FUEL CELL SCHEMATIC

HYDROGEN

OXYGEN

ANODE

ELECTROLYTE

CATHODE

H$^+$

H$^+$

CATALYST

CATALYST

H$_2$

ELECTRIC POWER

H$_2$O

EXCESS HYDROGEN (FOR REUSE)

WATER

−   +

Compendium of Hydrogen Energy

Volume 3: Hydrogen Energy Conversion

Edited by Frano Barbir,
Angelo Basile and T. Nejat Veziroğlu

WP
WOODHEAD PUBLISHING

Compendium of Hydrogen Energy

Related titles

Materials for fuel cells
(ISBN 978-1-84569-330-5)

Solid-oxide fuel cell technology
(ISBN 978-1-84569-628-3)

*Polymer electrolyte membrane and direct methanol fuel cell technology Volume 1:
Fundamentals and performance of low temperature fuel cells*
(ISBN 978-1-74569-773-0)

Compendium of Hydrogen Energy

Volume 3: Hydrogen Energy Conversion

Edited by

Frano Barbir, Angelo Basile and T. Nejat Veziroğlu

Notices
Knowledge and best practice in this field are constantly changing. As new research and experience broaden our understanding, changes in research methods, professional practices, or medical treatment may become necessary.

Practitioners and researchers must always rely on their own experience and knowledge in evaluating and using any information, methods, compounds, or experiments described herein. In using such information or methods they should be mindful of their own safety and the safety of others, including parties for whom they have a professional responsibility.

To the fullest extent of the law, neither the Publisher nor the authors, contributors, or editors, assume any liability for any injury and/or damage to persons or property as a matter of products liability, negligence or otherwise, or from any use or operation of any methods, products, instructions, or ideas contained in the material herein.

British Library Cataloguing in Publication Data
A catalogue record for this book is available from the British Library

Library of Congress Cataloging-in-Publication Data
A catalog record for this book is available from the Library of Congress

Library of Congress Number: 2015940509

For Information on all Woodhead Publishing publications
visit our website at http://store.elsevier.com/

Working together
to grow libraries in
developing countries

www.elsevier.com • www.bookaid.org

Contents

List of contributors

J.R. Anstrom The Pennsylvania State University, University Park, PA, USA

A.S. Aricò CNR-ITAE, Institute for Advanced Energy Technologies "Nicola Giordano", Messina, Italy

L. Blum Institute of Energy and Climate Research, Jülich, Germany

M. Cassir PSL Research University, Paris, France

K. Collier Collier Technologies Inc. (CTI), Reedsport, OR, USA

P. Cristiani Ricerca sul Sistema Energetico SpA, (RSE), Milan, Italy

L.M. Das Indian Institute of Technology, New Delhi, India

S. Di Iorio Istituto Motori—CNR, Naples, Italy

D.E. Eapen IIT Madras, Chennai, India

S. Etemad Precision Combustion, Inc., North Haven, CT, USA

M.L. Faro CNR-ITAE, Institute for Advanced Energy Technologies "Nicola Giordano", Messina, Italy

A.A. Franco Université de Picardie Jules Verne, Amiens Cedex; Réseau sur le Stockage Electrochimique de l'Energie (RS2E), Amiens, and ALISTORE European Research Institute, Amiens Cedex, France

V. Lair PSL Research University, Paris, France

H. Liang Eau2Energy, Nottingham, UK

A. Meléndez-Ceballos PSL Research University, Paris, France

V.N. Nguyen Institute of Energy and Climate Research, Jülich, Germany

S. Pasupathi Eau2Energy, Nottingham, UK

B.G. Pollet Eau2Energy, Nottingham, UK

R. Rengaswamy IIT Madras, Chennai, India, and Clarkson University and Texas Tech University, Lubbock, TX, USA

A. Ringuedé PSL Research University, Paris, France

J. Saint-Just H2 Plus Ltd., Farnham, Surrey, UK

P. Sementa Istituto Motori—CNR, Naples, Italy

G. Squadrito CNR—Istituto di Tecnologie Avanzate per l'Energia "Nicola Giordano", (CNR-ITAE), Messina, Italy

H. Su Eau2Energy, Nottingham, UK

S.R. Suseendiran IIT Madras, Chennai, India

S. Trocino CNR-ITAE, Institute for Advanced Energy Technologies "Nicola Giordano", Messina, Italy

B.M. Vaglieco Istituto Motori—CNR, Naples, Italy

K. Young BASF-Ovonic, Rochester Hills, MI, USA

S.C. Zignani CNR-ITAE, Institute for Advanced Energy Technologies "Nicola Giordano", Messina, Italy

Woodhead Publishing Series in Energy

This page intentionally left blank

Part One

Fuel cells

This page intentionally left blank

Proton exchange membrane fuel cells

1

B.G. Pollet*, *A.A. Franco*†,‡,§, *H. Su**, *H. Liang**, *S. Pasupathi**
*Eau2Energy, Nottingham, UK, †Université de Picardie Jules Verne, Amiens Cedex, France,
‡Réseau sur le Stockage Electrochimique de l'Energie (RS2E), Amiens, France, §ALISTORE
European Research Institute, Amiens Cedex, France

1.1   Fabrication and manufacturing of fuel cells

1.1.1   Introduction

Fuel cells have emerged as a vital alternative energy solution to reduce societal dependence on internal combustion engines and lead acid batteries. Fuel cells promise significantly improved energy efficiency with zero or low greenhouse gas emissions, and they are expected to play a key role in the hydrogen economy. Fuel cell technology is based upon the simple CHEMICAL reaction given in the following equation:

$$2H_2 + O_2 \rightarrow 2H_2O \tag{1.1}$$

The proton exchange membrane fuel cell (PEMFC) is one of the most elegant types of fuel cells, which is fed hydrogen, which is oxidized at the anode, and oxygen that is reduced at the cathode. The protons released during the oxidation of hydrogen are conducted through the proton exchange membrane to the cathode. As the membrane is not electrically conductive, the electrons released from the hydrogen travel along the electrical detour provided, and an electrical current is generated. These reactions and pathways are shown schematically in Figure 1.1.

1.1.2   Principles of membrane electrode assembly

The membrane electrode assembly (MEA) is the heart of PEMFCs, where the electrochemical reactions take place to generate electrical power. The MEA is pictured in the schematic of a single PEMFC shown in Figure 1.2. The MEA is typically sandwiched by two flow field plates that are often mirrored to make a bipolar plate when cells are stacked in series for greater voltages.

The MEA consists of a proton exchange membrane, catalyst layers (CLs), and gas diffusion layers (GDLs). Typically, these components are fabricated individually and then pressed to together at high temperatures and pressures. An ideal MEA would allow all active catalyst sites in the CL to be accessible to the reactant (H_2 or O_2), protons, and electrons and would facilitate the effective removal of produced water from the CL and GDL.
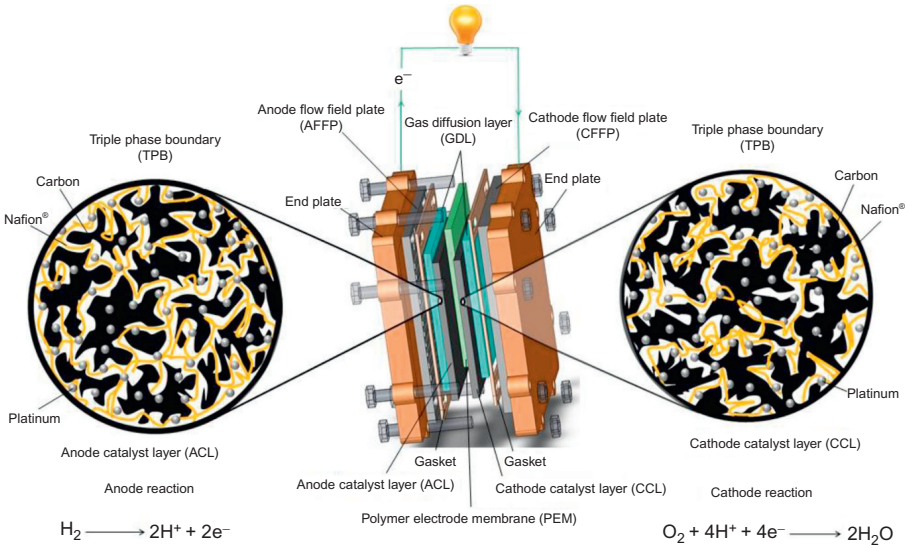
Figure 1.1 Schematic of a single typical PEMFC.
Copyright Bruno G. Pollet.
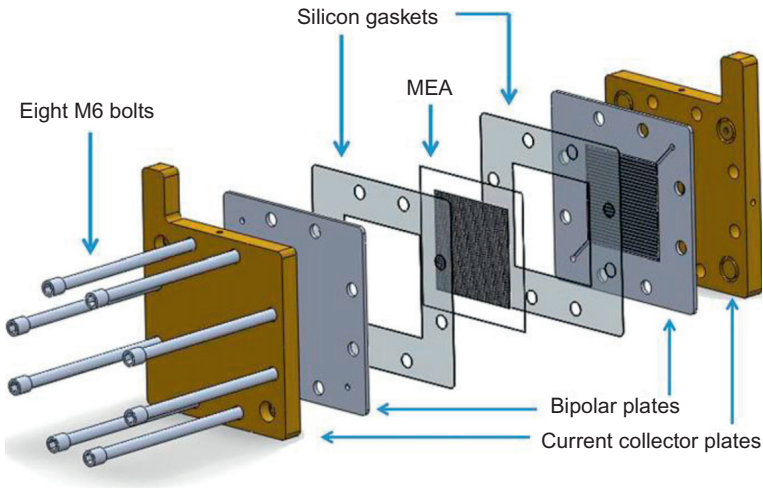
Figure 1.2 Single PEMFC schematic.

Analogous cathode and anode reactions in the MEA for a H_2/O_2 fuel cell are

$$\text{Cathode}: \quad \frac{1}{2}O_2 + 2H^+ + 2e^- \rightarrow H_2O \tag{1.2}$$

$$\text{Anode}: \quad H_2 \rightarrow 2H^+ + 2e^- \tag{1.3}$$

The flow of ionic charge through the electrolyte must be balanced by the flow of electronic charge through an outside circuit, and it is this balance that produces electrical power.

Several review articles in the literature cover specific aspects of PEMFC. The MEA fabrication technologies is a key element for creating a fuel cell that will perform at a high level. Over the past several decades, great efforts have been made to optimize the CL, MEA structures, and fabrication methods have been developed. In this chapter, we attempt to cover some MEA fabrication methods commonly practiced in a low-temperature fuel cell laboratory, with emphasis on applied aspects. Some mention of techniques that are useful in the investigation of various aspects of fuel cells, such as the alkaline fuel cell (AFC) and the phosphoric acid fuel cell (PAFC).

1.1.3   Overview of MEA components

1.1.3.1   Catalyst layer

The CL is a key component in the gas diffusion electrodes (GDEs), as the location where electrochemical reactions take place. The CLs need to be designed to generate high rates of the desired reactions and minimize the amount of catalyst necessary for reaching the required levels of power output. An ideal CL should maximize the active surface area per unit mass of the electrocatalyst and minimize the obstacles for reactant transport to the catalyst, for proton transport to exact positions, and for product removal from the cell; these requirements entail an extension of the three-phase boundary.

1.1.3.2   Gas diffusion layer

The porous GDL in PEMFCs ensures that reactants effectively diffuse to the CL. In addition, the GDL is the electrical conductor that transports electrons to and from the CL. Typically, GDLs are constructed from porous carbon paper, or carbon cloth, with a thickness in the range of 100–300 μm. The GDL also assists in water management by allowing an appropriate amount of water to reach, and be held at, the membrane for hydration. In addition, GDLs are typically waterproofed with a polytetrafluoroethylene (PTFE) (Teflon) coating to ensure that the pores of the GDL do not become congested with liquid water.

1.1.3.3   Membrane

The main function of the membrane in PEMFCs is to transport protons from the anode to the cathode; membrane polymers have sulfonic groups, which facilitate the transport of protons. The other functions include keeping the fuel and oxidant separated, which prevents mixing of the two gases and withstanding harsh conditions, including active catalysts, high temperatures or temperature fluctuations, strong oxidants, and reactive radicals. Thus, the ideal polymer must have excellent proton conductivity, chemical and thermal stability, strength, flexibility, low gas permeability, low water drag, low cost, and good availability (Zhang, 2008).

Though the membrane and GDL are the critical part of the MEA, a review of the design and fabrication of polymer electrolyte membranes (PEM) and GDL is beyond the scope of this chapter.

1.1.4   Methods for MEA fabrication

The process of MEA fabrication should be guided by both fuel cell performance and cost reduction. Table 1.1 identifies various methods available for the fabrication of MEAs. The following description provides an overview of two common MEA fabrication methods: ink-based method and *in situ* method.

1.1.4.1   Ink-based method

The first generation of polymer electrolyte membrane fuel cells (PEMFC) used PTFE-bound Pt black electrocatalysts that exhibited excellent long-term performance at a prohibitively high cost (Wilson et al., 1995). However, the CL formed by this Pt black catalyst has several disadvantages, including high platinum loadings (4 mg/cm^2); large platinum agglomerates ($\sim$1 μm on average); lower electrochemical surface area ($\sim$25 m^2/g); and poor access to the catalyst surface for gas, electrons, and protons. Approaches to improve the CL construction by significantly increasing the three-phase boundary in the CL can be achieved in two ways. First, a breakthrough was made by replacing pure Pt black with supported Pt catalysts (Wagner et al., 2008), which can significantly reduce the Pt loading from 4 down to 0.4 mg/cm^2 (Raistrick, 1986, 1989). Second, the PTFE-bound CLs are typically impregnated with Nafion by brushing or spraying to provide ionic transport to the catalyst site. The impregnation of an ionomer (Nafion) into these CLs was found to be extremely effective in improving the three-dimensional reaction zone for fuel cell applications. The latter can be accomplished by blending the solubilized ionomer and the platinized carbon into a homogeneous "ink" from which the thin film CL of the electrode can be made. However, the platinum utilization in this PTFE-bound CL still remains low: in the vicinity of 20% (Murphy et al., 1994; Cheng et al., 1999).

Numerous efforts have been made to improve existing thin film catalysts in order to prepare a CL with low Pt loading and high Pt utilization without sacrificing electrode performance. In thin film CL fabrication, the most common method is to prepare catalyst ink by mixing the Pt/C agglomerates with a solubilized polymer electrolyte such as Nafion ionomer and then to apply this ink on a porous support or membrane using various methods. In this case, the CL always contains some inactive catalyst sites not available

Table 1.1   Various methods available for the fabrication of MEAs

MEA fabrication methods	
Ink-based method	*In situ method*
Spray coating	Sputter deposition
Screen printing	Dual ion-beam-assisted deposition
Inkjet printing	Electrodeposition method
	Reactive spray deposition technology
	Atomic layer deposition

for fuel cell reactions because the electrochemical reaction is located only at the interface between the polymer electrolyte and the Pt catalyst where there is reactant access.

The procedure for forming a thin film CL on the membrane, according to Wilson (1993)'s patent, is as follows:

1. Combine a 5% solution of solubilized perfluorosulfonate ionomer (such as Nafion) and 20% wt Pt/C support catalyst in a ratio of 1:3 Nafion/catalyst.
2. Add water and glycerol to weight ratios of 1:5:20 carbon–water–glycerol.
3. Mix the solution with ultrasound until the catalyst is uniformly distributed, and the mixture is adequately viscous for coating.
4. Ion exchange the Nafion membrane to the Na^+ form by soaking it in NaOH, then rinse and let dry.
5. Apply the carbon–water–glycerol ink to one side of the membrane. Two coats are typically required for adequate catalyst loading.
6. Dry the membrane in a vacuum with the temperature of approximately 160 °C.
7. Repeat Steps 5 and 6 for the other side of the membrane.
8. Ion exchange the assembly to the protonated form by lightly boiling the MEA in 0.1 M H_2SO_4 and rinsing in deionized water.
9. Place carbon paper/cloth against the film to produce a GDL.

Alternatively, the CL ink can be (1) applied to a PTFE blank or some other substrate and then decal transferred onto the membrane, called as decal transfer method (Wilson and Gottesfeld, 1992; Xie et al., 2004); or (2) deposited onto the diffusion layer and then hot pressed to the membrane for MEA fabrication, called as hot pressing method (Antolini et al., 1999; Passalacqua et al., 1998; Sasikumar et al., 2004; Taylor et al., 1992; Paganin et al., 1996); or (3) deposited onto Nafion membranes and then assembled with two GDLs, called as catalyst-coating membrane method (Liang et al., 2012, 2013, 2014). Based on the nature of catalyst ink and its application method, several thin film CL fabrication techniques have been developed, including decal transfer (Wilson and Gottesfeld, 1992; Xie et al., 2004), brush painting (Ticianelli et al., 1988; Park et al., 2008), spray coating (Subramaniam et al., 2000; Møller-Holst, 1996), doctor blade coating (Bender et al., 2003), screen printing (Ihm et al., 2004; Kim et al., 1998; Rajalakshmi and Dhathathreyan, 2007), inkjet printing (Towne et al., 2007; Taylor et al., 2007), and rolling (Bolwin et al., 1995). Currently, screen printing and spray coating have become standard methods for conventional CL fabrication. Inkjet printing is also showing promise for fabricating low Pt-loading MEAs.

Spray coating

The spray-coating method (Kumar et al., 1995) is widely used for catalyst fabrication. Typically, the catalyst ink is coated on the gas diffusion layer or cast directly on the membrane. The application apparatus can be a manual spray gun or an auto-spraying system with programmed X–Y axes, movable robotic arm, an ink reservoir and supply loop, ink atomization, and a spray nozzle with adjustable flux and pressure. To prevent distortion and swelling of the membrane, Xu et al. developed a novel catalyst-coated membrane (CCM) approach—a catalyst-sprayed membrane under irradiation (CSMUI), for preparation of MEAs for low-temperature PEMFC. Catalyst ink was sprayed directly onto the membrane, and an infrared light was used simultaneously to evaporate the solvents. The resultant MEAs prepared by this method yielded very high performance.

Shin et al. (2002) prepared colloidal catalyst ink with a method similar to the conventional spray-coating approach, called a colloidal method. A mixture of Pt/C powder and Nafion ionomer was dripped drop by drop into the *n*-butyl acetate solvent to form the ionomer colloids. The ink was then treated ultrasonically to allow the colloids to absorb the Pt/C powder. The ink was then sprayed via airbrushing onto the carbon paper, which was to be used as the GDL. It was stated that the colloidal method is the preferred ink for spraying methods, as it forms larger agglomerates. Small agglomerates formed by the solution method have a tendency to penetrate too far into the GDL, blocking pores needed for gas transport. In addition, it was proposed that in the colloidal method the ionomer colloid absorbs the catalyst particles and larger Pt/C agglomerates are formed. The colloidal method is known to cast a continuous network of ionomer that enhances proton transport.

The colloidal method dramatically outperformed the solution method at high current densities. This is attributed to a significant increase in the proton conductivity, as well as a moderate enhancement of the mass transport in the CL formed with the colloidal ink. The increase in proton conductivity is due to the continuous network of ionomer in the colloidal CL. The increased mass transport is a product the larger agglomerates of Pt/C in the colloidal CL, which translates to a higher porosity, allowing a greater flux of the reactant and product gases.

Screen printing

Similar to spray coating, the screen-printing method is also widely used for CL fabrication. The major difference between the two is that the viscosity of the ink for spray coating is much lower than that for screen printing. In a typical screen printing process, the ink slurry is first cast onto certain substrates, and then the CL is transferred to a Nafion membrane by hot pressing. The membrane is converted into Na^+ form to avoid swelling during hot pressing and decal transfer because, in this form, the Nafion membrane is mechanically strong and stable for hot pressing from 150 to 160 °C. In the direct screen printing process (Wilson et al., 1995), the ink slurry is applied to a membrane in either Na^+ or TBA form to stabilize the catalytic layer, thereby enhancing the membrane's physical strength.

The coating apparatus consists of a silk screen mesh fixed to a frame with sufficient tension to squeeze the ink through the screen and onto the blank substrate (e.g., polyimide). The substrate is fixed on an *XY* table with adhesion tape, and the silken screen mesh is masked, with an open window in the center for screen printing. The silicon rubber squeeze is a fixed support and can be moved in both *X* and *Y* directions. A hot air or IR ramp is used to dry the coating for solvent removal.

The coating procedure consists of positioning the substrate layer under the silk screen mesh, which is not masked, and using a squeegee on top of the mesh at one side. An appropriate amount of ink is micropipetted near the squeegee, and the slurry is first spread across and then pushed through the mesh to the substrate layer by rapid movements of the squeegee. Hot air is used to dry the CL coated on the substrate. The same procedure is repeated until the pipette volume of catalyst ink has been transferred to the substrate layer.

Inkjet printing

Inkjet printers utilize drop-on-demand technology to deposit various materials or "inks." This is a popular deposition technique used not only in desktop printers, but also to deposit various other coating materials, such as those required for CL fabrication. Using inkjet-printing technology, a research group in the Pacific Northwest National Lab (PNNL) has successfully fabricated CLs for hydrogen-air PEMFCs (Towne et al., 2007). In their study, a slightly modified commercial desktop inkjet printer was used to deposit catalyst ink directly from a print cartridge onto the Nafion membrane to form a CL. The ink cartridges were filled with the catalyst inks. The membrane was secured to a cellulose acetate sheet and fed through the printer using the original paper feed platen. Computer software was used to control the print parameters, such as electrode dimensions, thickness, and resolution. Fuel cell testing on the fabricated CLs showed power densities up to 155 mW/cm^2, with a cathode catalyst loading of 0.20 mg Pt/cm^2.

These studies demonstrate some of the advantages of inkjet printing for CL fabrication, such as varied composition layer printing, and suggest that inkjet-based fabrication technology might be the way to cost-effective and large-scale fabrication of PEMFCs in the future. However, the question still remains of whether or not inkjet fabrication can offer any performance advantage and still lead to more efficient utilization of the Pt catalyst.

Similarly, Taylor et al. (2007) used inkjet printing to deposit catalyst materials onto GDLs. Their inkjet-printed CLs with a catalyst loading of 0.020 mg Pt/cm^2 showed high Pt utilizations. This research also demonstrated the capacity of the inkjet-printing technique to control ink volume precisely down to picoliters for ultralow catalyst loading, the flexibility of using different carbon substrates, and the functionality of gradient catalyst structure fabrication using these techniques.

1.1.4.2 In situ *method*

Numerous efforts have been made to develop *in situ* CL fabrication methods to lower Pt loading and increase platinum utilization without sacrificing electrode performance.

Sputter deposition (vacuum deposition methods)

Common vacuum deposition methods include chemical vapor deposition, physical, or thermal vapor deposition, and sputter deposition. Sputtering is commonly employed to form CLs and is known for providing denser layers than the alternative evaporation methods (Cavalca et al., 2001). The sputtering of CLs consists of a vacuum evaporation process that removes portions of a coating material (the target) and deposits a thin and resilient film of the target material onto an adjacent substrate. In the case of sputtered CLs, the target material is the catalyst material, and the substrate can be either the GDL or the membrane. Sputtering provides a method of depositing a thin CL (onto either the membrane or the GDL) that delivers high performance combined with a low Pt loading. The entire CL is in such intimate contact with the membrane that the need for ionic conductors in the CL is resolved (Cha and Lee, 1999). Moreover, platinum and its alloys are easily deposited by sputtering (Weber et al., 1987). The success of

the sputtering method on reducing platinum loading depends heavily on the reduction in the size of catalyst particles below 10 nm. State-of-the-art thin film electrodes feature Pt loading of 0.1 mg/cm^2 (Cha and Lee, 1999). A 5 nm sputtered platinum film amounts to a platinum loading of 0.014 mg/cm^2. However, the performance of a fuel cell with a sputtered CL can vary by several orders of magnitude depending on the thickness of the sputtered CL (O'Hayre et al., 2002).

The advantages of sputter deposition include:

1. Precise Pt loading and thickness, as well as controlled microstructure morphology.
2. Much smaller Pt particle size.
3. Homogeneous distribution of the Pt particles on the support and extremely low metal loadings (down to 10 ng/cm^2).
4. A simple preparation process that is easy to scale up.
5. Adaptiveness to various substrates, such as GDL and membrane.

Although the sputter deposition technique can provide a cheap and directly controlled deposition method, the performance of PEMFCs with sputtered CLs is still inferior to that of conventional ink-based fuel cells. In addition, other issues arise related to the physical properties of sputtered CLs, such as low lateral electrical conductivity of the thin metallic films (Wee et al., 2007; Kadjo et al., 2007). Furthermore, the smaller particle size of sputter-deposited Pt can hinder water transport because of the high resistance to water transport in a thick, dense, sputtered Pt layer (Kadjo et al., 2007). Currently, the sputter deposition method is not considered an economically viable alternative for large-scale electrode fabrication (Taylor et al., 1992), and further research is underway to improve methods.

Dual ion beam-assisted deposition

Saha et al. (2006) have proposed an improved ion deposition methodology based on a dual ion beam-assisted deposition (dual IBAD) method. Dual IBAD combines physical vapor deposition (PVD) with ion beam bombardment. The unique feature of dual IBAD is that the ion bombardment can impart substantial energy to the coating and coating/substrate interface, which could be employed to control film properties such as uniformity, density, and morphology. Using the dual IABD method, an ultralow, pure Pt-based CL (0.04–0.12 mg Pt/cm^2) can be prepared on the surface of a GDL substrate, with film thicknesses in the range of 250–750 Å. The main drawback is that the fuel cell performance of such a CL is much lower than that of conventional ink-based CLs. Further improvement in catalyst utilization and the gas/liquid diffusivity of the CLs prepared by IBAD is necessary.

Electrodeposition method

The first disclosure of electrodeposition of the catalytic layer in PEMFCs was in the form of (Vilambi Reddy et al., 1992) US patent (Vilambi Reddy et al., 1992). This patent detailed the fabrication of electrodes featuring low platinum loading in which the platinum was electrodeposited into their uncatalyzed carbon substrate in a commercial plating bath. The uncatalyzed carbon substrate consisted of a hydrophobic porous carbon paper that was impregnated with dispersed carbon particles and PTFE. Nafion was also impregnated onto the side of the carbon substrate that was to be catalyzed.

The Nafion coated carbon paper was placed in a commercial platinum acid-plating bath, along with a platinum counter electrode. The face of the substrate that was not coated with Nafion was most likely masked with some form of a nonconducting film. This step would have been taken to ensure that platinum would only be deposited in regions impregnated with Nafion. Thus, when an interrupted DC current was applied to the electrodes in the plating bath, catalyst ions would pass through the Nafion to the carbon particles and successfully be deposited only where protonic and electronic conduction coexists. This method was able to produce electrodes featuring platinum loadings of 0.05 mg/cm^2. This is a significant reduction in loading from the state-of-the-art thin film electrode.

In the following years, additional research on electrodeposition of platinum onto porous substrates was continued by Verbrugge (1994). According to Verbrugge, a distinguishing difference between his study and the aforementioned patent is the larger amount of sulfuric acid employed by Vilambi Reddy et al. (1992). Another distinguishing feature of Verbrugge's study is the employment of a membrane instead of a Nafion-impregnated layer. Using the area provided by the deposition channel, platinum was selectively electrodeposited through the membrane and into the membrane–electrode interfacial region. Verbrugge suggested that this method has the potential to increase platinum utilization because of the concentrated platinum found at the membrane–electrode interface. However, he did not provide the results of these electrodes implemented in a functional fuel cell.

The objective of studies by Hogarth et al. (1994), and later by Gloaguen et al. (1997), was to improve the reaction kinetics for the oxidation of methanol using electrodes fabricated with electrodeposition. Hogarth et al. placed electrodes in a plating bath that contained 0.02 M chloroplatinic acid and exposed only 1 cm^2 of the PTFE-impregnated carbon cloth electrode face by using a water seal. In this study, neither a Nafion layer nor a membrane film was applied to the carbon substrate prior to electrode position. The Gloaguen et al. study focused on the oxygen reduction reaction (ORR) kinetics of electrodes formed with the electrodeposition of platinum on carbon supports that were bound by Nafion onto a glassy carbon stick. One of the most significant conclusions of the study was that Pt activity is less related to particle size and more to the fine structure of the platinum surface.

A noticeable increase in catalyst utilization resulted when Pt deposition took place only in the three-phase reaction zone. Because Pt electrodeposition in aqueous solution only occurs in the region of the ionic and electronic pathways, it should be possible to reduce Pt loading significantly and increase Pt utilization in the CL. Pulse electrodeposition is promising and could replace conventional methods for fabricating cost-effective, low Pt-loading CLs. However, CL durability may be an issue if the active CL sites change with time.

Reactive spray deposition technology

Reactive spray deposition technology (RSDT) has been developed for direct catalyst deposition onto substrates, including PEM, to form CCMs (Maric et al., 2007). The process involves dissolving a Pt precursor in appropriate solvents, followed by

spraying the solution with an expansion gas through a nozzle to produce micron-sized droplets. The droplets are burnt out in a flame, resulting in metal atoms and/or metal oxide molecules in the gas phase. At the same time, a quench gas is used to induce rapid condensation of Pt vapors into Pt particles with a size of ∼5 nm. A mixture of carbon and Nafion ionomer is subsequently introduced into the gas stream. The cooling effect of the quench gas helps to avoid thermal damage to the ionomer and the membrane substrate. As a result, a thin film CL forms on the electrolyte membrane.

In the RSDT process, the steps for introducing catalyst, ionomer, and carbon into the gas mix are decoupled and can be independently controlled in such a manner that the Pt/C and ionomer/C ratios can be continuously modified during the deposition process. RSDT has the capacity and flexibility required to produce compositionally and structurally optimized CLs. The technology can be used to generate supported and unsupported platinum CLs with thicknesses from 10 to 200 nm and with varied morphologies, including dense films, porous films (packed particles), and dendritic and island-growth structures. However, the usage efficiency of the catalyst ink is quite low in the fabrication process, which is a major drawback of this technology for fuel cell CL preparation.

Pulsed laser deposition

Cunningham et al. (2003) used the pulsed laser deposition (PLD) method to deposit platinum onto E-TEK GDEs to prepare low catalyst-loading electrodes for PEMFCs. In the PLD process, the laser beam is focused by a quartz focus lens onto a polycrystalline platinum target. The Pt target is continuously rastered across the laser beam, via a dual rotation and translation motion, to obtain a uniform ablation over the entire target surface. The chamber is evacuated by a turbomolecular pump and filled with helium at a constant pressure throughout the PLD process. The platinum loadings are controlled by the number of pulses during deposition.

This technique yields a catalyst composed entirely of metal nanoparticles or nanocrystalline thin film, and it allows for control of size and distribution while eliminating the need for a dispersing and supporting medium. The obtained electrodes contained as little as 0.017 mg Pt/cm^2 and performed as well as standard E-TEK electrodes (Pt loading 0.4 mg/cm^2). The PLD technique may be of special interest as an alternative to the sputtering process in the production of micro fuel cells.

Atomic layer deposition

In order to lower the cost of PEMFCs, the catalytic activity and utilization efficiency of Pt must be increased; therefore, the CL structure must be modified (Lee et al., 2006). This may be achieved by the catalyst deposition method. Thin film methods have been used to prepare a Pt catalyst for PEMFC (Litster and McLean, 2004; Wee et al., 2007). Complex processes, such as reflux, centrifugation, and mixing with solvent before pasting on the GDL, are needed in the thin film method to prepare a supported catalyst (Litster and McLean, 2004; Chan et al., 2004). However, there is still a high Pt loading (>0.1 mg/cm^2) in the state-of-the-art thin film electrode

(Litster and McLean, 2004; Wee et al., 2007). Electrodeposition has been applied to increase Pt-utilization efficiency by depositing the catalyst on ionic and electronic pathways (Wee et al., 2007). However, it has relatively low productivity and high Pt loading. Sputtering can be used to directly deposit Pt on the substrate (Litster and McLean, 2004), but the Pt particles cannot penetrate into deep regions of the porous support (Chan et al., 2004). Consequently, atomic layer deposition (ALD) is introduced to overcome these difficulties. The particle density and loading of Pt could be controlled by the substrate surface condition and cycle number. Because ALD of Pt has the advantages of simple processing, large area, batch production, small particle size, lower loading, and good uniformity and conformality, it is a promising technique for applications in PEMFCs, especially for micro fuel cells where both lower loading and uniform, conformal coating of Pt with controlled particle size is required.

ALD is a gas phase thin film deposition method that is unique because the film growth proceeds through self-limiting surface reactions (Niinistö et al., 1996; Ritala, 1997; Klaus et al., 1997, 1999). As a consequence, ALD offers excellent large-area uniformity and conformality (Ritala et al., 1999) and enables simple and accurate control of film thickness and composition at an atomic layer level. All these characteristics make ALD an important film deposition technique for future microelectronics.

Liu et al. deposited Pt nanoparticles on carbon cloths and carbon nanotubes for applications in PEMFCs by using ALD method (Liu et al., 2009). In ALD of Pt (methylcyclopentadienyl) trimethylplatinum (MeCpPtMe3) and air or oxygen have been used as precursors to grow a uniform and thickness-controllable particle-like Pt film (Aaltonen et al., 2003, 2004). Conformal Pt nanoparticle coating on acid-treated CNTs was achieved, and good dispersion was observed on acid-treated carbon cloth and carbon nanotubes. ALD of Pt was conducted for 100 cycles to deposit 0.016 mg/cm^2 of Pt on the CNTs. In addition, the MEA prepared by Pt deposited on acid-treated CNTs using ALD method performs better than commercial E-TEK electrode. Platinum nanocatalyst deposited by ALD on CNTs has been demonstrated to have a higher utilization efficiency in PEMFCs than commercial E-TEK electrodes.

1.1.5 Conclusions

MEA is the core component of PEMFC, and electrochemical reaction only takes place at "triple-phase boundaries," where reactant, electrolyte, and electrons are brought together. The high cost of Pt and Pt-group metals, along with low Pt utilization in the CL, is a major barrier to the commercialization of fuel cell technology. The basic technical considerations and strategies and methodologies are how to maximize the three-phase interface of the CL, how to increase CL Pt utilization, and how to reduce Pt loading. Thus far, researchers have found that these goals can be achieved through optimizing existing CLs with respect to composition and structure, developing novel fabrication technologies, and introducing innovative CL approaches. This report outlined major advances made in the fabrication of MEA for PEMFCs from the PTFE-bound CLs of almost 20 years ago to the present investigation of low Pt loading MEA.

Those methods are not only used in PEMFC but also can be utilized for other low-temperature fuel cells such as the AFC and the PAFC.

1.2   Degradation mechanisms and mitigation strategies

The performance of a PEMFC or stack is affected by many internal and external factors, such as fuel cell design and assembly, degradation of materials, operational conditions, and impurities or contaminants (Borup et al., 2007; Cheng et al., 2007; Bruijn et al., 2008; Wu et al., 2008; Yousfi-Steiner et al., 2009; Yu et al., 2012; Zhang et al., 2009). Performance degradation is unavoidable, but the degradation rate can be minimized through a comprehensive understanding of degradation and failure mechanisms.

1.2.1   PEMFC components degradation

A schematic cross section of a single cell of a PEMFC showing individual components is shown in Figure 1.3.

An individual fuel cell consists of an anode, a cathode, and a polymer-electrolyte membrane. Each electrode has an electrocatalyst layer and a GDL. The CLs can be attached to either the membrane or at times to the GDL material (termed the GDE). The individual cells are electrically connected in series by bipolar plates to
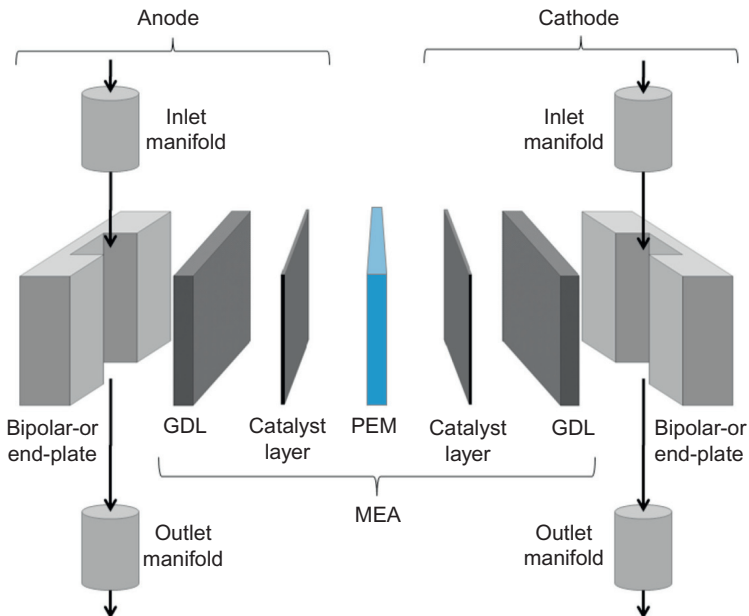
Figure 1.3 Schematic of a typical PEMFC.

form a fuel cell stack, and special end plates terminate the stacks to provide the compressive forces needed for the stack structural integrity. The bipolar plates provide conducting paths for electrons between cells, distribute the reactant gases across the entire active MEA surface area (through flow channels integrated into the plates), remove waste heat (through cooling channels), and provide stack structural integrity as well as barriers to anode and cathode gases. The aim of this section is to review the mechanisms that affect the lifetime of these fuel cell components and the mitigation strategies for these degradations.

1.2.1.1   Catalyst layer

In CLs, the electrocatalysts are nanoparticles of platinum or platinum alloys deposited on high surface area carbon supports. The nanoparticles increase the active catalytic surface area per unit mass of platinum. However, they also pose material stability and interaction issues. The stability of platinum, platinum alloys, and carbon particles, and the interaction of the nanocatalyst particles with the carbon supports are of concern for fuel cell durability.

Platinum dissolution and particle growth

Several studies have observed the growth of Pt particles as well as dissolution of Pt in the membrane phase. Both phenomena were already described for the PAFC and are closely related, as will be explained below. Thermodynamics predict substantial Pt dissolution in acid media strongly increasing with potential in the region of 0.85–0.95 V versus relative hydrogen electrode (RHE), according to the reaction

$$Pt \rightarrow Pt^{2+} + 2e^- \quad E_0 = 1.188 \text{ V versus RHE} \tag{1.4}$$

However, experiments on Pt thin film, Pt wire as well as on nanosized Pt on C have shown that at 80 °C in the region above 0.85 V versus RHE, Pt dissolution does not show the strong Nernstian potential dependence, and even has a maximum around 1.15 V. This was ascribed to the formation of an oxide layer, as also predicted by a kinetic model taking into account electrochemical formation of platinum oxide and its subsequent chemical dissolution:

$$Pt + H_2O \rightarrow PtO + 2H^+ + 2e^- \quad E_0 = 0.980 \text{ V versus RHE} \tag{1.5}$$

$$Pt^{2+} + H_2O \rightarrow PtO + 2H^+ \tag{1.6}$$

Also, the catalyst may lose its activity due to sintering or migration of Pt particles on the carbon support. Several mechanisms have been proposed to explain the coarsening in catalyst particle size during PEMFC operation: (1) Small Pt particles may dissolve in the ionomer phase and redeposit on the surface of large particles, leading to particle growth, a phenomenon known as Ostwald ripening. On the other hand, the dissolved Pt species may diffuse into the ionomer phase and subsequently precipitate in the membrane via reduction of Pt ions by the crossover hydrogen from the anode side,

which dramatically decreases membrane stability and conductivity. (2) The agglomeration of platinum particles on the carbon support may occur at the nanometer scale due to random cluster–cluster collisions, resulting in a typical log-normal distribution of particle sizes with a maximum at smaller particle sizes and a tail toward the larger particle sizes. (3) The growth in catalyst particles may also take place at the atomic scale by the minimization of the clusters' Gibbs free energy. In this case, the particle size distribution can be characterized by a tail toward the smaller particle sizes and a maximum at larger particle sizes.

Carbon corrosion

Corrosion of the catalyst carbon support is another important issue pertaining to electrocatalyst and CL durability. Thermodynamically, carbon (graphite) can be electrochemically oxidized to CO_2 at quite low potentials

$$C + 2H_2O \rightarrow CO_2 + 4H^+ + 4e^- \quad E_0 = 0.207 \text{ V versus RHE} \tag{1.7}$$

Due to the slow kinetics of these reactions, carbon can still be used in fuel cells. The presence of Pt catalysts the subsequent oxidation to CO_2 as verified by DEMS for carbon activated with 20% Pt. The mechanism consists of the following steps:

$$C + H_2O \rightarrow CO_{surf} + 2H^+ + 2e^- \quad E > 0.3 \text{ V versus RHE} \tag{1.8}$$

$$CO_{surf} + H_2O \rightarrow CO_2 + 2H^+ + 2e^- \quad E = 0.8 \text{ V versus RHE} \tag{1.9}$$
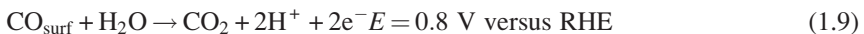
At a potential higher than 0.3 V versus RHE, CO_{surf} starts to form irreversibly on the carbon particle surface. CO_{surf} is oxidized on neighboring Pt sites to CO_2 at a potential of 0.8 V versus RHE. The amount of CO_2 formed is proportional to the total length of the two-dimensional grain boundaries between the Pt particles and the carbon support. Although carbon is stable in air at temperatures as high as 195 °C, a high platinum loading can lead to a loss of more than 80% of all carbon, where the time needed to reach the maximum amount of combusted carbon is determined by the temperature and the platinum loading. At platinum loadings used in commercial PEMFC catalysts, 40 wt% and higher, the loss of carbon at the lowest experimental temperature, 125 °C, amounted to 15% after 1000 h. From the relation between carbon loss and temperature, it was concluded that below 100 °C thermal oxidation of platinum-loaded carbon in air did not take place. However, the humidification of air substantially enhanced the thermal corrosion rate of carbon, by providing an additional pathway for chemical carbon oxidation through a direct reaction with water. In these studies, the corrosion rate was also found to be higher for high surface area carbon blacks, which was ascribed to a finer dispersion of Pt particles on this material.

Ionomer degradation

The ionomer in the electrode is susceptible to many of the same degradation mechanisms that were described for the fuel cell membrane. In comparison to the membrane, the ionomer is in a state that is more soluble than the Nafion membrane,

which only starts to dissolve when in water at 210 °C and high pressure of 68 atm for more than 2 h. The stability of recast Nafion ionomer in CL is reported to be much lower. The trace of the soluble ionomer is found in the cathode effluent water. The dissolution becomes more severe over time. As a result of the chemically ionomer degradation, the interface between catalyst and ionomer is lost, consequently reducing the electrochemically active surface of the electrode. As the ionomer acts as a binder in the electrode, it has a strong impact on the ionic and electronic conductivities of the electrode. The structural instability due to ionomer swelling and dissolution during long-time exposure in high-humidified conditions can change the electrical properties, leading to degradation of the fuel cell.

Mitigation strategies for CL degradation

Researchers have proposed and successfully employed several strategies to enhance catalyst durability. First of all, fuel cell-operating conditions play a major role in catalyst degradation. The dissolution of Pt from the carbon support is less favorable at low electrode potentials, which makes Pt catalysts more stable at the anode electrode than that at the cathode side. Secondly, corrosion of the carbon support due to fuel starvation can be alleviated by enhancing water retention on the anode, such as through modifications to the PTFE and/or ionomer, the addition of water-blocking components like graphite, and the use of improved preferable catalysts for water electrolysis. Thirdly, Pt-alloy catalysts such as PtCo, Pt–Cr–Ni have shown better activity and stability compared to pure Pt catalysts. By strengthening the interaction between the metal particles and the carbon support, sintering and dissolution of the metal alloy catalysts can be alleviated.

1.2.1.2   Membrane

Membrane degradation can be classified into three categories: mechanical, thermal, and chemical/electrochemical. Chemical degradation is a major cause of failure of perfluorosulfonic acid (PFSA) membrane. It is thought that hydroxyl ($\cdot$OH) or peroxy ($\cdot$OOH) radicals attack polymer end groups that still contain residual terminal H-groups. Characterization by X-ray photoelectron spectroscopy (XPS) revealed that during fuel cell operation the interactions between carbon, fluorine, and oxygen are changing. An example is the attack of hydroxyradicals on carboxylic end groups:

$$R_f - CF_2COOH + \cdot OH \rightarrow R_f - CF_2 \cdot + CO_2 + H_2O \tag{1.10}$$

$$R_f - CF_2 \cdot + OH \rightarrow R_f - CF_2OH \rightarrow R_f - COF + HF \tag{1.11}$$

$$R_f - COF + H_2O \rightarrow R_f - COOH + HF \tag{1.12}$$
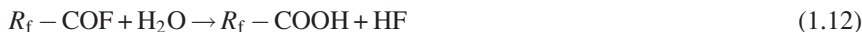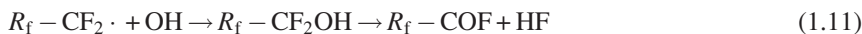
The exact mechanism of the direct radical pathway has not been established yet. Studies on chemical degradation have shown that the conditions leading to increased radical attack in PFSAs include higher temperature (especially above 90 °C), low

humidification, high gas pressure, use of pure hydrogen and pure oxygen, and high cell voltages.

Mechanical degradation causes early life failure due to perforations, cracks, tears, or pinholes, which may result from congenital membrane defects or from improper MEA fabrication processes. The local areas corresponding to the interface between the lands and channels of the flow field or the sealing edges in a PEMFC, which are subjected to excessive or nonuniform mechanical stresses, are also vulnerable to small perforations or tears. During fuel cell operation, the overall dimensional change due to nonhumidification, low humidification, and relative humidity (RH) cycling is also detrimental to mechanical durability. The constrained membrane in an assembled fuel cell experiences in-plane tension resulting from shrinkage under low RH and in-plane compression during swelling under wet conditions.

Several studies have addressed the issue of thermal stability and thermal degradation of PFSA membranes. The PTFE-like molecular backbone gives Nafion membranes their relative stability until beyond 150 °C due to the strength of the C—F bond and the shielding effect of the electronegative fluorine atoms. At higher temperatures, Nafion begins to decompose via its side sulfonate acid groups.

Mitigation strategies for membrane degradation

To prevent mechanical failure of the membrane, the MEA and flow field structure must be carefully designed to avoid local drying of the membrane, especially at the reactant inlet area. With respect to the chemical and electrochemical degradation of the membrane, developing membranes that are chemically stable against peroxy radicals has drawn particular attention. First of all, one solution is to develop novel membranes with higher chemical stability, such as a radiation-grafted FEP-g-polystyrene membrane, in which polystyrene was used as a sacrificial material owing to its low resistance to radicals. Free radical stabilizers and inhibitors such as hindered amines or antioxidants also have the potential to be mingled during membrane fabrication. Second, increased chemical stability can also be realized by modifying the structure of the available membrane. It was suggested that radical attack of the residual H-containing terminal bonds of the main chain of the PFSA membrane was the primary degradation mechanism. By eliminating the unstable end group, chemical stability was significantly enhanced. Third, the damage caused by hydrogen peroxide can be suppressed by redesigning the MEA. For example, a composite membrane, in which a thin recast Nafion membrane was bonded with a polystyrene sulfonic acid (PSSA) membrane, when positioned at the cathode of the cell could successfully prevent oxidation degradation of the PSSA membrane. Fourth, introduction of peroxide-decomposition catalysts like heteropoly acids within the membrane has proven to moderate or eliminate membrane deterioration due to peroxide. However, the advantage of this approach would be partially counteracted by a decrease in membrane stability and conductivity caused by the mixture of the catalysts. Last but not least, the development and implementation of new metal coatings with improved corrosion resistance and of catalysts that produce less hydrogen peroxide are long-term goals for membrane durability enhancement.

1.2.1.3 Gas diffusion layer

The GDL typically consists of two layers bonded together: a macroporous layer made of conductive carbon fibers and a microporous layer (MPL) made of carbon particles and a Teflon binder. The understanding of how a GDL degrades during operation and the effects of its degradation on fuel cell performance is based on only a few recent studies. Unfortunately, there is a large gap in the literature between studies of the GDL's physical properties and studies that relate these properties to PEMFC-durability data.

Some researchers found that the loss of GDL hydrophobicity increased with operating temperature and when sparging air was used instead of nitrogen. Additionally, they concluded that changes in the GDL properties were attributed mostly to the MPL. It was found that weight loss and the MPL contact angle increased with the time of exposure, and the increase was attributed to oxidation of the carbon in the MPL. As the fuel cell operates, the PTFE and carbon composite of the GDLs are susceptible to chemical attack (i.e., OH radical as electrochemical by-product) and electrochemical (voltage) oxidation. The loss of PTFE and carbon results in the changes in GDL physical properties, such as the decrease of GDL conductivity and hydrophobicity, which further lowers MEA performance and negatively affects the durability of the whole fuel cell. With regard to the quantitative correlation between performance loss and the changes in GDL properties, it was found that the decomposition of PTFE in the electrodes induced an approximately two times higher performance loss than that related to the agglomeration of the platinum catalyst after 1000 h of fuel cell operation.

Mitigation strategies for GDL degradation

Little information about mitigating GDL degradation is available from the literature. To improve GDL oxidative and electrooxidative stability, it was suggested using graphitized fibers during GDL preparation. It was also proposed that higher PTFE loading could benefit the water management ability of aged GDLs.

1.2.1.4 Bipolar plate

The bipolar plate serves as a separator between two adjacent cells. It conducts the electronic current between these two cells, separates the gases, and contains the flow patterns both for the reactants and for the coolant, in most cases a liquid coolant. With respect to the electric conductivity of bipolar plates, the contact resistance is more important than the bulk resistance, especially with regard to long-term behavior. Whereas a beginning of life resistance of 10 mΩ cm^2 is suggested as a specification, for long-term stability a combined specification for anode and cathode side of lower than 50 mΩ cm^2 has been used as a target specification, which has to be maintained up to 5000 h of fuel cell operation. The release of contaminants from the bipolar plates is a feature that can determine to a large extent the lifetime of the fuel cell. Whereas it does not so much affect the properties of the bipolar plate itself, it leads to poisoning of the membrane and the catalysts.

Mitigation strategies for bipolar plate degradation

For graphite and graphite composite plates, corrosion and release of contaminants under normal operation is not an issue. At normal operating conditions, the cathode potential is not high enough for oxide formation on the surface, and the contact resistance remains constant during fuel cell operation. Although not reported, under extreme conditions corrosion of the graphite is conceivable. Especially under start–stop or fuel starvation conditions, electrodes can be exposed to potentials promoting carbon corrosion.

For metal-based bipolar plates, the stability depends on the nature of the metal, the potential, and RH. Corrosion of the bipolar plates takes place when the plate material is oxidized at the potential to which it is exposed, and the surface oxide layer is soluble in the medium it is situated in. The medium is often not well defined. When in direct contact with the electrolytic membrane, the plate–membrane contact can lead to direct exchange of cations with protons of the electrolyte. On the other hand, the water produced in the fuel cell also contains ions, emanating from the electrodes and the membranes. When using stainless steel bipolar plates, corrosion is a generally observed phenomenon, which varies strongly between the various stainless steel grades.

Another common concern related to bipolar plates is the possible deformation or even fracture caused by the compressive forces that are used to ensure good electric contact and reactant sealing during fuel cell operation. Some operational factors, such as thermal cycling, nonuniform current, or thermal misdistributions over the active area, can impair the mechanical properties of the bipolar plate materials. A surface treatment method is particularly promising as the treatment is a modification to the surface rather than a coating procedure; therefore, delamination is not an issue. At the cathode side, the potential is high enough to form a partly conducting passive layer on the metal surface. Although, it protects the surface from corrosion, this layer results in an increase in contact resistance. Many metals show a buildup of such a passive layer under long-term testing in a fuel cell. This is a process that can take place over thousands of hours, thus finally exceeding a maximum tolerable resistance.

1.2.1.5   Seals

Sealing material is placed between the bipolar plates to prevent gas and coolant leakage and crossover. Typical sealing materials utilized in PEMFCs include fluorine caoutchouc, EPDM, and silicone. Not only are they meant to prevent leakage of the gases and the coolants outside their containments, seals function as electrical insulation, stack height control, and variability control as well. The degradation phenomena connected to seals do not only refer to the loss of the functionality of the seals themselves, but also to the leakage of seal components that could poison the MEA. In a recent study, the stability of various sealing materials has been tested in a simulated environment at 60 and 80 °C. This simulated environment consisted of solutions containing HF and H_2SO_4, in two different concentrations. It was concluded that silicone S and silicone G are heavily degraded in the concentrated solutions as well as the diluted concentrations, although most of the data are collected in the concentrated solutions. Degradation reveals itself by weight loss, complete disintegration, as well

as by leaching of Mg and Ca. The latter stem from magnesium oxide and calcium carbonate, which are used as fillers for obtaining the desired tensile strength, hardness, and resistance to compression.

Mitigation strategies for seals degradation

Only in a couple of long-term experiments was seal degradation observed, and this might have been the consequence of an inappropriate materials, selection. Silicone seals in direct contact with a perfluorosulfonic acid membrane suffer from degradation, at the anode as well as at the cathode. The degradation is probably caused by acidic decomposition of the sealing material, leading to coloration of the membrane and detectable amounts of silicon on the electrodes. No fuel cell performance loss or increase in gas leakage along the seal has been observed. Seal selection through *ex situ* and *in situ* screening processes should be based on the overall chemical and mechanical properties of the materials. With regard to seal material degradation, no available publications relevant to mitigation strategies have yet been found.

1.2.2   *Operational effects on degradation*

Operating conditions are known to have an impact on a fuel cell's durability. These effects include exposure to impurities (on both the cathode and anode sides of the fuel cell), exposure to and start-up from subfreezing conditions, potential cycling, fuel starvation, start/stop cycling, and changes in temperature and/or RH.

1.2.2.1   *Impurity effects*

The effect of contaminants on fuel cells is one of the most important issues in fuel cell operation and applications. Impurities in hydrogen fuel, such as CO, H_2S, NH_3, organic sulfur–carbon, and carbon–hydrogen compounds, and in air, such as nitrogen oxides (NO_x), SO_x, and small organics, are brought along with the fuel and air feed streams into the anodes and cathodes of a PEMFC stack, causing performance degradation and sometimes permanent damage to MEAs. For the PEM, the contaminants—in particular the cations—can get into the membrane to compete with the proton for the $-SO_3^-$ sites (Nafion membrane) and at the same time decrease the water content, resulting in a reduction in proton conductivity. On the other hand, metal ions such as Fe^{3+}/Fe^{2+} inside a membrane can also accelerate membrane degradation during a fuel cell operation through a peroxide formation mechanism.

Carbon oxide contamination

Both carbon monoxide and carbon dioxide have become major concerns in PEMFCs using reformate H_2-rich gas as fuel, particularly at conventional operating temperatures ($<80\,°C$). It is well documented that CO binds strongly to Pt sites, resulting in the reduction of surface active sites available for hydrogen adsorption and oxidation. The CO-poisoning effect was strongly related to the concentration of CO, the exposure time to CO, the cell operation temperature, and anode catalyst types. Normally, CO poisoning on Pt electrocatalysts becomes more severe with increases in CO

concentration and exposure time. The CO impurities from fuel streams, even at a level of a few ppm, can cause a substantial degradation in cell performance, especially at high current densities. The voltage losses became deeper with prolonged exposure to CO, due to its accumulation on the Pt catalyst surface over time. On the other hand, the severity of catalyst poisoning by CO can be strongly affected by fuel cell operation temperature; it may not be sensitive to pressure. At low temperatures (<80 °C), a trace amount of CO can cause a significant performance drop. The performance loss due to CO_2 contamination in anode fuel can be observed especially at higher current densities. On a Pt catalyst, CO_2 can be catalytically converted into CO, which then poisons the catalyst.

Hydrogen sulfide (H_2S)

Metal catalysts in general have a strong chemical affinity with H_2S, and Pt catalysts are not an exception and are particularly vulnerable. The degrading effects of the presence of this impurity in the FC are significant and commensurate with H_2S concentration and time of exposure. The electrochemical desorption of sulfur requires potentials unachievable in a continuously operating H_2/air fuel cell. About 10 ppb of H_2S has been shown during long operating times to have a degrading effect on fuel cell performance.

Ammonia (NH_3)

The presence of ammonia levels as low as 13 ppm in the fuel stream has rapid deleterious effects on performance. Higher concentrations (80, 200, and 500 ppm) of NH_3 have shown a marked decrease in performance in simulated reformate: cell performance decreases with exposure to NH_3 in reformate from 825 to 200 mA cm^{-2} at 0.6 V. Short-term exposure (<1 h) to NH_3 shows reversible effects. However, the negative effects caused by long-term exposure are irreversible, meaning that further operation on neat H_2 results only in a partial recovery. Cyclic voltammetry (CV) of the anode, after exposure, does not indicate any noticeable NH_3 adsorption onto the CL. Thus, the degradation mechanism appears to be due to protonic conductivity loss. The likely culprit is that NH_3 reacts with ionomeric H^+, generating NH^{4+} and consequently lowering the protonic activity. The negative effect gradually starts at the anode CL, the first region exposed, and continues into the membrane as the ammonia diffuses deeper and deeper.

Cationic ions

The foreign cationic ions that originate from impurities in fuel cell stack component materials, fuels, and coolants can cause water management problems in fuel cells. The cationic ions such as alkali metals, alkaline earth metals, transition metals, and rare earth metals were reported to directly affect the transport properties of the electrolyte membrane. Iron ions from stainless steel end plates resulted in severe Nafion degradation as evidenced by a massive fluoride loss. The iron contamination also led to several types of performance losses, including cathode and anode kinetic losses, ohmic loss, and mass transport loss. For example, metallic ions including Cu^{2+}, Fe^{3+}, Ni^{2+}, and Na^+ presented in sulfate salt solutions at a concentration level of

100 ppm were found to significantly decrease the ionic conductivity of a Nafion 117 membrane; among these, the ferric ions were more harmful. Researchers have discussed the critical role played by trace metallic ions in membrane degradation by reviewing the degradation modes of PEM, it was concluded that the displacement of H^+ with foreign cationic ions directly affected water flux and proton conductivity inside the membrane, leading to membrane degradation.

Sulfur dioxide (SO_2)

Sulfur dioxide is a common air contaminant resulting from fossil fuel combustion and can be found in high concentrations in urban areas with heavy traffic and in close proximity to some chemical plants. The effects of SO_2 on the cathode are similar to those produced by the presence of H_2S in the anode. Performance degradation appears to be a function of SO_2 concentration in the bulk, as the performance decrease was measured to be 53% at 2.5 ppm SO_2 as compared to a 78% decrease at 5 ppm SO_2 for the same applied dosage. Performance does not improve after impurity injection is turned off; thus, is not reversible just by normal operation. The severity of the effect is due to the strong chemisorption of SO_2 (or other S-species) onto the Pt catalyst surface. Electrochemical oxidation (during a CV) of adsorbed SO_2 shows full cell performance recovery.

Nitrogen dioxide (NO_x)

NO_x are air contaminants that mostly originate in the combustion of fossil fuels. Internal combustion engine emissions are the major source of NO_x; thus, they are abundant in urban areas. NO_2 has been shown to quickly degrade fuel cell performance, with a gradual decrease over 30 h of operation, after which degradation did not continue. The rate of poisoning of PEMFCs by NO_2 does not strongly depend on NO_2 bulk concentration. The degradation of performance of the fuel cell can reach 50%, while the cell performance completely recovers after applying neat air for 24 h. The poisoning effects of NO_2 do not appear to be a catalyst poisoning issue, as no surface species can be detected during CV; the poisoning mechanism is still not understood.

Sodium chloride (NaCl)

The presence of NaCl at the electrode decreases its performance. The performance loss is mostly due to a decrease of protonic conductivity as a consequence of exchange of H^+ by Na^+ at the CL and at the membrane. Large concentrations of the salt also decreased the hydrophobicity of the GDL, increased liquid water retention, and correspondingly decreased oxygen transport to the electrocatalyst at high current densities. Surprisingly, Cl^- does not appear to block adsorption on the catalyst surfaces, as revealed by CV measurements. However, chloride has a dramatic effect on the oxygen reduction kinetics of cathode electrocatalysts. Chloride has also been noted to affect GDL materials, which can lead to changes in water and gas transport.

Mitigation strategies for impurity effects

As discussed above, the impurities in the hydrogen stream and pollutants in the air stream can contaminate the fuel cell MEA in many ways, causing performance degradation and failure. Therefore, the measures and methods for mitigation

contamination have to be developed in order to minimize or eliminate its effects. For fuel, the reformed H_2-rich gas is the dominant source. As discussed above, this fuel contains appreciable amounts of CO and CO_2, which are the major fuel cell anode contaminants. There are several effective methods available to mitigate CO poisoning in PEMFCs, such as enhancing CO oxidation by pretreating reformate, introducing an anode oxidant-bleed, developing CO-tolerant catalysts, and optimizing fuel cell operating conditions. Pretreatment of reformate is one of the most popular ways to purify H_2-rich gas to reduce the CO concentration to as low as 10 ppm. Air or oxygen (or H_2O_2) bleeding has been demonstrated to be another effective way to reduce CO contamination if the fuel cell stack is operated with a reformate fuel stream. During fuel cell operation, air or oxygen will be intermittently blown into the anode. CO-tolerant catalyst development is another important mitigation method. As discussed above, the addition of a second or third metal into the Pt can form an alloying catalyst. The second or third metal can greatly help in CO oxidation. Operating a PEMFC at high temperatures (>80 °C) has a significant benefit for contamination tolerance due to the weaker adsorption and faster oxidation rate of CO on the Pt catalyst. It is worthwhile noting that for a long-term supply of hydrogen, reformate may not be an option due to the fossil hydrogen carbon shortage. It is expected that the external supply of hydrogen will rely on electrolysis and reformate from renewable biomass materials such as methanol and ethanol. For H_2 production from water electrolysis, CO fuel contamination may not be a problem. However, for short-term hydrogen supplies, reformate is still an option in terms of cost and reliability. For oxidant (air), the use of filters to purify the cathode feed stream effectively eliminated contamination from diesel and dust emission, hence improving the performance of a PEMFC operated in an underground mine.

1.2.2.2 Subfreezing temperature

One criterion PEMFCs are required to meet for automotive applications is the ability to survive at and startup from subfreezing temperatures. Early literature suggested that there was little degradation from freezing fuel cells to subfreezing temperatures for a limited number of cycles. However, a recent paper suggested that there could be significant degradation in the performance of PEMFCs subjected to cycling from −10 °C. These apparent discrepancies (from no degradation to 5.4% degradation/cycle) in the various literature results can be attributed to several factors. The preparation method of the MEA is critical in determining the freeze/thaw durability of the PEMFC. If the electrode/electrolyte adhesion is weak, then there is a greater degradation in the performance due to ice formation resulting in delamination. This may explain some of the discrepancies in the literature results where some electrodes were sprayed onto the GDL while others were prepared directly on the membrane. Moreover, the degradation is also a function of the rate of heating/cooling in addition to the freezing temperature. This is evidenced by rapid cycling (quenching) to −80 °C leading to delamination of the electrode while normal cycling to −40 °C (even for 100 cycles) shows no such delamination in an identically prepared MEA. Studies have also revealed that there is little loss in performance of even fully humidified cells using

carbon cloth backing. However, the breakage of carbon fibers in carbon paper backing leads to loss in performance during freeze/thaw cycles. Therefore, in addition to the preparation method and cycling conditions, the component materials used in the fuel cell assembly will also play a vital role in determining the durability of fuel cells subjected to multiple freeze/thaw cycling.

The reason for the performance of degradation at freezing temperature is thought to be the effect of freezing water on the MEA (including Nafion membrane, CL, and GDL) properties. The conductivity of Nafion is highly dependent upon the state of water in the polymer, and it has been shown to have an increased activation energy at lower temperatures, where the water in the membrane is likely in the frozen state. There is only limited literature available on the durability of the CL and GDL under freeze/thaw cycling. These reveal that even a freestanding hydrated CL can be subjected to cracking and peeling while cycling from -30 °C. This damage was associated with a loss in the electrochemical surface area of the catalyst that can be avoided by drying the catalyst.

Mitigation strategies for degradation due to subfreezing temperatures

The mitigation strategies utilized to avoid degradation due to subfreezing temperatures can fall into three categories: (1) those that prevent ice formation either by drying out the fuel cell or by replacing the water with a nonfreezing liquid; (2) those that prevent ice formation during start-up by providing heat; and (3) those that keep the fuel cell warm, thus preventing ice formation. Fuel cell stacks can be kept warm by providing insulation or by providing heat either through a battery or by operating the cell intermittently in a low-power mode. The freezing water can be avoided by eliminating carrying a water tank on board and by running the fuel cell at lower inlet RHs and reclaiming the exhaust water, though it is not clear if the current class of membrane materials will operate stably under such conditions. The water inside the stack can be minimized by running the cell under dry reactant gases (H_2, air) or dry nitrogen before shutdown or by vacuum drying the fuel cell. Moreover, during start-up, extra heat can be provided from a battery, by catalytically combusting hydrogen, or by preheating the reactant gases, and the heat carrying capacity of the reactant gases is rather low.

1.2.2.3 Relative humidity

Another aspect of fuel cell operation that is likely to affect the integrity of the cell is the changes in temperature and RH that are associated with transitions between low and high power. In general, for cells that operate at fixed stoichiometric ratios, operation at low current implies a relatively cool and wet cell; higher currents imply a hotter, drier cell. The fact that the ionomer swells with water uptake suggests that increases in water uptake as the membrane is exposed to high RH conditions can lead to compressive stresses in the membrane that then yield tensile residual stresses during drying. These stresses are suggested as a significant contributor to mechanical failures of the membrane. Another recent study suggests that drying can considerably strain the membrane–electrode assembly and that mechanical failure of membranes can result from gradual reduction in ductility combined with excessive strains induced

by constrained drying of the MEA. Both temperature and RH have been shown to affect the rate of catalyst surface area loss due to platinum particle growth. These studies suggest that more needs to be learned about material properties and how they change over the course of fuel cell operation.

1.2.2.4   Fuel starvation

Full-sized cells, on the order of several hundred square centimeters in area, will experience different conditions between the inlet and the outlet, and this can lead to current distributions that cannot easily be simulated in subscale testing. Furthermore, cells arranged in a stack configuration can experience different flows of fuel, air, and coolant resulting from imperfect manifolding. Therefore, adjacent cells in a stack can experience different conditions in terms of hydrogen and oxygen content, but they will be forced to carry the same current as their neighboring cells, as they are connected in series. It is noticed that, in the case of gross fuel starvation, cell voltages can become negative, as the anode is elevated to positive potentials and the carbon is consumed instead of the absent fuel. In the case of gross fuel starvation, for multiple cells in a stack, fuel maldistributions can lead to some cells having insufficient fuel to carry the current that is being pushed through them by adjacent cells. In the absence of a sufficient anodic current source from hydrogen, the cell potential climbs higher until oxidation occurs; in this case, the oxidation of the carbon support of the CL.

Mitigation strategies for degradation due to fuel starvation

Proper reactant distribution is critical to avoid this problem, and stack developers have accordingly sought to monitor the voltage of each cell to avoid such a problem. Obviously, such an extensive monitoring system will add considerable cost and complexity to the fuel cell stack and control scheme.

1.2.2.5   Load cycling

A fuel cell, particularly one that must meet the challenging dynamic load of an automotive application, will undergo many rapid changes in load over the course of its lifetime. As the fuel cell cycles from high to low current, its cell potential will also vary, generally between 0.6 and 1.0 V. For cells operating with relatively pure hydrogen as a fuel, the anode will stay fairly close to the reversible hydrogen potential, due to the facile nature of the hydrogen–oxidation reaction. This implies that the cathode experiences potential swings as cell potential changes to match variable power demands. The variation of the cathode potential will change several properties of the electrode materials, notably the degree of oxide coverage of both platinum and carbon, and the hydrophobicity of the surfaces. A more subtle distinction has to do with the fact that the oxide can actually serve to protect the platinum surface from dissolution at higher potentials. When the cathode potential rises rapidly to higher values, the platinum can dissolve at a rapid rate until a passivating oxide layer is formed.

Mitigation strategies for degradation due to load cycling

Any attempt to develop stable catalysts for fuel cell applications must consider the stability of the catalysts not only under constant potential conditions but also under potential cycling. To design catalysts that are robust to this degradation mode, considerably more information is needed about the nature of the oxide, the kinetics of its formation, and its ability to protect the catalyst from dissolution over the entire range of potentials.

1.2.2.6   Start/stop cycling

Performance degradation during start/stop cycling is considered an important issue affecting the durability and lifetime of PEMFCs. Due to the high potentials experienced by the cathode during start/stop cycling, the conventional carbon support for the cathode catalyst is prone to oxidation by reacting with oxygen or water. Both start-up and shutdown are dynamic processes that a fuel cell inevitably must confront in automobile applications. Compared to steady state processes, start/stop cycling processes experience different profiles under operating conditions. Under conditions of a prolonged shutdown, unless the stack is continually provided with fuel, hydrogen crossover from the anode to the cathode will eventually empty out the anode chamber and result in an air-filled flow channel. In this case, the starting flow of fuel will induce a transient condition in which fuel exists at the inlet, but the exit is still fuel-starved. As a result, starting and stopping the fuel cell can induce considerable damage to the cell. This phenomenon has been modeled and reveals that an unprotected start can induce local potentials on the cathode in excess of 1.8 V relative to a hydrogen reference electrode. On the other hand, catalyst degradation at the cathode is considered a major failure mode for PEMFCs when the catalysts are exposed to reverse current conditions during start/stop cycling.

Mitigation strategies for degradation due to start/stop cycling

The strategies for degradation due to start/stop cycling can be classified into two major categories: (1) material improvement for more stable catalyst supports and (2) system mitigation strategies for conventional carbon black supports. In the aspect of material improvement, replacing conventional carbon supports with corrosion resistant materials (e.g., graphitized carbon) is an important mitigation strategy. The use of graphitized carbon resulted in a reduced mass transport limitation of the GDL, in comparison with the mass transport limitation enhanced by conventional carbon oxidation at the MPL/electrode interface. In addition to graphitized carbon, other carbon materials, such as carbon nanotubes or carbon nanofibers, and carbon aerogel and xerogel, have also been considered as catalyst supports because of their more stable electrochemical behaviors. In the aspect of system mitigation strategies, it includes (1) gas purge to anode before start-up and after shutdown; (2) auxiliary load applied to consume residual oxygen at the cathode with potential control; (3) exhaust gas recycle as purging gas or reaction gas; and (4) electronic short to eliminate high potential at the cathode. In comparison with materials improvement by using graphitized carbon or noncarbon supports, system strategies are relatively simple and cheap to implement in real fuel cell engines.

1.3   Theoretical modeling for fundamental understanding

1.3.1   Introduction

The most complex components in PEMFCs are the electrodes, which are constituted by metallic nanoparticles of a few nanometers size having the role of electrocatalyst, and are supported on carbon particles of a few microns size having the role of electronic conductor. The resulting complex structure, arising from more than 30 years of research efforts to enhance the efficiency and reduce the loading by precious metals in these devices (Franco, 2014a), is in turn embedded within PFSA proton conducting polymers, leading to a composite electrode of few micrometers thick (Figure 1.4). During the PEMFC operation, a strong nonlinear multiscale dynamical coupling between several physicochemical phenomena takes place within the MEA: reactant transfers (hydrogen and oxygen through the GDL and CL pore phases), water transfers (biphasic water in CL and GDL meso/macropores, dissolved water in the PEM and CL ionomer), electrochemistry (hydrogen oxidation producing electrons and protons, and oxygen reduction producing water), and charge transfer (proton within the CL ionomer and PEM, electron within the CL and GDL). In fact, processes at the smaller scales (e.g., ORR on the cathode platinum nanoparticles) dominate the processes at the larger scales (e.g., liquid water transport through the cathode carbon support secondary pores), which in turn affect the processes at the smaller ones (e.g., through the water flooding limiting O_2 transport in the cathode). In addition to the electrochemical reactions, reactants, and biphasic water transport, other mechanisms limiting optimal platinum utilization are charge transfer, thermomechanical stresses and irreversible materials degradation. For instance, microstructural degradation leading to the
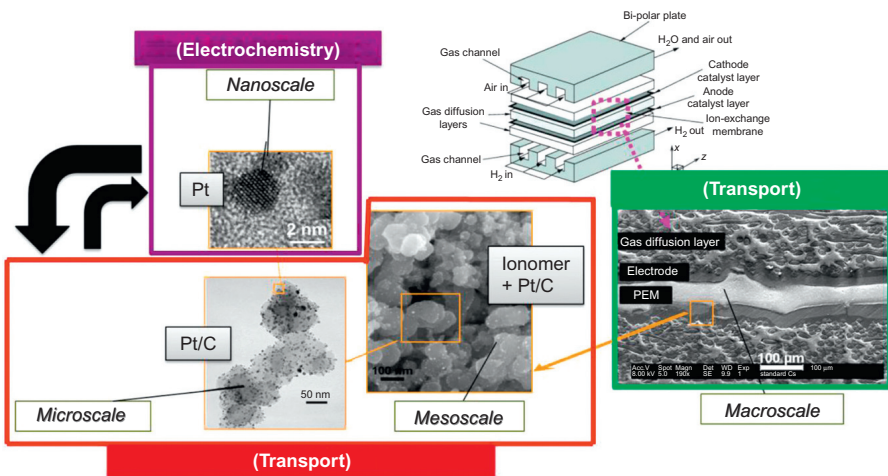
Figure 1.4 Multiscale structure of a PEMFC electrode.
Adapted from Franco (2014a).

PEMFC components aging is attributed to several complex physicochemical phenomena not yet completely understood (Franco, 2014b, 2012). These spatiotemporal nano/microstructural changes translate into irreversible long-term cell power degradation. Moreover, the ways of how aging mechanisms occur are expected to be strongly sensitive to the PEMFC operation mode.

Consequently, because of the structural complexity and multiphysics character of PEMFCs, interpretation of experimental observations and ultimate cell optimization remain a challenge. An analysis through consistent physical models is required to elucidate the efficiency limitations and their location, the degradation, and failure mechanisms. From a practical point of view, it is crucial to accurately predict their performance, state-of-health, and remaining lifetime. For that purpose, it is necessary to develop diagnostic schemes that can evaluate the cells/stack performance and state-of-health adequately. To achieve this, several steps are required:

- to develop via physical modeling a better understanding of several individual processes in the cell components;
- to understand the interplay between individual scales over the spatiotemporal hierarchies with their possible competitive or synergetic behavior;
- to identify the contribution of each mechanism into the global cell response under dynamic conditions.

A detailed understanding of the relevant processes on all these materials and components scales is required for a physically based optimization of the cell design and the cell embedded into the system, regarding its efficiency and durability.

1.3.2   Modeling concepts and methods: A general overview

1.3.2.1   Concepts

A mathematical model is a transcription of a physical theory describing a system into mathematical concepts and language. As mathematics is the most logical and organized way of thinking, it becomes natural using it when one wants to rationalize and to predict the behavior of physical systems.

The word *multiphysics* usually characterizes, in published literature, mathematical models that describe the interplaying of mechanisms belonging to different physical domains. Multiphysics models include models describing these multiple mechanisms within a single and unique spatial scale (e.g., a model describing the impact of heating on the mechanical stress of a material) (Holzapfel and Gasser, 2001). The majority of models developed to describe the operation of PEMFCs fall within this category, as they have to consider at least two different physical domains: the electrochemistry and the transport.

In this chapter, "multiscale models" refer to models which account for mathematical descriptions of mechanisms taking place at different spatial scales (Couenne et al., 2008). Multiscale models aim to significantly reduce empirical assumptions than can

be done in simple multiphysics models. Indeed they explicitly describe mechanisms in scales neglected in the simpler multiphysics model. Multiscale models have a hierarchical structure, which means that solution variables defined in a lower hierarchy domain have finer spatial resolution than those solved in a higher hierarchy domain. Consequently, physical and chemical quantities of smaller length-scale physics are evaluated with a finer spatial resolution to resolve the impact of the corresponding small-scale geometry. Larger-scale quantities are in turn calculated with coarser spatial resolution, homogenizing the smaller-scale features. Depending on the development context of these models (engineer- or physicist-based), they would be built following two complementary viewpoints: top-down or bottom-up. Top-down models connect detailed macroscopic descriptions of mechanisms with global parameters representing microscopic mechanisms. On the other hand, bottom-up cell models scale up detailed descriptions of microscopic mechanisms onto global parameters to be used in macroscopic models (Figure 1.5) (Franco, 2013b).

Finally, the mathematical descriptions in a multiscale model can be part of a single simulation paradigm (e.g., only continuum) or of a combination of different simulation paradigms (e.g., stochastic model describing a surface electrocatalytic reaction coupled with a continuum description of reactants transport phenomena). In the latter case, one speaks about "multiparadigm" models. Multiparadigm models, consisting of injecting data extracted from a single scale model into upper scale models via their
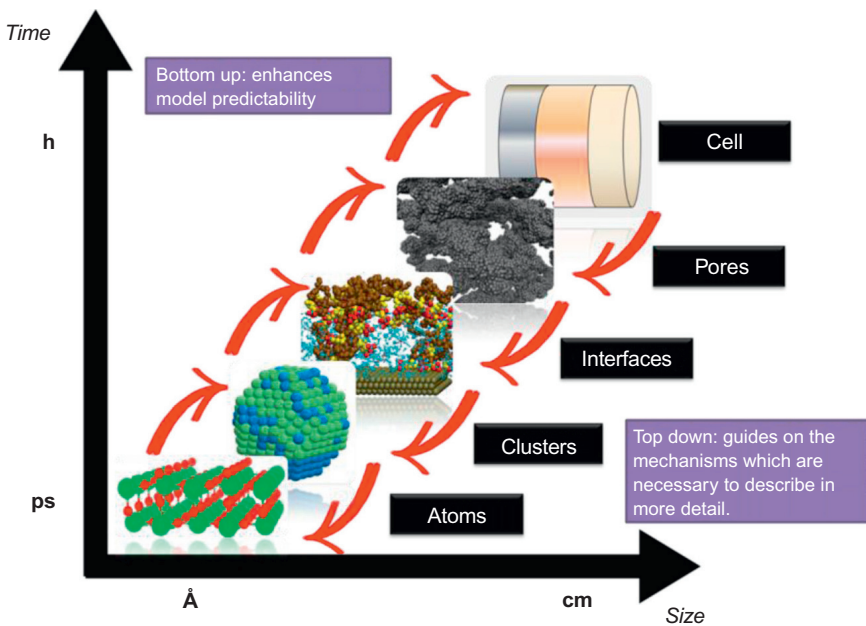
Figure 1.5 Bottom-up and top-down multiscale modeling.
Figure from Franco (2013b).
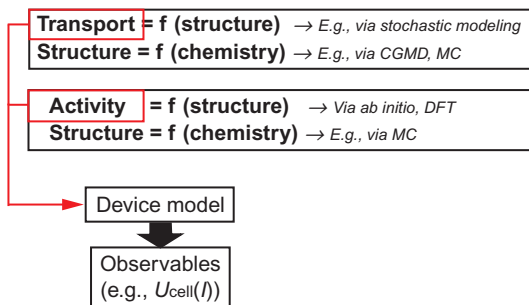
Figure 1.6 Schematics of a typical multiparadigm approach for the simulation of PEMFC. Figure from Franco (2013b).

parameters, constitute a powerful emerging approach in the PEMFC community, to connect the chemical and structural properties of the materials with the overall performance of the cell (e.g., cell potential U_{cell} in Figure 1.6) (Eberle and Horstmann, 2014; de Morais et al., 2011).

For example, in the field of electrocatalysis, one can use nudged elastic band calculations (Sheppard et al., 2008) to estimate the values of the activation energies E_{act} of single elementary reaction kinetic steps and then inject them into elementary kinetic rate expressions (de Morais et al., 2015a,b; Quiroga and Franco, 2015). Another example of multiparadigm model results from the use of coarse grain molecular dynamics (CGMD) for the calculation of the materials structural properties (e.g., tortuosity and porosity) as a function of the materials chemistry, which are used in turn for the estimation of the effective diffusion parameters used in continuum reactants transport models (Malek and Franco, 2011).

1.3.2.2 Methods available in the literature

Numerous models have been developed and reported in the literature in the last 30 years for the description and prediction of the PEMFC components and the interfaces structural properties (e.g., electrodes, membrane, GDL, catalyst/electrolyte interfaces) as well as their associated reactivity and transport properties; for example (Figure 1.7)

1. models devoted to investigate the components reactivity properties, with particular emphasis on electrochemical interfaces (electrolyte/catalyst) and
2. models devoted to investigate the components of transport properties regarding charges (electrons, protons), reactants (e.g., H_2/O_2), and products (H_2O/H_2O_2).

For each aspect, two subclasses of models are currently reported:

- distributed parameters' models, able to resolve locally the species spatial distribution on the catalyst surface, electrode volume, by accounting for thermomechanical stresses, and so on and
- lumped parameters' models, describing effective (mean field, MF) properties.
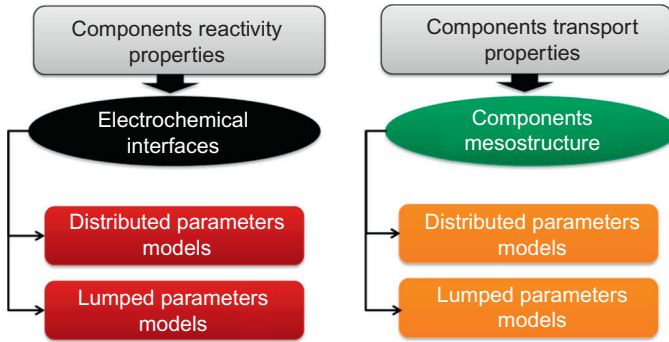
Figure 1.7 Classes of components models available in the literature.

These model subclasses concern a diverse number of computational methods as illustrated in Figure 1.8; for example, kinetic Monte Carlo (kMC), metropolis Monte Carlo, MF, CGMD, pore network modeling (PNM), and the multiscale (multiphysics, multiparadigm) simulation frameworks coupling on-the-fly atomistic and continuum-level descriptions of some of the electrochemical and transport mechanisms.

This section reviews some of the most advanced and promising modeling tools available in the literature for analyzing mechanisms and processes in PEMFCs. The section does not intend to be exhaustive, but instead, aims to provide a guide for a general public of researchers, engineers, and students through some practical illustrations. For other aspects and examples of PEMFC modeling, the readers are invited to consult (Franco, 2013c,e, 2012, 2014b).
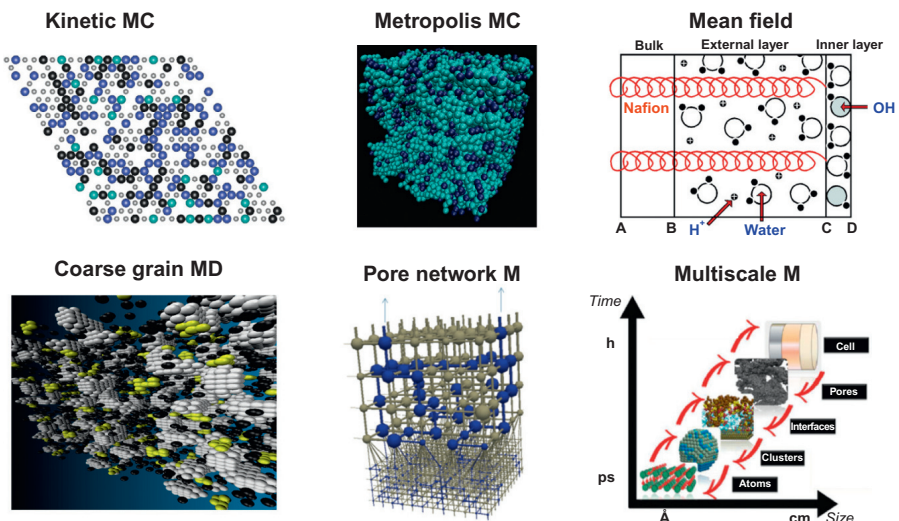
Figure 1.8 Some computational methods used for PEMFC assessment.

1.3.3   Models of the components structure

Several mathematical models have been reported attempting to capture the influence of the electrodes' structural properties on the ionic transport properties and cell capacity response. Approaches have consisted of building up artificial structures capturing the main features of the real electrodes (e.g., length scales, particles shapes) and computer-aided reconstruction (e.g., based on X-ray tomography and 3D focused ion beam (FIB)/scanning electron microscopy (SEM) of the real electrode structure. Defining an appropriate structural picture for the electrodes is crucial for the PEMFC models. Even if the PEMFC models have already been successfully applied in a variety of studies, including analysis of stress generation and cell design, a lack of knowledge of the model parameters can lead to a significant reduction of their prediction capability.

As an example of artificial structure, the spherical agglomerate model with a single diameter is a common approach to describe the average electrochemical reaction rate in the CLs. For instance, Hu et al. (2014), among many other authors before them, use a classical agglomerate model with thin film of polymer and liquid water to investigate the effects of the cathode catalyst later (CCL) properties on the PEMFC performance. This type of approach allows us, in a simple way, to capture the effects of the agglomerates radius, Pt loading and Pt particle radius, operation temperature, and pressure on the PEFMC performance and can be used to optimize it by suitable operational conditions and CL structure (Figure 1.9) (Xing et al., 2014; Song et al., 2004a,b, 2005; Wang et al., 2004a,b,c; Moore et al., 2014). Kulikovsky has recently revisited such agglomerates models (Kulikovsky, 2014) by deriving an analytical solution for the polarization curve of the cathode, taking into account oxygen transport in agglomerates of carbon particles. The author found that in agglomerates of the radius <100 nm, the oxygen transport in agglomerates manifests itself at cell potentials below 100 mV only, a performance region without practical interest. Thus, the account of this transport in CCL modeling is redundant; that is, the standard macro–homogeneous model is adequate for CCL performance simulations.
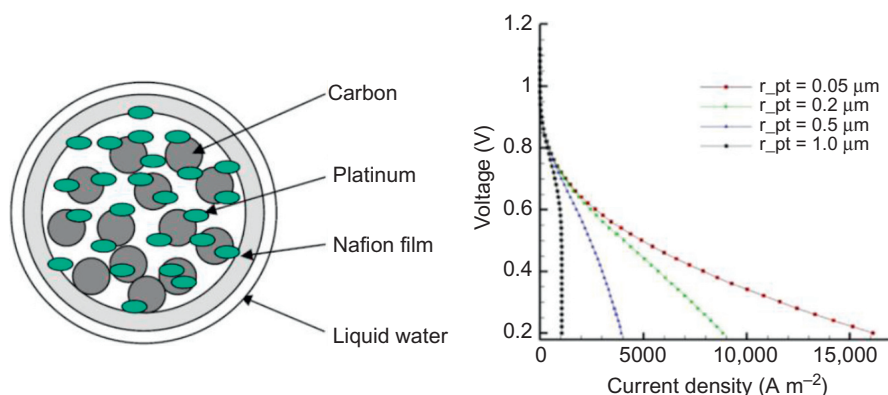
Figure 1.9 An example of agglomerate model and calculated cell performance curve for different agglomerate diameters.
From Hu et al. (2014).
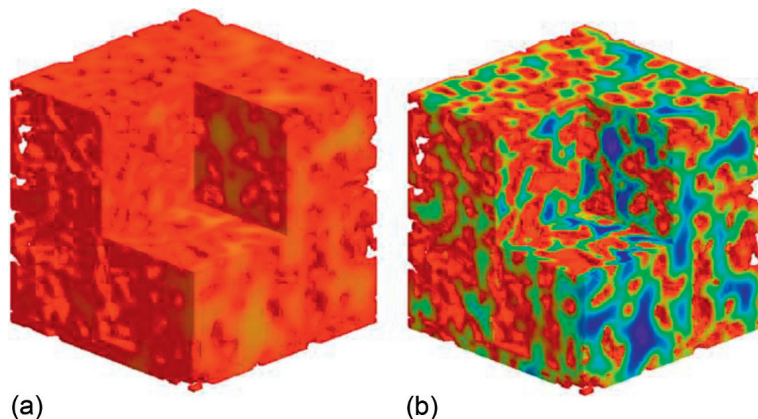
Figure 1.10 Distribution of the normalized oxygen concentrations in the CL under overpotential of 0.65 V (A) in comparison with that under overpotential of 0.85 V (B). The value of the normalized concentration changes from 1 (red) to 0.05 (blue). From Zhang et al. (2014).

However, real agglomerates are highly irregular, and approximating them by independent spheres could give rise to errors. Zhang et al. reported an investigation consisting of acquiring three-dimensional microstructure of a cathode by using FIB/SEM tomography (Figure 1.10) (Zhang et al., 2014). Oxygen diffusion and the associated electrochemical reaction in the microstructure were simulated using explicit pore-scale modeling. The simulations were then compared with the results predicted by a spherical agglomerate model using an average diameter estimated from the three-dimensional microstructure. The authors found that the spherical agglomerate model substantially overestimated the reaction rates and the overpotential. These findings implicate that the spherical agglomerate model needs to be used with care in CL design as its diameter is just a fitting parameter rather than a geometrical description of the agglomerates.

Furthermore, there are very few efforts so far aiming to predict the structural properties of the composite electrodes as a function of the fabrication parameters and the composition. For instance, Monte Carlo (MC) models consisting of multiparticles energy-based spatial arrangement optimization are just emerging and used to mimic electrodes fabrication and to estimate relevant structural and transport properties (Kriston et al., 2014). Because of their fully empirical parameterization, these techniques cannot predict the influence of the chemical composition (e.g., solvent and active material chemistries) on the arising electrode self-organization and structural properties.

Alternatively, electrode microstructures can be generated *in silico* by atomistic methods. To improve the understanding of the CL structure (e.g., in PEMFCs), the effects of applicable solvent, particle sizes of primary carbon powders, wetting properties of carbon materials, and composition of the CL ink should be explored (Malek and Mashio, 2013). These factors determine the complex interactions between Pt/C particles, ionomer molecules, and solvent molecules and, therefore, control the CL formation process. Mixing the ionomer with dispersed Pt/C catalysts in the ink suspension prior to

deposition will increase the interfacial area between ionomer and Pt/C nanoparticles. The choice of a dispersion medium determines whether ionomer is to be found in the solubilized, colloidal, or precipitated forms. With the aim of predicting these effects, CGMD models have been developed by Malek et al. to simulate the self-organization of the CLs and to understand its impact on the effective transport and electrochemical properties (Malek et al., 2007). CGMD is essentially a multiscale technique (parameters can be extracted from density functional theory (DFT) and/or molecular dynamics calculations). CGMD simulations have been employed for characterizing microstructure of CL in view of effect of solvent, ionomer, and Pt particles. For instance, based on this technique, it has been found that Pt content increase in CLs impacts the structure of the electrode, essentially by decreasing Nafion coverage on the C support, and also changes the CL pore size distribution (PSD) (Figure 1.11) (Malek et al., 2011).

Another important aspect that can be captured by CGMD simulations is the structure of the complex interfaces formed between the ionomer and the Pt/C surface. As recently demonstrated from these simulations (Damasceno Borges et al., 2013a,b), the hydrophilicity degree of the substrate can strongly impact the interfacial morphology of Nafion thin films and, thus, the protonic charge distribution over space (Figure 1.12). This is expected to impact the electrochemical double layer structure, which will impact in turn the effectiveness of the ORR. For instance, the following features are found:
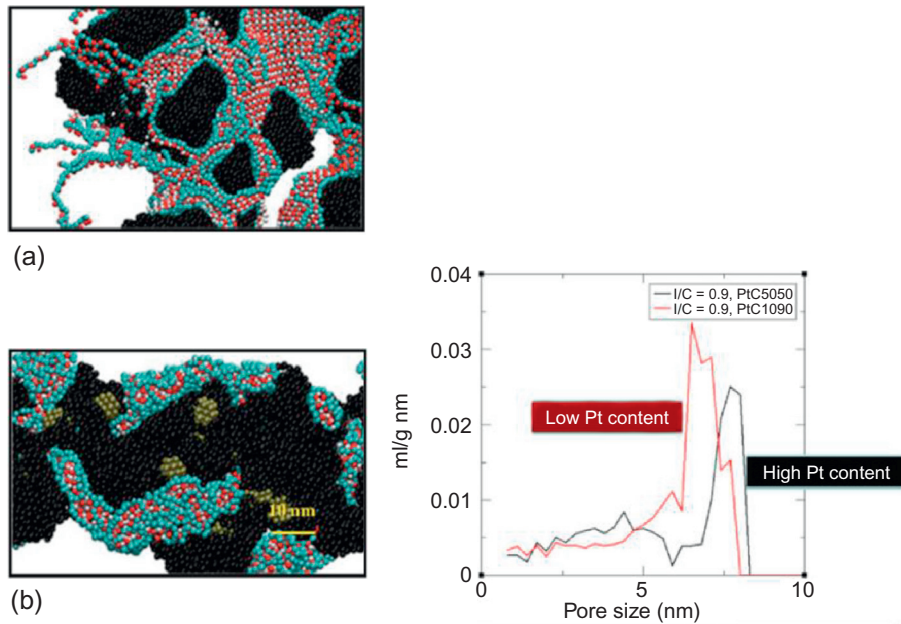
Figure 1.11 CGMD-calculated impact of the Pt content on the ionomer coverage on C and on the CL pore size distribution: (a) without Pt and (b) with Pt.
From Malek et al. (2011).
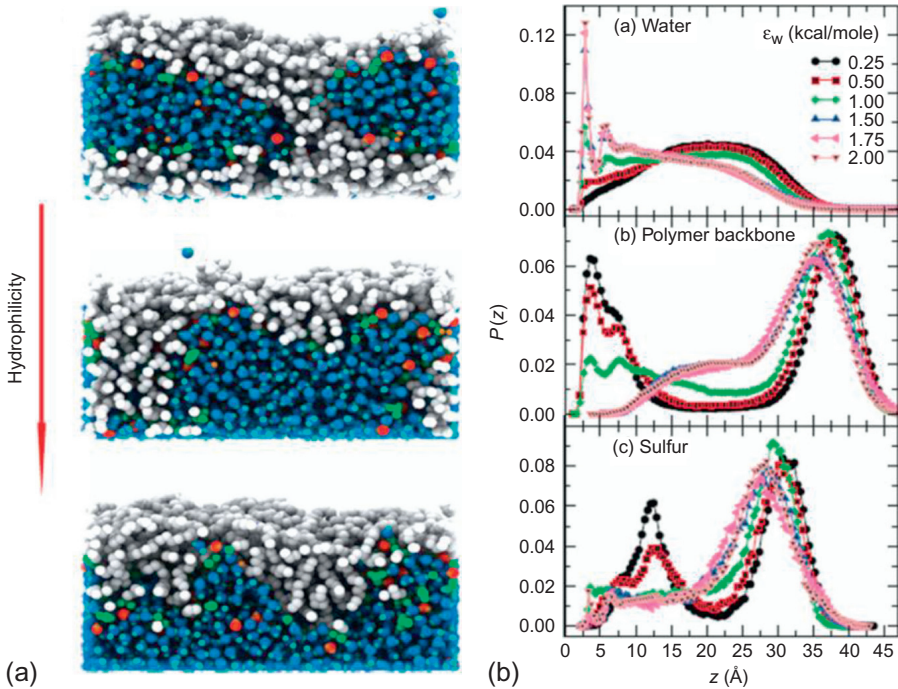
Figure 1.12 (a) Snapshots of CGMD-calculated structures of hydrated Nafion ultrathin films, at $T=350$ K and number of water molecules per sulfonic acid group $=22$, for an interaction with the support of increasing hydrophilic character from top to bottom. It is observed the formation of extended water pools (blue) that are separated from the confining polymer matrix (grey) by the charged sulfonic groups interface (green); hydronium complexes are also shown (red). (b) Mass probability distributions as a function of the distance from the support, z, at the indicated values of hydrophilicity (highest ew value $=$ highest hydrophilicity): representation of water oxygens, polymer backbone units and sulfur atoms.
From Damasceno Borges et al. (2013a).

→ The ionomer density at the vicinity of the substrate decreases as the substrate hydrophilicity increases, and the opposite trend occurs at the top of the film.
→ A compact water layer is formed in the hydrophilic cases.
→ For the hydrophobic case, the side chains are pointing out from the surface. No presence of water is observed on the top as a hydrophobic film surface is formed that could prevent gas and water absorption.
→ Still, in the most hydrophobic cases, the formation of hydrophilic water channels (inverted micelles) is more evident, and the formation of polymer layers is detected that would prevent the water and proton to diffuse through the film thickness.
→ The agglomeration of adsorbing anions (SO_3^-) is observed when the hydrophilicity increases.
→ For the most hydrophobic cases, the polymer is adsorbed mainly via backbone, and for the most hydrophilic cases, the presence of backbone is less evident at low hydration.
→ The backbone can be adsorbed even in the hydrophilic surfaces.

The ionomer film structure will be impacted by the catalyst/carbon oxidation state (which determines its hydrophilicity). As the distribution of charge at the vicinity of the substrate is strongly affected by the ionomer structure, the surface hydrophilicity is expected to impact the proton concentration at the reaction plane, and nonuniform reaction rates are expected inside the CL. It is important to note that the hydrophilicity of the Pt is expected to evolve during the PEMFC operation as its oxidation state changes. Thus, the structure of Nafion at the interface is also expected to evolve upon the PEMFC operation. All these structural features are expected to strongly impact the ORR kinetics through the polymer poisoning of the catalyst and the effective ionic transport and water uptake properties of the thin film.

The CGMD approach has been also used to model the structural change of carbon nanoparticles in terms of total mass loss during the oxidation process (Ban et al., 2013). The stability of Pt nanoparticles is investigated for various temperatures and roughnesses of the carbon surface. Simulation results show that migration and coalescence of Pt particles can occur. Detachment and transport of small Pt clusters were observed supporting the argument that the transport of molecular Pt species occurs on carbon surface (see Figure 1.13).

Finally, we just mention, without further details, that analogous to CL models, numerous sophisticated models are becoming available for the prediction of the three-dimensional microstructure of compressed fiber-based materials from stochastic simulations (Gaiselmann et al., 2014; Norouzifard and Bahrami, 2014). Such compression models are usually validated by comparing calculated structural characteristics with the experimental ones extracted from tomography characterizations (Figure 1.14). Similar stochastic approaches have been more recently developed, virtually creating full-length nonoverlapping fibers, carbonized binder, and PTFE as distinct phases according to the carbon paper manufacturing process (El Hannach and Kjeang, 2014). All these models are very helpful for analyzing the distribution of transport properties and determining correlations to structural features such as porosity, fiber alignment, and orientation.

1.3.4   Functional models

1.3.4.1   Water transport in CLs

Having appropriate controllers for PEMFCs operating at low relative humidities on the cathode side is crucial to speed up the integration of thermal management strategies into realistic systems for automotive applications. This necessarily requires developing mathematical models that capture the interplaying dynamics between water transport and thermal aspects. To achieve these goals, the understanding and the physically based modeling of the water transport in the CLs is a crucial aspect that has been the subject of numerous publications. In a pioneering work, Springer et al. (1991) reported an isothermal, one-dimensional, steady-state model of a complete PEMFC. In particular, the model predicted an increase in PEM resistance with increased current density and demonstrated the great advantage of a thinner PEM for alleviating the resistance problem. Bernardi and Verbrugge (1991, 1992) proposed a one-dimensional mathematical model of the PEMFC for liquid water transport in
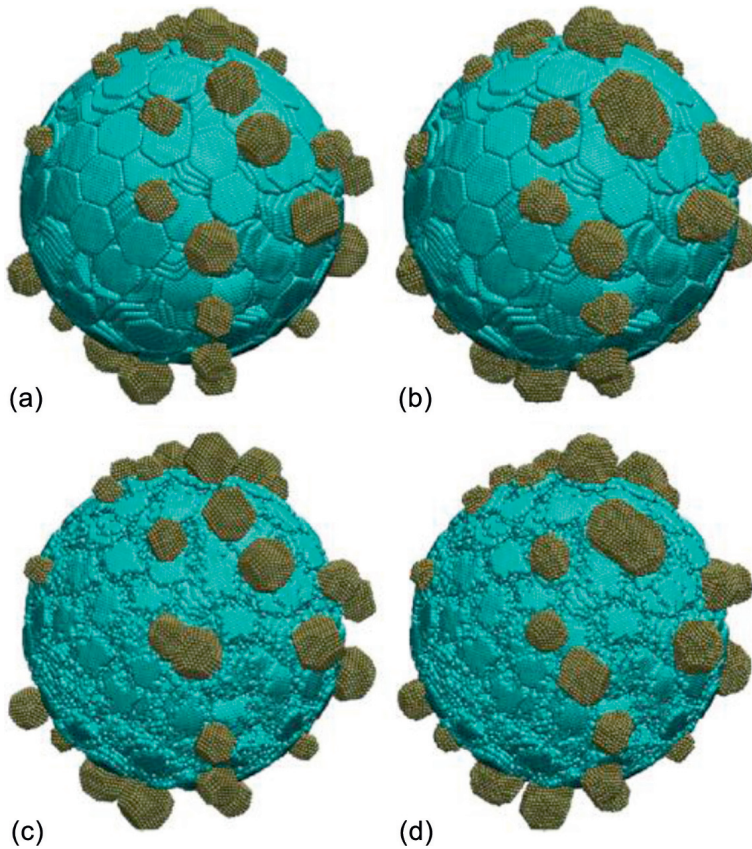
Figure 1.13 Simulation snapshots of Pt particles equilibrated on the surface of carbon black with 3.2 nm graphitic layers. (a) Pt particles on the surface of pristine carbon at 300 K. (b) Pt particles on the surface of pristine carbon at 873 K. (c) Pt particles on the surface of oxidized carbon black with 50% weight loss at 300 K. (d) Pt particles on the surface of oxidized carbon black with 50% weight loss at 873 K.
From Ban et al. (2013).

porous electrodes assuming a constant liquid water volume fraction and no interactions between liquid and gas flows. A number of CL models had then been developed, including interface models, thin film models, agglomerate models, and thin film agglomerate models mentioned in Section 1.3.3 (Broka and Ekdunge, 1997; Jaouen et al., 2002; Siegel et al., 2003, 2004; Sun et al., 2005a,b; Yin, 2005; Lin et al., 2004). Besides these models, the works of Wang and Wang (2005, 2006) treated the CL as an individual zone with various conservation equations employed for transient simulation.

Many different two-phase flow models have shown up in the literature during the last decade. Wang et al. (2001) pioneered the research on this issue through analytical
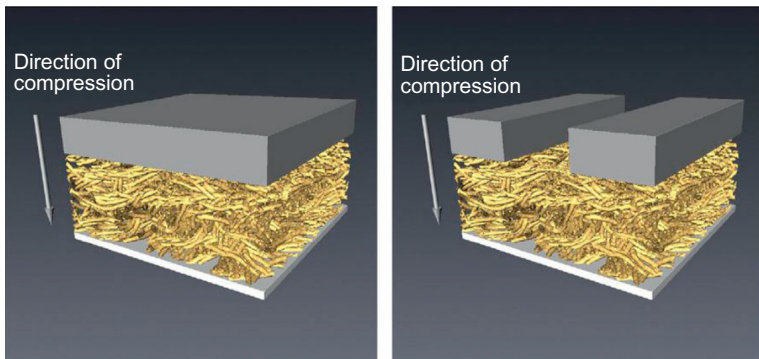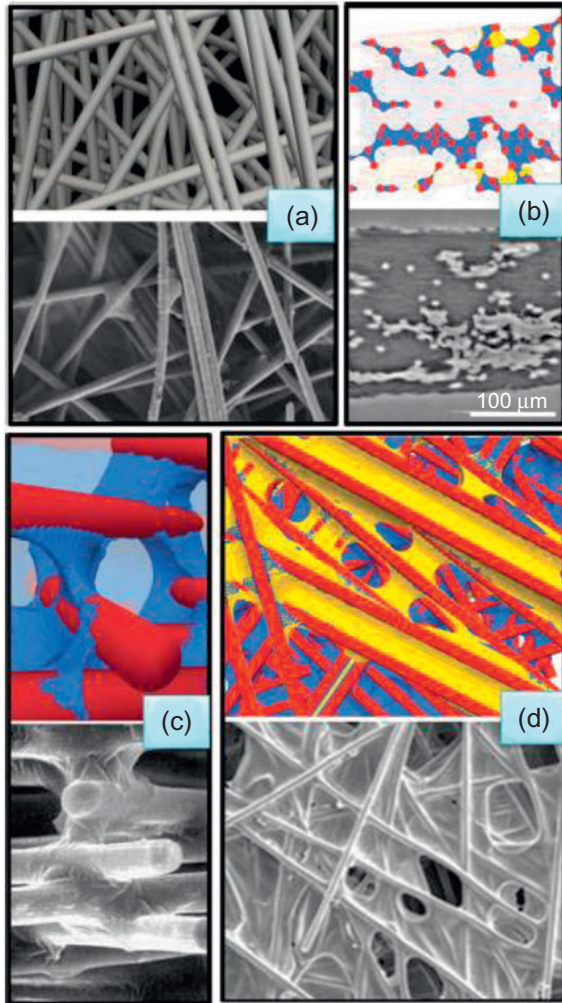
Figure 1.14 (Top) 3D image of nonwoven GDL (yellow fibers) with flat stamp (left) and with stamp of flow-field structure (right) (from Gaiselmann et al., 2014); (right) visual features of the generated GDL structure compared to typical SEM images of Toray TGP-H from the literature: (a) top view of the fiber structure; (b) side view of the GDL; (c) internal side view of fibers (red) and binder (blue); and (d) top view of the GDL with PTFE (yellow).
From El Hannach and Kjeang (2014).

and numerical methods. The model of Natarajan and Van Nguyen (2001, 2003), which considered evaporation and condensation of liquid water, also demonstrated the importance of the biphasic water transport on cell performance. Wu et al. (2009) discussed the different water transport modeling approaches and compared simulation results using various published expressions for liquid water saturation, relative permeability, evaporation/condensation rates, and absorption/desorption rates. In most reported models, the dynamics of evaporation and condensation are neglected due to the high surface area of porous media and the resulting relatively fast evaporation rate.

PNM can be used to estimate relationships between reactant transport properties and the liquid water saturation in the CL with a given PSD, estimated by porosimetry experiments for instance. PNM is an efficient method to investigate multiphase transport in porous media (Figure 1.15). It was used in the petroleum field for decades and was recently applied to study water management inside the GDLs and CLs of the PEMFC (Chapuis et al., 2008; Gostick et al., 2007; Wu et al., 2012).

These studies allowed understanding two-phase flow effects in the GDLs; for instance, the role of local mixed wettability on two-phase pattern and gas (H_2, O_2, N_2) diffusion, the role of adjacent layers on performance, as well as the role of rib/channel effects. The CL has been much less studied than the GDL within the framework of PNM. This is due to the more complex microstructure, the smaller pore sizes
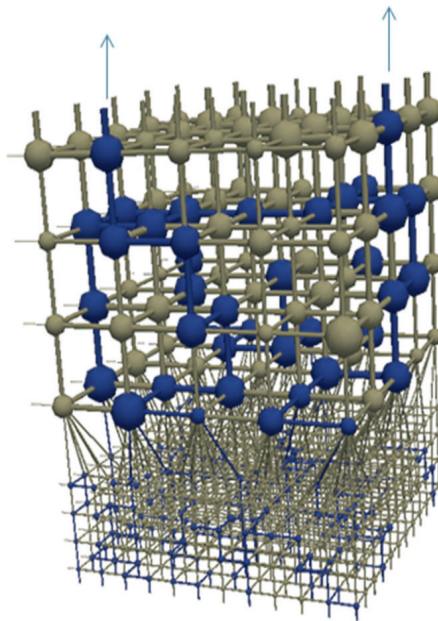
Figure 1.15 Example of calculated liquid water patterns in a porous structure through the PNM. Figure adapted from El Hannach et al. (2011).

involved, and the fact that the phenomena are more complex due to the electrochemical reactions (and the associated water production and charge transport).

PNM approaches provide the same outcomes as continuum PSD-based MF approaches (Eikerling, 2006); however, both approaches do not describe the filling dynamics of each single pore. PNM simulations need as an input the discretized PSD, which allows visualizing the transient water location and propagation along a set of pores. This allows explicitly setting pores with different properties in precise locations. To be representative for real CLs, PNM needs to account for a large number of pores. The continuum PSD approach inherently contains the information about the CL structure, whereas a PNM approach needs the CL structure as an input. Finally, statistical analysis of the results based on numerous simulations is needed with the same PNM to take an average of the results, as PNM is essentially an initial condition-dependent approach. However, it is highlighted that the pore-filling dynamics cannot be neglected as the evaporation within the CL pores has a major effect on the catalyst activity (Eikerling, 2006). The experimental work reported by Song et al. (2007) showed that the higher water evaporation flux at elevated temperature causes a reduction in active platinum sites, which is even more important when operating at low relative humidities (Zhang et al., 2007).

Understanding transport properties in CL structures is a complex task, in particular in relation with the PSD, the catalyst size distribution and the structure of the ionomer within the electrode. These parameters have been demonstrated to be crucial on the determination of the effective PEMFC performance (Malek et al., 2011; Ohma et al., 2010; Iden et al., 2011). As discussed in Section 1.3.3, during the CL fabrication process, the ionomer features a complex structure. It can only penetrate until a certain minimal pore size. The ionomer coverage for Ketjen Black for instance is estimated only about 60% of the coverage of Vulcan carbon supports due to the large number of primary pores ($r_{pp} < 15$ nm) in the Ketjen Black support (Ikeda et al., 2010). Thus, Pt particles in smaller pores are not in direct contact with the ionomer unlike in secondary pores (15 nm $< r_{sp} < 100$ nm). The proton conduction in these primary pores is guaranteed by the presence of liquid water. The work of Wang et al. (2004a) shows that Pt utilization in liquid water-filled pores is comparable to ionomer-filled pores, which underlies the strong effects of liquid water content in the CL on performance.

A recent work tackles the question of the PSD water-filling dynamics versus the active area variation, in the context of open cathode PEMFCs (Strahl et al., 2014). The authors propose a dynamic multiscale model describing two-phase water transport, electrochemistry, and thermal management within a framework that combines a computational fluid dynamics (CFD) approach with a microstructurally resolved model predicting the water-filling dynamics of the electrode pores and the impact of these dynamics on the evolution of the electrochemically active surface area (ECSA) (Figure 1.16). The model allows relating for the first time the cathode electrode structure to the cell voltage transient behavior during experimental changes in fuel cell temperature. The effect of evaporation rates, desorption rates, and temperature changes on the performance of four different electrode pore-size distributions is explored using steady state and transient numerical simulations. Four different CL structures, namely, only primary pores, only secondary pores, Super P, and Ketjen
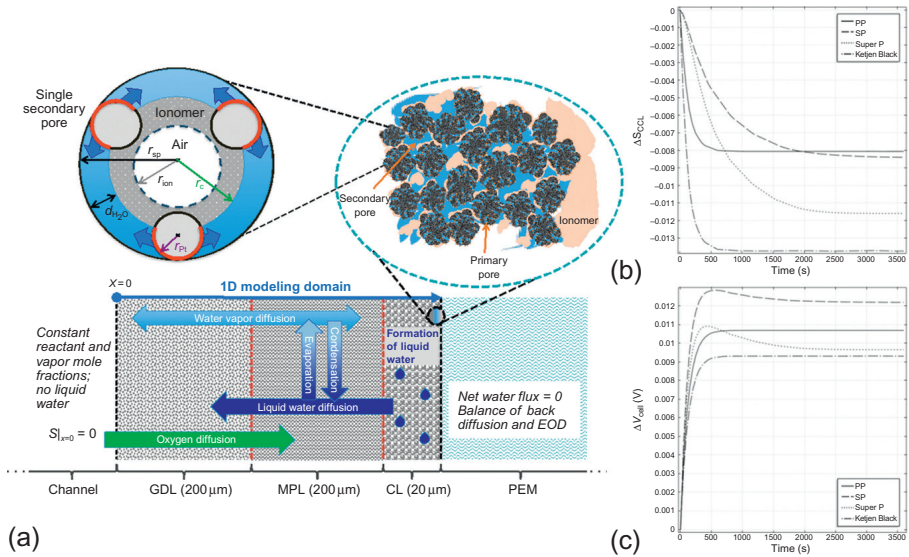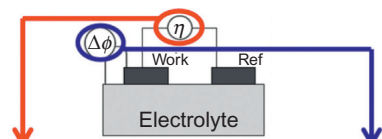
Figure 1.16 (a) Multiscale model of CCL PSD water filling and ECSA dynamics and (b) influence of different carbon structures (primary pores only, secondary pores only, Super P, Ketjen Black) on the liquid water saturation dynamics (b) and cell voltage dynamics (c) when a temperature step increase is applied.
Adapted from Strahl et al. (2014).

Black were analyzed in terms of liquid water transport characteristics and electrochemical activity. Transient simulations with the presented model allow for studying the influence of the CL pore structure on thermal and water management of a PEMFC. The model helps to understand experimentally observed thermal and electrochemical system dynamics, which is essential for the development of proper control strategies. It has been shown that for the relatively dry open-cathode system the evaporation rate constant and the liquid water sorption constant are crucial for proper representation of the CCL performance. The dynamics of the voltage response with respect to an increase in cell temperature are dominated by water desorption dynamics of the Nafion thin film in secondary pores.

1.3.4.2 Electrochemistry in CLs

In the most popular PEMFC models, the kinetic rates associated to the electrochemical reactions (e.g., ORR in the cathode) are described via Butler–Volmer equations with empirical parameters, not connected with atomistic processes and thus describing reactions through effective global steps, in contrast to the transition state theory (Figure 1.17) (Mocoteguy et al., 2007). The numerical estimation of the values of parameters such as the zero exchange current (i_0) or the symmetry factors (α) is often a difficult task (Eikerling et al., 2007). These macroscopic parameters show strong dependence on the PEMFC operation parameters such as the temperature or the

Figure 1.17 Main differences between the classical Butler–Volmer approach and a more physical approach based on transition state theory for the modeling of electrochemistry. From Franco (2013d).

reactants RH, the CL mesostructural properties, and even the MEA design (Song et al., 2007). Modeling-based optimization of CL reactants and water transport for enhanced performance and stability requires a good knowledge of these electrochemical parameters related to the chemical and nanostructural properties of the catalyst.

The possible impact of water and ionomer that are expected in the vicinity of the catalyst in realistic PEMFC environments on the ORR kinetics appears to be very rarely explored (Subbaraman et al., 2010). In fact, in many models, the electrochemical double-layer (EDL) capacity is usually assumed to be constant (i.e., the EDL structure been uncoupled from the elementary reactions) (Antoine et al., 2001). It is well known that this is a very significant assumption that can lead to contradictory interpretations of experimental data as the electrochemical interface is expected to evolve under transient conditions (such as in the case of aging nanoparticles, oxidation, and corrosion mechanisms), and the structure of the EDL influences in turn the electron transfer rate and thus the effective electroactivity properties of the catalyst surface (Biesheuvel et al., 2009; Frumkin, 1933; Bockris and Reddy, 1970). More refined Butler–Volmer models, splitting global reaction steps into a set of elementary steps, have been developed and mainly used to explore external contaminants impact on the PEMFC performance or MEA materials aging mechanisms (Camara et al., 2002; Darling and Meyers, 2003; Rinaldo et al., 2010). Kinetic parameters are usually estimated from experimental fitting, without checking the thermodynamic consistency of the proposed pathways at the atomistic level. The kind of electrochemical model used in a multiphysics model of a PEMFC can impact on estimated values

of the other model parameters (if fitted from experimental data) such as the ones related to transport phenomena. It is thus important to develop appropriate elementary kinetic models for robust optimization of the other model parameters (Franco, 2010).

First principles or *ab initio* calculations (such as the DFT method) can be used to predict important quantities such as adsorbate atomic structures and bonding energies and provide key information on the reaction mechanisms and pathways. This includes the determination of the controlling elementary reaction pathways and intrinsic kinetics involved in the ORR over Pt and Pt-based alloys and their potential-dependent behavior (Figure 1.18a). This is also related to the understanding of the influence of the reaction environment including the surface coverage, alloy composition, solution phase, and electrochemical potential. In this context, DFT has been largely used to explore different PEMFC reactions in the absence of interfacial electric field (e.g., ORR) (Wang and Balbuena, 2005a,b). However, a complete description of ORR kinetics from first principles calculations for pure Pt and PtM surfaces is still missing, and the influence of the nanoparticles morphology and the surrounding EDL structure (strongly influenced in turn by the micro and mesoscopic transport phenomena of reactants, charges, and water inside the electrodes) onto the effective ORR kinetics is not solved yet.

A multiscale modeling approach to close the gap between the DFT data and the realistic catalyst behavior in PEMFC environments has been reported (de Morais et al., 2011). By using DFT calculations, thermodynamically favorable reaction steps

	E_{act}
$O_{2(s)} + s \leftrightarrow 2O(s)$	30
$H_{(s)} + O_{2(s)} \leftrightarrow O_2H_{(s)} + s$	38
$O_{(s)} + H_{(s)} \leftrightarrow OH_{(s)} + s$	88
$OH_{(s)} + H_{(s)} \leftrightarrow H_2O_{(s)} + s$	19
$O_2H_{(s)} + H_{(s)} \leftrightarrow H_2O_{2(s)} + s$	24
$O_2H_{(s)} \leftrightarrow OH_{(s)} + O_{(s)}$	2
$OH_{(s)} + OH_{(s)} \leftrightarrow H_2O_{(s)} + O_{(s)}$	1
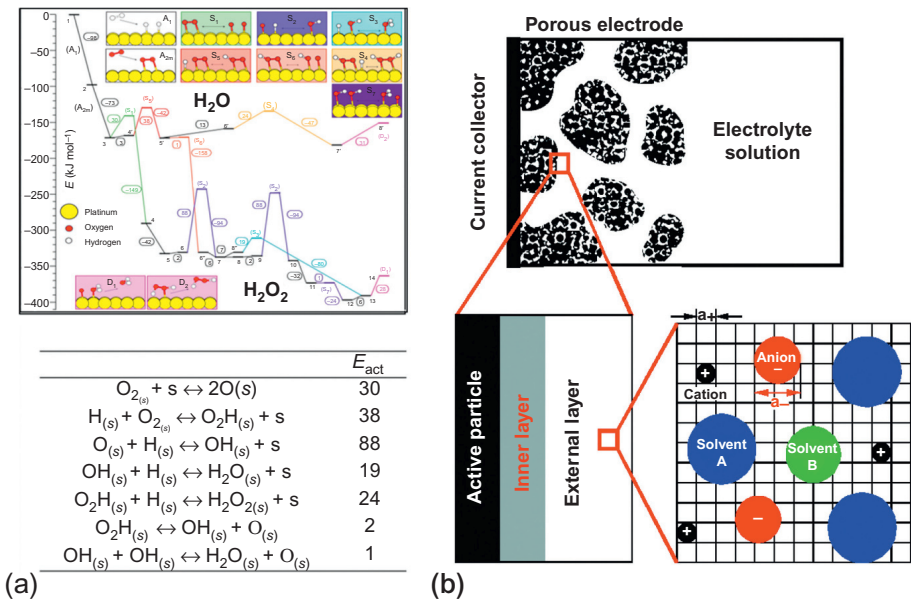
Figure 1.18 (a) Elementary kinetic steps detected as the most favorable ones for the ORR on Pt(111) with the associated activation energies (schematics built from de Morais et al., 2015; Franco, 2013d) and (b) recently reported EDL model developed on the basis of the statistical mechanics (from Quiroga et al. (2014)).

are detected, and the associated activation energies calculated: the related chemical and electrochemical processes are modeled by series–parallel elementary kinetic steps (e.g., O_2 dissociation followed by the H_2O formation), and Pt nanoparticles are modeled by a Pt(111) surface. For instance, this model neglects side effects (i.e., edge of sites on a nanoparticle and kink sites). Although not perfect, this approach is still sufficient enough for predicting relevant CL potential evolution trends. Full elementary kinetic modeling of reactions on 3D nanoparticles still remains a great challenge, at least for atomistic theoretical studies (Wang et al., 2009; Neurock, 2003; Calle-Vallejo et al., 2014, 2015). The calculated energy barriers are used to estimate the kinetic rate constants for each single reaction step involved in the ORR. A MF approach can be used to build the elementary kinetic model and describe the rate of the individual reactions in the CL.

A general EDL theory has been reported that applies to a large diversity of types of electrolytes used in electrochemical power generators, such as batteries, fuel cells, and super capacitors (Figure 1.18b) (Quiroga et al., 2014). The theory describes how interfacial electrolyte/electrode redox reactions impact the EDL structure (charge distribution) and, conversely, how the EDL structure affects the effectiveness of the interfacial redox reactions. The model applies for PEMFC, batteries, and ionic liquids, and any application where the complexity of involved species in the EDL makes it difficult to be treated with simpler models. In the case of PEMFC, the EDL complexity is due to the amount of different types of sulfonic acid groups involved that one can have, plus all the intermediary species in the ORR. In the ionic liquids case, the EDL complexity is due to the high electrolyte concentration bringing a huge amount of energy per second with large electric field values. The comparison between this theory and the ones previously reported can be summarized as follows:

- Classical description of the EDL neglects size effects of different adsorbed species and introduces semiempirical assumptions in considering the electric permittivity. The theory reported by the authors accounts for the size effects and relative size effects and calculates explicitly the impact of its electrostatic properties onto the effective interfacial reaction kinetics.
- Classical Poisson–Nernst–Planck (PNP) approaches consider electric permittivity as constant along the external layer (classically called diffuse layer). The theory reported by the authors explicitly calculates the electric permittivity along the EDL as function of the electrolyte composition. Moreover, the theory recovers the classical PNP equations in the range of diluted solutions at high electric field.

The theory opens a new perspective on scaling up DFT data into elementary kinetic models.

1.3.4.3 Cell models

From an engineering perspective, the use of continuum modeling represents an elegant way of tackling the competition and synergies between these mechanisms at the macroscopic level (Weber et al., 2014). In general, it is important to develop modeling tools that can evaluate the relative impact of each single scale onto the overall efficiency of the PEMFC. Continuum modeling consists on mathematically

describing electrochemical, transport, and thermomechanical mechanisms in the cells through a set of ordinary differential equations and partial differential equations. Depending on the aspects studied and the assumptions considered, this arises to mathematical problems of different levels of complexity to be solved numerically.

The number and complexity of the processes in the MEA together with sophisticated geometries of the flow fields almost inevitably lead to two- or three-dimensional CFD models. For instance, such models are used to investigate the effects of different components, flow channel designs, and operational parameters on the PEMFC performance in conditions close to the application level (Figure 1.19) (Ferng and Su, 2007; Tiss et al., 2014; Haddad et al., 2013; Amirfazli et al., 2014).

A finite element model was developed by Carral and Mele to investigate the influence of the assembly phase of MEA stacks on the mechanical state of the active layer (MEAs) (Carral and Mele, 2014). Validated by experimental measurements, this model offers the possibility to analyze the influence of different parameters through the use of a complete parametric set, such as the number of cells and their position in the stack. The simulations show that a better uniformity of the MEA compression is obtained with the greatest number of cells and at the center of the stack. The finite element analysis is finally found to be an effective tool to show the influence of the assembly on the performance of PEMFCs, and can support engineers to ensure the uniformity of the MEA mechanical strain within the stack.

Malek and Franco have proposed a multiscale approach to combine CGMD capabilities with a cell model for the simulation of the feedback between detailed electrochemistry and transport with materials aging mechanisms (Malek and Franco, 2011), which means that at each numerical simulation time step, the model describes how the calculated local conditions impact local materials degradation kinetics, simultaneously to how the materials' degradation affects, in the next time step, the local conditions (Figure 1.20).

CGMD simulations of a PEMFC electrode have been used to build a structural database for electrodes with different C contents in terms of interpolated mathematical
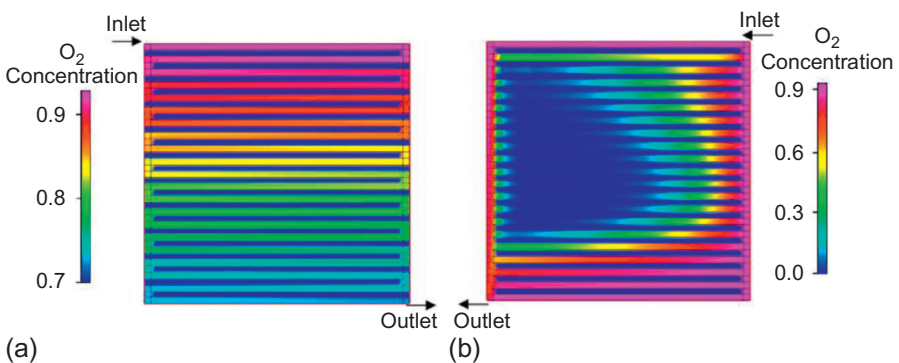
Figure 1.19 Calculated O_2 concentration in the cathode flow channel: (a) serpentine and (b) parallel.
From Ferng and Su (2007).
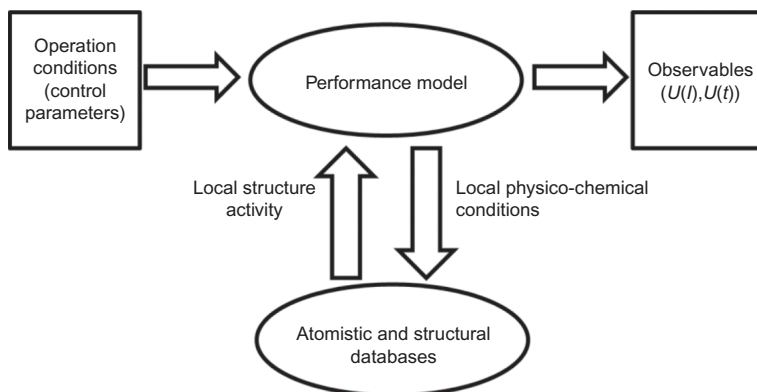
Figure 1.20 Multiscale modeling approach for the prediction of PEFMCs durability. From Malek and Franco (2011).

functions describing the impact of the C mass loss (induced by corrosion) on the evolution of the ionomer coverage on Pt and C, the electronic conductivity of the C, the C surface area, and the Pt surface area (which reorganizes during the C corrosion process). These functions are then integrated into a cell model to simulate the impact of C corrosion on the membrane-electrodes assembly performance decay (Figure 1.21).

Franco has recently reported a new multiscale simulation tool of electrochemical cells: MS LIBER-T (Multiscale Simulator of Lithium Ion Batteries and Electrochemical Reactor Technologies) (Figure 1.22) (www.modeling-electrochemistry.com). MS LIBER-T is coded on an independent C/Python language basis, highly flexible, and portable. It is fully modular, which means that the model represents explicitly the different physical phenomena in the PEMFC as nonlinear submodels in interaction. Such an approach allows the easy modification of submodels and the testing of new assumptions keeping the mathematical structure of the model. This model

- Implements algorithmic methods for the direct (on the fly) couplings between atomistic models (kMC for the electrochemical reactions, for instance) and continuum models (for instance, ionic transport across the EDL and reactants and products transports across the cell electrodes) (Quiroga and Franco, 2015). Thanks to these on the fly couplings, the model is built to allow investigating the impact of the catalyst surface heterogeneities (e.g., defects in the catalyst, adspecies surface diffusion limitations) onto the overall electrode performance.
- Implements effective microstructurally resolved models of water and reactants transport in the electrodes (pore size distribution-based).
- Implements a new nonequilibrium EDL model as described above.

1.3.5   The future

Several cost and durability challenges need still to be overcome for the widespread application of PEMFC. For instance, because of the numerous competing mechanisms at multiple scales, the design of these cells presents a complex optimization problem where different scales have to be considered simultaneously.
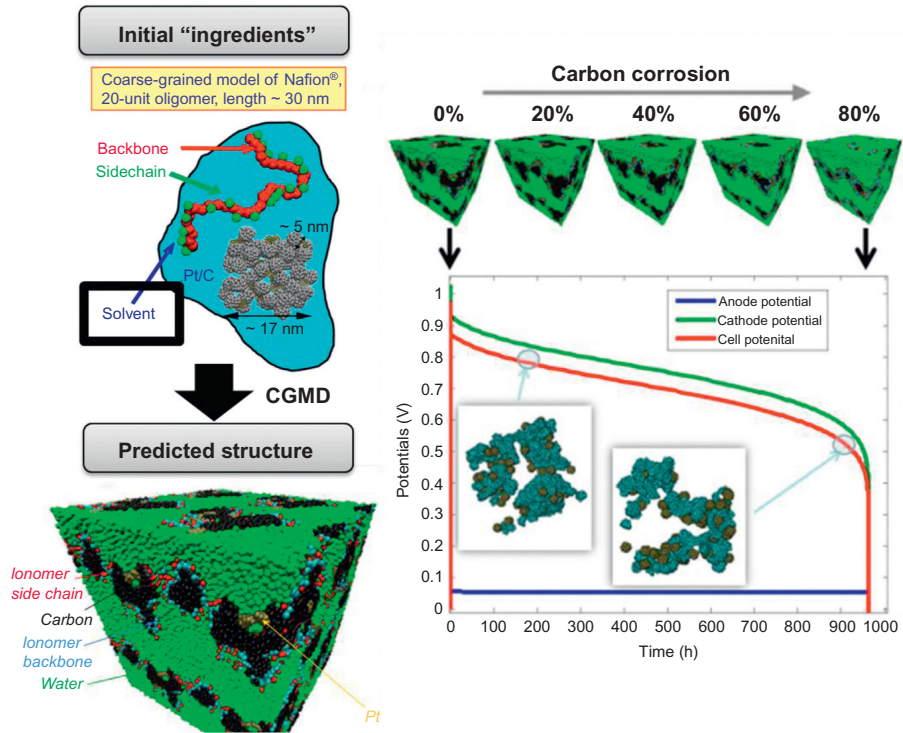
Figure 1.21 CGMD model of cathode carbon corrosion in PEMFCs and the associated prediction of performance decay by using a cell model.
Adapted from Malek and Franco (2011).

Thanks to the development of modern computational science over the past few decades, modeling and numerical simulation are now well established as powerful tools for *in silico* studies of mechanisms and processes in PEMFCs. Several application examples at both atomistic and macroscopic models have been reviewed in this section.

Moreover, the so-called multiscale modeling approaches allowing linking the chemical/microstructural properties of materials and components with their macroscopic efficiency also have been discussed. In combination with dedicated experiments, they can potentially provide tremendous progress in designing and optimizing the next-generation battery cells. Multiscale models aim, by construction, to considerably reduce empirical assumptions beyond what can be done in simple multiphysics models. This is because they explicitly describe mechanisms in scales neglected in the simple multiphysics model. These approaches utilize very powerful tools to bridge the gaps between the chemical/structural properties of materials, the components, and the efficiency of electrochemical power generators (Lopes Oliveira et al., 2012; Xue et al., 2014, 2015; Quiroga and Franco, 2015). These models already have been used to scale up the detailed chemical and structural properties of functional nanomaterials (through elementary kinetic models based on DFT
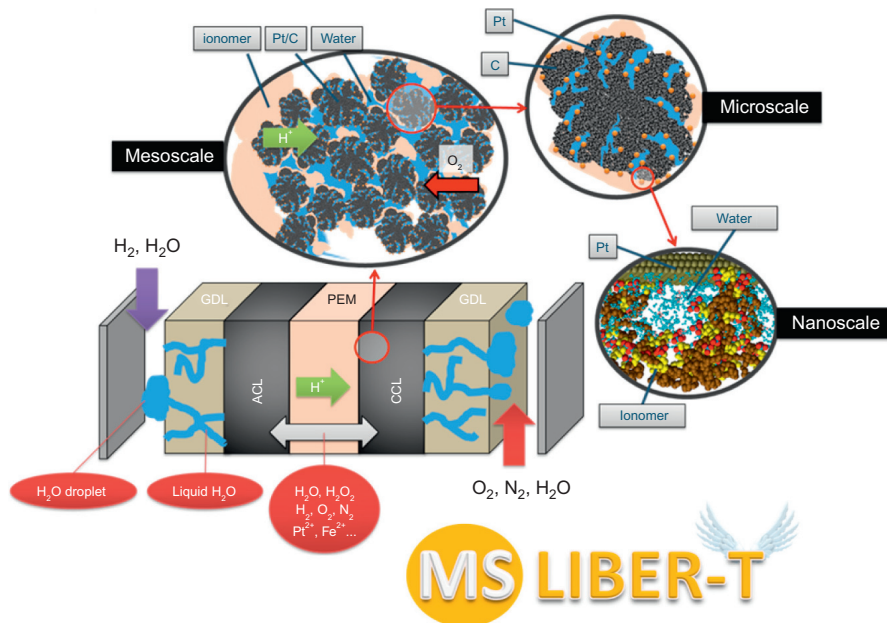
Figure 1.22 MS LIBER-T multiscale platform applied to PEMFCs.

parameters) onto complete cell simulators. New applications of these models are now emerging thanks to the straightforward knowledge transfer from the PEMFC field. For example, it has been used to predict the impact of particle-size and pore-size distributions on battery performance and durability (Figure 1.23).

Usually models need parameters fitting, through a code using a particular algorithm to optimize the parameter values to fit the calculated observables (e.g., cell potential) to experimental data. This process is done at a fixed set of physical assumptions associated to a model. Next generation of models will need the deployment of automata algorithms developing, testing, comparing with experimental data and optimizing multiple (evolutive) generations of models. In such a type of automata, we may imagine a master routine which automatically changes the physics of a model and then subroutines which optimize the parameters values in each model generation (Figure 1.24). These types of automata already exist in computer science, but still no major contribution is present for the field of PEMFCs.

Furthermore, to complement the modeling efforts themselves, an exploration of multiscale models through three-dimensional visualization with interaction in an informed virtual environment should allow (1) a better exploitation and understanding of the simulated three-dimensional electrode structures; (2) interactive, efficient, and fast simulations in real time; (3) a spread out of these new models for industry; and (4) provision of a powerful didactic tool for teaching purposes. Immersion in a virtual reality center is a powerful way to navigate through invisible or complex data

(a)

(b)

(c)
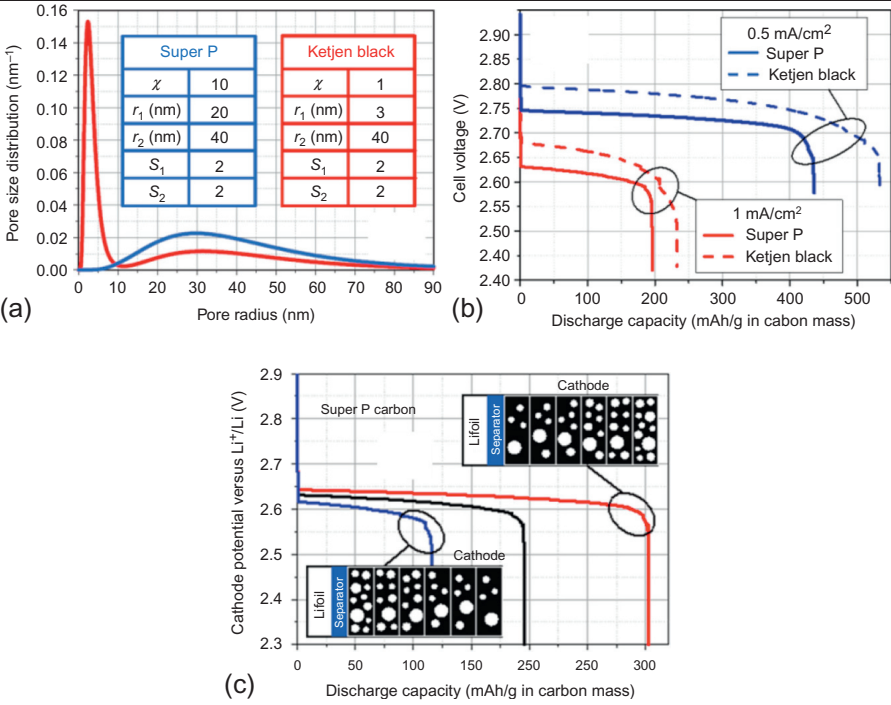
Figure 1.23 Model MS LIBER-T used for (a and b) the prediction of the performance of lithium air battery for different positive electrode structures (Ketjen Black vs. Super P carbons); (c) different pore size distributions and gradients along the electrode thickness. From Xue et al. (2014).
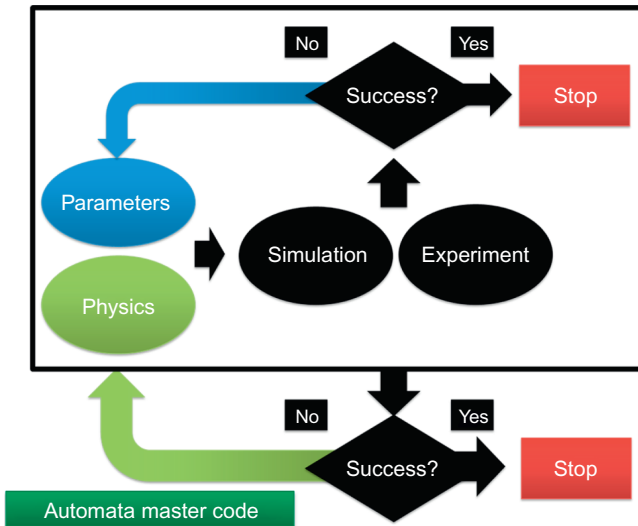
Figure 1.24 An automata algorithm for physics optimization.
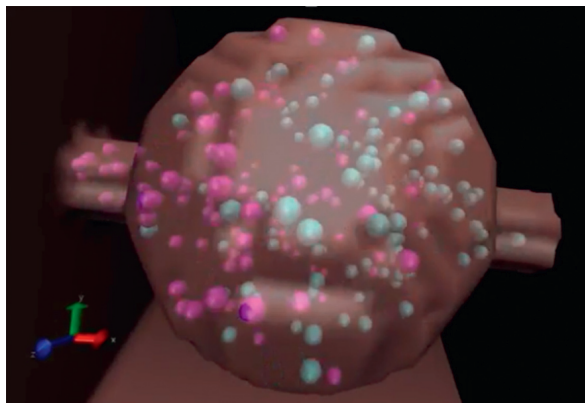
Figure 1.25 Example of virtually generated pore and associated simulation of ionic transport in a lithium air battery electrode (Blanquer et al., 2015).

(Figure 1.25). Multiphysical and multiscale electrode structures can be then explored with gradual complexity with adaptive guiding. It should be noticed that such a virtual environment has never been reported before in the modeling community of electrochemistry, and developments in this sense have been recently started at UPJV and UTC in Picardie Region, France (Franco et al., 2014).

Finally, a combination of multiscale modeling with statistical tools allowing understanding of how the uncertainties on a fabrication process (e.g., error percentage on an electrode formulation) propagates on the final product design performance, and durability appears to be strongly needed by the PEMFC industry to ensure the reliability of their products in the market.

Only multidisciplinary actions combining physics, chemistry, mathematics, informatics, and engineering skills will allow facing these major challenges for PEMFC modeling.

References

Aaltonen, T., Ritala, M., Sajavaara, T., Keinonen, J., Leskela, M., 2003. Chem. Mater. 15, 1924–1928.

Aaltonen, T., Ritala, M., Tung, Y.-L., Chi, Y., Arstila, K., Meinander, K., Leskelä, M., 2004. J. Mater. Res. 19, 3353–3358.

Amirfazli, A., 2014. J. Power Sources 268, 533.

Antoine, O., Bultel, Y., Durand, R., 2001. J. Electroanal. Chem. 499 (1), 85.

Antolini, E., Giorgi, L., Pozio, A., Passalacqua, E., 1999. J. Power Sources 77, 136–142.

Ban, S., Malek, K., Huang, C., 2013. J. Power Sources 221, 21.

Bender, G., Zawodzinski, T.A., Saab, A.P., 2003. J. Power Sources 124, 114–117.

Bernardi, D.M., Verbrugge, M.W., 1991. AIChE J. 37, 1151.

Bernardi, D.M., Verbrugge, M.W., 1992. J. Electrochem. Soc. 139, 2477.

Biesheuvel, P.M., Franco, A.A., Bazant, M.Z., 2009. J. Electrochem. Soc. 156 (2), B225–B233.

Blanquer, G., Yin, Y., Quiroga, M.A., Franco, A.A., 2015. in preparation.

Bockris, J.O., Reddy, A.K.N., 1970. Modern Electrochemistry. Plenum, New York.

Bolwin, K., Giilzow, E., Bevers, D., Schnurnberger, W., 1995. Solid State Ion. 77, 324–330.

Borup, R., Meyers, J., Pivovar, B., Kim, Y.S., Mukundan, R., Garland, N., Myers, D., Wilson, M., Garzon, F., Wood, D., 2007. Chem. Rev. 107, 3904–3951.

Broka, K., Ekdunge, P., 1997. J. Appl. Electrochem. 27, 281.

Bruijn, F., Dam, V., Janssen, G., 2008. Fuel Cells 8, 3–22.

Calle-Vallejo, F., Martínez, J.I., García-Lastra, J.M., Sautet, P., Loffreda, D., 2014. Fast prediction of adsorption properties for platinum nanocatalysts with generalized coordination numbers. Angew. Chem. 126 (32), 8456–8459.

Calle-Vallejo, F., Loffreda, D., Koper, M.T., Sautet, P., 2015. Introducing structural sensitivity into adsorption–energy scaling relations by means of coordination numbers. Nat. Chem. 7 (5), 403–410.

Camara, G.A., Ticianelli, E.A., Mukerjee, S., Lee, S.J., McBreen, J., 2002. J. Electrochem. Soc. 149, A748–A753.

Carral, C., Mele, P., 2014. Int. J. Hydrogen Energy 39, 4516.

Cavalca, C.A., Arps, J.H., Murthy, M., 2001. Fuel cell membrane electrode assemblies with improved power outputs and poison resistance. US Patent No. 6,300,000.

Cha, S.Y., Lee, W.M., 1999. J. Electrochem. Soc. 146, 4055–4060.

Chan, K.Y., Ding, J., Ren, J.W., Cheng, S.A., Tsang, K.Y., 2004. J. Mater. Chem. 14, 505–516.

Chapuis, O., Prat, M., Quintard, M., Chane-Kane, E., Guillot, O., Mayer, N., 2008. J. Power Sources 178, 258.

Cheng, X., Yi, B., Han, M., Zhang, J., Qiao, Y., Yu, J., 1999. J. Power Sources 79, 75–81.

Cheng, X., Shi, Z., Glass, N., Zhang, L., Zhang, J.J., Song, D., Liu, Z.S., Wang, H., Shen, J., 2007. J. Power Sources 165, 739–756.

Couenne, F., et al., 2008. Structured modeling for processes: a thermodynamical network theory. Comput. Chem. Eng. 32 (6), 1120–1134.

Cunningham, N., Irissou, E., Lefevre, M., Denis, M.C., Guay, D., Dodelet, J.P., 2003. Electrochem. Solid State Lett. 6, A125–A128.

Damasceno Borges, D., Franco, A.A., Malek, K., Gebel, G., Mossa, S., 2013a. ACS Nano 7 (8), 6767–6773.

Damasceno Borges, D., Malek, K., Mossa, S., Gebel, G., Franco, A.A., 2013b. ECS Trans. 45, 101.

Darling, R.M., Meyers, J.P., 2003. J. Electrochem. Soc. 150, A1523.

de Morais, R., Loffreda, D., Sautet, P., Franco, A.A., 2011. Electrochim. Acta 56 (28), 10842–10856.

de Morais, R., Franco, A.A., Sautet, P., Loffreda, D., 2015a. Coverage-dependent thermodynamic analysis of the formation of water and hydrogen peroxide on a platinum model catalyst. Phys. Chem. Chem. Phys. 17 (17), 11392–11400.

de Morais, R., Franco, A.A., Sautet, P., Loffreda, D., 2015b. Interplay between reaction mechanism and hydroxyl species for water formation on Pt (111). ACS Catal. 5 (2), 1068–1077.

Eberle, D., Horstmann, B., 2014. Electrochim. Acta 137, 714–720.

Eikerling, M., 2006. Water management in cathode catalyst layers of PEM fuel cells. A structure-based model. J. Electrochem. Soc. 153 (3), E58–E70.

Eikerling, M., Kornyshev, A.A., Kulikovsky, A.A., 2007. Physical modeling of fuel cells and their components. In: Bard, A.J., Stratmann, M., Macdonald, D., Schmuki, P. (Eds.), Encyclopedia of Electrochemistry, vol. 5. Electrochemical Engineering, VCH-Wiley, Weinheim, p. 447.

El Hannach, M., Kjeang, E., 2014. J. Electrochem. Soc. 161 (9), F951.

El Hannach, M., Pauchet, J., Prat, M., 2011. Pore network modeling: application to multiphase transport inside the cathode catalyst layer of proton exchange membrane fuel cell. Electrochim. Acta 56 (28), 10796–10808.

Ferng, Y., Su, A., 2007. Int. J. Hydrogen Energy 32, 4466.

Franco, A.A., 2010. A multiscale modeling framework for the transient analysis of PEMFCs—from theory to the engineering practice. Habilitation to become Research Director (H.D.R.) manuscript. Université Claude Bernard Lyon-1, France. Available for download in www.modeling-electrochemistry.com.

Franco, A.A., 2012. PEMFC degradation modeling and analysis. In: Hartnig, C., Roth, C. (Eds.), Polymer Electrolyte Membrane and Direct Methanol Fuel Cell Technology (PEMFCs and DMFCs), vol. 1. Fundamentals and Performance, Woodhead, Cambridge, UK.

Franco, A.A., 2013b. RSC Adv. 3 (32), 13027–13058.

Franco, A.A., 2013c. Toward a bottom-up multiscale modeling framework for the transient analysis of PEM Fuel Cells operation. In: Franco, A.A. (Ed.), Polymer Electrolyte Fuel Cells: Science, Applications and Challenges. Pan Stanford Distributor: Francis & Taylor.

Franco, A.A., 2013d. Multiscale modeling methods for electrochemical energy conversion and storage. In: Kondov, I., Sutmann, G. (Eds.), Multiscale Modeling Methods for Applications in Materials Science. CECAM-FZ Jülich IAS Series, vol. 19. ISBN : 978-3-89336-899-0 Germany.

Franco, A.A., 2013e. Polymer Electrolyte Fuel Cells: Science, Applications and Challenges. Francis & Taylor, Pan Stanford Distributor.

Franco, A.A., 2014a. Multiscale modeling. In: Kreysa, G., Ota, K., Savinell, R.F. (Eds.), Encyclopedia of Applied Electrochemistry. Springer, New York, pp. 1320–1334.

Franco, A.A., 2014b. Physical modeling and numerical simulation of direct alcohol fuel cells. In: Corti, H.R., Gonzalez, E.R. (Eds.), Direct Alcohol Fuel Cells. Springer, Netherlands, pp. 271–319.

Franco, A.A., et al., 2014. MASTERS Project (Region Picardie).

Frumkin, A., 1933. Z. Phys. Chem. Abt. A 164, 121.

Gaiselmann, G., et al., 2014. J. Power Sources 257, 52.

Gloaguen, F., Leger, J.M., Lamy, C., 1997. J. Electrochem. Soc. 27, 1052–1060.

Gostick, J.T., Ioannidis, M.A., Fowler, M.W., Pritzker, M.D., 2007. J. Power Sources 173, 277.

Haddad, D., 2013. Int. J. Hydrogen Energy 38, 8550.

Hogarth, M.P., Munk, J., Shukla, A.K., Hamnett, A., 1994. J. Appl. Electrochem. 24, 85–88.

Holzapfel, G.A., Gasser, T.C., 2001. Comput. Methods Appl. Mech. Eng. 190, 4379–4403.

Hu, G., Li, G., Zheng, Y., Zhang, Z., Xu, Y., 2014. J. Energy Inst. 87, 163–169.

Iden, H., Sato, K., Ohma, A., Shinohara, K., 2011. Relationship among microstructure, ionomer property and proton transport in pseudo catalyst layers. J. Electrochem. Soc. 158 (8), B987–B994.

Ihm, J.W., Ryu, H., Bae, J.S., Choo, W.K., Choi, D.K., 2004. J. Mater. Sci. 39, 4647–4649.

Ikeda, K., Nonoyama, N., Ikogi, Y., 2010. Analysis of the ionomer coverage of Pt surface in PEMFC. ECS Trans. 33 (1), 1189–1197.

Jaouen, F., Lindbergh, G., Sundholm, G., 2002. J. Electrochem. Soc. 149, A437.

Kadjo, A.J.J., Brault, P., Caillard, A., Coutanceau, C., Garnier, J.P., Martemianov, S., 2007. J. Power Sources 172, 613–622.

Kim, C.S., Chun, Y.G., Peck, D.H., Shin, D.R., 1998. Int. J. Hydrogen Energy 23, 1045–1048.

Klaus, J.W., Sneh, O., George, S.M., 1997. Science 278, 1934–1936.

Klaus, J.W., Sneh, O., Ott, A.W., George, S.M., 1999. Surf. Rev. Lett. 6, 435–448.

Kriston, A., Pfrang, A., Popov, B.N., Boon-Brett, L., 2014. J. Electrochem. Soc. 161 (8), E3235.

Kulikovsky, A.A., 2014. Electrochim. Acta 130, 826.

Kumar, G.S., Raja, M., Parthasarathy, S., 1995. Electrochim. Acta 40, 285–290.

Lee, K., Zhang, J.J., Wang, H.J., Wilkinson, D.P., 2006. J. Appl. Electrochem. 36, 507–522.

Liang, H., Zheng, L., Liao, S., 2012. Int. J. Hydrogen Energy 37, 12860–12867.

Liang, H., Dang, D., Xiong, W., Song, H., Liao, S., 2013. J. Power Sources 241, 367–372.

Liang, H., Huaneng, S., Pollet, B.G., Linkov, V., Pasupathi, S., 2014. J. Power Sources 266, 107–113.

Lin, G.Y., He, W.S., Van Nguyen, T., 2004. J. Electrochem. Soc. 151, A1999.

Litster, S., McLean, G., 2004. J. Power Sources 130, 61–76.

Liu, C., Wang, C.-C., Kei, C.-C., Hsueh, Y.-C., Perng, T.-P., 2009. Small 5, 1535–1538.

Lopes Oliveira, L.F., et al., 2012. Phys. Chem. Chem. Phys. 14, 10215.

Malek, K., Franco, A.A., 2011. J. Phys. Chem. B 115 (25), 8088–8101.

Malek, K., Mashio, T., 2013. Atomistic and molecular modeling of degradation mechanisms in PEMFCs. In: Franco, A.A. (Ed.), Polymer Electrolyte Fuel Cells: Science, Applications and Challenges. Pan Stanford, Singapore.

Malek, K., Eikerling, M., Wang, Q., Navessin, T., Liu, Z., 2007. J. Phys. Chem. C 111, 13627.

Malek, K., Mashio, T., Eikerling, M., 2011. Microstructure of catalyst layers in PEM fuel cells redefined: a computational approach. Electrocatalysis 2 (2), 141–157.

Maric, R., Roller, J., Vanderhoek, T., 2007. Reactive spray formation of coatings and powders. BC, Canada, WO Patent/2007/045089, April 26.

Mocoteguy, P., Druart, F., Bultel, Y., Besse, S., Rakotondrainibe, A., 2007. J. Power Sources 167, 349.

Møller-Holst, S., 1996. Denki Kagaku oyobi Kogyo Butsuri Kagaku 64, 699–705.

Moore, M., Wardlaw, P., Dobson, P., Boisvert, J.J., Putz, A., Spiteri, R.J., Secanell, M., 2014. J. Electrochem. Soc. 161, E3125.

Murphy, O.J., Hitchens, G.D., Manko, D.J., 1994. J. Power Sources 47, 353–368.

Natarajan, D., Van Nguyen, T., 2001. J. Electrochem. Soc. 148, A1324.

Natarajan, D., Van Nguyen, T., 2003. J. Power Sources 115, 66.

Neurock, M., 2003. J. Catal. 216 (1–2), 73.

Niinistö, L., Ritala, M., Leskelä, M., 1996. Mater. Sci. Eng. B 41, 23–29.

Norouzifard, V., Bahrami, M., 2014. J. Power Sources 264, 92.

O'Hayre, R., Lee, S.J., Cha, S.W., Prinz, F.B., 2002. J. Power Sources 109, 483–493.

Ohma, A., Fushinobu, K., Okazaki, K., 2010. Influence of Nafion® film on oxygen reduction reaction and hydrogen peroxide formation on Pt electrode for proton exchange membrane fuel cell. Electrochim. Acta 55 (28), 8829–8838.

Paganin, V.A., Ticianelli, E.A., Gonzalez, E.R., 1996. J. Appl. Electrochem. 26, 297–304.

Park, H.S., Cho, Y.H., Cho, Y.H., Park, I.S., Jung, N., Ahn, M., Sung, Y.E., 2008. J. Electrochem. Soc. 155, B455–B460.

Passalacqua, E., Lufrano, F., Squadrito, G., Patti, A., Giorgi, L., 1998. Electrochim. Acta 43, 3665–3673.

Quiroga, M.A., Franco, A.A., 2015. A multi-paradigm computational model of materials electrochemical reactivity for energy conversion and storage. J. Electrochem. Soc. 162 (7), E73–E83.

Quiroga, M.A., Xue, K.H., Nguyen, T.K., Huang, H., Tulodziecki, M., Franco, A.A., 2014. J. Electrochem. Soc. 161 (8), E3302.

Raistrick, I.D., 1986. In: Van Zee, J.W., White, R.E., Kinoshita, K., Burney, H.S. (Eds.), The Electrochemical Society Proceedings Series. The Electrochemical Society, Pennington, NY, p. 156.

Raistrick, I.D., 1989. Electrode assembly for use in a solid polymer electrolyte fuel cell. US Patent 4,876,115.

Rajalakshmi, N., Dhathathreyan, K.S., 2007. Chem. Eng. J. 129, 31–40.

Rinaldo, S.G., Stumper, J., Eikerling, M., 2010. J. Phys. Chem. C 114, 5773.

Ritala, M., 1997. Appl. Surf. Sci. 112, 223–230.

Ritala, M., Leskelä, M., Dekker, J.-P., Mutsaers, C., Soininen, P.J., Skarp, J., 1999. Chem. Vap. Depos. 5, 7–9.

Saha, M.S., Gullb, A.F., Allen, R.J., Mukerjee, S., 2006. Electrochim. Acta 51, 4680–4692.

Sasikumar, G., Ihm, J.W., Ryu, H., 2004. J. Power Sources 132, 11–17.

Sheppard, D., Terrell, R., Henkelman, G., 2008. J. Chem. Phys. 128, 134106.

Shin, S.-J., Lee, J.-K., Ha, H.-Y., Hong, S.-A., Chun, H.-S., Oh, I.-H., 2002. J. Power Sources 106, 146–152.

Siegel, N.P., Ellis, M.W., Nelson, D.J., von Spakovsky, M.R., 2003. J. Power Sources 115, 81.

Siegel, N.P., Ellis, M.W., Nelson, D.J., von Spakovsky, M.R., 2004. J. Power Sources 128, 173.

Song, D.T., Wang, Q.P., Liu, Z.S., Navessin, T., Eikerling, M., Holdcroft, S., 2004a. J. Power Sources 126, 104–111.

Song, D.T., Wang, Q.P., Liu, Z.S., Navessin, T., Holdcroft, S., 2004b. Electrochim. Acta 50, 731–737.

Song, D.T., Wang, Q.P., Liu, Z.S., Eikerling, M., Xie, Z., Navessin, T., Holdcroft, S., 2005. Electrochim. Acta 50, 3347–3358.

Song, C., Tang, Y., Zhang, J.L., Zhang, J., Wang, H., Shen, J., McDermid, S., Li, J., Kozak, P., 2007. PEM fuel cell reaction kinetics in the temperature range of 23–120°C. Electrochim. Acta 52 (7), 2552–2561.

Springer, T.E., Zawodzinski, T.A., Gottesfeld, S., 1991. J. Electrochem. Soc. 138, 2334.

Strahl, S., Hussar, A., Franco, A.A., 2014. Electrode structure effects on the performance of open-cathode proton exchange membrane fuel cells: a multiscale modeling approach. Int. J. Hydrogen Energy 39 (18), 9752–9767.

Subbaraman, R., Strmcnik, D., Stamenkovic, V., Markovic, N.M., 2010. J. Phys. Chem. C 114 (18), 8414.

Subramaniam, C.K., Rajalakshmi, N., Ramya, K., Dhathathreyan, K.S., 2000. Bull. Electrochem. 16, 350–353.

Sun, W., Peppley, B.A., Karan, K., 2005a. J. Power Sources 144, 42.

Sun, W., Peppley, B.A., Karan, K., 2005b. Electrochim. Acta 50, 3359.

Taylor, E.J., Anderson, E.B., Vilambi, N.R.K., 1992. J. Electrochem. Soc. 139, L45–L46.

Taylor, A.D., Kim, E.Y., Humes, V.P., Kizuka, J., Thompson, L.T., 2007. J. Power Sources 171, 101–106.

Ticianelli, E.A., Derouin, C.R., Redondo, A., Srinivasan, S., 1988. J. Electrochem. Soc. 135, 2209–2214.

Tiss, F., Chouikh, R., Guizani, A., 2014. Energy Convers. Manage. 80, 32–38.

Towne, S., Viswanathan, V., Holbery, J., Rieke, P., 2007. J. Power Sources 171, 575–584.

Verbrugge, M., 1994. J. Electrochem. Soc. 141, 46–53.

Vilambi Reddy, N.R.K., Anderson, E.B., Taylor, E.J., 1992. High utilization supported catalytic metal-containing gas-diffusion electrode, process for making it, and cells utilizing it. US Patent No. 5,084,144.

Wagner, N., Kaz, T., Friedrich, K.A., 2008. Electrochim. Acta 53, 7475–7482.

Wang, Y., Balbuena, P.B., 2005a. J. Chem. Theory Comput. 1, 935–943.

Wang, Y., Balbuena, P.B., 2005b. J. Phys. Chem. B 109, 18902–18906.

Wang, Y., Wang, C.Y., 2005. Electrochim. Acta 50, 1307.

Wang, Y., Wang, C.-Y., 2006. Electrochim. Acta 51, 3924.

Wang, Z.H., Wang, C.Y., Chen, K.S., 2001. J. Power Sources 94, 40.

Wang, Q.P., Eikerling, M., Song, D.T., Liu, Z.S., 2004a. J. Electroanal. Chem. 573, 61.

Wang, Q.P., Eikerling, M., Song, D.T., Liu, Z.S., Navessin, T., Xie, Z., Holdcroft, S., 2004b. J. Electrochem. Soc. 151, A950.

Wang, Q.P., Song, D.T., Navessin, T., Holdcroft, S., Liu, Z.S., 2004c. Electrochim. Acta 50, 725–730.

Wang, L., Roudgar, A., Eikerling, M., 2009. J. Phys. Chem. C 113, 17989.

Weber, M.F., Mamiche-Afare, S., Dignam, M.J., Pataki, L., Venter, R.D., 1987. J. Electrochem. Soc. 134, 1416–1419.

Weber, A.Z., et al., 2014. A critical review of modeling transport phenomena in polymer–electrolyte fuel cells. J. Electrochem. Soc. 161 (12), F1254–F1299.

Wee, J.H., Lee, K.Y., Kim, S.H., 2007. J. Power Sources 165, 667–677.

Wilson, M.S., 1993. Membrane catalyst layer for fuel cells. US Patent 5,234,777.

Wilson, M.S., Gottesfeld, S., 1992. J. Appl. Electrochem. 22, 1–7.

Wilson, M.S., Valerio, J.A., Gottesfeld, S., 1995. Electrochim. Acta 40, 355–363.

Wu, J., Yuan, X., Martin, J., Wang, H., Zhang, J., Shen, J., Wu, S., Merida, W., 2008. J. Power Sources 184, 104–119.

Wu, H., Li, X., Berg, P., 2009. On the modeling of water transport in polymer electrolyte membrane fuel cells. Electrochim. Acta 54 (27), 6913–6927.

Wu, R., Liao, Q., Zhu, X., Wang, H., 2012. Int. J. Hydrogen Energy 37 (15), 11255–11267.

Xie, J., Garzon, F., Zawodzinski, T., Smith, W., 2004. J. Electrochem. Soc. 151, A1841–A1846.

Xue, K.H., Nguyen, T.K., Franco, A.A., 2014. Impact of the cathode microstructure on the discharge performance of lithium air batteries: a multiscale model. J. Electrochem. Soc. 161 (8), E3028–E3035.

Xue, K.H., McTurk, E., Johnson, L., Bruce, P.G., Franco, A.A., 2015. A comprehensive model for non-aqueous lithium air batteries involving different reaction mechanisms. J. Electrochem. Soc. 162 (4), A614–A621.

Xing, L., et al., 2014. Int. J. Hydrogen Energy 39, 9087.

Yin, K.M., 2005. J. Electrochem. Soc. 152, A583.

Yousfi-Steiner, N., Moçotéguy, P., Candusso, D., Hissel, D., 2009. J. Power Sources 194, 130–145.

Yu, Y., Li, H., Wang, H., Yuan, X., Wang, G., Pan, M., 2012. J. Power Sources 205, 10–23.

Zhang, J., 2008. PEM Fuel Cell Electrocatalysts and Catalyst Layers: Fundamentals and Applications. Springer, Canada. doi:10.1007/978-1-84800-936-3.

Zhang, J., Tang, Y., Song, C., Cheng, X., Zhang, J., Wang, H., 2007. PEM fuel cells operated at 0% relative humidity in the temperature range of 23–120°C. Electrochim. Acta 52 (15), 5095–5101.

Zhang, S., Yuan, X., Hin, J., Wang, H., Friedrich, K., Mathias Schulze, M., 2009. J. Power Sources 194, 588–600.

Zhang, X., Ostadi, H., Jiang, K., Chen, R., 2014. Electrochim. Acta 133, 475.

Phosphoric acid fuel cells

2

D.E. Eapen*, S.R. Suseendiran*, R. Rengaswamy*, †
*IIT Madras, Chennai, India, †Clarkson University and Texas Tech University, Lubbock, TX, USA

2.1 Introduction

Phosphoric acid fuel cell (PAFC) is the most commercially advanced technology among the hydrogen–oxygen fuel cells. Research on the high-temperature hydrogen fuel cell began in the 1960s leading to the development of PAFCs. The PAFC differs from other fuel cell technologies mainly on the basis of the electrolyte used and the method of hydrogen generation for the cell reaction. Liquid phosphoric acid (PA) dispersed in a silicon carbide matrix acts as the electrolyte. This enables the working of PAFC at temperatures in the range of 160–220 °C. The higher temperature operation helps overcome many of the limitations of lower temperature fuel cells such as water management, high activation losses, and slow reaction kinetics. Higher temperature also permits the use of hydrogen directly from the reformer. Moreover CO poisoning of the platinum catalyst is also reduced. PA can tolerate CO_2 to any extent and CO to about 1–2 % accompanying the reformed hydrogen fuel.

PAFCs have been found useful in stationary power distribution, defense, and military applications. Heat and power cogeneration is another major advantage. In spite of these advantages, PAFC technology is constrained by various factors. Use of precious metal electrocatalyst makes it costly. The system weight is high owing to the use of heavier materials for bipolar plates. The power density of the PAFC systems is therefore low. These characteristics are discussed further in this chapter. PAFC performance in transport applications has been found to be less than optimal. This chapter aims at providing an overview of the principles behind the operation of PAFC, its various components, mathematical models available, and the performance characterization. Future developments possible for PAFC are also discussed.

2.2 Working

PAFC is an electrochemical cell, where the chemical energy of the fuel (hydrogen being the most common) is converted into electrical energy. The basic construction is similar to any other fuel cell. Liquid PA dispersed in silicon carbide medium acts as the electrolyte, which is packed between two platinum-coated carbon electrodes connected externally through a load. The catalyst is bound to the electrode with PTFE binder, which is also hydrophobic and inhibits the electrolyte from filling the electrode. Hydrogen fuel is supplied to the anode where oxidation occurs, producing protons and electrons. Electrons travel through the external circuit to the cathode. PA, being a good ionic conductor, carries the protons to the cathode side. Air or oxygen
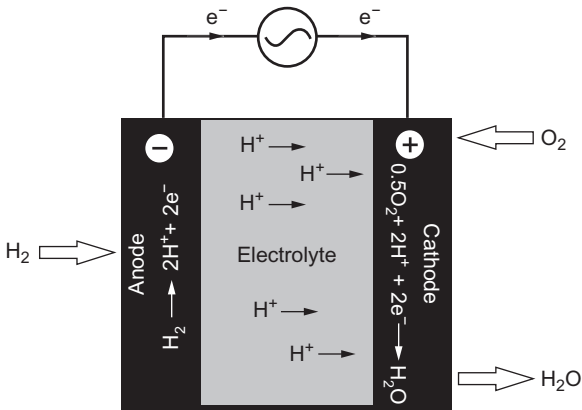
Figure 2.1 Basic elements of a fuel cell.

is sent to the cathode where the oxygen reduction reaction (ORR) consumes the proton and the electron.

Hydrogen is the most common fuel and atmospheric air is used as oxidant. A simple representation of PAFC working is depicted in Figure 2.1. The following reactions occur at the electrodes

Anode:	$H_2 \rightarrow 2H^+ + 2e^-$
Cathode:	$\frac{1}{2}O_2 + 2H^+ + 2e^- \rightarrow H_2O$
Overall:	$H_2 + \frac{1}{2}O_2 \rightarrow H_2O$

The potential produced in a single cell is low and in order to obtain specific power outputs, a sufficient number of cells are stacked in series or parallel. Further details of the working components and their characteristics are described in the following sections.

2.3 Components

The voltage output of an individual PAFC is in the range of 0.6–0.8 V. Thus, the actual fuel cell system would be a combination of several cells connected in series forming a stack. The structure of a PAFC stack is a bit more complex than the single cell described in Section 2.2. The single cells are combined in series using bipolar plates. One side of the bipolar plate forms the anode flow field for one cell and the other side forms the cathode flow field for the adjacent cell. Each cell has a silicon carbide matrix containing the electrolyte (PA) sandwiched between the anode and the cathode preventing direct contact between them. The catalyst layer is bound to the gas diffusion layer using PTFE binder forming the gas diffusion electrode (GDE). The gas diffusion layers are attached to the bipolar plate which acts as the current collector and supplies the fuel and oxidant to the cells. The cross-sectional view of a PAFC cell is depicted in Figure 2.2.
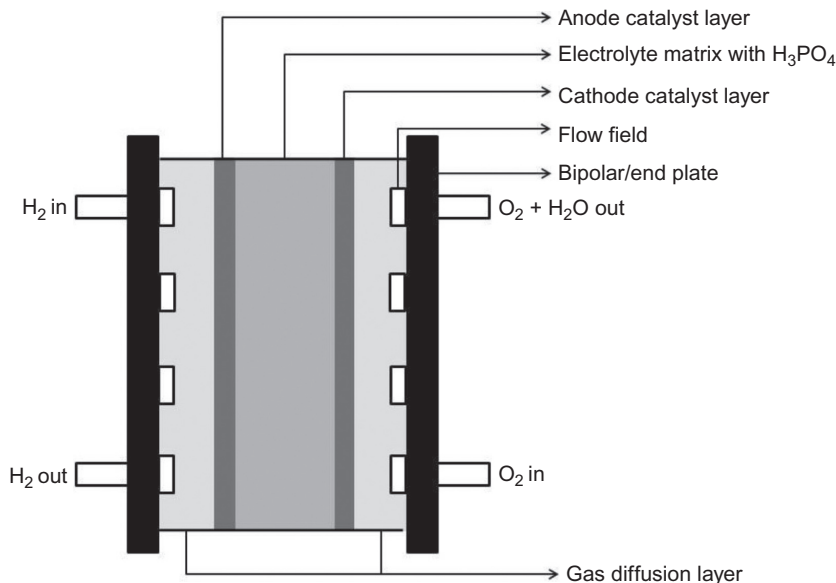
Figure 2.2 Components of a phosphoric acid fuel cell.

2.3.1 *Gas diffusion electrodes*

The GDEs comprises of a highly porous carbon cloth or carbon paper, which is bonded to the catalyst layer using polytetrafluoroethylene (PTFE). This PTFE not only acts as the binder but also imparts hydrophobicity to the GDEs. The GDE has porosity in the range 40–60 % with a PTFE content in the range 30–50 % (Giordano et al., 1990). The hydrophobicity of the GDE is to prevent the acid from blocking the pores so that the reactant gases can penetrate the pores and form a three-phase boundary with the catalyst surface and the electrolyte.

Both the anode and the cathode use platinum as the catalyst. However, the electrodes differ in terms of platinum loading and the alloying elements. The cathode ORR is slower than the hydrogen oxidation reaction at the anode. Hence, a higher loading of around $0.5 \, \text{mg/cm}^2$ is required at the cathode side compared to a platinum loading of nearly $0.1 \, \text{mg/cm}^2$ on the anode side.

The anode catalyst should be tolerant to catalyst poisons like CO, H_2S, and so on which may be present in the fuel supplied (Stonehart, 1992). To prevent deactivation of catalyst in the presence of these poisons, Palladium (Stonehart, 1984a) or Ruthenium (Ross et al., 1975) is loaded along with platinum in the anode catalyst layer. The inclusion of small amounts of oxygen in the fuel stream can also help eliminate the CO poisoning.

The ORR kinetics can be improved by alloying platinum with transition elements such as vanadium, chromium, cobalt, iron, or copper. Pt–V (Jalan, 1980) and Pt–Cr (Landsman et al., n.d.) were found to be the best combination among the binary alloys. During the operation of the fuel cell the non-platinum metal of the alloy leaches out

and goes into the PA leaving behind the high surface area platinum. Better kinetics observed for the ternary alloys such as Pt–Co–Cr (Landsman and Luczak, 1991) and Pt–Cu–Fe (Roh et al., 1996) are due to the decrease in the interatomic distances in the catalyst particles. The alloy structure has significant influence on the stability of the catalyst particles. The dissolution of the non-platinum metal is more in the disordered structure than the ordered structure during the initial operation of the cell. But, after several hours of operation, the disordered structure was observed to be more stable than the ordered structure.

2.3.2 Electrolyte and matrix

High-concentration PA retained in porous silicon carbide (SiC) matrix is employed as the electrolyte because of its low vapor pressure at the operating temperature range of PAFC. The main purpose is to transfer protons from the anode to the cathode and to physically separate the two electrodes. The PA electrolyte is also tolerant to trace amounts of CO and H_2S. PTFE binds the SiC particles and also provides the hydrophobic zones to the matrix. The inclusion of materials like zirconium silicate ($ZrSiO_4$), niobium carbide (NiC) (Caires et al., 1997), and zirconium phosphate ($Zr_3(PO_4)_4$) (Neergat and Shukla, 2001) improves the performance of the fuel cell.

Performance is better for SiC slurry prepared by ball milling (Dheenadayalan et al., 2002) than that by mechanical stirring. Polyethersulfone (PES) (Yoon et al., 2000) has been explored as an alternative for PTFE. Superior performance is demonstrated by PES prepared using non-volatile solvent (n-methyl-2-pyrrolidone) (Yoon and Yang, 2003) compared to PES prepared using a volatile solvent (dichloroethane). The improved performance is attributed to reduced pore sizes, which prevent reactant cross-over.

Recently, PA-doped polybenzimidazole membranes have been discovered as an alternative for the PA retained in SiC matrix. This new polymer electrolyte possesses all the advantages of the PA–SiC matrix such as CO tolerance, high-temperature operation, and so on. This electrolyte also allows the use of Pt-Ni/C as a cathode electrocatalyst. The conductivity of this membrane can be increased by increasing the PA doping levels. At 160 °C and a PA concentration of 1600 mol%, the conductivity of this electrolyte was found to be 0.13 S/cm, which is higher compared to the Nafion membrane used in PEMFCs (He et al., 2006). Studies show that the molecular weight of polybenzimidazole membrane affects the mechanical strength of the electrolyte. Higher levels of doping on low molecular weight polymer leads to reduced mechanical strength. However, higher doping level had no effect on the mechanical strength in the case of high molecular weight polymeric membrane (Lobato et al., 2007).

2.3.3 Bipolar plates

The bipolar plates in the fuel cell stack serve the purpose of supplying fuel to the anode and oxidant to the cathode and also provide the electrical conduction between the cells. Thus, the bipolar plate should have very good electrical conductivity and very low gas permeability. It needs to be very stable in the oxidative and reductive

environments. Only graphite has been successfully used as bipolar plates in PAFC. Ghouse (1998) report a bipolar plate prepared by lamination technique in which two porous graphite plates are bound to the sides of a non-porous graphite foil with PES as the binder. The flow fields for delivering hydrogen and oxygen to the catalyst layer were machined onto the porous graphite plates. An electrical resistivity of 4–14 mΩm and a gas permeability of 0.01 cm^2/s are reported for this bipolar plate.

2.4 Fuels for PAFC

Hydrogen is the main fuel used in a PAFC. The higher temperature operation of a PAFC enables the direct use of hydrogen produced by reforming hydrocarbons. While using hydrocarbon fuels, the sulfur compounds should be removed prior to reforming in order to prevent catalyst poisoning. The reformate hydrogen contains CO_2 and traces of CO, which could poison the catalyst at low temperature. PAFC is tolerant to CO_2 and it can tolerate 1–2 % of CO owing to the high temperature. Preprocessing of reformate is not needed for PAFC and it can be directly fed to the cell. The need for a reforming unit adds to the cost but is a necessity when considering the low energy density hydrogen storage, and the infrastructure available for transport of reformer fuel. Digester gas has also been used recently as fuel for PAFC.

2.5 Performance

2.5.1 Potential

PAFC has a working potential range of 0.6–0.8 V. A number of cells are stacked in parallel or series in order to provide for a particular voltage requirement. The potential varies with varying current density and also depends on a number of factors such as temperature, pressure, concentration or activity of the reactants and products, fuel and oxidant flow rates, electrode properties, electrolyte conductivity, contact resistances, and so forth (Hirschenhofer et al., 1998).

The open circuit voltage is determined by the Nernst equation. The terminal voltage obtained will be much lesser than the OCV owing to the activation losses, ohmic losses, and the concentration losses, which are strong functions of current density. Open circuit potential (OCP) is related to the Gibb's free energy as $E = -\Delta G/nF$. For a PAFC operating at a very high temperature, the OCP is expected to be lower. However, the increased reaction rates and electrode kinetics leads to lesser irreversible losses in a high-temperature PAFC.

2.5.2 Power density

Current density is defined as the amount of current produced per unit area of the electrode and is expressed in terms of A/m$_2$ or mA/cm^2. PAFCs can be operated at different current densities, with a typical range of 1000–4000 A/m^2. Typical potentials

obtained would be in the range of 0.6–0.8 V. The potential varies as current density varies. The various irreversible losses such as activation, ohmic, and concentration losses become significant at larger current densities and as a result the potential decreases rapidly with increasing current densities.

Power density for a fuel cell is the product of the working potential and the current density. It is expressed in W/m_2. A typical curve is shown in Figure 2.3. At high current densities, although power density increases to a certain extent, the potential decreases. Due to this, to achieve the required potential more cells should be added. At low current densities, although potential is satisfactorily large, the power density will be small and in order to achieve the power requirement at low currents, the electrode area should be increased.

2.5.3 Lifespan

PAFCs have a typical life span of about 40,000–50,000 h. The high-temperature operation prevents the use of Nafion membrane and hence the membrane degradation effects are lesser. Other components of the fuel cell basically consist of graphite and platinum carbon electrodes that are stable in the high temperatures (Sammes et al., 2004).
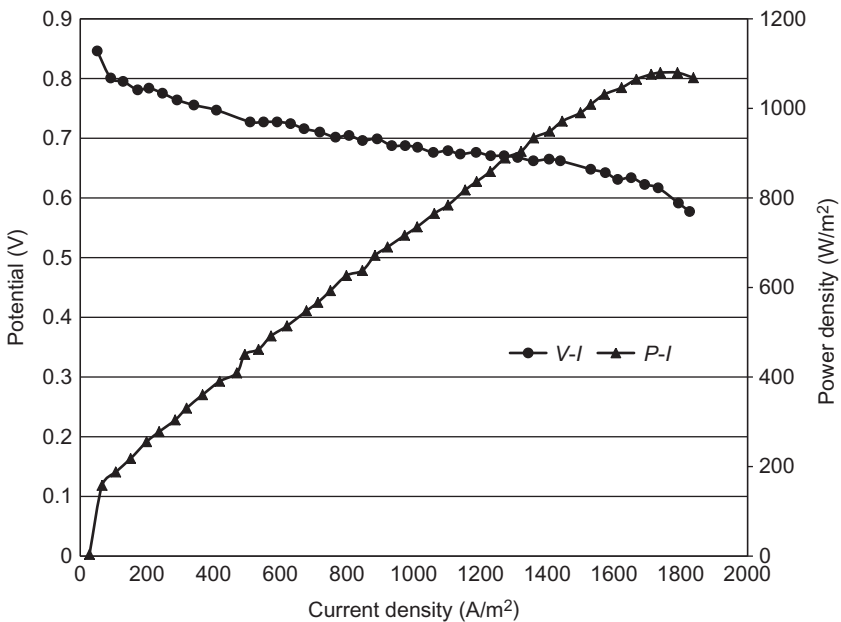
Figure 2.3 Characteristic curve (*V-I*, *P-I* plot) for PAFC.
Data from Zervas et al. (2006).

2.5.4 Efficiency

One important fuel cell specification used for performance comparison is the efficiency. There are many definitions for efficiency in the literature. The very basic definition of ratio of "energy output" to "energy input," is not very specific without a proper definition for the "energy input."

Because the reaction that takes place in a fuel cell is basically a combustion reaction (although through an electrochemical path), the enthalpy of combustion is considered as the "energy input." As ΔG is the maximum amount of electrical work obtained from the electrochemical reaction (Larmine et al., 2003), maximum efficiency or theoretical efficiency is defined as

$$\eta_{max} = \frac{\Delta G_f}{\Delta H_f} \times 100\%$$

$$= \frac{\Delta G_f/nF}{\Delta H_f/nF} \times 100\%$$

$$\eta_{voltage} = \frac{V_{OCV}}{V_{crit}} \times 100\%$$

For a PAFC operating at 200 °C this value is about 77%. This seems lower than PEMFCs, which operates at a lower temperature of 60–80 °C. However, due to irreversible losses such as activation loss, ohmic loss, and concentration loss, the actual OCV obtained will be lower than that corresponding to ΔG_f and this drop is significantly lower at higher temperatures. Thus, in practice, high-temperature PAFCs have higher efficiency than lower temperature fuel cells.

This definition of efficiency does not take into account various other information that are of importance. For example, all the fuel or oxidant supplied will not be utilized, and there is always some unreacted fuel that is lost. The voltage efficiency is multiplied by a fuel utilization factor, μ_f, which is the ratio of the fuel reacted to the fuel supplied in order to get a more informative efficiency value. This gives the ratio of the amount of current produced to the amount that would have been produced if the entire fuel supplied was utilized.

$$\eta_{cell} = \mu_f \times \eta_{voltage}$$

To draw good comparisons between various technologies, efficiency definition may need to be application dependent. For example, information about the energy used for processing the fuel to get hydrogen, should be included (one generally multiplies η_{cell} with $\eta_{process}$). Because a PAFC operates at a high temperature, hydrogen containing CO_2 and maybe CO can be directly fed to the cell. The process heat is not wasted and the electrode contamination is significantly reduced compared to PEMFC. In other words $\eta_{process}$ is large. Another important advantage of the PAFC is the useful heat cogeneration. This implies that most of the energy lost is recovered and utilized.

Because of combined power and heat generation, the PAFC can achieve very high cell efficiency, near 85%.

The parasitic energy losses due to the auxiliary systems such as pumps and sensors also should not be neglected. For stationary power generation, the grid losses, the generator or turbine losses and AC conversion losses should be considered. For automobile applications, a well-to-wheel or tank-to-wheel efficiency is defined to include the motor shaft efficiency and so on. Comparisons should be made based on an overall efficiency that can, for example, be obtained as

$$\eta_{overall} = \eta_{recovery} \times \eta_{processing} \times \eta_{cell} \times \eta_{motor}$$

2.6   Advantages and environmental impact

Generally all fuel cells are considered to be safe, silent, and pollution-free devices. When hydrogen is used as the fuel, the only by-product is water along with electricity and heat. For a high-temperature PAFC, even the heat produced as the by-product of the electrochemical reaction is utilized. A PAFC plant is capable of providing useful heat and low oxygen content air for storage rooms and other areas, along with electric power. Although at higher temperatures the OCV is expected to be low, the reduction in other reversible losses at higher temperature provides significant advantage. There are no harmful emissions or exhaust gases. The small amount of CO_2 released is well within the safety limits. Due to the high-temperature operation, the hydrogen–carbon dioxide mixture from the reformer can be directly sent to the cell stack, thereby preventing loss of useful heat to the environment. Even with the fuel processing unit, the PAFC systems are noise-free devices.

2.7   Design issues and disadvantages

The main disadvantage is the cost implications of PAFC. Use of platinum catalyst on both electrodes, graphitization of bipolar plates, auxiliary system requirement, fuel processing, overhaul maintenance, and so on makes the system expensive. The low potential associated with high temperature is another limitation. The size of PAFC also limits its application.

PAFC performance degrades over time. This loss in the performance can be seen from a voltage loss or a decreased power density as it is operated for a long time (1000 h for reference). Decrease in voltage will in turn cause a decrease in efficiency. Many experiments have been conducted to predict the factors responsible for this loss in performance. The major factors leading to the loss of PAFC performance were found to be the aggregation of platinum particles, corrosion of carbon support, and loss of electrolyte from the matrix.

2.7.1 Platinum agglomeration

Ghouse (1999) operated a PAFC at 175 °C for 1000 h. The current density obtained from the fuel cell was 175 mA/cm^2 at a voltage of 0.5 V versus RHE. The agglomerate size of the platinum particles was determined before the start of operation and also after 1000 h of operation. The agglomerate size increased from 22 to 40 Å at the anode and from 23 to 46 Å at the cathode. This increase in size corresponds to the loss in surface area of the platinum electrocatalysts, and this is the major reason for the degradation of the PAFC performance.

This increase in the crystallite size of the platinum particles is because of operating the fuel cell at OCV (0.9 vs. RHE) for about 45 min during the 1000 h of operation. This was supported by Honji (1988) who showed that the platinum dissolves into the electrolyte at a voltage above 0.8 V versus RHE and the dissolved platinum redeposit onto the cathode at a voltage of 0.9 V versus RHE. This increases the crystallite size of the platinum particles at the cathode. These deposited agglomerates migrate through the electrolyte and get deposited on the anode, thus increasing the crystallite size of platinum particles at the anode as well. So, it is not advisable to operate the cell at the OCV. While shutting down the cell it is necessary to cut down the hydrogen input and purge nitrogen to the anode side until the temperature of the cell comes down to 50 °C. The air input to the cell should be continued until the cell temperature reaches 50 °C.

2.7.2 Carbon corrosion

The morphology of the electrodes was examined by Ghouse et al. before the start of the operation of the fuel cell and also after completing 1000 h. After 1000 h of operation, cracks were observed on the electrode surface due to the corrosion of the carbon substrates. The carbon corrosion occurs in two ways. One is the formation of a surface oxide layer that keeps building up with time and cell potential. The second is the evolution of CO_2. The amount of CO_2 evolved also increases with time and cell voltage (Kinoshita and Bett, 1973). As both the CO_2 evolution and surface oxidation increases with time and cell potential, the corrosion current determined from the Tafel polarization also exhibits the same trend. Stonehart's (1984b) weight loss measurements showed that corrosion of carbon increases as time progresses. Stonehart (1984b) also determined the corrosion rate of carbon after heat treating it at various temperatures. Figure 2.4 shows how the corrosion rate changes with heat treatment temperature. The variation can be attributed to the fact that increase in the temperature of heat treatment reduces the surface area of the carbon, leading to "graphitization." This suggests that the corrosion of the carbon supports can be eliminated by graphitizing by heat treating it at higher temperatures.

2.7.3 Electrolyte depletion

The fuel and oxidant supplied to the electrodes can take the path of cracks developed on the electrodes due to carbon support corrosion and can possibly mix together. This leads to a decrease in the voltage of the fuel cell and also increases the cell
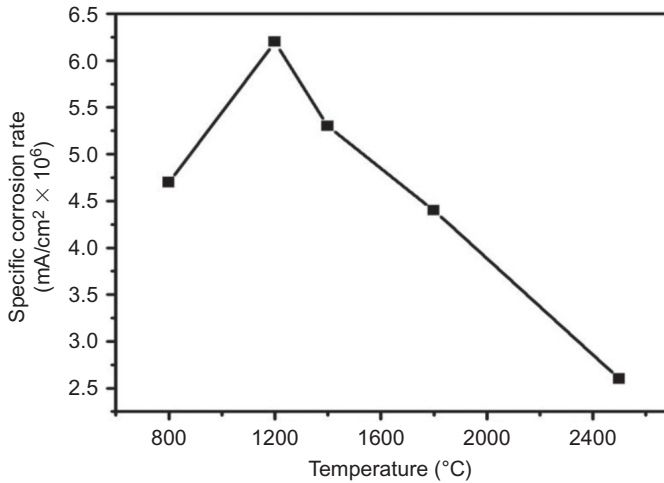
Figure 2.4 Corrosion rate of carbon versus heat treatment temperature.
Data obtained from Stonehart (1984b).

temperature. Because of this temperature rise, the electrolyte in the matrix can deplete due to evaporation, which again degrades the fuel cell performance by increasing the resistance of the cell. This electrolyte loss can be compensated by replenishing the electrolyte from the reservoir. The porous graphite plates bonded to the sides of the graphite foil in the bipolar plate is the electrolyte reservoir plate. PA can be impregnated into the pores of this plate by immersing it in 100% PA solution at 175 °C for 24 h (Ghouse, 1999).

2.7.4 Electrolyte flooding

The corrosion of the carbon support can also break the bonds between the PTFE and carbon leading to the loss of hydrophobicity of the electrodes (Alderucci et al., 1990). If the electrodes are not hydrophobic, the electrolyte can block the pores in the electrodes preventing the access of reactants to the catalyst particles. This phenomenon is known as electrolyte flooding and this is also one of the important reasons for the degradation of PAFC performance.

2.7.5 Effect of flow rate and fuel starvation

The effects of flow rate of the reactants and reactant starvation on the performance of the PAFC are studied in Song et al. (2000). The performance is increased when the flow rate of the reactants increases. When the flow of oxygen is reduced, the voltage of the cell drops suddenly at a limiting current density of 150 mA/cm^2. The concentration overpotential is increased because the decrease in the oxygen flow rate produces a sufficient demand for oxygen. The high flow rate of the reactants reduces

the OCV of fuel cells. This may be explained by the reactant cross-over through the membrane. When the supply of the reactants is cut off, the voltage of the cell gradually reduces to zero. Now if the reactants supply is restarted, the cell reaches a potential lesser than the previous potential. The change in the three-phase boundary area during reactant starvation is considered to be the possible reason for this loss in the voltage and it was found to be independent of time.

2.8 Modeling of PAFCs

General working of a PAFC is similar to a PEMFC except for the PA electrolyte, the high temperature and the corresponding influences. A number of models have been developed to simulate the phenomena in various types of fuel cells, which can be extended to PAFCs also.

Modeling of the various overpotentials, transport phenomena in the flow fields and diffusion layers, and reaction kinetics on the catalyst are similar to most fuel cells. The temperature variations can be justifiably neglected with an assumption of high and uniform temperature profile. The difficulty comes in modeling the catalyst electrode layer, where proper modeling of the three-phase contacting between the gas, electrolyte, and the solid catalyst is critical. The porous electrode theory can be modified to a flooded electrolyte theory which incorporates dual porosity to model the electrode. The carbon particles containing the platinum catalyst are bound to the electrodes with PTFE. According to the flooded electrolyte model, the carbon particles containing Pt catalyst forms agglomerates. These agglomerates are assumed to be spherical and are flooded with the electrolyte. The space between the agglomerates is only partly filled with electrolyte due to the hydrophobicity imparted by PTFE binder. The reactant diffuses through the porous electrode, reaches the agglomerate surface, and diffuses into the electrolyte in the agglomerate. Reaction happens inside the agglomerate and the product water diffuses out. This model can be effectively used for other electrodes also (Choudhury et al., 2002; Choudhury and Rengaswamy, 2006).

A 2-D steady state model for PAFC is presented in Choudhury et al. (2002) along with parameter sensitivity analysis to see dependence of current output on parameters such as Tafel slope, active catalyst area per unit volume, oxygen exchange current density and agglomerate size. The model was used for groove design, catalyst layer thickness optimization, and humidity management. A steady state three-dimensional model was used to study the effect of various parameters on the fuel cell operation (Zervas et al., 2006). The effect of current density and fuel utilization on the cell and stack potential, generated power, concentration distribution in the flow fields, and the potential distribution on the electrode surface were studied. Parameter effects on step response of a fuel cell are studied using a transient model in Choudhury et al. (2005). Various CFD techniques have been used for simulating more detailed 3-D steady state models applicable for PAFC (Zervas et al., 2008).

2.9   Applications

PAFC systems are generally used for stationary applications and are not preferred for automobile transport applications, due to the warm-up time required and the inability to provide sudden power surges for acceleration. The best efficiency for a PAFC is achieved when operated in cogeneration mode where the product heat and water are utilized for onsite heating, cooling, and hot water. They are applied in energy intensive areas such as hospitals, schools, office buildings, manufacturing centers, and similar places. In addition to electricity output, PAFC can be applied for space heating. It can also supply low oxygen content air for warehouses and other storage areas. Biogas and digester gas fuel utilization helps achieve higher revenue in farms, breweries, and so forth.

2.10   Future

Although the PAFC systems have attained a lifetime of 40,000 h, commercial deployment is still not substantial. One of the reasons is the high cost, which comes from almost all components of PAFC including fuel processor. These barriers may be mitigated to some extent if the lifetimes of PAFC systems cross 60,000 h without any further increase in the cost. Even then it is important to reduce the cost of the system. The cost of the system can be reduced by finding alternative electrocatalysts, and also by finding the alternative ways for manufacturing PAFC stacks

There is a strong demand for an alternate electrolyte that can be stable throughout the lifetime of a PAFC. PA-doped PBI membranes (He et al., 2006) can be considered as a suitable alternative for the conventional SiC matrix but it is still not well established. If the PBI-based PAFC systems are commercialized and also if they attain the required lifetime, then PAFCs can become a viable alternative for the fuel cell industry. The additional cost also comes from the carbon support, which is not stable in the PA environment. The graphitization of the carbon supports at high temperature is again a cost-intensive process, so alternative non-carbon or polymer-based supports have to be developed (Remick and Wheeler, 2010). The same applies to the bipolar plates as well.

Due to the high-temperature operation of the PAFCs, the voltage of the cell is limited to 0.8 V and this limits the power density. Therefore, the power density can be increased only by increasing the current density. This again calls for the development of alternative cathode electrocatalysts to increase the kinetics of ORR.

Efforts have been made to operate PAFC systems with anaerobic digester gas biogas, sewer digester gas, and so on, which are methane rich. This prospect has large implications for producing energy from waste. Other goals involve extending the time interval between overhaul maintenance, improving power utilization to achieve better range of applications, development of low-cost components, and finding better markets for commercialization. If the next generation PAFC can be developed with all these advancements, then PAFC systems can still be a viable alternative for stationary

and on-site power generation markets. The larger power demand as well as a need for higher quality power along with growing environmental concerns makes fuel cells a very promising technology, despite the cost limitations.

2.11 Additional sources

2.11.1 Books

EG&G Technical Services Inc., Fuel Cell Handbook, seventh ed., US Department of Energy publication, 2004, pp. 1–352.

Benjamin, T.G., Camara, E.H., Marianowski, L.G., 1980. Handbook of Fuel Cell Performance, Prepared by the Institute of Gas Technology for the US Department of Energy, under the contract number EC-77-C-03-1545, May 1980.

Vielstich, W., 1999–2014. Handbook of Fuel Cells—Fundamentals, Technology and Applications, vol. 1–6. Wiley.

Mench, M.M., Fuel Cell Engines. Wiley, pp. 1–515.

Li, X., 2005. Principles of Fuel Cells. Taylor & Francis, p. 592.

2.11.2 Web sites

www.fuelcelltoday.com
www.fuelcellindustryreview.com
www.fuelcell.org
www.doosanfuelcell.com

References

Alderucci, V., Recupero, V., Pino, L., Di Leonardo, R., Cocke, D.L., Giordano, N., Parmigiani, F., 1990. Characterization of the morphological modification induced by long term operations on phosphoric acid fuel cell (PAFC) electrodes. J. Appl. Electrochem. 20, 811–817.

Caires, M., Buzzo, M., Ticianelli, E.A., Gonzalez, E.R., 1997. Preparation and characterization of matrices for phosphoric acid fuel cells. J. Appl. Electrochem. 27, 19–24.

Choudhury, S.R., Rengaswamy, R., 2006. Characterization and fault diagnosis of PAFC cathode by EIS technique and a novel mathematical model approach. J. Power Sources 161 (2), 971–986.

Choudhury, S.R., Deshmukh, M.B., Rengaswamy, R., 2002. A two-dimensional steady-state model for phosphoric acid fuel cells (PAFC). J. Power Sources 112 (1), 137–152.

Choudhury, S., Choudhury, S., Rangarajan, J., Rengaswamy, R., 2005. Step response analysis of phosphoric acid fuel cell (PAFC) cathode through a transient model. J. Power Sources 140 (2), 274–279.

Dheenadayalan, S., Song, R.H., Shin, D.R., 2002. Characterization and performance analysis of silicon carbide electrolyte matrix of phosphoric acid fuel cell prepared by ball-milling method. J. Power Sources 107 (1), 98–102.

Ghouse, M., Aug. 1998. Fabrication and characterisation of the graphite bi-polar plates used in A 0.25 kW PAFC stack. Int. J. Hydrog. Energy 23 (8), 721–730.

Ghouse, M., 1999. Effect of the long term testing of the phosphoric acid fuel cell stacks on platinum catalyst crystallite size. J. New Mater. Electrochem. Syst. 2 (1), 79–84.

Giordano, N., Passalacqua, E., Recupero, V., Vivaldi, M., Taylor, E.J., Wilemski, G., 1990. An investigation of the effects of electrode preparation parameters on the performance of phosphoric acid fuel cell cathodes. Electrochim. Acta 35 (9), 1411–1421.

He, R., Li, Q., Bach, A., Jensen, J.O., Bjerrum, N.J., 2006. Physicochemical properties of phosphoric acid doped polybenzimidazole membranes for fuel cells. J. Membr. Sci. 277, 38–45.

Hirschenhofer, J.H., Stauffer, D.B., Engleman, R.R., Klett, M.G., 1998. Fuel Cell Handbook, 4th ed. FETC.

Honji, A., 1988. Agglomeration of platinum particles supported on carbon in phosphoric acid. J. Electrochem. Soc. 135 (2), 355.

Jalan, V.M., 1980. Noble metal/vanadium alloy catalyst and method for making. Google Patents.

Kinoshita, K., Bett, J., 1973. Electrochemical oxidation of carbon black in concentrated phosphoric acid at 135 °C. Carbon N.Y. 11, 237–247.

Landsman, D.A., Luczak, F.J., 1991. Ordered ternary fuel cell catalysts containing platinum and cobalt. Google Patents.

Landsman, I., Douglas, A., Hartford, W., Francis, J., 1983. Process using Noble Metal-Chromium Alloy Catalysts in an Electrochemical Cell. Google Patents.

Larmine, J., Dicks, A., 2003. Fuel Cell Systems Explained, 2nd ed. Wiley.

Lobato, J., Cañizares, P., Rodrigo, M.A., Linares, J.J., Aguilar, J.A., 2007. Improved polybenzimidazole films for H_3PO_4-doped PBI-based high temperature PEMFC. J. Membr. Sci. 306 (1–2), 47–55.

Neergat, M., Shukla, A.K., 2001. A high-performance phosphoric acid fuel cell. J. Power Sources 102 (1–2), 317–321.

Remick, R.J., Wheeler, D., 2010. MCFC and PAFC R&D Workshop Summary Report.

Roh, W., Cho, J., Kim, H., 1996. Characterization of Pt-Cu-Fe ternary electrocatalysts supported on carbon black. J. Appl. Electrochem. 26, 623–630.

Ross, P.N., Kinoshita, K., Scarpellino, A.J., Stonehart, P., Jul. 1975. Electrocatalysis on binary alloys. J. Electroanal. Chem. Interfac. Electrochem. 63 (1), 97–110.

Sammes, N., Bove, R., Stahl, K., 2004. Phosphoric acid fuel cells: fundamentals and applications. Curr. Opin. Solid State Mater. Sci. 8 (5), 372–378.

Song, R.H., Kim, C.S., Shin, D.R., 2000. Effects of flow rate and starvation of reactant gases on the performance of phosphoric acid fuel cells. J. Power Sources 86 (1), 289–293.

Stonehart, P., 1984a. Electrocatalyst advances for hydrogen oxidation in phosphoric acid fuel cells. Int. J. Hydrog. Energy 9 (11), 921–928.

Stonehart, P., 1984b. Carbon substrates for phosphoric acid fuel cell cathodes. Carbon N.Y. 22 (415), 423–431.

Stonehart, P., 1992. Development of alloy electrocatalysts for phosphoric acid fuel cells (PAFC). J. Appl. Electrochem. 22 (11), 995–1001.

Yoon, K.H., Yang, B.D., 2003. Preparation and characterization of matrix retaining electrolyte for a phosphoric acid fuel cell by non-volatile solvent, NMP. J. Power Sources 124 (1), 47–51.

Yoon, K.H., Choi, J.Y., Jang, J.H., Cho, Y.S., Jo, K.H., 2000. Electrode/matrix interfacial characteristics in a phosphoric acid fuel cell. J. Appl. Electrochem. 30 (1), 121–124.

Zervas, P.L., Koukou, M.K., Markatos, N.C., 2006. Predicting the effects of process parameters on the performance of phosphoric acid fuel cells using a 3-D numerical approach. Energy Convers. Manag. 47 (18–19), 2883–2899.

Zervas, P.L., Tatsis, A., Sarimveis, H., Markatos, N.C.G., 2008. Development of a novel computational tool for optimizing the operation of fuel cells systems: application for phosphoric acid fuel cells. J. Power Sources 185 (1), 345–355.

Molten carbonate fuel cells

3

M. Cassir, A. Meléndez-Ceballos, A. Ringuedé, V. Lair
PSL Research University, Paris, France

3.1 A unique molten salt fuel cell

Although the first attempt to use molten salts in energy devices such as fuel cells was made about a century ago, it is only in the last few decades that the molten carbonate fuel cell (MCFC) has become a mature product for market entry, representing in the last 3 years the first fuel cell in terms of large-size elements and megawatts produced. From 2012 up to the beginning of 2015, systems of 300 to several MW have been constructed for a total production of about 250 MW. Historically speaking, the MCFC concept was known already in 1921 but developed in the 1950s (Broers, 1958). It should be stressed that MCFC was first competing with a KOH molten salt system operating at a temperature of 400 °C. MCFC recognized as more efficient was finally selected in the family of high-temperature fuel cells together with solid oxide fuel cell that appeared later on in the fuel cell panorama (1970s). But let us see what makes the electrolyte membrane constituted by a molten carbonate eutectic and a lithium aluminate solid support attractive. Molten carbonates are nontoxic and highly conductive salts (1 S cm^{-1} at 650 °C) forming eutectics with low melting points (e.g., 488 °C for Li_2CO_3–K_2CO_3) (Sangster and Pelton, 1987). At their usual operating temperature of 650 °C allowing the cogeneration of heat and electrical power, the kinetics of hydrogen oxidation and oxygen reaction are high enough to avoid the use of noble metals used in low-temperature fuel cells (Maru, 1984). Thus, cheap and efficient nickel-based electrode materials can be used. Moreover, hydrogen can be produced by reforming of hydrocarbons at the same temperature, which simplifies the whole installation.

Our aim is to show the features sparking an interest in a fuel cell containing a molten carbonate electrolyte, how this unique characteristic is produced in the now competitive MCFC, and the new trends of similar systems for other promising applications, such as carbon capture and storage (CCS) and CO_2 valorization, or hybrid carbonate/oxide electrolytes, or direct carbon fuel cells (DCFC), and other strategic routes.

3.2 A glance to the operation principle

A molten carbonate electrolyte acts as any other solvent, such as water; its dissociation produces acidic-basic properties, which control its behavior. The self-ionization constant of a molten carbonate is characterized by the equilibrium

$$M_2CO_3(l) \Leftrightarrow M_2O(s) + CO_2(g) \tag{3.1}$$

(l), (s), and (g) are the liquid, solid, and gas phase, respectively.

As a molten carbonate is a strong electrolyte, this equilibrium can be expressed in terms of a simple ionic form as

$$CO_3^{2-} \Leftrightarrow CO_2 + O^{2-} \tag{3.2}$$

In the oxoacidity concept, O^{2-} is an electron pair donor associated an oxoacid CO_2 forming an oxobase CO_3^{2-} (Flood and Forland 1947, Yamada et al. 1994). The oxoacidity can be fixed by imposing a carbon dioxide partial pressure or by adding oxides in the melt. High partial pressures of CO_2 represent, for instance, highly oxoacidic media. This is a key concept in the chemistry of molten carbonates with a direct influence on the one hand, on the electrochemical reactions at the electrodes and, on the other hand, on the degradation/dissolution of the cathode and the stainless steel separator plates.

Figure 3.1 shows a scheme of an MCFC single cell with the reactions occurring at each electrode, knowing that the global cell reaction involves the consumption of CO_2 at the cathode and its recycling at the anode

$$H_2 + 0.5O_2 + CO_2(cat) \rightarrow H_2O + CO_2(an) \tag{3.3}$$
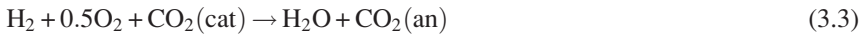
The cathode is constituted by lithiated nickel oxide and the anode by Ni with a small content of chromium or aluminum. They are separated by a carbonate eutectic containing lithium carbonate with another alkali carbonate (either sodium, or potassium, or both) supported by lithium aluminate. The specific redox reactions at each electrode are:
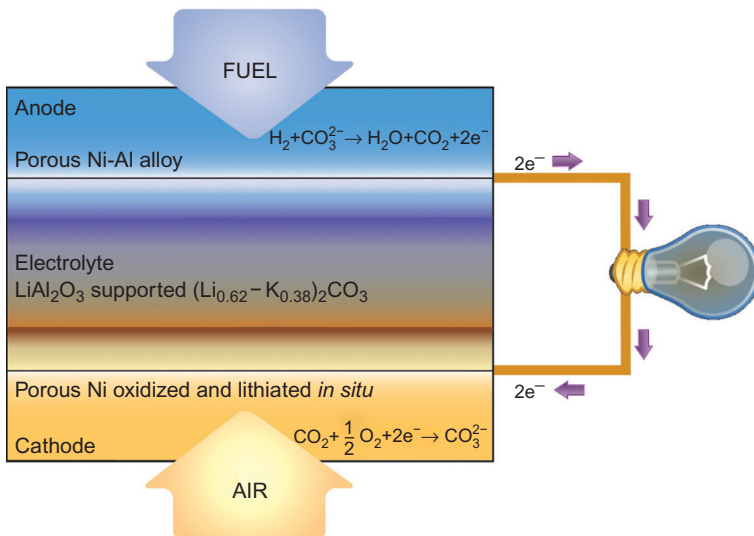
Figure 3.1 Scheme of an MCFC single cell.

3.2.1   At the cathode or air compartment

In all the present systems, the oxidant is always air containing CO_2, which has the particularity of being part of the reduction reaction, as follows:

$$0.5O_2 + CO_2 + 2e^- \rightarrow CO_3{}^{2-} \tag{3.4}$$

In fact, this mechanism is more complex because molecular oxygen is not stable in such media and produces reduced oxygen species, $O_2{}^{2-}$ and $O_2{}^-$ (Appleby et al., 1980; Nishina et al., 1990; Cassir et al., 1993, 1997; Weever et al., 1995). For example, in many cases the principal reduction pathway is due to the reduction of superoxides:

$$O_2{}^- + 2CO_2 + 3e^- \rightarrow 2CO_3{}^{2-} \tag{3.5}$$

tion of peroxides:

$$O_2{}^{2-} + 2CO_2 + 2e^- \rightarrow 2CO_3{}^{2-} \tag{3.6}$$

3.2.2   At the anode or hydrogen compartment

Even if hydrogen or a mixture of hydrogen and carbon monoxide are oxidized within the cell, they result from the transformation of hydrocarbons by reforming or thermal cracking.

Hydrogen oxidation, more rapid than oxygen reduction, is

$$H_2 + CO_3{}^{2-} \rightarrow H_2O + CO_2 + 2e^- \tag{3.7}$$

Of course, this representation is subdivided into different steps involving adsorbed hydrogen. Among the controversial mechanisms proposed in the literature, we will only show that given by Ang and Sammels (1980):

$$H_2 \rightarrow 2H_{ads.} \tag{3.8}$$

$$H_{ads.} + CO_3{}^{2-} \rightarrow OH^- + CO_2 + e^- \tag{3.9}$$

$$H_{ads.} + OH^- \rightarrow H_2O + e^- \tag{3.10}$$

3.3   Description of the components for building a stack

An MCFC stack is composed of a succession of single cells with the two electrodes separated by the electrolyte membrane. Single cells are interconnected by corrugated separator plates (or bipolar plates) ensuring the distribution of fuel and oxidant and the electrical connection of the whole system. Figure 3.2 is a schematic representation of an MCFC planar configuration; the only one used for this family of fuel cell.

Figure 3.2 Schematic representation of an MCFC planar configuration.

Fuel inlet

Cell frame
Corrugated plate
Collector plate
Anode
Electrolyte matrix
Cathode

Oxidant inlet
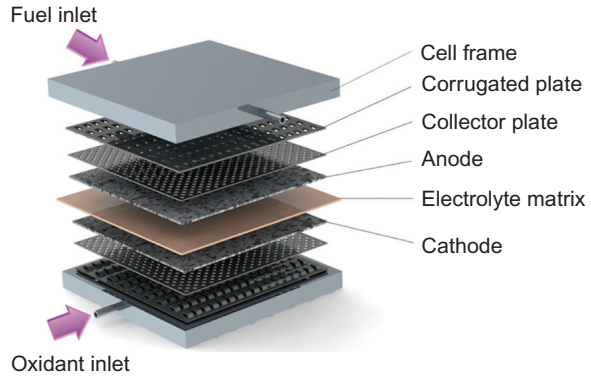
3.4 Issues on materials

3.4.1 Electrolyte membrane

The most conventional electrolytes are constituted by an alkali carbonate eutectic constituted by Li_2CO_3/K_2CO_3 (62/38 mol%) or Li_2CO_3/Na_2CO_3 (52/48 mol%) (Morita et al., 2002; Scaccia, 2005). They are held by a lithium aluminate porous ceramic matrix, which is composed of chemically inert and isolating particles insoluble in the carbonate melt. γ-$LiAlO_2$, the most stable crystalline structure of lithium aluminate, is the usual solid support impregnated by the carbonate eutectic to form a paste. The resulting matrix is composed by 55 wt.% of lithium aluminate and 45 wt.% of carbonate melt and is manufactured as a thin plate by tape casting (Durairajan et al., 2002). About 70% of the ohmic resistance of the cell being due to such matrix, it is necessary to reduce its thickness (about 0.3 mm) (Yuh et al., 1992). As γ-$LiAlO_2$ suffers stresses during operation, in particular by thermal cycling, it is often mixed with other, thicker particles of α-$LiAlO_2$ and fibers of α-$LiAlO_2$, in the following proportions: 55–30–15% (Bushnell et al., 1982; Paetsch et al., 1993; Yamamasu et al., 1993). The composition, structure, and porosity of the matrix are therefore required to be very well controlled (Kulkarni and Giddey, 2012). The porosity range to obtain the highest electrical conductivity is estimated by the Meredit–Tobias equation:

$$\rho = \rho_0 \delta^{-2} \tag{3.11}$$

with ρ, the specific resistance of the matrix; ρ_0, the specific resistance of the electrolyte; and δ, the porosity (Lacovangelo and Pasco, 1988). The optimum pore radius γ to retain the electrolyte under the pressure gradient between both electrodes is as follows (Young–Laplace equation):

$$\gamma = \frac{2\sigma\cos\theta}{\Delta P} \tag{3.12}$$

with σ the surface tension coefficient of the carbonate eutectic, θ the contact angle (electrolyte/support), and ΔP the pressure gradient between the electrodes (Bohme et al., 1994).

As an example for the of α-LiAlO$_2$ support and following the (3.11) and (3.12) equations, this material should have a pore diameter less than 8 μm (with 0.1 bar between the electrodes) and a porosity in the range of 40–70% for increased lifetime (Zhou et al., 2007). Coming back to the molten eutectic itself, the general requirements as in any electrochemical generator are a high ionic conductivity and a good chemical and mechanical stability. In MCFCs, only molten carbonates eutectics containing lithium are used (Li–K, Li–Na, and Li–Na–K). These melts have a density around 2.1 g cm^{-3}, a conductivity value between 1 and 2 S cm^{-1}, and a surface tension around 200 mN m^{-1} at 650 °C (Spedding, 1973; Kojima et al., 2007, 2008). A deeper insight in the chemical and physical properties of molten carbonates, such as viscosity, volatility, conductivity, or surface tension has been largely given in the literature (Ward and Janz, 1965; Spedding, 1973; Yuh et al., 1995; Cassir and Belhomme, 1999; Kojima et al., 2007, 2008; Kim et al., 2009; Lair et al., 2012; Kanai et al., 2013) and it is not our purpose here to provide more details. The main weakness of molten carbonates eutectics, whatever their nature, is their corrosiveness; we will address more specifically this particular point. In effect, one of the most limiting factors for MCFCs' lifetime is the dissolution of the lithiated nickel oxide cathode (and also of the stainless steel constituting the bipolar plates), which becomes severe in oxoacidic media (under high CO$_2$ partial pressures). Thus, it is important to optimize the nature and composition of the carbonate electrolyte from a balanced viewpoint by ensuring high conductivity and surface tension and low viscosity and volatility, and avoiding cathode dissolution by increasing the oxobasicity of the electrolyte either by changing the composition of the usual molten alkali carbonates; for example, by decreasing the potassium content in alkali carbonate eutectics or increasing the lithium content, which means that the Ni cathode is less soluble in Li–Na than in Li–K (Orfield and Shores, 1988), or by using additives. On the one hand, adding a few percent of alkali earth species, Mg, Ca, Sr, and Ba increases the oxobasicity of the electrolyte and, consequently, reduces the cathode solubility in the electrolyte (Cassir et al., 1998; Cassir and Belhomme, 1999; Scaccia, 2005; Morita et al., 2002; Tanimoto et al., 2003; Doyon et al., 1987) but, on the other hand, they decrease the conductivity and the performances of the cell (Selman and Maru, 1981). A compromise is therefore necessary. An increase in MCFC lifetime of about 20% has been obtained by adding CaCO$_3$ 9 mol% and BaCO$_3$ 9 mol%, in contrast to SrCO$_3$, which has a negative effect (Tanimoto et al., 2003).

It has also been shown that the logarithm of the solubility of the rare earth metal oxides has a linear relation with respect to the Coulomb force ratio between the rare earth and the alkaline metals (Ota et al., 2006). Nd$_2$O$_3$, which has the highest solubility in the carbonate eutectics among the three mentioned oxides, was the most efficient to reduce the NiO solubility; however, La$_2$O$_3$ is still the best additive with respect to solubility reduction. The positive effect of lanthanum is due to the formation of highly soluble oxycarbonates (La$_2$O) increasing the oxobasicity of the melt, which reduces

NiO solubility. From this point of view, it has been shown empirically that a good compromise between smaller radius and higher valence cations would be the best approach to select the best additive (Matsuzawa et al., 2005; Kulkarni and Giddey, 2012). Other elements such as Fe, La, and W have also been added to Li–K eutectic (Tanimoto et al., 2003; Terada et al., 1999); they inhibit the NiO dissolution but problems of cation segregation were observed at long-term cell operation. The effect of the addition of HF on the MCFC performance has also been analyzed (Smith and Winnick, 1999). HF consumes carbonates yielding fluoride, water, and carbon dioxide, which modifies the behavior of the melt. In fact, the MCFC device can generate electricity (0.065 W cm^{-2}) even if the electrolyte contains 40 mol% of LiF. However, the cell performance decreases for high fluoride concentrations. Although Li_2CO_3–Cs_2CO_3 melts are more oxoacidic than the common carbonate eutectics, they have been tested in single cells showing higher oxygen solubility, lower overpotentials, and higher cell potentials than the common carbonate eutectics (Yuh et al., 1992; Paetsch et al., 1993). The idea of using Cs or Rb carbonates as additives in Li_2CO_3–K_2CO_3 has been investigated recently and, in particular, their effect on the conductivity of the carbonate eutectic; a slight decrease can be observed at less than 5 mol % that be compensated by higher amounts of Li$^+$, a very mobile ion, in the melt (Lair et al., 2012).

3.4.2 Cathode

The state-of-the-art Ni cathode is oxidized and lithiated in situ in the carbonate eutectic under an oxidizing atmosphere (air/CO_2) and becomes $Li_xNi_{1-x}O$, a p-type semiconductor containing crystal defects in its lattice (Janowitz et al., 1999; Fukui et al., 1998). According to the literature, a value of 0.2 atm.% of lithium was estimated in this material by nuclear microprobe measurements (Belhomme et al., 2000). The relatively high solubility of $Li_xNi_{1-x}O$ provokes the formation of metallic nickel and short circuits between the anode and the cathode. Simplifying, the dissolution of the nickel oxide cathode material can be expressed as follows:

$$NiO + CO_2 \Leftrightarrow Ni^{2+} + CO_3^{2-} \tag{3.13}$$

$$Ni^{2+} + H_2 + CO_3^{2-} \Leftrightarrow Ni + CO_2 + H_2O \tag{3.14}$$

Acting on the electrolyte nature by increasing the oxoacidic properties is one of the ways to control NiO solubility. The effect of additives has already been developed in the previous paragraph. Another solution is either to recover the usual Ni cathode by protective coatings or to replace the material itself. In the first case, the literature is abundant in possibilities and several species and deposition techniques have been tested to process thin metal oxide layers onto porous nickel substrate. The principal attention has been given to $LiCoO_2$ or cobalt-based oxides, more corrosion-resistant than Ni and presenting interesting electrocatalytic properties (Yuh et al., 1995; Kim et al., 2011; Mendoza et al., 2003, 2004; Pauporté et al., 2005; Escudero et al., 2006;

Simonetti and Lo Presti, 2006; Lair et al., 2008; Paoletti et al., 2009). However, this material is expensive and other oxides have been tested, such as titanium and cerium, showing also an important decrease in the Ni solubility without affecting the properties of the cathode substrate (Albin et al., 2006; Meléndez-Ceballos et al., 2013, 2014). More exotic coatings such as gadolinium strontium cobaltite allowed fastening the oxygen reduction charge transfer (Song et al., 2011). In the second case, other cathode materials have been investigated, such as NiO-based materials containing other oxides less soluble and with the same performance as the classical device; alloys Ni–M (M = Nb, Al, Ti, Co) (Wijayasinghe et al., 2004; Ringuedé et al., 2006); or binary oxides $NiO–LiCoO_2$ (Kuk et al., 2001) and $NiO–CeO_2$ (Durairajan et al., 2002); or the ternary oxide $LiFeO_2–LiCoO_2–NiO$ (Fukui et al., 2000; Daza et al., 2000). A complete substitution of the Ni cathode has also been tested, such as single oxides: $LiFeO_2$, Li_2MnO_3, $La_{0.8}Sr_{0.2}CoO_3$, and $LiCoO_2$ (Janowitz et al., 1999; Fukui et al., 1998; Carewsca et al., 1997; Mohamedi et al., 2001; Belhomme et al., 2001). It should be concluded that for the moment the best solution seems to be the protection of Ni and the control of the electrolyte composition.

3.4.3   Anode

From the beginning of MCFCs, the anode material has been constituted by a porous nickel structure reinforced by a few percent of chromium, the role of which is to preserve its structural stability submitted to deformation under compressive load, compulsory to minimize the contact resistance between the components of the stack (Wendt et al., 1993; Frangini and Masci, 2004). In such a case, the surface of the anode in contact with the lithium-containing carbonate eutectic is recovered by $LiCrO_2$, which decreases significantly the wettability of the anode modifying its surface and, thus, affects hydrogen oxidation (Moon and Lee, 2003; Frangini and Masci, 2004). The sintered nickel tile has pore diameters of 3–5 μm and a porosity of 55–70%, with a surface area varying from 0.1 to 1 $m^2 g^{-1}$ and a thickness from 0.5 to 0.8 mm. The amount of Cr has been progressively reduced to ensure a better charge transfer, but the initial creep problem was back again and one of the best solutions is the addition of aluminum to nickel permitting a good mechanical resistance (Moon and Lee, 2003; Yoshiba et al., 2004). Furthermore, Kim et al. have studied a NiAl containing chromium inclusions, Ni/5 wt.% Ni_3Al/5 wt.% Cr, and have shown that the mechanical deformation of this material dramatically decreased due to the addition of Ni_3Al and chromium inclusions (Kim et al., 2002). Other alternatives have also been investigated, with the purpose of lowering the anode cost, which contributes to about 25% of the whole stack. Many additives have been considered, in particular Al, Ni–Cr–Al, Ni–Pd, Sn, Ti, and Ni recovered by a protective layer of Nb, doped CeO_2 and $LiFeO_2$, among which the addition of small amounts of cerium to Ni–Cr, improving creep resistance, seems of particular interest (Wee, 2006, 2007). In the case of the anode, the degradation due to the electrolyte in reducing atmosphere is very limited and is not a major issue;

however, another kind of dramatic degradation can be due to contaminants proceeding from the fuel, among which sulfur poisoning is the most harmful. This subject is too large to be presented in this chapter.

3.5   Variety of fuels

In principle, a huge number of fuels, based on hydrogen–carbon mixtures, are usable in MCFC systems: natural gas, carbon monoxide, syngas from coal or waste, coal gas, gasoil, ethanol, biogas, propane, and gasified biomass. The problem of impurities is less severe than for low-temperature fuel cells, but a cleanup of the fuel in necessary; for example, sulfur impurities can be critical and have been analyzed abundantly in the literature (Di Giulio et al., 2012, 2014). Even though the most used fuel for MCFC is natural gas, the fact that CO is used in MCFCs offers the possibility of converting fuel from organic origins; for example, biomass and, more recently, organic wastes. Biogas proceeding from anaerobic digestion of wastewater, organic waste, agricultural waste, industrial waste, animal by-products, or wood, are largely mentioned and are beginning to be used. However, most of the time, depending on its origin, its composition varies and some species such as HCl or H_2S must be removed if in a too important an amount. Thus, biogas pretreatment is required to avoid Ni-poisoning and corrosion of MCFC's components, with an elevation of methane and CO yields (Micoli et al., 2013, 2014). We will describe the case of an MCFC fed by natural gas, which produces syngas by vaporeforming:

$$CH_4 + H_2O \rightarrow CO + 3H_2 \tag{3.15}$$

The anode oxidation reaction is

$$H_2 + CO + 2CO_3{}^{2-} \rightarrow 3CO_2 + H_2O + 2e^- \tag{3.16}$$
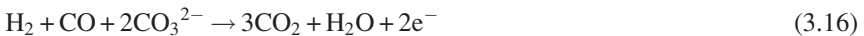
The reforming operation can either be external (out of the MCFC device), where syngas is introduced afterwards in the anode compartment, or direct and indirect internal reforming (Belhomme et al., 2000). In the external reformers operating at about 750 °C, used in the conventional MCFC, the heat required proceeds from the anode exhaust gas via heat exchangers. Internal reforming operates at 650 °C and, therefore, requires the use of well-adapted catalysts. The heat necessary for reaction (3.15), which is endothermic, proceeds from the exothermic fuel cell reaction. This system allows the use of other fuels, such as methanol and higher hydrocarbons. In the case of the indirect process, the reformer is separated, but adjacent to the anodic compartment of the electrochemical cell. The most interesting solution appears to be the direct internal reforming where syngas is produced directly in the anode compartment (Kordesch and Simader, 1996). Figure 3.3 summarizes the three types of reforming processes.
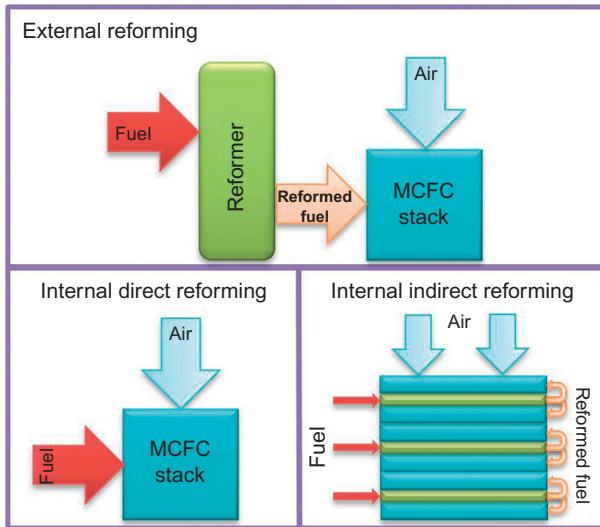
Figure 3.3 Reforming modes in MCFC systems.

3.6 Panel of stationary applications and market forces

MCFCs are available commercially for stationary generation with installations around the world, with power from 300 kW to 60 MW (Baran Industrial Complex Fuel Cell Facility, Korea). More than a hundred MCFC devices, alone or combined with microturbines, are installed all over the world for cogeneration, with or without grid connection and marine transportation. These installations are located in institutions (colleges, universities, hospitals, prisons) and industries (food and drink processing companies such a breweries, wastewater treatment plants, hotels, telecommunications, utilities). The electrical efficiency for this type of fuel cell varies from 47% to 48% with the potential to reach up to 57% and an overall efficiency above 80% when combining heat and power (Ghezel-Ayagh et al., 2007). This should be enough to ensure their place in the market, but the cost of this type of installation is still high. The overall cost of an MCFC installation could be divided into fuel cell stack (57%); balance of plant (BOP) (26%); installation, commissioning, and fuel conditioning (16%); and other (1%). Considering a clean fuel supply with a content of sulfur lower than 10 ppb, costs of fuel conditioning are low, and if the supplied fuel needs to be conditioned the cost of the system could increase as much as 50%; these estimates are based in the reported costs of fuel cell energy of a DFC 1500 system of about 4000 $/kW (Remick and Wheeler, 2010). Hence, cost reductions are an important requirement to compete with such emerging stationary technologies as PEMFC or SOFC, and the research opportunities to reduce costs are summarized in Table 3.1.

Historically, many companies produced demonstration MCFC devices (e.g., MC-Power and ERC in the United States, Ansaldo in Italy, ECN in the Netherlands, MTU in Germany, and IHI and Toshiba in Japan). Nevertheless, most of them have dropped this activity and, nowadays, the most important developer in the world is the U.S.-based company Fuel Cell Energy (FCE), which produces stationary systems

Table 3.1 Cost reduction issues for MCFC devices

Cost reduction by increasing power density		Cost reduction by increasing lifetime	
Actual 120–140 mW cm^{-2}	**Target** 160–180 mW cm^{-2}	**Actual** 5 years	**Target** 10 years
↑ Working temperature ↑ Electrolyte conductivity ↓ Polarization losses at electrodes ↓ Interfacial contact resistance between bipolar plates and electrodes		↓ Electrolyte losses ↓ Cathode dissolution ↓ Working temperature ↑ Lifetime of electrolyte matrix	

ranging from 300 kW to 2.8 MW. The principal market for these systems is Asia where FCE in alliance with POSCO Energy has sold many systems in South Korea. The second market is the United States where FCE has installed stationary systems powered by biogas from water treatment plants. POSCO Energy in South Korea is developing the biggest MCFC facility worldwide. Fuel Cell Energy Solutions (FCES) in Germany in alliance with FCE is pursuing the ambition of MTU creating the most important MCFC infrastructure and market in Europe. The potential of MCFC for CCS by redirecting the CO_2 at the exhaust gas of coal-fired power plants toward an MCFC that requires this gas for operation opens the possibility to expand its market as complementary equipment for conventional power generation plants as a way to mitigate CO_2 emissions. The contribution of MCFC stationary power plants to the overall power generated by fuel cells of all types is shown in Figure 3.4, where we can observe the MCFC
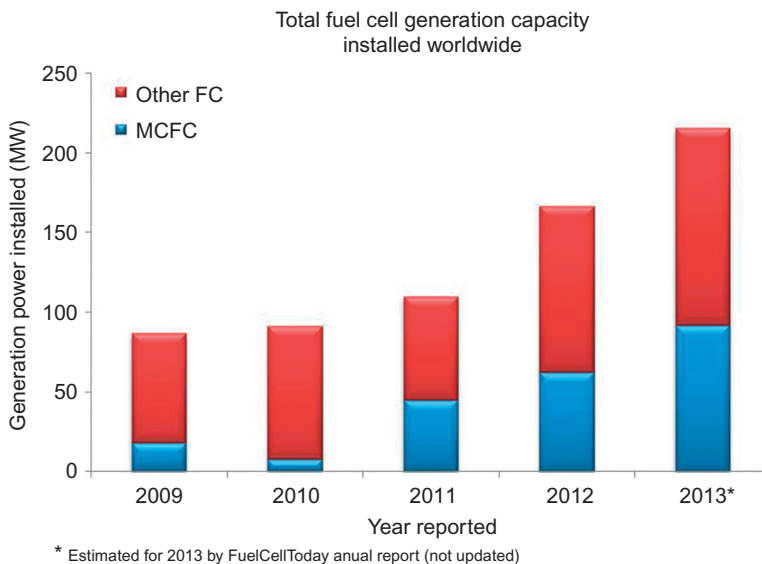
Figure 3.4 Overall power generated by fuel cells of all types and, in particular, MCFC devices.

contribute in 42% to the total fuel cell power installed and this will continue to grow in the years to come (Carter and Wing, 2013).

3.7 New trends

On the basis of the experience with molten carbonates and with MCFC devices, different other associated topics have appeared very recently (CO_2 valorization, water electrolysis), in the last decade (hybrid carbonate/oxide fuel cells,CCS) or have made a comeback after decades of silence (direct carbon fuel cell (DCFC)). We will briefly review the interest in some promising applications.

3.7.1 Hybrid fuel cells (MCFC/SOFC)

It has been shown recently that combining ceramics with molten salts presents a growing interest for innovative high-temperature fuel cell applications. In the last 10 years, doped-ceria oxides mixed with molten salts, such as chlorides, fluorides, carbonates, and sulfates (Zhu and Mat, 2006; Zhu et al., 2001 & 2010; Lapa et al., 2010; Di et al., 2010; Xia et al., 2010; Zhang et al., 2010; Benamira et al., 2011; Li and Sun, 2010; Raza et al., 2010) have been investigated. This phase being molten or partially molten at intermediate temperature (>500 °C for alkali molten carbonates) would create an interfacial conduction pathway. Oxide ions ensure the conductivity in the oxide phase, the conductivity being attributed mostly to carbonates in the carbonate phase. These composites form highly disordered interfacial regions ("superionic highways," "percolating conducting paths") between the oxide phase and the carbonate phase (Zhu et al., 2010). Some achievements have already been realized. Li and Sun (2010) have developed a so-called composite (oxide/molten carbonates) NANOSOFC (nanosolid oxide fuel cell), obtaining a maximum output power density of 140 mW cm^{-2}, stable for 200 h (Li and Sun, 2010; Di et al., 2010) studying the same kind of composites, obtained a maximum power density of 590 mW cm^{-2} at 600 °C (Di et al., 2010; Raza et al., 2010) showed that the use of Na_2CO_3 significantly improved the performance, reaching 1.15 W cm^{-2} at 500 °C.

3.7.2 Valorization of CO_2

The role of CO_2 in MCFC systems and the first experience in capturing this greenhouse gas in molten carbonates opened a space to another strategic field: the use of this gas as a source of energy and not as waste in the negative sense of the term (Cassir et al., 2012). The interest in processing CO_2 by electrolysis into carbon monoxide or graphite in molten carbonates has been pointed out in the recent literature (Le Van et al., 2009; Kaplan et al., 2010). Fundamental approaches have been developed on the electrochemical and thermodynamic properties of CO_2 in order to optimize its reactivity and transformation in these molten media (Chery et al., 2014, 2015). The feasibility of a large-scale development of CO_2 electrolyzers combining the production of CO or C with solar thermal energy has been proven by Licht and his coworkers (Licht, 2011; Licht et al., 2013).

3.7.3   Molten carbonate electrolysis cell (MCEC)

There is a growing interest in solid oxide electrolysis cells (SOECs) because high temperatures can theoretically be more efficient and materials cheaper; for example, at 800 °C the ratio of electric power compared to heat energy is 20% less than at low temperature. For similar reasons, MCECs could be also very interesting, but it is only recently that Hu et al. published the first results on the electrochemical performances of such devices, where they clearly showed that in short-time tests, MCEC exhibit lower polarization than MCFC systems (Hu et al., 2014). The reactions follow:

At the anode

$$CO_3{}^{2-} \rightarrow 0.5O_2 + CO_2 + 2e^- \tag{3.17}$$

At the cathode

$$H_2O + CO_2 + 2e^- \rightarrow H_2 + CO_3{}^{2-} \tag{3.18}$$

and the global cell reaction

$$H_2O \rightarrow H_2 + 0.5O_2 \tag{3.19}$$

At the cathode side in specific conditions, CO is also produced by the CO_2 reduction

$$2CO_2 + 2e^- \rightarrow CO + CO_3{}^{2-} \tag{3.20}$$

The coelectrolysis will globally produce syngas: $H_2 + CO$.

3.8   Conclusion

In brief, it can be stated from the experience of the last decade that MCFC devices are mature and are progressively entering the markets of cogeneration and stationary energy. More power has been produced in the last few years by MCFCs than by any other fuel cell. Moreover, molten carbonate science is alive, and progress is expected with respect to the performance and lifetime of such devices. In parallel, the use of molten carbonates in carbon capture, CO_2 valorization, DCFC, or electrolysis are becoming concrete scientific and technological goals.

References

Albin, V., Mendoza, L., Goux, A., Ringuedé, A., Billard, A., Briois, P., Cassir, M., 2006. Morphological, structural and electrochemical analysis of sputter-deposited ceria and titania coatings for MCFC application. J. Power Sources 160, 821–826.

Ang, P.G.P., Sammels, A.F., 1980. Influence of electrolyte composition on electrode kinetics in the molten carbonate fuel cell. J. Electrochem. Soc. 127, 1279–1294.

Appleby, A.J., Nicholson, S., 1980. Reduction of oxygen in lithium-potassium carbonate melt. J. Electroanal. Chem. 112, 71–76.

Belhomme, C., Cassir, M., Tessier, E., Berthoumieux, E., 2000. Lithium depth profile in NiO molten carbonate fuel cell cathode by nuclear microprobe. Electrochem. Solid-State Lett. 3, 216–219.

Belhomme, C., Gourba, E., Cassir, M., Tessier, C., 2001. Chemical and electrochemical behavior of NiO in the cathodic conditions used in molten carbonate fuel cells MCFC. J. Electroanal. Chem. 503, 69–77.

Benamira, M., Ringuedé, A., Albin, V., Vannier, R.-N., Hildebrandt, L., Lagergren, C., Cassir, M., 2011. Gadolinia-doped ceria mixed with alkali carbonates for SOFC applications: I—a thermal, structural and morphological insight. J. Power Sources 196, 5546–5554.

Bohme, O., Leidich, F.U., Salge, H.J., Wendt, H., 1994. Development of materials and production technologies for molten carbonate fuel cells. Int. J. Hydrog. Energy 19, 349–355.

Broers, G.H.J., 1958. High Temperature Galvanic Fuel Cells (Ph.D. thesis). University of Amsterdam, The Netherlands.

Bushnell, C.L., Bregoli, L.J., Scroll C.R., 1982. Electrolyte matrix for molten carbonate fuel cell, US Patent 4,322,482.

Carewsca, M., Scaccia, S., Croce, F., Arumugam, S., Yang, Y., Greenbaum, S., 1997. Electrical conductivity and ^{6,7}Li NMR studies of $Li_{1+y}CoO_2$. Solid State Ion 93, 227–237.

Carter, D., Wing, J., 2013. Fuel cell today industry review 2013. Fuel Cell Today. 36–37.

Cassir, M., Belhomme, C., 1999. Technological applications of molten salts: the case of the molten carbonate fuel cell. Plasmas Ion 2, 3–15.

Cassir, M., Moutiers, G., Devynck, J., 1993. Stability and characterization of oxygen species in alkali molten carbonate: a thermodynamic and electrochemical approach. J. Electrochem. Soc. 140, 3114–3122.

Cassir, M., Malinowska, B., Peelen, W., Hemmes, K., de Wit, J.H.W., 1997. Identification and electrochemical characterization of in situ produced reduced oxygen species in molten Li-K carbonate under $P(CO_2) = 1$ atm and $P(CO_2) = 0.1$ atm $+ P(O_2) = 0.9$ atm. Influence of oxide, peroxide and superoxide additions. J. Electroanal. Chem. 433, 195–205.

Cassir, M., Olivry, M., Albin, V., Malinowska, M., Devynck, J., 1998. Thermodynamic and electrochemical behavior of nickel in molten Li-Na carbonate modified by addition of calcium carbonate. J. Electroanal. Chem. 452, 127–137.

Cassir, M., McPhail, S., Moreno, A., 2012. Strategies and new developments in the field of molten carbonates and high-temperature fuel cells in the carbon cycle. Int. J. Hydrog. Energy 37, 19345–19350.

Chery, D., Albin, A., Lair, V., Cassir, M., 2014. Thermodynamic and experimental approach of electrochemical reduction of CO_2 in molten carbonates. Int. J. Hydrog. Energy 39, 12330–12339.

Chery, D., Lair, V., Cassir, M., 2015. CO_2 electrochemical reduction into CO or C in molten carbonates: a thermodynamic point of view. Electrochim. Acta. http://dx.doi.org/10.1016/j.electacta.2015.01.216.

Daza, L., Rangel, C.M., Cassais, M.T., Martinez, M.J., Alonso, J.A., 2000. Modified nickel oxides as cathode materials for MCFC. J. Power Sources 86, 329–333.

Di Giulio, N., Bosio, B., Cigolotti, V., Nam, S.W., 2012. Experimental and theoretical analysis of H_2S effects on MCFCs. J. Hydrog. Energy 37, 19329–19336.

Di Giulio, N., Bosio, B., Han, J., McPhail, S.J., 2014. Experimental analysis of SO_2 effects on molten carbonate fuel cells. J. Hydrog. Energy 39, 12300–12308.

Di, J., Chen, M., Wang, C., Zheng, J., Fan, L., Zhu, B., 2010. Samarium doped ceria–(Li/Na)$_2$CO$_3$ composite electrolyte and its electrochemical properties in low temperature solid oxide fuel cell. J. Power Sources 195, 4695–4699.

Doyon, J.D., Gilbert, T., Davies, G., Patsch, L., 1987. NiO solubility in mixed alkali/alkaline earth carbonates. J. Electrochem. 134, 3035–3038.

Durairajan, A., Colon-Mercado, H., Haran, B., White, R., Popov, B., 2002. Electrochemical characterization of cobalt-encapsulated nickel as cathodes for MCFC. J. Power Sources 104, 157–168.

Escudero, M.J., Mendoza, L., Cassir, M., Gonzalez, T., Daza, L., 2006. Studies on the behavior of porous nickel coated by cobalt oxide in molten carbonate. J. Power Sources 160, 775–781.

Flood, H., Forland, T., 1947. The acidic and basic properties of oxides. Acta Chem. Scand. 1, 592–604.

Frangini, S., Masci, A., 2004. Intermetallic FeAl based coatings deposited by the electrospark technique: corrosion behavior in molten (LiqK) carbonate. Surf. Coat. Technol. 184, 31–39.

Fukui, T., Okawa, H., Tsunooka, T., 1998. Solubility and deposition of LiCoO$_2$ in a molten carbonate. J. Power Sources 71, 239–243.

Fukui, T., Ohara, S., Okawa, H., Hotta, T., Naito, M., 2000. Properties of NiO cathode coated with lithiated Co and Ni solid solution oxide for MCFCs. J. Power Sources 86, 340–346.

Ghezel-Ayagh, H., Farooque, M., Maru Hansraj, C., 2007. Carbonate fuel cell: principles and applications. Recent Trends Fuel Cell Sci. Technol. 217–247.

Hu, L., Rexed, I., Lindbergh, G., Lagergren, C., 2014. Electrochemical performance of reversible molten carbonate fuel cells. Int. J. Hydrog. Energy 39, 12323–12329.

Janowitz, K., Kah, M., Wendt, H., 1999. Molten carbonate fuel cell research. Part I. Comparing cathodic oxygen reduction in lithium:potassium and lithium:sodium carbonate melts. Electrochim. Acta 45, 1025–1037.

Kanai, Y., Fukunaga, K.I., Terasaka, K., Fujioka, S., 2013. Mass transfer in molten salt and suspended molten salt in bubble column. Chem. Eng. Sci. 100, 153–159.

Kaplan, V., Wachtel, E., Gartsman, K., Feldman, Y., Lubomirsky, I., 2010. Conversion of CO$_2$ to CO by electrolysis of molten lithium carbonate. J. Electrochem. Soc. 157, B5552.

Kim, G., Moon, Y., Lee, D., 2002. Preparation of Ni-5 wt% Al alloy. J. Power Sources 69, 55–60.

Kim, J.-E., Patil, K.Y., Han, J., Yoon, S.-P., Nam, S.-W., Lim, T.-H., Hong, S.-A., Kim, H., Lim, H.-C., 2009. Using aluminum and Li$_2$CO$_3$ particles to reinforce the a-LiAlO$_2$ matrix for molten carbonate fuel cells. Int. J. Hydrog. Energy 34, 9227–9232.

Kim, Y.-S., Yi, C.-W., Choi, H.S., Kim, K., 2011. Modification of Ni-based cathode material for molten carbonate fuel cells using Co$_3$O$_4$. J. Power Sources 196, 1886–1893.

Kojima, T., Miyazaki, Y., Nomura, K., Tanimoto, K., 2007. Electrical Conductivity of Molten Li$_2$CO$_3$-X$_2$CO$_3$ (X: Na, K, Rb, and Cs) and Na$_2$CO$_3$–Z$_2$CO$_3$ (Z: K, Rb, and Cs). J. Electrochem. Soc. 154, F222–F230.

Kojima, T., Miyazaki, Y., Nomura, K., Tanimoto, K., 2008. Density, surface tension, and electrical conductivity of ternary molten carbonate system Li$_2$CO$_3$–Na$_2$CO$_3$–K$_2$CO$_3$ and methods for their estimation. J. Electrochem. Soc. 155, F150–F156.

Kordesch, K.V., Simader, G.R., 1996. Fuel Cells & Their Applications. VCH, Germany.

Kuk, S.T., Song, Y.S., Suh, S.I., Kim, J.Y., Kim, K., 2001. The formation of LiCoO$_2$ on a NiO cathode for a molten carbonate fuel cell using electroplating. J. Mater. Chem. 11, 630–635.

Kulkarni, A., Giddey, S., 2012. Materials issues and recent developments in molten carbonate fuel cells. J. Solid State Electrochem. 16, 3123–3146.

Lacovangelo, C.V., Pasco, W.D., 1988. Hot-roll-milled electrolyte structures for molten carbonate fuel cells. J. Electrochem. Soc. 135, 221–224.

Lair, V., Ringuedé, A., Albin, V., Cassir, M., 2008. Characterization in MCFC conditions of high-temperature potentiostatically deposited Co-based thin films on NiO cathode. Ionics 14, 555–561.

Lair, V., Albin, V., Ringuedé, A., Cassir, M., 2012. Theoretical predictions vs. experimental measurements of the electrical conductivity of molten Li_2CO_3-K_2CO_3 modified by additives. Int. J. Hydrog. Energy 37, 19357–19364.

Lapa, C.M., Figueiredo, F.M.L., de Souza, D.P.F., Song, L., Marques, F.M.B., 2010. Synthesis and characterization of composite electrolytes based on samaria-doped ceria and Na/Li carbonates. Int. J. Hydrog. Energy 35, 2953–2957.

Le Van, K., Groult, H., Lantelme, F., Dubois, D., Avignant, D., Tressaud, A., 2009. Electrochemical formation of carbon nano-powders with various porosities in molten alkali carbonates. Electrochim. Acta 54, 4566–4573.

Li, S., Sun, J., 2010. Electrochemical performances of NANOCOFC in MCFC environments. Int. J. Hydrog. Energy 35, 2980–2985.

Licht, S., 2011. Efficient solar-driven synthesis, carbon capture, and desalinization, STEP: solar thermal electrochemical production of fuels, metals, bleach. Adv. Mater. 23, 5592–5612.

Licht, S., Cui, B., Wang, B., 2013. STEP carbon capture—the barium advantage. J. CO2 Util. 2, 58–63.

Maru, H.C., 1984. Molten Salt Techniques, vol. 2. Plenum Press, New York.

Matsuzawa, K., Mizusaki, T., Mitsushima, S., Kamiya, N., Ota, K.-I., 2005. The effect of La oxide additive on the solubility of NiO in molten carbonates. J. Power Sources 140, 258–263.

Meléndez-Ceballos, A., Fernández-Valverde, S.M., Barrera-Díaz, C., Albin, V., Lair, V., Ringuedé, A., Cassir, M., 2013. TiO_2 protective coating processed by atomic layer deposition for the improvement of MCFC cathode. Int. J. Hydrog. Energy 38, 13443–13452.

Meléndez-Ceballos, A., Fernández-Valverde, S.M., Albin, V., Lair, V., Ringuedé, A., Cassir, M., 2014. ALD-processed CeO_2 protective layer and its electrochemical performance as MCFC cathode. Electrochim. Acta 140, 174–181.

Mendoza, L., Albin, V., Cassir, M., Galtayries, A., 2003. Electrochemical deposition of Co_3O_4 thin layers in order to protect the nickel-based molten carbonate fuel cell. J. Electroanal. Chem. 548, 95–107.

Mendoza, L., Baddour-Hadjean, R., Cassir, M., Pereira-Ramos, J.P., 2004. Raman evidence of the formation of LT-$LiCoO_2$ thin layers on NiO in molten carbonate at 650 °C. Appl. Surf. Sci. 225, 356.

Micoli, L., Bagnasco, G., Turco, M., 2013. HCl removal from biogas for feeding MCFCs: adsorption on microporous materials. Int. J. Hydrog. Energy 38, 447–452.

Micoli, L., Bagnasco, G., Turco, M., 2014. H_2S removal from biogas for fuelling MCFCs: new adsorbing materials. Int. J. Hydrog. Energy 39, 1783–1787.

Mohamedi, M., Hisamitsu, Y., Kihara, K., Kudo, T., Itoh, T., Ushida, I., 2001. Ni–Al alloy as alternative cathode for molten carbonate fuel cells. J. Alloys Compd. 315, 224–233.

Moon, Y., Lee, D., 2003. Corrosion resistance of 316 L stainless steel with surface layer of Ni_2Al_3 or NiAl in molten carbonates. J. Power Sources 115, 1–11.

Morita, H., Komoda, M., Mugikura, Y., Izaki, Y., Watanabe, T., Masuda, Y., Matsuyama, T., 2002. Performance analysis of molten carbonate fuel cell using a Li/Na electrolyte. J. Power Sources 112, 509–518.

Nishina, T., Takahashi, M., Uchida, I., 1990. Gas electrode reactions in molten carbonate media. J. Electrochem. Soc. 137, 1112–1121.

Orfield, D., Shores, A., 1988. Solubility of NiO in molten Li_2CO_3, Na_2CO_3, K_2CO_3, and Rb_2CO_3 at 910 °C. J. Electrochem. Soc. 135, 1662–1668.

Ota, K.-I., Matsuda, Y., Matsuzawa, K., Mitsushima, S., Kamiya, K., 2006. Effect of rare earth oxides for improvement of MCFC. J. Power Sources 160, 811–815.

Paetsch, L.M., Doyon, J., Farooque, M., 1993. In: Proceedings of the Third International Symposium of Carbonate Fuel Cell Technology. The Electrochemical Society, Pennington.

Paoletti, C., Carewska, M., Lo Presti, R., Mc Phail, S., 2009. Performance analysis of new cathode materials for molten carbonate fuel cells. J. Power Sources 193, 292–297.

Pauporté, T., Mendoza, L., Cassir, M., Galtayries, A., Chivot, J., 2005. Direct low temperature deposition of crystallized Co_3O_4 films by potentiostatic electrolysis. J. Electrochem. Soc. 152, C49–C53.

Raza, R., Wang, X., Ma, Y., Liu, X., Zhu, B., 2010. Improved ceria–carbonate composite electrolytes. Int. J. Hydrog. Energy 35, 2684–2688.

Remick, R., Wheeler, D., 2010. NREL Technical Report, NREL/TP-560-49072.

Ringuedé, A., Wijayasinghe, A., Albin, V., Lagergren, C., Cassir, M., Bergman, B., 2006. Solubility and electrochemical studies of $LiFeO_2$-$LiCoO_2$-NiO materials for the MCFC cathode application. J. Power Sources 160, 789–795.

Sangster, M., Pelton, A.D., 1987. Special report to the phase equilibria program. American Ceramic Society, Westerville, Ohio.

Scaccia, S., 2005. Investigation on NiO solubility in binary and ternary molten alkalimetal carbonates containing additives. J. Mol. Liq. 116, 67–71.

Selman, J.R., Maru, H.C., 1981. Advances in Molten Salt Chemistry, vol. 4. Plenum Press, New York.

Simonetti, E., Lo Presti, R., 2006. Characterization of Ni porous electrode covered by a thin film of $LiMg_{0.05}Co_{0.95}O_2$. J. Power Sources 160, 816–820.

Smith, D.S., Winnick, J., 1999. Cesium-containing electrolyte for the molten carbonate fuel cell. Electrochem. Solid State Lett. 2, 207–209.

Song, S., Jang, S.C., Han, J., Yoon, S.P., Nam, S.W., Lim, T., 2011. Enhancement of cell performance using a gadolinium strontium cobaltite coated cathode in molten carbonate fuel cells. J. Power Sources 196, 9900–9905.

Spedding, P.L., 1973. Electrical conductance of molten alkali carbonate binary mixtures. J. Electrochem. Soc. 120, 1049–1053.

Tanimoto, K., Kojima, T., Yanagida, M., Nomura, K., Miyazaki, Y., 2003. Optimization of the electrolyte composition in a $(Li_{0.52}Na_{0.48})_{2-2x} AE_xCO_3$ (AE = Ca and Ba) molten carbonate fuel cell. J. Power Sources 131, 256–260.

Terada, S., Higaki, K., Nagashima, I., Ito, Y., 1999. Addition of potassium tungstate to the electrolyte of a molten carbonate fuel cell. J. Power Sources 83, 178–185.

Ward, A.T., Janz, G.J., 1965. Molten carbonate electrolytes: electrical conductance, density and surface tension of binary and ternary mixtures. Electrochim. Acta 10, 849–857.

Wee, J., 2006. Creep and sintering resistance of a Ce and anode. Mater. Chem. Phys. 98, 273–278.

Wee, J., 2007. Effect of cerium addition to Ni-Cr anode electrode for molten carbonate fuel cells: surface fractal dimensions. Mater. Chem. Phys. 101, 322–328.

Weever, R., Hemmes, K., de Wit, J.H.W., 1995. The mechanism of hydrogen oxidation at gold and nickel flag electrodes in molten Li/K carbonate. J. Electrochem. Soc. 142, 389–397.

Wendt, H., Böhme, O., Leidich, F.U., Brenscheidt, T., 1993. In: Proceedings of the 3rd International Symposium on Carbonate Fuel Cell Technology. In: The Electrochemical Society Proceedings Series, vol. 93-3. The Electrochemical Society Inc., Massachussets.

Wijayasinghe, A., Bergman, B., Lagergren, C., 2004. A study on $LiCoO_2$-rich cathode materials for the MCFC based on the $LiCoO_2$–$LiFeO_2$–NiO ternary system. Electrochim. Acta 49, 4709–4717.

Xia, C., Li, Y., Tian, Y., Liu, Q., Wang, Z., Jia, L., Zhao, Y., Li, Y., 2010. Intermediate temperature fuel cell with a doped ceria–carbonate composite electrolyte. J. Power Sources 195, 3149–3154.

Yamada, K., Uchida, I., 1994. In-situ formation process of $LiCoO_2$ in the molten lithium-potassium carbonate eutectic at 923 K. Chem. Lett. 2, 299–302.

Yamamasu, Y., Kakihara, T., Kasai, E., Morita, E., 1993. Component development and durability test. In: Proceedings of the Third International Fuel Cell Conference, NEDO/MITI, Tokyo, Japan, pp. 161–164.

Yoshiba, F., Morita, H., Yoshikawa, M., Mugikura, Y., Izaki, Y., Watanabe, T., Komoda, M., Masuda, M., Zaima, N., 2004. Improvement of electricity generating performance and life expectancy of MCFC stack by applying Li/Na carbonate electrolyte. Test results and analysis of $0.44\ m^2$/10 kW- and $1.03\ m^2$/10 kW-class stack. J. Power Sources 128, 152–164.

Yuh, C., Farooque, M., Johnsen, R., 1992. In: Proceedings of the Fourth Annual Fuel Cells Contractors Review Meeting, US DOE/METC.

Yuh, C., Johnsen, R., Farooque, M., Maru, H., 1995. Status of carbonate fuel cell materials. J. Power Sources 56, 1–10.

Zhang, L., Lan, R., Petit, C.T.G., Tao, S., 2010. Durability study of an intermediate temperature fuel cell based on an oxide-carbonate composite electrolyte. Int. J. Hydrog. Energy 35, 6934–6940.

Zhou, L., Lin, H., Yi, B., 2007. Sintering behavior of porous α-lithium aluminate matrices in molten carbonate fuel cells at high temperature. J. Power Sources 164, 24–32.

Zhu, B., Mat, M.D., 2006. Studies on dual phase ceria-based composites in electrochemistry. Int. J. Electrochem. Sci. 1, 383–402.

Zhu, B., Liu, X., Zhou, P., Yang, X., Zhu, Z., Zhu, W., 2001. Innovative solid carbonate–ceria composite electrolyte fuel cells. Electrochem. Commun. 3, 566–571.

Zhu, B., Li, S., Mellander, B., 2010. Theoretical approach on ceria-based two-phase electrolytes for low temperature (300–600 °C) solid oxide fuel cells. Electrochem. Commun. 10, 302–305.

This page intentionally left blank

Solid oxide fuel cells

4

M.L. Faro, S. Trocino, S.C. Zignani, A.S. Aricò
CNR-ITAE, Institute for Advanced Energy Technologies "Nicola Giordano", Messina, Italy

Acronyms and symbols

$A\ cm^{-2}$	Ampere per square centimeter
ABO_3	typical perovskite formula
ASC	anode-supported cell
C(s)	carbon as solid
$Ce_{0.8}G_{0.2}O_2$	gadolinium-doped ceria
$Ce_{0.9}Gd_{0.1}O_{1.95}$	gadolinium-doped ceria
CeO_{2-x}	substoichiometric cerium dioxide
cermet	ceramic–metallic composite
$CH_4(g)$	methane in the gas phase
$CO_2(g)$	carbon dioxide in the gas phase
Crofer 22 APU	ferritic stainless steel brand name
E_a	activation energy
ESC	electrolyte-supported cell
GDC	gadolinia-doped ceria, $Ce_{0.9}Gd_{0.1}O_{1.95}$
$H_2(g)$	hydrogen in the gas phase
$H_2O(g)$	water in the gas phase
$La_{0.6}Sr_{0.4}Fe_{0.8}Co_{0.2}O_3$	lanthanum ferrite doped with strontium and cobaltum
$La_{0.8}Sr_{0.2}Cr_{0.93}V_{0.03}O_3$	lanthanum chromite doped with strontium and vanadium
$La_{0.8}Sr_{0.2}Ga_{0.8}Mg_{0.2}O_3$	lanthanum gallate doped with strontium and magnesium
$La_{0.8}Sr_{0.2}MnO_3$	lanthanum manganite doped with strontium
$La_{1-x}Sr_xCo_{1-y}Fe_yO_{3-\delta}$	generic formula of lanthanum cobaltite doped with strontium and iron
La_2NiO_4	lanthanum nickelate
$LaGaO_3$	lanthanum gallate
LSCV	$La_{0.8}Sr_{0.2}Cr_{0.03}V_{0.03}O_3$
LSFCO	$La_{0.6}Sr_{0.4}Fe_{0.8}Co_{0.2}O_3$
LSGM	$La_{0.8}Sr_{0.2}Ga_{0.8}Mg_{0.2}O_3$
LSM	$La_{0.8}Sr_{0.2}MnO_3$
MIECs	mixed electronic and ionic conductors
MSC	metal-supported cell
$O_2(g)$	molecular oxygen in the gas phase
$O^{2-}(s)$	oxygen ion on the surface
$O_2{}^{n-}$	molecular oxygen with a partial negative charge
pO^2	oxygen partial pressure
POX	partial oxidation

ppm	part per million
S cm^{-1}	Siemens per centimeter of conductor
SOFC	solid oxide fuel cell
SR	steam reforming
TPB	triple-phase boundary
wt.%	weight percentage
YSZ	yttria-stabilized zirconia
ZMG232	metal alloy brand name
γ-Al$_2$O$_3$	γ allotropic phase of aluminum oxide
δ	degree of oxygen substoichiometry
ΔG°	standard Gibbs energy change
ΔH	enthalpy change
ΔH°	standard enthalpy change
μm	micrometers
σ$_0$	oxygen ion conductivity

4.1 Introduction: What are solid oxide fuel cells?

A solid oxide fuel cell (SOFC) is a device allowing the direct conversion of chemical energy into electrical energy at high temperature, using an all solid-state cell equipped with ceramic materials. These systems can in principle achieve efficiency levels significantly higher than conventional technologies used to produce electricity (Ormerod, 2003). The reactions involved are simple and identical to those involved in an internal combustion engine; the main difference is based on the fact that electrochemical reactions are involved instead of direct chemical combustion. SOFCs consist of three elements assembled together to form a sandwich. A dense electrolyte is sandwiched between two porous electrodes, the anode and the cathode (Figure 4.1). The fuel is fed to the anode, where an oxidation reaction takes place, which releases electrons to the external circuit. The oxygen of air reacts at the cathode, accepting electrons from the external circuit, causing the occurrence of a reduction reaction.
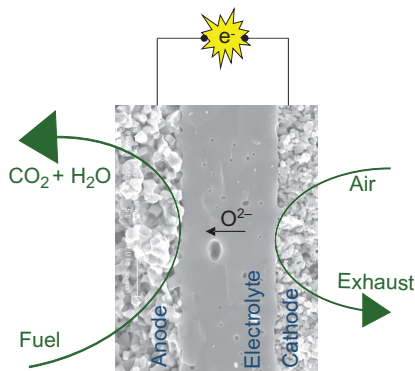
Figure 4.1 Scheme and microstructure of a solid oxide fuel cell.

The flow of electrons in the external circuit from the anode to the cathode is spontaneous and produces electricity. The number of charges transported externally is balanced by oxygen ions migration into the electrolyte in the opposite direction, that is, toward the anode (anionic electrolyte). The energy transported by the electrical current has as driven force the propensity that fuel and oxidant have to react to form water and CO_2. The "electrochemical" reaction occurs on the electrode surface in a region very close to the interface with the electrolyte (functional layer). Therefore, the electrodes must have a porous structure in order to facilitate the permeation of the reagents toward the region next to the electrolyte and to allow for removal of reaction products. The electrolyte must be full density, that is, impermeable to the reagents to prevent direct contact between fuel and oxidant. Basically, SOFCs can generate electricity as long as the reactants are fed to the electrodes.

The energy provided by a single cell is very low compared to the conventional electrical technologies, whereas the current density is high. To overcome this limitation, cells must be connected in series to form a stack through bipolar plates consisting of proper manifolds and flow fields while being electronically conductive.

At the present, this technology has not yet reached the maturity level required by the market of distributed energy production compared to direct combustion systems. However, it is expected that with the next developments in SOFCs' materials, components, and systems, they can replace the conventional technologies for stationary applications and auxiliary power units up to a maximum of 50 kW$_e$ (Singhal, 2002).

4.2 Ceramic components (anodes, cathodes, electrolytes) of an SOFC

The basic components of a ceramic SOFC are the electrolyte, the anode, and the cathode. The materials for different cell components are selected based on the following criteria:

(a) Suitable electrical conducting properties required by different cell components to perform their intended cell functions.
(b) Adequate chemical and structural stability at high temperature during cell operation as well as during cell fabrication.
(c) Minimal reactivity and interdiffusion among different cell components.
(d) Matching thermal expansion among different cell components.

In addition to the above materials selection criteria, the fabrication processes are chosen in such a way that every sequential component fabrication process does not affect those components already fabricated. The processes are optimized to minimize the cell fabrication cost. The fabrication routes for the individual cell components of SOFC differ significantly depending on which cell component is designed to perform the supporting function in the cell, whereas in most cases the electrolyte or the anode (in the case of planar configuration) and cathode (in the case of tubular configuration) ensure the mechanical stability of the cells.

4.2.1 Anode (fuel electrode)

In the SOFC, the fuel fed to the anode must be sufficiently reducing in nature to provide useful electrochemical driving force. Thus, the fuel electrode must be stable in the reducing environment of the fuel, have catalytic activity for the oxidation of hydrogen and organic fuels, and be characterized by high ionic and electronic conductivity (mixed conductivity) over a wide pO_2 range. Especially in the anode-supported SOFC design, it must have sufficient porosity to allow for the transport of the fuel to the interface and the transport of the products of fuel oxidation away from the electrolyte/fuel electrode interface where the fuel oxidation reaction takes place (i.e., Reactions 4.1 and 4.2):

$$O^{2-}(s) + H_2(g) = H_2O(g) + 2e^- \qquad (4.1)$$

$$4O^{2-}(s) + CH_4(g) = 2H_2O(g) + CO_2(g) + 8e^- \qquad (4.2)$$
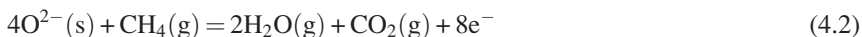
Furthermore, the anode must be characterized by chemical and physical compatibility with the other cell components.

In order to perform its electrochemical function, the anode must be able to transport oxygen ions to the active catalytic sites as well as release electrons from the active sites into the external circuit. As there are no adequate mixed-conducting materials available to perform both functions under reducing environment, ceramic–metallic or "cermet" composites of electronic and ionic conducting materials are used in the "commercial" SOFC anodes.

The reducing conditions present at the fuel compartment of an SOFC permit the use of nickel as anode in combination with ceramic materials; for example, yttria-stabilized zirconia (YSZ) or gadolinia-doped ceria (GDC). Alternatively, copper, cobalt, iron, and noble metals may be useful alternatives as SOFC anodes because they have excellent electrical conductivities in reducing atmosphere; however, Ni is the preferred one owing to the excellent catalytic properties for breaking hydrogen bonds and the fairly low cost. Porosity is engineered into the structure through the addition of pore-forming agents to the ceramic–metallic composite as well as through the volume contraction associated with the reduction of NiO to Ni (Wilson et al., 2006).

Electrocatalysis of hydrogen on metals such as Ni is relatively facile, and anode overpotential is just a small contribution to the overall drop in fuel cell voltage (Zhu and Deevi, 2003). The rate-limiting step is the adsorption of hydrogen onto the metal surface; the subsequent step is the reaction of absorbed hydrogen with O^{2-} to give water and electrons (Costamagna et al., 1998).

Nickel is also an excellent catalyst for cracking of hydrocarbons that may also cause deposition of carbon (McIntosh and Gorte, 2004). Carbon formation is responsible for the clogging of gas channels, physical delamination of the nickel layer, and fragmentation of the porous anode.

Preventing carbon deposition is, therefore, of primary importance for Ni-based catalysts used in the direct oxidation of carbon-based fuels (Finnerty et al., 1998).

Due to these drawbacks, it is challenging to develop new SOFC anodes capable of efficient operation in the presence of hydrogen and organic fuels while being tolerant to carbon deposition. In heterogeneous catalysis, a reduction of carbon deposits at intermediate temperatures has been observed for Ni catalysts supported on basic oxides, such as γ-Al_2O_3 (Dias and Assaf, 2004; Hoang and Chan, 2007), MgO (Rezaei et al., 2011), a combination of MgO–CaO (York et al., 2007) and MgO, and Al_2O_3 (Nagaoka et al., 2005). However, these oxides are characterized by insulating electrical properties; thus, they can be used in the electronic conducting phase of SOFC electrodes only at doping levels. A reduction of carbon deposits was also observed in unmodified Ni catalysts at low temperatures in the presence of a proper combination of GDC and zirconia-based electrolytes (YSZ) (Murray et al., 1999). This behavior has been interpreted in terms of enhanced oxygen ion transfer promoted by the doped-ceria in combination with the oxygen storage properties of CGO and YSZ. It also has been demonstrated for the bimetallic Ni-based alloys that the presence of a second metal (e.g., Cu) that interrupts the network of Ni-Ni, can improve the stability of the catalysts (Dal Santo et al., 2012). In fact, the network promotes the cracking process and the consequent formation and deposition of carbon fibers and soot (Reaction 4.3).

$$CH_4 \rightleftharpoons C(s) + 2H_2 \, \Delta H^\circ \simeq 90 \, kJ; \quad \Delta G^\circ \simeq -27 \, kJ \quad at \, 800 \, ^\circ C \tag{4.3}$$
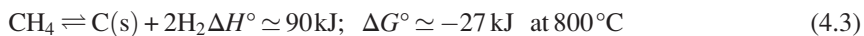
Among the alternative anode materials that are capable of withstanding sulfur contamination, volume instability upon redox cycling, and carbon deposition, perovskite oxides have drawn considerable attention. The catalytic oxidation of carbon-based fuels on such materials appears to involve lattice oxygen (Mars van Krevelen mechanism) (Mars and van Krevelen, 1954). They can be easily substituted on the A and B sites with alkali earth and transition metal elements, respectively. This allows interesting modifications of their electronic and catalytic properties. These perovskite materials are reported to be stable at the operating temperature of SOFCs (600–1000 $^\circ$C) and some of them across a wide oxygen partial pressure range (1–10^{-20} atm) (Vernoux et al., 2001). Several materials have been suggested, such as the lanthanum-doped strontium titanates proposed by Marina et al. (2002). High electrical conductivity has been observed for yttrium-doped $SrTiO_3$ under reducing condition (Hui and Petric, 2002). Madsen et al. have studied the influence of the addition of NiO to anodes based on $La_{0.8}Sr_{0.2}Cr_{0.93}V_{0.03}O_3$ (LSCV) that also contained $Ce_{0.9}Gd_{0.1}O_{1.95}$ (GDC). The microstructure of the anode was investigated in relation of the firing temperature and the performance of SOFCs fed with hydrogen was evaluated (Madsen and Barnett, 2005). Further developments are related to the utilization of a multifuel mixture by using mixed properties of different materials into the same anode. Lo Faro et al. studied the combination of Ni and $La_{0.6}Sr_{0.4}Fe_{0.8}Co_{0.2}O_3$ (LSFCO). After a thermal treatment at 1100 $^\circ$C of a Ni precursor deposited on LSFCO, a modification of the perovskite surface occurred (Figure 4.2) causing the extraction of lanthanum from the perovskite and the formation of La_2NiO_4 cluster over an Sr-enriched perovskite support (Lo Faro et al., 2012). This system showed the premises of good fuel flexibility without the aid of fuel processing or internal
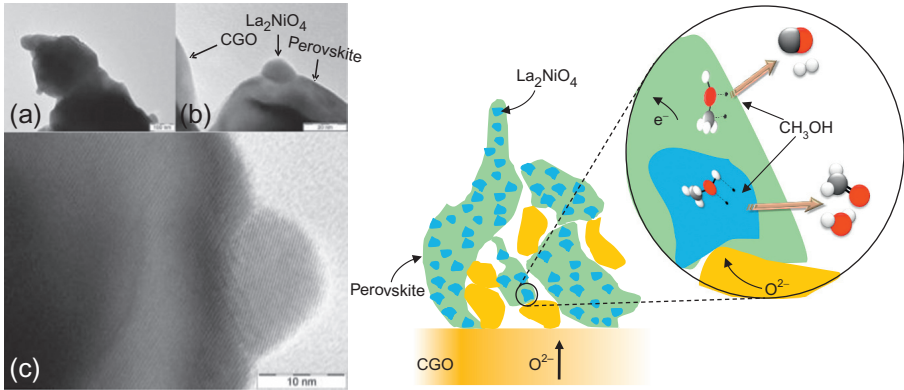
Figure 4.2 Ni-modified $La_{0.6}Sr_{0.4}Fe_{0.8}Co_{0.2}O_3$ micrograph (a, b, and c) and mechanism for the methanol oxidation promoted by the perovskite catalyst.

reforming. The potential advantage of this new anode consisted of the direct utilization of dry fuels that maximize the energy density and simplify the system as no significant water/thermal management is required. The direct use of odorized fuels in SOFCs causes specific problems (Lohsoontorn et al., 2008). This issue can be bypassed by using proper fuel processing consisting of a purification step, and reforming of fuel to syngas in a subsequent step. However, the fuel processing causes an evident increase of the complexity and cost of the system; moreover, the risk of poisoning is not completely avoidable. Direct oxidation of organic fuels at Ni-modified $La_{0.6}Sr_{0.4}Fe_{0.8}Co_{0.2}O_3$ (LSFCO) in combination with GDC was quite promising. A high conversion of propane (85%) and large stability (100 h without significant losses) at 800 °C in the presence of 80 ppm of H_2S was demonstrated (Lo Faro et al., 2013).

4.2.2   Cathode (air electrode)

The air electrode operates in an oxidizing environment of air or oxygen at temperatures between 600 and 1000 °C. Electrochemical reduction of oxygen from the gas phase to oxide ions consumes two electrons (Reaction 4.4).

$$\frac{1}{2}O_2(g) + 2e^- = O^{2-}(s) \tag{4.4}$$

The oxygen ions formed by reduction are then incorporated into the electrolyte, through oxygen vacancies, and migrate to the anode. In order to function properly, SOFC cathode materials must be catalytically active for the oxygen reduction and have to meet the following requirements.

(a) High ionic conductivity is required to facilitate transport of oxygen anions between the electrolyte and active reaction zone.
(b) High electronic conductivity is necessary to provide pathways between the reaction sites and external circuit.

(c) Chemical and dimensional stability during cell fabrication and operation.
(d) Thermal expansion should match with other cell components.
(e) Compatibility and minimum reactivity with the electrolyte and the interconnection is required for the electrodes.
(f) Sufficient porosity is necessary to facilitate transport of molecular oxygen from the gas phase to the air electrode/electrolyte interface.

In addition to being an electronic conductor, performance and activation overpotential can be significantly improved if the cathode is also an ionic conductor (Koep et al., 2005; Zurlo et al., 2014; Magnacca et al., 2013).

As the cathode is constantly exposed to an oxidizing atmosphere, the electrode materials are mostly oxide-based, which typically are not known for high electronic conductivities.

To satisfy these requirements, doped perovskite oxides of generic formula $La_{1-x}A_xCo_{1-y}B_yO_{3-\delta}$ (A = Sr, Ba, Ca, and B = Cr, Mn, Fe, Ni, Cu), such as lanthanum manganite (LSM), lanthanum ferrite/cobaltite (LSFCO), and lanthanum chromite/manganite (LSCM), show reversible oxidation–reduction behavior. The ABO_3 crystal structure type can be described as follows: The A-cations are located at the corners of a cube. O^{2-} ions occupy the face-centered positions and one of the smaller B-cations sits in the center of the cube. Hence, the B-site cations are surrounded octahedrally by oxide ions. In general, the cation with the larger ionic radius occupies the A-sites, the smaller cation the B-sites.

The partial substitution of cations in the ABO_3 perovskite structure by cations with a lower valence either leads to formation of oxygen vacancies or to charge compensation by electronic charge carriers (Mai et al., 2005; Skinner, 2001).

The material can have oxygen excess or deficiency depending upon the ambient oxygen partial pressure and temperature. Large amounts of disordered oxygen vacancies at elevated temperatures lead to high ionic conductivity. For example, in the series $La_{1-x}Sr_xCo_{1-y}Fe_yO_{3-\delta}$, the ionic conductivity in air at temperatures 700–1000 °C can be from one to two orders of magnitude larger than that of zirconia-based solid electrolytes (Teraoka et al., 1988). The presence of multivalent cations in the perovskite compositions, on the other hand, ensures a high and predominating electronic conductivity, whereas the stability and thermomechanical properties of the materials are determined by the specific cations. A balance is necessary between the need of high O^{2-} flux and the long-term stability.

Typical data of cathodic overpotentials obtained in the range between 600 and 800 °C for $La_{0.6}Sr_{0.4}Fe_{0.8}Co_{0.2}O_3$ (LSFC) and $La_{0.8}Sr_{0.2}MnO_3$ (LSM) are shown in Figure 4.3. As can be seen, especially at low temperature, the kinetics of the O_2 reduction prevail over the ohmic and mass transport properties and affect the final performance of a complete cell. Comparing the electrochemical behavior of LSFC and LSM, the LSFC performs more in the range of temperatures investigated.

Current SOFC technologies use porous multiphase composite electrodes where, in general, one phase provides ionic conductivity and another electronic percolation. The catalytic activity is usually provided by the electronically conducting phase. Mixed ionic and electronic conductors (MIECs) such as LSFC and LSM are mixed with CGO nanopowders in order to mitigate constraints related to the kinetics of O_2
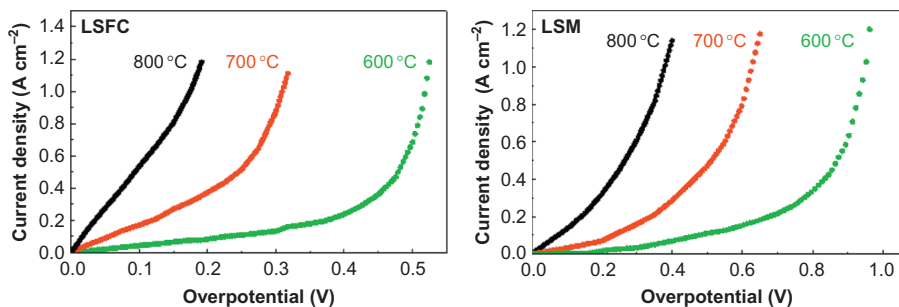
Figure 4.3 Electrochemical behavior for the O_2 reduction promoted by LSFC and LSM electrocatalysts.

reduction and mass transport. Electrochemical impedance spectroscopy analysis at 900 °C has provided information about the effect of CGO mixed to perovskite. The addition of CGO to LSFC did not much affect the electrochemical behavior, whereas the addition of CGO to LSM caused an increase of the polarization resistance and a decrease of the mass transport resistance. A compromise of these two trends may be achieved with 70 wt.% LSM+30 wt.% CGO (Figure 4.4).

The active area of such composite electrodes is inherently restricted to the interfacial regions between this phase and the ceramic membrane electrolyte. Mixed conducting materials can provide both ionic and electronic conductivity in one phase, greatly enhancing the active electrode area. The reaction sites in SOFC electrodes are commonly discussed using the concept of a triple-phase boundary (TPB). The TPB is the location at which the electron conducting, ion conducting, and gas phases come into contact.

The general macroscopic reaction pathways for the oxygen reduction process on a porous cathode/solid electrolyte structure were discussed more than 35 years ago (Pizzini, 1973), and are summarized in the diagram in Figure 4.5.
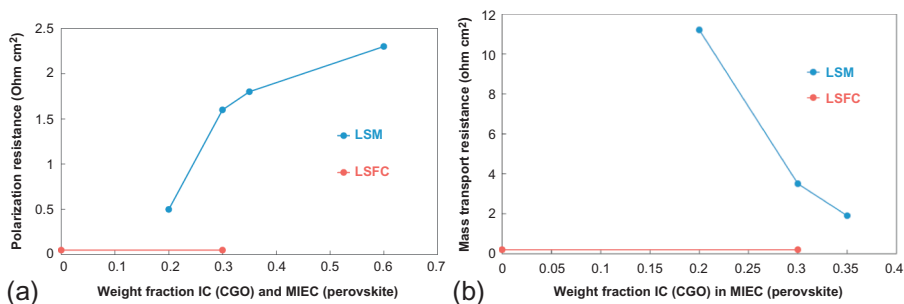
Figure 4.4 (a) Polarization and (b) mass transport resistance for MIECs ($La_{0.6}Sr_{0.4}Fe_{0.8}Co_{0.2}O_3$ (LSFC) or $La_{0.8}Sr_{0.2}MnO_3$ (LSM)) as a function of CGO content.
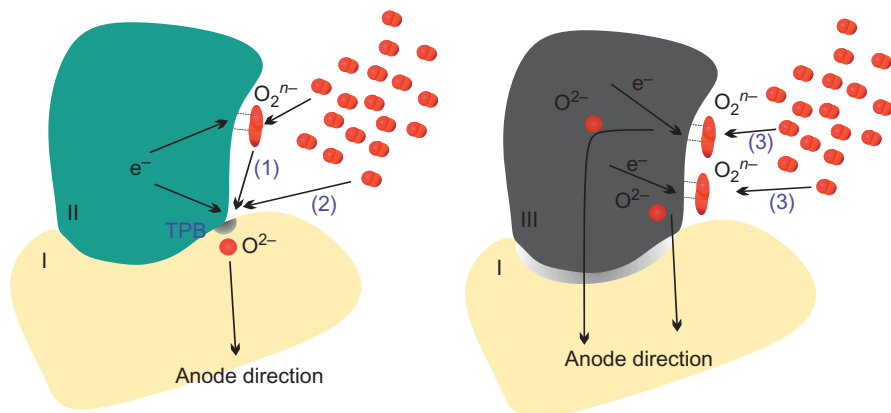
Figure 4.5 Oxygen reaction pathways between ionic (I), electronic (II), and mixed-conducting materials (III); (1) surface dissociation and diffusion followed by incorporation at the TPB, (2) direct incorporation at the TPB, (3) incorporation along the length of the MIEC followed by bulk diffusion.

Reaction pathway (1): The oxygen absorbs dissociatively on the surface of the perovskite phase before diffusing along the surface to the TPB where it is incorporated into the ionic phase.

Reaction pathway (2): Gas-phase oxygen is incorporated directly into the electrolyte phase at the TPB.

Reaction pathway (3): This involves incorporation of oxygen at the surface of the MIEC coupled to bulk diffusion to the electrolyte/MIEC interface. Bulk pathway is enabled when the electronic phase is replaced by a mixed conductor.

When this third mechanism occurs, the distance from the interface, λ, is determined by a balance between surface exchange rates and bulk ionic conductivity, which are related to the vacancy concentration. Low ionic conductivity and fast surface incorporation rates reduce the mechanism to that of the purely electronic conductor. In contrast, high ionic conductivity and low surface rates can extend the reaction zone far from the interface region. Using the characteristic thickness criterion as for MIEC membranes, the mixed conducting zone is estimated to extend up to $\sim 10\ \mu m$ from the interface (Adler et al., 1996).

At distances greater than this, the net current is electronic and only an equilibrium exchange occurs between gas-phase oxygen and the MIEC. This MIEC zone represents an extension of the TPB region, and increases the active electrode area.

Steele and Bae found that the performance of LSCF-GDC cathodes could be interpreted in terms of surface exchange kinetics that limit the performance of the cathode (Steele and Bae, 1998). Increased understanding of the relative importance of bulk versus surface kinetics in MIEC cathodes is required to provide guidelines for both cathode manufacture and development of new cathode materials.

4.2.3   Electrolyte (membrane)

The main purpose of an electrolyte is to conduct a specific ion between two electrodes in order to complete the overall electrochemical reaction. Without conduction of that specific ion, no appreciable current can flow through the fuel cell and only terminal potential can be recorded.

Ideally, an electrolyte is an ionic conductor and an electronic insulator. SOFC electrolytes work in a drastic environment: hydrogen- or carbon-based fuels on the anode side, air on the cathode side, and also high temperatures.

To achieve good cell performance, the electrolyte must be free of porosity to avoid gases to permeate from one side of the electrolyte to the other, it should be uniformly thin to minimize ohmic loss, and should have high ion conductivity with transport number for ions close to unity and a transport number for electrons as close to zero. Moreover, electrolytes with these desired properties must be deposited as thinly as possible in order to reduce ohmic loss.

The general criteria for the quality assessment of a solid electrolyte material to be used in an SOFC include

(a) Easy fabrication into a mechanically strong and dense membrane of small thickness and large area to minimize bulk resistance.
(b) An oxide-ion conductivity $\sigma_0 > 10^{-2}$ S cm^{-1} at the cell operating temperature.
(c) Excellent chemical and mechanical compatibility with electrodes to avoid formation of blocking interface phases and to minimize interfacial resistances.
(d) A negligible electronic conductivity at the cell operating temperature to retain a transport number close to 1.
(e) Compatibility of thermal-expansion coefficients between electrolyte, electrodes, interconnects, and seals from ambient temperature and cell operating temperature.
(f) Relatively low costs of material and fabrication.

SOFCs are based on the concept of an oxygen ion conducting electrolyte through which the oxide ions (O^{2-}) migrate from the air electrode (cathode) side to the fuel electrode (anode) side where they react with H_2 to form water and electricity.

When organic fuels are fed to the anode, an oxygen ion conductor offers, in principle, good perspective for a direct electro-oxidation (i.e., Reaction 4.5):

$$CH_4 + O^{2-} \rightarrow CO_2 + 2H_2O + 8e^- \tag{4.5}$$

However, at the high temperature of operation, oxygen ion conductors can also promote internal steam reforming (SR) (Reaction 4.6):

$$CH_4 + H_2O \rightarrow CO + 3H_2 \tag{4.6}$$

with CO and H_2 then used in the electro-oxidation reactions. Even in this condition, oxygen ion conducting electrolytes are preferred because CO can be more efficiently oxidized.

Generally an SOFC consists of yttrium-stabilized zirconia (YSZ) electrolyte operating at temperatures above 800 °C (Holtappels and Stimming, 2010;

Montinaro et al., 2006; Lo Faro et al., 2009; Pascual et al., 1983). This represents the present state of the art of commercial-type SOFCs. Many efforts have been addressed to materials able to operate at intermediate temperatures (500–800 °C) in order to increase stability and use of cheap ferritic steels (Cowin et al., 2011). Like zirconia, ceria forms a fluorite structure and is a well-known electrolyte material for SOFCs also in consideration to its good compatibility with conventional electrodes (Steele, 2000a; Inaba and Tagawa, 1996; Huijsmans et al., 1998). Despite its favorable ion transport properties in comparison to YSZ, ceria has not been considered as a realistic electrolyte for fuel cell applications because of its high electronic conductivity. In particular, under reducing conditions, CeO_2 is not stable and becomes CeO_{2-x} (Mogensen et al., 2000). Like zirconia, ceria is doped to increase conductivity, and also like zirconia, the highest conductivity occurs for ions with the lowest size mismatch. However, an increasing amount of dopants tends to form a second phase due to the solubility limit, resulting in a reduced conductivity. Among Gd, Sm, and Y, gadolinium is a common rare earth dopant, with ionic conductivity values that have exceeded those obtained with equivalent amounts of samarium doping (Steele, 2000b; Kudo and Obayashi, 1975; Yahiro et al., 1988).

Some novel oxygen ionic conductors have been recently suggested, including perovskite-type oxides derived from lanthanum gallate $LaGaO_3$ (Ishihara et al., 1994; Huang et al., 1998). The $La_{0.8}Sr_{0.2}Ga_{0.8}Mg_{0.2}O_3$ (LSGM) can be considered a promising electrolyte and an alternative to the conventional GDC due to its higher ion transport number at intermediate temperatures and suitable ionic conductivity (Wan et al., 2005; Tao et al., 2005; Liu et al., 2012). It is characterized by lower conductivity at intermediate temperature but similar activation energy toward the oxygen ion migration (Figure 4.6).

These characteristics reduce the loss of efficiency, allowing the achievement of higher cell voltages under practical operating conditions of current densities.
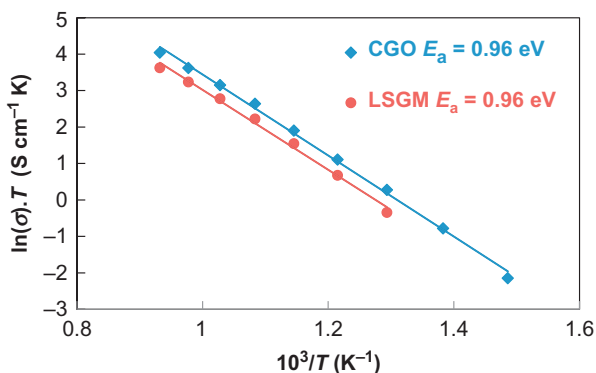
Figure 4.6 Arrhenius plot of ionic conductivity for alternative electrolytes for SOFCs operating at intermediate temperature (i.e., $Ce_{0.8}G_{0.2}O_2$) (CGO is as well known as Gadolinia-doped Ceria (GDC)) and $La_{0.8}Sr_{0.2}Ga_{0.8}Mg_{0.2}O_3$ (LSGM).

In principle, the overall reversibility expected for an all-perovskite-based SOFC at intermediate temperatures is higher than that of an SOFC equipped with a ceria-based electrolyte (Lo Faro and Aricò, 2013). Nevertheless, the use of LSGM as electrolyte has the disadvantage that it cannot be used in combination with the Ni/YSZ conventional anode due to the well-known reaction between NiO and LSGM during cell fabrication. This causes the formation of an undesired phase consisting of La_2NiO_4 (Huang et al., 1997). In order to minimize such constraint, some developments have regarded the formation of a barrier layer using an additional electrolyte layer such as samarium-doped ceria (SDC) or GDC between the Ni-based anode and LSGM electrolyte (Wang et al., 2011; Peña-Martínez et al., 2006). However, this approach makes the SOFC fabrication more complicated with an increase in manufacturing costs. Another possibility is the use of new anodes based on perovskites in order to solve such issues, as reported by Lo Faro and Aricò (2013).

The most recent research efforts are concerned with the investigation of ceramic proton conductors to replace conventional anionic ceramic electrolytes. They may offer an interesting combination of benefits because of their ability to transport both protons and oxygen ions at intermediate temperatures. Ceramic proton conductors have a larger ionic transport number than ceria-doped gadolinia (GDC) and better chemical compatibility with conventional SOFC materials than lanthanum strontium gallates (LSGM). Furthermore, these oxides can work in the temperature range of 400–750 °C in dependence of their lower activation enthalpies of their conductivity. Protonic SOFC may show higher thermodynamic efficiency for the conversion of chemical energy to electrical power rather than anionic SOFC (Demin and Tsiakaras, 2001).

However, the presence of protons in these materials is not due to structural protons. These materials derive their ionic conductivity from the incorporation of protonic defects that have sufficiently high mobility (Thomas and Lander, 1956). It has been suggested (Coors, 2003) that water can diffuse across the electrolyte membrane, inducing SR and even conversion of CO to CO_2 through the water–gas shift reaction

$$CO + H_2O \rightarrow CO_2 + H_2 \tag{4.7}$$
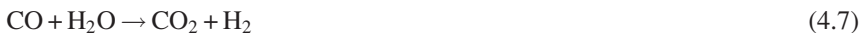
Hydrogen generated by reactions (4.6) and (4.7) is then electro-oxidized to form protons. In this case, hydrocarbons can be directly utilized and no water is produced at the anode, avoiding dilution effects. Fuel utilization increases although dilution due to CO_2 still occurs.

The most studied materials are concerned with acceptor-doped perovskite-type oxides $AB_{1-x}M_xO_3$ (A = Ba, Sr; B = Ce, Zr, Ti) where A and B are the main constituents, M is a trivalent dopant, such as a rare earth element, and x is the dopant concentration, usually less than 1. Among them, the best-known and most intensively investigated examples are alkaline earth cerates, zirconates, niobates, and titanates. It is widely recognized that oxides with high conductivity (e.g., $BaCeO_3$-based compounds) generally show very low-phase stability toward carbonation caused by atmospheric CO_2 (Kreuer, 1997).

4.3   Fuels used in SOFCs

Hydrogen is a commodity in many chemical and petroleum processing operations and is also a clean energy source. Although fuel cells work efficiently with hydrogen as a fuel, there are still some major problems related to hydrogen availability and acceptability. In the short- to medium-term future, the only realistic fuels for SOFCs are the carbon-based fuels, particularly natural gas and the so-called biofuels such as biogas and bioethanol. The performance of such energy devices depends crucially on the properties of their component materials; therefore, it is necessary to develop innovative materials with improved functional properties. The key issue is the utilization of novel anodes because the state-of-the-art anode (Ni-YSZ) is affected by carbon deposition and poisoning by sulfur contaminants. This causes a rapid as well as irreversible cell degradation (Park et al., 2000; Timmermann et al., 2008). Typically, these drawbacks may be mitigated by adding a purification step for the fuel and a chemical processor to produce clean syngas by conventional SR, partial oxidation reforming (POX), or autothermal reforming (ATR) (Ahmed and Krumpelt, 2001). Alternatively, the addition of a large amount of water steam to the fuel (steam-to-carbon ratio approx. 2.5) may mitigate the carbon deposition mechanisms by creating the condition for an internal reforming (Lee et al., 1990). In both cases, the associated increase in complexity and costs, as well as the risk of damages for the cells, may be an obstacle for the large diffusion of such technology. The development of SOFC anodes capable of operating with several fuels, without suffering from carbon deposition due to catalytic cracking, and resistant to contaminants, is still far from being achieved. Currently, one of the most exciting possibilities is the direct oxidation of fuels at the anode (Putna et al., 1995). Operation with dry organic fuels at the anode simplify both thermal and water management. For example, the direct oxidation of methane (Reaction 4.8) has the thermodynamic possibility to achieve 99.2% conversion efficiency at targeted temperatures. If this reaction is achieved, it is necessary to avoid or inhibit methane cracking. There is also considerable controversy as to whether the reaction is actually a single step (i.e., deep oxidation) or if it involves a series of intermediate reactions. The final products of both direct combustion and electrochemical processes are CO_2 and water (Reaction 4.9).

$$CH_4 + 2O_2 \Leftrightarrow CO_2 + 2H_2O, \quad \Delta H = -802\,\mathrm{kJ\,mol^{-1}} \tag{4.8}$$

$$CH_4 + 4O^{2-} \Leftrightarrow CO_2 + 2H_2O + 8e^-, \quad \text{Electrochemical} \tag{4.9}$$

Some experiments on competitive oxidation of hydrocarbons have revealed an activity pattern according to the sequence $C_3H_8 > C_2H_4 > C_3H_6 > C_2H_2 > i\text{-}C_4H_8$. Nevertheless, the reaction rates required in a fuel cell are not extremely high (Park et al., 2000).

For a current density of 1 A cm^{-2}, a porous anode with only 1 cm^2 of catalytic active surface area per cm^2 of planar fuel cell (very low for a porous catalyst) would require a turnover frequency (frequency of adsorption/desorption of reacting molecules on reaction sites) of less than 10. This is a reasonable value for an oxidation

catalyst. Most probably the direct oxidation of hydrocarbons is a multistep process involving dehydrogenation, C adsorption, and subsequently reaction with O^{2-} ions, desorption of CO_2 as reaction product.

Regarding the direct utilization of organic fuels in SOFCs, materials with mixed ionic and electronic conducting characteristics may be desirable. The mixed conductivity extends the active zones where electrochemical reactions can occur by distributing O^{2-} ions at the interfaces between the electronic conductor and gas phase.

Several materials, especially conductive oxides, have been proposed as possible alternatives for SOFC anodes. SOFC developers have used doped-ceria as an anode material to lower the operating temperature. Ceramics based on CeO_2 exhibit mixed ionic and electronic conductivity in a reducing atmosphere due to the reduction of Ce^{4+} to Ce^{3+}. In addition, it is believed that the excellent catalytic activity of CeO_2-based materials are related to the oxygen-vacancy formation and migration associated with reversible CeO_2–Ce_2O_3 transition (Sun et al., 2006; Skorodumova et al., 2002).

It has been reported that ceria-based ion conductors (Marina and Mogensen, 1999) have a high resistance to carbon deposition, which permits the direct supply of dry carbon-based fuels to the anode. The most effective method, however, is the addition of Ni, Co and some noble metals, such as Pt, Rh, Pd, and Ru to ceria. These materials are beneficial for the reforming reactions of organic fuels, due to their capability of breaking the C–H bond (La Rosa et al., 2009; LoFaro et al., 2014; Lo Faro et al., 2007; Saeki et al., 1994). Highly porous structures generally result in less carbon deposition. The use of mixed ionic-electronic conducting materials such as doped-ceria as ceramic matrix of the anode also yielded much lower carbon deposition than the conventional zirconia matrix.

Boosting the commercialization of such technology for the market of distributed energy, the chance is mainly based on the development of new anodic formulations that, at the same time, should not cause modifications in the well-established SOFC manufacturing process (Montinaro et al., 2006) and improve the reliability of SOFC technology toward the utilization of carbon-based fuels (Park et al., 2000). This aspect is in line with the strategies of several SOFC companies, which may take advantage from innovations in the short to medium term (Steele, 2000a; Cacciola et al., 2001).

Sin et al. (2007) have proposed a Ni-Cu alloy combined with ceria for the direct utilization of hydrocarbons. It has been observed that the interruption of the Ni-Ni network, which promotes the cracking process and the consequent formation and deposition of carbon fibers and soot, as well as the addition of CGO, can improve the ionic conduction, oxygen storage, and stability of the catalyst. Substitution of Ni-Ni-Ni with Ni-Cu-Ni patterns reduced the cracking process as demonstrated by a durability test of more than 1000 h in the presence of dry methane fed to the anode (La Rosa et al., 2009; Sin et al., 2007). These properties derive from the excellent synergy of Ni providing electrocatalytic activity and Cu ensuring resilience to cooking. Cu breaks the assemblies of Ni atoms, which activate carbon deposition. These insights have opened new scenarios in the investigation of the synthesis methods for the preparation of Ni-based alloys (Lo Faro et al., 2015) as well as of protective layers for conventional SOFCs.

Accordingly, the basic idea is to use Ni-based alloy composite as a thin protective layer for a thick conventional SOFC anode (LoFaro et al., 2014). The electrochemical
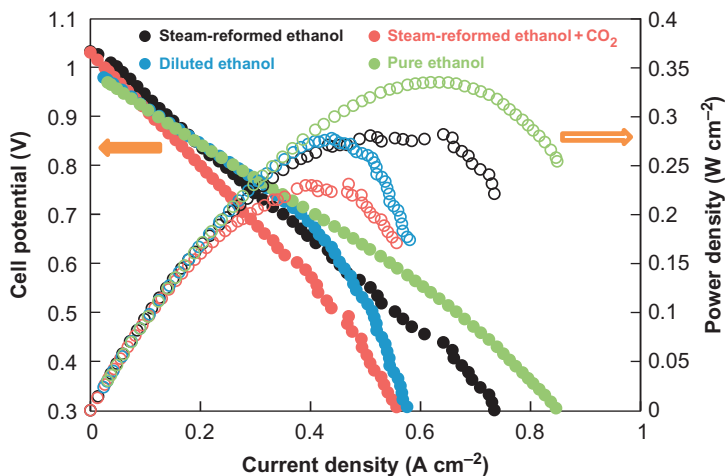
Figure 4.7 Polarization and power density curves collected at 800 °C for a protected commercial SOFC fed with ethanol (LoFaro et al., 2014).

performance achieved in the presence of pure, diluted, and reformed ethanol fuels (Figure 4.7) demonstrated that the protective layer plays a positive role in the presence of pure ethanol fed to the anode. Whereas significant carbon blockage under the feed of dry ethanol has been reported for conventional cells (Tsiakaras and Demin, 2001; Saunders and Kendall, 2002; Saunders et al., 2004).

Regarding the future of SOFCs, there are some perspectives for the utilization of heavy carbon-based fuels and carbon-free liquid fuels (Cimenti and Hill, 2009). In principle, SOFCs can take benefit from the high operating temperatures making possible the electrochemical conversion of any gas and/or liquid fuel. In this regard, conventional SOFCs have been explored for the direct utilization of dry oxygenated fuels such as dimethyl ether (Murray et al., 2002) and ammonia (Ma et al., 2007). However, the most interesting results have been achieved by replacing the Ni-YSZ anode of a conventional SOFC with innovative materials characterized by resilience to carbon deposition while being affordable in costs. Park et al. (2000) have proposed Cu instead of Ni as electronic conductor, whereas the catalytically active phase was assured by the presence of CeO_2 for the oxidation of various dry hydrocarbons including methane, ethane, 1-butene, n-butane, and toluene. Another approach is the use of materials characterized by both ionic and electronic conductions (MIEC) and able to promote the fuels oxidation and conversion of contaminants. Some perovskite oxides include stability under high temperature and under redox environment; effectiveness toward the cleavage of C–H, C–C, and C=C bonds through oxidative processes; and minimum chemical binding energy for sulfur species. Pioneering work has been reported on the fuel flexibility of perovskites toward the oxidation of several fuels and their combinations, including natural gas and H_2S (Pillai et al., 2008), syngas, methanol, glycerol, propane, and H_2S up to a maximum of 80 ppm (Lo Faro et al., 2012, 2013).

4.4   Advantages of SOFCs

As discussed above, SOFCs are solid-state devices that produce electricity from the electrochemical reaction of a fuel and an oxidant separated by an ionic-conducting oxide electrolyte.

Compared to several other types of fuel cells, SOFCs appear better suited for the small power systems market (e.g., less than 100 kW) for a distributed energy generation that includes cogeneration and trigeneration (Chicco and Mancarella, 2009). Because of the high operating temperature, SOFCs have the potential of offering high-level performance and efficiency, up to 70% of the electrical yield, and provide many advantages over traditional energy conversion systems including reliability, modularity, and extremely low emissions.

However, such technology compared to traditional energy conversion systems such as internal and external combustion engines is still higher in cost. The efficiency of fuel cells is much higher than those of combustion engines because fuel cells are not governed by the Carnot cycle (Minh and Takahashi, 1995); in fact, the energy conversion pathway does not proceed via thermal energy but directly from chemical into electrical energy. Thus, the chemical reaction is controlled in such a way that the electron exchange does not take place locally but via an external circuit; the fuel cell is therefore a part of the electrical circuit.

SOFC systems are presently rated at a cell voltage of 0.7 V/cell, where at suitable efficiency they exhibit a high electric power output (>50 % of the maximum). While this is a reasonable approach for performance comparisons, there are also some disadvantages. As can be seen in Figure 4.8, the cell efficiency is limited to 56% by the
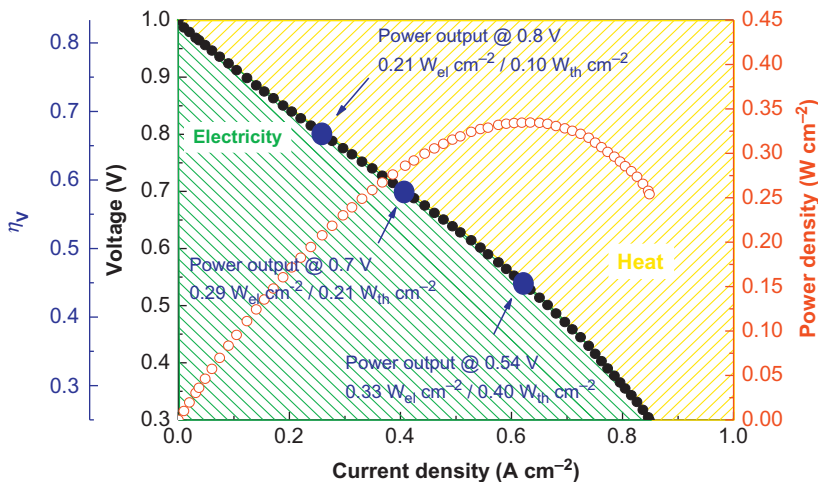
Figure 4.8 Electrical versus thermal power output in an SOFC operating at 800 °C in the presence of pure ethanol.

electricity to heat ratio. Removal of the heat needs large amounts of air feed. This affects stack, heat exchanger, and blower designs.

A rise of the cell voltage from 0.7 to 0.8 V/cell implies a 30% increase in cell area and therefore in stack size for the same electric output. However, the electricity to heat ratio increases from 1.4 at 0.7 V to 2 at 0.8 V. The cell electrical efficiency is raised by about 10%. A lower heat output can reduce the size of peripherals like tubing, heat exchanger, and blower, and also the power consumption of the active cooling systems like blowers and pumps.

4.5 Design issues and disadvantages of SOFCs

SOFCs have been tested since 1930 under several configurations, among which the most widespread and tested devices have been planar and tubular arrangements. However, a number of technological problems still need to be solved, basically related to the high operating temperature and then to thermal cycling issues. Research and development are therefore still proceeding toward the development of new materials and to optimize the design of single cells and complete stacks. The materials for cell components in these different designs are either the same or very similar in nature.

The materials for different cell components must be selected based on the following criteria:

(a) Suitable electrical conducting properties required by different cell components to perform their intended cell functions.
(b) Adequate chemical and structural stability at high temperatures during cell operation as well as during cell fabrication.
(c) Minimal reactivity and interdiffusion among different cell components.
(d) Matching thermal expansion among different cell components.

In addition to the above materials selection criteria, the fabrication processes must be chosen in such a way that every sequential component fabrication process does not affect those components already fabricated and to minimize the cell fabrication costs. The conventional architectures vary from tubular cell (Figure 4.9) to planar (Figure 4.10).

The fabrication routes for the individual cell components of SOFC differ greatly depending on which cell component design is to perform the mechanical supporting function in the cell, whereas in most cases the electrolyte or the anode and cathode ensure the mechanical stability of the cells. The designs shown above differ in terms of current path within a stack of cells, in gas flow configuration and gas manifolding, and cell-to-cell electrical connection.

It is noteworthy that planar cells experience lower stresses than tubular cells, suggesting that smart designs may alleviate possible stresses.

Ceramic interconnectors played a dominant role in the early SOFC developments, whereas the metallic interconnects have been frequently used in recent developments. Both variants have benefits and disadvantages and the final choice is therefore always a compromise depending, among other aspects, on the design, the operating
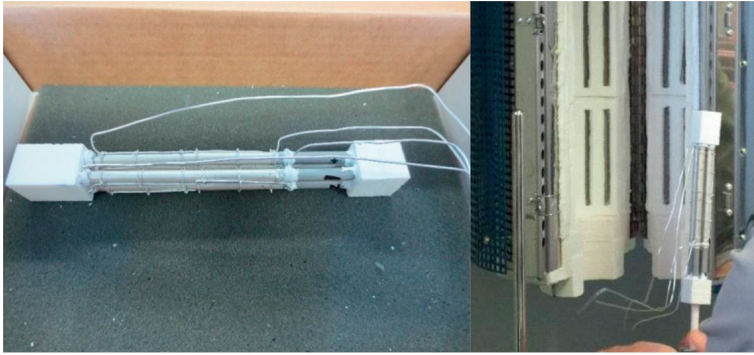
Figure 4.9 Example of a four-microtubular cell stack based on conventional materials.
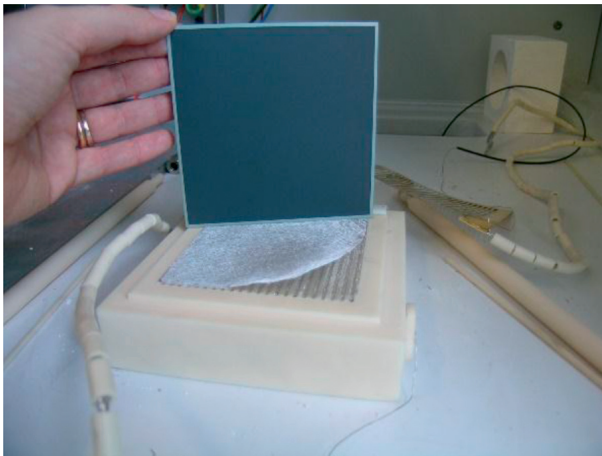
Figure 4.10 Example of a planar cell based on conventional materials.

temperature, the required service life as well as on the material and production costs of these components.

In general, advantages for metallic arrangements are considered to be high electrical conductivity, good processability, and low cost. Long-term resistance to corrosion behavior and low chromium evaporation are necessary; whereas high expansion coefficients are disadvantageous. Furthermore, the use of metallic interconnects and compressive sealing is fundamental for a practical application as well as to facilitate rapid start-up and thermal cycling. The success of metallic interconnects in SOFC systems will decisively depend on solving these problems. Though SOFCs operating at temperatures above 750 °C are currently performing better, they also cost almost 8 times more than those operating below that temperature. Lowering the operating

temperature into a range where cheap ferritic steel interconnects can be used reduces the interconnect materials cost by 200% and the cost approaches \$10 per kW. Research and development work on ferritic steels therefore concentrates on application temperatures <750 °C. The application range of interest for this material class coincides with the development goals for planar anode-supported fuel cells. For this reason, such materials are being used or developed by all companies working on this concept (e.g., Sanyo, FZJ, Hitachi Metals, ThyssenKrupp). Most used metallic interconnects are based on ZMG232, Crofer 22 APU, Haynes alloy series, stainless steels, and Fe-16Cr alloy (Yang et al., 2004; Brylewski et al., 2001; Kurokawa et al., 2004; Fontana et al., 2007).

In general, it can be stated that the long-term corrosion behavior of commercially available materials is not yet sufficient. For example, longevity for stationary applications has been fixed at 40,000–80,000 h and therefore degradation and aging mechanisms must be reduced considerably (Tu and Stimming, 2004). The solutions have not yet reached the cost goal. Intensive work is being performed to find cheaper solutions by simplifying and adapting the design and using other modern manufacturing techniques (e.g., punching, laser cutting, brazing).

4.6   Applications of SOFCs

SOFCs are under consideration for a number of other auxiliary power applications. For example, cars and other vehicles, from trucks to airplanes, have power requirements beyond those for propulsion. Today, batteries or alternators, or a combination of the two, usually supply these additional electronics needs, but several technologies—including fuel cells—are under development to supply power for electronics in the future. Auxiliary power requirements are likely to grow significantly as developers incorporate additional electronics into vehicles.

Small fuel cell systems, typically less than 10 kW, are under consideration for many applications that traditional electric utilities have not supplied widely. These applications are a subset of distributed generation. In this area, fuel cells may enable new companies to enter the power generation business as equipment providers or electricity providers. For example, companies that supply commodities, fuels, and wastes are forming partnerships with fuel cell companies to bring fuel cell-based electricity to consumers in remote locations that are off the grid. Among the applications under consideration are

– backup for residential, commercial, or industrial users
– high-quality power for commercial or industrial users
– remote power for residential, commercial, or industrial users in developed or developing counties
– grid-independent power for residential, commercial, or industrial users

Resource issues are some of the most significant in the stationary power sector, particularly for companies that want to introduce large, grid-connected units. The scale of investments in such units is significant, and risks are high if systems do not work properly or integrate properly with the grid.
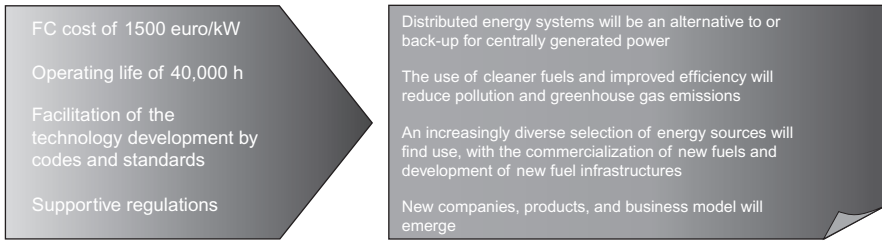
Figure 4.11 Introducing SOFC to the market.

The stationary sector appreciates the following properties of SOFCs:

- Power quality and reliability. Some manufacturing operations are very sensitive to power fluctuations and disruptions and will pay a premium for high-quality, reliable power.
- Environmental benefits. Building new conventional power sources, particularly in environmentally sensitive areas or near urban areas, is increasingly difficult.
- Remote power. Power transmission and distribution are expensive. Placing a plant near the point of power use avoids these costs.

Deregulation of the electric utility industry has led to the creation of numerous energy service companies, which view SOFCs as an attractive technology for introducing on-site power generation to small and midsize electricity users. Distributed generation is increasingly attractive to utility companies because it can improve reliability, increase asset use, and avoid transmission and distribution costs. SOFCs suit distributed generation.

Establishing codes and regulations that allow SOFCs to connect safely to the grid is important if they are to achieve widespread commercial use.

Figure 4.11 outlines the factors and events that will enable stationary application of SOFCs.

One of the main implications is the consumer's ability to use an increasingly diverse selection of energy sources. New business models could be especially important in the stationary power sector as SOFC-based distributed energy systems become an alternative to or backup for centrally generated power. Although fuel cells are already addressing market needs in niche applications, significant commercial markets will emerge only as products come on the market at competitive price points and with superior performance.

4.7 Market diffusion and future trends

To make SOFCs economically competitive, both materials and system fabrication costs must be dramatically reduced. Precommercial planar SOFC cells generally present an architecture consisting of Ni-based anodes supporting the electrolyte as well as the cathodes. The requirement of significant cost reduction, as well as robustness of the ceramic membranes, has prompted the exploration of alternative cell architectures
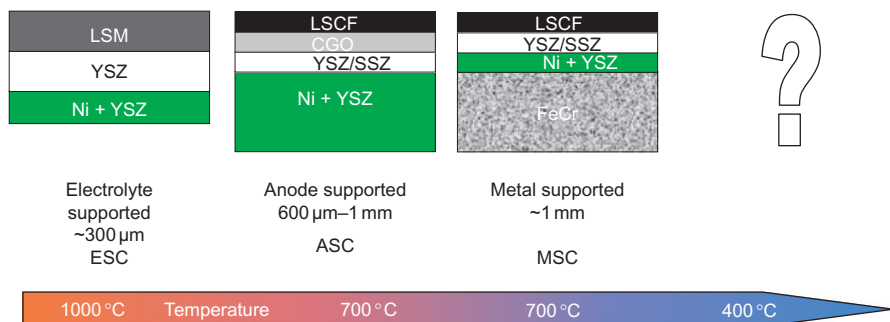
Figure 4.12 Cell architecture trend for planar SOFCs.

in which the structural and the catalytic functions of the supporting porous electrode are separated. An alternative to the traditional anode-supported architecture is represented by a porous metallic alloy that provides the mechanical support for the electrolyte film and serves as the electrical connection, while the electrocatalytic function is maintained by a thin (10–15 μm) layer of Ni-based anode at the solid electrolyte/porous steel alloy interface (Figure 4.12).

Unfortunately, this approach appears unsuitable for the direct oxidation process because cheap ferritic stainless steel porous supports are quite affected by carbon deposition and difficult to be treated with protective coatings. Furthermore, the use of strong reducing atmospheres for the high-temperature sintering irreversibly modifies the anode catalyst. The performances reported in the literature for this approach are quite small despite the fact that it has been proposed for about a decade. According to the concepts and objectives reported above, the progress beyond the state of the art to promote the commercialization of such technology mainly relies on the development of innovative nanostructured SOFC anode materials for direct oxidation at intermediate temperatures of organic fuels and characterized by resilience to carbon deposition, stability toward the presence of contaminants, and suitable catalytic activity with reaction rates comparable to methane internal reforming at 800 °C.

The cathode-supported cell approach also appears reliable in terms of performance, appropriate sealing, and simplicity of design. The use of a cathode support does not preclude any aspect of SOFC operation. Cathode-supported cells are currently used in conjunction with tubular design for high-temperature operation (i.e., $T > 900$ °C); such cathode is based on $La_{0.8}Sr_{0.2}MnO_3$ (LSM) that has suitable electrocatalytic properties only at very high temperatures and this precludes its use at lower temperatures. However, an LSFCO cathode that possesses good stability and electocatalytic activity at temperatures lower than 800 °C may be one of the possible solutions for the reduction of the working temperature. This material has not been significantly investigated as support for devices with suitable geometric area (>10 cm $\times$ 10 cm). A thin anode layer is a prerequisite for the direct oxidation process, allowing appropriate tolerance to redox and thermal cycles.

4.8 Conclusions

The issues addressed in this chapter concern the perspectives of SOFCs diffusion into the market of distributed energy power generators. As outlined above, most of the issues related to materials, fuels, and cell configuration can be addressed by using approaches useful for the intermediate temperature operation as well as providing scalability for the industry supply chain. Besides, the high conversion efficiency assured by the direct oxidation of organic fuel in SOFCs, in combination with cogeneration, the use of fuels derived from renewable sources in high-efficiency SOFC systems appears to be in good agreement with the need for sustainable processes.

References

Adler, S.B., Lane, J.A., Steele, B.C.H., 1996. Electrode kinetics of porous mixed-conducting oxygen electrodes. J. Electrochem. Soc. 143, 3554–3564.

Ahmed, S., Krumpelt, M., 2001. Hydrogen from hydrocarbon fuels for fuel cells. Int. J. Hydrog. Energy 26, 291–301.

Brylewski, T., Nanko, M., Maruyama, T., Przybylski, K., 2001. Application of Fe–16Cr ferritic alloy to interconnector for a solid oxide fuel cell. Solid State Ion 143, 131–150.

Cacciola, G., Antonucci, V., Freni, S., 2001. Technology up date and new strategies on fuel cells. J. Power Sources 100, 67–79.

Chicco, G., Mancarella, P., 2009. Distributed multi-generation: a comprehensive view. Renew. Sustain. Energy Rev. 13, 535–551.

Cimenti, M., Hill, J.M., 2009. Direct utilization of liquid fuels in SOFC for portable applications: Challenges for the selection of alternative anodes. Energies 2, 377–410.

Coors, W.G., 2003. Protonic ceramic fuel cells for high-efficiency operation with methane. J. Power Sources 118, 150–156.

Costamagna, P., Costa, P., Antonucci, V., 1998. Micro-modelling of solid oxide fuel cell electrodes. Electrochim. Acta 43, 375–394.

Cowin, P.I., Petit, C.T.G., Lan, R., Irvine, J.T.S., Tao, S., 2011. Recent progress in the development of anode materials for solid oxide fuel cells. Adv. Energy Mater. 1, 314–332.

Dal Santo, V., Gallo, A., Naldoni, A., Guidotti, M., Psaro, R., 2012. Bimetallic heterogeneous catalysts for hydrogen production. Catal. Today 197, 190–205.

Demin, A., Tsiakaras, P., 2001. Thermodynamic analysis of a hydrogen fed solid oxide fuel cell based on a proton conductor. Int. J. Hydrog. Energy 26, 1103–1108.

Dias, J.A.C., Assaf, J.M., 2004. Autothermal reforming of methane over Ni/γ-Al$_2$O$_3$ catalysts: the enhancement effect of small quantities of noble metals. J. Power Sources 130, 106–110.

Finnerty, C.M., Coe, N.J., Cunningham, R.H., Ormerod, R.M., 1998. Carbon formation on and deactivation of nickel-based/zirconia anodes in solid oxide fuel cells running on methane. Catal. Today 46, 137–145.

Fontana, S., Amendola, R., Chevalier, S., Piccardo, P., Caboche, G., Viviani, M., Molins, R., Sennour, M., 2007. Metallic interconnects for SOFC: characterisation of corrosion resistance and conductivity evaluation at operating temperature of differently coated alloys. J. Power Sources 171, 652–662.

Hoang, D.L., Chan, S.H., 2007. Experimental investigation on the effect of natural gas composition on performance of autothermal reforming. Int. J. Hydrog. Energy 32, 548–556.

Holtappels, P., Stimming, U., 2010. Solid oxide fuel cells (SOFC). John Wiley & Sons, Ltd. http://onlinelibrary.wiley.com/book/10.1002/9780470974001.

Huang, K., Feng, M., Goodenough, J.B., Milliken, C., 1997. Electrode performance test on single ceramic fuel cells using as electrolyte Sr- and Mg-doped $LaGaO_3$. J. Electrochem. Soc. 144, 3620–3624.

Huang, K., Tichy, R., Goodenough, J.B., Milliken, C., 1998. Superior perovskite oxide-ion conductor; strontium- and magnesium-doped $LaGaO_3$: III, performance tests of single ceramic fuel cells. J. Am. Ceram. Soc. 81, 2581–2585.

Hui, S., Petric, A., 2002. Electrical properties of yttrium-doped strontium titanate under reducing conditions. J Electrochem Soc 149, J1–J10.

Huijsmans, J.P.P., Van Berkel, F.P.F., Christie, G.M., 1998. Intermediate temperature SOFC—a promise for the 21st century. J. Power Sources 71, 107–110.

Inaba, H., Tagawa, H., 1996. Ceria-based solid electrolytes. Solid State Ion 83, 1–16.

Ishihara, T., Matsuda, H., Takita, Y., 1994. Doped $LaGaO_3$ perovskite type oxide as a new oxide ionic conductor. J. Am. Chem. Soc. 116, 3801–3803.

Koep, E., Mebane, D.S., Das, R., Compson, C., Liu, M., 2005. Characteristic thickness for a dense $La_{0.8}Sr_{0.2}MnO_3$ electrode. Electrochem. Solid-State Lett. 8, A592–A595.

Kreuer, K.D., 1997. On the development of proton conducting materials for technological applications. Solid State Ion 97, 1–15.

Kudo, T., Obayashi, H., 1975. Oxygen ion conduction of the fluorite-type $Ce1-x$ Ln x O $2-x/2$ (Ln = lanthanoid element). J. Electrochem. Soc. 122, 142–147.

Kurokawa, H., Oyama, Y., Kawamura, K., Maruyama, T., 2004. Hydrogen permeation through Fe-16Cr alloy interconnect in atmosphere simulating SOFC at 1073 K. J. Electrochem. Soc. 151, A1264–A1268.

La Rosa, D., Sin, A., Lo Faro, M., Monforte, G., Antonucci, V., Arico, A., 2009. Mitigation of carbon deposits formation in intermediate temperature solid oxide fuel cells fed with dry methane by anode doping with barium. J. Power Sources 193, 160–164.

Lee, A.L., Zabransky, R.F., Huber, W.J., 1990. Internal reforming development for solid oxide fuel cells. Ind. Eng. Chem. Res. 29, 766–773.

Liu, B., Guo, W., Chen, F., Xia, C., 2012. Ga site doping and concentration variation effects on the conductivities of melilite-type lanthanum strontium gallate electrolytes. Int. J. Hydrog. Energy 37, 961–966.

Lo Faro, M., Aricò, A.S., 2013. Electrochemical behaviour of an all-perovskite-based intermediate temperature solid oxide fuel cell. Int. J. Hydrog. Energy 38, 14773–14778.

Lo Faro, M., La Rosa, D., Monforte, G., Antonucci, V., Arico, A., Antonucci, P., 2007. Propane conversion over a Ru/CGO catalyst and its application in intermediate temperature solid oxide fuel cells. J. Appl. Electrochem. 37, 203–208.

Lo Faro, M., La Rosa, D., Antonucci, V., Arico, A.S., 2009. Intermediate temperature solid oxide fuel cell electrolytes. J. Indian Inst. Sci. 89, 363–381.

Lo Faro, M., Antonucci, V., Antonucci, P., Arico, A., 2012. Fuel flexibility: a key challenge for SOFC technology. Fuel 102, 554–559.

Lo Faro, M., Modafferi, V., Frontera, P., Antonucci, P., Aricò, A.S., 2013. Catalytic behavior of Ni-modified perovskite and doped ceria composite catalyst for the conversion of odorized propane to syngas. Fuel Process. Technol. 113, 28–33.

Lo Faro, M., Frontera, P., Antonucci, P., Aricò, A.S., 2015. Ni–Cu based catalysts prepared by two different methods and their catalytic activity toward the ATR of methane. Chem. Eng. Res. Des. 93, 269–277. http://dx.doi.org/10.1016/j.cherd.2014.05.014.

LoFaro, M., Reis, R.M., Saglietti, G.G.A., Sato, A.G., Ticianelli, E.A., Zignani, S.C., Aricò, A.S., 2014. Nickel–copper/gadolinium-doped ceria (CGO) composite

electrocatalyst as a protective layer for a solid-oxide fuel cell anode fed with ethanol. ChemElectroChem 1 (8), 1395–1402. http://dx.doi.org/10.1002/celc.201402017.

Lohsoontorn, P., Brett, D.J.L., Brandon, N.P., 2008. Thermodynamic predictions of the impact of fuel composition on the propensity of sulphur to interact with Ni and ceria-based anodes for solid oxide fuel cells. J. Power Sources 175, 60–67.

Ma, Q., Ma, J., Zhou, S., Yan, R., Gao, J., Meng, G., 2007. A high-performance ammonia-fueled SOFC based on a YSZ thin-film electrolyte. J. Power Sources 164, 86–89.

Madsen, B.D., Barnett, S.A., 2005. The influence of NiO content on ceramic-based solid oxide fuel cell anodes, 2005, pp. 1185–1194.

Magnacca, G., Spezzati, G., Deganello, F., Testa, M.L., 2013. A new in situ methodology for the quantification of the oxygen storage potential in perovskite-type materials. RSC Adv. 3, 26352–26360.

Mai, A., Haanappel, V.A.C., Uhlenbruck, S., Tietz, F., Stöver, D., 2005. Ferrite-based perovskites as cathode materials for anode-supported solid oxide fuel cells: part I. Var. Compos. Solid State Ionics 176, 1341–1350.

Marina, O.A., Mogensen, M., 1999. High-temperature conversion of methane on a composite gadolinia-doped ceria–gold electrode. Appl. Catal. Gen. 189, 117–126.

Marina, O.A., Canfield, N.L., Stevenson, J.W., 2002. Thermal, electrical, and electrocatalytical properties of lanthanum-doped strontium titanate. Solid State Ion 149, 21–28.

Mars, P., van Krevelen, D.W., 1954. Oxidations carried out by means of vanadium oxide catalysts. Chem. Eng. Sci. 3 (Suppl. 1), 41–59.

McIntosh, S., Gorte, R.J., 2004. Direct hydrocarbon solid oxide fuel cells. Chem. Rev. 104, 4845–4866.

Minh, N.Q., Takahashi, T., 1995. Principles of operation. In: Takahashi, N.Q.M. (Ed.), Science and Technology of Ceramic Fuel Cells. Elsevier Science Ltd, Oxford, pp. 15–40 (Chapter 2).

Mogensen, M., Sammes, N.M., Tompsett, G.A., 2000. Physical, chemical and electrochemical properties of pure and doped ceria. Solid State Ion 129, 63–94.

Montinaro, D., Sglavo, V., Bertoldi, M., Zandonella, T., Arico, A., Lo Faro, M., Antonucci, V., 2006. Tape casting fabrication and co-sintering of solid oxide "half cells" with a cathode–electrolyte porous interface. Solid State Ion 177, 2093–2097.

Murray, E.P., Tsai, T., Barnett, S.A., 1999. A direct-methane fuel cell with a ceria-based anode. Nature 400, 649–651.

Murray, E.P., Harris, S.J., Jen, H., 2002. Solid oxide fuel cells utilizing dimethyl ether fuel. J. Electrochem. Soc. 149, A1127–A1131.

Nagaoka, K., Jentys, A., Lercher, J.A., 2005. Methane autothermal reforming with and without ethane over mono- and bimetal catalysts prepared from hydrotalcite precursors. J. Catal. 229, 185–196.

Ormerod, R.M., 2003. Solid oxide fuel cells. Chem. Soc. Rev. 32, 17–28.

Park, S., Vohs, J.M., Gorte, R.J., 2000. Direct oxidation of hydrocarbons in a solid-oxide fuel cell. Nature 404, 265–267.

Pascual, C., Jurado, J.R., Duran, P., 1983. Electrical behaviour of doped-yttria stabilized zirconia ceramic materials. J. Mater. Sci. 18, 1315–1322.

Peña-Martínez, J., Marrero-López, D., Ruiz-Morales, J.C., Buergler, B.E., Núñez, P., Gauckler, L.J., 2006. Fuel cell studies of perovskite-type materials for IT-SOFC. J. Power Sources 159, 914–921.

Pillai, M.R., Kim, I., Bierschenk, D.M., Barnett, S.A., 2008. Fuel-flexible operation of a solid oxide fuel cell with $Sr_{0.8}La_{0.2}TiO_3$ support. J. Power Sources 185, 1086–1093.

Pizzini, S., 1973. General aspects of the kinetics of ion transfer across interfaces. In: van Gool, W. (Ed.), Fast Ion Transport in Solids. North-Holland Publishing Co., Amsterdam, p. 461

Putna, E.S., Stubenrauch, J., Vohs, J.M., Gerte, R.J., 1995. Ceria-based anodes for the direct oxidation of methane in solid oxide fuel cells. Langmuir 11, 4832–4837.

Rezaei, M., Meshkani, F., Ravandi, A.B., Nematollahi, B., Ranjbar, A., Hadian, N., Mosayebi, Z., 2011. Autothermal reforming of methane over Ni catalysts supported on nanocrystalline MgO with high surface area and plated-like shape. Int. J. Hydrog. Energy 36, 11712–11717.

Saeki, M., Uchida, H., Watanabe, M., 1994. Noble metal catalysts highly-dispersed on Sm-doped ceria for the application to internal reforming solid oxide fuel cells operated at medium temperature. Catal. Lett. 26, 149–157.

Saunders, G.J., Kendall, K., 2002. Reactions of hydrocarbons in small tubular SOFCs. J. Power Sources 106, 258–263.

Saunders, G.J., Preece, J., Kendall, K., 2004. Formulating liquid hydrocarbon fuels for SOFCs. J. Power Sources 131, 23–26.

Sin, A., Kopnin, E., Dubitsky, Y., Zaopo, A., Aricò, A.S., La Rosa, D., Gullo, L.R., Antonucci, V., 2007. Performance and life-time behaviour of NiCu–CGO anodes for the direct electro-oxidation of methane in IT-SOFCs. J. Power Sources 164, 300–305.

Singhal, S.C., 2002. Solid oxide fuel cells for stationary, mobile, and military applications. Solid State Ion 152–153, 405–410.

Skinner, S.J., 2001. Recent advances in perovskite-type materials for solid oxide fuel cell cathodes. Int. J. Inorg. Mater. 3, 113–121.

Skorodumova, N.V., Simak, S.I., Lundqvist, B.I., Abrikosov, I.A., Johansson, B., 2002. Quantum origin of the oxygen storage capability of ceria. Phys. Rev. Lett. 89, 166601.

Steele, B.C.H., 2000a. Materials for IT-SOFC stacks: 35 years R&D: the inevitability of gradualness? Solid State Ion 134, 3–20.

Steele, B.C.H., 2000b. Appraisal of $Ce1 - yGdyO2 - y/2$ electrolytes for IT-SOFC operation at 500 °C. Solid State Ion 129, 95–110.

Steele, B.C.H., Bae, J.-M., 1998. Properties of $La_{0.6}Sr_{0.4}Co_{0.2}Fe_{0.8}O_3 - x$ (LSCF) double layer cathodes on gadolinium-doped cerium oxide (CGO) electrolytes: II. Role of oxygen exchange and diffusion. Solid State Ion 106, 255–261.

Sun, C., Sun, J., Xiao, G., Zhang, H., Qiu, X., Li, H., Chen, L., 2006. Mesoscale organization of nearly monodisperse flowerlike ceria microspheres. J. Phys. Chem. B 110, 13445–13452.

Tao, S.W., Irvine, J.T.S., Kilner, J.A., 2005. An efficient solid oxide fuel cell based upon single-phase perovskites. Adv. Mater. 17, 1734–1737.

Teraoka, Y., Zhang, H.M., Okamoto, K., Yamazoe, N., 1988. Mixed ionic-electronic conductivity of La_1-xSrxCo$_1$-yFeyO$_3$-δ perovskite-type oxides. Mater. Res. Bull. 23, 51–58.

Thomas, D.G., Lander, J.J., 1956. Hydrogen as a donor in zinc oxide. J. Chem. Phys. 25, 1136–1142.

Timmermann, H., Sawady, W., Campbell, D., Weber, A., Reimert, R., Ivers-Tiffee, E., 2008. Coke formation and degradation in SOFC operation with a model reformate from liquid hydrocarbons. J. Electrochem. Soc. 155, B356–B359.

Tsiakaras, P., Demin, A., 2001. Thermodynamic analysis of a solid oxide fuel cell system fuelled by ethanol. J. Power Sources 102, 210–217.

Tu, H., Stimming, U., 2004. Advances, aging mechanisms and lifetime in solid-oxide fuel cells. J. Power Sources 127, 284–293.

Vernoux, P., Djurado, E., Guillodo, M., 2001. Catalytic and electrochemical properties of doped lanthanum chromites as new anode materials for solid oxide fuel cells. J. Am. Ceram. Soc. 84, 2289–2295.

Wan, J.-H., Yan, J.-Q., Goodenough, J.B., 2005. LSGM-based solid oxide fuel cell with 1.4 W/cm^2 power density and 30 day long-term stability. J. Electrochem. Soc. 152, A1511–A1515.

Wang, W., Yang, Z., Wang, H., Ma, G., Gao, W., Zhou, Z., 2011. Desirable performance of intermediate-temperature solid oxide fuel cell with an anode-supported $La_{0.9}Sr_{0.1}Ga_{0.8}Mg_{0.2}O_3 - \delta$ electrolyte membrane. J. Power Sources 196, 3539–3543.

Wilson, J.R., Kobsiriphat, W., Mendoza, R., Chen, H.Y., Hiller, J.M., Miller, D.J., Thornton, K., Voorhees, P.W., Adler, S.B., Barnett, S.A., 2006. Three-dimensional reconstruction of a solid-oxide fuel-cell anode. Nat. Mater. 5, 541–544.

Yahiro, H., Eguchi, Y., Eguchi, K., Arai, H., 1988. Oxygen ion conductivity of the ceria-samarium oxide system with fluorite structure. J. Appl. Electrochem. 18, 527–531.

Yang, Z., Walker, M.S., Singh, P., Stevenson, J.W., Norby, T., 2004. Oxidation behavior of ferritic stainless steels under SOFC interconnect exposure conditions. J. Electrochem. Soc. 151, B669–B678.

York, A.P.E., Xiao, T.C., Green, M.L.H., Claridge, J.B., 2007. Methane oxyforming for synthesis gas production. Catal. Rev. 49, 511–560.

Zhu, W.Z., Deevi, S.C., 2003. A review on the status of anode materials for solid oxide fuel cells. Mater. Sci. Eng. A 362, 228–239.

Zurlo, F., Di Bartolomeo, E., D'Epifanio, A., Felice, V., Natali Sora, I., Tortora, L., Licoccia, S., 2014. $La_{0.8}Sr_{0.2}Fe_{0.8}Cu_{0.2}O$ 3-δ as "cobalt-free" cathode for $La_{0.8}Sr_{0.2}Ga_{0.8}Mg_{0.2}O$ 3-δ electrolyte. J. Power Sources 271, 187–194.

Reversible fuel cells

5

V.N. Nguyen, L. Blum
Institute of Energy and Climate Research, Jülich, Germany

Symbols used, units, abbreviation

$\eta_{\text{Fc,c}}$	fuel cell efficiency of the cell
$\eta_{\text{RT,RFC}}$	round-trip efficiency of reversible fuel cell
$\eta_{\text{RT,sys}}$	round-trip system efficiency
$\eta_{\text{el,c}}$	electrolysis efficiency of the cell
ΔG	Gibbs free energy change
ΔH	enthalpy change
ΔS	entropy change
° (**superscript**)	at standard atmospheric conditions
A	cell surface area
AE	alkaline electrolysis
ASR	area-specific resistance
F	Faraday constant, 96,485 Cmol^{-1}
FT	Fischer–Tropsch
GDL	gas diffusion layer
HER	hydrogen evolution reaction
HOR	hydrogen oxidation reaction
i	current density (in A cm^{-2})
I	total current (in Ampere)
ICC	ionic charge carries
LSCF	lanthanum strontium cobalt ferrite
LSM	$La_{0.8}Sr_{0.2}MnO_3$
MEA	membrane-electrode assembly
MH	metal hydride
N_{cells}	number of cells in the stack0
OER	oxygen evolution reaction
ORR	oxygen reduction reaction
p	pressure in Pascal
PEE	polymer electrolyte electrolysis
PEFC	polymer electrolyte fuel cell
PEM	proton exchange membrane
PTFE	polytetrafluoroethylene
Q	thermal energy
R	ideal gas constant ($R = 8.31451$ $\text{Jmol}^{-1}\,\text{K}^{-1}$)
RAFC	reversible alkaline fuel cell
RFC	reversible fuel cell
RPEFC	reversible polymer electrolyte fuel cell
RSOFC	reversible solid oxide fuel cell
SOC	solid oxide cell

SOE	solid oxide electrolysis
SOEC	solid oxide electrolysis cell
SOFC	solid oxide fuel cell
T	temperature
V_N	reversible cell voltage (Nernst voltage)
V_{act}	activation overvoltage
V_{cell}	real cell voltage (the applied operating potential)
V_{con}	concentration overvoltage
V_{ohm}	Ohmic overvoltage
V_{stack}	voltage of a stack
V_{tn}	thermoneutral voltage
x_j	mole fraction of the component j
YSZ	yttria-stabilized zirconia
z	number of electrons exchanged

5.1 Introduction

Providing affordable, reliable, environmentally sustainable energy to the world's population presents a major challenge for this decade and the future. The development of renewable energies, especially those dedicated to electricity generation, has been spectacular in recent years. Fuel cells have the potential to convert hydrogen and other fuels into electricity very efficiently, producing negligible pollution. Hydrogen technologies can help to cope with these challenges and to contribute to the new system's development (Winter, 2009; Ursua et al., 2012).

Solar energy and wind energy are intermittent resources; that is, their energy availability changes from hour to hour, from day to night, and from season to season.

Reversible fuel cells (RFCs) offer a solution to producing fuel through the use of surplus electricity and reconverting this into electricity using the same device. In autonomous systems with surplus energy during periods of high solar radiation in summer, an RFC system can in electrolysis mode produce hydrogen and oxygen, which are then stored in tanks. If there is a lack of energy, the unit is fed with the stored gases operating in fuel cell mode to produce electricity (Wittstadt et al., 2005).

The high specific energy and the increased energy density of RFCs are attractive for aerospace applications and for energy storage in terrestrial regenerative systems (Barbir et al., 2005). RFCs based on H_2–O_2–H_2O chemistries are also attractive as all three species are environmentally friendly and inexpensive and water is the primary input. As such, RFCs constitute a promising technology for large-scale energy storage.

An overview on RFCs is presented by Pettersson et al. (2006), Müller (2012), Mogensen et al. (2006), Soloveichik (2014), and Gabbasa et al. (2014).

The original idea of Bacon in 1946 as summarized by Kordesch and Steininger (1988) was the storage of energy by means of electrolysis of water and storing of the gases produced, later recombining them in the same unit to produce electricity.

An RFC is a fuel cell that can function efficiently in fuel cell mode for electricity generation, as well as in electrolysis mode for hydrogen/chemicals production.

In general, an electrochemical cell is composed of two half-cells. Each half-cell consists of an electrode and an electrolyte. The two half-cells may use the same electrolyte, or they may use different electrolytes. The chemical reactions in the cell may involve the electrolyte, the electrodes, or an external substance (as with fuel cells that may use hydrogen gas as a reactant).

Faraday defined the cathode of a cell as the electrode to which cations (positively charged ions) flow within the cell, to be reduced by reacting with electrons (negatively charged) from that electrode; and the anode as the electrode to which anions (negatively charged ions) flow within the cell, to be oxidized by depositing electrons on the electrode.

The oxidation of ions or neutral molecules occurs at the anode and the reduction of ions or neutral molecules occurs at the cathode. The names of the electrodes change from fuel cell mode to electrolysis mode. For simplicity, we indicate the two electrodes in an RFC as the oxygen electrode and the fuel electrode.

RFCs have the potential to reduce device cost, installation space, and to raise the operating rate compared to the more traditional systems with individual units of water electrolyzer and fuel cell.

In principle, stack design for RFCs is the same for the conventional fuel cell stacks described in Chapters 1–4.

Because electricity production using fuel cells is already treated in detail in Chapters 1–4, this chapter will describe only the basic principle of electrolysis for hydrogen/chemical production.

5.2 Fundamentals of electrolysis

In chemistry, electrolysis is a method of using a direct electric current (DC) to drive an otherwise nonspontaneous chemical reaction via an electrolytic cell. Electrical energy can be used to drive the dissociations of H_2O, for example, by means of electrolysis. Water electrolysis consists of circulating a direct current through water to separate its molecules into hydrogen and oxygen. The current flows between two electrodes that are separated and immersed in an electrolyte to increase ionic conductivity. The electrolysis process usually requires the implementation of a diaphragm or separator to avoid a combination of hydrogen and oxygen being generated at the electrodes. The electrodes, the diaphragm and the electrolyte are elements that configure the electrolytic cell. The key process of electrolysis is the interchange of atoms and ions by the removal or addition of electrons from the external circuit. The overall reaction of water electrolysis is expressed as

$$H_2O(g/l) + \text{electric energy} + \text{heat} \rightarrow \frac{1}{2}O_2 + H_2 \tag{5.1}$$

Three main technologies, according to the electrolyte, are used in an electrolytic cell:

- Alkaline electrolysis with a liquid electrolyte (AE);
- Polymer electrolyte electrolysis with an acidic ionomer electrolyte (PEE);
- High-temperature solid oxide electrolysis with a dense oxide ion-conducting electrolyte (SOE).

An overview of water electrolysis is given by Smolinka et al. (2010), Ursua et al. (2012), Smolinka (2009), Carmo et al. (2013), Mergel et al. (2013), Zahid et al. (2010), and Laguna-Bercero (2012).

Apart from steam electrolysis, solid oxide electrolysis cells (SOECs) are also capable of electrolyzing carbon dioxide to form carbon monoxide and oxygen (Green et al., 2008; Bidrawn et al., 2008; Ebbesen and Mogensen, 2009; Dipu et al., 2012; Yan et al., 2014) as well as the coelectrolysis of CO_2/H_2O mixtures for the purpose of syngas and fuel production (Laguna-Bercero, 2012; Zhan et al., 2009; Graves et al., 2011; Nguyen et al., 2013; Ni, 2012; Nguyen and Blum, 2015). The overall reaction of CO_2 electrolysis is expressed as

$$CO_2 + electric\ energy + heat \rightarrow CO + \tfrac{1}{2}O_2 \tag{5.2}$$
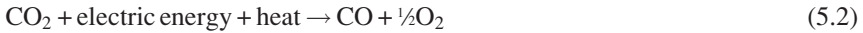
The coelectrolysis of CO_2/H_2O mixtures in SOECs is much more complex than the electrolysis of H_2O or CO_2 alone, respectively. This is because the reversible shift reaction (RSR) (Equation 5.3) and methanation reactions or reversed direct internal reforming (DIR) reactions (Equation 5.4–5.6) may occur in the porous cathode (fuel electrode) (Nguyen et al., 2013),

$$CO + H_2O \leftrightarrow H_2 + CO_2 \tag{5.3}$$

$$CO + 3H_2 \leftrightarrow CH_4 + H_2O \tag{5.4}$$

$$2CO + 2H_2 \leftrightarrow CH_4 + CO_2 \tag{5.5}$$

$$CO_2 + 4H_2 \leftrightarrow CH_4 + 2H_2O \tag{5.6}$$
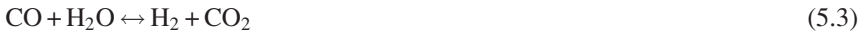
The hydrogen or the syngas (a mixture of H_2 and CO) that is produced by Equations (5.1) and (5.2) can be used to produce synthetic fuels such as synthetic natural gas (methane) (Equations 5.4–5.6) or Fischer–Tropsch (FT) liquid fuels (methanol, dimethylether, hydrocarbons) or other chemicals (Dry, 2002).

The amount of electrical energy that must be added equals the change in the Gibbs free energy of the reaction plus losses in the system. The required energy for the electrolysis reaction is determined by the process enthalpy change ($\triangle H$), consisting of the entropy term ($T \cdot \triangle S$) as thermal energy (Q) and the Gibbs free energy change ($\triangle G$) as electric energy. The following expression shows the relation among these thermodynamic magnitudes:

$$\Delta G = \Delta H\text{-}Q = \Delta H\text{-}T^{\cdot}\Delta S \tag{5.7}$$

The electrolysis process is an endothermic ($\triangle H > 0$) and nonspontaneous ($\triangle G > 0$) chemical reaction.

From a thermodynamic point of view, the Gibbs free energy change ($\triangle G$) is an expression of the minimum cell voltage V_N (or the reversible cell voltage, or Nernst voltage) required for the electrolysis to take place, expressed as

$$V_N = \frac{\triangle G}{zF} \tag{5.8}$$

where z is the number of electrons transferred per molecule of hydrogen products and F is the Faraday constant, $96{,}485 \ \mathrm{Cmol}^{-1}$.

The reversible cell voltage is determined through the Nernst equation as Equation (5.9), which predicts the minimum electrical potential required to split H_2O at a particular location along the cell with a specific temperature and gas concentration, assuming ideal gas behavior.

The Nernst equation for water electrolysis can be written as

$$V_N = V_N^0 - \frac{RT}{zF} \ln \left[\left(\frac{x_{H_2O}}{x_{H_2} x_{O_2}^{1/2}} \right) \left(\frac{p}{p_{st}} \right)^{-1/2} \right] \tag{5.9}$$

where R is the ideal gas constant ($R = 8.31451 \ \mathrm{Jmol}^{-1} \ \mathrm{K}^{-1}$), T is the temperature in Kelvin, x_j is the mole fraction of the gas j in the gaseous mixture, p is pressure and p_{st} is the reference pressure at standard conditions. V_N^0 represents the standard potential or open-cell potential.

If the thermal energy $T \cdot \triangle S$ is provided by means of electricity, as is the case in most commercial electrolyzers, the minimum voltage for electrolysis to occur is known as the thermoneutral voltage (V_{tn}).

$$V_{tn} = \frac{\triangle H}{zF} \tag{5.10}$$

Energy consumed in the electrolysis process depends, nevertheless, on temperature and pressure. The thermodynamic properties are plotted in Figure 5.1 as a function of temperature for the H_2–H_2O system from 0 to 1200 °C at standard pressure. It shows that the Gibbs free energy change, $\triangle G$, for the reacting system decreases with increasing temperature, while the product of the temperature and the entropy change, $T \cdot \triangle S$, increases. Therefore, for reversible operation, the electrical work requirement decreases with temperature, while a larger fraction of the total energy required for electrolysis, $\triangle H$, can be supplied in the form of heat.

At standard temperature and pressure (298.15 K and 1 atm) the reversible and thermoneutral voltages of an electrolytic cell for water electrolysis are $V_N^0 = 1.229$ V and $V_{tn}^0 = 1.481$ V, respectively.

The voltage of an operating electrolysis cell is significantly higher than the theoretical reversible cell voltage derived from thermodynamics. The real cell voltage V_{cell} can be regarded as the sum of the reversible cell voltage (Nernst voltage) and the overpotentials.
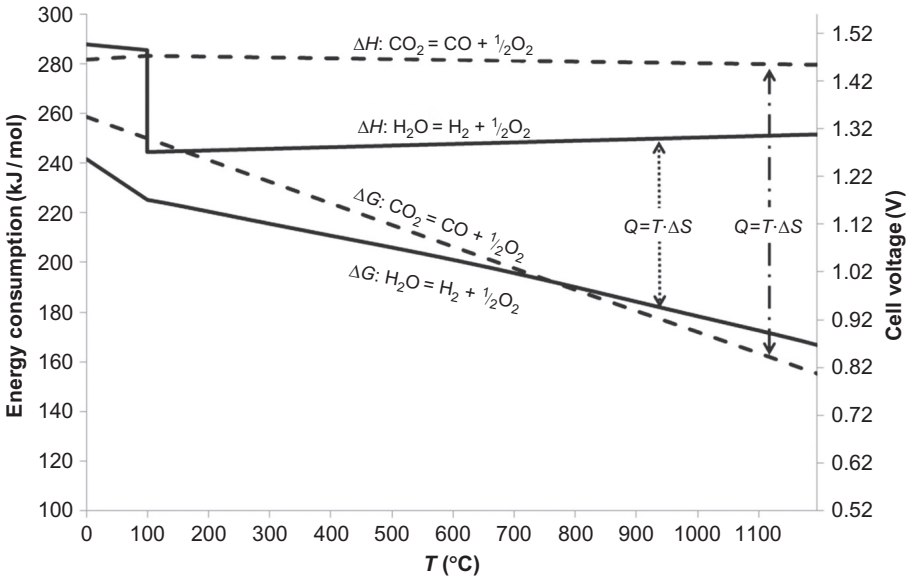
Figure 5.1 Temperature dependency of energy demand of CO_2 and H_2O reduction reactions. Calculated from data in Daubert et al. (1992).

$$V_{cell} = V_N + V_{ohm} + V_{act} + V_{con} \qquad (5.11)$$

In Equation (5.11) the term V_{ohm}, known as ohmic overvoltage, is caused by the ohmic resistance of the cell elements (electrodes, current collectors, etc.) to the electron flow and of the electrolyte to the ion flow. V_{ohm} is mainly proportional to the electric current I that flows through the cell and the area-specific ohmic resistance of the cell R_A, ($V_{ohm} = IR_A$). The term V_{act}, known as the activation overvoltage, is caused by the energy required, to overcome the charge transfer between the chemical species and the electrodes. The term V_{con}, known as concentration overvoltage, is caused by mass transport processes (convection and diffusion). Transport limitations reduce reactant concentration while increasing the concentration of the products in the interface between the electrode and electrolyte (Ursua et al., 2012).

The relationship between cell voltage and current density (i) is given by the i–V characteristic curve. Figure 5.2 shows typical results for the voltage versus current density of solid oxide cells (SOCs) operated at 800 °C (Zhan et al., 2009), as well as a typical low-temperature (60 °C) RPEFC (Barbir et al., 2005).

The i–V curve is highly dependent on the electrolysis temperature. For a given current, reversible, ohmic, and activation voltages decrease as temperature increases, and thus the necessary cell voltage decreases with temperature.

The cell consumes extra power [$(V_{cell} - V_{tn})I_{cell}$] due to cell losses.

The applied voltage V_{cell} travels in the opposite direction to the Nernst voltage V_N created by differing oxygen partial pressures p_{O_2} ($p_{O_2} = x_{O_2}$) at the two electrodes. When $V_{cell} < V_N$, the cell does work on the external sink (charging the externally
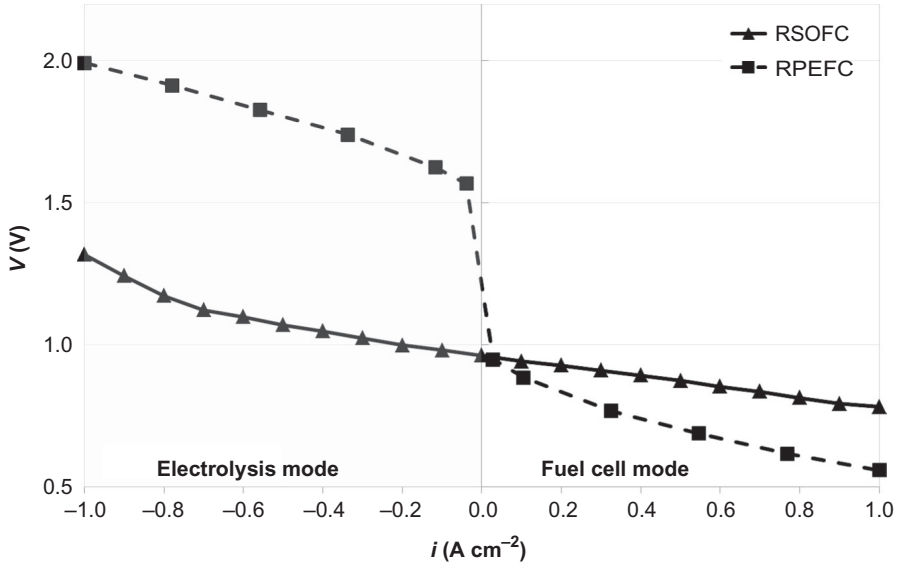
Figure 5.2 *i–V* characteristic curve for RPEFC at 60 ˚C and for RSOFC (50% H$_2$, 50% H$_2$O) at 800 ˚C.

For RPEFC: data from Barbir et al. (2005) and for RSOFC: data from Zhan et al. (2009).

connected battery). This is the fuel cell mode. When $V_{cell} > V_N$, the external source does work on the cell. This is the electrolyzer mode.

An important performance parameter that quantifies the ohmic loss associated with the operation of electrolysis cells is the area-specific resistance (ASR). This quantity is defined as

$$\text{ASR} = \frac{V_{cell} - V_N^0}{i} = \frac{V_{cell} - V_N^0}{I/A} \tag{5.12}$$

where I is the current, A is the cell surface area, and i is the current density.

The voltage of a stack is determined by

$$V_{stack} = N_{cells} V_{cell} \tag{5.13}$$

where N_{cells} is the number of cells in the stack.

Depending on the operating voltage, the electrolyzer can work in three different modes: thermoneutral, endothermic, and exothermic.

In thermoneutral mode, the enthalpy increment of the reaction system is exactly balanced by the electrical energy input to the system ($V_{cell} = V_{tn} \rightarrow Q = 0$). The electrolyzer operates adiabatically. No external heater or cooler is used, and the electrolyzer outlet temperature varies as a function of operating voltage. As the operating voltage decreases, the electrolyzer outlet temperature decreases to maintain the energy balance.

In endothermic mode, the operating voltage is lower than the thermoneutral, and extra heat energy input is needed to balance the enthalpy change ($V_{cell} < V_{tn} \rightarrow Q > 0$). In exothermic mode, the operating voltage is higher than the thermoneutral voltage and extra heat energy has to be removed from the electrolyzer ($V_{cell} > V_{tn} \rightarrow Q < 0$).

Electrolysis efficiency of the cell, $\eta_{el,c}$, can be defined for electrolysis, analogous to the definition of fuel cell efficiency (Larminie and Dicks, 2003). The electrolysis cell efficiency can be expressed strictly in terms of cell operating potentials as

$$\eta_{el,c} = \frac{\Delta H / zF}{V_{cell}} = \frac{V_{tn}}{V_{cell}} \tag{5.14}$$

The round-trip efficiency is a key figure of merit for a renewable energy cycle and constitutes the fraction of the original electrical energy obtained after the storage and utilization cycle. The ideal round-trip efficiency $\eta_{RT,RFC}$ at current density i of an RFC for electrolysis operation at voltage V_{el} and fuel cell operation at V_{FC} might be written as (Barbir et al., 2005; Zhan et al., 2009)

$$\eta_{RT,RFC} = \eta_{el} \cdot \eta_{FC} = \frac{V_{FC} Q_{FC}}{V_{el} Q_{el}} \tag{5.15}$$

where Q_{FC} is the charge transferred during fuel cell operation and Q_{el} is the charge transferred during electrolysis operation. In a closed-loop H_2/H_2O storage system, if the electrolyte does not have a leakage current due to mixed conductivity and none of the reactants are lost due to gas leakage, $Q_{FC} = Q_{el}$, Equation (5.15) reduces to Equation (5.16) (Bierschenk et al., 2011)

$$\eta_{RT,RFC} = \frac{V_{FC}}{V_{el}} \tag{5.16}$$

For example, using data from Figure 5.2 (current density ± 500 mA cm^{-2}) Equation (5.16) yields $\eta_{RT,RFC} = 80\%$ for a reversible solid oxide fuel cells (RSOFC) and $\eta_{RT,RFC} = 39\%$ for an RPEFC. These figures do not take into account fuel utilization in fuel cell mode nor the energy consumption of the different systems.

The round-trip system efficiency $\eta_{RT,sys}$ is defined as the quotient of net energy generated in fuel cell mode to the total energy supplied in electrolysis mode (Wendel et al., 2015)

$$\eta_{RT,sys} = \frac{V_{FC} Q_{FC} - W_{BOP,FC}}{V_{el} Q_{el} + W_{BOP,El}} \tag{5.17}$$

where $W_{BOP,FC}$ and $W_{BOP,El}$ are the total balance of plant component energy required during fuel cell mode and electrolysis mode, respectively. The total balance of plant component energy includes parasitic power loads from components, such as compressors, power produced from turbines and energy entering the system in the form of fuel or process streams (Wendel et al., 2015).

5.3   Reversible alkaline fuel cell

Reversible alkaline fuel cells (RAFCs) normally use an aqueous solution of potassium hydroxide (KOH) as the electrolyte, operate under fuel cell mode in the range of 60–120 °C, and can yield the highest voltage at comparable current densities while operated with pure hydrogen and oxygen. The electrolysis of aqueous alkaline hydroxide solutions has historically been one of the most popular means of producing hydrogen and oxygen from water.

Figure 5.3 shows the schematic of an RAFC that involves interconversions between H_2, O_2, and H_2O in an alkaline environment. Reactions and ionic charge carriers (ICC) are presented in Table 5.1.

If the RAFC is operating as an electrolyzer (upper dashed line in Figure 5.3), the oxygen electrode is the anode and the hydrogen electrode (fuel electrode) is the cathode. The half-cell reactions for electrolysis mode are the oxygen evolution reaction (OER) and the hydrogen evolution reaction (HER) (Table 5.1). If the RAFC is operating as a fuel cell (lower solid line in Figure 5.3), the oxygen electrode is the cathode and the fuel electrode the anode. The half-cell reactions for fuel cell mode are the oxygen reduction reaction (ORR) and the hydrogen oxidation reaction (HOR) (Table 5.1).

A porous Raney nickel metal electrode or a noble metal catalyzed carbon electrode such as a hydrogen electrode can be used reversibly, without any damage to be expected from the hydrogen evolution (Kordesch and Steininger, 1988).
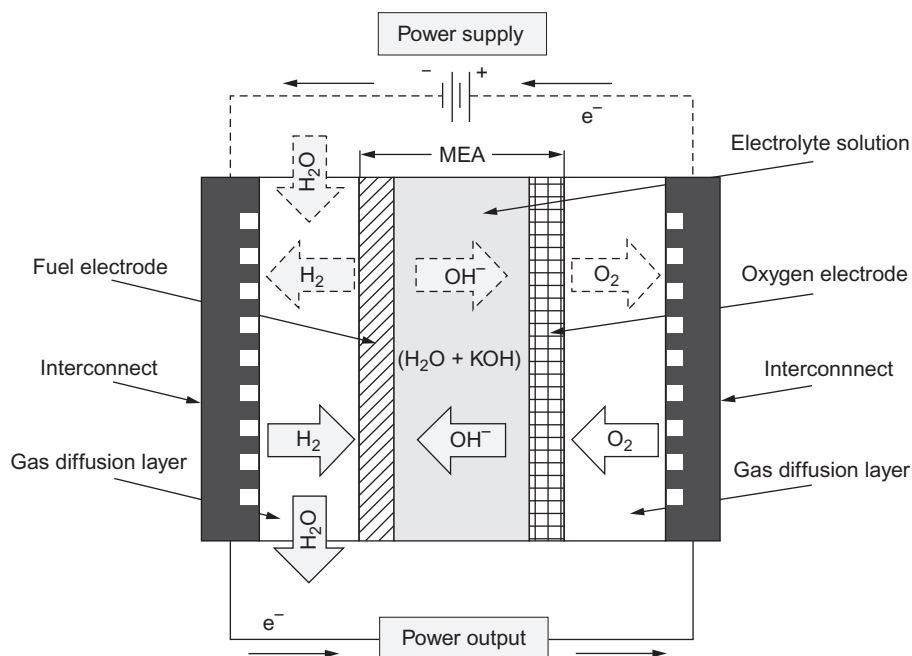

Figure 5.3 Schematic of reversible alkaline fuel cell (RAFC).

Table 5.1 Half-cell reactions and ionic charge carriers in the H_2–O_2–RAFC

Process	Fuel electrode	ICC	Oxygen electrode
Electrolysis mode	$2H_2O + 2e^- \rightarrow H_2 + 2OH^-$	OH^-	$2OH^- \rightarrow \frac{1}{2}O_2 + H_2O + 2e^-$
Fuel cell mode	$H_2 + 2OH^- \rightarrow 2H_2O + 2e^-$	OH^-	$\frac{1}{2}O_2 + H_2O + 2e^- \rightarrow 2OH^-$

The key technology in the development of RAFC is the fabrication of active electrocatalysts only for both the oxygen reduction and the water oxidation at the oxygen electrode. Catalyst development is critical in these fields. The best catalysts for the ORR are made of platinum (Pt) (Gasteiger et al., 2005), but Pt has only moderate activity in OER (Trasatti, 1984). Ruthenium (Ru) and iridium (Ir) oxides are the best OER catalysts (Trasatti, 1984), but are not as active in ORR as Pt. As a result, alloys of Pt, Ir, and Ru have been evaluated for bifunctional oxygen electrode activity, and have been shown to perform better than the pure metals or metal oxides (Chen et al., 2002; Zhang et al., 2007). Swette et al. (1991) developed a highly efficient bifunctional oxygen electrocatalyst and a "dual-character" $Na_xPt_3O_4$ electrode.

Recently, Mn oxide thin film was found to be highly active for both the ORR and the OER (Gorlin and Jaramillo, 2010). X-ray diffraction (XRD), scanning electron microscopy (SEM), and X-ray photoelectron spectroscopy (XPS) were used to investigate the nature of the bifunctional activity of Mn oxides. The authors developed a thin film analog consisting of a nanostructured Mn(III) oxide. This inexpensive and earth-abundant catalyst could potentially be employed as the bifunctional oxygen electrode in an RAFC.

Ng et al. (2013) developed a precious-metal-free, high-performance O_2 electrode for RAFCs. They fabricated an O_2 electrode with both the Ni/C catalyst and the MnOx/glassy carbon particles. As Ni is known to be catalytically active for the HOR and the HER they developed a bifunctional Ni on a carbon black (Ni/C) catalyst for the H_2 electrode by mean of an adapted impregnation-reduction technique (Brown et al., 1982; Schulze et al., 2001). The device of Ng et al. (2013) was cycled between electrolyzer mode and fuel cell mode eight times. The round-trip efficiency had decreased from 40% to 34% by the eighth cycle.

Electrode stability is another key design parameter that warrants attention. Carbon, which is typically used as a catalyst support and electrode substrate, easily corrodes in the highly oxidative electrochemical potentials encountered during water oxidation (Pettersson et al., 2006). To solve this problem, researchers have been developing electronically conductive carbon substitutes such as titanium oxide and boron carbide as catalyst supports, as well as Ni foam and titanium metal sheets as gas diffusion layers (GDLs) (Pettersson et al., 2006). Another noncarbon support candidate of interest is stainless steel (SS), an iron-based alloy that is low in cost and oxidation resistant. Wu and Scott (2012) successfully prepared and applied a non-precious metal bifunctional oxygen electrode from $Cu_xMn_{0.9-x}Co_{2.1}O_4$ in a regenerative H_2-O_2 fuel cell using alkaline anion exchange membranes. The fuel cell to electrolyser voltage ration achieved about 32%, which may be taken as an indicator of good efficiency.

Ng et al. (2014) developed a carbon-free, precious metal-free, high-performance O_2 electrode for RAFCs. This electrode is a thin, porous, nanostructured layer (thin film) of Mn(III) oxide that coats the OER-active stainless steel substrate. As NiO_x is known to be an even more active OER catalyst than MnO_x (Subbaraman et al., 2012), NiO_x is added to stainless steel. The round-trip efficiency of this device in both modes showed a smaller decrease from 45% to 42% over 10 cycles. The work of Ng et al. (2014) provides a propitious route for designing high performance and scalable precious metal-free and carbon-free O_2 electrodes for RAFCs.

5.4 Reversible polymer electrolyte fuel cells

Polymer electrolyte-based RFCs (RPEFCs) are a new type of energy device that make use of hydrogen. They can be operated as both fuel cell and water electrolyzer. A typical RPEFC consists of two porous electrodes, that are separated by a polymer electrolyte membrane (Figure 5.4).

If the unit is operating as an electrolyser (upper dashed line in Figure 5.4), the oxygen electrode is the anode (oxidation reaction) and the fuel electrode is the cathode (reduction reaction). If the unit is operating as a fuel cell (lower solid line in Figure 5.4), the oxygen electrode is the cathode (reduction reaction) and the fuel electrode is the anode (oxidation reaction). It is therefore important that both electrodes do not degrade during operation in an oxidizing environment.
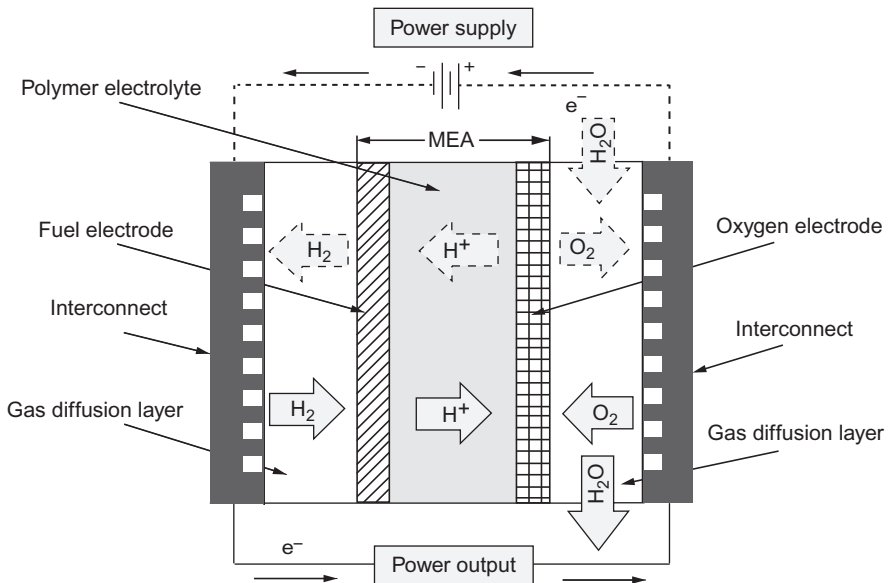

Figure 5.4 Schematic of reversible polymer electrolyte fuel cell (RPEFC).

The membrane in RPEFCs is usually a perflourosulfonic acid polymer. This is a polytetrafluoroethylene (PTFE, trade name Teflon) chain with side chains terminating in an SO_3H group. It is the hydrogen in this sulfonate group that dissociates from the polymer when it is wet and appears as protons in the solution; polymer acids have the advantage that the anion (SO_3^{2-} tail) is fixed in the electrolyte rather than dissolved (Pettersson et al., 2006). Most commonly, Nafion, a polymer developed by DuPont, is used as the electrolyte in RPEFCs.

5.4.1 Electrocatalysis at the fuel (hydrogen) electrode

Electrocatalytic processes are of first-order importance in the operation of fuel cells and electrolyzers (Greeley and Markovic, 2012).

The HER ($2H^+ + 2 e^- \rightarrow H_2$) is the cathodic half-cell reaction in acid-based electrolyzers. The HOR ($H_2 \rightarrow 2 H^+ + 2 e^-$) is the corresponding anodic half-cell reaction in the hydrogen oxidation fuel cell (Table 5.2).

To understand the electrocatalytic processes, a combination of fundamental surface rate modeling with atom-specific free energy data obtained from density functional theory (DFT) calculations was used for the rapid calculation of the hydrogen adsorption free energy as a descriptor for trends in the HER rates of both metals and metal alloys (Greeley and Markovic, 2012). An alloy of PtBi has subsequently been confirmed to be both stable and more active than any known pure metal HER catalysts (Skulason et al., 2010). Furthermore, nonprecious metal catalysts for the HER, which, although generally less active than Pt alloys, are less expensive than catalysts containing Pt, can also be identified (Björketun et al., 2010).

A good catalyst for the HER is also a good catalyst for the HOR; thus, practical fuel cell anode materials are based on Pt as a catalyst. The long-term activity of noble metals for HOR is usually affected by the adsorption of impurities. Adsorbed CO is one key impurity. Both experimental and computational investigations have determined that the use of bifunctional catalysts, including alloys of Pt and Ru or related metals, is effective in reducing the CO overpotential (Maillard et al., 2005).

5.4.2 Bifunctional electrocatalysts on the oxygen electrode

The cathodic half-cell reaction in the hydrogen-oxygen fuel cell is the ORR ($O_2 + 2H^+ + 2e^- \rightarrow H_2O$). The anodic half-cell reaction in acid-based electrolyzers is the more complex OER ($H_2O \rightarrow O_2 + 2H^+ + 2e^-$) (Table 5.2).

Table 5.2 Half-cell reactions and ionic charge carriers in the H_2–O_2–RPEFC

Process	Fuel electrode	ICC	Oxygen electrode
Electrolysis mode	$2H^+ + 2e^- \rightarrow H_2$	H^+	$H_2O \rightarrow \tfrac{1}{2}O_2 + 2H^+ + 2e^-$
Fuel cell mode	$H_2 \rightarrow 2H^+ + 2e^-$	H^+	$\tfrac{1}{2}O_2 + 2H^+ + 2e^- \rightarrow H_2O$

The ORR and the OER are multielectron reactions that include a number of elementary steps involving different reaction intermediates.

Because the kinetics of HER and HOR are very fast on platinum-based materials, the key technology in the development of the RPEFC is the fabrication of active electrocatalysts for both the oxygen reduction and the water oxidation at the oxygen electrode.

There is an urgent need for the development of bifunctional catalysts that are highly active for both the ORR and OER and are durable under high potential conditions during the OER in the charging process. Bioperational electrocatalysts for RPEFC applications have been developed using a combination of unsupported metallic platinum and OER electrocatalysts such as ruthenium (oxide) and iridium (oxide).

An overview of bifunctional electrocatalyst is given by Park et al. (2012), Xuan et al. (2011), Altmann et al. (2011), Jörissen (2006), and Pettersson et al. (2006).

Swette et al. (1994) prepared various bifunctional electrocatalysts for different electrodes. The single-layer electrode was composed of a bifunctional electrocatalyst, while the double-layer electrode was composed of a platinum transition layer and a metal–metal oxide layer for oxygen redox reactions. Most of the double-layer bifunctional oxygen electrodes showed better performance in both fuel cell and electrolysis mode, as compared with the single-layer ones. Catalyst arrays consisting of combinations of all five noble metals (Pt, Ru, Os, Ir, and Rh) were prepared, screened, and physically and electrochemically characterized by Chen et al. (2001). Of 715 unique combinations, they found that $Pt_{4.5}Ru_4Ir_{0.5}$ is highly active for both ORR and OER activity. The study showed that the addition of Ru to the Pt/Ir electrodes increased the reaction rate by stabilizing the surface atom/oxygen bonds.

Yim et al. (2004) tested various commercially available and in-house bifunctional electrocatalysts in the RFCs. The performance in fuel cell mode with different electrocatalysts appeared to increase in the sequence of $Pt > Pt\text{-}Ir > Pt\text{-}RuO_x > Pt\text{-}Ru \sim Pt\text{-}Ru\text{-}Ir > Pt\text{-}IrO_x$, with $Pt\text{-}Ir \sim Pt\text{-}IrO_x > Pt\text{-}Ru > Pt\text{-}Ru\text{-}Ir > Pt\text{-}RuO_x \sim Pt$ obtaining in water electrolysis mode. For a mixed electrocatalyst of platinum and iridium black in an RPEFC, a small amount of iridium led to high performance in both fuel cell and electrolysis mode (Jung et al., 2009).

Recently, Lee and Kim (2014) found that when Pt in the oxygen electrode of RPEFCs is in contact with the carbon-based GDL, the Pt accelerates the electrochemical carbon corrosion, resulting in poor cyclic performance of the RPEFC. The three-layered $IrO_2/Pt/IrO_2$ electrode structure, proposed by Lee and Kim (2014), showed significantly improved cyclic performance compared with the conventional, homogeneously mixed Pt and IrO_2 oxygen electrode.

5.4.3   Electrocatalyst supports

The importance of support in electrocatalysis is well recognized (Borup et al., 2007; Garcia et al., 2013; Roca-Ayats et al., 2014). Generally, electrocatalyst support improves the dispersion of electrocatalyst particles, which is necessary for achieving a high surface area. For electrochemical reactions, the support provides good electronic conductivity and controls wettability. However, carbon materials, such as

catalyst support, porous electrode structures (carbon fiber paper or carbon cloth), and bipolar plates, commonly used in fuel cells, cannot be used on the oxygen side of a proton exchange membrane (PEM) electrolyzer due to corrosion, as indicated by the following reaction (Kangasniemi et al., 2004):

$$C + 2H_2O \rightarrow CO_2 + 4H^+ + 4e^- \tag{5.18}$$

Conductive oxide supports, particularly reduced titanium oxides, and titanium-ruthenium oxide composites have been used in electrolyzers and are important candidates for use in the oxygen electrodes of RPEFCs.

Lee et al. (2004) developed a technique for the direct deposition of Pt catalyst onto the solid membrane using a thin film catalyst layer impregnated with polypyrole. Polypyrole improved the fabrication of the catalyst layer directly onto the surface of the Nafion membrane and, overall, improved the performance of the RPEFC.

The RPEFC investigating results of Hwang et al. (2012) showed that the round-trip energy conversion efficiency of the supported Pt-Ir/TiO$_2$ (42%) was significantly higher than that of unsupported Pt-Ir black (30%).

The properties of Pt$_3$Ir nanoparticle supported on TiC, TiCN, and TiN material as bioperational oxygen electrode catalysts were investigated by Roca-Ayats et al. (2014). The Pt$_3$Ir/TiCN material shows the highest activity toward ORR and OER as well as the best compromise between catalytic activity and stability. The Pt$_3$Ir/TiN shows good activity toward ORR and OER, but with high degree of passivation by dissolved oxygen. The Pt$_3$Ir/TiC catalyst is the worst one. The results indicate that nitrogen loading appears to be an important factor for the catalyst performance. Lin et al. (2014) investigated the effect of O$_2$ gas on the electrochemical behavior of the TiN/ZrN-coated SS304 stainless steel and Ti in the O$_2$-rich environment of RPEFC with acid and fluoride (F-) ions. The results showed that the corrosion rate of the TiN/ZrN coating on Ti was about 243 times lower than that of the bare Ti. The TiN/ZrN coating on the SS304 substrate improved corrosion resistance about six times, as compared with uncoated SS304 stainless steel.

A new procedure for a simple wet coating of carbon paper with Nb-doped TiO$_2$ was presented by Alvar et al. (2014). Titanium tetraisopropoxide and niobium ethoxide were added to a vigorously stirred solution of acetylacetone and ethanol under N$_2$ atmosphere. The solution was then acidified to a pH value of about 3 by addition of HCl. The coated carbon papers were then dried in air at 450 °C. Cyclic voltammetry measurements of all samples revealed that the oxidatively functionalized carbon paper coated with Nb-doped TiO$_2$ is by a factor of 4.3 more stable than untreated carbon paper.

5.4.4   Membrane-electrode assembly (MEA) for RPEFC

The conventional membrane-electrode assembly for PEFC is not commonly applied to water electrolysis because the GDL may inhibit the diffusion of reactants and products. Therefore, most MEAs used in RPEFCs are constructed of two-layer structure electrodes consisting of the membrane and a gas diffusion electrode (GDE).

The GDE is most commonly a thin film electrocatalyst layer and consists of a catalyst, a proton conducting polymer, and a solvent (Pettersson et al., 2006).

Bifunctional oxygen electrodes must be combined into a single electrode. Three different electrode designs are described by Altmann et al. (2011) as follows:

- Option 1: the MEA is the mixture of two different catalysts for separate chemical reactions and involves compromises in structure and reactivity. Because there are no specific reaction areas, the properties of the GDL have to be a compromise between hydrophobic and hydrophilic properties.
- Option 2 is a multilayered electrode. Here two electrode layers, one for the FC mode and another for the electrolysis mode, are applied onto the membrane. The use of multilayer electrodes offers fully active areas of the electrode for each mode, and good performance can be expected. However, the electrical and ionic contacts between the electrode, membrane, and current collector can be a problem. While the inner layer exhibits superior proton transfer to the membrane, the outer layer has better electronic conductivity to the bipolar plate.
- Option 3 is a segmented electrode. In the third design, the active areas are split into separate zones for the fuel cell and the electrolysis reactions. The segmented electrode allows the use of partially optimized gas diffusion media. The GDLs can be structured with an adapted level of hydrophobicity. However, by dividing the electrode into different parts, the active area is effectively reduced.

Altmann et al. (2011) compared different combinations for structuring bifunctional electrodes based on the two catalysts Pt and IrO_2. The mixture of both catalysts performs best for the present stage of electrode development. The multilayer electrodes yield promising results with the potential for optimization by improving the electronic conductivities and mass transport properties of the specific layers.

Chen et al. (2009) investigated the effect of fabrication methods of bifunctional catalyst layers on RPEFC performance and found that Pt layers formed by spraying onto the GDL showed a more homogeneous and porous surface than that sprayed onto the membrane. The cell potentials of the RPEFC with Pt layers sprayed onto the GDL are more than 100 mV higher (at 800 mAcm^{-2} in fuel cell mode) than those using Pt layers sprayed onto the membrane. From the voltage against current density characteristics they concluded that the cells with Pt sprayed onto the GDL displayed significantly higher round-trip efficiency at high current density than those with Pt sprayed onto the membrane.

5.4.5   Gas diffusion layer (GDL)

A porous, conductive GDL plays an important role in electric connection between bipolar plate with channel-land structure and electrode. The GDL also performs the following essential functions: passage for reactant transport and heat/water removal, and mechanical support to the MEA.

In RPEFCs, the GDL has to achieve an appropriate balance between hydrophilic and hydrophobic properties for the both fuel cell and water electrolyzer.

Ioroi et al. (2003) looked at using titanium, which is a corrosion-resistive and electron-conductive material in highly cathodic and acidic environments, as a GDL for RPEFCs. A variety of titanium GDLs coated with different amounts of hydrophilic

solutions of PTFE were prepared and tested. The study found that the hydrophilic content of the hydrogen GDL did not affect the performance, but the amount of hydrophilic content of oxygen GDL changed the performance of the RPEFC significantly.

In the studies of Ito et al. (2011) and Hwang et al. (2012) a titanium (Ti)-felt is applied to the GDL substrate at the oxygen electrode and, additionally, titanium powders are loaded in the GDL substrate. The Ti-power loading in the Ti-felt substrate creates hydrophobic mesopores. Based on measured i–V characteristics and the analysis of overpotential the results indicated that the change of pore size distribution brings a significant improvement in fuel cell performance under full humidification conditions, but the influence of this treatment is small for the electrolysis performance.

The effect of through-plane PTFE distribution in GDL on RPEFC performance was investigated by Hwang et al. (2013). A Ti-felt was used for the oxygen-side GDL and was treated with PTFE. The RPEFC performance was evaluated based on measured current–voltage characteristics in both the electrolysis and fuel cell modes. Electrolysis performance was independent not only of the PTFE distribution but also of the PTFE loading of the Ti-felt GDL. In contrast, during fuel cell operation, the cell performance was significantly improved by the PTFE loading, and the level of improvement depended on the drying condition of the Ti-felt GDL. The results verified that compared with nonuniform distribution, a uniform distribution in the Ti-felt GDL yields a better fuel cell performance.

5.4.6   RPEFC stack

The RPEFC stack includes several cells containing a bipolar plate, a fuel electrode, an oxygen electrode and an electrolyte matrix. The bipolar plate connects the cells in sequence and also supplies gas for the electrodes. The low temperature, low pollution, and high power density of an RPEFC stack make it attractive. However, the high material cost is considered a major drawback facing worldwide RPEFC application. Moreover, the durability issue is another barrier for RPEFC commercialization (Gabbasa et al., 2014). The expenses of RPEFC stacks must be reduced by improving their design, materials and performance through further investigations.

5.5   Reversible solid oxide fuel cell (RSOFC)

5.5.1   Principle of RSOFC

The development and successful demonstration of SOCs for electrolytic hydrogen production began more than three decades ago (Isenberg, 1981; Dönitz and Erdle, 1985). Dönitz presented results from the HOTELLY project for single cell and stack including the durability test. In the past few years, the solid oxide electrolysis field has attracted many research groups and the results suggest that this technology can be much more efficient than low-temperature electrolyzers.
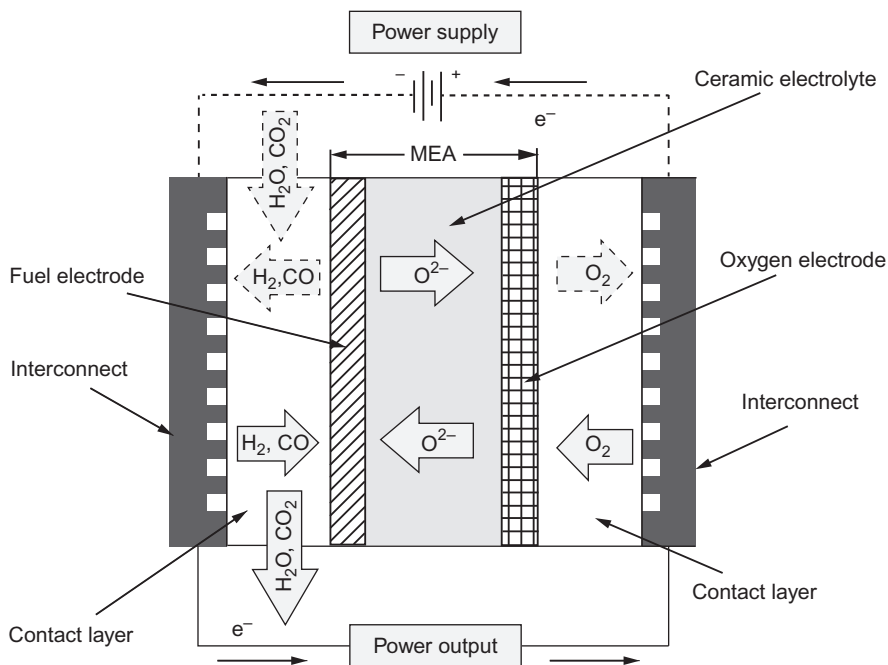
Figure 5.5 Schematic of reversible solid oxide fuel cell (RSOFC).

Table 5.3 Half-cell reactions and ionic charge carriers in the H_2–O_2–RSOFCs

Process	Fuel electrode	ICC	Oxygen electrode
Electrolysis mode	$H_2O + 2e^- \rightarrow H_2 + O^{2-}$	O^{2-}	$O^{2-} \rightarrow \frac{1}{2}O_2 + 2e^-$
Fuel cell mode	$H_2 + O^{2-} \rightarrow H_2O + 2e^-$	O^{2-}	$\frac{1}{2}O_2 + 2e^- \rightarrow O^{2-}$

In Figure 5.5, a typical RSOFC is shown, which essentially consists of two porous electrodes, separated by a dense, oxide ion-conducting electrolyte. The reactions for both the electrolysis and fuel cell modes are presented in Table 5.3.

The state-of-the-art solid oxide fuel cell (SOFC) materials formed a starting point for SOEC and RSOFC development. Typical electrolytes utilized are made of doped zirconia, which is a fluorite-structured oxide; for example, yttria-stabilized zirconia ($8YSZ = 8$ mol.% Y_2O_3-stabilized ZrO_2) or scandia-stabilized zirconia (ScSZ). Fuel electrodes are made of composites of zirconia and Ni-metal catalyst (Ni/YSZ), while oxygen electrodes are made of perovskite materials.

5.5.2 Durability evaluation of RSOFCs

Even though SOCs are reversible in theory and can attain comparable initial performance in electrolysis and fuel cell mode, the degree of degradation of the cells during long-term testing during fuel cell and electrolysis operation modes can be

dramatically different (Yildiz, 2012). Whereas voltage degradation rates below 1%/1000 h under constant current operation are demonstrated for SOFCs, degradation in electrolysis mode tends to be higher. Hauch and coworkers (Hauch et al., 2008) tested state-of-the-art SOCs in electrolysis mode at the Risø National Laboratory at temperatures in the range of 650–950 °C. A long-term degradation rate of 2%/1000 h was obtained at 850 °C at a current density of -0.5 A cm^{-2}, whereas the degradation rate increased to 6%/1000 h at 950 °C and a current density of -1.0 A cm^{-2}. Stack degradation tends to be faster than cell degradation alone due to additional impacts from piping, interconnects, and seals (Nabielek et al., 2009). Performance degradation results from a 25-cell SOEC stack at INL were presented by O'Brien et al. (2007). The ASR increased more than 40% over approximately 900 h.

The delamination of the oxygen electrode from the electrolyte has been observed as a major problem leading to SOEC performance degradation (Sohal et al., 2012). The buildup of a high oxygen partial pressure at the electrode/electrolyte interface is thought to be one major reason for the detachment of the electrode layer from the electrolyte. Therefore, a key requirement for the oxygen electrode in reversible SOCs is a flexible structure that accommodates oxygen excess in electrolysis mode and is also stable when oxygen poor conditions prevail in fuel cell mode (Yildiz, 2012).

Several efforts have been made to identify an optimal materials set for stable stack operation in electrolysis mode (Marina et al., 2007; Laguna-Bercero et al., 2011).

A report by Laguna-Bercero et al. (2011) presents $La_{2-x}Sr_xCo_{0.5}Ni_{0.5}O_{4+\delta}$ (LSCN) as a novel electrode for reversible SOCs. From electrochemical tests, LSCN was found to perform well and stable in both the electrolytic and fuel cell operating modes.

Mixed conducting oxygen electrodes like lanthanum strontium cobalt ferrites (LSCFs) are presented as good candidates for reversible oxygen electrodes in high-temperature electrolysis cells (Minh, 2011, 2013; Laguna-Bercero et al., 2011). The performance of LSCF and LSM/YSZ oxygen electrodes for RSOFCs were presented and discussed by Laguna-Bercero et al. (2011). Total ASR values have been found to decrease in accordance with LSM/YSZ > LSCF. Performance degradation in terms of the ASR of various oxygen electrodes (LSM, LSF, LSCF) in both fuel cell and electrolysis operating modes was presented by Minh (2011), where the LSCF electrodes showed the best performance and stability due to having the lowest values of ASR. The loss in performance (the voltage degradation) during SOFC operation (fuel cell mode) of an anode-supported 5×5 cm^2 single cell with an LSCF electrode is only approximately 1%/1000 h (Tietz et al., 2006). The recently reported cell performance (Schefold et al., 2012) of a circular anode-supported single cell with an LSCF electrode during 9000 h of electrolysis operation with an applied current of -1 A cm^{-2} under steady state operation showed a voltage increase of 3.8%/1000 h.

Recently, a Jülich two-cell planar short stack with LSCF oxygen electrodes was tested by Nguyen et al. (2013) in both fuel cell and electrolysis modes. The voltage degradation under fuel cell operation mode of 4000 h is 0.6%/1000 h at current density of 0.5 A cm^{-2} (fuel utilization: FU = 40%) and $T = 750$ °C. There is nearly no degradation after 2000 h of steam electrolysis (800 °C, H$_2$/H$_2$O = 1/1, FU = 15%) at

current density of -0.3 A cm^{-2}. The results verified that LSCF present a good candidate for reversible oxygen electrodes in high-temperature electrolysis cells.

Minh (2013) tested the reversibility of a 10-cell reversible SOFC stack (cells consisting of a YSZ electrolyte, Ni/YSZ hydrogen electrode, LSCF oxygen electrode and stainless steel current collectors) over 1000 h. The stack ran very successfully with a high power density of 480 mW cm^{-2} at 0.7 V and 80% fuel utilization in fuel cell mode and >6 standard liter per minute (SLPM) hydrogen production in steam electrolysis mode using about 1.1 kW of electrical power. The degradation rate was in the order of 100–300 mΩ cm^2/1000 h.

The effect of Mo doping on the crystal structure and thermal, electrical and electrochemical properties of the SrCo$_{1-x}$Mo$_x$O$_{3-\delta}$ ($x=0.05, 0.1$) system was studied by Aguadero et al. (2012). The good performance of these compounds in both cathodic and anodic conditions makes this system a promising candidate for reversible oxygen electrodes in RSOFCs.

Symmetrical solid oxide fuel cells (SSOFCs) have been developed in the past few years as a new concept of RSOFCs. In this configuration, the same electrode material is used for both the oxygen and fuel electrodes. An overview of the most common materials tested as symmetrical electrodes for RSOFCs, into electrolytes employed, configurations tested and into new fabrication processes and procedures for microstructural engineering was given by Ruiz-Morales et al. (2011). One of the most promising SSOFC systems seems to be the double perovskite Sr$_2$Fe$_{1.5}$Mo$_{0.5}$O$_6$ (SFM). This material exhibits conductivities higher than 300 S cm^{-1} in both oxidizing and reducing conditions, and performances in excess of 800 mW cm^{-2} at 900 °C with lanthanum strontium gallium magnesium oxide (LSGM) electrolyte. The most remarkable feature is its good functionality as a symmetrical electrode for SOEC (Ruiz-Morales et al., 2011).

A novel design for RSOFCs is the dual cells concept by Viviani et al. (2012). The dual membrane cell is an innovative RSOFC concept combining protonic and anionic conductivity, thereby providing an independent compartment for water formation. The cell comprises a series of five layers with different compositions, alternating two dense electrolytes and three porous layers. Such a three-chamber configuration promises many advantages related to fuel dilution, materials corrosion and reversibility between fuel cell and electrolyzer operational modes at high temperature (Figure 5.6). Dual conductivity can be achieved by joining two dense electrolytes BCY (BaCe$_{0.85}$Y$_{0.15}$O$_{3-\delta}$) and YDC (Ce$_{0.85}$Y$_{0.15}$O$_{2-\delta}$) through a porous ceramic central membrane made up of both materials.

Complete anode-supported dual cells have been fabricated through a combination of pressing, casting, printing, wet spraying and plasma spraying techniques (Viviani et al., 2012).

Single RSOFCs with different configurations from several manufacturers have been evaluated for initial performance and long-term durability by Zhang et al. (2013).

According to these authors, cells from Ceramatec Inc. and from Materials and Systems Research Inc. (MSRI) showed excellent overall durability in electrolysis mode and acceptable degradation in both the fuel cell and electrolysis modes. Cells from
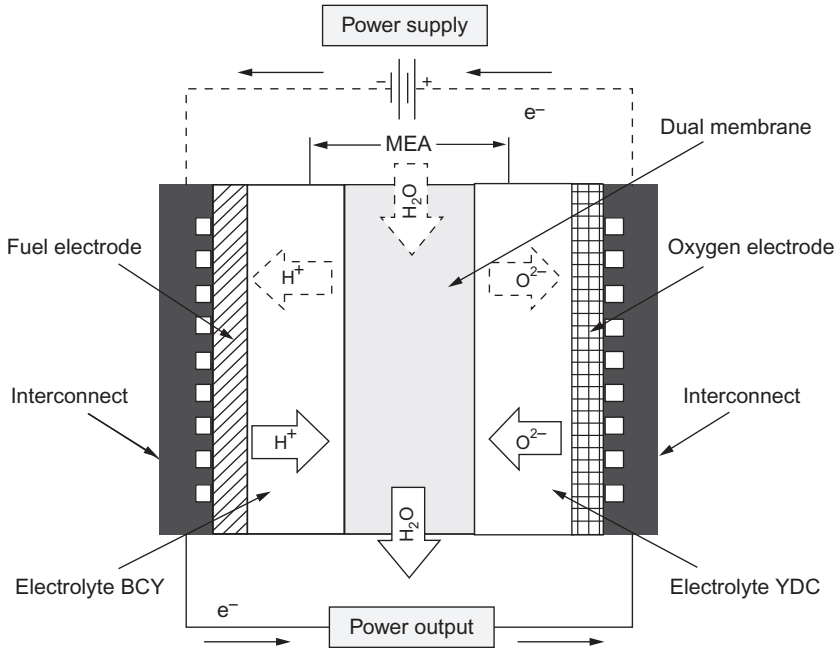
Figure 5.6 RSOFC with dual cell concept by Viviani et al. (2012).

Saint Gobain Advanced Materials Inc. (St. Gobain) and SolidPower Inc. demonstrated stable performance in fuel cell mode but rapid degradation in electrolysis mode, especially at high current density. These results confirm that cells developed for SOFC applications are not necessarily suitable for electrolysis mode without modification.

Graves et al. (2015) investigated whether electrolysis-induced performance loss might be decreased by operating the cell reversibly, periodically cycling between fuel cell and electrolysis modes. They found that the ohmic resistance slightly decreased during 4,000 h of reversible cycling. The work of Nguyen et al. (2013) showed a similar result. For the test in both fuel cell and electrolysis modes, nearly no degradation after 2000 h of steam electrolysis (figure 4 in Nguyen et al., 2013) was also observed. Operating in charge–discharge energy storage cycles suggests a variety of other possibilities for controlling operating conditions to repair the deterioration of materials or to eliminate other types of electrochemical cell degradation (Graves et al., 2015).

5.6   Applications and alternative concepts for RFCs

Applications of the regenerative fuel cell system based on the combination of an electrolyzer subsystem and a fuel cell subsystem for spacecraft on-board energy storage are presented in the literatures by authors such as Müller (2012), Sone (2011), Xiaojin

et al. (2010), and Markgraf et al. (2012). The key components of such systems are the fuel cell, the electrolyzer and the hydrogen/oxygen storage system.

The realization of an RFC system has not been reported up until now.

5.6.1   Production of hydrogen via water electrolysis

Because the application of fuel cells is already addressed in Chapters 1–4, in this chapter only the application of electrolyzers is presented.

At present, commercial electrolyzers are available for hydrogen production in the areas of AE and PEE. Commercial alkaline electrolyzers operate at about 80 ˚C and at low current densities in the range of -0.2 to -0.4 A cm^{-2} (Mergel et al., 2013). They have been produced in a variety of power classes up to 750 sm^{3}h^{-1}. The leading manufacturers of alkaline electrolyzers are Hydrogenics, H2 Logic, NEL Hydrogen, Sagim S.A., McPhy, Teledyne Energy Systems, and Wasserelektrolyse Hygrotechnik GmbH (Mergel et al., 2013).

Commercial PEM electrolyzers currently operate at higher current densities (by a factor of five in comparison to alkaline electrolyzers) but require about 2–3 mg cm^{-2} of iridium in the oxygen electrode and about 1–2 mg cm^{-2} of platinum in the fuel electrode as catalysts (Carmo et al., 2013). There are few commercial products on the market (<65 sm^3 h^{-1}) (Mergel et al., 2013). The leading manufacturers of PEM electrolyzers are Giner Electrochemical Systems, H-TEC Systems, Hydrogenics, ITM Power, Proton OnSite, and Siemens. Proton OnSite recently achieved a lifetime of more than 15,000 h for a prototype stack in polymer electrolyte electrolyzers of 50 kg H$_2$/day (Ayers et al., 2012). The production costs of PEM electrolysis systems were also reduced by approximately 44% in the time period from 2008 to 2014 (Ayers et al., 2014).

5.6.2   The production of hydrogen, synthesis gas and fuels from H$_2$O and CO$_2$ using RSOFC

RSOFC can be quite easily applied in the areas of high-temperature electrolysis. The high-temperature SOE has the advantage that it can operate with lower electricity consumption because a part of the energy required for water splitting is obtained in the form of heat (Figure 5.1); furthermore, it speeds up the reaction kinetics. According to Mogensen et al. (2006), electricity cost is the major constituent of the production price and the potential H$_2$ production price using SOE technology is almost half that of using ordinary AE.

SOEs has the advantage that they can also split CO$_2$ into CO and O$_2$. RSOFCs have potential for the production of synthetic fuel from renewable energy sources in places where electricity can be generated extremely cheaply (Mogensen et al., 2006) or with excess heat energy.

Figure 5.7 shows an example of a novel electrical energy storage system that is based on H–C–O chemistry using high-temperature RSOFCs.
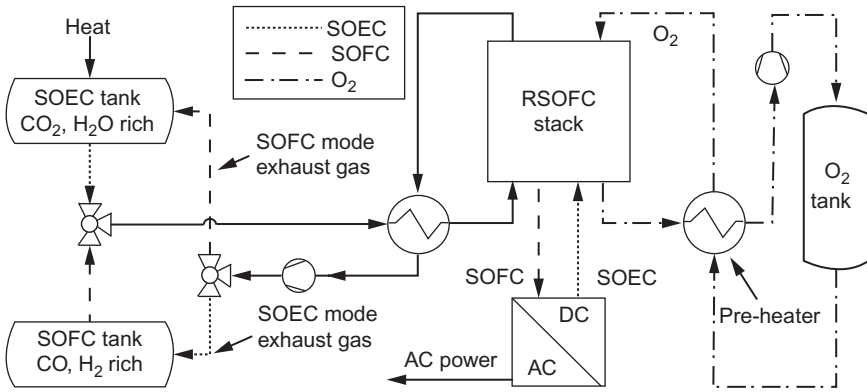
Figure 5.7 Schematic of electrical energy storage system using RSOFCs.
Adapted from Kazempoor and Braun (2014).

The proposed device operates reversibly, storing energy electrochemically in tanks like a flow battery. In SOFC mode, electricity is produced through the electrochemical oxidation of the $H_2/CO/CH_4$ fuel mixture as the fuel flows from the "SOFC tank" through the MEA after preheating, with the exhaust collected in the "SOEC tank." In SOEC mode, syngas is produced as fuel via the high-temperature coelectrolysis of H_2O/CO_2-rich gas mixture and is stored chemically in the "SOFC tank."

Based on electrolysis, in principle two pathways exist to produce liquid fuels from H_2O and CO_2. First, hydrogen generated in electrolyzer mode can react with CO_2 to produce storable liquid fuels such as gasoline or diesel fuel via the modified FT synthesis (i.e., the original FT process combined with a water–gas-shift reactor) (Riedel et al., 1999). The total reaction of CO_2 hydrogenation is

$$CO_2 + 3H_2 \rightarrow -CH_2 - + 2H_2O \tag{5.19}$$

where $-CH_2-$ is part of a hydrocarbon chain.

The second pathway employs the high-temperature coelectrolysis of steam/CO_2 mixtures to produce syngas. The syngas can then be used to make various kinds of liquid fuels, such as synthetic diesel, by using the original FT process:

$$CO + 2H_2 \leftrightarrow -CH_2 - + H_2O \tag{5.20}$$

The $-CH_2-$ is the chain growth molecule on which higher hydrocarbons are built.

An overview for the production of FT liquid fuels from high-temperature solid oxide coelectrolysis units is given by Graves et al. (2011), Becker et al. (2012), and Nguyen and Blum (2015).

Wendel et al. (2015) presented a novel system based on RSOFCs that employ a thermal management strategy of promoting exothermic methanation within the RSOFC stack to provide thermal energy for the endothermic steam/CO_2 electrolysis

reactions during charging mode (fuel cell mode). The modeling results indicate that round-trip efficiencies greater than 70% can be achieved at a stack temperature of 680 ˚C and elevated stack pressure of 20 bar.

5.6.3   Innovative electrical energy storage concepts

5.6.3.1   Investigation of the hybrid photovoltaic/RPEFC system

The hybrid photovoltaic (PV)/RPEFC system in the tropics was investigated by Dihrab et al. (2012). With the assistance of power from PV during sunny hours, hydrogen as an energy carrier is produced by RPEFC in electrolyzer mode. The system then uses stored hydrogen to produce energy in cell mode after sunset or on cloudy days. The measured results showed the ability of the system to meet the load proposed by system modeling. Under Malaysian weather condition its total efficiency was about 4.5%.

5.6.3.2   The proton flow battery concept

An innovative concept for integrating a metal hydride (MH) storage electrode into a reversible proton exchange membrane fuel cell (RPEFC) is described and investigated experimentally by Andrews and Mohammade (2014).

In this new "proton flow battery concept," many steps in the conventional process are completely avoided. In the charge mode (upper dashed line in Figure 5.8), water is split by electrolysis on the oxygen side of a PEFC membrane with the assistance of a catalyst. Protons (H^+) pass through the polymeric acid membrane (Nafion) to the MH storage electrode. A key feature of the system is that the hydrogen storage material is integrated into the hydrogen-side electrode of the RPEFC. In the discharge or fuel cell mode (lower solid line in Figure 5.8), hydrogen atoms are released from their weak bonds with the metal atoms of the storage electrode. These liberated hydrogen atoms move to the surfaces of the metal particles where they each give an electron on the metal atoms to reform protons. The protons then move through the storage material into the Nafion membrane. Once in the membrane, protons are electrically attracted back toward the oxygen side of the RPEFC through the Nafion membrane.

The key innovation is in electrolysis mode to inject protons emanating from the Nafion membrane directly into the MH storage electrode. Steps including the conversion of protons produced during electrolysis into hydrogen gas, the compression of this gas, and, subsequently, the splitting of gas molecules in the fuel cell to release protons and generate electricity are completely avoided (Andrews and Mohammade, 2014). Therefore, the proton flow battery has, in principle, the potential for higher round-trip efficiency than the conventional hydrogen storage system. Other advantages of the proton flow battery might include (1) longer lifetimes than other batteries as a solid-state electrolyte is used; (2) low-temperature operation; and (3) the Pt catalyst normally required on the hydrogen side of an RPEFC is not required in the proton flow battery.

Andrews and Mohammade (2014) reported preliminary results of the RPEFC with an integrated solid-state MH powder electrode and of the other with an integrated
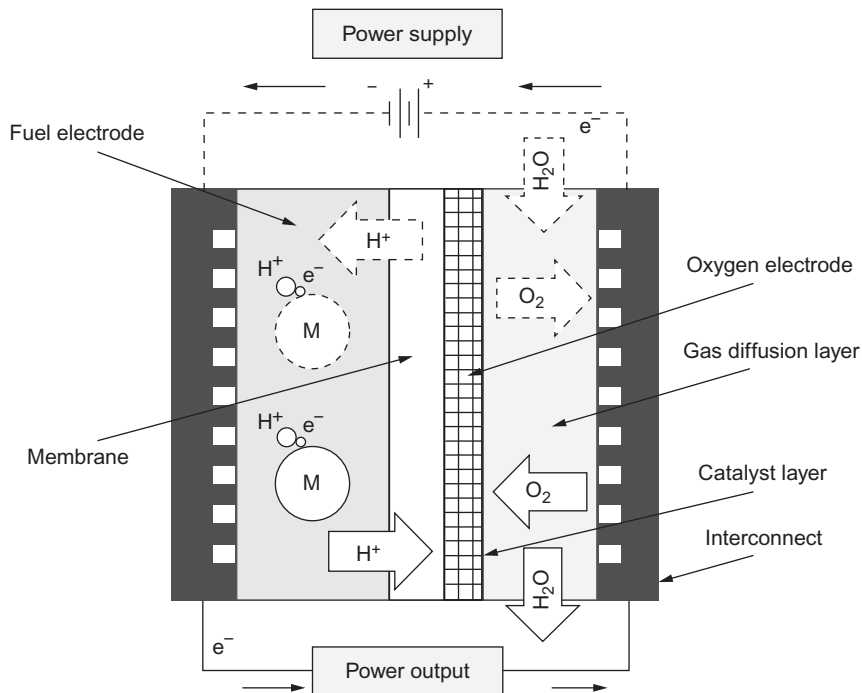
Figure 5.8 Schematic design of a modified RPEFC with an integrated solid proton storage electrode (Andrews and Mohammade, 2014). *M* represents a metal atom of the solid storage to which a hydrogen atom is bonded.

solid-state MH-Nafion storage electrode. The RPEFC had a Nafion membrane and a catalyst layer of Pt black/IrO_2 on the oxygen side but no catalyst or gas diffusion backing on the hydrogen side. The composite MH-Nafion electrode stored up to 0.6 wt.% of hydrogen, but only a small fraction of this was able to be recovered to run the device in fuel cell mode. The MH powder electrode stored hydrogen more reversibly, although the total storage capacity was much lower, at 0.07 wt.%. The results provide initial confirmatory evidence that the proton flow battery concept is feasible and promising.

5.6.3.3   Rechargeable high-temperature solid oxide batteries

Another possibility for an RFC also ascribed as a high-temperature metal–air battery is described by Leonide et al. (2014) and Drenckhahn et al. (2013). In this concept fuel and water vapor are not supplied from external storage, but are stored internally in the stack on the fuel electrode side through a metal/metal-oxide RedOx pair (e.g., iron–iron oxide). On the fuel side there is a stagnant gas atmosphere as a mixture of hydrogen and water vapor. Under charging mode the metal oxide is reduced to its metallic state by the hydrogen that is produced by electrolysis. The water vapor produced as a
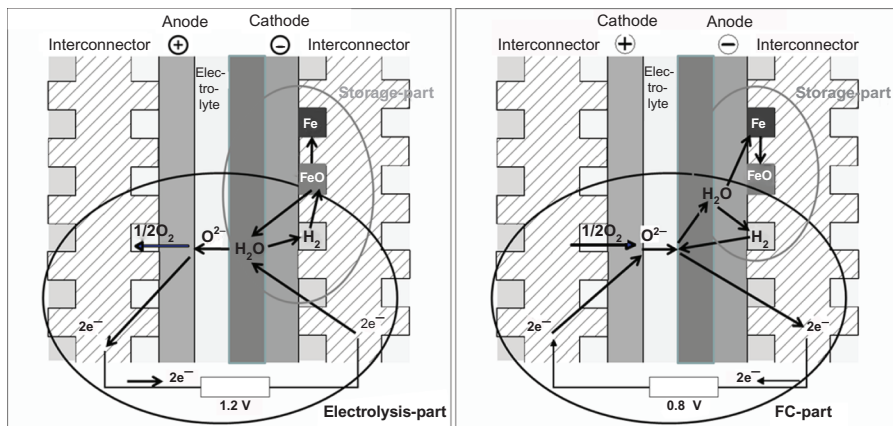
Figure 5.9 Functional principle of rechargeable solid oxide battery.

result of reduction of the metal oxide then keeps the electrolysis process going, without an external supply of water. In this way, the electrical energy is stored in the metal (see Figure 5.9 left) and the "battery" can be charged until no metal oxide can be further reduced. Under discharging mode, the "battery" is operated like a fuel cell. The consumed hydrogen through the fuel cell reaction leads to increased oxygen partial pressure in the stagnant atmosphere, which in turn leads to oxidation of the metal by the water vapor, which is produced in fuel cell reaction. During the oxidation process, hydrogen is released to continue the fuel cell reaction (see Figure 5.9 right). The "battery" can be discharged until no metal can be further oxidized. This concept offers the possibility of comparatively high energy and power densities. The electrodes will be the same as those used in SOFCs and SOECs. Research is mainly focused on the development of a suitable and long-term stable storage material (see Menzler et al., 2013).

5.7   Need for further research and development

In all areas of electrochemistry, basic science is the key to driving technological innovation.

For RPEFCs, due to the high price and the limited reserves of Pt, Ir, and Ru, they can only be used as catalyst materials to a limited extent in the future (Trasatti, 1984). Activities in catalyst development for PEM electrolysis are therefore concentrated on reducing or completely replacing noble metals in the catalyst-coated membranes while retaining comparable performance.

Degradation of the currently used SOFC materials in electrolytic or reversible mode is an ongoing challenge (Yildiz, 2012). A massive R&D effort is probably necessary in order to obtain inexpensive electrolyzers with sufficiently high durability and efficiency for broad commercial RSOFC application. Fundamentally, the following research areas are important (Mogensen et al., 2006):

- materials research in order to identify improved materials and fabricate effective structures;
- surface science in order to understand the nature of the interfaces between the electrodes and electrolyte (at the electronic and atomic level); and
- solid-state electrochemistry in order to understand the processes and losses involved (electrochemical reactions and degradation mechanisms at the molecular level are necessary).

References

Aguadero, A., Perez-Coll, D., Alonso, J.A., Skinner, S.J., Kilner, J., 2012. A new family of Mo-doped $SrCoO_3 - \delta$ perovskites for application in reversible solid state electrochemical cells. Chem. Mater. 24, 2655–2663.

Altmann, S., Kaz, T., Friedrich, K.A., 2011. Bifunctional electrodes for unitised regenerative fuel cells. Electrochim. Acta 56, 4287–4293.

Alvar, E.N., Zhou, B., Eichhorn, S.H., 2014. Oxidative treatment to improve coating and electrochemical stability of carbon fiber paper with niobium doped titanium dioxide sols for potential applications in fuel cells. Electrochim. Acta 132, 347–355.

Andrews, J., Mohammade, S.S., 2014. Towards a "proton flow battery": investigation of a reversible PEM fuel cell with integrated metalhydride hydrogen storage. Int. J. Hydrog. Energy 39, 1740–1751.

Ayers, K.E., et al., 2014. High performance, low cost hydrogen generation from renewable energy, Technical Report, Proton OnSite, Wallingford, CT, DOI:10.2172/1117668.

Ayers, K.E., Capuano, C.B., Anderson, E.B., 2012. Recent advances in cell cost and efficiency for PEM-based water electrolysis. ECS Trans. 41, 15–22.

Barbir, F., Molter, T., Dalton, L., 2005. Efficiency and weight trade-off analysis of regenerative fuel cells as energy storage for aerospace applications. Int. J. Hydrog. Energy 30 (4), 351–357.

Becker, W.L., Braun, R.J., Penev, M., Melaina, M., 2012. Production of Fischer—Tropsch liquid fuels from high temperature solid oxide co-electrolysis units. Energy 47, 99–115.

Bidrawn, F., Kim, G., Corre, G., Irvine, J.T.S., Vohs, J.M., Gorte, R.J., 2008. Efficient reduction of CO_2 in a solid oxide electrolyzer. Electrochem. Solid-State Lett. 11, B167–B170.

Bierschenk, D.M., Wilson, J.R., Miller, E., Dutton, E., Barnett, S.A., 2011. A proposed method for high efficiency electrical energy storage using solid oxide cells. ECS Trans. 35, 2969–2978.

Björketun, M.E., Bondarenko, A.S., Abrams, B.L., Chorkendorff, I., Rossmeisl, J., 2010. Screening of electrocatalytic materials for hydrogen evolution. Phys. Chem. Chem. Phys. 2010 (12), 10536–10541.

Borup, R., et al., 2007. Scientific aspects of polymer electrolyte fuel cell durability and degradation. Chem. Rev. 107, 3904–3951.

Brown, D.E., Mahmood, M.N., Turner, A.K., Hall, S.M., Fogarty, P.O., 1982. Low overvoltage electrocatalysts for hydrogen evolving electrodes. Int. J. Hydrog. Energy 7, 405–410.

Carmo, M., Fritz, D.L., Mergel, J., Stolten, D., 2013. A comprehensive review on PEM water electrolysis. Int. J. Hydrog. Energy 38, 4901–4934.

Chen, G.Y., Delafuente, D.A., Sarangapani, S., Mallouk, T.E., 2001. Combinatorial discovery of bifunctional oxygen reduction water oxidation electrocatalysts for regenerative fuel cells. Catal. Today 67, 341–355.

Chen, G.Y., Bare, S.R., Mallouk, T.E., 2002. Development of supported bifunctional electrocatalysts for unitized regenerative fuel cells. J. Electrochem. Soc. 149, A1092–A1099.

Chen, G.Y., Zhang, H., Ma, H., Zhong, H., 2009. Effect of fabrication methods of bifunctional catalyst layers on unitized regenerative fuel cell performance. Electrochim. Acta 54, 5454–5462.

Daubert, T.E., et al., 1992. Physical and Thermodynamic Properties of Pure Chemicals Evaluated Process Design Data. Hemisphere Publishing Corporation, New York.

Dihrab, S., Khatib, T., Sopian, K., Al-Ani, H., Zaidi, S.H., 2012. On the performance of hybrid PV/unitized regenerative fuel cell system in the tropics. Int. J. Photoenergy 2012, Article ID 942784, 1–7. http://dx.doi.org/10.1155/2012/942784,.

Dipu, A.L., Ryu, J., Kato, Y., 2012. Carbon dioxide electrolysis for a carbon-recycling iron-making system. ISIJ Int. 52, 1427–1432.

Dönitz, W., Erdle, E., 1985. High-temperature electrolysis of water vapor—status of development and perspectives for application. Int. J. Hydrog. Energy 10, 291–295.

Drenckhahn, W., Greiner, H., Kühne, M., Landes, H., Leonide, A., Litzinger, K., Lu, C., Schuh, C., Shull, J., Soller, T., 2013. A novel high temperature metal-air battery. ECS Trans. 50, 125–135.

Dry, M.E., 2002. The Fischer–Tropsch process: 1950–2000. Catal. Today 71, 227.

Ebbesen, S.D., Mogensen, M.J., 2009. Electrolysis of carbon dioxide in solid oxide electrolysis cells. J. Power Sources 193, 349–358.

Gabbasa, M., Sopian, K., Fudholi, A., Asim, N., 2014. A review of unitized regenerative fuel cell stack: material, design and research achievements. Int. J. Hydrog. Energy 39, 17765–17778.

Garcia, G., Roca-Ayats, M., Lillo, A., Galante, J.L., Pena, M.A., Martinez-Huerta, M.V., 2013. Catalyst support effects at the oxygen electrode of unitized regenerative fuel cells. Catal. Today 210, 67–74.

Gasteiger, H.A., Kocha, S.S., Sompalli, B., Wagner, F.T., 2005. Activity benchmarks and requirements for Pt, Pt-alloy, and non-Pt oxygen reduction catalysts for PEMFCs. Appl. Catal. B 56, 9–35.

Gorlin, Y., Jaramillo, T.F., 2010. A Bifunctional nonprecious metal catalyst for oxygen reduction and water oxidation. J. Am. Chem. Soc. 132, 13612–13614.

Graves, C., Ebbesen, S.D., Mogensen, M., Lackner, K., 2011. Sustainable hydrocarbon fuels by recycling CO_2 and H_2O with renewable or nuclear energy. Renew. Sustain Energy Rev. 15, 1–23.

Graves, C., Ebbesen, S.D., Jensen, S.H., Simonsen, S.B., Mogensen, M.B., 2015. Eliminating degradation in solid oxide electrochemical cells by reversible operation. Nat. Mater. 14, 239–244.

Greeley, J., Markovic, N.M., 2012. The road from animal electricity to green energy: combining experiment and theory in electrocatalysis. Energy Environ. Sci. 5, 9246–9256.

Green, R.D., Liu, C.C., Adler, S.B., 2008. Carbon dioxide reduction on gadolinia-doped ceria cathodes. Solid State Ion 179, 647–660.

Hauch, A., Ebbesen, S.D., Jensen, S.H., Mogensen, M., 2008. Solid oxide electrolysis cells: microstructure and degradation of the Ni/yttria-stabilized zirconia electrode. J. Electrochem. Soc. 155, B1184–B1193.

Hwang, C.M., Ishida, M., Ito, H., Maeda, T., Nakano, A., Kato, A., Yoshida, T., 2012. Effect of titanium powder loading in gas diffusion layer of a polymer electrolyte unitized reversible fuel cell. J. Power Sources 202, 108–113.

Hwang, C.M., Ito, H., Maeda, T., Nakano, A., Kato, A., Yoshida, T., 2013. Effect of through-plane polytetrafluoroethylene distribution in a gas diffusion layer on a polymer electrolyte unitized reversible fuel cell. ECS Trans. 58, 1059–1068.

Ioroi, T., Oku, T., Yasuda, K., Kumagai, N., Miyazaki, Y., 2003. Influence of PTFE coating on gas diffusion backing for unitized regenerative polymer electrolyte fuel cells. J. Power Sources 124, 385–389.

Isenberg, A.O., 1981. Energy-conversion via solid oxide electrolyte electrochemical cells at high-temperatures. Solid State Ion 3 (4), 431–437.

Ito, H., Maeda, T., Nakano, A., Hwang, C.M., Ishida, M., Yokoi, N., Hasegawa, Y., Kato, A., Yoshida, T., 2011. Effect of titanium powder loading in microporous layer on a polymer electrolyte unitized reversible fuel cell. ECS Trans. 41, 469–477.

Jörissen, L., 2006. Bifunctional oxygen/air electrodes. J. Power Sources 2006 (155), 23–32.

Jung, H.-Y., Park, S., Popov, B.N., 2009. Electrochemical studies of an unsupported PtIr electrocatalyst as a bifunctional oxygen electrode in a unitized regenerative fuel cell. J. Power Sources 191, 357–361.

Kangasniemi, K.H., Condit, D.A., Jarvi, T.D., 2004. Characterization of vulcan electrochemically oxidized under simulated PEM fuel cell conditions. J. Electrochem. Soc. 151, E125–E132.

Kazempoor, P., Braun, R.J., 2014. Model validation and performance analysis of regenerative solid oxide cells for energy storage applications: reversible operation. Int. J. Hydrog. Energy 39, 5955–5971.

Kordesch, K., Steininger, K.-H., 1988. An improved bifunctional oxygen (air) electrode for reversible alkaline fuel cell systems and for rechargeable metal-air batteries. In: Proceedings of the Intersociety Energy Conversion Engineering Conference 23th, Vol. 2, pp. 283–285.

Laguna-Bercero, M.A., 2012. Recent advances in high temperature electrolysis using solid oxide fuel cells: a review. J. Power Sources 203, 4–16.

Laguna-Bercero, M.A., Kilner, J.A., Skinner, S.J., 2011. Development of oxygen electrodes for reversible solid oxide fuel cells with scandia stabilized zirconia electrolytes. Solid State Ion 192, 501–504.

Larminie, J., Dicks, A., 2003. Fuel Cell Systems Explained. John Wiley & Sons, New York.

Lee, W.H., Kim, H., 2014. Optimization of electrode structure to suppress electrochemical carbon corrosion of gas diffusion layer for unitized regenerative fuel cell. J. Electrochem. Soc. 161, F729–F733.

Lee, H., Kim, J., Park, J., Joe, Y., Lee, T., 2004. Performance of polypyrrole-impregnated composite electrode for unitized regenerative fuel cell. J. Power Sources 131, 188–193.

Leonide, A., Drenckhahn, W., Greiner, H., Landes, H., 2014. Long term operation of rechargeable high temperature solid oxide batteries. J. Electrochem. Soc. 161 (9), A1297–A1301.

Lin, M.T., Wan, C.H., Wu, W., 2014. Enhanced corrosion resistance of ss304 stainless steel and titanium coated with alternate layers of TiN and ZrN in a simulated O_2-rich environment of a unitized regenerative fuel cell. Int. J. Electrochem. Sci. 9, 7832–7845.

Maillard, F., Lu, G.Q., Wieckowski, A., Stimming, U., 2005. Ru-decorated Pt surfaces as model fuel cell electrocatalysts for CO electrooxidation. J. Phys. Chem. B 2005 (109), 16230–16243.

Marina, O.A., Pederson, L.R., Williams, M.C., Coffey, G.W., Meinhardt, K.D., Nguyen, C.D., Thomsen, E.C., 2007. Electrode performance in reversible solid oxide fuel cells. J. Electrochem Soc. 154, B452–B459.

Markgraf, S., Hörenz, M., Schmiel, T., Jele, W., Lucas, J., Henn, N., 2012. Alkaline fuel cells running at elevated temperature for regenerative fuel cell system applications in spacecrafts. J. Power Sources 201, 236–242.

Menzler, N.H., Hospach, A., Niewolak, L., Bram, M., Tokariev, O., Berger, C., Orzessek, P., Quadakkers, W.J., Fang, Q., Buchkremer, H.P., 2013. Power-to-storage—the use of an anode-supported solid oxide fuel cell as a high-temperature battery. ECS Trans. 57 (1), 255–267.

Mergel, J., Carmo, M., Fritz, D.L., 2013. Status on technologies for hydrogen production by water electrolysis. In: Stolten, D., Scherer, V. (Eds.), Transition to Renewable Energy Systems. Wiley-VCH, Weinheim, pp. 425–450.

Minh, N.Q., 2011. Development of reversible solid oxide fuel cells (RSOFCs) and stacks. ECS Trans. 35, 2897–2904.

Minh, N.Q., 2013. SOFC operation: direct fuel utilization, pressurization and reversibility. ECS Trans. 57, 197–204.

Mogensen, M., Jensen, S.H., Hauch A., Chorkendorff, I., Jacobsen, T., 2006. Performance of Reversible Solid Oxide Cells: A Review, http://www.risoe.dk/rispubl/art/2006_90_paper.pdf.

Müller, M., 2012. Regenerative fuel cells. In: Stolten, D., Emonts, B. (Eds.), In: Fuel Cell Science and Engineering—Materials, Processes, Systems and Technology, vol. 1. Wiley-VCH Verlag GmbHCo. KGaA, Weinheim, chapter 8.

Nabielek, H., Blum, L., Buchkremer, H.P., Haanappel, V.A.C., de Haart, L.G.J., Quadakkers, W.J., et al., 2009. Reducing degradation effects in SOFC stacks manufactured at Forschungszentrum Jülich—approaches results. Ceram. Eng. Sci. Proc. 28, 65–77.

Ng, J.W.D., Gorlin, Y., Hatsukade, T., Jaramillo, T.F., 2013. A precious-metal-free regenerative fuel cell for storing renewable electricity. Adv. Energy Matter 3, 1545–1550.

Ng, J.W.D., Tang, M., Jaramillo, T.F., 2014. A carbon-free, precious-metal-free, high-performance O_2 electrode for regenerative fuel cells and metal-air batteries. Energy Environ. Sci. 7, 2017–2024.

Nguyen, V.N., Blum, L., 2015. Syngas and synfuels from H_2O and CO_2: current status. Chem. Ing. Tech. 87, 354–375.

Nguyen, V.N., Fang, Q., Packbier, U., Blum, L., 2013. Long-term tests of a Jülich planar short stack with reversible solid oxide cells in both fuel cell and electrolysis modes. Int. J. Hydrog. Energy 38, 4281–4290.

Ni, M., 2012. An electrochemical model for syngas production by co-electrolysis of H_2O and CO_2. J. Power Sources 202, 209–216.

O'Brien, J.E., Stoots, C.M., Herring, J.S., Hartvigsen, J.J., 2007. Performance of planar high-temperature electrolysis stacks for hydrogen production from nuclear energy. Nucl. Technol. 158, 118–131.

Park, S., Shao, Y., Liu, J., Wang, Y., 2012. Oxygen electrocatalysts for water electrolyzers and reversible fuel cells: status and perspective. Energy Environ. Sci. 5, 9331–9344.

Pettersson, J., Ramsey, B., Harrison, D., 2006. A review of the latest developments in electrodes for unitized regenerative polymer electrolyte fuel cells. J. Power Sources 157, 28–34.

Riedel, T., Claeys, M., Schulz, H., Schaub, G., Nam, S.S., Jun, K.W., Choi, M.J., Kishan, G., Lee, K.W., 1999. Comparative study of Fischer–Tropsch synthesis with H_2/CO and H2/CO2 syngas using Fe- and Co-based catalysts. Appl. Catal. A Gen. 186, 201.

Roca-Ayats, M., Garcia, G., Galante, J.L., Pena, M.A., Martinez-Huerta, M.V., 2014. Electrocatalytic stability of Ti based-supported Pt3Ir nanoparticles for unitized regenerative fuel cells. Int. J. Hydrog. Energy 39, 5477–5484.

Ruiz-Morales, J., Marrero-Lopez, D., Canales-Vazquez, J., Irvine, J.T.S., 2011. Symmetric and reversible solid oxide fuel cells. RSC Adv. 1, 1403–1414.

Schefold, J., Brisse, A., Tietz, F., 2012. Nine thousand hours of operation of a solid oxide cell in steam electrolysis mode. J. Electrochem. Soc. 159, A137–A144.

Schulze, M., Gülzow, E., Steinhilber, G., 2001. Activation nickel-anode for alkaline fuel cells. Appl. Surf. Sci. 179, 251–256.

Skulason, E., Tripkovic, V., Bjorketun, M.E., Gudmundsdottir, S., Karlberg, G., Rossmeisl, J., Bligaard, T., Jonsson, H., Nørskov, J.K., 2010. Modeling the electrochemical hydrogen oxidation and evolution reactions on the basis of density functional theory calculations. J. Phys. Chem. C 114, 22374.

Smolinka, T., 2009. Water electrolysis. In: Garche, J. (Ed.), Encyclopedia of Electrochemical Power Sources. Elsevier Ltd, Oxford, pp. 394–413.

Smolinka, T., Rau, S., Hebling, C., 2010. Polymer electrolyte membrane (PEM) water electrolysis. In: Stolten, D. (Ed.), Hydrogen and Fuel Cells, Fundamentals, Technologies and Applications. Wiley-VCH, Weinheim, Germany, pp. 271–289.

Sohal, M.S., O'Brien, J.E., Stoots, C.M., Sharma, V.I., Yildiz, B., Virkar, A., 2012. Degradation issues in solid oxide cells during high temperature electrolysis. J. Fuel Cell Sci. Technol. 9, 011017-1–011017-10.

Soloveichik, G.L., 2014. Regenerative fuel cells for energy storage. Proc. IEEE 102, 964–975.

Sone, Y., 2011. A 100-W class regenerative fuel cell system for lunar and planetary missions. J. Power Sources 196, 9076–9080.

Subbaraman, R., Tripkovic, D., Chang, K.-C., Strmcnik, D., Paulikas, A.P., Hirunsit, P., Chan, M., Greeley, J., Stamenkovic, V., Markovic, N.M., 2012. Trends in activity for the water electrolyser reactions on 3d M(Ni, Co, Fe, Mn) hydr(oxy)oxide catalysts. Nat. Mater. 11, 550–557.

Swette, L., Kackley, N., McCatty, S.A., 1991. Oxygen electrodes for rechargeable alkaline fuel cells. III. J. Power Sources 36, 323–339.

Swette, L.L., LaConti, B., McCatty, S.A., 1994. Proton-exchange membrane regenerative fuel cells. J. Power Sources 47, 343–351.

Tietz, F., Haanappel, V.A.C., Mai, A., Mertens, J., Stöver, D., 2006. Performance of LSCF cathodes in cell tests. J. Power Sources 156, 20–22.

Trasatti, S., 1984. Electrocataysis in the anodic evolution of oxygen and chlorine. Electrochim. Acta 29, 1503–1512.

Ursua, A., Gadia, L.M., Sanchis, P., 2012. Hydrogen production from water electrolysis: current status and future trends. Proc. IEEE 100, 410–426.

Viviani, M., Canu, G., Carpanese, M.P., Barbucci, A., Sanson, A., Mercadelli, E., Nicolella, C., Vladikova, D., Stoynov, Z., Chesnaud, A., Thorel, A., Ilhan, Z., Ansar, S., 2012. Dual cells with mixed protonic-anionic conductivity for reversible SOFC/SOEC operation. Energy Procedia 28, 182–189.

Wendel, C.H., Kazempoor, P., Braun, R.J., 2015. Novel electrical energy storage system based on reversible solid oxide cells: system design and operating conditions. J. Power Sources 276, 133–144.

Winter, C.J., 2009. Hydrogen energy—abundant, efficient, clean: a debate over the energy-system-of change. Int. J. Hydrog. Energy 34, 1–52.

Wittstadt, U., Wagner, E., Jungmann, T., 2005. Membrane electrode assemblies for unitised regenerative polymer electrolyte fuel cells. J. Power Sources 145, 555–562.

Wu, X., Scott, K., 2012. A non-precious metal bifunctional oxygen electrode for alkaline anion exchange membrane cells. J. Power Sources 206, 14–19.

Xiaojin, L., Yu, Y., Zhigang, S., Baolian, Y., 2010. Mass minimization of a discrete regenerative fuel cell (RFC) system for on-board energy storage. J. Power Sources 195, 4811–4815.

Xuan, J., Leung, D.Y.C., Leung, M.K.H., Ni, M., Wang, H., 2011. A computational study of bifunctional oxygen electrode in air-breathing reversible microfluidic fuel cells. Int. J. Hydrog. Energy 36, 9231–9241.

Yan, J., Chen, H., Dogdibegovis, E., Stevenson, J., Cheng, M., 2014. High-efficiency intermediate temperature solid oxide electrolyzer cells for the conversion of carbon dioxide to fuels. J. Power Sources 252, 79–84.

Yildiz, B., 2012. Reversible solid oxide electrolytic cells for large-scale energy storage: challenges and opportunities. In: Kilner, J.A., Skinner, S.J., Irvine, S.J.C., Edwards, P. (Eds.), Functional Materials for Sustainable Energy Applications. Woodhead Publishing Series in Energy, vol. 35. Elsevier, UK, pp. 149–178.

Yim, S.D., Lee, W.Y., Yoon, Y.G., Sohn, Y.J., Park, G.G., Yang, T.H., Kim, C.S., 2004. Optimization of bifunctional electrocatalyst for PEM unitized regenerative fuel cell. Electrochim. Acta 50, 713–718.

Zahid, M., Schefold, J., Brisse, A., 2010. High-temperature water electrolysis using planar solid oxide fuel cell technology: a review. In: Stolten, D. (Ed.), Hydrogen and Fuel Cells, Fundamentals, Technologies and Applications. Wiley-VCH, Weinheim, Germany, pp. 227–242.

Zhan, Z., Kobsiriphat, W., Wilson, J.R., Pillai, M., Kim, I., Barnett, S.A., 2009. Syngas production by co-electrolysis of CO_2/H_2O: the basis for a renewable energy cycle. Energy Fuels 23, 3089–3096.

Zhang, Y.J., Wang, C., Wan, N.F., Mao, Z.Q., 2007. Deposited RuO_2-IrO_2/Pt electrocatalyst for the regenerative fuel cell. Int. J. Hydrog. Energy 32, 400–404.

Zhang, X., O´Brien, J.E., O´Brien, R.C., Housley, G.K., 2013. Durability evaluation of reversible solid oxide cells. J. Power Sources 242, 566–574.

This page intentionally left blank

Microbial and enzymatic fuel cells

6

G. Squadrito*, P. Cristiani†
*CNR—Istituto di Tecnologie Avanzate per l'Energia "Nicola Giordano",
(CNR-ITAE), Messina, Italy, †Ricerca sul Sistema Energetico SpA, (RSE), Milan, Italy

Abbreviations

BES	bioelectrochemical system
EFC	enzyme fuel cells
FC	fuel cell
MEA	membrane electrode assembly
MFC	microbial fuel cells
MPL	micro porous layer
PEFC	polymer electrolyte fuel cell
SOFC	solid oxide fuel cell

6.1 Introduction: What novel fuel cells exist?

Any exothermic oxy-reductive reaction can be used for energy generation. Combustion of different fuels for heating and cooking has been used since prehistory and, more recently, for moving machines and cars, and for generating electricity. Volta battery opened the way for electrochemistry that allows a direct conversion of chemical energy into electric power and vice versa, also gaining in energy conversion efficiency. Fuel cells, which can be considered as no cycling batteries, opened a new scenario for continuous power generation by using electrochemistry for controlling the oxidation of a fuel.

Silent, no polluting, and efficient power generation capability allowed fuel cells to become a candidate for future distributed heat and power generation (Squadrito et al., 2014; Environmental Protection Agency, 2008; The Fuel Cell Industry Review, 2014; Fuel cells for ship, 2012; McConnell, 2010).

Usually fuel cell classification is made by electrolyte type, because it defines the working temperature and the main characteristics of the fuel cell. A standard classification considers five technologies extensively treated in the first five chapters of this volume: alkaline (AFC), phosphoric acid (PAFC), molten carbonate (MCFC), polymer electrolyte (PEFC), and solid oxide fuel cell (SOFC). These technologies are today well developed and known, although further advancement in efficiency, endurance, and costs are required for large-scale commercialization. Water formation from hydrogen and oxygen is the reference reaction for all of these, although in addition to hydrogen, or hydrogen-rich streams, some kinds of fuel cells can be fueled also with methanol or light alcohols (Li and Faghri, 2013; Bahrami and Faghri, 2013; Kamarudin et al., 2013; Bretta et al., 2005). In addition to these, a number of alternate

fuels have been proposed and studied over time like methane or natural gas, formic acid, dimethyl-ether, sodium borohydride, carbon, ammonia (Cimenti and Hill, 2009; Giddey et al., 2012; Ma et al., 2010; Rice et al., 2002).

Considering PEFC, for example, a large number of liquid fuels have been proposed, and there is the habit to rename these PEFC "direct (fuel name) fuel cells"; for example, there are "direct methanol fuel cells," "direct alcohol fuel cells," "direct sodium borohydride fuel cells," and so forth. Although of applicative interest, these kinds of FCs are not considered a new type, but simply a PEFC supplied by a different fuel; meaning a PEFC subclass. Catalysts and sometime also the transported ion changes in these cells, but all are based on a polymer electrolyte.

Since about 2000, a lot of work has been dedicated to high-temperature PEFC (HT-PEFC) (Chandan et al., 2013; Zhang et al., 2006; Li et al., 2009). In reality, many of these are based on a porous polymer doped/impregnated with phosphoric acid. The ion conduction is related to phosphoric acid, not an inner property of the polymer, although some authors speculate about a kind of chemical link between the polymer and phosphoric acid. Also, in this case it is not a different class but a PAFC using a polymer matrix as separator and acid support, or a hybrid PA/PEFC, or finally a PEFC in which the polymer has intrinsic ion-conducting properties.

A completely new fuel cell technology requires a totally new working process or a different electrolyte, such as proposed by Staiti et al. (Giordano et al., 1996; Staiti et al., 1997; Giordano et al., 1997) with EtheroPolyAcid fuel cells. The development of this kind of fuel cell was actually stopped many years ago, due both to technological difficulties and a lack of interest from industry and the scientific community.

Since the mid-1990s there has been an increasing interest in biofuel cells (Higgins et al., 2011; Tayhas et al., 1994; Minteer et al., 2007a; Ivanov et al., 2010; Song et al., 2011; Allen and Benedetto, 1993). The name derives from the use of bioentities as catalysts: enzymes or bacteria. The electrolyte nature is less determinant for their characterization than in conventional fuel cells and batteries, while cathode and anode are often separated by the same polymeric membranes, that is selective for passage of ions, and electrons are transported through an external circuit. Like other fuel cells, biofuel cells need a fuel to produce power. But unlike conventional fuel cells, where metal catalysts are usually used for reactions at both electrodes, biofuel cells utilize enzyme-based catalysts; either they occur as isolated proteins or in microorganisms, at the least at the anode. Today, biofuel cells are classified in two main classes: enzymatic and microbial. In the enzymatic systems, a single enzyme or isolated proteine aggregates are used as catalyst. In microbial fuel cells (MFCs), living bacteria act at the electrodes, in electrolytic biofilm. It is expected that the development of the technology based on electro-active biofilm in electrochemical cells could lead to a new, energetically competitive, system to produce hydrogen (Ruiz et al., 2015; Sasakia et al., 2012; Villano et al., 2011).

An overview of the state of the art of these new fuel cell concepts and their potentialities is given in the following sections.

6.2   MFCs: Description, working principles, and components

MFC is a fuel cell technology operating at low temperature. In this fuel cell, hydrogen comes from an organic feedstock dissolved in the water that is the "fuel." At the anode, the catalyst consists in a bacterial biofilm growing on the electrode and providing the
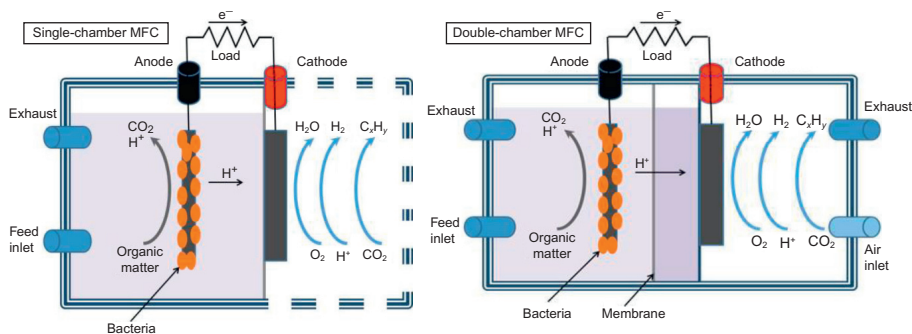
Figure 6.1 Basic working principles of microbial fuel cells in single-chamber (left) and double-chamber (right) configuration.

conversion of the chemical energy of organic matter directly into electrons and positive ions. The positive ions migrate to the cathode where they react with oxygen (Figure 6.1).

Different cell configurations and architectures are under investigation, each one having advantages and drawbacks. They are often divided into two different main types: single-chamber and double-chamber configurations. In a double-chamber configuration, the cathode and anode compartments are separated by an ion-conducting membrane or a salt bridge, and anolyte and catholyte solutions could be different; while in a single-chamber configuration the cathoic chamber is absent and the two electrodes are in contact with the same solution when the membrane is eliminated also.

This bioelectrochemical technology has a distinct advantage with respect to other fuel cell technologies as it can oxidize, without heavy pretreatments, marginal biomass dispersed in wastewater, combining in this way water treatment with electricity generation, with the help of microbes.

The exchange of knowledge between an increasing number of different specialists who are attracted to this amazing and transversal technology is responsible for its rapid development in the last few years, although the main experiments in progress are still at a basic level in the laboratory.

Several challenges remain and are currently the object of studies, including the fate of electrons between bacteria and conductive materials and the modeling of the whole process. As a matter of fact, tentative scaling-up is at a beginning level and the validation of MFC technology is still far off.

Last but not least, efforts to develop standards allowing the comparison of results obtained by different specialists and laboratories will have to be approached (Harnisch and Rabaey, 2012). A comparison with older and better-known fuel cell technologies and other energy technologies is the final challenge for this technology.

6.2.1   MFC: A multidisciplinary approach

As was true for other types of fuel cells, studies on MFC started around the 1960s but increased after the early studies carried out by Allen and Benedetto in the 1980s on the chemical mediators enhancing the electron transfer from microbes to anode substrate

in fuel cells (Allen and Benedetto, 1993). Because very little current was generated by the "microbial batteries," across a potential difference as low as a half volt, the industrial world did not pay much attention to the new biofuel cell approach in the beginning. Several studies concerning the effect of bioelectroactive biofilms on industrial materials were focused in the past on the prevention of microbial-induced corrosion (biocorrosion) that can strongly affect heat exchangers of fossil and nuclear power plants and other industrial cooling circuits (Cristiani, 2014a; Roberge, 1999; Dexter, 1986) and in biofilm sensors for soils more recently (Cristiani et al., 2008).

The development of biotechnology, the problems related to waste disposal, the pollution of waters and soils, and the focus on finding ways to produce renewable energy have completely changed the scenario. The possible use of bacterial biofilms in fuel cells to produce energy was reconsidered in the early 2000s, when it was demonstrated how some microbes are able to transfer electrons directly to the anode substrate (Chaudhuri and Lovley, 2003), opening the way to mediator-less microbial fuel cells.

Since 2000, a significant contribution to the MFC exploitation has been coming from Bruce Logan publications (Penn State University, US) and a few European groups (Liu and Logan, 2004; Rabaey and Verstraete, 2005; Logan et al., 2006; Aelterman et al., 2006), which triggered a crescent of worldwide interest in MFC. Experts in water purification concentrated all their efforts on the microbial oxidation of the organic substance at the bioanode, initially neglecting the possibility of using a similar approach to the cathodic half-reaction, for which they relied on expensive platinum, already used in conventional fuel cells (Liu and Logan, 2004; Cheng et al., 2006a,b; Fan et al., 2007; Cheng and Logan, 2011). In contrast, the corrosionists that initially centered their studies on the effect of microbial catalysis of oxygen and hydrogen reduction (Pope, 1987; Lee and Newman, 2003; Hamilton, 2003; Lewandowski et al., 1997), posed negligible attention to the anodic reactions other than those that involved the dissolution of metals. The bioanode and biocathode "approaches" meet a little later in 2008 (Erable et al., 2012; Dumas et al., 2008; Bergel et al., 2010). The challenge to create completely microbial electrochemical systems for technological purposes including the bioelectrochemical hydrogen production, and not only for the production of electricity, ranged on worldwide in the following years.

The number of research activities and publications in this area has exploded in recent years from less than 100 publications in 2001 to more than 5000 in 2014 (research on Scopus database at www.scopus.com), mostly driven with reactors of less than 1L-reactor volume and often using synthetic wastewater or well-defined substrates (Pant et al., 2010).

Tentatives of prototypal stacks and applications also started (Logan et al., 2006; Aelterman et al., 2006; Ieropoulos et al., 2012a; Rinaldi et al., 2008; Santoro et al., 2013a; Santoro et al., 2013b; Elmekawy et al., 2013; Erable et al., 2012; Oh and Logan, 2007; Shungui, 2009; Wang and Ren, 2013), opening the way also to a number of microbial bioelectrochemical systems (BESs) both for energy and chemical production (Wang and Ren, 2013; Harnisch and Rabaey, 2012; Zhou et al., 2013), although there are still a few studies that focus on system scaling-up.

The transition from basic research to the realization of large-scale devices requires deeper communication between specialists with different skills, including biology,

electrochemistry, physics, engineering, electronics, as well as systems modeling, design, and optimization. Sharing of preexisting know how might be most strategic than to develop new one to overcome the major issues and bottlenecks of the BESs. The multidisciplinary approach that was crucial to develop other kinds of fuel cells is even more relevant in the case of MFCs.

6.2.2   MFC working principles

A BES differs from an electrochemical system in that it uses biological molecules (enzymes, complexes and chains of enzymes, whole cells, bacteria, other microorganisms, etc.) for the catalysis of the half-reactions at the anode and/or at the cathode.

The natural prerogative of microorganisms to induce electrical phenomena through the reactions of oxidation-reduction enzymes can be exploited in various ways in BES: for the production of energy, chemical compounds, or to accelerate degradation processes of complex organic compounds and not very biodegradable (Harnisch and Rabaey, 2012).

In an MFC, bacteria grow on one or both electrodes, depending on the configuration, forming an electroactive biofilm. The electrochemical reactions from the fuel oxidation and the transfer of electrons from the anode compartment to the cathode until the final acceptor (usually oxygen) can be driven by the bacteria and biofilm. In the anode compartment, anaerobic or microaerophilic bacteria (Cristiani et al., 2013a; Rosenbaum et al., 2011) degrade organic substances in the absence of oxygen, producing, in extreme brief: carbon dioxide, hydrogen ions, and electrons (Figure 6.1). Oxygen, in charge of the electromotive force of the electrons flow, reduces at the cathode with the help of microbial or chemical catalyst layer.

Although still controversial and debated, several mechanisms for electron transfer to anodes, from cathodes, or both, have been proposed, subdivided mainly into four different types (Lovley, 2008): direct electron transfer (DET) via outer-surface enzymes (such as c-type cytochromes), long-range electron transfer via microbial "nanowires," electron flow through a conductive biofilm matrix, and soluble electron shuttles (mediators). The single mechanism seems prevalently adopted by the microorganisms depending on the bacteria consortium, the biofilm thickness, and the distance between bacteria and the conductive surface. It should be noted that the mechanisms found in bio-geo-chemical cycles of some key compounds that have characterized the development of life (oxygen, nitrogen, sulfur, manganese, etc.; Cypionka, 2000) play an important role in the BESs.

6.2.3   Bioanode

Microbial catalysis oxidation of organic compound, total or partial, can occur at the anode through several mechanisms, each one still controversial and debated, but that may operate alone or also in synergy. The main mechanisms actually studied can be resumed as following (Lovley, 2008):

1. enzymes electrocarriers (cytochromes) on the cell membrane or in the extracellular area in direct contact with the anode;

2. different extracellular mediators (enzymes) released into solution (as flavins and other enzymes fenazine reducing);
3. conductive biopolymers integrated in the cell membrane; and
4. microconductive pili (nanowire), secreted by bacteria, plugging to the electrode.

Anode bacteria are usually classified in either DET or mediated electron transfer (MET) classes. In the first class there are bacteria able to transfer the electrons directly to the anode electrode, such as *Aeromonas hydrophila* (Pham et al., 2003), *Geobacter metallireducens* (Min et al., 2005), *Rhodoferax ferrireducens* (Chaudhuri and Lovley, 2003), and *Shewanella putrefaciens* (Kim et al., 1999).

The MET class includes bacteria that need redox-active chemical species (mediators) to carry out indirect electron transfer, such as *Actinobacillus succinogenes* (Park and Zeikus, 2000; Park and Zeikus, 1999), *Alcaligenes faecalis* (Rabaey et al., 2004), *Enterococcus gallinarum* (Rabaey et al., 2004), *Proteus vulgaris* (Thurston et al., 1985), and *Shewanella oneidensis* (Ringeisen et al., 2006). The mediators could be produced by the same bacteria or by other bacteria of the consortium. In any case the bacteria need to contact the electrode in a way to transfer it to the electrons. Consequently, the anode electrode works both as charge collector and bacteria support. From this necessity the electrode's material must be biocompatible, good electron conductor, high surface, stable under electrochemical condition, and stable against bacterial corrosion. Usually carbon-based materials are chosen for their low cost, biocompatibility, and biochemical stability.

The simplest one is in the form of a pipe brush where two lengths of stainless steel wire are twisted together trapping short lengths of carbon fiber between them. In this case, the anode has a cylindrical shape, the bacteria growth is on the carbon fibers, and the electric current is extracted trough the stainless steel core. Other materials, like titanium, are also used as collector instead stainless steel. Figure 6.2 is a sketch of a typical single-chamber configuration largely used in the literature.

For increasing the available surface for unit volume, carbon grains or activated carbon powders can be used. In this case a porous bag is necessary for containing the powder or grains. The bag can have different shapes, so that we can have more versatility in defining the cell architecture. Moreover, as in PEFC, carbon grains or activated carbon powders in a micro porous layer (MPL) can be used for increasing the available surface of the electrode per unit volume (Santoro et al., 2011). Carbon grains or MPL of different structure produces different cell architectures.

For these approaches, the generated current can be extracted directly from the carbon tissues used for the bags or as support of the MPL layer or by inserting a network of electric wires inside the carbon grain (powder).

Finally, the electrode can be built by using a carbon cloth or a carbon paper sheet, materials already used as supports in PEFC.

It must be underlined that the variety of possible anode configurations, the different volumes used, and the practices of the batch configuration create difficulties in comparing results coming from different laboratories.
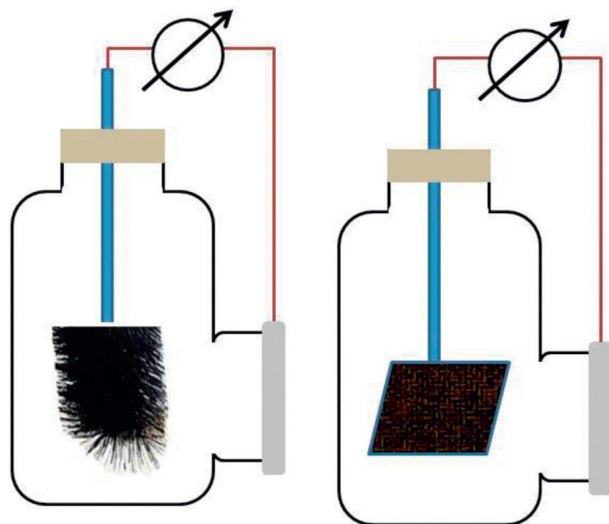
Figure 6.2 Typical MFC's single-chamber single-cell configuration for lab test. Usually the bottle has an internal volume in the range 50–500 cm^3, and the cathode active area range is 1–5 cm^2. The anode is placed in the center of the bottle, and usually has a "pipe cleaner" or a bag shape, and it is realized with carbon-based materials (like carbon fibers and carbon cloth). Conversely, the cathode has a planar configuration with disk shape, and usually the external side of the cathode is directly exposed to air. The bottle could have also two tubes for changing the anode solution or for tests in flowing conditions.

6.2.4 Cathode and biocathode

The cathode must be in contact with an oxygen supplier, usually air, on one side and with the electrolyte solution on the other side. This means that cathode structure must be porous, for allowing oxygen diffusion, and at the time impermeable to water, for avoiding electrolyte leakage.

The ORR can be catalyzed both with conventional electrocatalysts, such as platinum, or by bacteria.

There is a specific issue for Pt-loaded cathodes interacting with organic substances in membraneless MFCs, beside the cost (Santoro et al., 2012). The oxidation byproducts generated from the degradation of organic substances could cover the Pt catalyst on cathodes (Yang et al., 2009). This phenomenon substantially reduces the Pt efficiency (Postole and Auroux, 2011). Finally, Pt has high-catalyst capability at low pH (Erable et al., 2009). Neutral or alkaline conditions (typical of wastewater) decrease the Pt electrocatalytic activity (Seo et al., 2011).

Microbial catalysis of the oxygen reduction on biocathode may take place with similar mechanisms as on the bioanode and, especially, by external mediators secreted by a complex community of microorganisms that adapt their metabolism as a function

of external conditions and sources of available energy (Chung et al., 2011; Daghio et al., 2014). Among the bacteria species that already demonstrated DET, *Acidithiobacillus ferrooxidans* (Yarzabal et al., 2002), *Desulfovibrio vulgaris* (Kloeke et al., 1995; Jones and Garland, 1997), *Geobacter sulfurreducens* (Reguera et al., 2005; Cadena et al., 2007), and *S. putrefaciens* (Freguia et al., 2010) can be mentioned. While for MET, *Acinetobacter calcoaceticus* (Borole et al., 2009), *Clostridium beijerinckii* (Hatch and Finneran, 2008), *Pseudomonas* spp. (Venkataraman et al., 2010), and *S. oneidensis* (Marsili et al., 2008) are well representative.

The biocatalysis of the oxygen reduction to water on stainless steel was studied in lab-scale marine MFCs (Erable et al., 2010) and previously exploited in biofilm sensors for industrial cooling waters and soil (Cristiani et al., 2008) as well. From brackish water/sediments MFC tests (De Schamphelaire et al., 2010) the capability of carbon biocathodes to catalyze the oxygen-reduction reaction (Wei et al., 2011a) was also underlined. It was demonstrated that cathodic biofilms have the ability to transform inorganic cathodes into more active microbial catalyzed biocathodes also in MFCs fed with wastewater, thus avoiding the use of expensive Pt catalysts and reducing the MFCs costs (Santoro et al., 2012; Cristiani et al., 2013b). The power generation in MFCs with Pt-free cathodes approaches that of MFCs with Pt-loaded cathode when anaerobic conditions were established in the chamber. The electrochemical results showed how the performance of inorganic cathodes (with and without Pt catalyst) improves after biofilm growth. The increase of anodic overpotential due to the rise of pH in the tested MFCs was one of the factors limiting the power density during long-term operation.

A schematic of different mechanisms for anaerobic or microaerophilic biocathode is reported in Figure 6.3, where the global biocatalized reaction of acetate degradation to CO_2 and water is illustrated.

Understanding and optimizing the synergy of anaerobic bacterial metabolism on anodes/cathodes seems to be the fundamental solution to develop cost-effective MFCs for higher power generation.

6.2.5 MFC issues: Design and components

In designing the MFC cells the specific necessities of the biotic electrodes must be considered. From the literature the design of cells is classified as follows:

- MFC general configuration: single chamber, dual chamber (see Figure 6.1). These reference configurations could be evolved to roll-type and multichamber according to the necessity to reduce volume and increase efficiency.
- Reactor geometry: flat plate, tubular. Flat plate reactor could have either a polygonal or circular shape; in this case, anode and cathode are opposite one another in planar configuration. In tubular geometry the anode and cathode could be on the two opposite faces of the membrane or separator tube, or placed on the round surfaces of two concentric cylinders.
- The separator could be a membrane (anion or cation exchange), a salt bridge, or a mechanical separator hosting the culture media (membraneless reactors).
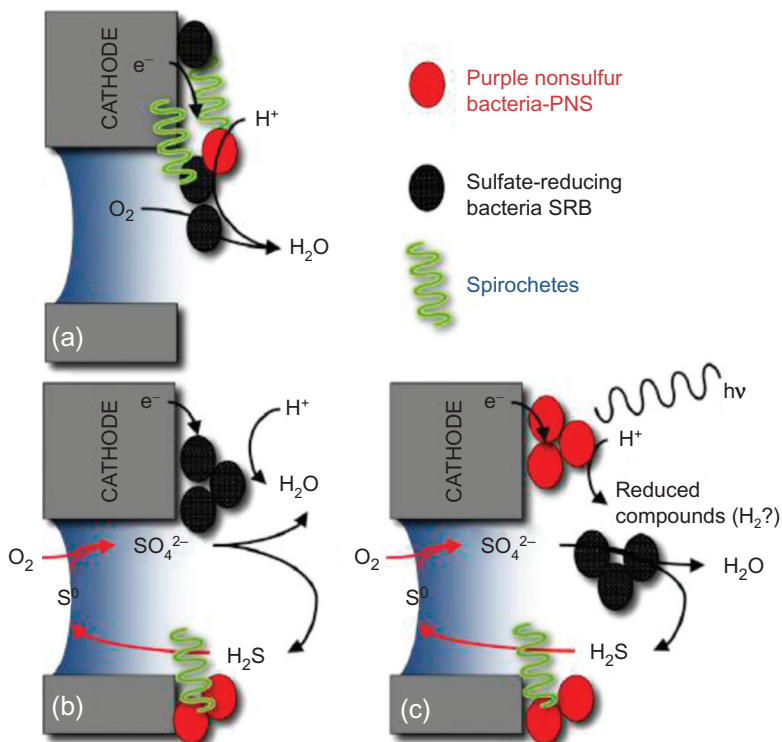
Figure 6.3 Schematic of three different ORR pathways (a, b, and c) each one involving the bacteria consortium forming the biocathode: (a) microaerobic metabolism; (b) anaerobic metabolism; (c) anaerobic plus phototropic metabolism (Cristiani et al., 2013a).

- Flow type could be batch or continuous flow. In batch operation the MFC is "recharged" periodically at suitable time intervals to supply food to microbes.
- Cathode type: conventional air cathode, biocathode, chemical cathode. Conventional air cathodes work like the gas diffusion cathodes of PEFC and use noble metals as catalyst. Biocathode do not use noble metals. The chemical cathode uses a chemical reduction-reaction that could also not involve the oxygen.

Combinations of different elements give different cell designs. A number of issues are in common with conventional electrochemical devices (batteries, supercapacitors, fuel cells) in designing a bioelectrochemical device. In practical applications, the following items have significant relevance to increase cell efficiency, power outputs, and reliability:

- Minimize internal resistance
- Low cost materials and manufacturing
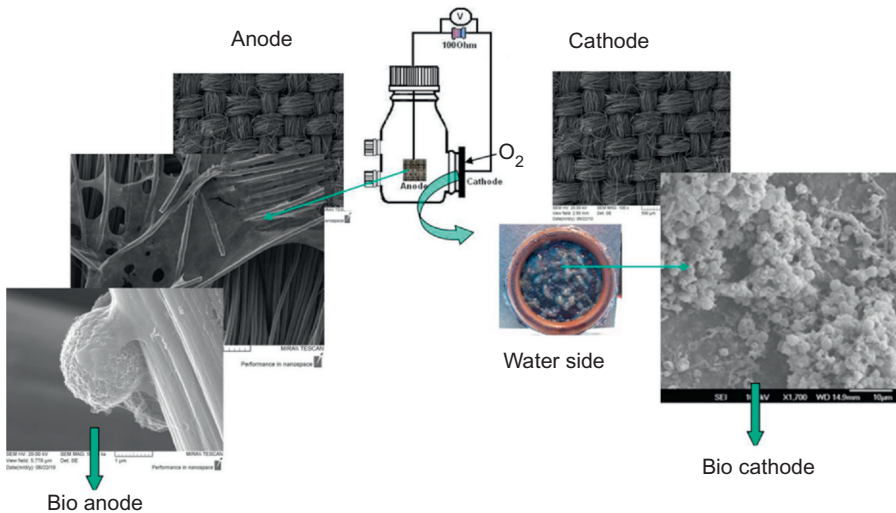- Maximize electrode activity (and surface)

Figure 6.4 Bacteria and biofilms making bioanode and biocathode in a single-chamber MFCs (partially modified from Cristiani, 2014b).

- Long endurance of components
- User friendly management
- Safety (both for user and environment)

The minimizing of internal resistance can be achieved by (1) reducing the distance between cathode and anode; (2) increasing electrolyte ion conduction and selectivity; (3) reducing contact resistance; and (4) optimizing electrode and current collectors' conductivity and design.

Electrode activity is improved by catalyst optimization/microbes consortia selection (where this applies); electrode composition and structure optimization; electrode–electrolyte matching optimization; and optimization of reactant supply (where this applies).

Different approaches might be used for each issue, and several experimental techniques are available for demonstrating the quality of the obtained results. Each research group defined its own protocol according to its experience and the previous literature, conducted by approaches similar but not totally overlapping, and often results coming from different authors are not easy to be compared each other. In spite of the increasing number of common tests used to characterize the performances of BESs, agreement on reference tests and fundamental data is still far from established both to compare results existing in the literature and to supply adequate information for new applications. This is an additional issue of this science sector.

Many MFC studies still use the components derived from low-temperature hydrogen fuel cell devices such as polymeric electrolyte membrane (PEM) and abiotic, chemically catalyzed cathodes, based on platinum-loaded materials (Feng et al., 2010). These

components are the most expensive parts of FCs and actually act as a bottleneck for developing large-scale MFC systems.

The study of very simple types of membraneless MFC, where both cathode and anode are directly exposed to the same microbial consortium, represent a promising way to overcome the existing bottleneck for the scale-up of technology. In these systems (Figure 6.2) the same bacteria play different roles, acting as (1) the catalysts at the anode, (2) the catalyst at the cathode, and (3) active components of the electrolyte that actually preserves the anaerobiosis at the anode, consuming oxygen.

The biofilm, consisting of 80% or more of water, is in fact a good electrolytic conductor. It is also capable of consuming entirely the oxygen that diffuses from the outside through the pores of the porous cathode electrode (Ieropoulos et al., 2013; Santoro et al., 2012), blocking the path to the anode. Moreover, the metabolism aerobic/anaerobic can be appropriately modulated in the biofilm, as a function of the environmental conditions.

Several studies have greatly explored the range of electroactive microorganisms able to catalyze the anodic or the cathodic process in a fuel cell, demonstrating the wide variety of bacteria potentially involved, although the single species can return different feedback to polarization (Zhou et al., 2013). These studies underline how consortia of microorganisms act synergistically, better that a single species, although innovative genetic studies promise to develop new and artificial microorganisms suitably designed to boost their electrical performances in the near future (Biffinger et al., 2009; Rosenbaum and Angenent, 2010).

A large number of studies devoted to the investigation and engineering of single components of MFC exist; for example, on electrode materials (Cheng and Logan, 2011) or ion exchange membranes (Harnisch et al., 2008).

Advances in configurations and operations of BESs for wastewater treatment, bioenergy, and bioproducts have been reviewed by a number of publications.

Several comprehensive reviews of MFC mechanisms and reactor configurations are available in the literature (Zhou et al., 2013; Du et al., 2007). They include MFCs electrodes geometries (Wei et al., 2011b), materials used to partition anodic and cathodic chambers such as various membrane and salt bridges (Patil et al., 2010), substrates (Pant et al., 2010; Huang and Angelidaki, 2008; Huang et al., 2008) including artificial media and various wastewater, and microsized MFCs (Puig et al., 2010; Qian et al., 2009, 2011).

It must be underlined that up to now, in front of these efforts and variety of approaches the reported power densities are really low, if compared with other fuel cells or conventional electrochemical devices. Typical power densities are on the order of 1–3 W/m^2, with the higher outputs obtained by using simulated feedstocks, like acetate buffer culture media. Power densities on the order of tens of W/m^2 have been also reported (Oliveira et al., 2013; Logan, 2012).

This low power is due not only to early stage development, but also to some intrinsic limits of MFC related to

- limited ion conductivity of the culture media (that acts also as electrolyte at least in the anode chamber);

- bacteria will use a part of the fuel energy to live and to reproduce themselves; and
- mediators, self-produced or added, may have a significant mass that limits their diffusion.

On these bases the logical conclusion is that the power production don't represent the strength of this kind of fuel cell. The main advantage of MFCs is their capability to produce energy from wastewater. Wastewater treatment is a strong energy-consuming process; MFC provides the possibility to reduce considerably this energy consumption. So, wastewater may be is an ideal fuel of MFC, although in this moment many developers work with artificial feedstocks. This situation complicates the development of MFC, because wastewater composition differs from site to site. It can be foreseen that the first applications will be developed for special cases in the food industry. In these cases, in fact, the composition of processed wastewater is more controllable and constant.

6.2.6   MFC issues: Operation

MFC can operate in both batch and flow configuration. In flow configuration the substrate is continuously supplied to the media in the cell, while in batch configuration the culture media is static and the media must be periodically replaced or enriched to assure the bacteria's survival. For this reason, an appropriated refilling approach must be defined for maintaining anaerobic conditions at the anode.

A large part of the experimental results reported in the literature for MFCs is in batch operation, using the cell configuration reported in Figure 6.2. Moreover, batch cells used in different laboratories have different sizes and shapes. This situation creates some difficulties in data comparison and in developing scale-up approaches.

Flowing conditions appear more attractive because this can assure a stable output, can allow for a more simple management of large volumes of culture media, and its volume is related only to its design and electrodes characteristic, not to the storage of a suitable reactant reservoir close to electrodes as in batch configuration. This last characteristic could allow higher volumetric power densities.

Finally, in flow configuration it's easier to maintain stable some operative parameters that have great influence on MFC performances.

Examples of operational parameters that have been studied are the effects of pH (Puig et al., 2010; Patil et al., 2011; Guerrini et al., 2013) or temperature (Patil et al., 2010) on current generation, and of substrate loading on Coulombic efficiency (Sleutels et al., 2011).

Operative parameters, such as temperature, pH, and redox potential of solution, influence strictly the single electrochemical responses of anodes or cathodes, being crucial for getting the global reaction under anodic or cathodic kinetic control (Puig et al., 2010; Patil et al., 2010; Guerrini et al., 2013).

A pH decrease in MFCs during the first days of MFC operation can be due to the process of fermentation, whose final result is the production of an anaerobic environment inside the MFC. As the solution gets anaerobic, MFCs start to produce electricity, and colonization of electrodes takes place.

Prefermentation of the wastewater speeds power production by making the environment completely anaerobic. Experimental evidence demonstrated that the MFC, even if equipped with an open-air cathode, is populated by anaerobic bacteria that use sulfur in their life cycle (Cristiani et al., 2013a; Rosenbaum et al., 2011). Microanalyses by RX microprobe EDX demonstrated the presence of sulfur in the cathodic electrode and the precipitation of carbonates on its wet surface (Santoro et al., 2012). The carbonate precipitation, due to the alkalinity produced at the cathode, causes pore clogging. The CO_2 produced at the anode may mitigate the increasing of pH in the MFC and the carbonate precipitation (Guerrini et al., 2013), and the pore clogging by carbonates deposits seems the main cause of the decay of performance of the MFCs observed in time.

Nevertheless, other concomitant and contrasting mechanisms must be involved in pH determination in MFCs (Guerrini et al., 2013). If the reactions in Equations (6.1) and (6.2) are predominant in the MFC, a gradual accumulation of hydroxyls should accompany acetate oxidation and oxygen reduction.

$$2O_2 + 8e^- + 8H^+ \rightarrow 4H_2O \tag{6.1}$$

$$CH_3COO^- + 2H_2O \rightarrow 2CO_2 + 8e^- + 7H^+ \tag{6.2}$$

As a result, pH should gradually increase with time, becoming more alkaline as more acetate is removed. Thus, MFCs with higher voltages (at equal CE) would cause a bigger increase in pH.

Scaling-up BES from the lab-scale to pilot and even larger scales require a relevant study of operating parameters. The optimization of them will play an important role for the stabilization of MFC electrical performance, in particular. In fact, the actual electrical output of lab systems is usually nonconstant in time (Feng et al., 2010; Martinucci et al., 2015).

The base assumption for comparing different systems may be that the system under evaluation is in a dynamic steady state in which the microbial community is adapted to the incoming substrate and that microbial growth/death rates hold the balance so that the maximum amount of substrate is being utilized (Cristiani et al., 2013; Mudrack and Kunst, 1986). In this case a linearly increasing chemical oxygen demand (COD) loading rate should result in a linearly increasing COD removal rate and at a constant removal efficiency. Therefore, due to anodic respiration (Lovley, 2006) in a BES, this should ideally correlate to linearly increasing current density at a constant Coulomb efficiency. In the case of other parameters, such as nitrogen removal, the elimination paths are different but the final results can still be compared to one another (Brown et al., 2014).

6.3   Application in field and perspectives

The BESs, find a natural, non-exclusive, application in industrial biotechnological plant, like wastewater plants, as they could potentially contribute in various ways to the optimization of purification processes, in addition to the energy needs of the plant.

A requirements of a wastewater treatment plant are removing organics and some specific pollutants, such as phosphor (in the form of phosphate) and nitrogen compounds (ammonium and nitrate in particular), from the influent, and lowering the pollutants concentration under the threshold fixed by the discharge regulations (Brown et al., 2014). The treatment efficiency (in terms of pollution and COD removal) must be maintained for a wide range of loading rates and therefore MFCs, eventually integrated with other BESs, must achieve comparable treatment efficiency as the primary requirement for their potential application in wastewater treatment lines. The recovery and utilization of resources such as phosphorous and nitrogen is becoming an increasingly important economic factor in the wastewater treatment sector, other than for the development of BES for wastewater treatment (Elmekawy et al., 2013; Kelly and He, 2014). For this reason, studies with human urine and other common components of civil wastewater have been carried out, and the ability to break down the water pollutants, such as phosphorus and nitrogen compounds, has been verified and documented (Ieropoulos et al., 2013a,b; Santoro et al., 2014).

One in-field test is in progress at the treatment plant Nosedo in Milan, Italy, one of the largest and most modern in Europe. A power of 600 kW may be sufficient to cover the energy demand of this wastewater plant. Water purification requires energy, especially to ensure the supply of oxygen in a uniform manner inside the tanks where the treatment of aerobic degradation is carried out. Being able to repeat in the plant the MFC's performance obtained in the laboratory (greater than 30% CE) at the total amount of the water bulk, the power generated may be, in principle, sufficient to cover the energy demand of the wastewater plant.

It has to be underlined that the same bacteria in the inoculum of the wastewater treatment plant, as well as the strains used for the anaerobic fermentation in biogas plants operate in the different BESs.

Exploitation of the mechanisms of bioelectrolysis applied to more complex matrices, solids, such as sewage sludge, agro-food, lignocellulosic, and other benefits are expected in terms of products, including second-generation biofuels and new systems of biosanitation (Rabaey and Rozendal, 2010).

Being able to contribute both to the solution of the energy problem and the disposal of waste, MFC has attracted the attention of specialists in very different fields. Although still at the frontier, this research is predicted to result in amazing innovation in the medium term, although it may seem to be just an enjoyable learning experience at present. One example of the future is the case of robot prototypes powered with waste designed at the University of Bristol, where I. Jeropoulos and his team of the Laboratory of Robotics has already successfully experimented with the use of microbial fuel cells to capture insects, such as mosquitoes, and to power a phone with human urine (Ieropoulos et al., 2012b, 2013a,b).

Concerning plant applications, the floating system in experimentation at Nosedo wastewater plant (Italy) demonstrates the possibility to apply the technology at low-level COD, inferior to 50 mg/L (Cristiani, 2014b).

The power produced in the laboratory with the microbial system tested is of the order of 1 W per cubic meter of wastewater, still far from the value of 1 kW/m^3 suggested in 2008 by the pioneers of the technology and, in fact, has not yet been reached in any laboratory even under ideal conditions. In the controlled conditions of the experiment carried out at

the laboratory level, in addition to providing a substrate very easy to digest, such as acetate, the solution can be made very conductive by the addition of phosphate, controlling in this way also the pH. The cells are also usually made of very small size (a few centimeters), although the productivity is then arbitrarily normalized to the meter, on a scale that refers to the geometric surface of the electrode or to the volume of the solution containing the wastewater to be treated. Because of these and other concerns, even before their use in power plants, BESs will be applied for the treatment of pollutants and for the electrosynthesis of valuable chemical new products from wastes (Rabaey et al., 2010).

6.4   Enzyme fuel cells: Description, working principles, and components

Like conventional fuel cells, enzyme fuel cells (EFCs) can burn pure hydrogen (Krishnan and Armstrong, 2012). Like MFCs, they are bioelectrochemical devices able to directly convert organic substance (currently glucose and alcohols) into energy. The main difference in respect to MFCs is linked to the use of pure enzyme as catalysts at the anode and, in large part of cases, also at the cathode. EFCs received increasing attention between 2000 and 2009, supported by a high number of publications about the use of enzymes as catalysts for a great number of electrochemical devices, including processes for hydrogen production from organics (Willner et al., 2009; Minteer et al., 2007b; Osman et al., 2011; Barton et al., 2004; Woodward et al., 2002). The attention to EFCs recently moved mostly to other fields of chemistry. Enzymes are not low-cost catalysts, although they could offer significant cost advantages over traditional precious-metal catalysts through economies of scale. The main advantage is their high selectivity, which is balanced by the necessity to have very stable operating conditions and environment inside the cell. These characteristics and their biocompatibility created great expectations for EFCs as a micropower supplier for implanted medical devices (Barton et al., 2004; Woodward et al., 2002; Kerzenmacher et al., 2008). The main drawback is related to enzyme stability and survival, which usually is only a few days.

6.4.1   EFC working principles

EFCs, like MFCs, are biofuel cells, but in this case enzymes attached to the electrodes are directly used for catalyzing the oxidant-reductive reaction. The electricity production is related to enzyme action also in MFC, but the enzyme concentration produced by bacteria is limited and their activity is controlled by their metabolism. Extracting enzymes from biomass and using them more concentrated in EFC seems a good way to increase the power output in a more controlled way than for MFC. This is because the use of pure enzymes will avoid the necessity to maintain the bacteria living on the electrode, improving the diffusion path for the reactants and products also. The enzymes that are largely used in EFC are oxidoreductase, responsible for reactions involving electron transfer. This class of enzyme includes a number of subclasses defined by the type of the substrate they act on and by the reaction mechanism. Typical

enzymes used at cathode in the development of EFCs systems are the bilirubine oxidase (Habrioux et al., 2010; Salaj-Kosla, 2012; Lopez et al., 2014) and the group of laccase (Brunela et al., 2007; Scodeller et al., 2010; Gutiérrez-Sánchez et al., 2012) and at anode the glucose oxidase (Ivnitski et al., 2006; Barriere et al., 2006), or other sugar-based enzymes like fructose (Kamitata et al., 2007).

Apparently, the EFC seems to be a system closer to the conventional low-temperature fuel cell, where the anode catalyst is substituted with an enzyme. Actually, the schemes and the geometries normally used differ from these reported in Figure 6.2 for MFC. Furthermore, the electrode surfaces have a more complex structure than for MFCs, as enzymes are usually entrapped on the electrodes in a conductive and complicated matrix. There are several and particular kinds of EFC configurations with membranes (Mano et al., 2003) and membraneless ones (Santoro et al., 2013c). In general, the EFC process is more critical than MFC and it has main limits in the enzyme properties summarized below:

- Enzymes have a limited life: during cellular life the enzyme are replaced continuously;
- Enzymes are selective: they work just on specific substrates and in well-defined conditions, and usually control a well-defined reaction step;
- Enzymes are active in a limited range of operative conditions, like temperature and pH.

Enzyme endurance and stability of a biological cell is one of the main issues, with reported stabilities usually ranging from few hours to a few days (Osman et al., 2011). This is not the case in MFC because the bacteria replace the enzyme before their deactivation. However, the reported power densities for EFC, usually in the range of 0.1–1.1 mW/cm^2, are an order of magnitude larger than MFC ones.

Enzyme selectivity is another big issue for two reasons: a number of enzymes working in sequence are necessary for the multistep oxidation of organic fuels and enzymes need mediators for electron transfer/product release (Kerzenmacher et al., 2008; Sokic-Lazic et al., 2010; Kar et al., 2011; Bathnagar et al., 2011; Cao, 2005). This creates the necessity of an accurate design of the EFC, supported by an appropriate modeling, and the obligation to maintain deep control of the fuel solution composition.

Changes in operating conditions, when enzyme operates out of bio cellules, are not mediated by the cellular environment. This also means that a small shock in temperature or pH changes can deactivate or destroy the enzymes. This aspect could be an advantage for specific applications; for example, in biomedical applications where EFC might be self-activated under specific conditions or in biosensors, which can be built with the same enzymes used for BES (i.e., in Kanga et al., 2009; Grattieri et al., 2015).

6.4.2   Enzyme and mediator immobilization

Immobilization of the enzyme is used to increase stability and operating life; immobilizing both enzyme and mediator is also possible to reduce the charge transfer losses. Within the immobilization techniques, the entrapping and the encapsulation of the enzyme in a defined matrix gives relevant advantages that need to be mentioned: (1) isolation of the enzyme from specific poisoning elements, (2) increased selectivity,

(3) improved mass transfer, and (4) increased long-term stability of the enzyme. Moreover, the separation of the enzyme from the mixture containing the substrate allows for more modular cell designs (Cao, 2005; Cooney et al., 2008).

Drawbacks include that it can affect the stability and/or activity of the enzyme, it can introduce additional mass-transfer limitations on the substrate, and it involves additional costs.

The stability of the immobilized enzyme will depend on the nature and strength of the bonds to the support material, the treatment required for immobilization, the degree of confinement, and the enzyme reaction working conditions. Enzyme denaturation and loss of structural freedom (necessary for their activity) must be carefully avoided. Just as with other kinds of FCs, the conclusion is that an accurate construction of the three-dimensional structure of the electrode is fundamental to achieve the best performance and endurance, and both material and methods must be accurately evaluated (Cao, 2005; Cooney et al., 2008).

Physical surface adsorption with diffusional mediators, or mediators coadsorbed with an enzyme, is the most common immobilization technique.

In this case, enzymes can be adsorbed, for example, onto conductive particles such as low-cost carbon black or graphite powder or nanostructured carbons and the method is relatively simple, cost-effective, and well known to the FC industry. Moreover, conductivity of support and its porosity is usually sufficient to grant adequate ion, electron, and reactant/product transport. In this case, the binding forces are primarily electrostatic, and then the characteristic of the support in respect to the enzyme ones play an important role: if interaction is too weak, enzymes can desorb during operation with progressive loss of performances; if they are too strong, enzyme denaturation (i.e., irreversible catalyst deactivation) can occur.

Other immobilization techniques are the entrapment in conducting polymer matrices or gels; wiring or covalent attachment to functionalized polymers; and enzyme cross-linking.

The entrapment of the enzyme within a polymer matrix, a sol–gel, a redox hydrogel, or behind a semipermeable membrane were also proposed (Sheldon, 2007; Kandimalla et al., 2006). The structure of the hosting matrix must grant an adequate degree of enzyme movement, without allowing any leaching of the enzyme and/or mediator. Also, this technique could be considered relatively simple and easy to be scaled-up. Care to both ion and electron release and transmission also must be taken into account, especially for this technique and the following ones. Enzyme covalently bonding to supports (like porous glass, cellulose, ceramics, and metallic oxides) is a more complex process that links the enzyme to the support by the enzyme's functional groups not essential for the catalytic activity.

Cross-linking is a technique largely used in polymer science, in this case consisting of joining enzymes to form three-dimensional aggregates via covalent bonding between some of their active groups. Usually the obtained structures exhibit low mechanical stability and the loss of a significant part of the catalytic activity (Sheldon, 2007).

Continuous efforts and improvements have been made in the last 10 years on each of these techniques, both in evolving new materials and optimizing the procedures, but more research is needed for obtaining suitable long-term stability and effectiveness.

6.4.3   Fuel

Usually EFCs are fueled with one kind of saccharide (e.g., glucose, lactose, fructose) or alcohols, mainly ethanol. More recently, other fuels have been considered, such as glycerol due to its high energy density and availability as a by-product of biodiesel production or aminoacids (Sokic-Lazic et al., 2010). But a single enzyme, due to its selectivity, is not able to catalyze all the steps necessaries for the complete conversion of these chemicals into CO_2 and water. This creates the necessity to use more enzymes acting in cascade to avoid both partial operative voltages and intermediate chemicals in cell effluent. Although this has been known since the early stages of EFC history, working success of enzyme cascade systems was first reported starting from about 2005. This approach allowed, in a few years, the achievement of power densities over $1mW/cm^2$ by totally burning glycerol and alcohols (Osman et al., 2011; Sokic-Lazic et al., 2010). However, enzyme cascade base anodes results were more complicated to produce and also less tolerant to operating conditions variation such as, for example, fuel concentrations.

In addition to enzyme/electrode preparation methods development, optimization of the buffer type and concentration, redox polymer composition, and binder-to-enzyme ratios have been the object of a number of studies aimed at increasing power densities and endurance, but most of the proposed solutions were specific to the setup used and cannot easily be used for other configurations (Zebda et al., 2011; Sakai et al., 2009; Togo et al., 2008; Nazaruk et al., 2010; Mano et al., 2005; Kontani et al., 2009).

6.4.4   EFC issues: Design and components

Concerning design and components for EFC, the first question is which application?

EFCs have approached power densities close to $1mW/cm^2$ that are acceptable for portable electronic applications, especially for biomedical applications if linked to high-energy density fuels such as ethanol and glycerol or to locally available bioresources (Barton et al., 2004; Sokic-Lazic et al., 2010). This must be associated with the developments in overall system design. Like in MFCs, by removing the separator membrane (Stoica et al., 2009; Korani et al., 2015), the realization of single-chamber air-breathing systems could improve design simplicity and effectiveness without significant loss in power output. Cells with chemistries that allow single-compartment operation and possess constructional simplicity would be highly advantageous for practical engineering applications. As for other FCs, the development of low-cost, modular, and scalable designs is very important (Sakai et al., 2009). The rapid progress in PEFC MEA/stack performance over the past 25 years could give important indications: the integration of modeling and experimental studies allowed the development of engineering protocols able to maximize the power output and durability and to reduce the cost. For many proposed EFCs' applications, in fact, further substantial improvements in performance are required both in terms of power densities and energy efficiencies.

Electrode architectures, materials, and design need to be improved for maximizing the enzyme catalytic activity and minimizing deactivation. Efforts to develop new methods

and materials for integrated enzyme electrodes that maximize enzyme loading could receive significant support by modeling. Also, the use of nanostructures shows great promise, but as is the case for other kinds of FCs, for application purposes the materials must be safe and cost-effective, and the fabrication techniques must be practical.

It is also important to study time-dependent performance over practical periods, also considering the replacement of perishable components where necessary. These efforts must be supported by a better understanding of the reaction environment and the development of models to be used in conjunction with laboratory studies to accelerate the development of practical systems.

6.5   Future trends and expectations

Both for MFC and EFC a forecast about their market force and possible large-scale application is quite unpredictable. The two technologies are still in early stages of development compared to the other FC technologies.

In the last two centuries humanity enjoyed the availability of low-cost energy as a simple fact of life. Now, a large natural reservoir of new technologies for a better life are being created, but we have often disregarded the downside of all this. The increasing request for energy and the growing human population have created environmental and energy availability problems that need to be solved. Energy availability and the security of the energy supply are now top questions of international politics and, more recently, so is accessing clean water for sanitation purposes, mainly for drinking water. A few of the barriers to address for the 2.5 billion people in the world who don't have access to safe sanitation facilities include the expense of wastewater infrastructure and the pollution of water in many regions where the electric grid is not available. Both MFC and EFC could contribute to solving the water problem for those countries, depurating and sanitizing water, at low cost and high efficiency, in principle.

References

Aelterman, P., Rabaey, K., Pham, H.T., Boon, N., Verstraete, W., 2006. Continuous electricity generation at high voltages and currents using stacked microbial fuel cells. Eviron. Sci. Technol. 40, 3388–3394.

Allen, R.M., Benedetto, H.P., 1993. Microbial fuel-cells electricity production from carbohydrates. Appl. Biochem. Biotechnol. 34/40, 27–40.

Bahrami, H., Faghri, A., 2013. Review and advances of direct methanol fuel cells: part II: modeling and numerical simulation. J. Power Sources 226, 303–320.

Barriere, F., Kavanagh, P., Leech, D., 2006. A laccase–glucose oxidase biofuel cell prototype operating in a physiological buffer. Electrochim. Acta 51, 5187–5192.

Barton, S.C., Gallaway, J., Atanassov, P., 2004. Enzymatic biofuel cells for implantable and microscale devices. Chem. Rev. 104, 4867–4886.

Bathnagar, D., Xu, S., Fischer, C., Arechederra, R.L., Minteer, S.D., 2011. Mitochondrial biofuel cells: expanding fuel diversity to amino acids. Phys. Chem. Chem. Phys. 13, 86–92.

Bergel, A., Feron, D., Flemming, H.C., 2010. From fundamentals to microbial power plants: electrochemically active biofilms. Bioelectrochemistry 78, 1.

Biffinger, J., Ribbens, M., Ringeisen, B., Pietron, J., Finkel, S., Nealson, K.H., 2009. Characterization of electrochemically active bacteria utilizing a high-throughput voltage-based screening assay. Biotechnol. Bioeng. 102, 436–444.

Borole, A.P., Hamilton, C.Y., Vishnivetskaya, T., Leak, D., Andras, C., 2009. Improving power production in acetate-fed microbial fuel cells via enrichment of exoelectrogenic organisms in flow-through systems. Biochem. Eng. J. 48, 71–80.

Bretta, D.J.L., Atkinson, A., Cumming, D., Ramírez-Cabrera, E., Rudkin, R., Brandona, N.P., 2005. Methanol as a direct fuel in intermediate temperature (500–600 °C) solid oxide fuel cells with copper based anodes. Chem. Eng. Sci. 60, 5649–5662.

Brown, R.K., Harnisch, F., Wirth, S., Wahlandt, H., Dockhorn, T., Dichtl, N., Schröder, U., 2014. Evaluating the effects of scaling up on the performance of bioelectrochemical systems using a technical scale microbial electrolysis cell. Bioresour. Technol. 163, 206–213.

Brunela, L., Denele, J., Servat, K., Kokoh, K.B., Jolivalt, C., Innocent, C., Cretin, M., Rolland, M., Tingry, S., 2007. Oxygen transport through laccase biocathodes for a membrane-less glucose/O_2 biofuel cell. Electrochem. Commun. 9 (2), 331–336.

Cadena, A., Texier, A.C., Gonzalez, I., Cervantes, F.J., Gomez, J., 2007. Qualitative and quantitative determination of a humic model compound in microbial cultures by cyclic voltammetry. Environ. Technol. 28, 1035–1044.

Cao, L., 2005. Immobilised enzymes: science or art? Curr. Opin. Chem. Biol. 9, 217–226.

Chandan, A., Hattenberger, M., El-kharouf, A., Du, S., Dhir, A., Self, V., Pollet, B.G., Ingrama, A., Bujalski, W., 2013. High temperature (HT) polymer electrolyte membrane fuel cells (PEMFC)—a review. J. Power Sources 231, 264–278.

Chauduri, S.K., Lovley, D.R., 2003. Electricity generation by direct oxidation of glucose in mediator less microbial fuel cells. Nat. Biotechnol. 21, 1229–1232.

Cheng, S., Logan, B.E., 2011. Increasing power generation for scaling up single-chamber air cathode microbial fuel cells. Bioresour. Technol. 102, 4468–4473.

Cheng, S., Liu, H., Logan, B.E., 2006a. Power densities using different cathode catalysts (Pt and CoTMPP) and polymer binders (nafion and PTFE) in single chamber microbial fuel cells. Environ. Sci. Technol. 40, 364–369.

Cheng, S., Liu, H., Logan, B.E., 2006b. Increased performance of single chamber microbial fuel cells using an improved cathode structure. Electrochem. Commun. 8, 489–494.

Chung, K., Fujiki, I., Okabe, S., 2011. Effect of formation of biofilms and chemical scale on the cathode electrode on the performance of a continuous two-chamber microbial fuel cell. Bioresour. Technol. 102, 355–360.

Cimenti, M., Hill, J.M., 2009. Direct utilization of liquid fuels in SOFC for portable applications: challenges for the selection of alternative anodes. Energies 2, 377–410.

Cooney, M.J., Svoboda, V., Lau, C., Martina, G., Minteer, S.D., 2008. Enzyme catalysed biofuel cells. Energy Environ. Sci. 1, 320–337.

Cristiani, P., 2014a. Risk assessment of biocorrosion in condensers, pipework and other cooling system components". In: Liengen, T., Féron, D., Basseguy, R., Beech, I. (Eds.), European Federation of Corrosion (EFC) Series (#66). Woodhead Publishing, pp. 357–384, Chapter: 15.

Cristiani, P., 2014b. Elettricità dai batteri. Le Scienze (Italian edition of Scientific American), May 2014, page 54.

Cristiani, P., Franzetti, A., Bestetti, G., 2008. Monitoring of electro-active biofilm in soil. Electrochim. Acta 54 (1), 41–44.

Cristiani, P., Franzetti, A., Gandolfi, I., Guerrini, E., Bestetti, G., 2013a. Bacterial DGGE fingerprints of biofilms on electrodes of membraneless microbial fuel cells. Biodeter. Biodegr. J. 84, 211–219.

Cristiani, P., Carvalho, M.L., Guerrini, E., Daghio, M., Santoro, C., Li, B., 2013b. Cathodic and anodic biofilms in single chamber microbial fuel cells. Bioelectrochemistry 92, 6–13.

Cypionka, H., 2000. Oxygen respiration by Desulfovibrio species. Annu. Rev. Microbiol. 54, 827e–848e.

Daghio, M., Gandolfi, I., Bestetti, G., Franzetti, A., Guerini, E., Cristiani, P., 2014. Anodic and cathodic microbial communities in single chamber microbial fuel cells. New Biotechenol. 32, 79–84.

De Schamphelaire, L., Boeckx, P., Verstraete, W., 2010. Evaluation of biocathodes in freshwater and brackish sediment microbial fuel cells. Appl. Microbiol. Biotechnol. 87, 1675–1687.

Dexter, S.C. (Ed.), 1986. Biologically Induced Corrosion. NACE-8, Houston.

Du, Z., Li, H., Gu, T., 2007. A state of the art review on microbial fuel cells: a promising technology for wastewater treatment and bioenergy. Biotechnol. Adv. 25, 464–482.

Dudzik, J., Chang, W.C., Kannan, A.M., Filipek, S., Viswanathan, S., Li, P., Renugopalakrishnan, V., Audette, G.F., 2013. Cross-linked glucose oxidase clusters for biofuel cell anode catalysts. Biofabrication 5 (3), 035009.

Dumas, C., Basseguy, R., Bergel, A., 2008. Microbial electrocatalysis with Geobacter sulfurreducens biofilm on stainless steel cathodes. Electrochim. Acta 53, 2494–2500.

Elmekawy, A., Hegab, H.M., Dominguez-Benetton, X., Pant, D., 2013. Internal resistance of microfluidic microbial fuel cell: challenges and potential opportunities. Bioresour. Technol. 142, 672–682.

Technology characterization: fuel cells, prepared for Environmental Protection Agency, Combined Heat and Power Partnership Program; by Energy and Environmental Analysis, Dec. 2008; http://www.epa.gov/chp/documents/catalog_chptech_fuel_cells.pdf.

Erable, B., Etcheverry, L., Bergel, A., 2009. Increased power from a two-chamber microbial fuel cell with a low-pH air-cathode compartment. Electrochem. Commun. 11, 619–622.

Erable, B., Vandecandelaere, I., Faimali, M., Delia, M.-L., Etcheverry, L., Vandamme, P., Bergel, A., 2010. Marine aerobic biofilm as biocathode catalyst. Bioelectrochemistry 78, 51–56.

Erable, B., Feron, D., Bergel, A., 2012. Microbial catalysis of the oxygen reduction reaction for microbial fuel cells: a review. ChemSusChem 5, 962–967.

Fan, Y., Hu, H., Liu, H., 2007. Enhanced Coulombic efficiency and power density of air-cathodemicrobial fuel cells with an improved cell configuration. J. Power Sources 171, 348–354.

Feng, Y., Lee, H., Wang, X., Liu, Y., He, W., 2010. Long-term cathode performance and the microbial communities that develop in microbial fuel cells fed different fermentation end products. Bioresour. Technol. 102, 361–366.

Freguia, S., Tsujimura, S., Kano, K., 2010. Electron transfer pathways in microbial oxygen biocathodes. Electrochim. Acta 55, 813–818.

Fuel cells for ship, 2012. Research and Innovation, Position Paper 13–2012, published by Det Norske Veritas (Norway).

Giddey, S., Badwal, S.P.S., Kulkarni, A., Munnings, C., 2012. A comprehensive review of direct carbon fuel cell technology. Prog. Energy Comb. Sci. 38, 360–399.

Giordano, N., Staiti, P., Hocevar, S., Aricò, A.S., 1996. High performance fuel cell based on phosphotungstic acid as proton conducting electrolyte. Electrochim. Acta 41, 397–403.

Giordano, N., Staiti, P., Aricò, A.S., Passalacqua, E., Abate, L., Hocevar, S., 1997. Analysis of the chemical cross-over in a phosphotungstic acid electrolyte based fuel cell. Electrochim. Acta 42, 1645–1652.

Guerrini, E., Cristiani, P., Trasatti, S.P., 2013. Relation of anodic and cathodic performance to pH variations in membraneless microbial fuel cells. Int. J. Hydrog. Energy 38, 345–353.

Gutiérrez-Sánchez, C.M., Pita, C., Vaz-Domínguez, S., Shleev, A.L., De Lacey, J., 2012. Gold nanoparticles as electronic bridges for laccase-based biocathodes. Am. Chem. Soc. 134 (41), 17212–17220.

Hamilton, W.A., 2003. Microbially influenced corrosion as a model system for the study of metal microbe interactions: a unifying electron transfer hypothesis. Biofouling 19, 65–76.

Harnisch, F., Rabaey, K., 2012. The diversity of techniques to study electrochemically active biofilms highlights the need for standardization. ChemSusChem 5, 1027–1038.

Harnisch, F., Schröder, U., Scholz, F., 2008. The suitability of monopolar and bipolar ion exchange membranes as separators for biological fuel cells. Environ. Sci. Technol. 42, 1740–1746.

Hatch, J.L., Finneran, K.T., 2008. Influence of reduced electron shuttling compounds on biological H_2 production in the fermentative pure culture *Clostridium beijerinckii*. Curr. Microbiol. 56, 268–273.

Higgins, S., Lau, C., Minteer, S.D., Atanassov, P., Cooney, M., 2011. Hybrid biofuel cell: microbial fuel cell with an enzymatic air-breathing cathode. ACS Catal. 1 (9), 994–997.

Huang, L.P., Angelidaki, I., 2008. Effect of humic acids on electricity generation integrated with xylose degradation in microbial fuel cells. Biotechnol. Bioeng. 100 (3), 413–422.

Huang, L.P., Zeng, R.J., Angelidaki, I., 2008. Electricity production from xylose using a mediator-less microbial fuel cell. Bioresour. Technol. 99, 4178–4184.

Ieropoulos, I.A., Greenman, J., Melhuish, C., Horsfield, I., 2012a. Microbial fuel cells for robotics: energy autonomy through artificial symbiosis. ChemSusChem 5, 1020–1026.

Ieropoulos, I., Greenman, J., Lewis, D., Knoop, O., 2013a. Energy production and sanitation improvement using microbial fuel cells. J. Water Sanit. Hyg. Dev. 3, 383–391.

Ieropoulos, I., Greenman, J., Melhuish, C., 2013b. Miniature microbial fuel cells and stacks for urine utilisation. Int. J. Hydrog. Energy 38 (1), 492–496.

Ivanov, I., Vidaković-Koch, T., Sundmacher, K., 2010. Recent advances in enzymatic fuel cells: experiments and modeling. Energies 3, 803–846.

Ivnitski, D., Branch, B., Atanassov, P., Apblett, C., 2006. Glucose oxidase anode for biofuel cell based on direct electron transfer. Electrochem. Commun. 8 (8), 1204–1210.

Jones, R.W., Garland, P.B., 1997. Sites and specificity of reaction of bipyridylium compounds with anaerobic respiratory enzymes of *Escherichia coli*—effects of permeability barriers imposed by cytoplasmic membrane. Biochem. J. 164, 199–211.

Kamarudin, M.Z.F., Kamarudin, S.K., Masdar, M.S., Daud, W.R.W., 2013. Review: direct ethanol fuel cells. Int. J. Hydrog. Energy 38, 9438–9453.

Kamitaka, Y., Tsujimura, S., Setoyama, N., Kajino, T., Kano, K., 2007. Fructose/dioxygen biofuel cell based on direct electron transfer-type bioelectrocatalysis. Phys. Chem. Chem. Phys. 9, 1793–1801.

Kandimalla, V.B., Tripathi, V.S., Ju, H.X., 2006. Immobilization of biomolecules in sol–gels: biological and analytical applications. Crit. Rev. Anal. Chem. 36, 73–106.

Kanga, X., Wanga, J., Wua, H., Aksayc, I.A., Liua, J., Lin, Y., 2009. Glucose oxidase–graphene–chitosan modified electrode for direct electrochemistry and glucose sensing. Biosens. Bioelectron. 25, 901–905.

Kar, P., Wen, H., Li, H., Minteer, S.D., Barton, S.C., 2011. Simulation of multistep enzyme-catalyzed methanol oxidation in biofuel cells. J. Electrochem. Soc. 158 (5), B580–B586.

Kelly, P.T., He, Z., 2014. Nutrients removal and recovery in bioelectrochemical systems: a review. Bioresour. Technol. 153, 351–360.

Kerzenmacher, S., Ducre´, J., Zengerlea, R., von Stetten, F., 2008. Energy harvesting by implantable abiotically catalyzed glucose fuel cells. J. Power Sources 182, 1–17.

Kim, B.H., Kim, H.J., Hyun, M.S., Park, D.H., 1999. Direct electrode reaction of Fe(III)-reducing bacterium, *Shewanella putrifaciens*. J. Microbiol. Biotechnol. 9, 127–131.

Kloeke, F.V., Bryant, R.D., Laishley, E.J., 1995. Localization of cytochromes in the outer membrane of *Desulfovibrio vulgaris* (Hildenborough) and their role in anaerobic biocorrosion. Anaerobe 1, 351–358.

Kontani, R., Tsujimura, S., Kano, K., 2009. Air diffusion biocathode with CueO as electrocatalyst adsorbed on carbon particle-modified electrodes. Bioelectrochemistry 76, 10–13.

Korani, A., Salimia, A., Hadadzadeh, H., 2015. Nickel-phendione complex covalently attached onto carbon nanotube/cross linked glucose dehydrogenase as bioanode for glucose/oxygen compartment-less biofuel cell. J. Power Sources 282, 586–595.

Krishnan, S., Armstrong, F.A., 2012. Order-of-magnitude enhancement of an enzymatic hydrogen-air fuel cell based on pyrenyl carbon nanostructures. Chem. Sci. 3, 1015–1023.

Lee, A.K., Newman, D.K., 2003. Microbial iron respiration: impacts on corrosion processes. Appl. Microbiol. Biotechnol. 62, 134–139.

Lewandowski, Z., Dickinson, W., Lee, W., 1997. Electrochemical interactions of biofilms with metal surfaces. Water Sci. Technol. 36, 295–302.

Li, X., Faghri, A., 2013. Review and advances of direct methanol fuel cells (DMFCs) part I: design, fabrication, and testing with high concentration methanol solutions. J Power Sources 226, 223–240.

Li, Q., Jensen, J.O., Savinell, R.F., Bjerrum, N.J., 2009. High temperature proton exchange membranes based on polybenzimidazoles for fuel cells. Prog. Polym. Sci. 34, 449–477.

Liu, H., Logan, B.E., 2004. Electricity generation using an air-cathode single chamber microbial fuel cell in presence and absence of a proton exchange membrane. Environ. Sci. Technol. 38, 4040–4046.

Logan, B.E., 2012. Essential data and techniques for conducting microbial fuel cell and other types of bioelectrochemical system experiments. ChemSusChem 5, 988–994.

Logan, B.E., Hamelers, B., Rozendal, R., Schröder, U., Keller, J., Freguia, S., Aelterman, P., Verstraete, W., Rabaey, K., 2006. Microbial fuel cells: methodology and technology. Eviron. Sci. Technol. 40, 5181–5192.

Lopez, R.J., Babanova, S., Ulyanova, Y., Singhal, S., Atanassov, P., 2014. ChemElectroChem 1 (1), 241–324.

Lovley, D., 2006. Bug juice: harvesting electricity with microorganisms. Nat. Rev. Microbiol. 4, 497–508. http://dx.doi.org/10.1038/nrmicro1442.

Lovley, D.R., 2008. The microbe electric: conversion of organic matter to electricity. Curr. Opin. Biotechnol. 19, 564–571.

Ma, J., Choudhury, N.A., Sahai, Y., 2010. A comprehensive review of direct borohydride fuel cells. Renew. Sustain Energy Rev. 14, 183–199.

Mano, N., Mao, F., Heller, A., 2003. Characteristics of a miniature compartment-less glucose–O_2 biofuel cell and its operation in a living plant. J. Am. Chem. Soc. 125 (21), 6588–6594.

Mano, N., Mao, F., Heller, A., 2005. On the parameters affecting the characteristics of the "wired" glucose oxidase anode. J. Electroanal. Chem. 574, 347–357.

Marsili, E., Baron, D.B., Shikhare, I.D., Coursolle, D., Gralnick, J.A., Bond, D.R., 2008. Shewanella secretes flavins that mediate extracellular electron transfer. Proc. Natl. Acad. Sci. USA 105, 3968–3973.

Martinucci, E., Pizza, F., Guerrini, E., Colombo, A., Trasatti, S.M., Lazzarini Barnabei, A., Liberale, A., Cristiani, P., 2015. Int. J. Hydrog. Enery 2015. http://dx.doi:10.1016/j.bioelechem.2015.05.008.

McConnell, V.P., 2010. Now, voyager? The increasing marine use of fuel cells. Fuel Cells Bull. 2010, 12–17.

Min, B., Cheng, S., Logan, B.E., 2005. Electricity generation using membrane and salt bridge microbial fuel cells. Water Res. 39, 1675–1686.

Minteer, S.D., Liaw, B.Y., Cooney, M.J., 2007a. Enzyme-based biofuel cells. Curr. Opin. Biotechnol. 18, 228–234.

Mudrack, K., Kunst, S., 1986. Biology of sewage treatment and water pollution control. Biologie der Abwasserreinigung (English translator: Hemmings, B.D.), (translation editor: Pike, E.B.), E. Horwood Limited, Chichester, England.

Nazaruk, E., Sadowska, K., Biernat, J.F., Rogalski, J., Ginalska, G., Bilewicz, R., 2010. Enzymatic electrodes nanostructured with functionalized carbon nanotubes for biofuel cell applications. Anal. Bioanal. Chem. 398, 1651–1660.

Oh, S.E., Logan, B.E., 2007. Voltage reversal during microbial fuel cell stack operation. J. Power Sources 167, 11–17.

Oliveira, V.B., Simões, M., Melo, L.F., Pinto, A.M.F.R., 2013. Overview on the developments of microbial fuel cells. Biochem. Eng. J. 73, 53–64.

Osman, M.H., Shah, A.A., Walsh, F.C., 2011. Recent progress and continuing challenges in biofuel cells. Part I: enzymatic cells. Biosens. Bioelectron. 26, 3087–3102.

Pant, D., Van Bogaert, G., Diels, L., Vanbroekhoven, K., 2010. A review of the substrates used in microbial fuel cells (MFCs) for sustainable energy production. Bioresour. Technol. 10, 1533–1543.

Park, D.H., Zeikus, J.G., 1999. Utilization of electrically reduced neutral red by *Actinobacillus succinogenes*: physiological function of neutral red in membrane-driven fumarate reduction and energy conservation. J. Bacteriol. 181, 2403–2410.

Park, D.H., Zeikus, J.G., 2000. Electricity generation in microbial fuel cells using neutral red as an electronophore. Appl. Environ. Microbiol. 66, 1292–1297.

Patil, S.A., Harnisch, F., Kapadnis, B., Schröder, U., 2010. The role of temperature on the formation and performance of bioelectrocatalytic active mixed culture biofilms for microbial bioelectrochemical systems. Biosens. Bioelectron. 26, 803–808.

Patil, S.A., Harnisch, F., Koch, C., Hübschmann, T., Fetzer, I., Carmona-Martínez, A.A., Müller, S., Schröder, U., 2011. Electroactive mixed culture derived biofilms in microbial bioelectrochemical systems: the role of pH on biofilm formation, performance and composition. Bioresour. Technol. 102, 9683–9690.

Pham, C.A., Jung, S.J., Phung, N.T., Lee, J., Chang, I.S., Kim, B.H., Yi, H., Chun, J., 2003. A novel electrochemically active and Fe(III)-reducing bacterium phylogenetically related to *Aeromonas hydrophila*, isolated from a microbial fuel cell. FEMS Microbiol. Lett. 223, 129–134.

Pope, D.H., 1987. Microbial Corrosion in Fossil-Fired Power Plants. EPRI CS-5495 Project 2300–12 Final Report November 1987, Research, 43: 1–15.

Postole, G., Auroux, A., 2011. The poisoning level of Pt/C catalysts used in PEM fuel cells by the hydrogen feed gas impurities: the bonding strength. Int. J. Hydrog. Energy 36, 6817–6825.

Puig, S., Serra, M., Coma, M., Cabré, M., Balaguer, M.D., Colprim, J., 2010. Effect of pH on nutrient dynamics and electricity production using microbial fuel cells. Bioresour. Technol. 101, 9594–9599.

Qian, F., Baum, M., Gu, Q., Morse, D.E., 2009. A 1.5 μL microbial fuel cell for on-chip bioelectricity generation. Lab Chip 9, 3076–3081.

Qian, F., He, Z., Thelen, M.P., Li, Y., 2011. A microfluidic microbial fuel cell fabricated by soft lithography. Bioresour. Technol. 102, 5836–5840.

Rabaey, K., Rozendal, R.A., 2010. Microbial electrosynthesis: revisiting the electrical route for bioproduction. Nat. Rev. Microbiol. 8, 706–716.

Rabaey, K., Verstraete, W., 2005. Microbial fuel cells: novel biotechnology for energy generation. Trends Biotechnol. 23, 291–298.

Rabaey, K., Boon, N., Siciliano, S.D., Verhaege, M., Verstraete, W., 2004. Bio-fuel cells select for microbial consortia that self-mediate electron transfer. Appl. Environ. Microbiol. 70, 5373–5382.

Reguera, G., McCarthy, K.D., Mehta, T., Nicoll, J.S., Tuominen, M.T., Lovley, D.R., 2005. Extracellular electron transfer via microbial nanowires. Nature 435, 1098–1101.

Rice, C., Ha, S., Masel, R.I., Waszczuk, P., Wieckowski, A., Barnard, T., 2002. Direct formic acid fuel cells. J. Power Sources 111, 83–89.

Rinaldi, A., Mecheri, B., Garavaglia, V., Licoccia, S., di Nardo, P., Traversa, E., 2008. Engineering materials and biology to boost performance of microbial fuel cells: a critical review. Energy Environ. Sci. 1, 417–429.

Ringeisen, B.R., Henderson, E., Wu, P.K., Pietron, J., Ray, R., Little, B., Biffinger, J.C., Jones-Meehan, J.M., 2006. High power density from a miniature microbial fuel cell using *Shewanella oneidensis* DSP10. Environ. Sci. Technol. 40, 2629–2634.

Roberge, P.R., 1999. Handbook of Corrosion Engineering. McGraw-Hill Professional Publishing, New York.

Rosenbaum, M., Angenent, L.T., 2010. Genetically modified microorganisms for bioelectrochemical systems. In: Rabaey, K., Angenent, L., Schröder, U., Keller, J. (Eds.), Bioelectrochemical Systems: From Extracellular Electron Transfer to Biotechnological Application. IWA Publishing, London, UK, ISBN: 978184339233X.

Rosenbaum, M., Aulenta, F., Villano, M., Angenent, L.T., 2011. Cathodes as electron donors for microbial metabolism: which extracellular electron transfer mechanisms are involved? Bioresour. Technol. 102, 324–333.

Ruiz, Y., Baeza, J.A., Guisasola, A., 2015. Enhanced performance of bioelectrochemical hydrogen production using a pH control strategy. ChemSusChem. 8 (2), 389–397.

Sakai, H., Nakagawa, T., Tokita, Y., Hatazawa, T., Ikeda, T., Tsujimura, S., Kano, K., 2009. A high-power glucose/oxygen biofuel cell operating under quiescent conditions. Energy Environ. Sci. 2, 133–138.

Salaj-Kosla, U., Pöller, S., Beyl, Y., Scanlon, M.D., Beloshapkin, S., Shleev, S., Schuhmann, W., Magner, E., 2012. Direct electron transfer of bilirubin oxidase *(Myrothecium verrucaria)* at an unmodified nanoporous gold biocathode. Electrochem. Commun. 16 (1), 92–95.

Santini, M., Guilizzoni, M., Lorenzi, M., Atanassov, P., Marsili, E., Fest-Santini, S., Cristiani, P., Santoro, C., 2015. Three-Dimensional X-ray Micro Computed Tomography of Carbonates and Biofilm on Operated Cathode in Single Chamber Microbial Fuel Cell. Biointerphases. http://dx.doi.org/10.1116/1.4930239.

Santoro, C., Agrios, A., Pasaogullari, U., Li, B., 2011. Effects of gas diffusion layer (GDL) and micro porous layer (MPL) on cathode performance in microbial fuel cells (MFCs). Int. J. Hydrog. Energy 36, 13096–13104.

Santoro, C., Lei, Y., Li, B., Cristiani, P., 2012. Power generation from wastewater using single chamber microbial fuel cells (MFCs) with platinum free cathodes and pre-colonized anodes. Biochem. Eng. J. 62, 8–16.

Santoro, C., Li, B., Cristiani, P., Squadrito, G., 2013a. Power generation of microbial fuel cells (MFCs) with low cathodic platinum loading. Int. J. Hydrog. Energy 38, 692–700.

Santoro, C., Stadlhofer, A., Hacker, V., Squadrito, G., Schröder, U., Li, B., 2013b. Activated carbon nanofibers (ACNF) as cathode for single chamber microbial fuel cells (SCMFCs). J. Power Sources 243, 499–507.

Santoro, C., Babanova, S., Atanassov, P., Li, B., Ieropoulos, I., Cristiani, P., 2013c. High power generation by a membraneless single chamber microbial fuel cell (SCMFC) using enzymatic bilirubin oxidase (BOx) air-breathing cathode. J. Electrochem. Soc. 160 (10), 720–726.

Santoro, C., Babanova, S., Artyushkova, K., Atanassov, P., Greenman, J., Cristiani, P., Trasatti, S., Schuler, A.J., Li, B., Ieropoulos, I., 2014. The effects of wastewater types on power generation and phosphorus removal of microbial fuel cells (MFCs) with activated carbon (AC) cathodes. Int. J. Hydrog. Energy 39, 21796–21802.

Sasakia, K., Morita, M., Sasakia, D., Matsumoto, M., Ohmura, N., Igarashi, Y., 2012. Single-chamber bioelectrochemical hydrogen fermentation from garbage slurry. Biochem. Eng. J. 68, 104–108.

Scodeller, P., Carballo, R., Szamocki, R., Levin, L., Forchiassin, F., Calvo, E.J., 2010. Layer-by-layer self-assembled osmium polymer-mediated laccase oxygen cathodes for biofuel cells: the role of hydrogen peroxide. J. Am. Chem. Soc. 132 (32), 11132–11140.

Seo, M.H., Choi, S.M., Kim, H.J., Kim, W.B., 2011. The graphene-supported Pd and Pt catalysts for highly active oxygen reduction reaction in an alkaline condition solution. Electrochem. Commun. 13, 182–185.

Sheldon, A., 2007. Enzyme immobilization: the quest for optimum performance. Adv. Synth. Catal. 349, 1289–1307.

Shungui, Z.H.O.U., 2009. U.S. Patent Application 12/498,023.

Sleutels, T.H.J.A., Darus, L., Hamelers, H.V.M., Buisman, C.J.N., 2011. Effect of operational parameters on Coulombic efficiency in bioelectrochemical systems. Bioresour. Technol. 102, 11172–11176.

Sokic-Lazic, D., Arechederra, R.L., Treu, B.L., Minteer, S.D., 2010. Oxidation of biofuels: fuel diversity and effectiveness of fuel oxidation through multiple enzyme cascades. Electroanalysis 22, 757–764.

Song, Y., Penmasta, V., Wang, C., 2011. Recent development of miniatured enzymatic biofuel cells. In: dos Santos Bernardes, M.A. (Ed.), Biofuel's Engineering Process Technology. InTech. chp 28, Available from: http://www.intechopen.com/books/biofuel-s-engineering-processtechnology/recent-development-of-miniatured-enzymatic-biofuel-cells-657, ISBN: 978-953-307-480-1.

Squadrito, G., Andaloro, L., Ferraro, M., Antonucci, V., 2014. Chapter 16—hydrogen fuel cell technology. In: Basile, A., Iulianelli, A. (Eds.), Advances in Hydrogen Production, Storage and Distribution. Woodhead Publishing, Cambridge (UK), ISBN: 978-0-85709-768-2.

Staiti, P., Hocevar, S., Giordano, N., 1997. Fuel cells with $H_3PW_{12}O_{40} \cdot 29H_2O$ as solid electrolyte. Int. J. Hydrog. Energy 22, 809–8014.

Stoica, L., Dimcheva, N., Ackermann, Y., Karnicka, K., Guschin, D.A., Kulesza, P.J., Rogalski, J., Haltrich, D., Ludwig, R., Gorton, L., Schuhmann, W., 2009. Membrane-less biofuel cell based on cellobiose dehydrogenase (anode)/laccase (cathode) wired via specific os-redox polymers. Fuel Cells 9, 53–62.

Tayhas, G., Palmore, R., Whitesides, G.M., 1994. Microbial and enzymatic biofuel cells. In: Himmel, M.E., Baker, J.O., Overend, R.P. (Eds.), Enzymatic Conversion of Biomass for Fuels Production. American Chemical Society, ACS Symposium Series No. 566.

"The Fuel Cell Industry Review 2014", E4Tech, November 2014; free download from http://www.e4tech.com/FuelCellIndustryReview/

Thurston, C.F., Bennetto, H.P., Delaney, G.M., Mason, J.R., Roller, S.D., Stirling, J.L., 1985. Glucose metabolism in a microbial fuel cell. Stoichiometry of product formation in a thionine-mediated *Proteus vulgaris* fuel cell and its relation to Coulombic yields. J. Gen. Microbiol. 131, 1393–1401.

Togo, M., Takamura, A., Asai, T., Kaji, H., Nishizawa, M., 2008. Structural studies of enzyme-based microfluidic biofuel cells. J. Power Sources 178, 53–58.

Venkataraman, A., Rosenbaum, M., Arends, J.B.A., Halitsche, R., Angenent, L.T., 2010. Quorum sensing regulates electric current generation of *Pseudomonas aeruginosa* PA14 in bioelectrochemical systems. Electrochem. Commun. 12, 459–462.

Villano, M., De Bonisa, L., Rossetti, S., Aulenta, F., Majone, M., 2011. Bioelectrochemical hydrogen production with hydrogenophilic dechlorinating bacteria as electrocatalytic agents. Bioresource Technol. 102 (3), 3193–3199.

Wang, H., Ren, Z.J., 2013. A comprehensive review of microbial electrochemical systems as a platform technology. Biotechnol. Adv. 31, 1796–1807.

Wei, J., Liang, P., Cao, X., Huang, X., 2011a. Use of inexpensive semicoke and activated carbon as biocathode in microbial fuel cells. Bioresour. Technol. 102, 10431–10435.

Wei, J., Liang, P., Huang, X., 2011b. Recent progress in electrodes for microbial fuel cells. Bioresour. Technol. 102, 9335–9344.

Willner, I., Yan, Y.-M., Willner, B., Tel-Vèred, R., 2009. Integrated enzyme-based biofuel cells—a review. Fuel Cell 9, 7–24.

Woodward, J., Heyer, N.I., Getty, J.P., O'Neill, H.M., Pinkhassik, E., Evans, B.R., 2002. Efficient Hydrogen Production Using Enzymes of the Pentose Phosphate Pathway. Proceedings of the 2002 U.S. DOE Hydrogen Program Review, NREL/CP-610-32405. Available on web at http://www.nrel.gov/docs/fy02osti/32405a6.pdf (last view on 20th February 2015).

Yang, S., Jia, B., Liu, H., 2009. Effects of the Pt loading side and cathode-biofilm on the performance of a membrane-less ad single chamber microbial fuel cell. Bioresour. Technol. 100, 1197–1202.

Yarzabal, A., Brasseur, G., Ratouchniak, J., Lund, K., Lemesle-Meunier, D., DeMoss, J.A., Bonnefoy, V., 2002. The high-molecular-weight cytochrome c Cyc2 of *Acidithiobacillus ferrooxidans* is an outer membrane protein. J. Bacteriol. 184, 313–317.

Zebda, A., Innocent, C., Renaud, L., Cretin, M., Pichot, F., Ferrigno, R., Tingry, S., 2011. Enzyme-based microfluidic biofuel cell to generate micropower. In: Dos Santos Bernardes, M.A. (Ed.), Biofuel's Engineering Process Technology. InTech. Available from: http://www.intechopen.com/books/biofuel-s-engineering-process-technology/enzyme-based-microfluidicbiofuel-cell-to-generate-micropower, ISBN: 978-953-307-480-1.

Zhang, J., Xie, Z., Zhang, J., Tang, Y., Song, C., Navessin, T., Shi, Z., Song, D., Wang, H., Wilkinson, D.P., Liu, Z.-S., Holdcroft, S., 2006. High temperature PEM fuel cells. J. Power Sources 160, 872–891.

Zhou, M., Wang, H., Hassett, D.J., Gu, T., 2013. Recent advances in microbial fuel cells (MFCs) and microbial electrolysis cells (MECs) for wastewater treatment, bioenergy and bioproducts. J. Chem. Technol. Biotechnol. 88, 508–518.

This page intentionally left blank

Part Two

Hydrogen combustion and metal hydride batteries

This page intentionally left blank

Hydrogen-fueled internal combustion engines

7

L.M. Das
Indian Institute of Technology, New Delhi, India

7.1 Introduction

Fossil fuels are dwindling fast, leading to an energy (fuel) crisis. Additionally, combustion of fossil fuels is causing rapid degradation of the environment. Internal combustion (IC) engines have become an easy victim to these twin crises. However, there is no room for doubt that IC engines, in view of their versatility, will continue to dominate the transport and power sectors. So it has become essential that "clean-burning" fuels, obtainable from renewable sources, be expeditiously identified to ensure a safe and long survival of IC engines. Hydrogen fuel is gifted with the potential of providing an eventual freedom from both fossil fuel starvation and environmental degradation due to the combustion of fossil fuels.

Hydrogen offers the unique advantage of being a fuel whose basic resource is recyclable in a short time cycle, as shown in Figure 7.1. The molecule of water could be split using either fossil fuel or many of the nonfossil sources such as solar, wind, nuclear, organic waste, and others. Upon combustion of hydrogen, water vapor comes out of the exhaust of the engine and this water goes back to the biosphere from where it came.

An integrated picture of the versatility of hydrogen can be projected if each of the stages such as production, transmission, storage, and utilization are elaborately discussed. However, efforts will be made here to restrict the discussion to the use of hydrogen in IC engines. With the present level of technology it is possible to have hydrogen-fueled IC engines to be used for automotive and agricultural applications (Das, 2002a).

7.1.1 Properties of hydrogen fuel

Hydrogen as a fuel has a set of distinctive features that sets it apart from conventional fuels. As will be evident from the following description, hydrogen has some very temperamental properties. If appropriately used, these properties contribute to better performance and lower emission characteristics as well as smooth combustion at low engine load operation. Interestingly, the same properties have been observed to be responsible for causing a series of undesirable combustion problems such as preignition/backfire and higher level of NO_x emissions at relatively high engine loads. Table 7.1 lists the physicochemical characteristics of hydrogen fuel *vis-à-vis* those of methane and gasoline. Properties such as diffusion, density, quenching distance, minimum ignition energy, flammability limit, flame speed, and autoignition temperature have proven to be very relevant to engine operation (see Table 7.2).
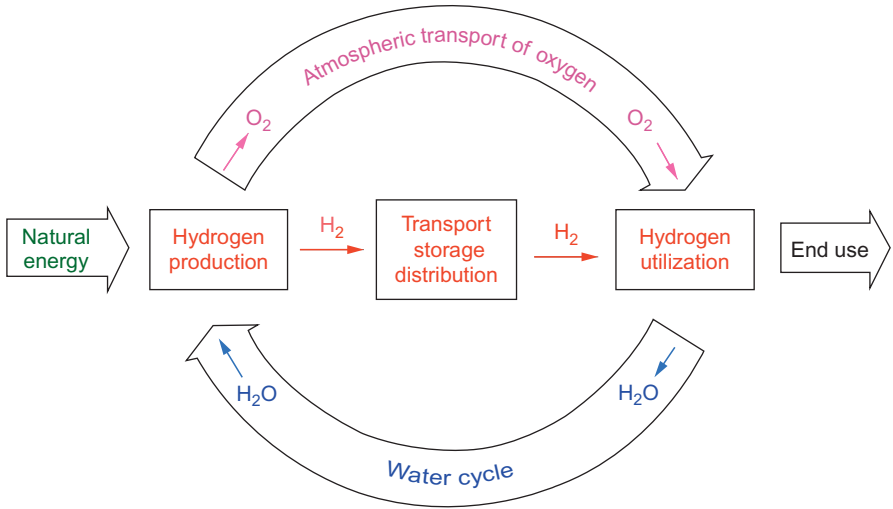
Figure 7.1 Hydrogen cycle.

Table 7.1 Thermodynamic properties of hydrogen, methane, and gasoline (generally accepted values from the literature)

Properties	Hydrogen	Methane	Gasoline
Molecular weight	2.016	16.043	107.0
Density of gas at NTP (g m^{-3})	83.764	651.19	4400
Heat of combustion (low) (kJ g^{-1})	119.93	50.02	44.5
Heat of combustion (high) (kJ g^{-1})	141.86	55.53	48
Specific heat (c_p) of NTP gas (J g^{-1} K^{-1})	14.86	2.22	1.62
Viscosity of NTP gas (g cm^{-1} s^{-1})	0.0000875	0.000110	0.00005
Specific heat ratio (γ) of NTP gas	1.383	1.308	1.05
Gas constant (R) (cm^2 atm g^{-1} K^{-1})	40.7030	5.11477	0.77
Diffusion coefficient in NTP air (cm^2 s^{-1})	0.61	0.16	0.005

Table 7.2 Combustion properties of hydrogen, methane, and gasoline (generally accepted values from the literature)

Properties	Hydrogen	Methane	Gasoline
Limits of flammability in air (volume %)	4.0–75.0	5.3–15.0	1.0–7.6
Stoichiometric composition in air (volume %)	29.53	9.48	1.76
Minimum energy for ignition in air (mJ)	0.02	0.29	0.24
Auto-ignition temperature (K)	858	813	501–744
Flame temperature in air (K)	2318	2148	2470
Burning velocity in NTP air (cm s^{-1})	265–325	37–45	37–43
Quenching gap in NTP air (cm)	0.064	0.203	0.2
Percentage of thermal energy radiated from flame to surrounding (%)	17–25	23–32	30–42
Diffusivity in air (cm^2 s^{-1})	0.63	0.2	0.08
Normalized flame emissivity (2000 K, 1 atm)	1.00	1.7	1.7
Limits of flammability (equivalence ratio)	0.1–7.1	0.53–1.7	0.7–3.8
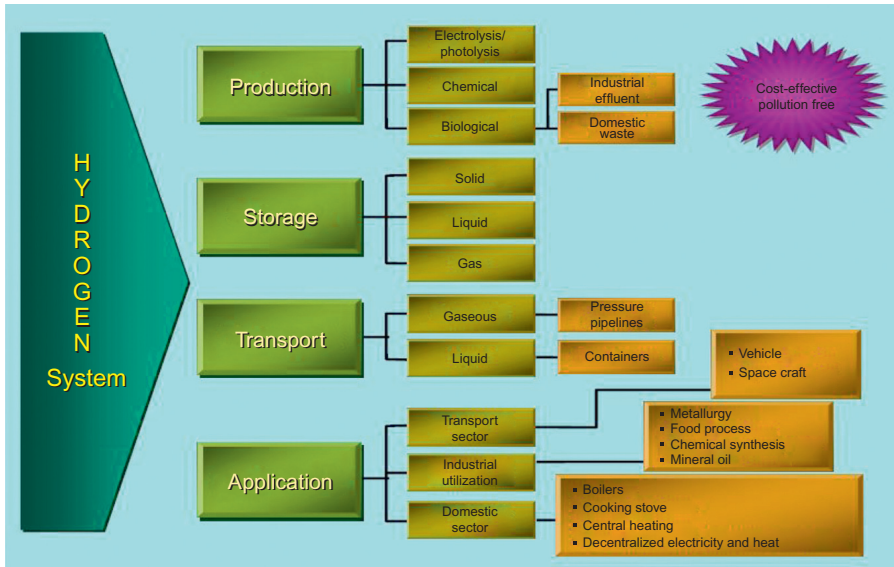
Figure 7.2 Hydrogen energy systems.

7.1.2 Energy density and diffusivity

Hydrogen, being the lightest element, has a low specific volume and also an extremely low density both as a fuel and as a gas. So there is a drop in efficiency when hydrogen is added to the intake of an engine. Figure 7.2 shows the different aspects of an integrated hydrogen energy system.

The positive feature of low energy density is sometimes useful in causing rapid dispersion into the atmosphere. High diffusivity demonstrates a tendency of faster leakage through openings, which also helps leaked hydrogen to diffuse to an incombustible proportion within a short period.

7.1.3 Minimum ignition energy and quenching distance

It is clear from Figure 7.3, taken after Lewis and Elbe (1987), that the minimum ignition energy of hydrogen air mixture is about one-tenth that of methane air mixture. This property facilitates hydrogen engine ignition with a very low energy spark. In contrast, any residual energy concentration (after a combustion cycle) in the form of a hot spot can cause surface ignition. Quenching distance of hydrogen is much lower compared to that of methane and gasoline.

Considering the properties such as minimum ignition energy and lower quench distance, hydrogen combustion is not only initiated with a low energy spark, but also is more difficult to quench and hence easier to sustain.
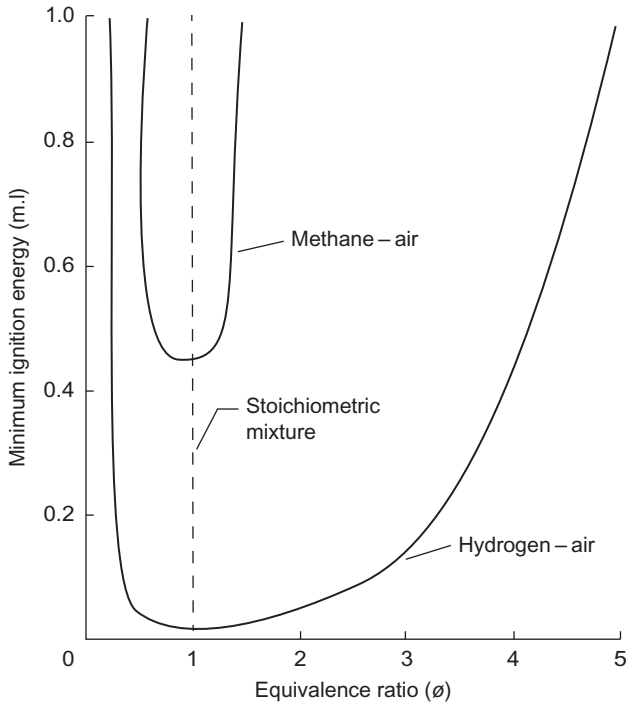
Figure 7.3 Minimum ignition energy for hydrogen and methane.

7.1.4 Flammability limit, flame speed, and flame temperature

The wide flammability range of hydrogen makes it possible for the engine to operate at a very low equivalence ratio. As the equivalence ratio falls below unity, the amount of fuel (thus the amount of energy) decreases, thereby decreasing the power output. The high flame speed of hydrogen has some definite implication to engine operation. Figure 7.4 shows the stable operating range of equivalence ratio for a hydrogen engine.

The spark timing of a hydrogen engine has to be substantially different from that of a gasoline engine. For the stoichiometric hydrogen operation, it has to be highly retarded for the timing set initially for a gasoline engine. As far as the lean hydrogen operation is concerned, it also has to be relatively advanced from the corresponding stoichiometric value fixed for a hydrogen setting. The spark timing depends upon the equivalence ratio of the lean operation.

Rapid flame propagation has been one of the major causes of backfire in hydrogen engines resulting in severe damages. In a properly designed hydrogen-specific engine it is also essential that the valve timing of both the intake and exhaust valves should be adjusted from the existing gasoline setting.
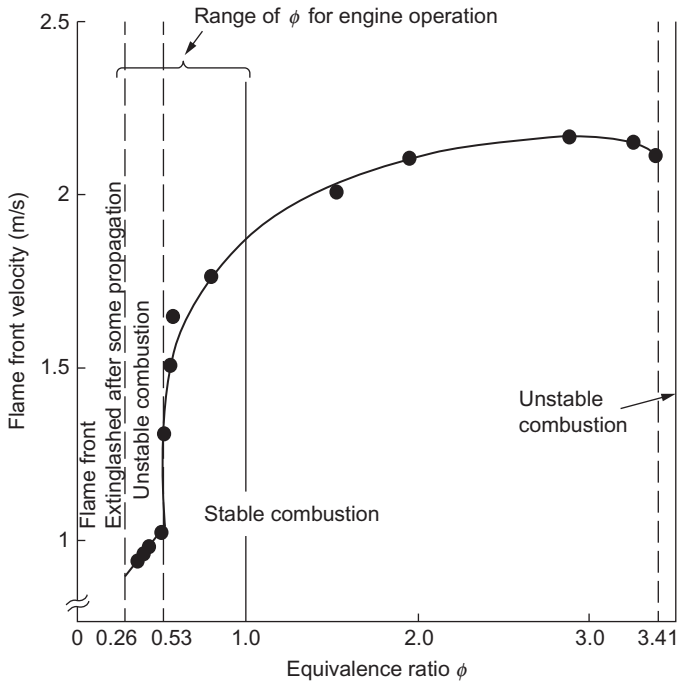
Figure 7.4 Stable operating range of a hydrogen engine.

Hydrogen flame is higher than other fuels at the stoichiometric mixture and there-fore the hydrogen engine is capable of giving a much higher thermal efficiency as compared to the gasoline engine at all ranges of equivalence ratio. At the same time, high flame temperature of hydrogen engine results in higher levels of NO_x emissions near stoichiometric mixtures. Exhaustive tests by researchers in the Indian Institute of Technology (IIT) Delhi in the laboratory have shown that it is possible to operate a hydrogen engine that is capable of ultra lean operation thereby producing extremely low levels of NO_x emissions.

Compression ignition (CI) of hydrogen is extremely difficult because of hydro-gen's auto-ignition temperature and therefore a hydrogen-operated diesel cycle is not easily achievable. At the same time, this property of high self-ignition temperature can be very useful to a spark ignition (SI) engine in which the compression ratio can be substantially increased, thereby increasing the thermal efficiency.

After a critical review of some of the properties of hydrogen, it is clear that an optimal hydrogen engine can be designed on the basis of unique properties of hydrogen so as to have a much higher thermal efficiency and substantially lower exhaust emission as compared with the existing conventional gasoline engine.

7.2   Evolution of hydrogen engine technology

It may be relevant to mention here that the hydrogen engine is not a radically new concept. Chronologically, the research and development activities with hydrogen engine operation could be classified into three different phases and for three distinct criteria related to sociotechnical priorities.

In an earlier phase of IC engine development, hydrogen was tried as a fuel for laboratory curiosity. Again, after a long lull of several decades, hydrogen received attention as an alternative engine fuel because of the threatened shortage of petroleum fuel during the war years. Another distinct military advantage of a hydrogen–oxygen system was also thought to have completely condensable exhaust, which could be of great benefit to submarines during war operations. The recent phase of work began in 1970s only after the importance of hydrogen was realized as an alternative fuel that also was extremely "clean burning" and can provide a solution to the growing problem of vehicular pollution.

The Rev. Cecil (1822) presented a paper "On Hydrogen Gas as a moving power in Machinery" before the Cambridge Philosophical Society that included the observations that "the engine in which hydrogen is employed to produce moving force may be inferior in some respects to many engines at present employed, yet it will not be wholly useless, if together with its own defects and it should be found to possess advantages peculiar to itself." A closer analysis of his observations shows that he had experienced some hydrogen-specific features that were very promising and also had identified some problems that were difficult to solve at that time. The literature reveals that Rudolf Erren did a lot of work on hydrogen engines in Germany and also in England. He not only had identified the problems of backfire and preignition, but also had made efforts to solve these problems by direct cylinder injection. One of his papers even suggested the commercial application of the hydrogen engine. Erren's (Erren and Campell, 1933) research work is still very relevant today. Apart from carrying out extensive tests to evaluate an engine's performance characteristics, Erren, even at that point of time had emphasized the nonpolluting characteristics of hydrogen. In fact, he had developed several hydrogen-operated buses with banks of high-pressure cylindrical tanks. Unfortunately, all his valuable research documents were destroyed due to bombing during World War II. Some additional information about Erren's work was given by Weil (1972). Oehmichen's is an excellent detailed investigation on hydrogen injection (Oehmichen, 1942) that provides very significant information on the desirable mode of injection. He discussed the implication of sonic velocity with regard to the injection system, which was also subsequently studied by Homan (1978).

Ricardo (1924) conducted extensive tests and experienced the problem of "popping back into the carburetor." Thus the problem of backfire was perhaps the major stumbling block in the growth of hydrogen engine technology. King and his team (King et al., 1957, 1958; King and Rand, 1955) in their research pursuits had put special emphasis on the study of hot spot-induced backfire. They also built up systems to get rid of backfire. Special tests were conducted over a wide range of engine operating

conditions to identify the causes of backfire. Influence of the two most significant parameters (compression ratio and equivalence ratio) was thoroughly investigated.

Interest in the hydrogen engine was glaringly visible in the 1970s. Individuals, industries, universities, and government organizations contributed to several areas of technology and system development. The prospective role of hydrogen in the transport sector gained significance because the long-term damaging effects due to vehicular emissions on the rapid degradation of the environment and human health had already created a tremor in different spheres of society. Research and development activities on the hydrogen engine were few and far between until the 1970s. However, since the 1970s, the activities related to different aspects of the hydrogen engine including the magnitude of publications has been so enormous it is beyond the scope of the chapter to discuss each of them. Some research papers give an overview (Das, 1990a; White et al., 2006; Escher, 1975; Verhelst and Wallner, 2009; Billings, 1974; Murray et al., 1972) of several aspects of technology. Results of several significant research activities carried out in the subject (Stebar and Parks, 1974; Finegold and Van Vorst, 1974; Van Vorst and Finegold, 1975; Adt et al., 1973; De Boer et al., 1976; McLean et al., 1977; Fagelson et al., 1975; Varde and Frame, 1982; Das, 1986; Eichlseder et al., 2003) have established the fact that hydrogen engine technology does possess the desired potential for being practically implemented in reciprocating IC engines. These studies have demonstrated several practical routes of adopting hydrogen supplementation as well as neat hydrogen operation in existing designs of engines without any substantial modification in the original hardware.

Figure 7.5 shows the results of a study made by Professor Veziroglu, indicating clearly that transition to a hydrogen economy is taking place much faster than previously thought.
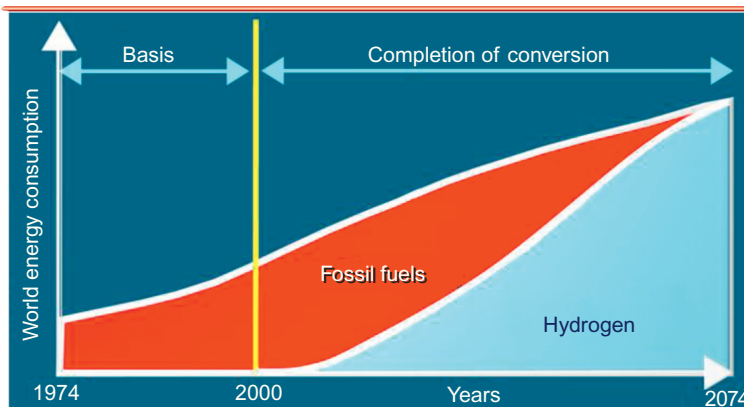
Figure 7.5 Transition to hydrogen economy.
Source: T. Nejat Veziroglu, Hydrogen Energy Technologies, UNIDO.

7.2.1   Classification of engines

It is well known that there are broadly two families of IC engines: SI engines and CI engines. The SI engines are largely fueled by gasoline, and the CI engines by diesel as the conventional fuel. The combustion process in an SI engine is very different from that in a CI engine. Thus the mixture formation technique plays a crucial role in the performance, emission, and combustion characteristics of the engine.

An SI engine can use neat hydrogen as the fuel and also can adopt hydrogen supplementation along with gasoline. But diesel engines cannot be converted to total hydrogen operation because autoignition temperature of hydrogen is about 576 °C. The literature shows that, even at a compression ratio of 29, it was not possible to achieve CI of hydrogen (Homan, 1978). Essentially, the diesel engines can run on a dual-fuel mode using both diesel and hydrogen.

Test results reported in the literature are based on engines that are designed to operate on gasoline and diesel and have been "converted" to hydrogen operation. Any converted system is likely to exhibit some degree of reliability problem in the long run. However, such problems offer adequate guidelines to develop a "hydrogen-specific" system.

The initial discussion in this chapter is related to the "hydrogen-operated SI engine." For the sake of brevity, this is referred to here as only the "hydrogen engine" in the following description. In the characterization of the hydrogen engine, it is important to classify the engines with respect to the timing of fuel induction to the engine cylinder. In this context, the classification could be made into two major categories such as "pre-IVC" (before intake valve closure) and "post-IVC" (after the intake valve closure). The pre-IVC configurations are those in which hydrogen is inducted into the engine cylinder prior to the intake valve closure; in the post-IV configurations, hydrogen is inducted after the closing of the intake valve. One important feature that needs to be emphasized here that in a post-IVC engine, hydrogen is ingested at a high pressure, whereas in a pre-IVC configuration the fuel is ingested at a relatively much lower pressure.

Apart from the basic design of developing a test rig to operate on hydrogen, it is also important to assess the engine configuration, which is capable of giving optimum performance and low-emission characteristics without causing any undesirable combustion symptoms (such as backfire). Apart from controlling the charge density with the throttle, a hydrogen-fueled pre-IVC engine can control the load by way of altering the mixture strength. This is a unique distinctive feature of the hydrogen engine because such unthrottled (quality-controlled) operation is possible because of the high flame speed of hydrogen over a wide range of mixture strength. Power control and power improvement techniques are important to ensure good performance. However, appropriate steps should be adopted in the integrated system so as to suppress backfire and control NO_x emissions.

The post-IVC engine configurations sometimes demonstrate a relatively lower thermal efficiency. This trend is closely linked with the combustion characteristics. Under certain engine operating conditions, the flame front progresses so rapidly that there is no scope for adequate diffusion of oxygen. This oxygen-deficient situation results in the extinction of the flame.

Pre-IVC engines can be designed to establish a hydrogen concentration gradient. A rich mixture near the spark plug can facilitate easy ignition near the spark plug and lean mixture at locations away from the plug. This is a very distinctive feature of pre-IVC configuration of hydrogen engines that permits engine operation at ultra-lean mode.

7.2.2   Difference and similarities between conventional and hydrogen-fueled IC engines

It is perhaps relevant to define a "hydrogen-specific" engine in the context of this chapter. A hydrogen-specific engine is one that is designed on the typical combustion characteristics of hydrogen fuel. In fact, most of the research results have been generated on retrofitted and converted systems. Such systems are bound to exhibit some reliability problems in the long run. Conversion technology has its intrinsic limitations, which prevent any configuration to evolve into its mature stage of technology.

As far as the exhaust emissions are concerned, a petroleum-fueled engine throws a host of noxious pollutants such as CO, HC, SO_x, particulate matter, and so on. All these are intrinsically absent in a hydrogen-fueled engine. Absence of particular matter prevents fouling of the spark plug and so wear will be minimized. Any traces of carbon monoxide and hydrocarbons found in the hydrogen engine exhaust are due to the engine's lubricating oil. Some researchers have also reported emissions of a small quantity of hydrogen peroxide.

A broad comparison of safety aspects between petroleum-fueled engines vis-à-vis hydrogen engines can be looked at from several angles. Radiation hazards from hydrogen-air fire are relatively much less as compared to corresponding hydrocarbon fire because of the low emissivity of hydrogen flame. Additionally, radiation from hydrogen fire is at a wavelength that is readily absorbed by the atmosphere.

Hydrogen is very light. In the event of leakage, it rises rapidly through air, thereby confining the risk of explosion to the space immediately above the leak. On the other hand, spilled gasoline spreads over the ground, thereby endangering a larger area around the spill. In the event of an accident of a gasoline-operated vehicle, splashed gasoline will present a hazard for hours, whereas hydrogen would disperse to incombustible proportions within moments.

The basic difference between the operation of a gasoline-fueled engine and a hydrogen-fueled engine stems mainly from the physicochemical properties of the two fuels. The most noticeable difference is that petroleum fuels are liquid at room temperature while hydrogen remains a gas even at a much lower temperature. The other properties that are responsible for engine operation are low density, low energy content per unit volume, wider flammability range, minimum ignition energy, high flame speed and smaller quench distance. These properties of hydrogen are responsible for the difference in performance and emission features between hydrogen engine and gasoline engine.

A comparative assessment between gasoline and hydrogen engines very clearly brings out the influence of two distinct properties of hydrogen fuel: flame velocity and adiabatic flame temperature. These two properties are very important for
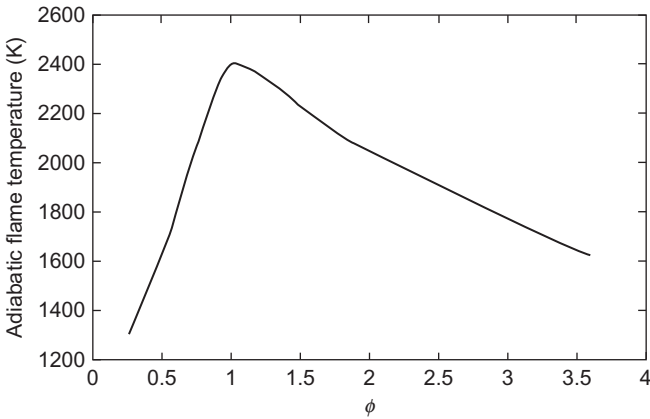
Figure 7.6 Adiabatic flame temperature for hydrogen–air mixture (Drell and Belles, 1958).

hydrogen engine operation from the point of view of thermal efficiency, combustion stability, and exhaust emission. Figures 7.6 and 7.7 show the effect of adiabatic flame temperature and laminar flame velocity of hydrogen–air mixture (Drell and Belles, 1958).

The ill-famous combustion problem (such as backfire) that occurs glaringly in the hydrogen engine can be eliminated by way of a well-designed fuel induction system. Backfire can also occur in a petroleum-fueled engine, but this is very mild and can be ignored. Hydrogen, unlike the liquid fuels, does not suffer from issues like vapor lock and cold wall quenching. As the wall quenching of hydrogen is a difficult phenomenon it can be considered as a factor that contributes to the backfire. Backfire could
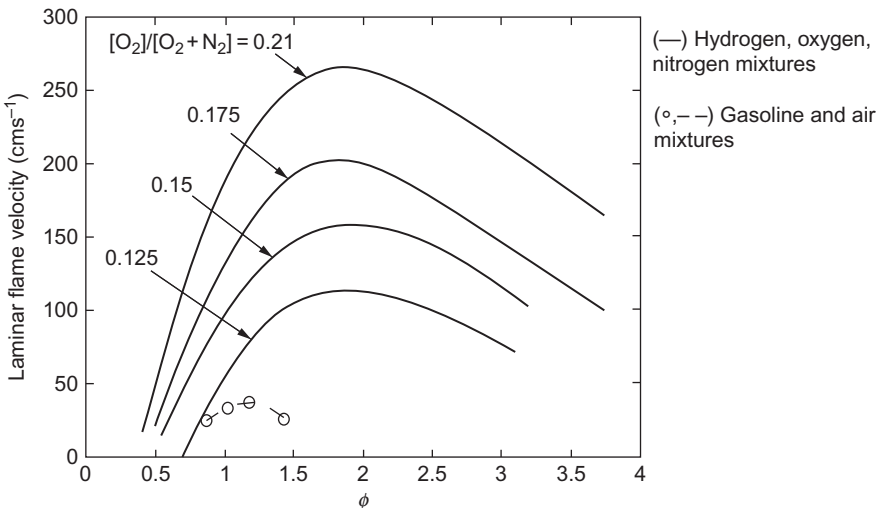
Figure 7.7 Laminar flame velocity versus equivalence ratio (Drell and Belles, 1958).

be caused by a large concentration of thermal masses as in the combustion chamber surfaces such as cylinder walls, pistons, valves, and spark plugs. At the same time there is a high possibility of backfire occurring by low thermal masses such as surface deposits or hot residual gases (Sirens, 2001; Das, 1990b).

Flame initiation failure happens to be one of the important practical problems encountered in the operation of the hydrogen engine. Such a situation occurs primarily because of the inappropriate function of the ignition system. Flame initiation failure can result in a series of operational and safety problems such as frequent misfire, flashback, and overheating of the exhaust manifold. These problems of high magnitude do not occur in gasoline engines.

7.2.3 Fueling of hydrogen engine configuration

7.2.3.1 Neat hydrogen engine

The hydrogen engine is capable of operating over a wide range of equivalence ratio: from ultra-lean mode to stoichiometric conditions. However, it has been observed that the engine gives maximum thermal efficiency and minimum NO_x emissions and without any problems of backfire if operated within a definite range of lean operation. Fuel induction technique has been found to be very crucial to hydrogen engine development. Apart from the performance and emission characteristics of the engine, the major thrust has been on controlling the tendency of backfire. As indicated in Table 7.3, several fuel induction techniques have been exhaustively investigated for a neat hydrogen engine (Das, 1990b).

Table 7.3 Fuel induction techniques (Das, 1990b)

Mixture formation	Classification	Hydrogen flow timing	Supply pressure
Continuous carburetion (CC)	Pre-IVC	Continuous flow	A little above atmospheric
Continuous manifold injection (CMI)	Pre-IVC	Continuous flow	Slightly greater than atmospheric
Timed manifold injection (TMI)	Pre-IVC	Hydrogen flow commences after opening of the intake valve but completed prior to intake valve closure	$1.4–5.5$ kgf/cm^2
Low-pressure direct cylinder injection (LPDI)	Post-IVC	Hydrogen flow commences after intake valve closure and is completed before significant compression pressure rise	$2–8.0$ kgf/cm^2

Extensive tests in the IIT Delhi's lab were carried out to assess the comparative benefits and shortcomings of each mode of fuel induction. The carbureted version is perhaps the simplest configuration to operate a hydrogen engine. But, it is highly susceptible to backfire and preignition problems. Sometimes, in the higher ranges of equivalence ratio the intensity and frequency of backfire are very high. Hence the carburetion technique is not acceptable for long-term application.

Continuous carburetion and continuous manifold injection techniques were also observed to be highly susceptible to flashback and thus cannot be recommended for long-term application. Timed manifold injection (TMI) and direct cylinder injections have proven effective in getting rid of backfire (Das, 2002b; Mathur and Das, 1991). Direct cylinder injection, by definition, is a sound mixture formation concept because it intrinsically precludes the possibility of backfire as the air–fuel mixture is formed in the cylinder after the intake valve closure. Direct cylinder injection in a hydrogen engine can be accomplished by two routes: high-pressure direct cylinder injection (HPDI) and low-pressure direct cylinder injection (LPDI). A properly designed LPDI system facilitates hydrogen injection early in the compression stroke and hence there exists a higher degree of possibility for better mixing of hydrogen and air. In an HPDI system, the pressure is so high that hydrogen fuel can be directly injected into the combustion chamber even during the compression stroke. An effective HPDI system prevents backfire in the intake manifold and auto-ignition during combustion and thus makes it possible to achieve controlled combustion. A significant feature experienced by the IIT Delhi team during laboratory tests shows that it is difficult for the injector to survive in the severe thermal environment of the combustion chamber. It was a very difficult task to develop a leak-proof injector that could be continuously used over a long period of tests. Engine system safety is of utmost significance for a hydrogen-fueled engine, and hydrogen should not leak at any point. From this point of view, the engines requiring high-pressure injection systems should preferably be avoided as far as possible Moreover, in-cylinder turbulence is essential to ensure adequate mixing and also to avoid the situations leading to heterogeneous charge. Such an objective could not also be achieved during the HPDI system in a series of tests at IIT Delhi.

An appropriately designed TMI provides the most pragmatic solution to backfire. In a TMI system, hydrogen fuel is introduced at an appropriate time into the intake manifold and at an appropriate location. TMI provides a means of delayed fuel delivery, whereby the small thermal masses and residual exhaust gases are cooled and the possibility of hot spot-induced backfire is reduced. The design criteria of the injector and the corresponding actuation mechanism toward an optimum system development have been described elsewhere (Mathur and Das, 1991). TMI system design is still being used for engine tests in IIT Delhi and it has been subsequently observed that it is not necessary to go to the higher level of pressure range (5.5 kgf/cm^2) as indicated in Table 7.3. The system functions very effectively at about 2 kgf/cm^2.

Several investigators have reported test data on the hydrogen engine. Almost all have reported on the improvement in performance characteristics. Level of NO_x emissions have been reported to be dependent upon the operating condition related to equivalence ratio. Efforts will be made in this chapter to analyze NO_x emission concentration with the help of test data generated.

7.3 Direct injection system for hydrogen-fueled IC engines

The role of direct cylinder injection in getting rid of the combustion problems related to the hydrogen engine has long since been realized. Smooth combustion helps improve the performance characteristics and lowers the exhaust emissions (Verhelst and Wallner, 2009). In the IC engine literature, the injection process has been described from different angles depending upon the predominant feature. Direct injection (DI) has been classified as early DI if the injection takes place during the early phase of the compression stroke soon after the intake valve is closed. Similarly, late DI signifies the situation when injection takes place in the later phase of the compression stroke. In a similar way, the injection process could be classified as high-pressure or low-pressure injection. The pressure varies over a very wide range (between 5 and 300 bars) and, in fact, there is no distinct well-defined boundary between these techniques. During the in-cylinder injection, the injector has to survive the hostile environment due to high temperature and pressure and should ensure smooth combustion and meet the requirement of extremely high volume flow rate (Das, 1990b; Boretti, 2011). A closer analysis of the DI system clearly shows that injection timing plays a very critical role as far as the mixture formation and subsequent combustion characteristics are concerned. Thus the injection parameters such as injection timing, start of injection, and injection duration have some influence on NO_x emissions. As reported (Verhelst and Wallner, 2009), Figure 7.8 reflects some test data indicating the NO_x concentration level in response to the start of injection and at various equivalence ratios (Kirchweger et al., 2007; Blotevogel et al., 2004).

Optical techniques such as LIF (laser-induced fluorescence), LIBS (laser-induced breakdown spectroscopy), and SIBS (spark-induced breakdown spectroscopy) have
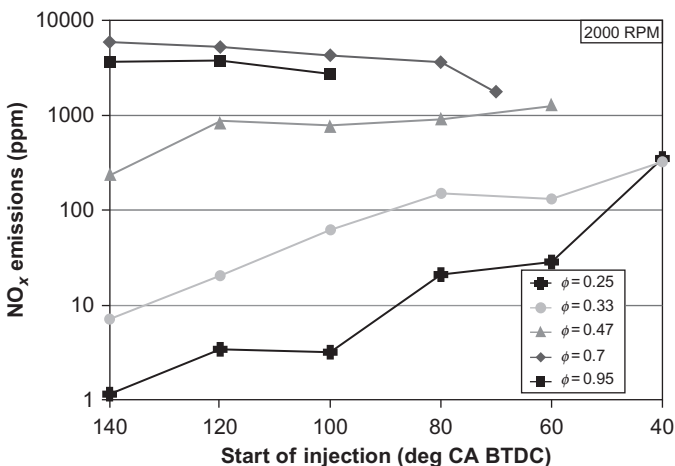
Figure 7.8 NO_x emission with different injection timings (Verhelst and Wallner, 2009).

been adopted by several researchers (Shudo and Oba, 2009; Salazar et al., 2009; Roy, 2013) to critically investigate the effect of mixture strength, localized equivalence ratio, and combustion characteristics in DI engines. Researchers at Sandia National Laboratory have studied the effect of mixture strength and the character of flame propagation in DI hydrogen-operated optical engine (Kaiser and White, 2009).

The turbocharged diesel engine adopting direct cylinder injection can be very useful in a dual-fuel mode of application in the transport sector. Such a system can utilize the operational advantages due to higher compression ratio, lean mixture strength, and use of exhaust energy. The most ideal configuration for hydrogen-diesel injection strategy could perhaps be the installation of two separate injectors in the combustion chamber to ensure efficient and timely injection of both the fuels. A research paper by de Oliveira et al. (2013) discusses an electronic control system for hydrogen injection in a diesel power generator.

Many advantages of the DI system were also reported by Mohammadia et al. (2007), who carried out some work on the technique on internal mixing of hydrogen with air. These research results bring out the significance of optimal injection timing in raising thermal efficiency and power output and at the same time lowering the NO_x emission level under smooth engine combustion conditions.

7.4   Performance characteristics of a hydrogen engine

The lower flammability limit of hydrogen is about 4% by volume and the upper limit is about 75% by volume. This property of hydrogen is best suited for quality regulation in which air intake need not be throttled. It has often been observed that part load operation by throttling brings down the efficiency because of the pressure drop across the throttle. In an unthrottled operation the mixture strength can be altered at wide-open throttle condition. The engine design has also been observed to be critical to the engine's thermal efficiency at low load conditions. Throttled engines show lower thermal efficiency.

In the course of exhaustive tests with TMI configuration at IIT Delhi, it was observed that during the ultra-lean operation of the hydrogen engine (equivalence ratio in the range of around 0.24–03) some amount of throttling was essential for continued stable operation. Such a feature has also been reported by other researchers on the hydrogen engine (Furuhama et al., 1977; Li et al., 1984; Adt et al., 1974; Pischinger, 1977) even though the fuel induction technique was not through TMI. Thus it is evident that, due to an excessive amount of unburnt hydrogen in the very lean mixture zone, some amount of throttling becomes necessary to achieve stable engine operation. Figure 7.9 shows an experimental research test rig that has the facility of changing several operating parameters (such as compression ratio, spark timing, etc.) under dynamic condition. A specially designed cam-actuated injection system (Das, 1986) has been installed on the engine to facilitate timed manifold injection of hydrogen fuel.

An appropriately designed TMI system embraces the benefit of both the SI and the CI engine. The engine can run on a higher compression ratio as compared to a gasoline-fueled engine. As shown in Figure 7.10, an SI hydrogen-fueled engine using

Cam-actuated hydrogen injection system installed on a variable compression ratio engine

Cam actuated
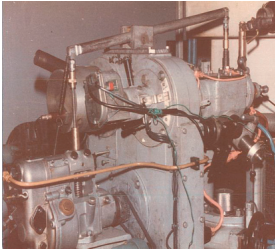
- Uses a lift rod moved by a cam and the motion being transmitted through a especially designed linkage

- Engine control depends on the response controllability, durability and the fuel — feeding capacity of the injector

Figure 7.9 A specially designed cam-actuated hydrogen gas injection system.
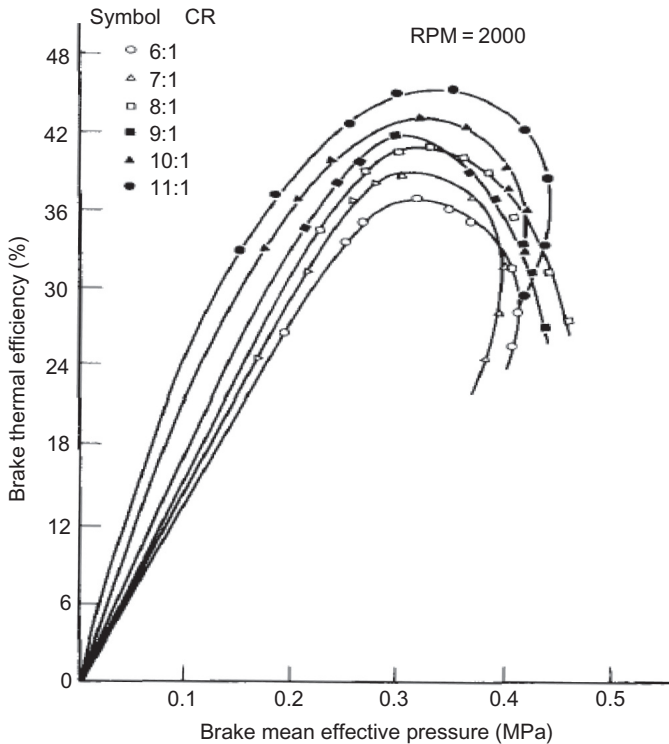
Figure 7.10 Variation of brake thermal efficiency with varying compression ratio (Mathur and Das, 1991).

TMI is capable of giving a thermal efficiency of more than 40%. Besides, there are several research results indicating that the response of the engine to run at a range of high mixture dilution (adopted by exhaust gas recirculation (EGR) or by way of introducing an excess air) is another dominant feature of the engine's increased thermal efficiency.

It is perhaps not a technically justified exercise to compare the power developed by a hydrogen engine with that of a gasoline engine. The only apparent logic to carry out this comparison hinges upon the fact that, at present, there is no specific engine system designed on properties of hydrogen fuel. All the studies are carried out on gasoline engines converted to hydrogen operation.

Maximum power output capabilities for a hydrogen engine is dependent on the design of the engine The pre-IVC configurations develop lesser power due to partial displacement of air by gaseous hydrogen fuel. In such engines, use of a supercharger can improve the power output. It has been reported by researchers that volumetric efficiency can be improved by supercharging. However it results in very high combustion chamber pressure and also high rate of pressure rise. As far as the noise level is concerned, in limited tests carried out in IIT Delhi, relatively higher noise was experienced. This aspect of hydrogen engine has not been adequately investigated and there is scanty literature available.

In-cylinder injection, by definition, increases the effective fuel charge per cylinder as hydrogen gas enters into the cylinder, which is already filled with air. In a broader sense, this can be considered to be a "supercharging effect" as the density of the charge gets increased. Essentially the post-IVC configurations give out higher power output mainly because of high-pressure injection. At this stage of hydrogen engine development, if an injected system can compensate for the power loss to a very great extent, the engine weight penalty from using supercharger in a carbureted engine does not seem justified. In a TMI configuration, some efforts were made to adopt hydrogen pressurization by increasing the supply pressure. The objective of these sample tests was to determine if any substantial improvement occurs in volumetric efficiency loss. There was no significant improvement.

Ignition timing plays a very crucial role for the power output depending upon the strength of mixture. As the equivalence ratio is reduced, the power output occurs at further advanced timings. Such a trend could be attributed to the decrease in the flame speed of hydrogen with the decreasing equivalence ratio. Such a phenomenon could be prevented by earlier ignition of the fuel charge so as to complete the combustion process.

Compression ratio has been a decisive operating parameter for the entire family of IC engines, as it influences the cycle temperature, burn rate, and end gas temperature. Thus it is very closely related to backfire conditions in a hydrogen engine. It has been reported in the literature that CI of hydrogen could not be attained even at a compression ratio of 29. On the other hand, hydrogen engines can run on a relatively higher compression ratio as compared to gasoline fueling. In the SI engines, increased compression ratio causes an increase of the area-to-volume ratio of the combustion chamber. This reduces the amount of residual gases and thus increases the cooling rate. The cooling effect helps to reduce the possibility of backfire due to residual gas ignition.

7.5   Undesirable combustion

It is essential that the undesirable combustion phenomena should be avoided in a hydrogen engine so as to get benefit from its performance and emission features. The abnormal undesirable combustion phenomena, depending upon the engine

operation, manifest themselves in different forms such as backfire, surface ignition, preignition, knocking, and rapid rate of pressure rise. Preignition, by definition, refers to the condition when the air–fuel mixture gets ignited before timed SI. Preignition is often caused by surface ignition at engine hot spots such as engine deposits, spark electrodes, and valves. If preignition occurs near the fuel intake valve, it results in the flame front traveling to the fuel induction system. The magnitude of damage has been reported to be from a simple misfire to the complete destruction of the fuel induction system and even the other engine components. In a different situation, when the preignition occurs away from the intake valve it gives rise to combustion knock. It is well known from the literature that knocking conditions take place when the end gas spontaneously ignites, thereby causing the rapid release of the remaining energy, which, in turn, gives rise to high-amplitude pressure waves. Some studies related to knock have been carried out using critical operating parameters such as intake air temperature, equivalence ratio, and compression ratio. These studies have clearly shown that knocking has very adversely affected the operating conditions of the hydrogen engine. Some research results have shown that knocking conditions were not so glaringly observed (as in the case of a conventional gasoline engine). This aspect needs to be further investigated to arrive at definite conclusions with respect to the hydrogen engine. Combustion knock is often characterized by rapid oscillation in cylinder pressure accompanied by a pinging noise. However, a knocking condition does not result in such severe damage as compared to the effects of backfire, but it affects the engine power output and efficiency.

It has been reported that steps such as use of the proper design of spark plug (for hydrogen ignition), provision of efficient case ventilation, and use of sodium-filled exhaust valve have proven effective in controlling the preignition phenomenon. Appropriately TMI and direct cylinder injection also avoid preignition tendency. Backfire occurs due to combustion of fresh charge during intake stroke either at the intake manifold or in the combustion chamber. It has not been widely studied to support the theory that backfire is often is preceded by preignition. As preignition results in heating up the combustion chamber, it also creates a situation conducive to backfiring in a consecutive cycle. Thus any preventive steps taken to get rid of pre-ignition, to some extent, also helps in suppressing backfire tendency.

Several techniques have been adopted to control the tendency of backfire, which has been reduced by the use of water injection or by adopting EGR. Both EGR and water injection have proven to be useful in cooling the "hot spots" and increasing the resistance of the mixture to preignition. These methods have often reduced the severity of the backfire, but have not been capable of totally getting rid of the problem. In some cases, these techniques demonstrate only short-term effectiveness. The experience in IIT Delhi has shown that water induction needs an onboard storage arrangement along with a pump. Sometimes distilled water becomes necessary. Sometimes "normal" engine deposits lead to flashback unless the water flow is increased in the induction system. All such steps indicate that water induction, even though it can effectively reduce the frequency of backfire, cannot be recommended as a long-term solution.

Formation of the appropriate quality of mixture in the combustion chamber also depends largely on the fuel induction technique. The chances of a homogeneous

mixture formation are relatively higher in a pre-IVC engine, because the air and the gaseous hydrogen fuel have enough time to mix. TMI is designed to inject hydrogen fuel only after an adequate quantity of air enters the combustion chamber and cools down the potential hot spots, thereby rendering them incapable of causing preignition and flashback. The designed TMI system prevents a situation leading to uncontrolled combustion. Figure 7.11 shows the smooth combustion attained in a TMI-operated hydrogen engine.

The inherent merit of direct cylinder injection in precluding the backfire has been well documented in the literature. Recent efforts to develop leak-proof injectors for prolonged engine operation have been successful in obtaining part load and full load efficiency improvement with extremely low emissions. Combustion improvement strategies with split injection have been successful in achieving stratification (Shudo and Oba, 2009; Wallner et al., 2009).

A paper by Sebastian et al. (Verhelst and Wallner, 2009) discusses many critical combustion features such as backfire, preignition, auto-ignition, and knocking related to hydrogen combustion in engines. The paper also compares the in-cylinder cylinder pressure with intake manifold pressure against crank angle for a combustion cycle with preignition phenomenon (Figure 7.12). As shown in this diagram, when the pre-ignition occurs, the peak pressure increases as compared to a normal combustion cycle. Verhelst et al. (Verhelst and Wallner, 2009), apart from preignition, have also provided very significant information on cylinder pressure and intake pressure under conditions of backfire.

Figure 7.13 presents a comparative picture of typical cylinder pressure and intake pressure variation with respect to crank angle in a backfiring cycle as compared to regular pressure traces (Verhelst and Wallner, 2009). A closer look at the two figures (Figures 7.12 and 7.13) provides adequate information to conclude that preignition and backfire are very closely interrelated. Quite often the combustion chamber gets heated up by preignition and thus the situation becomes conducive to subsequent backfire.
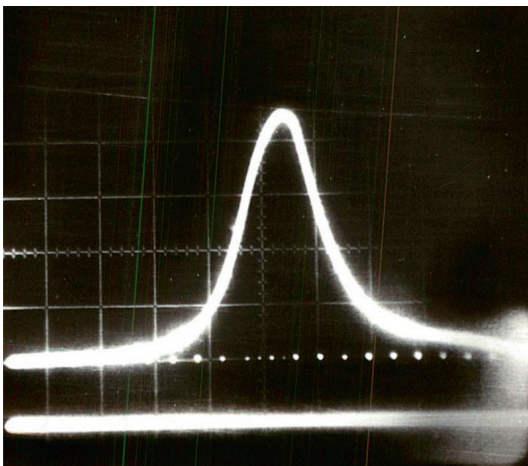
Figure 7.11 Pressure trace of hydrogen combustion (Das, 1986).
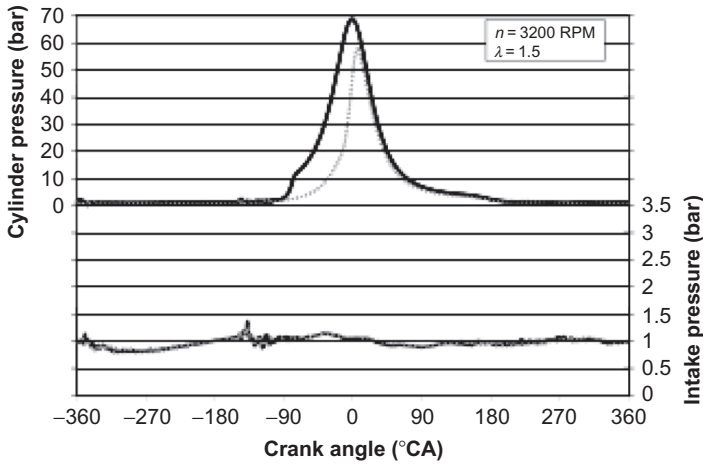
Figure 7.12 Typical cylinder and intake manifold pressure traces with preignition (solid lines), compared to regular pressure traces (dotted lines) (Verhelst and Wallner, 2009).
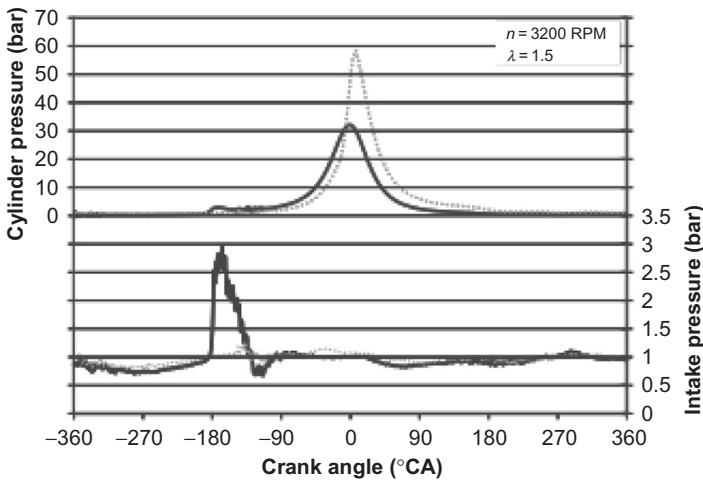
Figure 7.13 Typical cylinder and intake pressure traces for backfiring cycle (solid lines), compared to regular pressure traces (dotted lines) (Verhelst and Wallner, 2009).

The spontaneous auto-ignition of the end gas resulting in rapid release of energy produces high amplitude pressure waves, thereby resulting in knock. Figure 7.14 represents the cylinder pressure signal indicating the pressure oscillation of a mild knocking cycle. On the other hand, Figure 7.15 shows a heavily knocking cycle for the same engine at the same operating conditions of load and speed. A comparative assessment between the two figures (Figures 7.14 and 7.15) very distinctly shows the high magnitude of pressure and the corresponding high-pass filtered signal in the knocking cycle.
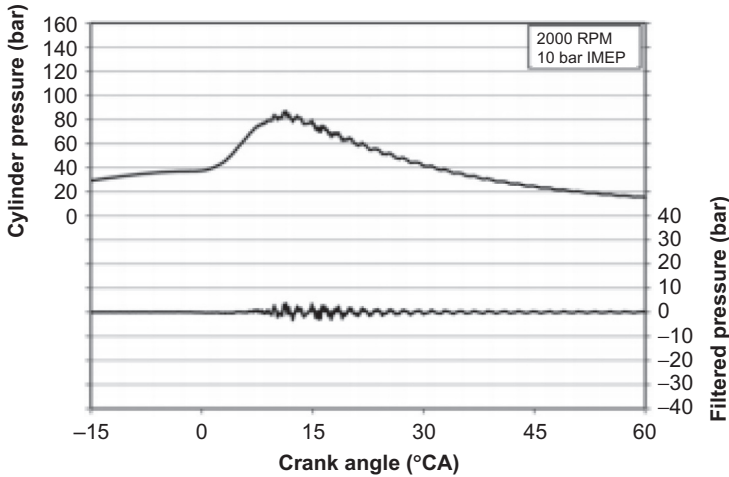
Figure 7.14 Typical cylinder pressure trace for light knocking cycle (Verhelst and Wallner, 2009).
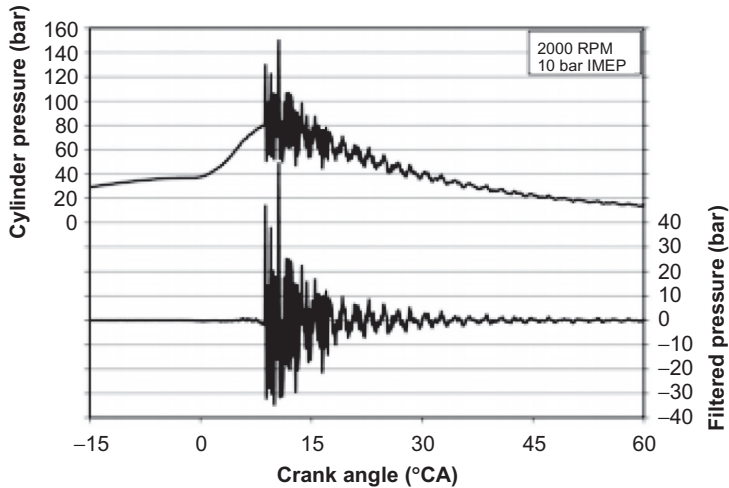
Figure 7.15 Typical cylinder pressure trace for heavy knocking cycle (Verhelst and Wallner, 2009).

7.6 Safety

Hydrogen happens to be one of the most flammable and explosive fuels; it must be handled with appropriate respect and safeguards. Safety aspects of hydrogen are the most common concern of the general public. The spontaneous fear reaction is probably attributable to "hydrogen bomb" and the Hindenburg fire. On a volume-of-gas basis, hydrogen has a lower explosion potential than either methane or propane;

but on a mass-of-fuel basis, hydrogen has the most explosion potential. It is important to recall here that volume considerations are more pertinent to storage safety. It has been discussed earlier that hydrogen, being the smallest and lightest element in nature, diffuses rapidly to the surroundings in noncombustible proportions. Low molecular weight of hydrogen results in high molecular diffusivity, such that hydrogen diffuses 3–8 times faster than air. Hudson et al. have discussed the technological advances and the challenges faced in the area of hydrogen storage from a safety point of view (Hudson et al., 2009).

Hydrogen fires burn very rapidly and radiate very little heat, and thus are relatively short lived. A person can be closer to a hydrogen fire than a gasoline fire without being burned. Hydrogen needs very little energy to ignite as compared to methane or gasoline but in a weak ignition source such as an electrostatic spark, there is already sufficient energy to ignite hydrogen. Sometimes during tests in the laboratory, it has been extremely useful to install a nonreturn valve (Figure 7.16) in the engine induction manifold so that reverse flow of hydrogen from the engine cylinder to the induction manifold is avoided (Das, 1991a). It is perhaps important to stress here that inherent reliability criteria connected with leakage, wear, corrosion, and material incompatibility of several parts used in a hydrogen engine system should be evaluated from strength, hardness, and machinability points of view depending upon the application. Permeability of steel to hydrogen is relatively low at room temperature, whereas the diffusion coefficient of hydrogen in steel is quite high (Das, 1991a). Flame arrestors are quite often used in several hydrogen-operated systems.

Flame arrestor is a system for suppressing explosions inside a hydrogen-containing system. In general, flame arrestors are installed upstream and downstream of possible ignition sources in piping systems containing hydrogen gases.

Hydrogen flame is invisible. This property is a big threat. As indicated in Figure 7.17, there have been some studies with conditions of making the hydrogen flame visible.

Leak detection and necessary remedial action form a very important design aspect of a safe hydrogen system. Sensors can be installed in enclosed areas to detect concentrations of hydrogen approaching 4% by volume (the lowest point at which ignition can occur). BMW's prototype cars, running on liquid hydrogen, have windows and sunroofs that open if hydrogen is detected.

M. R. Swain of the University of Miami carried out a very exhaustive study on several configurations of hydrogen engines. During his long career in hydrogen research, he probably felt that the safety aspects of hydrogen should be shared with the general public. Figure 7.18 clearly demonstrates that hydrogen could be safer than gasoline if properly handled.
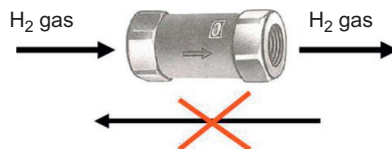
Figure 7.16 Nonreturn valve for hydrogen routing.
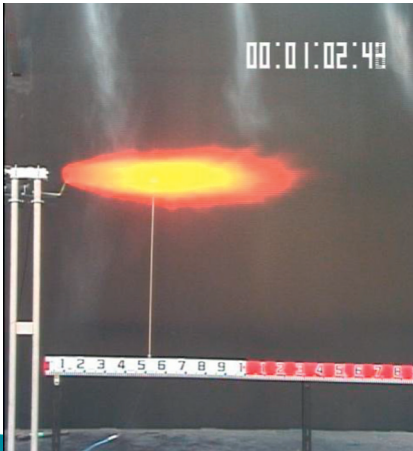
This photograph shows the measurement of the size and temperature of a high-pressure hydrogen jet flame. Since a hydrogen flame is almost invisible, the flame was made visible by using sodium.

Source:
http://www.unit.aist.go.jp/rces

Figure 7.17 Jet flame of high-pressure hydrogen.

Hydrogen flame versus gasoline flame

Photo from a video comparing an intentional hydrogen tank release and a small gasoline fuel line leak. After 60 seconds, the hydrogen flame has begun to subside, while the gasoline fire is intensifying. After 100 seconds, all of the hydrogen was gone and car's interior was undamaged (the maximum temperature inside the back window was 67 °F). The gasoline car continued to burn for several minutes and was completely destroyed.

Dr. Michael Swain, University of Miami

Figure 7.18 Demonstration of hydrogen safety: hydrogen fire versus gasoline fire.

7.6.1   Exhaust emissions

As far as the exhaust emissions from hydrogen engines are concerned, pollutants such as carbon monoxide (CO), hydrocarbons, oxides of sulfur, particulates, and a host of other common vehicular pollutants are intrinsically absent. Hydrogen fuel, upon combustion, does not produce either benzene (a carcinogen) or formaldehyde (a toxin). As has been mentioned elsewhere, traces of HC and CO are sometime present in the exhaust, which are due to lube oil (Das, 1991b). Such low quantities could be almost eliminated if a regular inspection and maintenance program is adopted to ensure normal oil combustion without any excess oil combustion. Some researchers have observed the presence of hydrogen peroxide and NO_x in the engine exhaust (Homan et al., 1983). It is appropriate to recall here that hydrogen peroxide, decomposed in the atmosphere, forms hydroxyl radicals that contribute to the formation of photochemical smog. Hence the hazardous effects of hydrogen peroxide on the environment cannot be ignored. Not enough studies have been carried out on the measurement of the hydrogen peroxide concentration from the exhaust of a hydrogen-operated engine. Sinclair and Wallace (1984) have suggested that hydrogen peroxide concentration at lower equivalence ratio results from quenching of preflame reactions. However, the available research results have indicated that the concentration level is too low to pose any threat. Tests carried out in a multicylinder hydrogen engine over a wide range of equivalence ratios (from 0.2 to stoichiometric) have shown that hydrogen peroxide is practically zero at a lean mixture less than 0.5. Some researchers have reported water condensed from exhaust had low levels of hydrogen peroxide.

NO_x happens to be the only pollutant of concern for a hydrogen-operated SI engine. NO_x often causes long-term respiratory problems. NO_x, in a series of chemical reactions along with reactive hydrocarbons, has been responsible for ozone formation. The bad effects of ozone on health are too well known to be further amplified. Breathing ozone can trigger a series of health problems ranging from simple coughing and throat irritation to severe health problems such as chest pain, bronchitis, and asthma.

NO_x emissions in any IC engine are dependent upon the reaction temperature, combustion duration, and available oxygen. Thus the equivalence ratio has a definite role to play. There are several ways to control the NO_x level in a hydrogen engine's exhaust. Operating the engine in a lean or ultra-lean mode decreases the temperature, thereby reducing the NO_x level. Engine operation with a very rich mixture can also be fruitful because it reduces the oxygen supply. However, running the engine in a rich mixture increases the possibility of backfire; therefore, this should preferably be avoided. Monitoring the engine combustion to reduce the burn time or lowering the engine RPM to ensure better heat dissipation are also some of the operating conditions that help reduce the NO_x level. Water injection and EGR have also been successful in controlling the NO_x level to some extent in the exhaust. Tests have been carried out employing all these techniques in IIT Delhi. But none of them have demonstrated enough long-term effectiveness to be adopted in hydrogen-operated vehicles. On the other hand, lean engine operation using hydrogen injection has proven to be a very sound technique, which could drastically reduce the NO_x emission and can produce a nearly "zero-emissions" system as shown in Figure 7.19 (Das, 1991b).
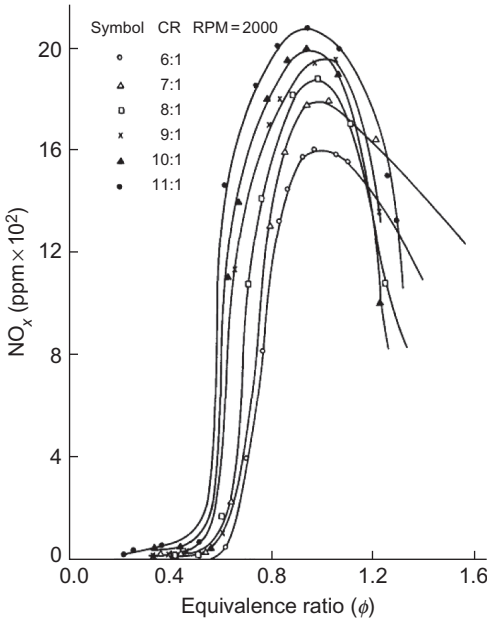
Figure 7.19 NO_x emissions from a hydrogen-operated engine.

7.7 IC engine-based vehicle development

In course of this historical review of hydrogen engine development, it was noted that several researchers made efforts to buildup hydrogen-operated IC engine at different phases of engine development. The efforts of Erren have been mentioned earlier. Furuhama and his team persistently followed hydrogen engine research (Furuhama et al., 1978; Furuhama, 1981; Furuhama and Fukuma, 1986) in several configurations of engines and converted vehicles to operate on hydrogen. In 1975 they successfully demonstrated the satisfactory operation of a hydrogen car. This accomplishment sent a very strong signal in favor of hydrogen-fueled vehicles as a technical reality.

There were several other successful efforts and achievements by several groups during that period (the 1970s). The UCLA car (Finegold et al., 1973) developed by a group of very enthusiastic students also received a lot of appreciation from hydrogen researchers. Frank Lynch, a member of this team of students, continued to engage in the hydrogen engine/vehicle R&D program, and has made valuable contributions to the technology over the years. In one of his early research publications, he suggested a simple method of parallel induction for fueling the hydrogen engine (Lynch, 1983). As far as the tests on vehicular engines are concerned, many groups at several places have carried out successful demonstrations. And as far as prototype vehicles are concerned, BMW and Ford have developed dedicated hydrogen vehicles built on IC engines (Gopalakrishnan et al., 2007; Lapetz et al., 2006; Wallner et al., 2008; BMW, 2006).

The world's first hydrogen-powered three-wheeler, HyAlfa, was launched at the Pragati Maidan, New Delhi, India, on January 9, 2012. The United Nations Industrial Development Organization (UNIDO) funded this project to a consortia consisting of IIT Delhi, Mahindra, and Air Products (USA). Exhaustive lab tests were carried out on the vehicular engine at IIT Delhi under varying operating conditions. The lab test results provided the technical guidelines and thus the existing designs of engines were converted to run on hydrogen. Based on these tests, hydrogen-operated three-wheelers for passenger and cargo version vehicles have been developed and these vehicles were launched during Auto Expo 2012, in Delhi. A hydrogen refueling station has also been set up by Air Products. These vehicles are still undergoing road trials for long-term road tests. After the completion of the phase of the project funded by UNIDO, the government of India (Ministry of New and Renewable Energy) has sponsored the continuation of extensive field trials. Figure 7.20 shows a typical passenger vehicle and Figure 7.21 shows the arrangement of a bank of cylinders installed in the fueling station. Figure 7.22 shows the NO_x emissions from these vehicles, and it can be seen that

Figure 7.20 Hydrogen-powered passenger three-wheeler.

Figure 7.21 Cylinder bank/cascade installed at the hydrogen fueling station.

	1200	1600	2000	2400	2800	3200	3600
■ Gasoline	95.28	12.22	2.373	1.871	1.535	1.507	1.469
■ Hydrogen	3.4	2.619	4.618	4.98	0.253	0.196	1.656

Engine speed, rpm
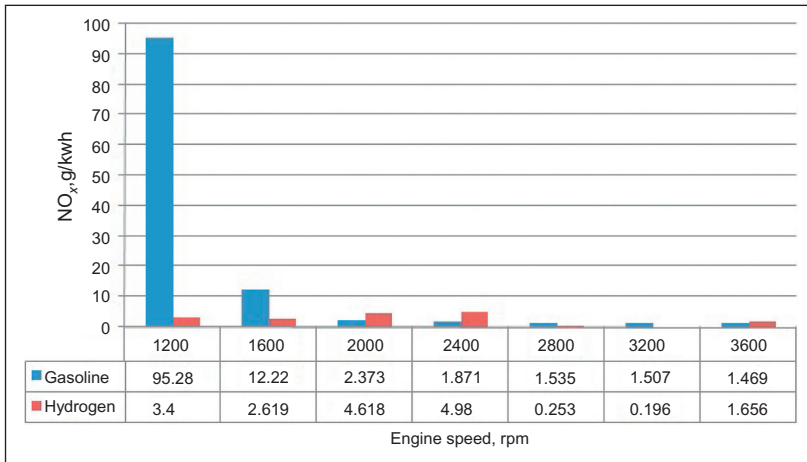
Figure 7.22 NO_x emission from hydrogen three-wheeler.

the NO_x level from hydrogen operation is negligible as compared to those from gasoline fueling (Natarajan et al., 2013).

7.8 Criteria for hydrogen-specific engine design

By now a lot of test data have been generated on the hydrogen-operated engine in various configurations. Even though dedicated hydrogen engines have not yet been developed, pertinent data on the engineering description toward an optimal hydrogen engine is now available. In this context it is perhaps desirable to have a look at the different aspects of design that are relevant to a hydrogen-specific engine. In the following paragraphs some efforts are made to highlight the operating parameters of engines that are critical to an optimum hydrogen engine. The design features should concentrate on three major shortcomings related to power output, NO_x emission in the engine exhaust, and undesirable combustion symptoms.

It was discussed earlier that power density of a naturally aspirated pre-IVC hydrogen engine is lower than a corresponding gasoline-fueled engine. Therefore, some steps have been adopted to recover the power density. Intake air pressure boosting has been a well-proven technique that has been successfully adopted to increase peak engine power. The same technique could also be used for pre-IVC hydrogen engine configurations. Experimental activities on boosted hydrogen engines have been investigated by several researchers. The well-known group of hydrogen engine researchers at Mushashi Institute of Technology carried out a series of tests on engines as well as vehicles (Furuhama and Kobayashi, 1982, 1980; Furuhama and Azuma, 1978) and reported tests on a turbocharged two-stroke liquid hydrogen engine and also

performed the tests on the vehicle. The literature reveals that tests using hydrogen-hybrid vehicles also showed a similar trend of increased power output due to boosting. Automobile manufacturers such as BMW and Ford also reported to have achieved substantial improvement though these techniques. Several research investigations have already shown that power density of a hydrogen engine can be enhanced by way of supercharging and adopting a variable equivalence ratio strategy. Such a strategic control technique has also been successfully adopted (Stockhausen et al., 2002; Natkin et al., 2003) to achieve increased power output under lean-burn conditions.

Despite so many distinct advantages, boosting pressure has very strong limitations from an application point of view. Boosting pressure results in raising the temperature and pressure of the charge that, in turn, amplifies the possibility of uncontrolled combustion and also results in an increased NO_x emission level.

Another configuration of hydrogen engine using multimode strategies has been observed to be characteristically closer to pressure-boosted hydrogen engines. Two modes of fueling techniques are incorporated into the system. The dual injection mechanism (Lee et al., 2002) is carried out such that the port fuel injection is used during the low to medium load engine operation and direct cylinder injection is done at peak load conditions. Research results have been very useful with dual injection strategies. A comparative assessment shows that a dual injector thermal efficiency with port fuel injection shows an improvement of about 15–30% over direct cylinder injection at low to medium loads. On the other hand, a direct cylinder injection strategy results in an improvement in power to the tune of 60–70% over the corresponding port fuel injection system. These results provide ample guidelines for the design of hydrogen-specific engines.

Judging the fuel induction techniques exclusively from a smooth combustion point of view, one can appreciate the potential benefit of direct cylinder injection because it is the sole technique that, by definition, avoids backfire. It is perhaps appropriate to mention here that cycle variation is higher in the case of a DI engine as compared to TMI or port fuel injection. This is so mainly because of the inadequate time available for mixing. It has been reported that cycle variation in a hydrogen engine increases gradually with the increase in speed. The optimum injection timing coincides with the timing of inlet valve closure, and any deviation from this timing results in sudden cycle variation. The causes leading to cyclic variation in a hydrogen engine with direct cylinder injection has been investigated by Kim and coauthors (Kim et al., 2005). Interesting research results on cyclic variation in combustion and the heat release delay has been reported by Nakagawa and his team (Nakagawa et al., 1982).

The spark plugs used for gasoline-fueled SI engines are designed to operate at the higher temperature necessary to burn off the combustion chamber deposits. However, combustion in the hydrogen-operated engine does not result in any such deposits. Thus, the standard spark plug, which falls in the "hot range" can often be at a temperature higher than the ignition temperature of hydrogen. So the spark plug itself is a vulnerable potential hot spot to promote backfire. Besides, if the spark plug gap is excessive, the ignition energy required is significantly increased. If the ignition system of the engine fails to supply this level of energy consistently, the SI becomes

unreliable. Under such circumstances, thermal ignition may occur late in the compression stroke or early in the power stroke. In the absence of any control of timing of combustion, the usual problems associated with overadvanced or overretarded spark timing take place resulting in either high peak temperature or delayed peak temperature. This might make the combustion temperature hotter when the intake valve opens. Hence the spark gap setting is crucial to hydrogen operation. Therefore, the spark plug is gapped at a narrow setting so as to take advantage of the low minimum quenching distance of hydrogen and to ensure stable combustion. Spark plugs with platinum electrodes are not recommended for use in a hydrogen engine as they can function as catalysts to hydrogen oxidation. Extensive tests at IIT Delhi have shown that cold spark plugs have been observed to be very useful in avoiding backfire condition (Mathur and Das, 1991) because the spark plug electrode temperature is maintained below auto-ignition temperature.

It was repeatedly discussed earlier that equivalence ratio ensuring ultra-lean operation improves efficiency, reduces NO_x emissions, and at the same time avoids a situation leading to backfire. Therefore one design strategy is to limit to ultra-lean mode only. Engine operation in high ranges of power output is one of the major constraints. This effect can be counterbalanced either by raising the compression ratio or by adopting supercharging. The other design feature could be to increase the engine displacement such that the size of the engine is increased. The cylinder operating pressure is lower than the pressure corresponding to stoichiometric condition. The temperatures are also lower. These conditions of temperature and pressure provide the option to select appropriate alternative materials of lighter weight. Such an approach requires a very substantial alteration in engine design, and could raise questions of system complexity. Raising the compression ratio and adopting the most effective fuel induction mechanism and load control have to be optimized, taking into consideration several significant parameters. In-cylinder turbulence and consequent flow characteristics need to be very carefully investigated.

7.9   Hydrogen blended fuels

The preceding discussions were related to total hydrogen operation in SI engines. That was because the SI engines could be converted to total hydrogen operation. However, in view of its "clean-burning" characteristics hydrogen fuel is also being considered for use in combination with other conventional and alternative fuels. Combustion effects of hydrogen on the other hydrocarbon fuels have been reported in bomb experiments as well as in IC engines. Lewis and Elbe (1987) also have provided very useful information indicating the influence of hydrogen on the combustion phenomena of other fuels such as methane. Several investigations in different parts of the world are being carried out using hydrogen in combination with gasoline, diesel, compressed natural gas (CNG), liquefied petroleum gas, biodiesel, and many other alternative fuels in IC engines. Many interesting results have come out of these tests. In some

cases, the field application of this blended fuel has been successfully demonstrated. An elaborate discussion on all these aspects is beyond the scope of the present work. Only restricted discussions have been attempted about some of the blended fuels that are being seriously considered for practical field application as regular alternative fuels. Thus we propose to discuss briefly (i) hydrogen-CNG blend and (ii) hydrogen-diesel dual-fuel engines. As will be evident from the following discussions, a great degree of success has been achieved in these engine technologies. A lot of research has already been done on the hydrogen-supplemented gasoline-fueled engine. The present work does not attempt to discuss this topic because presently the global thrust is on neat hydrogen for SI engines with the objective to develop a "zero-emissions" vehicle.

7.10   Hydrogen–CNG blend

Recently, there has been widespread use of hydrogen blended to CNG in engines and vehicles. It is advocated by some researchers that the change from a liquid fuel (petroleum) economy to a gas fuel (CNG) economy is taking place rapidly, and the transition to a "hydrogen economy" will occur much faster. If the ultimate goal is to introduce the ultra-clean fuel hydrogen by way of displacing fossil fuels, it must be simultaneously realized that an abrupt change is not possible from either an economics or a technological point of view. Thus the transition to a total hydrogen economy can take place through a middle path. In this context it is relevant to mention the progress in the technology of blending hydrogen to CNG and use of the blended fuel (HCNG) in IC engines.

Natural gas is being successfully used as an alternative vehicular fuel for IC engines in several countries. One of the major limitations of CNG has been its low flame speed. Methane (the most predominant constituent of CNG) has a much lower flame speed than most of the hydrocarbons, including gasoline at engine cylinder pressure. This property reduces the burning time of HCNG blend as compared to that of neat CNG. Lesser burning time results in improved efficiency. However, as far as the exhaust emissions are concerned, pollutants such as carbon monoxide, carbon dioxide, and hydrocarbons are found to be less for hydrogen-CNG blend. HCNG NO_x emissions show an increasing trend with respect to neat CNG; tests at IIT Delhi have shown that at least 5–7% of hydrogen addition is necessary for a significant improvement in efficiency as well as power output (Das and Polly, 2005).

The high flame speed of hydrogen can greatly compensate the low flame speed of CNG in a blended fuel. The other benefit from mixing hydrogen and natural gas helps to increase the hydrogen-to-carbon ratio of the fuel. This characteristic of the fuel helps in bringing down the carbon-based pollutants such as carbon monoxide and carbon dioxide. Thus the engine can adopt lean-burn operation, which results in achieving higher thermal efficiency. It has been observed that for a given power, BTE is higher for HCNG than pure natural gas for a given power output. It had also been

observed from tests that HCNG operation shows an improvement in efficiency. Karim et al. (1996) carried out studies on the combustion aspects of the engine by adding some amount of hydrogen to methane (Swain et al., 1993). The study included a very informative analysis of optimum spark timing, combustion duration, and rate of flame propagation. Swain et al. (1993) carried out some investigations on the influence to an engine's performance characteristics by adding hydrogen to methane. This study reported that the brake thermal efficiency takes a decreasing trend as the excess air ratio is increased. Bysveen (2007) carried out tests to evaluate the performance and exhaust emission characteristics of an engine fueled with CNG and a blend of hydrogen and CNG (referred to as HCNG).

It is evident in Figure 7.23 that for a given power, the brake thermal efficiency for the HCNG operation is substantially higher with respect to neat natural gas operation. These important results provide adequate guidelines for designing of specific HCNG engines. Ma et al. (2007) carried out a series of tests on a natural gas-operated SI engine enriched with various proportions (0%, 10%, 30%, and 50% by volume) of hydrogen. As usually expected, the lean-burn limit could be extended by adding hydrogen because of hydrogen's wide flammability range and fast flame speed. Figure 7.24 provides some test data on combustion duration at various operating conditions of mixture strength.

It is evident in Figure 7.24 that for a given value of lambda, combustion duration is decreased as the hydrogen fraction is increased. This is a very useful trend of behavior because it shows that hydrogen addition could speed up the flame propagation.
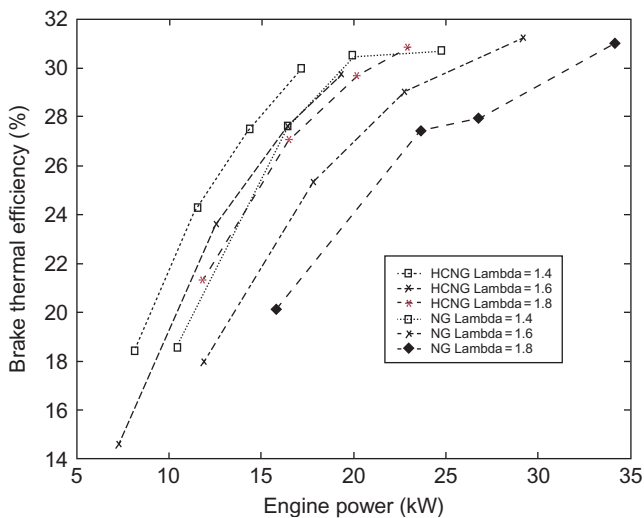
Figure 7.23 Brake thermal efficiency as a function of engine power (Bysveen, 2007).
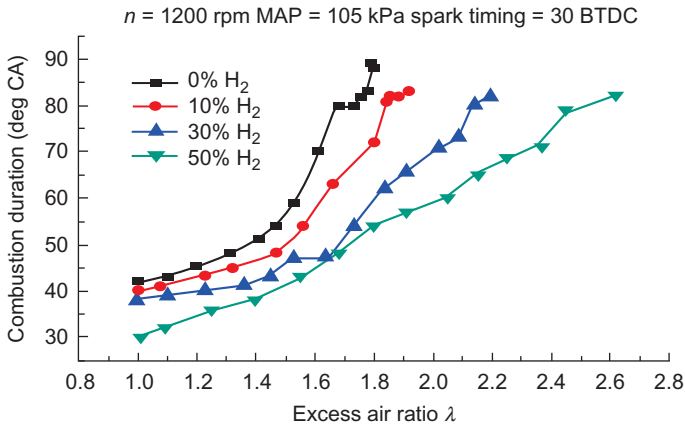
Figure 7.24 Combustion (0–98%) duration versus excess air ratio for fuel blends of various hydrogen fraction, engine speed: 1200 r/min, MAP = 105 kPa, spark advance = 30° (Ma et al., 2007).

7.11 Hydrogen-diesel dual-fuel engine

Use of hydrogen in the CI engine offers a lot of scope for use in developing countries where diesel engines are used for applications such as heavy traction vehicles that need relatively higher power output. In consideration of better thermal efficiency and long-term durability, these engines are used in transport, agriculture, and for decentralized energy applications. However, there are some practical problems in using hydrogen as the only fuel in diesel engines. The low cetane rating of hydrogen makes it unsuitable for use in diesel engines. It has already been discussed that it is difficult to achieve CI of hydrogen because of its high auto-ignition temperature. It has been estimated that a compression ratio of about 55:1 (for the ideal specific heat ratio for air being 1.4) is required to achieve CI of hydrogen. Considering the actual heat transfer in a diesel engine, the heat is transferred to the walls during compression. In such a case it has been estimated that the diesel engine should have a compression ratio of 83:1 (at a specific heat ratio of 1.3) to ensure CI of hydrogen. No diesel engines can have such an abnormally high compression ratio. Therefore, hydrogen diesel cycles have an auxiliary ignition source. Combustion triggering devices such as spark plugs/glow plugs have been partially successful in operating diesel engines of relatively higher compression ratio. Ikegami and his coworkers (Ikegami, 1975; Ikegami et al., 1982) studied the application of hydrogen in a CI engine. The team used a conventional swirl chamber diesel engine. Two different approaches were adopted for tests in this study. One set of experiments used CI on an air-aspirated engine system, and the other set was on an engine operating with an argon-oxygen charge. Interesting results were achieved in these sets of experiments, which showed

that both pilot injection and fuel leakage from the injector can be useful to ensure ignition in a diesel engine and bring about smooth engine operation. It is perhaps interesting to mention here that ignition in a hydrogen-operated diesel engine can also take place if the injector is leaking, even without the knowledge of the operator. Therefore, the amount of hydrogen leaking (either intentionally or inadvertently) must be carefully monitored to enable stable ignition from the viewpoint of thermal interactions between the engine cycles.

Welch and Wallace (1986) are reported to be successful in their work on a diesel engine using a glow plug. However, the use of a glow plug has been successful in demonstrating the operation of hydrogen in a diesel engine. But this cannot be accepted as a reference for the design of a hydrogen-specific CI engine.

Wong (1990) made some novel attempts to adopt direct cylinder diesel injection in a diesel engine. The engine configuration was modified by installing ceramic parts to build up the desired thermal environment. This was necessary to hold heat to raise the combustion chamber temperature. The technique did not prove successful because the maximum temperature that could be attained in these engines was less than the auto-ignition temperature of hydrogen.

Use of hydrogen in a CI engine has been actively pursued at the Indian Institute of Technology, Delhi. One of the major objectives of this study was to build up the engine on such technology that the systems could be transferred from lab to land. As will be discussed later, an effective method of charge dilution technique (Mathur et al., 1992a, 1993) was adopted to get rid of knocking, which is one of the most serious combustion problems in diesel engines. It is perhaps appropriate here to stress that the countries where the diesel consumption rate is relatively much higher because of its widespread use in several applications can use hydrogen for several decentralized applications such as DG set, pump set lawn mower, and others. The technique for suppressing knocking tendency has been described earlier and is shown in Figures 7.25 and 7.26 (Mathur et al., 1992a,b 1993).

Hydrogen-fueled diesel engine

Figure 7.25 Hydrogen fueled genset.
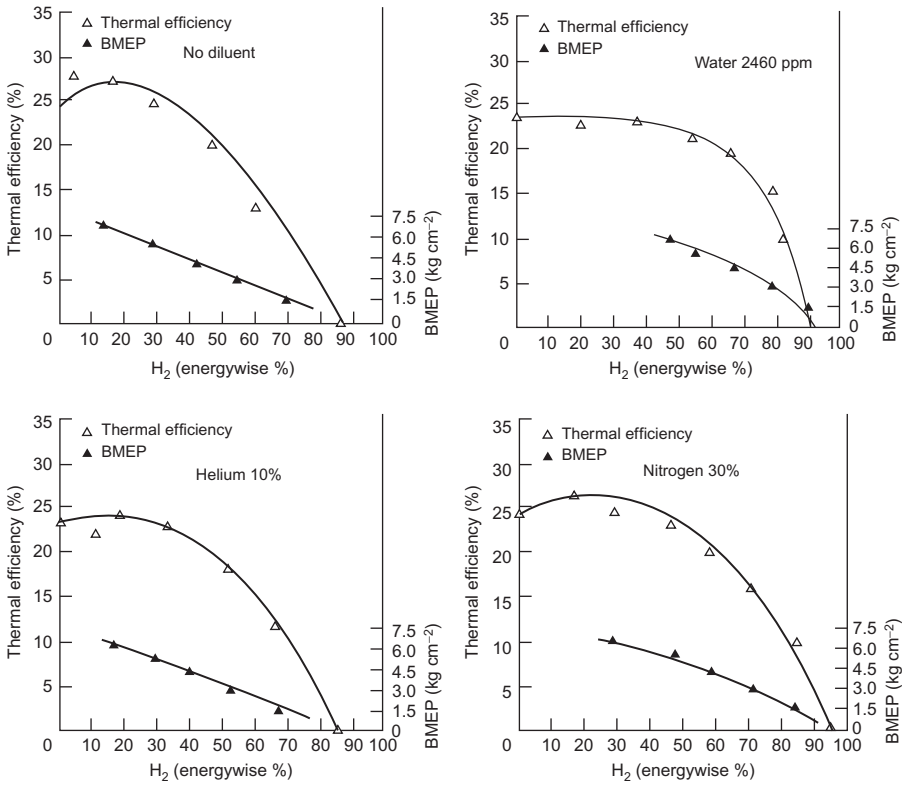
Figure 7.26 Effect of charge dilution on thermal efficiency (Mathur et al., 1993).

It has already been discussed that a reliable fuel induction technique for hydrogen into diesel engines is based upon the mode of dual-fuel operation (see Figure 7.27). In such a configuration, a hydrogen–air mixture can be inducted during suction stroke and a pilot diesel charge could be injected, as usual, to trigger combustion. Studies have been conducted to improve the performance and reduce the exhaust emissions of a hydrogen-diesel dual-fuel engine by using charge dilution technique. Extensive tests were carried out in small utility diesel engines with varying degrees of hydrogen substitution so as to ensure smooth engine operation with optimum performance and emission characteristics. Knocking conditions were effectively got rid of by using charge diluents such as helium, nitrogen, and water vapor.

Diluents such as helium, nitrogen, and water vapor in different proportions were mixed with the inducted charge (see Figure 7.28). Additions of all the three diluents along with the inducted charge resulted in improvement of the knock-limited engine operation. Nitrogen was a better diluent for engine performance, but water vapor proved to be more effective in controlling NO_x and smoke emission. The addition of 2460 ppm of water has been successful in achieving about 66% hydrogen energy substitution.
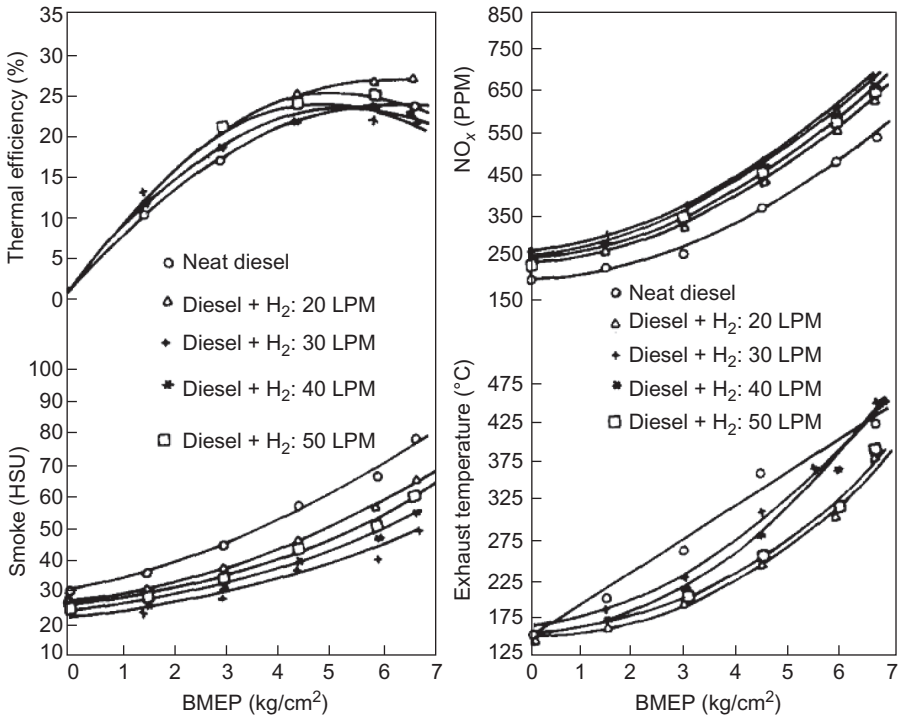
Figure 7.27 Hydrogen supplementation effect on a diesel engine (Mathur et al., 1992b).
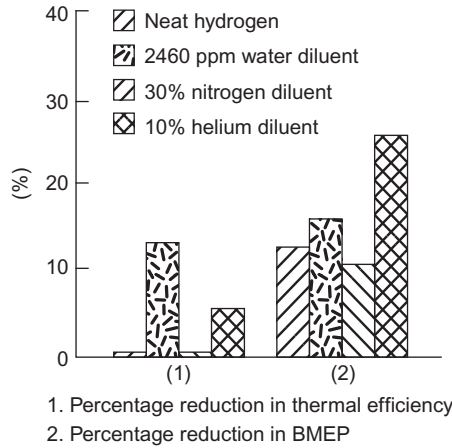
Figure 7.28 Performance parameter comparison with neat hydrogen and different diluents (Mathur et al., 1993).

7.12 HCCI mode of operation for the hydrogen IC engine

Another way of operating hydrogen that provides improvement in performance and emission characteristics of a hydrogen-fueled IC engine is the homogeneous charge compression ignition (HCCI) mode of operation. Neat hydrogen-fueled HCCI operation was possible with equivalence ratios between 0.19 and 0.30 with a compression ratio of 16:1 and intake charge temperatures in the range of 130–80 °C. Significant work was carried out by Ibrahim and Ramesh (2014a,b). HCCI is a concept where in a lean homogeneous mixture of air and fuel is compressed and ignited. Compression of this mixture leads to auto-ignition in multiple locations, followed by combustion that is significantly faster than the conventional Otto or Diesel modes. In HCCI engines, combustion rate is controlled by chemical kinetics. This mode of combustion is known to produce extremely low levels of NO_x emissions because of the low peak temperatures that are reached. HCCI engines have the potential to work with high thermal efficiencies. However, controlling combustion at relatively high equivalence ratios and sustaining combustion at very low equivalence ratios without misfire are some of the problems that are faced.

The addition of hydrogen to the charge in a diesel-fueled HCCI engine was found to be beneficial. HCCI engines with hydrogen being inducted and diesel being injected into the cylinder using a common rail system have been successfully demonstrated. An increase in the amount of hydrogen improved the thermal efficiency (as seen in Figure 7.29) of diesel-fueled HCCI operation by correctly phasing the combustion process. Extremely low levels of NO_x could be reached as seen in Figure 7.30. The NO_x levels were also lower than the diesel HCCI mode. The HC levels that are normally high in the diesel HCCI mode are reduced with the introduction of hydrogen (Ibrahim and Ramesh, 2014b).
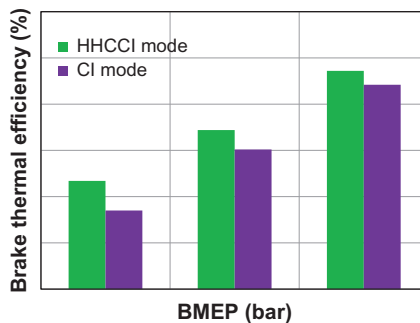
Figure 7.29 Comparison of diesel (CI) and hydrogen HCCI modes: brake thermal efficiency (Ibrahim and Ramesh, 2014a).
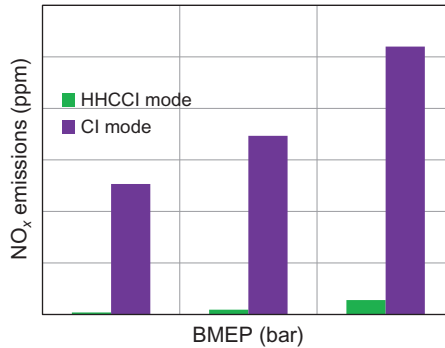
Figure 7.30 Comparison of diesel (CI) and hydrogen HCCI modes: brake thermal efficiency (Ibrahim and Ramesh, 2014b).

7.13   Future outlook and market penetration

By now a lot of test data have been generated on several configurations of hydrogen engine. Thus hydrogen-operated engines can enter into the transport sector, power sector, and several other applications as a production-ready technology that can penetrate into the market.

The objectives of having optimum performance characteristics with low exhaust emission can be attained right now with the excellent manufacturing infrastructure already existing for petroleum-fueled IC engines.

The major part of the discussions presented in this chapter centered around the conversion of existing gasoline or diesel engines. In some cases retrofits, subsystems, and other additional features have been installed at different locations of the engine system without interfering substantially with the basic engine hardware. It was emphasized earlier in this discussion that the conversion technology suffers from some fundamental shortcomings related to onboard storage and fueling the vehicle. Thus it is less likely that conversion technology will evolve to a level so as to be considered for actual prototype system development. However, the tests carried out in the converted engines will provide adequate technical information that can be adopted as guiding factors for building up an actual hydrogen-specific vehicle.

Designing a hydrogen-specific engine can result in a high-quality improved prototype product because the development of such an engine would not only take into account the unique combustion-related properties of hydrogen fuel, but also would incorporate the design features generated from extensive tests with retrofitted and converted engines. Several important aspects of engine development dealing with broad approaches for performance improvement and potential for low emission have been investigated. Verhelst (2014), in one of his recent papers, highlights the progress made in the area of the hydrogen engine in several significant features related to DI of hydrogen, in-cylinder heat transfer, and combustion characteristics. The appropriate technology of fueling the engine has a lot of influence on performance, combustion, and emission characteristics of the engine. Engine technology development should have

long-term endurance and durability tests to determine the long-term effects such as the effect of friction, wear and tear, dilution of lube oil, and so on.

Vehicular pollution has been globally identified as one of the most serious environmental problems. The factors that govern the penetration of hydrogen-fueled IC engine into the field depends upon an economic trade-off between the added cost of development of a hydrogen-specific vehicle and the cost of hydrogen fuel over conventional gasoline or diesel. In view of this, it is expected that hydrogen fuel will be introduced in the transport sector much sooner than anticipated. CNG has been adopted as a regular transportation fuel in many countries. Well-established infrastructures for CNG-fueling of vehicles have been adequately demonstrated. In this context, it is probably worthwhile considering the blend of hydrogen and CNG to be used in vehicles. A lot of research and development work in this area is still being carried out. However, there need not be a specific quantity of hydrogen (by volume %) prescribed at this point in time. Depending upon the availability of natural gas, a country can use HCNG as the bridging fuel until the hydrogen-based infrastructure/systems are developed. Several countries throughout the world have already prepared a road map with time-bound goals such that hydrogen energy penetrates faster into the field.

The descriptions provided above with respect to the hydrogen engine clearly show that the technology has matured to use hydrogen in IC engines. Some of these design features have been installed in vehicular engines and exhaustively tested, and these tests provide achievable optimum solutions for the design and development of prototype vehicles. The cost of any application-specific prototype depends upon a number of facts. Any precise life cycle analysis would depend upon a number of factors. The overall economics of utilization in engines is dependent upon production, transmission, and storage of hydrogen depending upon the character of the system and the amount of hydrogen used. However, in the context of this work it would perhaps be appropriate to restrict the discussion to the broader aspect of the hydrogen-fueled IC engine. Therefore, the production of hydrogen is beyond the scope of this chapter. The cost is dependent on the mode of hydrogen storage depending upon the application (for example, if is it for a mobile application in a hydrogen-fueled vehicle or a stationary application such as genset/pump set/lawn mower/burner and so on). This affects the overall economics if a comparative assessment is carried out between a hydrogen-operated system and a petroleum-fueled one.

References

Adt, R.R., Hershberger, D.L., Kartage, T., Swain, M.R., 1973. The hydrogen air fueled automobile engine, Part I.

Adt, R.R., Greenwell Jr., H., Swain, M.R., 1974. The hydrogen and methanol fueled air breathing automobile engine. In: Paper Presented at the THEME Conference, University of Miami.

Billings, R.E., 1974. Hydrogen's potential as an automotive fuel billings energy corporation, Pub. No. 74004.

Blotevogel, T., Egermann, J., Goldlücke, J., Leipertz, A., et al., 2004. Developing planar laser-induced fluorescence for the investigation of the mixture formation process in hydrogen engines. SAE Technical Paper 2004-01-1408. http://dx.doi.org/10.4271/2004-01-1408.

BMW, 2006. BMW Hydrogen 7 rescue guidelines.

Boretti, A., 2011. Advantages of the direct injection of both diesel and hydrogen in dual-fuel H₂ICE. Int. J. Hydrog. Energy 36, 9312–9317.

Bysveen, M., 2007. Engine characteristics of emissions and performance using mixtures of natural gas and hydrogen. Energy 32, 482–489.

Cecil, W., 1822. On the Application of Hydrogen Gas to Produce a Moving Power in Machinery; with a Description of and Engine Which is Moved by the Pressure of Atmosphere upon a Vacuum Caused by Explosion of Hydrogen Gas, vol. I Cambridge Philosophical Society.

Das, L.M., 1986. Studies of timed manifold injection in hydrogen operated spark ignition engine: performance, combustion and exhaust emission characteristics (Ph.D. dissertation), Department of Mechanical Engineering Indian Institute of Technology, Delhi.

Das, L.M., 1990a. Hydrogen engines: a view of the past and look into the future. Int. J. Hydrog. Energy 15 (6), 425–433.

Das, L.M., 1990b. Fuel induction techniques for hydrogen operated engine. Int. J. Hydrog. Energy 15, 833–842.

Das, L.M., 1991a. Safety aspects of hydrogen fueled enginesystem development. Int. J. Hydrog. Energy 16, 619–624.

Das, L.M., 1991b. Exhaust emission characterization of hydrogen-operated engine system: nature of pollutants and their control techniques. Int. J. Hydrog. Energy 16 (11), 765–775.

Das, L.M., 2002a. Near-term introduction of hydrogen engines for automotive and agricultural application. Int. J. Hydrogen Energy 27 (5), 479–487.

Das, L.M., 2002b. Hydrogen engine: research and development (R&D) programmes in Indian Institute of Technology (IIT), Delhi. Int. J. Hydrog. Energy 27, 953–965.

Das, L.M., Polly, M., 2005. Experimental evaluation of a Hydrogen Added Natural Gas (HANG) Operated SI engine. Symposium on International Automotive Technology, SAE Paper No 2005-26-29.

De Boer, P.C.T., McLean, W.J., Homan, H.S., 1976. The performance and emission of hydrogen fueled internal combustion engines. Int. J. Hydrog. Energy 1 (2), 153–172.

de Oliveira, A., dos Santos, E.C.M., Botelho, G.C., Valente, O.S., Sodre´, J.R., 2013. Hydrogen electronic injection system for a diesel power generator. Int. J. Hydrog. Energy 38, 7986–7993.

Drell, I.L., Belles, F.E., 1958. Survey of hydrogen combustion properties. Technical Report 1383. National Advisory Committee on Aeronautics.

Eichlseder, H., Wallner, T., Freymann, R., Ringler, J., 2003. The potential of hydrogen internal combustion engine in a future mobility scenario. SAE Technical Paper 2003-01-2267. http://dx.doi.org/10.4271/2003-01-2267.

Erren, A.R., Campell, W.H., 1933. Hydrogen: a commercial fuel for internal combustion engine and other purposes. J. Inst. Fuel VI (29), 277–290.

Escher, W.J.D., 1975. Hydrogen-fueled internal combustion engine, a technical survey of contemporary U.S Projects, ETA Report PR-51.

Fagelson, J.J., McLean, W.J., DoBoer, P.C.T., 1975. Analysis of hydrogen as a reciprocating engine fuel. In: Symposium on Chemistry of Combustion in Engines. American Chemical Society, Philadelphia.

Finegold, J.G., Lynch, F.E., et al., 1973. The UCLA hydrogen car: design, construction and performance. SAE Paper 730507, 1626–1637.

Finegold, J.G., Van Vorst, W.D., 1974. Engine performance with gasoline and hydrogen. In: Paper Presented at Theme Conference, Miami.

Furuhama, S., 1981. State of the art and future trend of hydrogen fueled engines. JSAE Review No 4.

Furuhama, S., Azuma, H., 1978. Hydrogen injection engine. In: Proceedings of 2nd World Hydrogen Energy Conference, vol. 4.

Furuhama, S., Fukuma, T., 1986. High output power hydrogen engine with high pressure fuel injection, hot surface ignition and turbocharging. Int. J. Hydrog. Energy 11, 399–407.

Furuhama, S., Kobayashi, Y., 1980. LH2 car with a two-stroke direct injection engine and LH2 pump. Int. J. Hydrog. Energy 7 (10), 809–820.

Furuhama, S., Kobayashi, Y., 1982. Development of a hot-surface-ignition hydrogen injection two-stroke engine. In: Proceedings of 4th World Hydrogen Energy Conference, Pasadena, California, vol. 3, p. 1069.

Furuhama, S., Yamane, K., Yamaguchi, I., 1977. Combustion improvement in hydrogen-fueled engines. Int. J. Hydrog. Energy 2 (3), 329–340.

Furuhama, S., Hiruma, M., Enomoto, Y., 1978. Development of a liquid hydrogen car. Int. J. Hydrog. Energy 8, 61–81.

Gopalakrishnan, R., Throop, M., Richardson, A., Lapetz, J., 2007. Engineering the ford H2 IC engine powered E-450 shuttle bus. SAE Technical Paper 2007-01-4095. http://dx.doi.org/10.4271/2007-01-4095.

Homan H.S., 1978. An experimental study of reciprocating internal combustion engines operated on hydrogen (Ph.D. Thesis), Cornell University.

Homan, S.H., De Boer, P.C.T., McLean, W.J., 1983. Theeffect of fuel injection on NO_x emissions and undesirablecombustion for hydrogen-fueled piston engines. Int. J. Hydrog. Energy 8, 131–146.

Hudson, M.S.L., Dubey, P.K., Pukazhselvan, D., Pandey, S.K., Singh, R.K., Raghubanshi, H., Shahi, R., Srivastava, O.N., 2009. Hydrogen energy in changing environmental scenario: Indian context. Int. J. Hydrog. Energy 34, 7358–7367.

Ibrahim, M.M., Ramesh, A., 2014a. Investigations on the effects of intake temperature and charge dilution in a hydrogen fueled HCCI engine. Int. J. Hydrog. Energy 39 (26), 14097–14108.

Ibrahim, M.M., Ramesh, A., 2014b. Experimental investigations on a hydrogen diesel homogeneous charge compression ignition engine with exhaust gas recirculation. Int. J. Hydrog. Energy 38 (24), 10116–10125.

Ikegami, M., et al., 1975. A study of Hydrogen-fueled diesel combustion. JSME Meeting Sendai, P Japan, 1975.

Ikegami, M., Miwa, K., Shioji, M., 1982. A study of hydrogen-fueled compression ignition engine. Int. J. Hydrog. Energy 7 (4), 341–353.

Kaiser, S., White, C., 2009. PIV and PLIF to evaluate mixture formation in a direct-injection hydrogen-fueled engine. SAE Int. J. Engines 1 (1), 657–668. http://dx.doi.org/10.4271/2008-01-1034.

Karim, G.A., Wierzba, I., Al-Alousi, Y., 1996. Methane hydrogen mixture as fuels. Int. J. Hydrog. Energy 21, 625–631.

Kim, Y.Y., Lee, J.T., Choi, G.H., 2005. An Investigation on the causes of cycle variation in direct injection hydrogen fueled engines. Int. J. Hydrog. Energy 30, 69–76.

King, R.O., Rand, M., 1955. The oxidation, decomposition, ignition and detonation of fuel vapors and gases. XXVII: the hydrogen engine. Can. J. Technol. 33, 445–469.

King, R.O., Wallace, W.A., Mahapatra, B., 1957. The oxidation, decomposition, ignition and detonation of fuel vapors and gases-V. The hydrogen engine and detonation of the end by the igniting effect of carbon nuclie formed by pyrolysis of lubricating oil vapor. Can. J. Technol. 34, 442–454.

King, R.O., Hayes, S.V., Allan, A.B., Anderson, R.W.P., Wacker, B.J., 1958. The hydrogen engine: combustion knock and related flame velocity. Trans. Eng. Inst. Can. 2 (4), 442–454.

Kirchweger, W., Haslacher, R., Hallmannsegger, M., Gerke, U., 2007. Application of LIF method for the diagnostics of the combustion process of gas-IC engine. Exp. Fluids 43, 329–340.

Lapetz, J., et al., 2006. The design, development, validation and delivery of the Ford H2 ICE E-450 shuttle bus. In: 1st (Int) Symposium on Hydrogen Internal Combustion Engines, pp. 20–33.

Lee, J.T., Kim, Y.Y., Caton, J.A., 2002. The development of a dual injection hydrogen fueled engine with high power and high efficiency. In: Wong, V.W. (Ed.), In: Proceedings of the ASME-ICED 2002 Fall Technical Conference, vol. 39, pp. 323–324.

Lewis, B., Elbe, G.V., 1987. Combustion, Flames, and Explosions of Gases. Academic Press. http://dx.doi.org/10.1016/B978-0-12-446751-4.50001-9.

Li, J.D., Lu, Y., Du, T.S., 1984. Improvement on the combustion of hydrogen-fueled engine. Hydrogen Energy Progress V. Pergamon Press, Oxford.

Lynch, F.E., 1983. Parallel induction: a simple fuel control method for hydrogen engine. Int. J. Hydrog. Energy 8 (9), 721–730.

Ma, F., Wang, Y., Liu, H., Li, Y., Wang, J., Zhao, S., 2007. Experimental study on thermal efficiency and emission characteristics of a lean burn hydrogen enriched natural gas engine. Int. J. Hydrog. Energy 32, 5067–5075.

Mathur, H.B., Das, L.M., 1991. Performance characteristics of hydrogen fueled SI engine using timed manifold injection. Int. J. Hydrog. Energy 16, 115–127.

Mathur, H.B., Das, L.M., Patro, T.N., 1992a. Effects of charge diluents on the emission characteristics of a hydrogen-fueled diesel engine. Int. J. Hydrog. Energy 17 (8), 635–642.

Mathur, H.B., Das, L.M., Patro, T.N., 1992b. Hydrogen fuel utilization in CI engine powered end utility systems. Int. J. Hydrog. Energy 17, 369–374.

Mathur, H.B., Das, L.M., Patro, T.N., 1993. Hydrogen fueled diesel engines: performance improvement through charge dilution techniques. Int. J. Hydrog. Energy 18, 421–431.

McLean, W.J., DeBoer, P.C.T., Homan, H.S., 1977. Hydrogen as a reciprocating engine fuel. Future Automotive Fuels; Prospects, Performance and Perspective. Plenum Press, New York.

Mohammadia, A., Shiojib, M., Yasuyuki, N., Ishikurab, W., Taboc, E., 2007. Performance and combustion characteristics of a direct injection SI hydrogen engine. Int. J. Hydrog. Energy 32, 296–304.

Murray, R.G., Schoeppel, R.J., Gray, C.L., 1972. The hydrogen engine in perspective. In: Proceedings of the Seventh IECEC, SanDiego, California, Paper 729216.

Nakagawa, Y., Nakai, M., Hamai, K., 1982. A study of the relationship between cycle-to-cycle variations of combustion and heat release delay in a spark-ignited engine. JSME 25 (199), 54–60.

Natarajan, S., Abraham, M., Rajesh, M., Subash, G., Das, L.M., 2013. DelHy 3 W—Hydrogen fueled Hy-Alfa Three Wheeler. SAE Technical Paper 2013-01-0224. http://dx.doi.org/10.4271/2013-01-0224.

Natkin, R.J., Tang, X., Boyer, B., Oltmans, B., Denlinger, A, Heffel, J.W., 2003. Hydrogen IC engine boosting performance and NO_x study. SAE Paper 2003,2003-011-3210.

Oehmichen, M., 1942. WasserstoffalsMotorTreibmittel. Deutsche Kraft Fahart-Forschung, Heft 68. VDI-VerlagGmbH, Berlin.

Pischinger, F., 1977. Schaffrath, 5–1 Untersuchungen and EniemWasserstoff Motor and MassahmanJurProfosesverbesserrung, University of Aachen, Germany.

Ricardo, H.R., 1924. Further note on fuel research. Proc. Inst. Automotive Eng. XVIII (I), 327–341.

Roy, M.K., 2013. Jet-guided combustion characteristics and local fuel concentration measurements in a hydrogen direct injection spark ignition engine. Proc. Combust. Inst. 34, 2977–2984.

Salazar, V., Kaiser, S., Halter, F., 2009. Optimizing precision and accuracy of quantitative PLIF of acetone as a tracer for hydrogen fuel. SAE Int. J. Fuels Lubr. 2 (1), 737–761. http://dx.doi.org/10.4271/2009-01-1534.

Shudo, T., Oba, S., 2009. Mixture distribution measurements using laser induced breakdown spectrosopy in hydrogen direct injection stratified charge. Int. J. Hydrog. Energy 34, 2488–2493.

Sinclair, L.A., Wallace, J.S., 1984. Lean limit emission of hydrogen-fueled engine. Int. J. Hydrog. Energy 9, 123–128.

Sirens, R., 2001. Influence of injection parameters on the efficiency and power output of a hydrogen fueled engine. In: ICE Technical Conference, Vol. 36. ICE, p. 1.

Stebar, R.F., Parks, F.B., 1974. Emission control with lean operation using hydrogen supplemented fuel. General Motors Research, Publication, GMR1537.

Stockhausen, W.F., Natkin, R.J., Kabat, D.M., Reams, L., Tang, X, Hashemi, S., et al., 2002. Ford P2000 hydrogen engine design and vehicle development program. SAE Paper 2002-01-0240.

Swain, M.R., Yusuf, M.J., Dugler, Z., Swain, M.N., 1993. The effects of hydrogen addition on natural gas engine operation. SAE Paper No.932775.

Van Vorst, Wm.D, Finegold, J.G., 1975. Automotive Hydrogen Engines and Onboard storage Methods. In: Hydrogen Energy Fundamentals, Miami.

Varde, K.S., Frame, G.A., 1982. A study of combustion and engine performance using electronically hydrogen fuel injection. In: Paper Presented at World Hydrogen Energy Conference-IV, Pasadena, California.

Verhelst, S., 2014. Recent progress in the use of hydrogen as a fuel for internal combustion engines. Int. J. Hydrog. Energy 39, 1071–1085.

Verhelst, S., Wallner, T., 2009. Hydrogen-fueled internal combustion engines. Prog. Energy Combust. Sci. 35, 490–527.

Wallner, T., et al., 2008. Fuel economy and emission evaluation of a BMW hydrogen 7 monofuel demonstration vehicle. Int. J. Hydrog. Energy 33, 7607–7618. http://dx.doi.org/10.1016/j.ijhydene.2008.08.067.

Wallner, T., Scarcelli, R., Nande, A., Naber, J., 2009. Assessment of multiple injection strategies in a direct-injection hydrogen research engine. SAE Int. J. Engines 2 (1), 1701–1709. http://dx.doi.org/10.4271/2009-01-1920.

Weil, K.H., 1972. The hydrogen IC engine-its origin and future in the emerging energy-transportation-environment. In: Proceedings of 7th IECEC, pp. 1355–1363.

Welch, A.B., Wallace J.S., 1986. Performance characteristics of a hydrogen fueled diesel engine with ignition assistance. Final Report, NRCC, Report No.DSS, Contract File No.24SU.31155-2-2664. Serial No. ISu 82-00340.

White, C.M., Steeper, R.R., Lutz, A.E., 2006. The hydrogen-fueled internal combustion engine: a technical review. Int. J. Hydrog. Energy 31, 1292–1305.

Wong, J.K.S., 1990. Compression ignition of hydrogen in direct injection diesel engine modified to operate as low heat rejection engine. Int. J. Hydrog. Energy 7, 507–514.

This page intentionally left blank

Blended hydrogen–natural gas-fueled internal combustion engines and fueling infrastructure

8

J.R. Anstrom[*], *K. Collier*[†]
[*]The Pennsylvania State University, University Park, PA, USA, [†]Collier Technologies Inc. (CTI), Reedsport, OR, USA

Glossary

CH_4	Methane
CI	Compression ignition engine uses high pressure to ignite fuel
CNG	Compressed natural gas
CO	Carbon monoxide
CTI	Collier Technologies Inc.
DME	Dimethyl ether is a synthetic fuel that can be blended with diesel or used as a diesel substitute
E10	A fuel blend of gasoline with up to 10% ethanol
E85	A fuel blend of gasoline with up to 85% ethanol
ECM	Engine control module or the computer and software that run modern engines
EGR	Exhaust gas recirculation into air–fuel mixtures within IC engines
ETC	European transient cycle for heavy duty engine dynamometer testing
FFV	Flex-fuel vehicles sense and adapt to various fuel blend ratios, typically gasoline and ethanol
FSEC	Florida Solar Energy Center
GHG	Greenhouse gas emissions, in this case related to vehicle tailpipe emissions
HC	Hydrocarbon
HCI	Hydrogen Components Inc.
Hythane®	HCI trademarked blend of 20% hydrogen with NG to match gasoline flame speed
HCNG or H₂NG	Hydrogen and compressed natural gas blends above 20% hydrogen volume
HPDI	High pressure direct injection engine technology
IC	Internal combustion engines burn fuel in an expandable chamber to convert pressure to mechanical power
IGT	Institute for Gas Technology
JPL	Jet Propulsion Laboratory
LH_2	Liquefied hydrogen
LLC	Lean limit of combustion
LNG	Liquefied natural gas
NG	Natural gas
NMHC	Nonmethane hydrocarbon emissions

NO$_x$	Various oxides of nitrogen-regulated emissions resulting from high-temperature combustion
OH—	Hydroxyl ions
OEM	Original equipment manufacturer of cars and trucks
PEM	Proton exchange membrane fuel cell
PSA	Pressure swing adsorption
SCR	Selective catalytic reduction of NO$_x$ after treatment of exhaust
SI	Spark ignition internal combustion engines ignite fuel with an electric spark
THC	Total hydrocarbon emissions
WTW	Well-to-wheel vehicle emissions

8.1   Introduction

The mixing of conventional and alternative transportation fuels has historically been practiced to obtain blends with advantages over conventional fuels including more desirable combustion properties, lower regulated and greenhouse gas (GHG) emissions, petroleum displacement, increased range, lower cost, or as a bridging technology to promote alternative fuel production and infrastructure. For example, a blend of gasoline with up to 10% ethanol (E10) is dispensed from existing stations into gasoline vehicles in the United States, providing an early market for ethanol (US Energy Information Administration, 2015). This blend works very well in spark ignition (SI) internal combustion (IC) engines designed for gasoline without significantly degrading vehicle range, reliability, or performance. Flex-fuel vehicle (FFV) SI engines and fuel systems are further modified to operate on blends of 15–85% ethanol with gasoline referred to as E85. Likewise, blends of diesel with biodiesel or dimethyl ether (DME) have created early markets for biomass-derived alternative diesel fuels that run acceptably in compression ignition (CI) engines.

The abovementioned systems all have a single onboard fuel tank to which the blended fuel is dispensed from a single fueling dispenser. So-called dual-fuel engine systems are designed to blend either diesel or gasoline with gaseous fuels such as hydrogen, propane, and natural gas from secondary onboard storage tanks. "Bifuel" systems can operate on either of two onboard fuels from separate tanks, such as gasoline or natural gas. Table 8.1 summarizes many conventional and alternative fuel blends along with their common names and relative attributes compared to conventional fuels.

The concept of fuel blending has been applied to gaseous alternative fuels as well, including the very promising blends of hydrogen with compressed natural gas (CNG) for SI engines. Table 8.2 lists the relative combustion properties of gasoline, natural gas, and hydrogen (Eichlseder et al., 2009). Unless otherwise mentioned, all percentages of fuel composition for hydrogen and natural gas blends will be on a volume basis. Up to 20% hydrogen has been blended with natural gas for service in gasoline SI engines without changes to engine design or tuning parameters (Lynch and Marmaro, 1992). This blend, typically called Hythane®, is designed to produce the same combustion flame speed as gasoline under stoichiometric conditions. This facilitates the utilization of the unmodified OEM ECM programming in a gasoline vehicle

Table 8.1 Alternative and conventional fuel blends

Fuel blends

Name	Constituent fuel	Constituent fuel	Attributes
E10	90% gasoline	10% ethanol	Runs in unmodified SI engines Displaces petroleum with renewable ethanol Lowers well-to-wheel GHG emissions Promotes ethanol production
E85	17–50% gasoline	50–83% ethanol	Runs in flex-fuel SI engines Flex-fuel retains gasoline option if E85 unavailable Displaces petroleum with renewable ethanol Lowers well-to-wheel GHG emissions Promotes ethanol production
Bxx biodiesel blends	1–99% diesel	99–1% biodiesel	Runs in diesel CI engines Displaces petroleum Lowers GHG emissions Promotes biodiesel production
Diesel DME Blend	75–90% diesel	25–10% DME	Displaces petroleum with renewable DME
Hythane®	80% natural gas	20% hydrogen	Runs in unmodified gasoline and natural gas engines Promotes hydrogen as combustion fuel Promotes engine conversions to CNG Modest power and range loss
HCNG or H₂CNG	50–80% natural gas	20–50% hydrogen gas	Runs in modified natural gas SI engines Greatly improved NO_x, methane tailpipe emissions Slightly improved thermal efficiency Significant power and range loss
Onboard Fuel Blending or Dual Fuel Systems			
CNG gasoline dual-fuel	Either 100% gasoline	Or 100% natural gas	Displaces petroleum with natural gas Lower fuel cost with CNG option Allows 100% CNG operation

Table 8.1 Continued

Fuel blends			
Name	**Constituent fuel**	**Constituent fuel**	**Attributes**
Diesel bifuel with CNG or propane	30–100% diesel	70–0% natural gas or propane	Retains gasoline operation and range if CNG unavailable ECM switchable between gasoline and CNG tunings and injectors Displaces petroleum with natural gas or propane Lowers average fuel cost Modest power gains with some efficiency loss Can use CNG, LNG, or propane
High pressure direct injection HPDI	Diesel for ignition only	~100% natural gas	Displaces nearly 100% of petroleum with natural gas Lower fuel cost Requires LNG for onboard evaporation to high pressure

Table 8.2 Relative combustion properties of gasoline, hydrogen, and natural gas

Property	Units	Gasoline	Methane	Hydrogen
Density (liquid)	kg/m^3	750–770	423	70.8
At	°C	15	−162	−253
Density (gaseous)	kg/m^3	–	0.716	0.09
Lower calorific value	MJ/kg	41.4	50	120
Energy density liquid	MJ/dm^3	31.7	21	8.5
Energy density gaseous	MJ/dm^3	–	12.6	3.0
Ignition limits	vol%	1.0–7.6	4.4–15.0	4.0–76.0
Ignition limits	λ-range	1.4–0.4	2.0–0.6	10–0.13
Auto-ignition temperature	°C	230–450	595	585
Minimum ignition energy	mJ	0.24	0.29	0.017
Laminar flame speed	cm/s	~40	~42	~230
Proportions by mass				
C	%	85.6	74.9	0
H	%	12.2	25.1	100
O	%	2.2	0	0

conversion. Emissions from Hythane®, particularly NO_x, have not been significantly reduced relative to the OEM gasoline engine. However, the main impetus for Hythane® has been to simplify the transition from gasoline as a primary transportation fuel to natural gas by eliminating the need for significant engine modifications.

Higher blends of hydrogen with natural gas, referred to as hydrogen-enriched compressed natural gas (HCNG) or H_2NG, were specifically developed to operate IC engines in extreme lean-burn conditions, thereby reducing engine out NO_x emissions. Lean-burn engine technology requires substantial tuning modifications to succeed and results in a significant loss of engine specific power which must be compensated for with increased displacement, turbocharging, or supercharging. HCNG blends between 30% and 50% hydrogen in lean-burn operation have demonstrated significantly reduced NO_x tailpipe emissions and improved efficiency compared to gasoline, CNG, or Hythane®.

Although 100% hydrogen can achieve a higher degree of lean-burn than HCNG, the amount of excess air required to achieve similar NO_x emissions results in very low specific power output. Also, the combination of low energy density for compressed hydrogen tanks and thermal efficiencies well below 50% for currently available hydrogen IC engines makes it difficult to achieve vehicle range over 500 km. The major advantage of pure hydrogen over HCNG is lower GHG tailpipe emissions if the hydrogen is produced from low-carbon feedstocks. Under current US air quality regulations, however, methane emissions are not regulated because in the atmosphere methane is very unreactive in the creation of photochemical smog.

Blended fuels can have significant impacts on the design of onboard fuel tanks and fueling station configurations. Bifuel CNG and diesel high-pressure direct injection (HPDI) systems mix diesel and natural gas in the engine and, therefore, require separate fueling dispensers and separate CNG and diesel onboard tanks. In contrast, blended fuel systems such as HCNG require only one fuel dispenser and a single onboard tank. HCNG blending can occur upstream of the fueling station in the pipeline or on-site at the fueling station. HCNG can be blended at the fueling station either prior to compression or postcompression. HCNG can be stored in a buffer tank for later dispensing or blended on demand immediately upstream of the dispenser. These various blend configurations impact station design, operations, equipment cost, footprint, maintenance, and mode of fuel delivery. On-site HCNG blending is most often deployed at fueling stations where both CNG and hydrogen fueling infrastructure already exist.

8.2 HCNG engine and after-treatment technologies

Before the advent of catalysts for IC engine emissions control, the Jet Propulsion Lab (JPL) tested fuel mixtures of hydrogen and gasoline as an emissions control strategy (Houseman and Hoehn, 1974). Although their results did show NO_x reductions, the advent of catalytic converter systems for vehicles proved to be a more cost-effective strategy.

The blending of hydrogen and natural gas was an offshoot of research aimed at making a transition from fossil fuels to hydrogen, the "hydrogen economy." Research at the Florida Solar Energy Center (FSEC) postulated that this transition must first make the transition from liquid to gaseous fuels. Hydrogen could then be introduced in ever-increasing proportions to the existing natural gas infrastructure. Institute of Gas Technology (IGT) published that up to 20% hydrogen could be added to the existing NG pipeline infrastructure with no modifications necessary (IGT, 1972). The Bureau of Mines Research Center performed experiments with hydrogen mixed with natural gas as a fuel for IC engines (Eccleston and Fleming, 1972). Up to 20% hydrogen was tested.

Frank Lynch at Hydrogen Components Inc. (HCI) received a patent for mixtures of hydrogen and natural gas up to 20% hydrogen (Lynch and Marmaro, 1992). This patent specifically identified that the purpose of this fuel mixture was to match the flame speed of gasoline in an IC engine. HCI also trademarked the term "Hythane®" to identify any specific mixture of hydrogen and methane.

A different approach was taken by Kirk Collier and colleagues at FSEC. The idea was to mix hydrogen and natural gas to extend the lean limit of combustion (LLC) beyond that achievable by natural gas alone. It is well known that NO_x emissions from IC engines are reduced as more air is added without increasing the amount of fuel. The rationale for the FSEC research was to determine the amount of hydrogen needed to achieve the most stringent exhaust emissions' standards without exhaust aftertreatment. Major results from the FSEC research are shown in Figure 8.1. NO_x emissions are plotted against degree of lean-burn for hydrogen fractions from 0% to 50% mixed with natural gas. The first major conclusion of this work was to show that hydrogen addition actually increases NO_x for the same power and relative air/fuel ratio. The second major conclusion is that hydrogen addition does increase the lean limit of combustion and hydrogen fractions greater than 10% can reduce NO_x emissions relative to natural gas alone. The third major conclusion is that 30% hydrogen addition results in a near optimal mixture when considering emissions, fuel cost, and onboard fuel storage density. This can be seen clearly in Figure 8.1 where the 30% H_2 curve is the lowest concentration to reach near zero NO_x emissions, representing a point of diminishing returns versus higher concentrations. FSEC was awarded several patents for mixtures of hydrogen and natural gas from 21% to 50% hydrogen while operating the engine within specified conditions (Collier et al., 1997).

Collier Technologies Inc. (CTI) continued the development and testing of HCNG. They received several additional patents pertaining to this fuel mixture (Collier, 2004). Exhaust gas recirculation (EGR) was included as an alternative technique to reduce NO_x emissions. The principle action is fundamentally the same as lean-burn; that is, adding heat capacity to the combustion event will decrease the maximum temperature while maintaining the average temperature. The advantage of using EGR as the dilution mechanism allows exhaust gas oxygen levels commensurate with stoichiometric combustion, thereby allowing further reduction in tailpipe emissions by incorporating three-way catalyst systems.
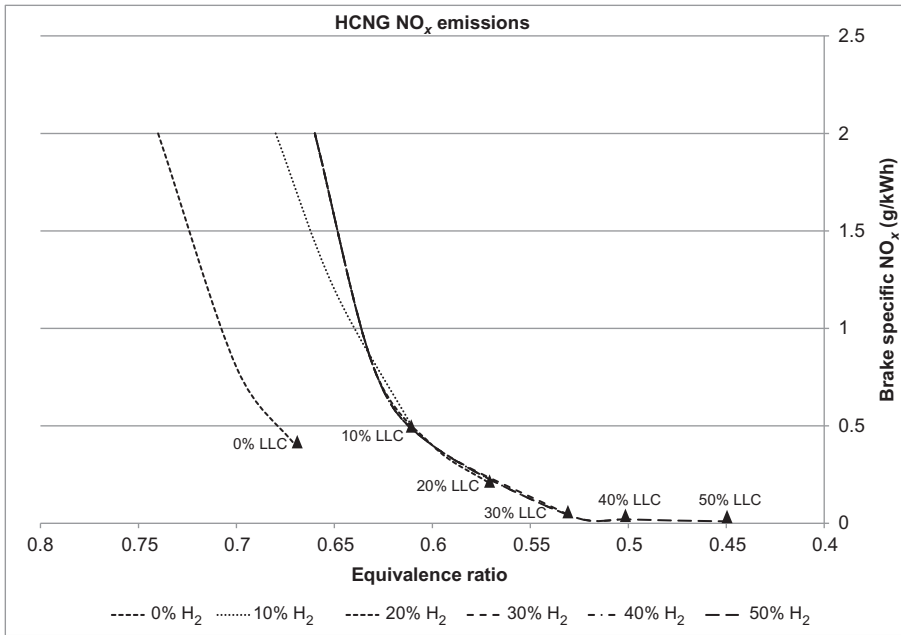
Figure 8.1 NO_x emissions versus degree of lean-burn for hydrogen fractions from 10% to 50%.

Another important technology to come out of CTI was the description of the intake port configuration that results in the lowest combination of NO_x and hydrocarbon HC emissions for HCNG. It was shown that configurations that impart angular momentum to the charge mixture increased both NO_x and HC emissions. The configuration was described that imparted the minimum angular momentum to the mixture.

The chemistry associated with hydrogen addition and combustion dynamics is due to the role of hydroxyl ions (OH^-). The process rate associated with removing the first hydrogen from methane (CH_4 to CH_3) is very slow when compared to other, more complex, hydrocarbons. This process relies on the creation of hydroxyl ions to speed up this reaction. Hydrogen produces hydroxyl ions at approximately 10 times the rate of methane. It is this strong ability of hydrogen to make hydroxyl ions that are able to react with CH_4 that explains the role of hydrogen in enhancing combustion with high charge–dilution ratios (Wang et al., 2010).

Performance benchmarks for these demonstrations were a Ford F150 truck with 30% HCNG, 30% EGR, and a stoichiometric air–fuel ratio. A prototype was developed to compete in the (year) Michelin Bibendum held at Fontana Raceway in California. Testing by an independent laboratory resulted in identical NO_x emissions of 0.009 g/km (0.015 g/mile) compared to a Toyota Prius over the same FTP driving cycle. A bus engine project in cooperation with Doosan Infracore and Penn State

University demonstrated NO_x emissions of 0.107 g/kW h (0.08 g/hp h) on the eight-mode steady state emissions test. Incorporating a selective catalytic reduction (SCR) system resulted in achieving less than 0.013 g/kW h (0.01 g/hp h) (limit of measuring equipment) on the same test.

HCI supported many Hythane® demonstrations while CTI also supported many HCNG demonstrations. Early Hythane® demonstrations were first completed on GM pickup truck platforms in Denver, CO, and then transit buses in Palm Desert, CA. HCNG demonstrations with cars and pickup trucks were also deployed in Vancouver, Canada; Phoenix, AZ; Washington, DC; State College, PA; Las Vegas, NV; and Reno, NV. These vehicles incorporated EGR and stoichiometric air–fuel ratio. HCNG bus demonstrations were performed in Los Angeles, CA; Las Vegas, NV; and State College, PA incorporating lean-burn technology. In the State College demonstration, a 12-l HCNG engine developed by the CTI/Doosan partnership replaced an 8.5-l Detroit Diesel Series 50 CNG engine in regular transit service demonstration from 2006 to 2009 on the Penn State campus.

One of the largest international Hythane® demonstrations to date has been the Mumbai, India, bus demonstration begun in 2010 and targeted at reducing transit bus contribution to India's significant NO_x and smog issues in urban areas. Australia's Eden Energy and their subsidiary Hythane® Company developed a nonturbocharged 6.l Hythane® engine and tested it on the European transient cycle (ETC) dynamometer cycle for heavy duty vehicles to meet the Bharat V (Euro V) requirements. They reported a NO_x reduction of 16.6%, total hydrocarbon (THC) of 15.1%, nonmethane hydrocarbon (NMHC) reduction of 66.6%, and CO_2 reduction of 6.2% compared with an equivalent CNG engine (NGV Global News, 2010). An improved fuel economy of 6.5% was also reported.

8.3   HCNG onboard storage and fueling infrastructure

Similar to HCNG engine technology, HCNG onboard storage and fueling infrastructure also borrows heavily from existing CNG and hydrogen-fueling systems. Starting with onboard storage, this section will discuss the various methods for achieving accurate and cost-effective blending and dispensing of HCNG.

8.3.1   Onboard HCNG storage

Hydrogen storage in high-strength steel tanks has the potential problem of hydrogen embrittlement where hydrogen atoms penetrate the steel crystal structure, degrading elasticity. This phenomenon becomes more pronounced the higher the hydrogen partial pressure and the higher the yield strength of the steel alloy. High-carbon steels are particularly susceptible. For this reason, high concentrations of hydrogen should not be allowed in high-strength steel tanks commonly used for low-cost storage of CNG onboard vehicles at the 250 bar pressure standard. Although hydrogen embrittlement is also a possibility with HCNG, the hydrogen

partial pressure is low relative to pure hydrogen. For example, a 30% HCNG mixture in a 250-bar storage tank will only be 7.5 bar of hydrogen partial pressure. Arizona Public Service Company conducted long term demonstrations of HCNG-converted F150 trucks. The storage tanks used were OEM fiber-reinforced 4130 steel. After 1 year of service, destructive testing of these tanks showed no signs of hydrogen embrittlement (Brayer et al., 2006). If the goal is total elimination hydrogen embrittlement risk, composite and aluminum construction tanks should be used instead because these are not subject to hydrogen embrittlement. Composite tanks are also favored for their lighter weight but are about twice as expensive as high-strength steel equivalents. Their price is falling with ongoing material advancements and growing production volumes across CNG and hydrogen markets. From successful field experience, it has been shown that all other components such as the plumbing, sensors, valves, regulators, and engine fuel systems can be identical to the common CNG 250 bar standard. A typical 250 par CNG fuel system schematic showing component layout within a vehicle is shown in Figure 8.2.

8.3.2 HCNG dispensing

HCNG fueling requires a designated dispenser separate from other gaseous fuels at the fueling station, which may include CNG at 250 bar and hydrogen at either 350 or 700 bar. Each gaseous fuel dispenser must have a specific nozzle mechanically keyed to never interchange with vehicle-mounted receptacles for other fuels. This is necessary to prevent dispensing of the wrong fuel into a vehicle but, more importantly, to prevent higher-pressure gas from being dispensed into lower-pressure fuel systems and thereby causing a rupture. Currently, there are no specific standards for HCNG-fueling nozzles. In many demonstrations, standard hydrogen or CNG nozzles have been repurposed to dispense HCNG and Hythane®. In the case of the Penn State University HCNG demonstration, a 250-bar hydrogen nozzle—obsoleted by the higher 350 and 700 bar hydrogen standards—was repurposed for HCNG dispensing into CTI-modified Ford Econoline service vans. A larger hydrogen nozzle, initially designed for fuel cell buses, was repurposed for dispensing into an HCNG bus.
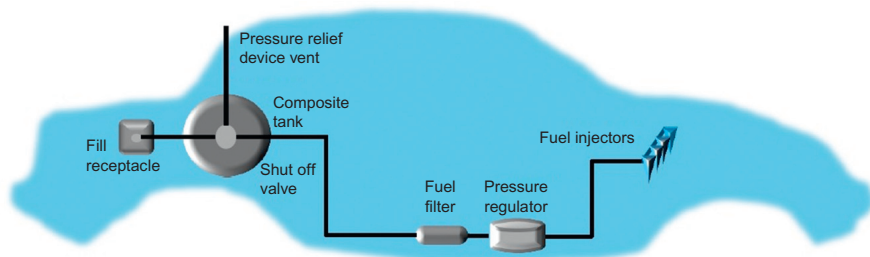
Figure 8.2 Schematic of HCNG onboard storage.

Beyond the nozzle and receptacle hardware, HCNG dispenser hardware closely resembles a typical CNG noncommunication fill system. HCNG and Hythane® leak detection can be accomplished with the natural gas odorant alone. However, best engineering practice would be to include additional leak detectors into the station as hydrogen may lower the flammability limit of the blend compared to straight natural gas.

8.3.3   HCNG sources, delivery, and blending

Implementing an HCNG dispenser always requires a source of both hydrogen and natural gas at the point of blending. There are four major sources of pure hydrogen available for fuel stations: hydrogen pipelines, delivered hydrogen gas, delivered liquefied hydrogen (LH_2), and on-site hydrogen production typically from electrolysis or small-scale steam–methane reformers. Natural gas in the pipeline is a mix of mostly methane with small traces of other gases, which can include up to 2% hydrogen. As up to 20% hydrogen could be safely transmitted in the existing natural gas pipelines, hydrogen could be delivered in the natural gas pipeline from various sources, including electrolysis of renewable wind and solar- or biomass-based sources. Several technologies exist to extract purified hydrogen from pipeline blends, including pressure swing adsorption (PSA), membrane separation, and electrochemical hydrogen separation (Melaina et al., 2013). This is an alternative to building out a dedicated hydrogen pipeline infrastructure, which is often cost prohibitive.

Common practice to date has been to blend HCNG at the fueling station using pure hydrogen gas already on-site for fuel cell and hydrogen IC engine vehicles. On-site blending eliminates the need for hydrogen extraction from the natural gas pipeline or a dedicated HCNG pipeline. Figure 8.3 depicts the possible process configurations for blending of hydrogen with natural gas at the station. HCNG blending can occur upstream of compression at the cost of a dedicated HCNG compressor. Alternatively, HCNG can be blended downstream of natural gas and hydrogen compression from separate high-pressure CNG and hydrogen buffer tanks. HCNG can be blended in advance and stored at high pressure or blended on-demand as the vehicle fuels with full mixing occurring in the vehicle tank.

8.4   Current and future use of HCNG in transportation

The main advantages of HCNG as a fuel blend are its potential to significantly reduce tailpipe emissions, of which NO_x is a source of smog in urban areas and methane is a powerful GHG. If HCNG technology is limited to retrofits of existing engines and 20% H_2 concentrations or less, then reduction of NO_x will be under 50% and the reduction of unburned methane will vary. These less than dramatic results for HCNG demonstrations have led some to question the cost benefit of implementing HCNG (Nelsson et al., 2010; National Petroleum Council, 2012). However, more dramatic reductions of both NO_x and unburned methane are achievable if lean-burn technology is implemented at H_2 concentrations at or above 30% and HCNG engines are upgraded
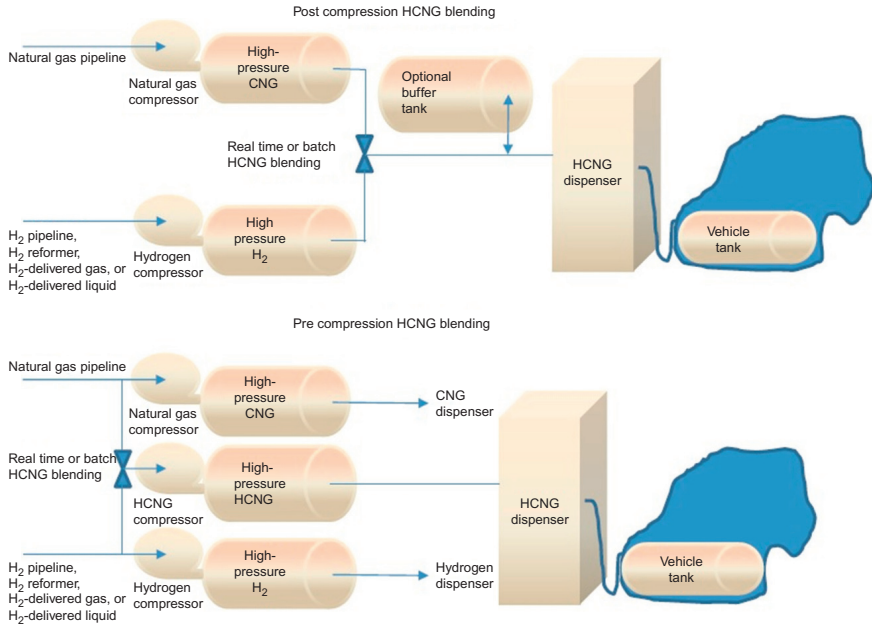
Figure 8.3 On-site HCNG blending processes.

in design and displacement (Collier et al., 1996, 1997; Collier, 2004). These upgrades may increase engine size, weight, and cost, but long-term savings due to improved fuel economy may also offset the initial investment. The increased thermal efficiency of HCNG lean-burn engines further improves both GHG and NO_x emissions. (Nelsson et al., 2010)

There are several other advantages of HCNG that make it attractive now and will likely keep it relevant into the distant future. As with many other alternative fuel blends, HCNG can be considered as a bridging technology that promotes early market penetration for hydrogen prior to widespread deployment of hydrogen fuel cell vehicles and hydrogen-fueling infrastructure. Fuel storage density decreases with increasing H_2 concentration in HCNG. Higher onboard energy storage density for HCNG provides significantly greater range than hydrogen alone for IC engine vehicles, making HCNG the preferred fuel choice for all except fuel cell powertrains and short-range IC powertrains such as airport shuttles and local delivery trucks. Maximum range is a reason to designate 30% H_2 as the optimal value for both range and emissions. Hydrogen fuel purity is far less of an issue for HCNG IC engines compared to proton exchange membrane (PEM) fuel cell powertrains because HCNG engines can safely burn carbon monoxide (CO) without damage. PEM fuel cell membranes are permanently damaged by even very low concentrations of CO on the order of 10 ppm. The fact that the hydrogen in HCNG promotes near complete methane combustion without exhaust after-treatment equipment is an cost advantage over CNG alone, leading to savings in cost, space,weight, and design complexity. Due to the

reduced amount of hydrogen required for HCNG (30% hydrogen mixture is 11% hydrogen energy content), renewable sources could more easily meet the demand of an early HCNG market and benefit from it. If hydrogen fuel cell vehicle markets do become established, HCNG will benefit from lower hydrogen costs.

However, HCNG has some significant challenges going forward. In terms of GHG, adding the equivalent energy of locally derived biogas to CNG is may be a superior alternative to HCNG derived totally from natural gas (Nelsson et al., 2010). HCNG engines should also be designed and certified for operation on both HCNG and CNG, adapting back to pure CNG during times when the HCNG-fueling infrastructure is down. Installation costs for an HCNG-fueling station will be significantly greater than for a hydrogen- or CNG-fueling station alone.

Transit buses and local delivery fleets are excellent venues for HCNG deployment because they do not require a large, dispersed, publicly available fueling infrastructure. Their captive-fueling infrastructure allows for the gradual implementation of HCNG and can tolerate minor difficulties with emerging HCNG technology.

Development of an HCNG version of flex-fuel technology—which would allow combustion of any mixture of hydrogen and natural gas—would enable HCNG vehicles to randomly fuel with either hydrogen, HCNG, or CNG based on current price and availability. HCNG flex-fuel would, therefore, further promote hydrogen market expansion from all sources.

Most importantly, further expansion of HCNG will depend on the development of international standards for nozzle/receptacle designs for one or more HCNG blends. These new standards could include both 20% and 30% HCNG blend versions. The existence of these standards would encourage manufacturers to offer production engine and dispensing products for HCNG.

8.5   Sources of further information

The US Department of Energy Alternative Fuels Data Center is an excellent resource for comparing various alternative fuels as they continue to develop (US DOE, Alternative Fuels Data Center, 2015).

Doosan Infracore acquired CTI in 2007 and is developing HCNG engine products (Doosaninfracore, 2015).

8.6   Conclusions

HCNG is now a well-understood and demonstrated technology that borrows heavily from widely used CNG engines and widely available CNG-fueling infrastructure. HCNG engines are essentially modified and retuned versions of existing CNG engines with the potential to switch back and forth between these fuels with reprogramming. HCNG requires dedicated fill nozzle and receptacle equipment at the filling station.

Blending HCNG on-site from available CNG and hydrogen is a straightforward process that uses common process flow equipment. HCNG and Hythane® provide varying levels of emission improvements over CNG and diesel, while vehicle range is maintained close to CNG levels. Both HCNG and Hythane® provide a "bridging technology" for emerging hydrogen production and fueling infrastructure.

Given that, HCNG and Hythane® fuel blends are viable low-emission alternatives that are competing with other alternatives to be widely adopted and displace petroleum-based gasoline and diesel. These other alternatives include a fully deployed hydrogen fuel cell and fueling infrastructure, CNG from biogas, battery electric technology, biodiesel, DME, and ethanol to name a few. Both HCNG and CNG will likely benefit from increased natural gas production and reserves due to recent advances in drilling technology. Ongoing technology development and, more importantly, market forces will over time determine which of these alternative fuels will become established.

References

Brayer, R., Karner, D., Francfort, J., 2006. 'U.S. Department of Energy FreedomCAR & Vehicle Technologies Program – Hydrogen and Hydrogen/Natural Gas Station and Vehicle Operations – 2006 Summary Report', Idaho National Laboratory, INL/EXT-06-11689.

Collier, R.K., et al. 1996. Untreated Exhaust Emissions of a Hydrogen-Enriched CNG Production Engine Conversion. SAE Paper 960858.

Collier, R.K., et al. 1997. Hydrogen enriched natural gas as a clean motor fuel. US Patent 5,660,602.

Collier, R.K., 2004. Low-emission internal combustion engine. US Patent 6,883,852.

Doosan Infracore Acquires CTI in 2007. http://www.doosaninfracore.com/en/intro/history.do Available at: http://www.doosaninfracore.com/en/intro/history.do (last accessed March 2015).

Eccleston, D.B., Fleming, R.D., 1972. Clean Automotive Fuel. Technical Progress Report 48. US Bureau of Mines Automotive Exhaust Emissions Program, February 1972.

Eichlseder, H., Klaus, S., Leiner, D., 2009. Potential of Synergies in a Vehicle for Variable Mixtures of CNG and Hydrogen. Society of Automotive Engineers, SAE Paper, Warrendale, PA, 2009-01-01420.

Houseman, J., Hoehn, F.W., 1974. A Two-Charge Engine Concept: Hydrogen Enrichment. SAE Paper 741169.

IGT (1972). A Hydrogen-Energy System. Institute of Gas Technology, report prepared for the American Gas Association, Catalog No. L21173, August.

Lynch, F., Marmaro, R., 1992. Special purpose blends of hydrogen and natural gas to Hydrogen Consultants, Inc., August 18, 1992. US Patent 5,139,002.

National Petroleum Council. Hydrogen Compressed Natural Gas (HCNG) Transport Fuel. Topic Paper #25, August 1, 2012.

Nelsson, C., Hulteberg, C., Saint-Just, J., Kaiadi, M., 2010. HCNG—a dead end or bridge to the future. In: 18th World Hydrogen Energy Conference 2010—WHEC 2010, ISBN: 978-3-89336-655-2.

NGV Global News, 2010. Eden Energy Hythane Test Produces Significant Results, May 31, 2010. Available at: http://www.ngvglobal.com/eden-energy-hythane-test-produces-significant-results-0531 (last accessed February 2015).

Melaina, M., Antonia, O., Penev, M., 2013. Blending Hydrogen into Natural Gas Pipeline Networks: A Review of Key Issues. NREL Technical Report NREL/TP-5600-51995, March 2013.

US DOE, Alternative Fuels Data Center, 2015. Available at: http://www.afdc.energy.gov/ (Last accessed July 2015).

US Energy Information Administration, 2015. How Much Ethanol Is in Gasoline and How Does It Affect Fuel Economy? Available at: http://www.eia.gov/tools/faqs/faq.cfm?id=27& t=10 (last accessed January 2015).

Wang, J., Huang, Z., Chenglong, T., Zheng, J., 2010. Effect of hydrogen addition on early flame growth of lean burn natural gas–air mixtures. Int. J. Hydrog. Energy 35, 7246–7252.

Optical diagnostics for the analysis of hydrogen–methane blend combustion in internal combustion engines

9

S. Di Iorio, P. Sementa, B.M. Vaglieco
Istituto Motori—CNR, Naples, Italy

Acronyms

AFR	air–fuel ratio
ASOS	after start of spark
ATDC	after top dead center
BFSC	brake fuel-specific consumption
BTDC	before top dead center
cad	crank angle degree
CoV	coefficient of variance
DOC	duration of combustion
DOI	duration of injection
EC	energy consumption
EOI	end of injection
FL	full load
FWHM	full width at half maximum
ICCD	intensified charge coupled device
IMEP	indicated mean effective pressure
LDV	laser Doppler velocimetry
LIF	laser-induced fluorescence
LHV	lower heating value
MBT	maximum brake torque
NGI	natural gas injector
PFI	port fuel injection
Pinj	injection pressure
PL	partial load
P_{max}	maximum in-cylinder pressure
ROHR	rate of heat release
RON	research octane number
rpm	revolution per minute
SOS	start of spark
TDC	top dead center

THC	total HC
UHC	unburned HC
UV	ultraviolet
θ50	center of combustion

9.1   Introduction

Both energy consumption and greenhouse gas (GHG) emissions have increased over the years as well as fuel depletion. Moreover, environmental pollution has reached serious limits for human health and for their surroundings mainly because of the use of fossil fuels for internal combustion engines (Kalghatgi, 2014; Nicoletti et al., 2015). For this reason it is mandatory that there be improvement in fuel efficiency, a reduction of emissions from engines, and the development of clean, renewable energy sources to replace carbon-based fuels. Nevertheless, the efficient use of existing supplies can be the fastest, cheapest, and cleanest solution to meet future energy and environmental needs until a large-scale production and distribution of alternative energy is developed (Karim and Wierzba, 1983; Rousseau et al., 1999).

In this context, the gaseous fuels and hydrogen can contribute to reduce fossil fuel consumption and solve environmental problems (Verhelst and Wallner, 2009). Methane is widely used in spark ignition (SI) engines because of its physical and chemical properties such as high knocking resistance (Karim and Wierzba, 1983). The major drawbacks of the use of methane in engines are the slow flame propagation speed and its poor lean-burn capability (Rousseau et al., 1999). The addition of hydrogen is very effective in the acceleration of methane combustion (Di Iorio et al., 2014; Ranson, 2000; Dimopoulos et al., 2007) as well as the reduction of cyclic variation (Ji and Wang, 2009, 2010; Wang and Ji, 2012; Wang et al., 2010; Yousufuddin and Masood, 2009; Dimopoulos et al., 2008). The wide flammability limits and the low quenching gap contribute to the extension of lean operation limit (Park et al., 2011; Xu et al., 2010; Ma et al., 2010; Wang et al., 2008) enhancing thermal efficiency. Moreover, CO_2 can be further reduced because of the absence of carbon in hydrogen fuel.

Unlike methane, hydrogen is not an energy source but rather an energy carrier, as it does not occur naturally on Earth. It might become a viable transport fuel if it overcomes significant barriers in production, transport, storage, and safety (Kalghatgi, 2014). Hydrogen can be produced using renewable sources through an expensive process, such as integrated wind-to-hydrogen (power to gas) plants. Nevertheless, as of 2014, 95% of hydrogen is made from methane, waiting for other exploring technologies that can reduce the production cost enough, and produce quantities of hydrogen great enough, to compete with the traditional energy sources (Wind-to-Hydrogen Project, 2009).

Hydrogen has been presented primarily as a fuel for fuel cell (FC) applications, as proposed by the US Department of Energy (2002). In recent years, many companies have researched the feasibility of commercially producing hydrogen cars, and some have introduced demonstration models in limited numbers (WHEC, 2012). At the 2012 World Hydrogen Energy Conference, Daimler AG, Honda, Hyundai, and Toyota confirmed plans to produce hydrogen fuel cell vehicles for sale by 2015 (Verhelst

et al., 2013). General Motors had not abandoned fuel cell technology and still plans to introduce hydrogen vehicles like the GM HydroGen4 to retail customers by 2015. They stated that the company believes that both fuel cell vehicles and battery electric vehicles are needed for the reduction of GHGs and the reliance on oil (WHEC, 2012). Nevertheless, great efforts are also devoted to develop technologies that might efficiently exploit the potential of hydrogen energy for motor vehicles. Hydrogen internal combustion engine cars are different than hydrogen fuel cell cars. The hydrogen internal combustion car is a slightly modified version of the traditional gasoline internal combustion engine car. The hydrogen engines burn fuel in the same manner that gasoline engines do (Verhelst et al., 2013). For this reason, the most extensive research activity has been performed on port fuel ignition (PFI) SI engines, where hydrogen and methane have been premixed and injected. The addition of hydrogen improves the combustion of methane/compressed natural gas. In particular, the methane/hydrogen blend is characterized by higher thermal efficiency at stoichiometric and lean combustion (Ma et al., 2009; Baratta et al., 2013; Kahraman et al., 2009; Ceper et al., 2009), lower combustion time and ignition delay (Ma et al., 2008, 2009; Wallner et al., 2007) with respect to methane combustion. The cycle-by-cycle variation (Ma et al., 2008; Baratta et al., 2014) is reduced as well as CO, CO_2, and UHC emissions (Ma et al., 2009; Kahraman et al., 2009; Wallner et al., 2007). The spark advance for mean brake torque at stoichiometric and lean combustion (Di Iorio et al., 2014; Wallner et al., 2007) can be reduced. On the other hand, the wall heat losses as well as the NO_x emissions (Ma et al., 2009; Wallner et al., 2007) increase because of the higher combustion temperatures and the lower quenching distance. The effect of the addition of hydrogen on knock tendency was studied as well. Hydrogen, in fact, improves the knock tendency in an SI engine as it reduces the combustion period (Shinagawa et al., 2004; Topinka et al., 2004). The experimental investigations on the effects of hydrogen addition on SI engines running under lean and diluted conditions on combustion characteristics and emissions were well presented in a paper by Tahtouh et al. (2011). They demonstrated that the dilution and the lean engine operability limits, which are beneficial in reducing both emission levels and fuel consumption, are extended only when the hydrogen percentage in the fuel is higher than 40% by volume. On the other hand, at a fixed engine load, HC and CO emissions decrease with the increase of the hydrogen fraction in the intake mixture, while NO_x emissions are mainly affected by the equivalence ratio and by the amount of dilution. Pumping losses, combustion efficiency and indicated efficiency were also improved combining hydrogen addition with lean and/or diluted conditions (Tahtouh et al., 2011). The use of hydrogen directly injected is also widely studied following the experience of a research group that operated on a lean-burn natural gas engine with direct injection (Reynolds and Evans, 2004). The effect of engine design was also characterized. In particular, Salazar and Kaiser (2011) have considered the effect of tumble. Verhelst et al. (2013) studied the effects of injection angle and start of injection on engine efficiency and emissions. They observed that a wide range of injection timings can be operated at stable low engine load conditions if the hydrogen is injected toward the spark plug. Moreover, recent studies have illustrated the effects of different injection strategies for methane, hydrogen, and hydrogen-enriched methane in a single-cylinder SI engine fueled with methane–hydrogen blends, and split injection

of methane (port injected) and comparably small amounts of hydrogen (direct injected). The split injection of methane alone (i.e., port injected and direct injected) was studied to distinguish between enhanced chemical reactions and flow effects. The results demonstrated that late fuel injection toward the spark plug can produce a significant advantage due to increased turbulence or charge stratification. It is also shown that the extension of the lean limits by the direct injection of comparably small amounts of methane is very similar to the lean limit extension using hydrogen addition (Biffiger and Soltic, 2015).

In this chapter, the studies carried out with conventional and advanced optical diagnostics to better understand the phenomena occurring in an engine fueled with methane–hydrogen blends are described. The effect of hydrogen addition on engine performance and pollutant emissions was investigated through a combined thermodynamic and optical investigation of the combustion process. The measurements were performed on an optical SI (PFI SI) engine. The findings are compared to those obtained with methane, considered as the reference case. This study allowed the analysis of some complex mechanisms involved in the combustion process, giving relevant information for the definition of the optimal configuration for methane–hydrogen engine configuration.

9.2   Optical diagnostics for combustion analysis

The combustion process occurring in internal combustion engines is characterized by complex chemical reactions of the hydrocarbon mixture at temperatures and pressures that change rapidly. It is influenced by many factors, such as fuel properties, chemistry, fluid dynamic processes, and the local equivalence ratio. In SI engines, combustion can proceed as a normal or abnormal phenomenon depending on engine operating conditions. The normal one, which is initiated solely by a timed spark, generates a flame front moving across the cylinder volume in a uniform manner at normal velocity. The abnormal combustion depends mainly on the temperature and the pressure history of the end gas as well as on the rate of development of the flame and can cause two major phenomena: surface ignition and knock (Ciatti et al., 2007). The knock phenomena causes reduced efficiency, increased heat transfer, and severe engine damage. A more detailed evaluation of these phenomena is performed when conventional techniques are coupled to optical techniques. In particular, the optical techniques allows the study of the combustion process without interfering with the phenomena that occurs in the cylinder. Moreover, the high spatial and temporal resolution makes possible the local analysis of the combustion process.

In recent years, optical techniques have been widely used to characterize the different processes involved in the combustion process. Laser Doppler velocimetry was applied to get information on the in-cylinder fluid dynamics. Shadowgraphy and the Schlieren measurements give relevant information on SI and flame propagation. Laser-induced fluorescence (LIF) was used for the analysis of the air–fuel mixture. Moreover, LIF as well as natural flame emission spectroscopy can be applied to follow the combustion evolution and the formation of the main chemical species. Natural flame emission spectroscopy allows for the analysis of the flame propagation and quantitative measurements of normal and abnormal combustion processes.

This section gives a brief overview of the most widely used natural flame emissions spectroscopy and their application for combustion analysis in SI engines: 2D digital imaging and ultraviolet (UV)–visible spectroscopy (Schefer, 2003; Tahtouh et al., 2010; Aleiferis and Rosati, 2012; White, 2007; Ciatti et al., 2007; Shudo et al., 2000; Gupta et al., 2011). These techniques can be considered the most flexible among the optical diagnostics because they can be applied in real engines and transparent research engines. In the first case, endoscopic devices, optical probes through a modified spark plug or engine head gasket are used. Nevertheless, the use of a partially transparent elongated piston offers a more accurate analysis of the complex phenomena involved in the SI combustion process (Zhao and Ladommatos, 1998).

Two-dimensional digital imaging is widely used to follow the combustion process in terms of gas/liquid fuel spray evolution and luminous combustion as well as to evaluate the fundamental in-cylinder processes, such as the flame propagation characteristic, cycle-to-cycle variability, and the equivalence ratio (Higgins et al., 2001; Ikeda et al., 2001; Anders et al., 1999). In particular, the analysis of the flame front diameter overcomes the limitation of pressure measurements in determining the initial flame kernel development very useful in characterizing the combustion process (Aleiferis et al., 2000; Aleiferis and Rosati, 2012; Bates, 1991). This technique was used by several authors to study the methane and hydrogen combustion in the internal combustion engine (White, 2007; Shudo et al., 2000; Tahtouh et al., 2010). A typical natural chemiluminescence emission of methane combustion detected in a small displacement single-cylinder optical engine is shown in Figure 9.1.

Natural flame emission spectroscopy, from UV to short visible range, allows a comprehensive analysis of the structure of the flame front, offering qualitative information on the spatial and temporal distribution of the radicals generated during the combustion, such as OH*, CH*, and C_2*, which are indicative of the reacting conditions in the flame. OH* chemiluminescence is used to measure flame propagation characteristics, cycle-to-cycle variability, and to evaluate global trends related to in-cylinder mixture formation (Ciatti et al., 2007). Moreover, OH* and C_2* chemiluminescence emissions can be correlated to the flame temperature (Dieke and
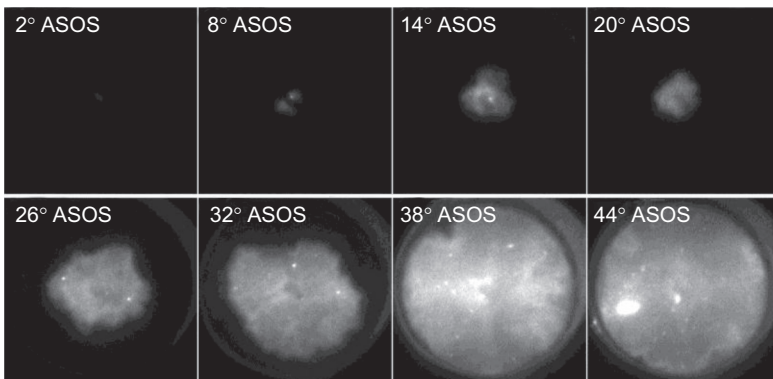
Figure 9.1 Natural flame emissions of methane combustion (Catapano et al., 2015).

Crosswhite, 1962). CH* is an important indicator of prompt NO formation (Lee et al., 2004), it is strongly dependent on the temperature (Higgins et al., 2001), and it is a marker of the break of the fuel into simple hydrocarbons.

Typical spectra detected at the inception of the spark, corresponding to a bright arc, and during combustion, in a transparent SI engine fueled with methane hydrogen blend (Di Iorio et al., 2014) are shown in Figure 9.2.

The radical species CN*, NH*, and C_2* are evident only at the SI timing. CN* and NH* mark the interaction between the excited hydrocarbon species of the fuel and the surrounding air molecules (Gaydon, 1957; Alkemade and Herrmann, 1979). C_2* is related to the carbon in the fuel (Gaydon and Wolfhard, 1953). OH* and CH* are instead well resolvable during the whole combustion process as well as a significant background of the broadband emission due to chemiluminescence of CO_2*, the convolution of HCO* Vayda bands, and HCHO* Emeleus bands (Miao et al., 2008; Garland and Crosely, 1988; Najm et al., 1998; Gupta et al., 2011; Shudo et al., 2000).

9.3   Characterization of the effect of hydrogen addition on methane combustion

The optical diagnostic techniques were applied together with conventional methods to better understand the effect of the hydrogen addition on flame stability, engine efficiency, and the pollutant formation and emissions of a methane-fueled engine.

9.3.1   Experimental setup

9.3.1.1   Engine

The investigation was carried out on an optically accessible single-cylinder SI engine whose specifications are listed in Table 9.1. The engine was equipped with the cylinder head of a commercial single-cylinder PFI 250 cm^3 engine. The head had four valves and a centrally located spark plug. The engine was characterized by an elongated cylinder and an elongated piston provided with a sapphire window, which replaces the flat-bottom piston bowl. This system enables the passage of optical signals coming from the combustion chamber. The engine was also equipped with a quartz cylinder to provide a lateral view of the combustion chamber. To reduce the window contamination by lubricating oil, the elongated piston arrangement was used together with self-lubricating Teflon-bronze composite piston rings in the optical section. A four-valve, pent-roof chamber engine was fitted on the elongated piston. The engine was not equipped with any after-treatment device. The air–fuel ratio (AFR) was measured by a linear lambda sensor installed at the exhaust. Gaseous fuels were supplied by a pressurized bottle using a pressure regulator typically set to 5 bar. A natural gas injector Bosch single-hole injector was used for all the gaseous fuels. The injection parameters, such as the ignition timing and the injection duration, were set by means of an electronic unit. A closed loop control allows the adjustment of the
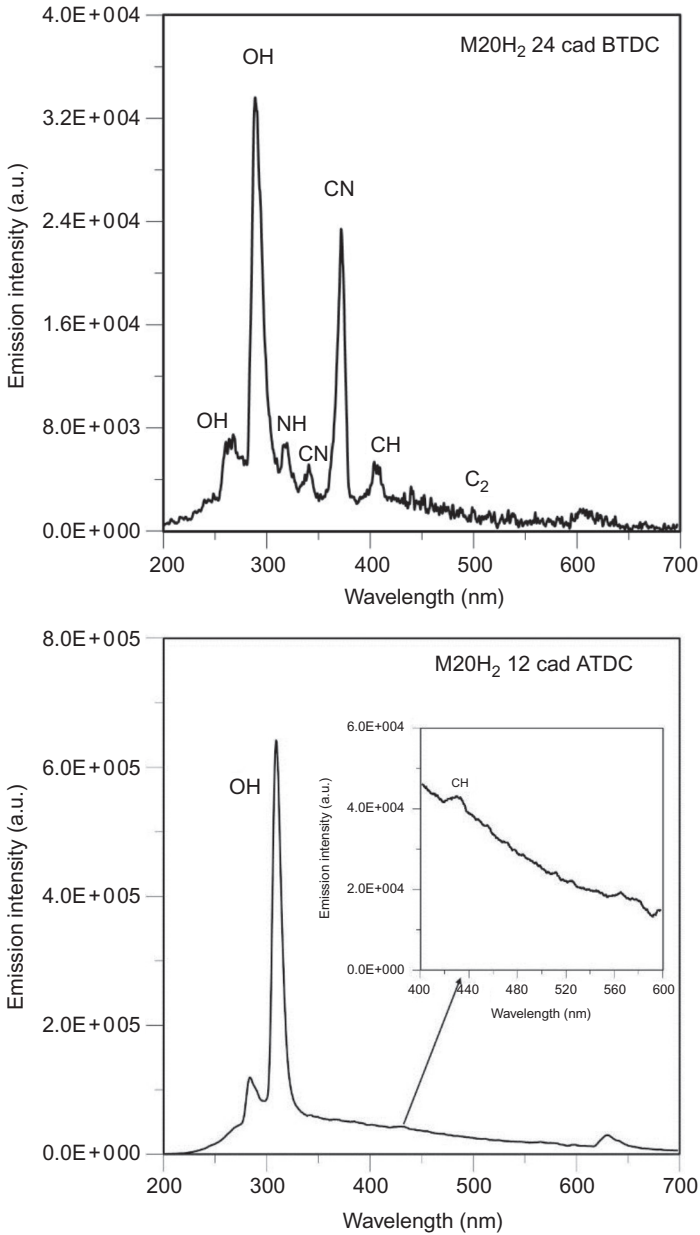
Figure 9.2 Emission spectra for M20H$_2$ in the central location of the chamber at 2000 rpm at different crank angles.

Table 9.1 Specifications of the PFI SI single-cylinder engine

Displacement (cm^3)	250
Bore (mm)	72
Stroke (mm)	60
Connecting road (mm)	130
Compression ratio	10.5:1

fuel injection in order to work with the desired AFR value. An optical shaft encoder was used to transmit the crankshaft position to the electronic control unit. A quartz pressure transducer was flush installed in order to measure the in-cylinder pressure.

Steady state measurements of CO, CO_2, O_2, UHC (unburned hydrocarbon), and NO_x were performed at the raw exhaust by commercial analyzers. CO, CO_2, and HC were measured by nondispersive infrared detectors; NO_x and O_2 were detected through electrochemical sensors. The methane component of HC emissions was measured by means of a Hewlett Packard 5890 gas chromatograph.

9.3.1.2 Fuels

The engine was fueled with pure methane (M) and blends of methane in hydrogen at 20% (v/v) (20MH2) and 40% (v/v) (40MH2) of hydrogen in methane. Methane and hydrogen were mixed by the supplier prior to the filling of the fuels into specific high-pressure gas bottles (approximately 200 bar). The main chemical and physical properties for pure methane and pure hydrogen are reported in Table 9.2.

9.3.1.3 Optical apparatus and procedures

Two-dimensional digital flame chemiluminescence imaging and natural flame emission spectroscopy measurements from UV to visible were performed by means of the optical experimental setup shown in Figure 9.3. During combustion the light emission

Table 9.2 Chemical and physical properties for methane and hydrogen

	Methane	Hydrogen
Molecular weight (g/mol)	16.04	2.02
C/H ratio (%)	0.25	0
Density (kg/Stm^3)	0.67	0.08
Low heating value (MJ/kg)	50	120
Flammability limits (vol.%)	5.3/14	4/75
Stoichiometric air/fuel ratio (kg\kg)	17.24	34.20
Max laminar burning velocity in air (m/s)	0.3–0.35	2–4
Net ignition energy (MJ)	0.29	0.02
Quenching distance (mm)	1.9	0.6
Energy density (MJ/l)	35.8	10.3
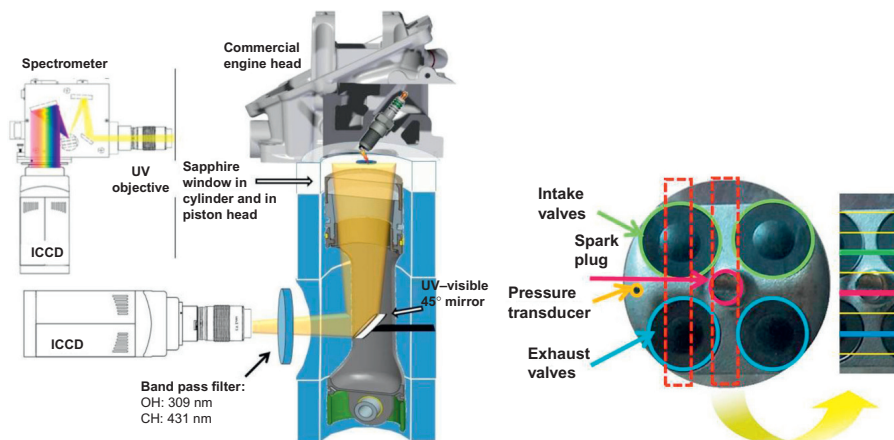
Figure 9.3 Optical apparatus for UV–visible imaging and spectroscopic measurements (left) and image of the combustion chamber with locations of measurement (right).

passed through the sapphire window and it was reflected toward the optical detection assembly by a 45° inclined UV–visible mirror located in the bottom of the engine and then recorded by means of the acquisition system.

The chemiluminescence signals were detected with a high spatial and temporal resolution by means of a Pimax intensified charged couple device (ICCD) camera. The chemiluminescence of the combustion process was recorded to follow the combustion propagation under different hydrogen levels. A postprocessing of the 2D digital imaging data was carried out to obtain the mean radius of the flame front and then the flame front mean propagation speed (Sementa et al., 2011).

For the spectroscopic investigations, combustion light emission was focused onto a micrometer controlled entrance slit of a spectrometer coupled to an ICCD camera (Figure 9.3). The central wavelength of the spectrometer was fixed at 375 and 575 nm to investigate the natural emissions from the UV (250 nm) to the visible (750 nm). The measurements were performed in correspondence of the central slice, chosen to detect the emission spectra from the spark inception to the combustion close to the spark plug, and of the lateral location of the combustion chamber, to follow the combustion in correspondence of intake and exhaust valves (Sementa et al., 2011).

9.3.2 Results and discussion

Experimental tests were carried out to study the complex mechanisms involved in the combustion process of methane and methane–hydrogen blends. The engine was fueled with pure methane (M), 20% (v/v) of hydrogen in methane (M20H_2) and 40% (v/v) of hydrogen in methane (M40H_2). The experimental investigations were carried out at 2000 rpm full load (FL) and 3000 rpm partial load (PL), corresponding to the same torque of 2000 rpm FL, around 8 Nm. The injection and ignition timing were kept constant to analyze the effect of the hydrogen on the combustion behavior

independently from the combustion phasing. In particular, the end of injection (EOI) was set at 250 cad before top dead center (BTDC). The start of spark (SOS) was the spark timing for maximum brake torque with pure methane. It was 24 cad BTDC at 2000 rpm and 22 cad BTDC at 3000 rpm. The methane and blends were injected at a pressure of 5 bar. The engine was operated at stoichiometric condition, and then the duration of fuel injection was properly chosen for each fuel. In particular, it increases at the increase of the hydrogen content because of the lower density of the fuel.

The in-cylinder pressure, the rate of heat release (ROHR), and the related parameters were assessed on an individual cycle basis and/or averaged on 400 cycles (Heywood, 1988). The performance in terms of the indicated mean effective pressure (IMEP) and the coefficient of variance (CoV) of IMEP was assessed as well. The values of the main engine parameters, such as the IMEP and lambda with the related coefficients of variance (CoV) for all the engine operating conditions and the tested fuels are reported in Table 9.3. The CoV both for IMEP and lambda was measured over 400 consecutive cycles.

Useful information on the combustion stability and the engine lean-burn limits can be obtained by the CoV for the IMEP, which represents the cyclic variability derived from pressure data (Deluchi, 1989). The CoV of the IMEP is always less than 3% indicating a very stable combustion. Moreover, from this result it can be argued that the thermal evolution and fluctuation of the maximum pressure signal due to the cyclic variation and the heat transfer between the different components of the optically accessible engine are negligible. It is possible to observe a slight increase of IMEP values for the hydrogen blends, looking at the data shown in Table 9.3. Moreover, the IMEP is slightly higher for $M20H_2$ with respect to $M40H_2$. For the percentage of hydrogen larger than 20% (v/v), the lower energy density likely prevails on the beneficial effect of hydrogen addition. The analysis of the impact of the addition of hydrogen on the combustion can be depicted by the in-cylinder pressure and the ROHR, shown in Figure 9.4.

The maximum in-cylinder pressure and the ROHR increase linearly with the hydrogen addition. Moreover, for the blends the combustion evolves faster and closer to the top dead center (TDC), as evidenced by the ROHR curves. These results evidenced that the hydrogen addition accelerates the combustion process, as also observed by Moreno et al. (2012) and Wang et al. (2009).

Table 9.3 Engine operating conditions

Fuel	Speed (rpm)	DOI (cad)	IMEP (bar)	CoV IMEP	Lambda	CoV lambda	Torque (Nm)
M	2000	82	4.3	2.9	1.0	0.5	7.4
$M20H_2$	2000	87	5.1	1.8	1.0	1.1	8.8
$M40H_2$	2000	97	4.8	2.0	1.0	0.7	8.2
M	3000	217	5	2.0	1.0	1.7	8.1
$M20H_2$	3000	234	5.2	1.1	1.0	0.4	8.4
$M40H_2$	3000	258	5.1	1.4	1.0	0.9	8.2
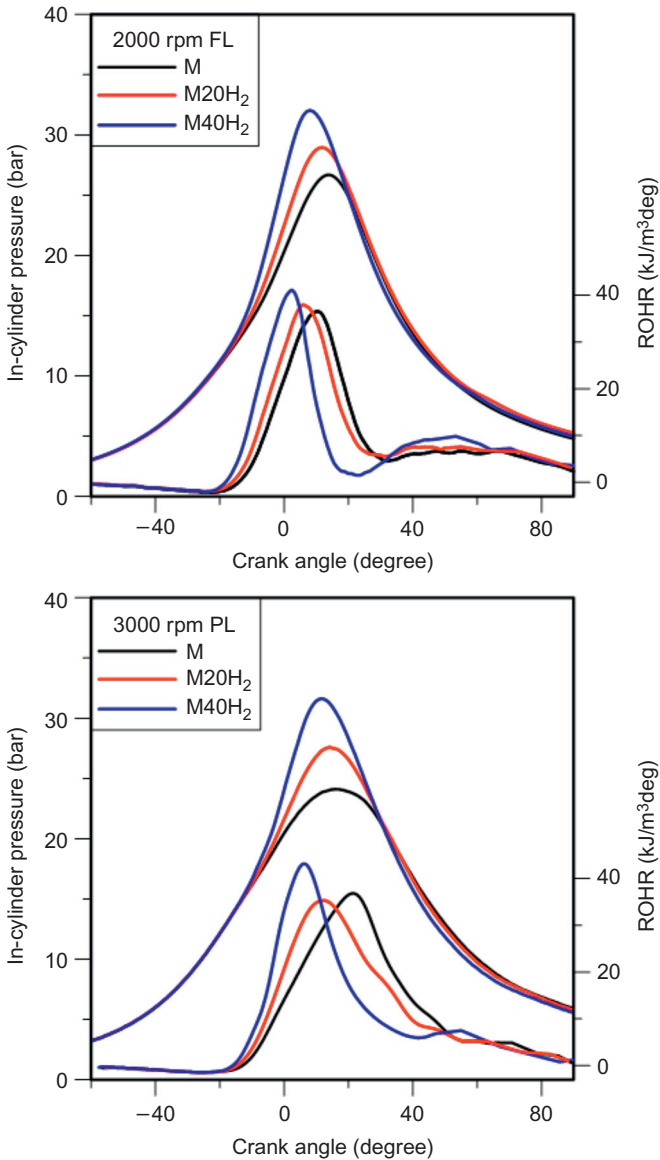
Figure 9.4 In-cylinder pressure and ROHR averaged curves for the engine fueled with pure methane and methane/hydrogen blends at 2000 rpm FL (up) and 3000 rpm PL (down).

The duration of combustion (DOC) and the center of combustion ($\theta50$), defined as the angle between the 5% and 90% of mass burnt ($\theta90$–$\theta5$) and the elapsed period for burning 50% of the total mass fuel, respectively, can give interesting information on methane combustion acceleration due to hydrogen addition. In Table 9.4, the

Table 9.4 **Combustion parameters**

Fuel	Speed (rpm)	θ50 (cad)	DOC (cad)	P_{max} (bar)
M	2000	10	45	27
M20H$_2$	2000	6	43	29
M40H$_2$	2000	2	39	32
M	3000	24	77	22
M20H$_2$	3000	19	67	24
M40H$_2$	3000	14	61	27

maximum in-cylinder pressure, the DOC, and the θ50 for all of the engine operating conditions and fuels are listed.

At the increase of the content of hydrogen, the center of combustion moves closer to the TDC. At the same time, the DOC decreases and the in-cylinder pressure and then the combustion temperature increase. It can be hypothesized that the addition of the hydrogen can promote the flame kernel formation and the flame propagation at the early stage of the mixture combustion. The faster burning velocity prompts a more advanced and shorter combustion duration with respect to methane, resulting in an increase of the cylinder gas temperature and in lower heat loses; as a result, the effective thermal efficiency is increased.

The combustion acceleration can be attributed to the effect of the addition of hydrogen to the chemical and physical processes occurring in flames. As shown by Collier et al. (2005), the methane combustion flame speed is limited by the slow reaction

$$CH_4 + O \rightarrow CH_3{}^+ + OH^-$$
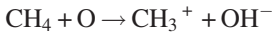
On the other hand, the reactions for completing the combustion, leading to H_2O and CO_2 formation, are very fast. The presence of the radicals obtained through hydrogen dissociation prompt a complete combustion, and then a faster one, allowing removing the first hydrogen atom from methane molecule (Schefer, 2001).

9.3.2.1 *Two-dimensional digital flame chemiluminescence imaging*

The temporal evolution of the integral of flame luminosity measured over all the combustion chamber and ROHR under different hydrogen content is shown in Figure 9.5.

The acceleration of combustion due to the addition of hydrogen as well as the improvement of combustion is well recognizable looking at the chemiluminescence intensity. The combustion emission intensity increases and the peak value advances with the hydrogen content. Moreover, it is evident that the addition of hydrogen can promote flame kernel formation and flame propagation at the early stage of combustion. These data are consistent with the ROHR results, and highlight the effect of the addition of hydrogen on early flame kernel development.

More details on flame propagation features can be obtained by an analysis of the images of the combustion shown in Figure 9.6.
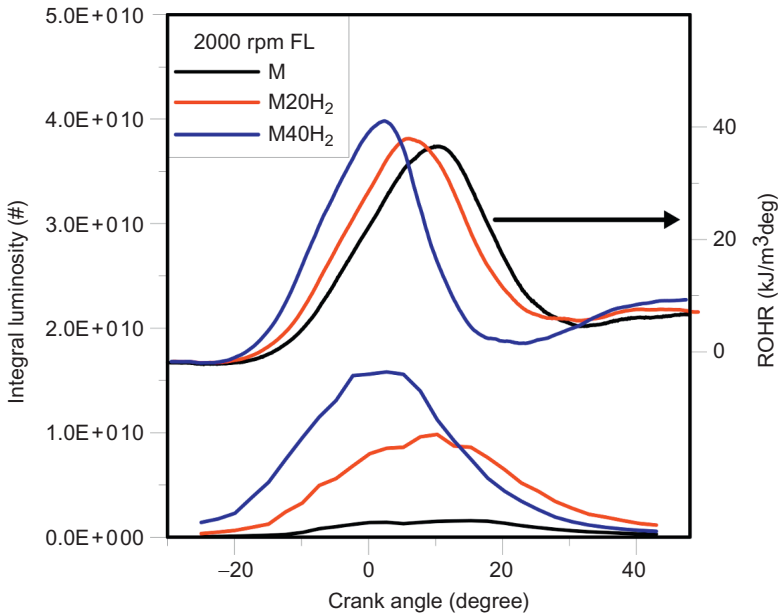
Figure 9.5 Integral of flame luminosity and ROHR for M (left), M20H$_2$ (right), and M40H$_2$ (down) at 2000 rpm FL.

The combustion develops almost radially toward the combustion chamber surface. However, distortion in the shape, in terms of symmetry and roughness of the boundaries, can be observed. In particular, the flame shows deviations of the flame's shape from a "circle," and it is generally wrinkled, as also observed in Aleiferis and Rosati (2012). The methane flame shows a more evident distortion and more wrinkled boundaries.

For a comprehensive analysis of the effect of hydrogen on flame propagation and distortion, the optical data were postprocessed using a shape descriptor of the flame front. Every image was processed by subtracting the background and fixing a threshold of 5% with respect to its maximum light intensity. This procedure allowed us to obtain the flame outline used to calculate the circularity of the flame front as well as the flame front diameter. The flame circularity is defined as circularity $=$ $(4 \cdot \pi \cdot \text{area})/\text{perimeter}^2$, where area $=$ flame front area and perimeter $=$ flame front perimeter. A value of 1.0 indicates a perfect circle. As the value approaches 0.0, it indicates an increasingly distorted shape. Figure 9.7 shows the circularity for all the tested fuels at 2000 rpm FL and 3000 PL.

At 2000 rpm the value of circularity is quite similar for all the tested fuels until 15 cad BTDC; after that, it increases with the hydrogen content in the blends. At 3000 rpm PL, instead, the effect of the addition of hydrogen on flame distortion is more evident. The circularity values calculated for methane are always lower than for hydrogen blends. These results highlight the positive effect of hydrogen on the flame front shape. Typically, the asymmetry of the flame is related to the in-cylinder
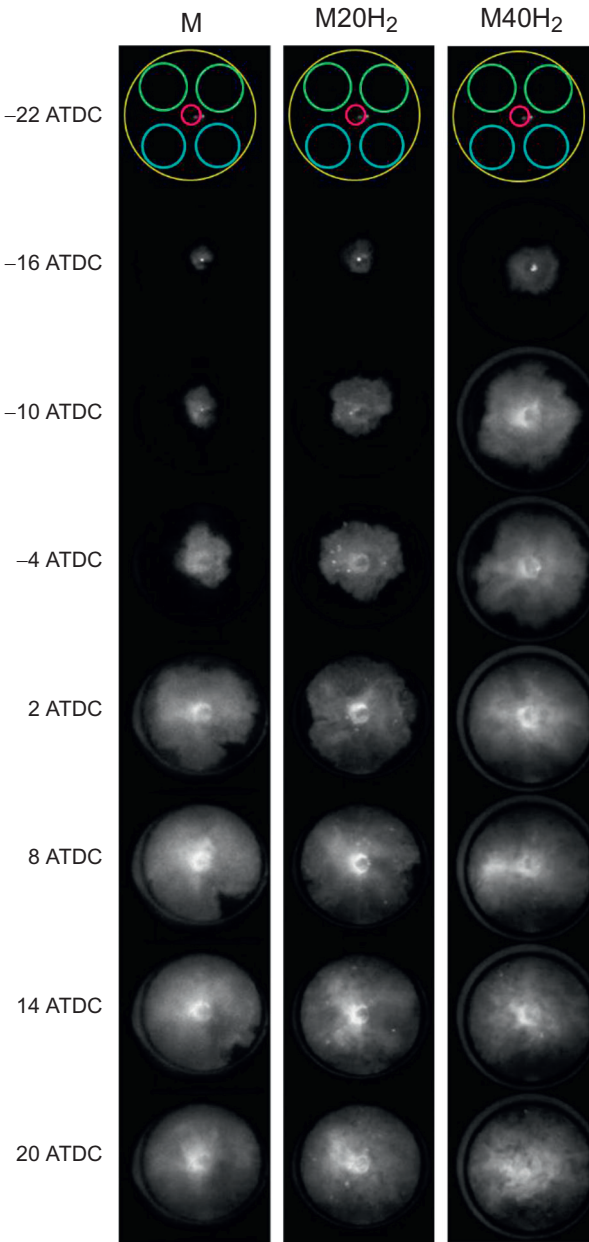
Figure 9.6 Images of the flame front propagation for M, M20H$_2$, and M40H$_2$ at 2000 rpm FL.

turbulence and the combustion reaction rate (Changwei et al., 2013). The in-cylinder turbulence enhances the distortion of the flame front of all fuels. The effect of turbulence is more evident for the methane because of the different fuel properties. The enhanced laminar flame speed due to the addition of hydrogen could improve the local
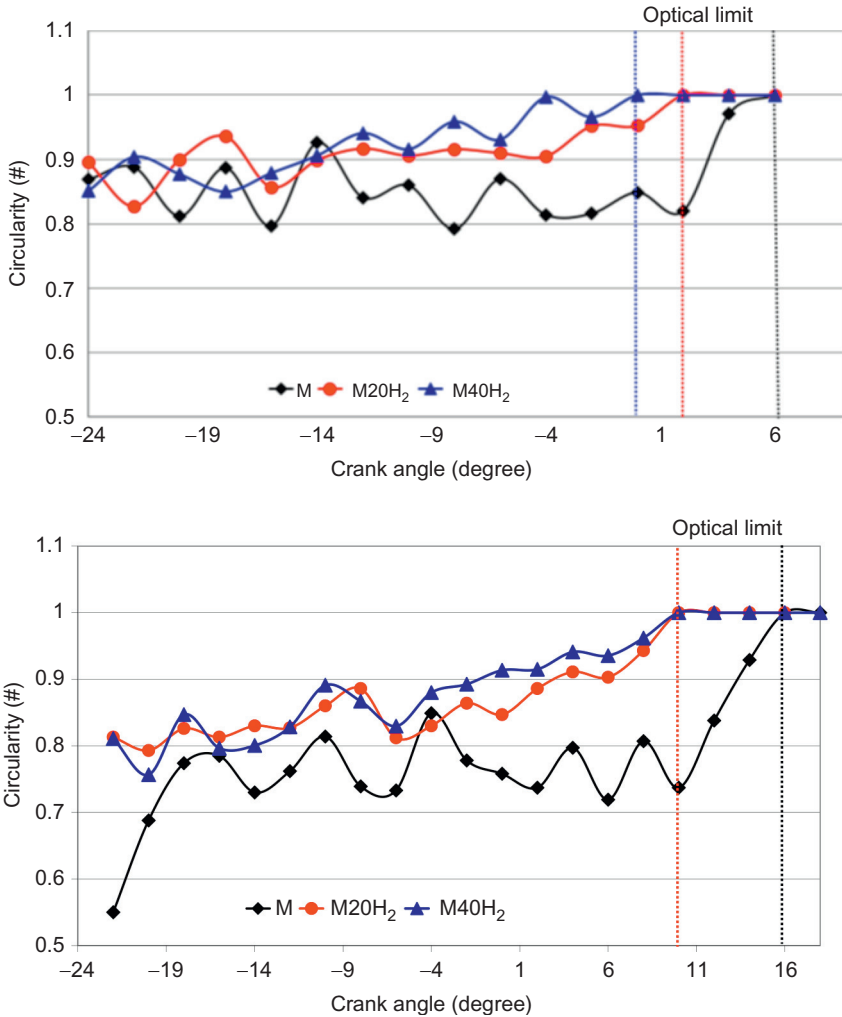
Figure 9.7 Flame front circularity for pure methane and methane/hydrogen blends at 2000 rpm FL (up) and 3000 rpm PL (down).

reaction rate contributing to the generation of the flame surface (Emadi et al., 2012) resulting in a more uniform flame front propagation. Moreover, the addition of hydrogen could increase the flame thickness (Miao et al., 2008), making the flame less sensitive to the local turbulence and consequently less irregular. Another aspect to take into account is the rapid diffusivity (3.8 × faster than methane) that enhances the formation of a uniform charge; therefore, when released it spreads quickly into a non-flammable concentration. The more the inhomogeneity of the mixture, the more the presence of fuel rich/lean zones, which slow down the flame front and worsen the efficiency of flame propagation. Furthermore, the wider flammability limits as

well as the lower ignition energy and quenching distance (Table 9.2) of the hydrogen with respect to the methane are positive to promote the combustion reaction rate and then to provide a more uniform propagation of the combustion.

The analysis of the flame front diameter allows overcoming the limitation of pressure measurements in determining the initial fame kernel development. Moreover, it is very useful in characterizing the combustion process as it heavily influences engine thermal efficiency and operating stability (Aleiferis et al., 2000, 2004; Bates, 1991).

The flame diameter was calculated from the flame area; the flame front propagation speed was evaluated as the time rate of the change of the flame radius. Figure 9.8 depicts the variation of the flame front diameter and the flame front propagation speed with crank angle for methane and blends at different engine operating condition.

The flame diameter increases almost linearly with time. The flame front propagation speed shows a similar behavior for all the fuels and operating conditions: quickly
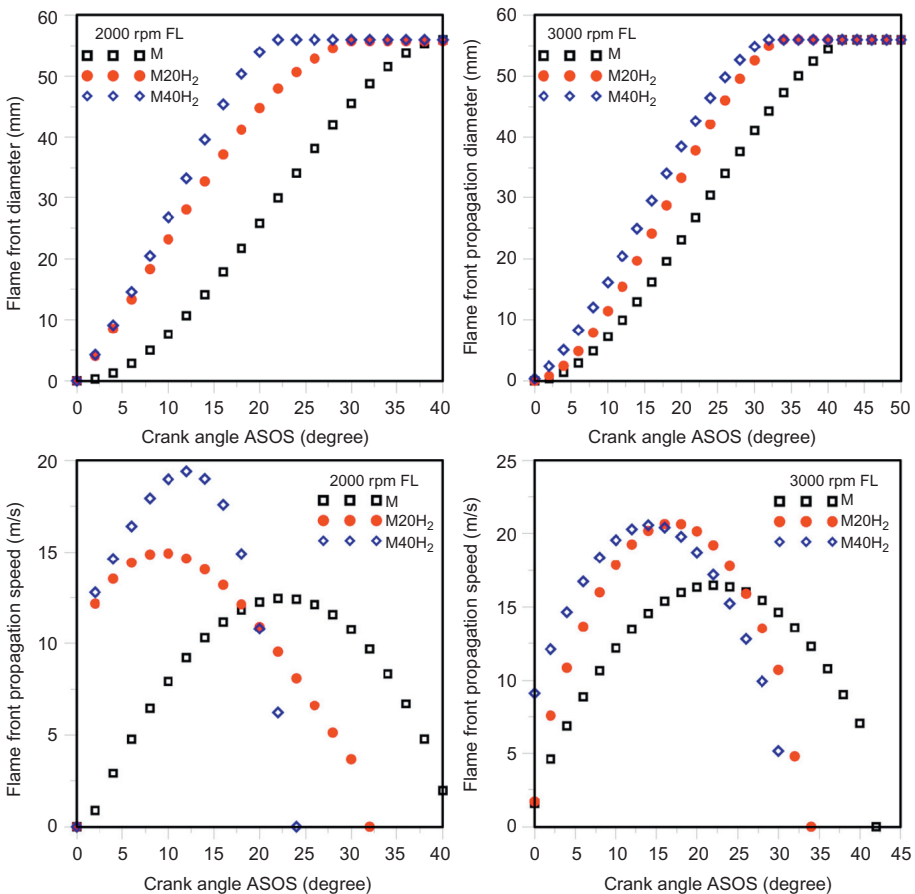
Figure 9.8 Flame front diameter (up) and propagation speed (down) vs. crank angle for M, $M20H_2$, and $M40H_2$ at 2000 rpm FL (left) and 3000 rpm PL (right).

rises, reaches a maximum, and then decreases. The low in-cylinder temperature and weak turbulence intensity around the spark plug, typical of the early phase of combustion, results in a relatively low flame propagation speed. Moving toward the center of the combustion, the enhanced turbulence intensity and the higher temperature cause the rise of the flame propagation speed, which reaches the peak value. During the last stage of combustion, the flame propagation speed decreases because of the increased fraction of combustion products, the reduced temperature, and weakened turbulence intensity near the cylinder linear. The flame growth was affected by the quality of the mixture. The flame propagation speed, in fact, increases and the peak advances with the increase of hydrogen volume fraction. These results are consistent with ROHR analysis. The improved flame propagation speed can be due, as said before, to the higher laminar flame speed of hydrogen with respect to methane. The higher diffusivity widens the total flame surface area, enhancing the turbulent reaction rate and accelerating the flame development process. Moreover, the addition of hydrogen prompts the formation of H*, O*, and OH* radicals, which are effective in accelerating the chain reactions and consequently improving the local laminar flame speed (Heywood, 1988). The advanced maximum flame front speed values can be attributed to the different evolution of the early stage of combustion. As said the hydrogen addition improves the local laminar flame speed and promotes the combustion reaction, enhancing the flame propagation speed also at the early stage of combustion. According to these data, it can be stated that the addition of hydrogen can promote flame kernel formation and flame propagation at an early stage of mixture combustion. Consequently, the flame propagates earlier with respect to methane. The advanced and accelerated flame propagation is beneficial for improving engine thermal efficiency and cycle-to-cycle variation as the combustion is closer to a theoretical combustion and the combustion duration is shortened as well as the heat exchange duration with cylinder walls.

A 3D graph representation of the combustion chemiluminescence emission makes more evident the effect of hydrogen addition on the combustion process. Figure 9.9 displays the combustion emission intensity measured at 34 cad after SOS for all the tested fuels.

This representation highlights the increase of the emissions intensity with the hydrogen content and the more evident distortion of the methane combustion flame. Moreover, it emphasizes the faster combustion propagation of the blends.

9.3.2.2 UV–visible spectroscopy

A comparison of the emission spectra detected in correspondence of a typical chamber position allows the analysis of the spatial evolution of the radical chemiluminescence (Figure 9.10).

The emission intensity is higher in correspondence of the spark plug and lower in correspondence of the intake valves. These results are consistent with the chemiluminescence images, and highlight the asymmetric evolution of the flame attributable to the motion of air that moves the combustion toward the exhaust valves.
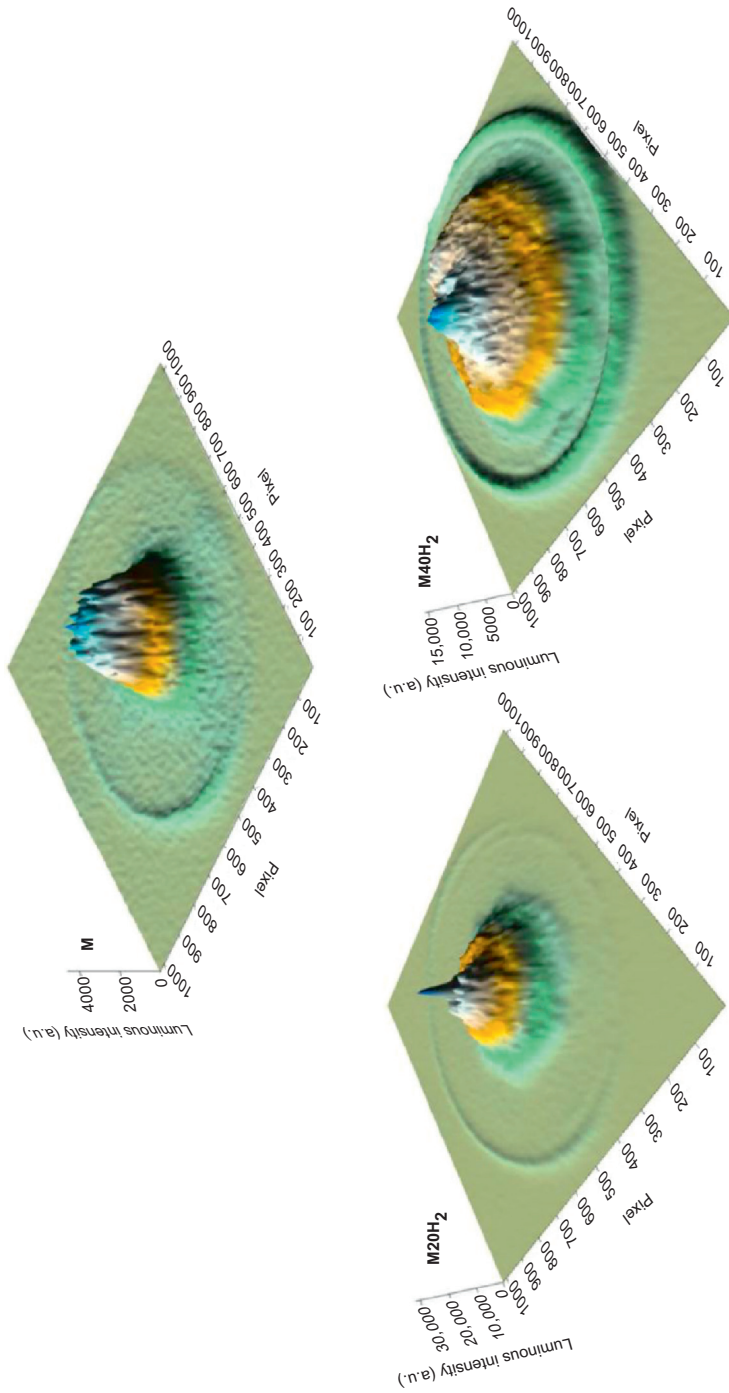
Figure 9.9 Images of the combustion flame luminosity for M (up), M20H$_2$ (left), M40H$_2$ (right) at 2000 rpm FL at 34 cad ASOS.
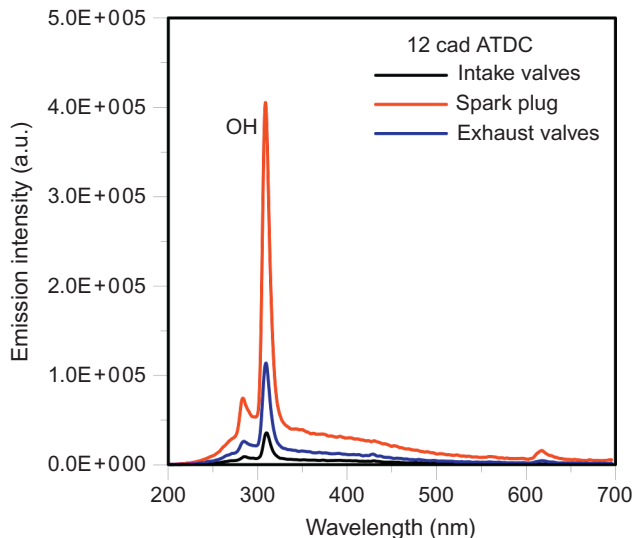
Figure 9.10 Emission spectra for methane in the central location in three typical locations of the chamber at 2000 rpm FL.

The comparison between the chemiluminescence emission spectra of methane and methane–hydrogen blends combustion in the same location and time is shown in Figure 9.11.

The chemiluminescence emission intensity increases at the increase of the hydrogen content in the blend, confirming that the faster combustion evolution of the blends is enhanced by the higher concentration of radicals due to hydrogen addition (Collier et al., 2005; Schefer, 2003).

The temporal evolution of the emission spectra for the three tested fuels is shown in Figure 9.12.

The intensity of the chemiluminescence emissions follows the combustion process: it increases during the first phase of combustion, reaches a maximum in correspondence of the center of combustion, and then decreases. The OH* is the predominant specie for all the tested fuels. Its temporal evolution is in good agreement with the flame front propagation speed results. The peak of the radical emission moves, in fact, closer to TDC at the increase of the hydrogen content (Najm et al., 1998). The OH* temporal evolution shows a rather rough profile. The emission spectra in the graph refer to different engine cycles. Therefore, the irregularity of the temporal evolution of OH* emission can be considered a marker of the instability of the combustion. It is worth noting that OH* temporal evolution becomes smoother as hydrogen concentration increases in the blends, indicating a more stable combustion. The extension of the lean stability limits and reduction of the cycle-to-cycle variability (Najm et al., 1998; Schefer, 2003; Larsen and Wallace, 1997; Meyers and Kubesh, 1997) obtained with hydrogen addition can be attributed to the enhanced reaction rates (Phillips and Roby, 1999). The larger H*, O*, OH* radical concentrations, due to hydrogen addition,
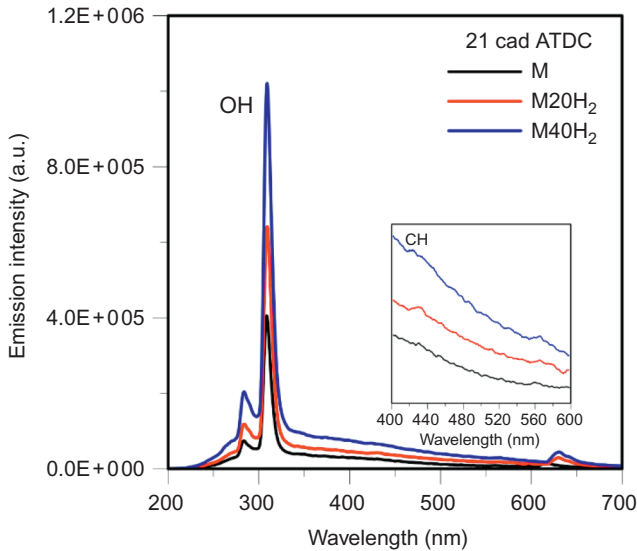
Figure 9.11 Emission spectra for methane/hydrogen blends in the central location in correspondence of the spark plug at 2000 rpm FL.

increase several key reaction rates. For example, H* is important for flame stability because of its relevant role in the chain branching reaction $H + O_2 \leftrightarrow OH + O$. This result makes stronger the hypothesis made for the digital imaging analysis regarding the irregularity of the flame front due to the inhomogeneity of the mixture in the pure methane condition.

9.3.2.3 Performance and emissions

To better analyze the effect of hydrogen addition on engine performance and emissions, their variation with respect to methane was considered:

$$\Delta X = X(\text{methane})/X(\text{MH2})$$

The variation of the brake fuel-specific consumption (ΔBSFC) and of the energy consumption (ΔEC) measured for all the tested fuels and the operating conditions are shown in Figure 9.13.

For all the tested conditions, fuel consumption decreases with the hydrogen content in the blend in accordance with the increase of the stoichiometric value. This effect is more evident for M20H$_2$ than for M40H$_2$ because the effect of the higher stoichiometric value is compensated by the lower energy density. Interesting information can be obtained from the analysis of the energy consumption evaluated as EC = BSFC × net heat value. The lowest energy consumption of the blends can be ascribed to the faster combustion promoted by hydrogen addition, which prompts a more efficient combustion. The combustion of M40H$_2$ blends can be further improved by a proper ignition calibration.
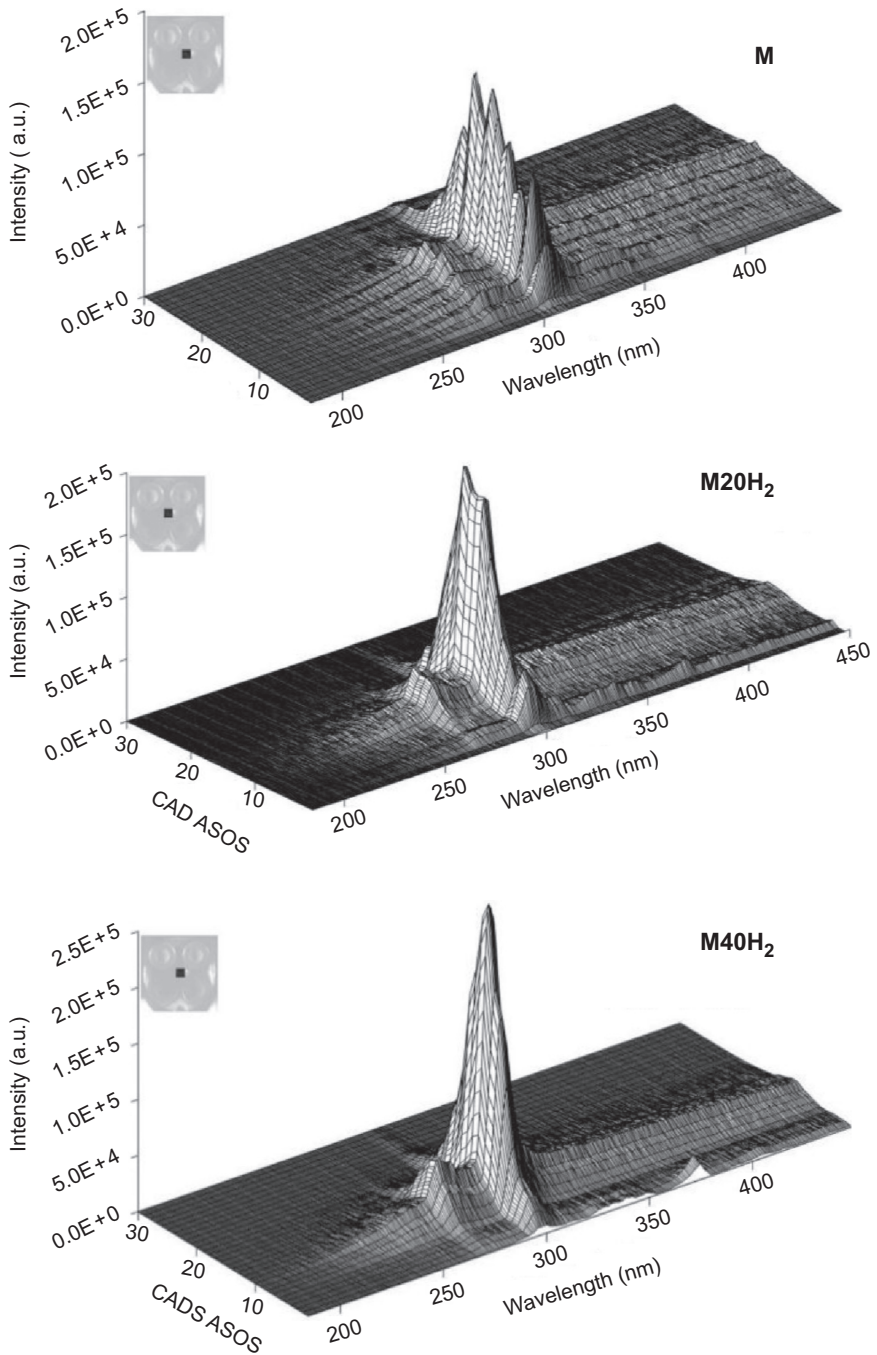
Figure 9.12 Temporal evolution of the emission spectra for methane (up), M20H$_2$ (center) and M40H$_2$ (down) detected at 2000 rpm FL at the central location of the combustion chamber.
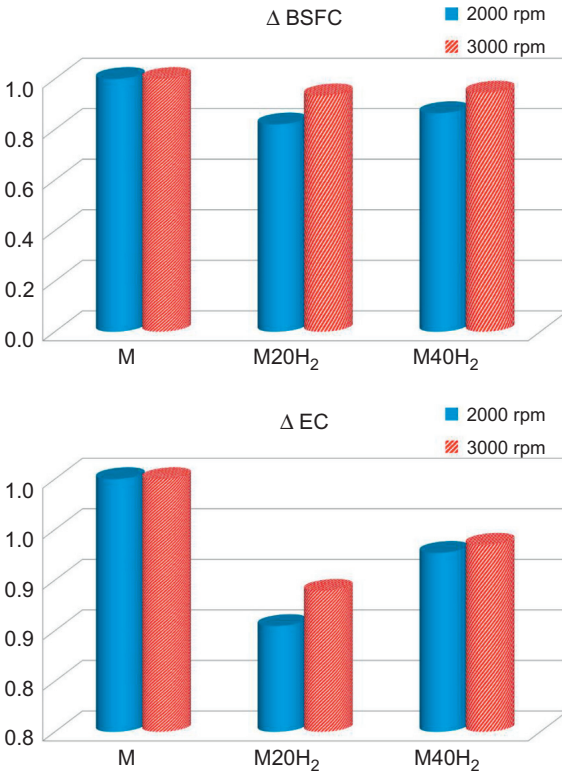
Figure 9.13 Brake fuel specific consumption and energy consumption for M, M20H$_2$, and M40H$_2$ at 2000 rpm FL (up) and 3000 rpm PL (down).

The variation of CO and CO$_2$ emissions with respect to methane fueling are reported in Figure 9.14.

CO and CO$_2$ emissions decrease at the increase of hydrogen content because of the lower carbon content of the blends. Moreover, as the hydrogen addition ratio is increased the radical pool increases, too. Higher OH* concentrations likely promotes the CO oxidation in CO$_2$ via the OH* radical. Figure 9.15 shows the variation of HC methanic and nonmethanic with respect to methane operation.

The HC emissions decrease at the increase of the hydrogen percentage in the blend. This result can be due to the lower carbon atom. The nonmethanic-HC emissions reduction is more evident than the methanic HC reduction because the addition of hydrogen to natural gas results in an increase in temperature, leading to a more effi-cient HC oxidation (Kahraman et al., 2009; Wang and Ji, 2012). Nevertheless, the lower quenching distance of hydrogen implies that when the flame approaches closer to the cylinder walls (Dimopoulos et al., 2007; Wallner et al., 2007) the hydrogen can still burn. On the other hand, the local conditions do not allow the methane combustion (Wallner et al., 2007). This implies a relative increase of methane in the THC emis-sions with the hydrogen addition ratio and this can be a shortcoming of the use of methane–hydrogen blends in engines. The oxidation treatment control of methane emissions is, in fact, more difficult than for the nonmethanic HC (Jordan et al.,
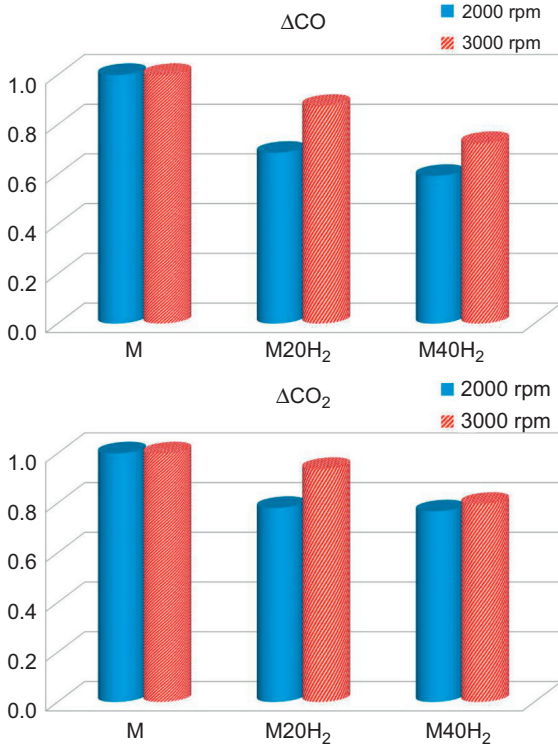
Figure 9.14 Variation of CO (up) and CO_2 (down) emissions for all the tested fuels.
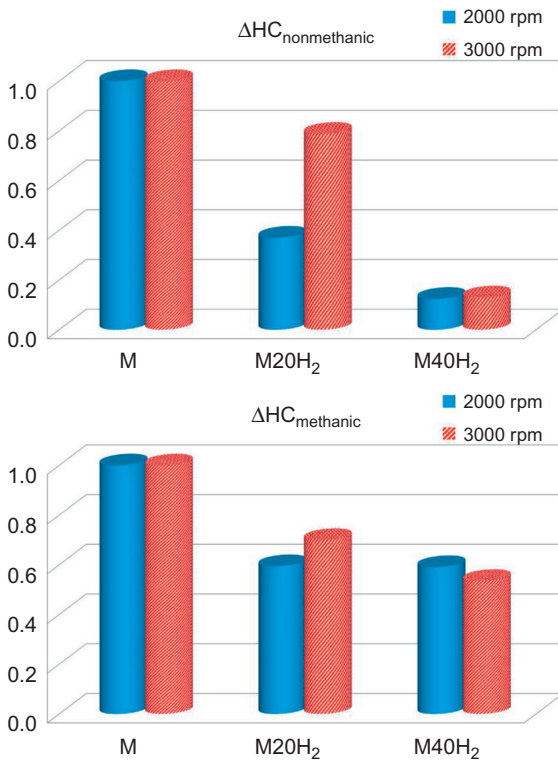
Figure 9.15 Variation of methanic (up) and nonmethanic HC (down) emissions for all the tested fuels.

1997; Tabata et al., 1995). Methane is regulated as a GHG; therefore, technology should be improved to satisfy the next-generation emissions standards.

Figure 9.16 represents the variation of NO_x emissions with respect to methane fueling.

The NO_x emissions increase at the increase of the hydrogen content in the blend because of the higher in-cylinder temperature, due both to the higher adiabatic temperature of the hydrogen and the faster and more advanced combustion. However, with the optimization of the spark advance timing, NO_x emissions can be reduced.

It is interesting to point out the benefit of the methane–hydrogen operation with respect to the conventional gasoline PFI engine (Catapano et al., 2015). In this sense, a comparison among the energy combustion related to a gasoline, methane, and methane–hydrogen blends operation is shown in Figure 9.17.

Methane operation is characterized by a lower EC with respect to gasoline. Nevertheless, the hydrogen addition improves the combustion process, resulting in a more efficient combustion also compared to the conventional gasoline operation.
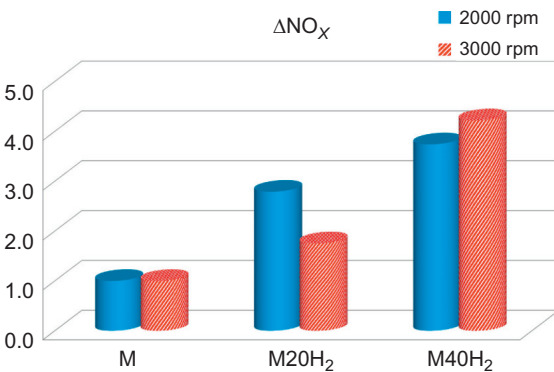
Figure 9.16 Variation of NO_x emissions with respect to methane operation for all the tested fuels at 2000 rpm FL.
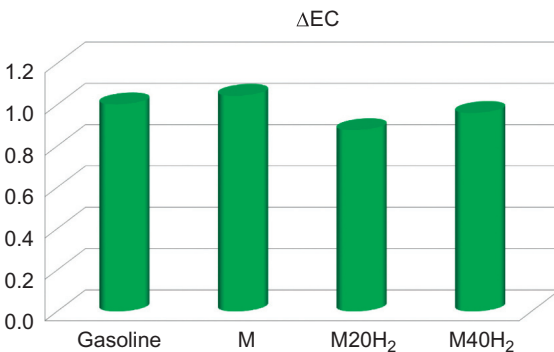
Figure 9.17 Variation of EC with respect to gasoline operation at 2000 rpm FL.

9.4   Conclusions

This chapter provided an experimental analysis of the effect of hydrogen addition on methane combustion. The strong effect of hydrogen addition on methane combustion was evaluated by the combustion process as well as on the engine performance and emissions. In particular, CO, CO_2, and methanic HC emissions decrease at the increasing of hydrogen content in the blends. On the other hand, NO_x emissions increase with the hydrogen fraction because of the increased in-cylinder temperature. Optical techniques allowed a more detailed analysis of the combustion process, highlighting that hydrogen addition results in a better flame kernel formation. Moreover, the flame propagation speed increases at the increase of the hydrogen content, and the flame front propagation is more uniform in all directions. Natural emission spectroscopy in the UV–visible range pointed out that the combustion promotion due to hydrogen addition and the increase of the stability can be ascribed to the larger H, O, and OH radical concentrations, which increases several key reaction rates. The improvement of the combustion due to the methane addition results in a more efficient combustion also compared to the conventional gasoline operation.

References

Aleiferis, P.G., Rosati, M.F., 2012. Flame chemiluminescence and OH LIF imaging in a hydrogen-fuelled spark-ignition engine. Int. J. Hydrogen Energy 37, 1797–1812.

Aleiferis, P., Taylor, A., Whitelaw, J., Ishii, K., Urata, Y., 2000. Cyclic variations of initial flame kernel growth in a Honda VTEC-E lean-burn spark-ignition engine. SAE Technical Paper 2000-01-1207. doi:10.4271/2000-01-1207.

Aleiferis, P., Taylor, A., Ishii, K., Urata, Y., 2004. The nature of early flame development in a lean-burn stratified-charge spark-ignition engine. Combust. Flame 136, 283–302.

Alkemade, C.T.J., Herrmann, R., 1979. Fundamentals of Analytical Flame Spectroscopy. Hilger, Bristol, UK.

Anders, H., Christensen, M., Johansson, B., Franke, A., Alden, M., Richter, M., et al., 1999. A study of the homogeneous charge compression ignition combustion process by chemiluminescence imaging. SAE Technical Paper 1999-01-3680. doi:10.4271/1999-01-3680.

Baratta, M., D'Ambrosio, S., Misul, D., 2013. Performance and emissions of a turbocharged spark ignition engine fuelled with CNG and CNG/hydrogen blends. SAE Technical Paper 2013-01-0866. http://dx.doi.org/10.4271/2013-01-0866.

Baratta, M., D'Ambrosio, S., Misul, D., Spessa, E., 2014. Effects of H_2 addition to compressed natural gas blends on cycle-to-cycle and cylinder-to-cylinder combustion variation in a spark ignition engine. J. Eng. Gas Turbines Power 136 (5), article no 051502.

Bates, S., 1991. Further insights into SI four-stroke combustion using flame imaging. Combust. Flame 85, 331–352.

Biffiger, H., Soltic, P., 2015. Effects of split port/direct injection of methane and hydrogen in a spark ignition engine. Int. J. Hydrogen Energy 40, 1994–2003.

Catapano, F., Di Iorio, S., Magno, A., Sementa, P., Vaglieco, B.M., 2015. A comprehensive analysis of the effect of ethanol, methane and methane-hydrogen blend on the combustion process in an optical PFI engine. http://dx.doi.org/10.1016/j.energy.2015.02.051.

Ceper, B., Akansu, S., Kahraman, N., 2009. Investigation of cylinder pressure for H_2/CH_4 mixtures at different loads. Int. J. Hydrogen Energy 34 (11), 4855–4861.

Changwei, J., Xiaolong, L., Binbin, G., Shuofeng, W., Jinxin, Y., 2013. Numerical investigation on the combustion process in a spark-ignited engine fueled with hydrogen gasoline blends. Int. J. Hydrogen Energy 38, 11149–11155.

Ciatti, S.A., Bihari, B., Wallner, T., 2007. Establishing combustion temperature in a hydrogen-fuelled engine using spectroscopic measurements. Proc. Inst. Mech. Eng. D: J. Automob. Eng. 221, 699.

Collier, K., Mulligan, N., Shin, D., Brandon, S., 2005. Emission results from the new development of a dedicated hydrogen-enriched natural gas heavy duty engine. SAE Technical Paper 2005-01-0235. doi:10.4271/2005-01-0235.

Deluchi, M., 1989. Hydrogen vehicles: an evaluation of fuel storage performance, safety, environment impacts, and cost. Int. J. Hydrogen Energy 14 (2), 81–130.

Di Iorio, S., Sementa, P., Vaglieco, B.M., 2014. Experimental investigation on the combustion process in a spark ignition optically accessible engine fueled with methane/hydrogen blends. Int. J. Hydrogen Energy 39 (18), 9809–9823.

Dieke, G.H., Crosswhite, H.M., 1962. The ultraviolet bands of OH. J. Quant. Spectrosc. Radiat. Transf. 2, 97–199.

Dimopoulos, P., Boulouchos, K., Rechsteiner, C., Soltic, P., Hotz, R., 2007. Combustion characteristics of hydrogen–natural gas mixtures in passenger car engines. SAE Technical Paper 2007-24-0065. doi:10.4271/2007-24-0065.

Dimopoulos, P., Bach, C., Soltic, P., Boulouchos, K., 2008. Hydrogen–natural gas blends fuelling passenger car engines: combustion, emissions and well-to-wheels assessment. Int. J. Hydrogen Energy 33, 7224–7236.

Emadi, M., Karkow, D., Salameh, T., Gohil, A., Ratner, A., 2012. Flame structure changes resulting from hydrogen-enrichment and pressurization for low-swirl premixed methane–air flames. Int. J. Hydrogen Energy 37, 10397–10404.

Garland, N. L., Crosely, D. R., 1986. On the collisional quenching of electronically excited OH, NH and CH in flames. Twenty-first Symposium (International) on Combustion. The Combustion Institute, Pittsburgh, PA, USA, 1693–1702.

Gaydon, A.G., 1957. The Spectroscopy of Flames. Chapman and Hall Ltd., London.

Gaydon, A.G., Wolfhard, H.G., 1953. Mechanism of formation of CH, C_2, OH and HCO radicals in flames. Symp. (Int.) Combust. 4 (1), 211–218.

Gupta, S.B., Bihari, B.P., Biruduganti, M.S., Sekar, R.R., Zigan, J., 2011. On use of CO_2 chemiluminescence for combustion metrics in natural gas fired reciprocating engines. Proc. Combust. Inst. 33, 3131–3139.

Heywood, J.B., 1988. Internal Combustion Engine Fundamentals. McGraw-Hill, New York.

Higgins, B., McQuay, M., Lacas, F., Rolon, J.C., Darabiha, N., Candel, S., 2001. Systematic measurements of OH chemiluminescence for fuel-lean, high-pressure, premixed, laminar flames. Fuels 80, 67–74.

Ikeda, Y., Kaneko, M., Nakajima, T., 2001. Local A/F measurement by chemiluminescence OH*, CH* and C2* in SI engine. SAE Technical Paper 2001-01-0919. doi:10.4271/2001-01-0919.

Ji, C., Wang, S., 2009. Effect of hydrogen addition on the idle performance of a spark ignited gasoline engine at stoichiometric condition. Int. J. Hydrogen Energy 34, 3546–3556.

Ji, C., Wang, S., 2010. Combustion and emissions performance of a hybrid hydrogen–gasoline engine at idle and lean conditions. Int. J. Hydrogen Energy 35, 346–355.

Jordan, L., Shahjahan, K., Robert, F., 1997. Palladium catalyst performance for methane emissions abatement from lean burn natural gas vehicles. Appl. Catal. B 14 (3e4), 211e23.

Kahraman, B., Ceper, S., Akansu, S., Aydin, K., 2009. Investigation of combustion characteristics and emissions in a spark-ignition engine fuelled with natural gas–hydrogen blends. Int. J. Hydrogen Energy 34 (2), 1026–1034.

Kalghatgi, G., 2014. Fuel/Engine Interactions, first ed. SAE International, Warrendale, PA, USA.

Karim, G.A., Wierzba, I., 1983. Comparative studies of methane and propane as fuels for spark ignition and compression ignition engines. SAE Technical Paper 831196. SAE Transaction vol. 92 SP-548.

Larsen, J.F., Wallace, J.S., 1997. Comparison of emissions and efficiency of a turbocharged lean-burn natural-gas and hythane-fueled engine. J. Eng. Gas Turbines Power 119 (1), 218–226.

Lee, C.L., Oh, C.B., Kim, J.H., 2004. Numerical and experimental investigations of the NO_x emissions characteristic of CH_4–air co-flow jet flames. Fuels 83 (17–18), 2323–2334.

Ma, F., Wang, Y., Liu, H., Li, Y., Wang, J., Ding, S., 2008. Effects of hydrogen addition on cycle-by-cycle variations in a lean burn natural gas spark-ignition engine. Int. J. Hydrogen Energy 3 (2), 823–831.

Ma, F., Ding, S., Wang, Y., Wang, M., Jiang, L., Naeve, N., Zaho, S., 2009. Performance and emission characteristics of a spark-ignition (SI) hydrogen-enriched compressed natural gas (HCNG) engine under various operating conditions including idle conditions. Energy Fuels 23 (6), 3113–3118.

Ma, F., Wang, M., Jiang, L., Deng, J., Chen, R., Naeve, N., Zhao, S., 2010. Performance and emission characteristics of a turbocharged spark-ignition hydrogen enriched compressed natural gas engine under wide open throttle operating conditions. Int. J. Hydrogen Energy 35, 12502–12509.

Meyers, D.P., Kubesh, T.J., 1997. The hybrid rich-burn/lean-burn engine. J. Eng. Gas Turbines Power 119 (1), 243–249.

Miao, H., Jiao, Q., Huang, Z., Jiang, D., 2008. Effect of initial pressure on laminar combustion characteristics of hydrogen enriched natural gas. Int. J. Hydrogen Energy 33, 3876–3885.

Moreno, F., Arroyo, J., Munoz, M., Monnè, C., 2012. Combustion analysis of a spark ignition engine fueled with gaseous blends containing hydrogen. Int. J. Hydrogen Energy 37, 13564–13573.

Najm, H.N., Paul, P.H., Mueller, C.J., Wyckoff, P.S., 1998. On adequacy of certain experimental observables as measurements of flame burning rate. Combust. Flame 113, 312–332.

Nicoletti, G., Arcuri, N., Bruno, R., 2015. A technical and environmental comparison between hydrogen and some fossil fuels. Energy Convers. Manage. 89, 205–213.

Park, C., Kim, C., Choi, Y., Won, S., Moriyoshi, Y., 2011. The influences of hydrogen on the performance and emission characteristics of a heavy duty natural gas engine. Int. J. Hydrogen Energy 36, 3739–3745.

Phillips, J.N., Roby, R.J., 1999. Enhanced gas turbine combustor performance using H_2-enriched natural gas. ASME Paper 99-GT-115.

Ranson, R., 2000. Hydrogen-Enriched Natural: Gas Bus Demonstration. NRG Technologies, Inc., Edison Way Reno, NV.

Reynolds, C., Evans, R., 2004. Improving emissions and performance characteristics of lean burn natural gas engines through partial stratification. Int. J. Engine Res. 5 (1), 105–114.

Rousseau, S., Lemoult, B., Tazerout, M., 1999. Combustion characteristics of natural gas in a lean burn spark-ignition engine. Proc. Inst. Mech. Eng. D: J. Automob. Eng. 213 (D5), 481–489.

Salazar, V., Kaiser, S., 2011. Influence of the flow field on flame propagation in a hydrogen-fueled internal combustion engine. SAE Int. J. Eng. 4 (2), 2376e94. http://dx.doi.org/10.4271/2011-24-0098.

Schefer, R.W., 2001. Combustion of Hydrogen-Enriched Methane in a Lean Premixed Swirl Burner. Combustion Research Facility Sandia National Laboratories, Livermore, CA.

Schefer, R.W., 2003. Hydrogen enrichment for improved lean flame stability. Int. J. Hydrogen Energy 28, 1131–1141.

Sementa, P., Vaglieco, B.M., Catapano, F., 2011. Non-intrusive investigation in a small GDI optical engine fuelled with gasoline and ethanol. SAE Technical Paper 2011-01-0140; SAE International Journal of Engines—Electronic Version, V120-3EJ.

Shinagawa, T., Okumura, T., Furuno, S., Kim, K.-O., 2004. Effects of hydrogen addition to SI engine on knock behavior. SAE Technical Paper 2004-01-1851. doi:10.4271/2004-01-1851.

Shudo, T., Shimamura, K., Nakajima, Y., 2000. Combustion and emissions in a methane DI stratified charge engine with hydrogen pre-mixing. JSAE Rev. 21, 3–7.

Tabata, T., Baba, K., Kawashima, H., 1995. Deactivation by poisoning of three-way catalyst for natural gas-fuelled engines. Appl. Catal. B 7 (1e2), 19–32.

Tahtouh, T., Halter, F., MounaÏm-Rousselle, C., Samson, E., 2010. Experimental Investigation of the initial stages of flame propagation in a spark-ignition engine: effects of fuel, hydrogen addition and nitrogen dilution. SAE Int. J. Eng. 3 (2), 1–19. http://dx.doi.org/10.4271/2010-01-1451.

Tahtouh, T., Halter, F., Samson, E., Mounaïm-Rousselle, C., 2011. Effects of hydrogen addition under lean and diluted conditions on combustion characteristics and emissions in a spark-ignition engine. Int. J. Eng. Res. 12, 466–482.

Topinka, J.A., Gerty, M.D., Heywood, J.B.,Keck, J.C., 2004. Knock behavior of a lean-burn, H2 and CO enhanced, SI gasoline engine concept. SAE Technical Paper 2004-01-0975. doi: 10.4271/2004-01-0975.

US Department of Energy, 2002. Freedom CAR Partnership (Society of Automotive Engineers, New York). Planning Document, January.

Verhelst, S., Wallner, T., 2009. Hydrogen-fueled internal combustion engines. Prog. Energy Combust. Sci. 35, 490–527.

Verhelst, S., Demuynck, J., Sierens, R., Scarcelli, R., Matthias, N.S., Wallner, T., 2013. Update on the progress of hydrogen-fueled internal combustion engines. In: Renewable Hydrogen Technologies Production, Purification, Storage, Applications and Safety, pp. 381–400 (Chapter 16), Elsevier.

Wallner, T., Ng, H., Peters, R., 2007. The effects of blending hydrogen with methane on engine operation, efficiency and emissions. SAE Technical Paper 2007-01-0474. http://dx.doi.org/10.4271/2007-01-0474.

Wang, S., Ji, C., 2012. Cyclic variation in a hydrogen-enriched spark-ignition gasoline engine under various operating conditions. Int. J. Hydrogen Energy 37, 1112–1119.

Wang, J., Chen, H., Liu, B., Huang, Z., 2008. Study of cycle-by-cycle variations of a spark ignition engine fueled with natural gas–hydrogen blends. Int. J. Hydrogen Energy 33, 4876–4883.

Wang, J., Huang, Z., Tang, C., Miao, H., Wang, X., 2009. Numerical study of the effect of hydrogen addition on methane—air mixtures combustion. Int. J. Hydrogen Energy 34, 1084–1096.

Wang, S., Ji, C., Zhang, B., 2010. Effect of hydrogen addition on combustion and emissions performance of a spark-ignited ethanol engine at idle and stoichiometric conditions. Int. J. Hydrogen Energy 35, 9205–9213.

WHEC, 2012. Conference Proceedings—19th World Hydrogen Energy Conference Toronto Canada, Energy Procedia, vol. 29, pp. 1–754.

White, C.M., 2007. OH* chemiluminescence measurements in a direct injection hydrogen-fuelled internal combustion engine. Int. J. Engine Res. 8 (2), 185–204.

Wind-to-Hydrogen Project, 2009. Hydrogen and Fuel Cells Research. National Renewable Energy Laboratory, US Department of Energy, Golden, CO, Retrieved 7 January 2010.

Xu, J., Zhang, X., Liu, J., Fan, L., 2010. Experimental study of a single-cylinder engine fuelled with natural gas–hydrogen mixtures. Int. J. Hydrogen Energy 35, 2909–2914.

Yousufuddin, S., Masood, M., 2009. Effect of ignition timing and compression ratio on the performance of a hydrogen–ethanol fuelled engine. Int. J. Hydrogen Energy 35, 6945–6950.

Zhao, H., Ladommatos, N., 1998. Optical diagnostics for in-cylinder mixture formation measurements in IC engines. Prog. Energy Combust. Sci. 24 (4), 297–336.

This page intentionally left blank

Catalytic combustion of hydrogen for heat production

10

J. Saint-Just*, *S. Etemad*†,‡

*H2 Plus Ltd., Farnham, Surrey, UK, †Precision Combustion, Inc., North Haven, CT, USA

Abbreviations

CCS	carbon capture and storage
CEN	Comité Européen de Normalisation, European Committee for Standardization
CENELEC	Comité Européen de Normalisation Électrotechnique, European Committee for Electrotechnical Standardization
CHP	combined heat and power
CO	carbon monoxide
EC	European Commission
EU	European Union
FP	Framework Programme [of the European Commission]
H$_2$	hydrogen
HV	heating value
IAHE	International Association for Hydrogen Energy
IGCC	integrated gasification combined cycle
IGT	Institute of Gas Technology
LHV	lower heating value, low heating value
LPG	liquefied petroleum gas
NO$_x$	nitrogen oxides
PAR	passive autocatalytic recombiner
PM	precious metal
PtG	Power to Gas
UHCs	unburned hydrocarbons

10.1 Introduction

At first, it is necessary to define what is meant by "catalytic combustion" in this chapter, as catalytic combustion does not have the same meaning for all scientists. For most of them, it is a reaction of total oxidation involving a catalyst and carried out with the purpose of producing heat. The operating conditions are chosen so that a flame does not develop. However, the catalyst community has long used the term "catalytic combustion" to describe all complete catalytic oxidations, even when the objective is not

‡Fairfield University, Fairfield, CT, USA.

to create heat (Lamb et al., 1922). The elimination of hydrogen traces in the oxygen stream of electrolyzers falls in that category as well as the oxidations of carbon monoxide (CO) and unburned hydrocarbons (UHCs) in the automotive catalytic converter. Catalytic combustion is also the working principle of a fraction of the hydrogen sensors. In this review, the focus is on hydrogen catalytic combustion for heat production, in line with the subject of Volume 3 "Hydrogen energy conversion." The applications not targeting the production of heat are only briefly described. Noncatalytic flameless combustion (Milani and Wünning, 2002), which has become a successful commercial process since the early 1990s, is not described.

The incentive for using catalytic combustion rather than traditional flame combustion is either to minimize pollutant emissions (nitrogen oxides NO_x, CO, UHCs), combust lean gas mixtures that would not burn in a stable fashion otherwise, or increase the stability and efficiency of radiant heaters. Catalytic combustion has been developed essentially for natural gas.

Currently, there is no significant market for pure hydrogen as an energy source (vehicles or heating fuel), except as a fuel for rockets. However, new markets are emerging (fuel cell electric vehicles, backup power, etc.), encouraged by the forthcoming availability of "green" hydrogen.[1] Hydrogen is now perceived as a future storage medium for renewable energies. The integration of this idea in the overall energy system has given rise to the Power to Gas (PtG) concept currently demonstrated in Europe. One of the options of PtG is to introduce green hydrogen in the natural gas grid and utilize the blend as such in all the traditional natural gas appliances (200 million in Europe).

Also, hydrogen-rich streams will originate from the clean fossil fuel plants that will incorporate carbon capture and storage (CCS). "Clean" hydrogen[2] will be converted to power in these plants. The issue of the clean conversion of pure hydrogen and blends is therefore becoming crucial. Burners, engines, turbines, and fuel cells are the candidate conversion devices. Several of these devices have tentatively used catalytic combustion, mostly for natural gas, but the number of commercial products has remained low. The main reason is that catalytic combustors, which can be only more expensive than their noncatalytic counterparts, have not yet found an entry application of sufficient added value. Their commercialization will take place only when environmental regulations on emissions impose lower emissions limits or when some application requires enhanced combustion stability. Another reason for the low market penetration is that technical issues remain for catalytic combustors, in particular, the trade-off between catalyst activity and durability.

In the mid-1970s, the oil crisis and the consequent search for alternatives to fossil fuels generated a lot of interest and government research funds for hydrogen as a carrier of renewable energies or nuclear energy, in particular. The interest has perpetuated up to today with vision and persistence by the International Association for

---

[1] Hydrogen is "Green" when it is obtained from renewable sources via electrolysis (PV, wind) or gasification (biomass).

[2] Hydrogen is "clean" when it is obtained via reforming or gasification, from fossil fuels which have been decarbonized for carbon capture and storage (CCS) or carbon capture and utilization (CCU).
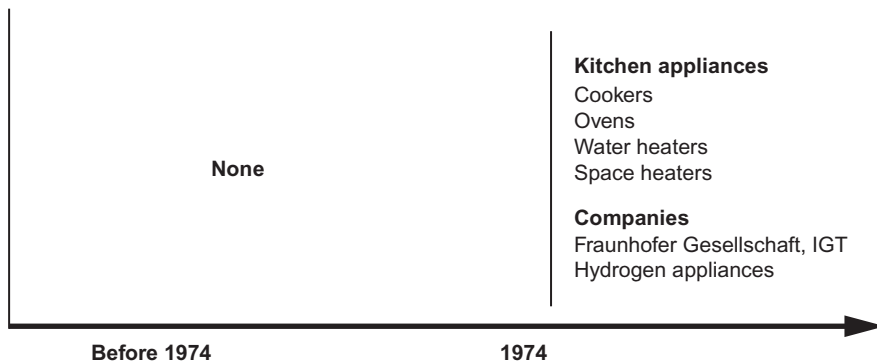
Figure 10.1 Hydrogen catalytic combustion applications developed in the hydrogen programs of the 1970s (Veziroglu, 1995).

Hydrogen Energy (IAHE). Excellent accounts of the achievements of the time concerning a wide array of devices featuring hydrogen catalytic combustion were published (Veziroglu and Escher, 1979) and are mentioned in Figure 10.1.

There was no significant commercial follow-up of the development of these devices as the availability of hydrogen energy was very low, but many ideas of the time could be revived for the current developments.

At stoichiometry in air, all usual fuels, including hydrogen, have adiabatic flame temperature above 1950 °C and the formation of NO_x may take place. Increasing the air–fuel ratio is one of the means to decrease the flame temperature and NO_x formation. For hydrocarbon fuels, including natural gas, the maximum amount of excess air that can be used without endangering flame stability in a traditional burner does not permit the very low NO_x, CO, and UHC levels required in a few countries and specific locations to be reached. Expensive and cumbersome exhaust gas cleanup technologies such as ammonia selective catalytic reduction have to be used. Catalytic combustion is one of the alternative control technologies that have been developed as it permits air–fuel mixtures outside the flammability limits to be combusted at temperatures below the threshold of thermal NO_x formation. This principle was applied in several turbine development programs in the United States, Japan, and Europe that started in the late 1970s (Dennis, 2006). After several R&D campaigns over decades in the United States, Japan, and Europe, the commercial stage for natural gas catalytic turbines was nearly reached, but the edge over competing noncatalytic technologies, which were developed in parallel, was not sufficient. Significant progress was made on the key issue of catalyst durability, but not to the point that it could be considered that the problem had been definitely solved. So, the effort on turbines did not expand the commercial market of catalytic combustion, which remained restricted essentially to industrial gas radiant heaters for paint drying and plastic forming.

Environmental regulations contributed to maintaining the interest in catalytic combustion for domestic boilers as catalytic combustion and, to a lesser extent, surface combustion in properly designed burners may prevent the formation of a concentrated

high-temperature hot spot where NO_x are formed. A hot spot develops because the heat transfers in the gas phase are slow compared to the rate of heat produced by the chemical reaction of oxygen with the fuel. In catalytic/surface combustion, the heat can be released by the surface supporting the catalyst while the presence of the catalyst permits the reaction to proceed at the lower temperature. As usual, the role of the catalyst is to increase the reaction rate of oxidation by lowering the activation energy and increasing the preexponential factor in the Arrhenius rate law formulation. Like many oxidation reactions, the reaction of methane with oxygen may be governed by an Eley–Rideal mechanism: reaction initiation at the catalyst surface and completion in the above boundary layer. However, matters are not that simple and the actual rate expression may be catalyst specific (Deutschmann and Warnatz, 2002). Catalyst activity and reaction conditions determine the thickness of that boundary layer. When the catalyst is very active and well spread over the supporting surface, the boundary layer is very thin and the combustion may appear flameless.[3] It has been experimentally demonstrated with a performing precious metal (PM) catalyst that the transition between initial flame combustion and final flameless combustion could proceed quite smoothly as a function of combustion conditions and catalyst temperature (Dzubiella and Eder, 1977). In catalytic combustor design, heat transfer issues and catalyst durability are prime movers.

Hydrogen has combustion specificities compared to methane:

- higher flame velocity (up to $\sim$8 times),
- wider range of flammability (5–75 vs. 5–15 vol.%),
- lower ignition energy (0.02 vs. 0.3 mJ),
- extreme sensitivity to the presence of catalytic surfaces during reaction with oxygen. The reaction starts at 77 K on platinum vs. $\sim$858 K without catalyst (Ladaki et al., 1965).

The catalytic oxidation of H_2 is a truly remarkable reaction. It is probably the reaction that is the most sensitive to the action of a catalyst. On platinum, the reaction has been reported to start at or even below 77 K, while in the gas phase it only starts above 858 K (Ladaki et al., 1965). This represents a rate acceleration of many orders of magnitude. Catalysts active at such low temperatures are sought for the operation of rockets fueled with liquid hydrogen.

The high flame velocity can induce flashback. Flashback can occur in premix burners when the flame velocity is greater than the flow rate of the burning mixture. The flame front then propagates back, eventually up to where the fuel and primary air are being mixed, and this is likely to damage the burner and cause accidents. Flame arrestors can alleviate this undesired phenomenon but they may not be practical in low-pressure devices such as residential burners, because of the pressure drop they induce in the flow. Diffusion burners are perceived as more suitable for hydrogen, including in turbines, if safety only is taken into account.

The wider range of flammability permits air to be added in large proportion to diminish the flame temperature and consequently the production of NO_x (lean combustion in

---

[3] At least for human eyes. A cat may not agree when looking at the same supposedly flameless device. One has to use some caution when defining what a flame is, as it involves human perception.

excess air). A similar result can be obtained in performing the combustion in the rich rather than in the lean-burn mode. Safety issues are also of concern as the hydrogen flame is not visible, especially for residential applications such as domestic cooking gas burners. Catalytic combustion may provide a solution with the presence of a catalytic material, which would glow in proportion of the temperature of the burner.

In view of these very different combustion characteristics of hydrogen compared to methane, it is mandatory to reassess the interest in and potential benefits of catalytic combustion when H_2 is the fuel, neat or in blends with other gases such as natural gas or CO. Syngas, which is composed of hydrogen and CO, is commonly available in industry as a reactive intermediate for the conversion of the chemically inert hydrocarbons found in nature such as methane and higher alkanes. Refinery fuel gases also contain hydrogen. Town gas, which was a mixture of hydrogen, CO, methane, and CO_2, is no longer distributed, except in Asia (not to be confused with the "City Gas" distributed in Japan, which is natural gas boosted with some liquefied petroleum gas (LPG)).

The following sections describe hydrogen catalytic combustion, achievements, and prospects, in the domains that are traditionally considered by the gas industry: residential, commercial, and industrial sectors.

The three main traditional energy conversion devices for converting gas into useful end products (vehicle fuels, heat, and power) are burners, engines, and turbines. Fuel cells must now be included in the list. The areas where hydrogen catalytic combustion may play a role are described below. To date, there are only a few commercial applications, as the current availability of hydrogen as an industrial gas is not adapted to the widespread utilization of hydrogen as an energy source. An exception is the industrial sector, where syngas is a traditional fuel. However, the amounts of hydrogen needed for the emerging fuel cell electric vehicles and the foreseen availability of green hydrogen are modifying the situation.

10.2   Commercial and residential applications

10.2.1   Burners

Prototype catalytic burners and hobs for hydrogen were featured in the numerous solar houses that have been demonstrated in the past 40 years (Hoffmann, 2012). The prime incentives to adopt catalytic combustion are safety, as the hydrogen flame is hardly visible, and low NO_x production. Catalytic combustion may provide a safety solution with the presence of a catalytic material that would glow in proportion to the temperature of the burner and would indicate that the burner is turned on.

An early prototype of such a burner was featured in the 1975 Homestead project of Roger Billings. It consisted of a two-story residence that was heated and cooled with hydrogen and demonstrated hydrogen-run kitchen appliances, fireplace, outdoor grill, automobile, and farm tractor. The burner was described as a "flame-assisted catalytic burner." A thick stainless steel wool mat was used to surround the burner ports, as described in Figure 10.2.
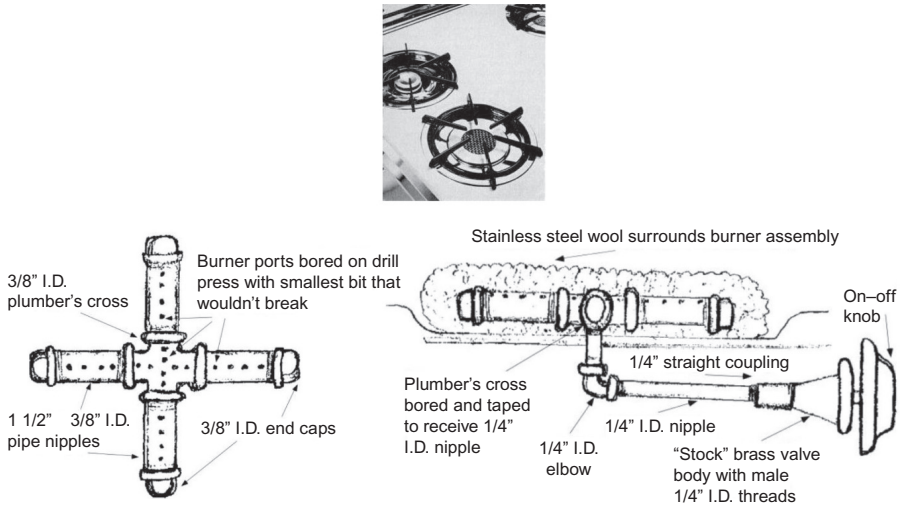
Figure 10.2 "Flame assisted catalytic burner," as featured in the 1975 Billings Hydrogen House, with "stainless steel as the catalyst" (Booth and Pyle, 1993).
Reprinted with permission. © 2015 Home Power Inc., www.homepower.com.

The surrounding stainless steel mat inhibited the mixing of air and hydrogen and created a stable hydrogen-rich zone around the burner head (100% flame diffusion burner, no premixing). The low NO_x production was attributed to the catalytic activity of the stainless steel wool, but other explanations could now be put forward. In any case, the phenomenological difference between catalytic and surface combustion when heat transfer phenomena are taken into account is small (Howell et al., 1996). Catalytic combustion with a deactivated catalyst evolves toward surface combustion and remains beneficial (Dzubiella and Eder, 1977).

The issue of indoor air quality has become of critical importance today (Logue et al., 2014), and there were recent attempts to design cooking stove catalytic burners for natural gas in order to curb the NO_x production (Jannasch, 2010). These attempts have been commercially unsuccessful but they are instructive for the design of burners for hydrogen or "hydrogen-enriched natural gas," a potentially future gas that may become available if green hydrogen is injected in the natural gas distribution grid, as one of the options of PtG, under demonstration in Europe (Benjaminsson et al., 2013). The natural gas is considered enriched because the value of green hydrogen is high, whatever the final energy content of the enriched gas, which is lower as the volumetric energy density of hydrogen is one-third that of natural gas.

One of the few successful commercial launches of a catalytic domestic burner was achieved by the French company Camping Gaz for the recreational camping market (>30,000 units sold). The incentive to use catalytic combustion was to provide the user with a camping stove that could operate even in windy situations. The technical challenges were numerous. In order to grill a steak in a pan, a temperature of 350 °C is necessary at the pan surface. In the chosen burner design, the catalyst (platinum on a

zirconia monolith slab, presumably) was located below a refractory glass plate, maintained in place and attached to the body of the device by a circular steel plate (Figure 10.3). The heat transfer from the catalyst to the pan is by radiation and conduction plus some convection.

To obtain the necessary 350 °C at the pan surface, the catalyst temperature had to be around 1350 °C, as a consequence of the various heat transfer limitations. The fuel was a mixture of butane and propane. The catalyst durability was 200 h (i.e., a few years of occasional utilization by a typical camper), which was acceptable for the targeted market.

For the home market with natural gas or LPG, this range of durability is not acceptable. The Swedish company Catator managed to significantly improve the durability in a design using also a glass plate (Figure 10.4).

Catator used its patented wire mesh catalysts (Jannasch, 2010). NO_x emissions were low (1–3 mg NO_x/kWh) and CO levels (0–15 mg CO/kWh) were acceptable. Relatively high thermal efficiencies were observed over a broad range of power inputs (40–50% for 1–4 kW). Durability was very good (>10,000 h).

These good performances did not, however, lead to commercial development because the catalytic burner has a very significant drawback compared to the traditional open flame burner: it would deprive natural gas cooking of its main advantage over electricity cooking; namely, the high reactivity of the open flame and the low inertia of the burner assembly. That advantage has already been challenged by induction stoves. In addition, the current absence of regulations on emissions and

Figure 10.3 Trek 270 camping stove by Camping Gaz (http://www.ipernity.com/home/26252; picture by Demetrius Chryssikos).
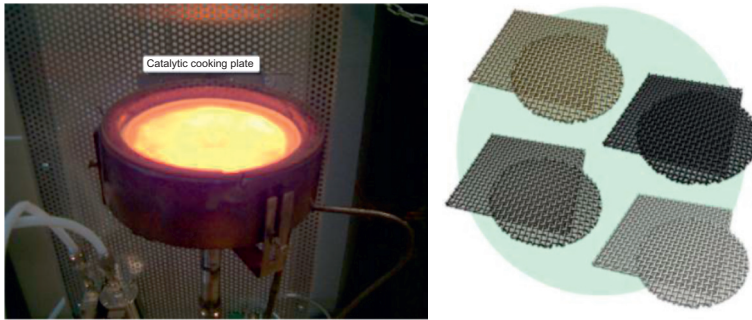
Figure 10.4 Catator's catalytic burner for gas stove and cooking plate applications.

performances does not provide an incentive for the commercialization of the higher-priced catalytic burners.

Developing hydrogen catalytic burners should prove easier than natural gas because of the high reactivity of hydrogen with catalysts and wider flammability limits. However, the diminishing prices of induction cooking stoves and the incipient successful commercialization of domestic combined heat and power (CHP) fuel cells cast a doubt on the urgency or even the necessity to develop domestic catalytic hydrogen burners. Safety will be a prime concern in the future hydrogen dwellings and all solutions that will minimize the opportunities for hydrogen to leak and accumulate in the house will prevail. For the cooking burner, the combination of a hydrogen fuel cell, electric wires (no hydrogen lines in the house if the fuel cell is outside), and induction heating may be hard to beat.

In these conditions, are there still incentives to develop domestic catalytic burners? The answer is yes, as natural gas, thanks to the existing distribution infrastructure, will continue to be distributed for the next several decades but its nature and the regulations may gradually change. There is a possibility that green hydrogen could be added to natural gas in higher and higher quantities over the years, as it is one of the options of the PtG concept. This topic is generating a flurry of activities, to the point that two standardization bodies of the European Union (EU), CEN and CENELEC, will intervene in order to identify and clarify the issues at every step of the chain. The end users are concerned and there is no doubt that burners and hobs performance will be under scrutiny. This is especially true as a new EcoDesign directive is being drafted for Europe (Shankleman, 2015).

Since the pioneering work of the Institute of Gas Technology (IGT) in the 1970s (Sharer and Pangborn, 1975), several major programs/studies have investigated the conditions under which hydrogen could be blended with natural gas and the blend distributed to consumers (Melaina et al., 2013). The presence of hydrogen influences the load (Wobbe index), the efficiency, and the flame stability. In that respect, what has to be feared with hydrogen/natural gas blends is flashback. This propensity has been utilized by CEN, a standardization body of the EU, to define a test gas, G222—77% $CH_4 + 23\%$ H_2, which serves to evaluate the ability of the newly commercialized

domestic burners to resist flashback. This means that, with the exception of old burners, all the domestic burners in Europe have the ability to burn blends of natural gas and hydrogen safely up to approximately 23 vol.%, which is well above what is foreseen today for the medium term. However, the new EcoDesign directive mentioned above may impose performances in terms of efficiency and emissions that may require new burner designs for Europe, including catalytic ones. Hopefully, these burners will be also designed to withstand hydrogen over the several years of their expected lifetime, as the conformity to the G222 test gas does not guarantee durability (the certification test lasts only about 1 h).

The catalytic combustion of hydrogen/methane or natural gas blends has been the subject of numerous academic investigations but only a few have been concerned with the design of domestic burners. The technology of porous radiant burners shows environmental advantages compared to traditional diffusion flame burners. In a comprehensive evaluation of premixed combustion of natural gas–hydrogen mixtures, monoliths, ceramic foams, and wire meshes, impregnated with catalysts or bare, have been compared, with various percentages of hydrogen in the blends (Roesler, 2009). Considering the various criteria of importance, namely, emissions (NO_x, CO, UHCs), operating range in terms of H_2 concentration, and flashback occurrence, it was concluded that the most attractive system was the wire mesh without precious metal catalysts. In the absence of catalysts, durability was not an issue. The presence of PM catalysts was actually detrimental as it increased the propensity of flashback. It was pointed out that the wire meshes themselves (bare FeCr alloy or impregnated with a few ceramic layers) may have some catalytic properties. This is reminiscent of the comments concerning the role of stainless steel wool for the Billings pure hydrogen burner, described previously.

A recent survey of commercial hydrogen technologies has pointed out the absence of commercial hydrogen cooking devices (Element Energy, 2006). No reference was made to the burners of the town gas era (up to 65% H_2). The barrier to hydrogen cooking was identified as the lack of a safe, simple, reliable, and viable technology. Catalytic/hybrid combustion was the recommended technology to develop for hydrogen burners. The insufficient size of the market was not mentioned as one of the barriers to commercialization. It is probably the main barrier as the knowledge accumulated on the catalytic/surface combustion of natural gas, natural gas/H_2 mixtures, and syngas should help the design of future pure hydrogen catalytic burners. However, as mentioned earlier, it is not obvious that the market will ever be sufficient in view of the safety issue with in-house hydrogen lines and the competition with induction cooking.

In contrast, the need for improved burners for natural gas and hydrogen/natural gas blends may appear if new environmental legislation comes into play. The current burners are appropriate in terms of resistance to flashback, as they have been tested in Europe with the G222 test gas but they have not been designed for long-term durability with hydrogen and they may not meet future environmental legislation. In view of the current interest in PtG and the option for injecting green hydrogen in the natural gas network, there is a chance that the companies that are developing the better technologies mentioned before, such as the wire mesh burners, will succeed in commercializing them.

10.2.1.1   Radiant heaters

According to Cowan (1986), industrial gas radiant heaters were first used in the United
States during World War II. At that time, they contributed to the war effort in short-
ening the time necessary for the paint curing of freshly painted military gear. After
that, the residential market expanded with gas surface combustion heaters, which
worked essentially with propane. A few of these heaters used catalytic combustion
with platinum catalysts. One catalytic radiant heater was actually demonstrated suc-
cessfully with hydrogen in 1991 (Pyle et al., 1993), but there was no commercial
follow-up because of the absence of a sufficient market.

   The future for pure hydrogen catalytic radiant heaters is uncertain, as the added
value of catalysts in hydrogen radiant heaters is not proven. Catalysts may help sta-
bilize outdoor operation in windy conditions.

10.2.1.2   Boilers

For the larger boiler market, which requires higher heat loads, the potential of catalytic
combustion to reduce NO_x emissions was recognized but catalyst durability is a very
challenging issue. Very significant progress in that respect was made by the German
company Viessmann with the design of the MatriX burner for natural gas. The original
burner was a hemispheric metallic wire mesh, impregnated with a precious metal cat-
alyst (Figure 10.5).
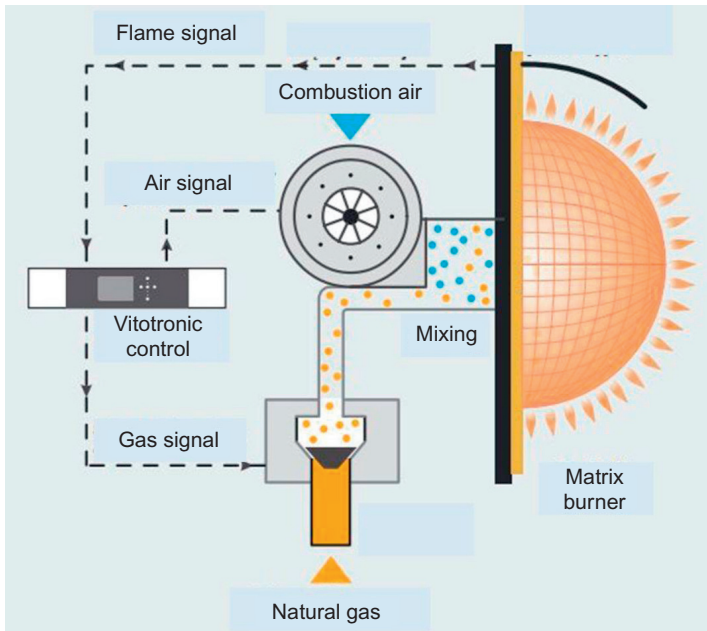
Figure 10.5 Original matrix burner and ancillary gas supply equipment (~1991). The heat is
transferred by radiation and convection to a high thermal inertia water tank.
Adapted from Viessmann: "Matrix, a unique gas burner, Jubilee, 20 years in Poland."

The main objective beyond the design of the burner was to develop a very low NO_x boiler, with performances below the requirements of the Blaue Engel label; namely, nitrogen monoxide and nitrogen dioxide below 60 mg/kWh (34 ppm) and CO below 50 mg/kWh (46 ppm). The approach was based on a thorough observation and understanding of the transition between the blue flame mode of operation and the flameless radiant catalytic mode once the catalyst has reached its optimum steady state temperature (Dzubiella and Eder, 1977). The objective was met with NO_x at 9 mg/kWh and CO at 17 mg/kWh. The performances deteriorated slightly with time, with NO_x levels reaching a stable value of ~20 mg/kWh after a few months of operation. What was very instructive is that low NO_x levels could still be observed after years of operation with platinum particles that had sintered to a very large extent.

Nevertheless, Viessmann had to update its MatriX burner concept, considering that, in view of their two-dimensional structure, radiant burners could not be made sufficiently compact for the modern, small household heating system. Moreover, the radiant burners are relatively unstable against changes in thermal load or air-ratio and difficult to modulate. Sufficiently low NO_x levels can be obtained by means other than pure catalytic combustion, such as noncatalytic surface or flameless combustion.

The value of the wire mesh concept for ultralow emission combustion and durability was demonstrated by the Swedish company Catator in more than two decades of development. One of their latest achievements is a 5–60 kW boiler that is able to combust a wide range of gases: natural gases, LPG, and low-heating value (LHV) gases with extremely low pollutant emissions (Figure 10.6).
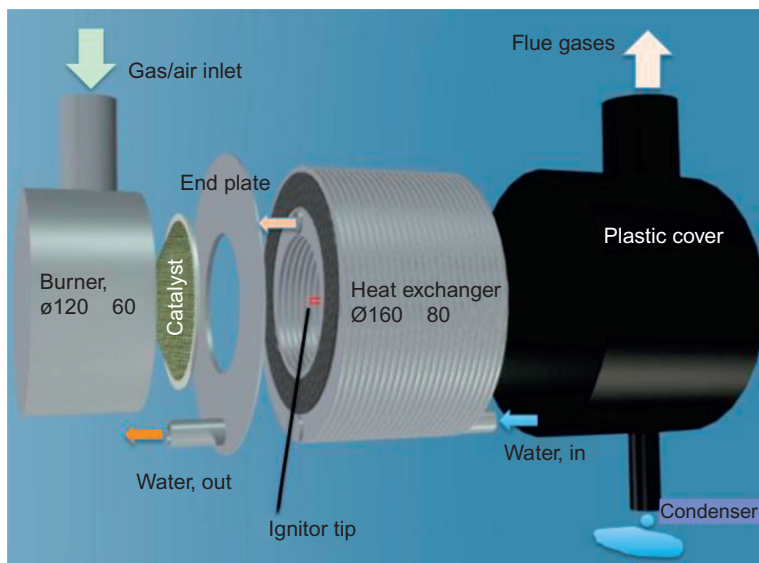
Figure 10.6 Catator's fuel flexible catalytic burner integrated with compact HeatCore™ heat exchanger (Silversand, 2013).

Despite its excellent performances, the burner is not yet commercialized because less expensive burners are able to meet the current environmental regulations. Its good behavior with LHV gases indicates that the burner could be adapted easily to hydrogen, possibly by diminishing the catalytic activity of the mesh in order to eliminate the chances of flashback.

A similar conclusion on the interest of catalytic combustion for hydrogen/natural gas blends was reached by Roesler (2009), who pointed out the suitability of moderately active catalytic metallic meshes while, at their operating conditions, ceramic foam supports were prone to initiate flashback.

The future for pure hydrogen boilers is uncertain, as the competition with hydrogen fuel cell CHP units will be severe. In the medium term, the market for natural boilers will be not be modified by the few percents of green hydrogen that may be added to the natural gas (Altfeld and Pinchbeck, 2013).

10.2.2   Engines

10.2.2.1   Propulsion and stationary applications

Engines for compressed natural gas currently represent a small but sizeable fraction of the automotive market ($\sim$2%). In contrast, hydrogen engines for propulsion, in the modern era, with gaseous or liquid hydrogen, never went beyond a limited commercialization (MAN, Ford, BMW). Catalytic combustion has played no role in hydrogen engines and the appearance of fuel cell electric vehicles has probably definitely sealed the fate of the hydrogen internal combustion (IC) engine for the road vehicle market.

Gas engines for stationary applications (power generation, CHP, etc.) are extremely popular. They operate with a wide variety of fuels, with the exception of hydrogen. Fuel cells have started to occupy a fraction of that market and they should rapidly displace the gas engine for micro-CHP.

10.2.3   Turbines

The application of turbines for residential and commercial markets is rather limited. Only a few vehicles operate with turbines. Microturbines for stationary power production exist now in the 30–250 kW range (COSPP, 2014). Hydrogen is not a fuel of choice and no application of hydrogen catalytic combustion can be foreseen in this area for the short to medium term.

10.2.4   Fuel cells

Fuel cells stacks operate with hydrogen, but not all the hydrogen is consumed and a small fraction is rejected, occasionally as a blend with other gases such as CO_2, which have entered the fuel cell without reacting. This small outlet flux, which is potentially hazardous, can be burned catalytically, and the recovered energy is used to increase the efficiency of the fuel cell system. Catalytic combustion is necessary because when hydrogen ends up

in a blend with inert gases, the anode gas is too lean to burn without a catalyst. In addition, catalytic combustors may be easily coupled with efficient heat exchangers (Johnson and Kanouff, 2012). The catalysts employed are usually platinum based.

10.2.5 Market forces and trends

Until recently, hydrogen catalytic combustion played no role in the residential and commercial markets. However, the incipient commercialization of fuel cells and hydrogen technologies will modify that situation because fuel cells often contain a hydrogen catalytic combustor, as mentioned above.

For the residential market, the increased availability of green hydrogen is not going to boost the development of hydrogen technologies other than fuel cells, because the presence of hydrogen lines in confined spaces is a touchy issue in terms of safety and because there are safer alternatives (see the discussion above on domestic burners). The town gas experience (hydrogen content of up to 65% hydrogen) is too old to contribute to the efforts that are now undertaken (HyIndoor, 2014) to build a new framework for the utilization of hydrogen in confined spaces in terms of regulation, codes, and standards. That framework will apply also to incipient commercial markets, for which hydrogen is already distributed, such as forklifts and backup power.

In conclusion, the emergence of fuel cells and hydrogen technologies will permit the interest in hydrogen catalytic combustion to be maintained.

10.3   Industrial applications

10.3.1   Burners

Industrial burners are used routinely to combust fuel gases with often high hydrogen contents. Premix burners can handle fuels with H_2 contents as high as 90 vol.%. Diffusion flame burners can burn pure H_2 (Baukal, 2001). The current mandatory emissions levels are met without necessarily using catalytic combustion or other advanced low-emissions combustion technologies such as FLOX® flameless combustion (Milani and Wünning, 2002). Postcombustion treatment technologies are also used to ensure environmental compliance.

Catalytic combustion was considered for providing the heat necessary for hot air balloons to reduce the combustion noise. While propane is the fuel of choice, climate change pressures toward hydrogen could also lead to this situation changing.

10.3.1.1   Radiant heaters

As mentioned earlier, industrial gas radiant heaters were first used in the United States during WWII (Cowan, 1986). Subsequently, the technology was commercialized by many small companies in an attempt to displace electric heaters, which were already addressing the industrial markets of paint drying and plastic forming. Gas heaters have
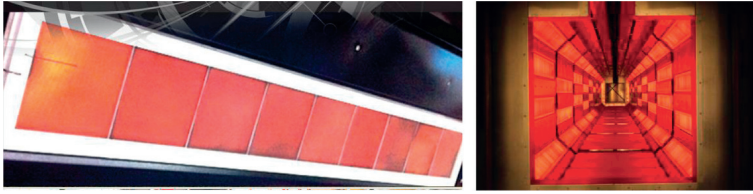
Figure 10.7 The Catherm® radiant unit emits infrared and convective energy through the catalytic combustion of natural gas or propane (Courtesy of Sunkiss Matherm).

a number of advantages: they have an operational flexibility that permits the spectrum of the emitted radiation to be adapted to the absorbing medium, which may be a painted object or a plastic sheet. A typical industrial setup is shown in Figure 10.7. The various designs, countercurrent and cocurrent, are described by Hayes and Kolaczkowski (1997). Catalyst durability is a manageable issue as low operating temperatures are sufficient ($<650\ °C$).

If natural gas with a few percent of hydrogen becomes available, the operation of the radiant heaters should not be affected. There is no incentive to use pure hydrogen, as the low-temperature operation with natural gas does not entail the creation of pollutants nor large CO_2 emissions. On the other hand, if hydrogen is available, only the countercurrent convective diffusive-type heaters should ensure safe operation.

10.3.2 Engines

Large industrial gas engines (up to 18 MW) can burn a wide array of gases from natural gas to refinery fuel gases and steel gases. Coke oven gas is of particular interest as it contains up to 70% hydrogen and methane as balance. Specific control systems and air ratios are used to deal with the higher risks of engine knocking or backfiring.

At the lower end of the power spectrum, the U.S. company HEC-TINA commercializes engines from 100 kW and up that have been modified to burn hydrogen. The objective is to offer the same benefits as fuel cells at a lower cost.

The use of hydrogen catalytic combustion has not been reported in the domain of gas engines at this time. However, an intense search for environmentally cleaner marine propulsion is currently underway, which includes hydrogen as a fuel.

10.3.3 Turbines

Refinery fuel gases and coal gasification gases are high hydrogen content gases that have been combusted in gas turbines for decades. However, turbine operation has always represented a challenge because of the ever-tighter emission regulations that had to be met without sacrificing efficiency improvements or turbine integrity. NO_x levels of 2 ppmv are now sought. New challenges are facing the industry, with the prospect of having to deal with integrated gasification combined cycle (IGCC) gases in relation with CCS and pure hydrogen in relation with the precombustion option for CCS.

Catalytic combustion has been one of the attractive potential solutions to reduce the NO_x emissions of combustion turbines (Dennis, 2006). Research on the topic started in the United States at the end of the 1970s (DeCorso et al., 1977), with the support of the Environmental Protection Agency, after the discovery of the concept of catalytically stabilized combustion in 1974 by Pfefferle (1973).

Catalytic combustion permits air–fuel mixtures outside the flammability limits to be combusted at temperatures below those of thermal NO_x formation. This principle was applied in numerous turbine development programs in the United States, Japan, and Europe. These initial programs investigated the fuel-lean catalyst system option but more recently, Precision Combustion, Inc. developed a fuel-rich catalyst design.

The first successful development for the fuel-lean catalyst system option was achieved by Catalytica Inc. and Kawasaki, who brought their system very close to commercialization (Dalla Betta et al., 1997), unfortunately with Enron as the first prospective customer. A circular metallic monolithic combustor, made out of a corrugated foil coated on one side only with palladium oxide catalyst, was at the heart of the system (Figure 10.8).

Depending on temperature, palladium can be in the metallic or oxide form. PdO has high activity for methane oxidation, while Pd metal has low activity. As the exothermic reaction proceeds, the heated palladium oxide turns into less active palladium metal and the reaction slows down. In theory, palladium can therefore act as a "thermostat" to contribute to maintaining the temperature of the system below that of NO_x formation (3 ppm at 1525 °C). In reality, matters are more complicated as the ignition temperatures of PdO is rather too high (>300 °C) and the PdO/Pd transition temperature is too low. Only half of the incoming fuel was oxidized catalytically. The other fraction was preheated in the monolith channels not coated with the catalyst and oxidized in a homogeneous flameless fashion at the exit of the monolith.

Hydrogen and syngas feeds were not part of the programs that investigated the fuel-lean catalyst system option.
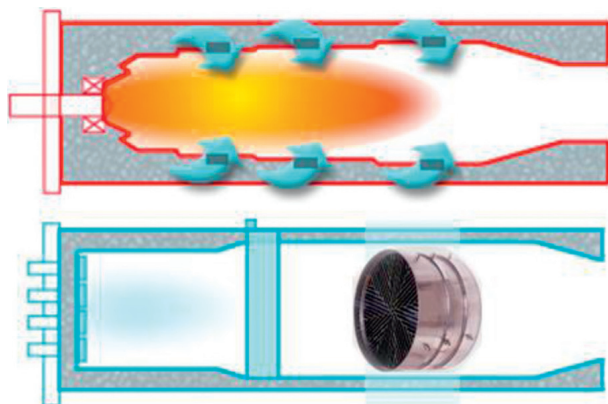
Figure 10.8 Conventional and "cool" Catalytica Inc. combustor.

To address the needs of high firing temperature gas turbine applications delivering low NO$_x$ emissions, the fuel-rich catalyst system option was developed by Precision Combustion, Inc. during the late 1990s under the concept of rich-catalytic lean-burn combustion, RCL®. The nonoxidizing reactor environment provides greater flexibility in terms of catalyst choice.

The system developed by Precision Combustion, Inc. is shown schematically in Figure 10.9. The system is based on fuel-rich operation of the catalyst and sustains fuel-lean gas phase combustion downstream of the catalyst via recirculation-based flame holding.

All the fuel and part of the air pass through the catalyst with the remainder of the air providing catalyst cooling. This cooling air then mixes with the catalyst effluent establishing a fuel-lean flame. Fuel-rich operation of the catalyst provides greater catalyst activity than fuel-lean operation. Consequently, a preburner is not normally required during low-emissions engine operation. Catalyst extinction temperature is particularly low, and is generally less than 200 °C (400 °F) for the precious metal catalysts used (i.e., once the catalyst has been lit off, the catalyst remains lit at inlet air temperatures as low as 200 °C (400 °F). A more complete discussion of fuel-rich versus fuel-lean catalysts behavior is given by Lyubovsky et al. (2003). Flashback and auto-ignition issues are also precluded because fuel oxidation and heat release in the catalyst stage are limited by available oxygen, rather than fuel reactivity as in a completely lean system. The system can therefore be operated safely even at the highest desired combustion-stage temperatures. The RCL system has been successfully tested in both rig and engine tests for natural gas fuel. Results from work with Solar Turbines, Incorporated (Smith et al., 2005), showed achievable NO$_x$ emissions as low as 1 ppm in rig tests. Engine tests in a modified industrial engine, using a cluster of four catalyst modules were tested demonstrating NO$_x$ emissions around 2 ppm, with CO below 10 ppm. Engine testing demonstrated excellent operability though the entire range of engine operating conditions, including transient events such as start-up, shutdown, and load shifting.

As an alternate approach to entire combustor modification for catalytic combustion as described above, a rich catalytic pilot concept has also been explored, wherein only the pilot fuel (a major source of NO$_x$ emission) is flowed through a rich catalytic pilot
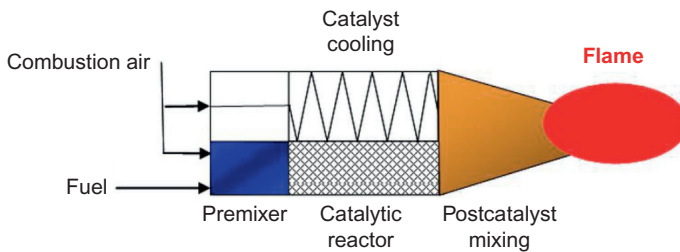
Figure 10.9 Precision combustion's two-stage catalytic combustion system. Fuel-rich catalyst effluent mixes with catalyst cooling air prior to fuel-lean gas-phase combustion. The system is therefore called rich-catalytic lean-burn combustion, trademarked as RCL® by Precision Combustion, Inc. (Smith et al., 2006a).

system within an otherwise conventional lean combustor. This makes catalytic combustion adaptability easier and has major benefit to retrofit as well as new engine applications. Full-scale single-injector rig test was demonstrated in Solar Turbines, Incorporated, high pressure rig (Karim et al., 2003) and full-size Solar Turbines, Incorporated, engine test (Baird et al., 2010), demonstrating low single-digit NO_x with CO below 10 ppm for good engine operability.

Following the above development work of fuel-rich catalytic combustion for gas turbine integration, additional parallel work by Siemens on natural gas and preliminary work on syngas were performed (Laster, 2005). Operation on natural gas demonstrated 3 ppm NO_x and 10 ppm CO emissions for high-firing application. Similar reactor was attempted to operate on high-hydrogen syngas fuel (24% H_2, 60% CO, 7% CH_4, 8% CO, 1% N_2). New modifications to design were required for syngas applications. In addition, parallel work by Alstom (Carroni, 2009) was also performed using rich catalytic combustion and catalytic pilot concept with major focus on natural gas.

Fuel-rich operation also allows similar catalyst and reactor performance with various fuel types, as rich catalyst-stage reactions and heat release are oxygen-limited regardless of the fuel's intrinsic reactivity on the catalyst. Catalytic combustion extends the range of fuels that can be combusted properly, from weak natural gas with an LHV of 6.5 MJ/m^3 (175 BTU/ft^3) to natural gas fuels containing higher hydrocarbons (e.g., propane) with LHV of 37.6 MJ/m^3 (1000 Btu/ft^3) or higher fractions of hydrogen. Fuels such as blast furnace gas (BFG) with LHV of 85 Btu/ft^3 have also been tested (Smith et al., 2006a,b). The rich catalytic reactor provided stability and extended turndown to low HV fuels due to catalytic prereaction. In addition, the catalytic region preferentially prereacts the higher hydrocarbons and hydrogen with no events of flashback or auto-ignition in the premixer, allowing lean operation with low NO_x and CO emissions. Consequently, and in contrast with the abovementioned fuel-lean catalyst system projects that focused exclusively on natural gas, the PCI system has been successfully tested in collaboration with Siemens and Solar Turbines, Inc., on high-firing temperature gas turbine applications using natural gas and hydrogen fuels as well as hydrogen-rich fuels such as simulated refinery fuel gas and syngas in relation with the requirements of IGCC (Smith et al., 2005).

PCI investigated hydrogen catalytic combustion at Solar Turbines' high-pressure facility (Etemad et al., 2011; Smith et al., 2005). They demonstrated in the Solar Turbines single-injector full-scale test rig at 8 bar that the rich catalytic system could burn hydrogen efficiently with low single-digit NO_x emissions and acceptable flame stability. In-house testing was performed up to 65% blend of hydrogen and nitrogen and at Solar Turbines up to 52% for safety constraints at the test facility. H_2 subscale testing was performed. By increasing the catalytic reactor conversion, lower NO_x levels were demonstrated (Smith et al., 2006a,b). Rich catalytic combustion has also been used for refinery fuel gas composition of 30% H_2 and 70% CH_4, indicating preferential reaction and downstream stable combustion with no sign of auto-ignition and flashback. Low single-digit NO_x was demonstrated.

Pure hydrogen has already been combusted in a turbine. In August 2009, Enel began operating a 16 MWe industrial-scale hydrogen power plant at Fusina in the Veneto region of Italy. It featured a gas turbine burner developed in collaboration with General Electric.

General Electric has long experience with hydrogen-rich fuels, with 28 turbines operating on blends containing more than 45 vol.% H_2 with a maximum of 97 vol.% for a 40 MW turbine at the Samsung General Chemicals petrochemical plant at Daesan in Korea (Moliere, 2004). Operation was not ideal, with NO_x control by steam/water injection, which diminishes efficiency, and with operational constraints during start-up, shutdown, and fuel changeover sequences to prevent undesirable ignition events.

NO_x emissions remain an issue for efficient premixed hydrogen turbines, and Enel also investigated catalytic combustion with lean premixed combustion to alleviate the problem. NO_x levels below 1 ppm were achieved with a cordierite-supported Pd catalyst, but attempts to replace Pd with perovskite catalysts were not successful (Gasperetti et al., 2007). Durability tests were not reported.

Liquid hydrogen has long been considered as a potential jet fuel. A thorough assessment of the technical feasibility was performed in the European Commission (EC)-supported CRYOPLANE project, which lasted for 24 months and was completed in 2003. The project, which was led by Airbus Deutschland, was carried out by a European consortium of 35 partners. The technical assessment concluded that hydrogen-fueled engines would be as energy efficient as kerosene engines and that conventional turbo engines could be converted to run on hydrogen. However, the aircraft would require fuel tanks four times larger than current kerosene ones, and the larger exterior surface areas would increase energy consumption by over 10%. With low NO_x turbines already developed prior to the project, the NO_x emissions would be much lower than those generated by the kerosene turbines and NO_x emissions were not considered a serious issue. Catalytic combustion was not mentioned among the turbine low-NO_x technologies considered at the time.

Today, interest in alternative jet fuels has shifted toward biofuels. The interest for hydrogen has not vanished, but the chances to witness aero-turbines featuring hydrogen catalytic combustion are now rather long-term.

In conclusion, it has been demonstrated that catalytic combustion remains a candidate technology for stationary premixed hydrogen turbines to reduce further NO_x emissions and improve operational stability. In the United States, the current development programs do not appear to support the scale-up of the technologies, but this may just reflect the relatively slow pace at which the clean coal projects advance. In Europe, a new momentum is provided by the emergence of PtG. The EC is supporting related projects on hydrogen turbines, as the current ones, which can handle hydrogen, are relatively low-efficiency diffusion turbines. The EC FP6 ENCAP project aimed at developing large-scale, certified stationary turbines to be run on hydrogen-rich fuels. National projects have also been initiated, with the involvement of the major gas turbine manufacturers (Anonymous, 2015). None of the current projects in Europe are mentioning catalytic combustion as an option.

10.3.4 Fuel cells

Molten carbonate fuel cells are currently the only fuel cells that address the industrial market. Catalytic combustors are used for the combustion of anode off-gas (Lee et al., 2012), which contains too much CO_2 to burn without catalyst. In addition, NO_x

production is minimized. The purified exhaust gas can be recirculated into the cathode channel for CO_2 supply to improve thermal efficiency.

10.3.5   Market forces and trends

In terms of industrial applications, turbines are the major likely domain for hydrogen catalytic combustion. Although the urgency to tackle greenhouse gas accumulation in the atmosphere has never been so clear, the current low oil and gas prices, which diminish government incomes, are slowing down the demonstration programs for clean coal programs and H_2 turbine developments. The efforts on hydrogen catalytic combustion for turbines have been drastically reduced. Future efforts on integrated clean coal and carbon capture sequestration may still consider hydrogen catalytic combustion as an alternative solution for low-emission applications.

The strong interest for PtG in Europe provides another incentive to keep developing catalytic combustion for turbines. In that concept, hydrogen is the storing medium for green electricity. Hydrogen may be stored underground and various options exist for its utilization. One of them is power production, which may be achieved only with turbines when large quantities are at stake. Hydrogen catalytic combustion may be of interest as very low NO_x production will be sought. Another option for the utilization of the stored hydrogen is its injection in the natural gas grid (up to 10 vol.% in the short to medium term) and the utilization of the blend as such. Currently, hydrogen concentrations of above 5 vol.% are not acceptable for most of the turbines in operation (Altfeld and Pinchbeck, 2013). If serious natural gas quality issues emerge and, more broadly, the necessity to deal with a wide variety of fuels, fuel flexible applications will have to consider hydrogen catalytic combustion concepts as an approach to achieve a safe, stable, low-emission combustion.

10.4   Applications not targeting the production of energy

10.4.1   Hydrogen safety sensors

Safety has always been a prime concern when dealing with hydrogen and it will be even more so as hydrogen technologies are now reaching the general public. Safety sensors for hydrogen detection play a key role in any hydrogen safety strategy and the importance of the topic cannot be overestimated. This importance has been recognized at the level of international bodies like ISO. ISO has long been involved as a partner in R&D efforts with major U.S. and European stakeholders from academia, industry, and government institutes (Burgess et al., 2009). There is indeed a need for standardization in terms of performance requirements and assessment: the database established by the EC-supported project H2sense (2014) has identified more than 400 different models of detectors. The National Energy Laboratory of the US Department of Energy has identified 120 manufacturers (Burgess et al., 2009). Four key parameters determine the quality of sensors: performance (sensitivity, range), lifetime, reliability, and cost. So far, no sensors exist that can satisfy all the criteria in all contexts.
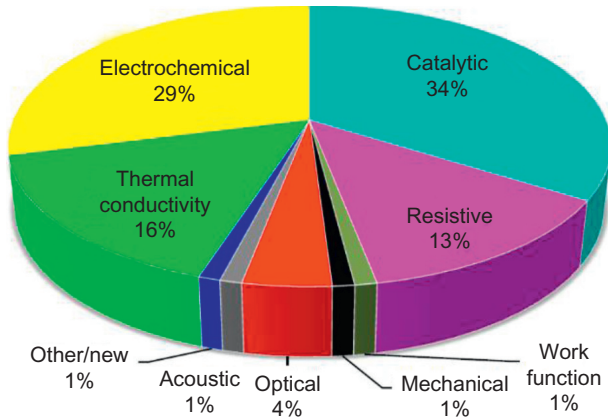
Figure 10.10 2014 market survey of hydrogen sensors (fuel cells and hydrogen joint undertaking project H2sense (2014).

There are more than 10 different working principles that have been used to design commercial sensors (Figure 10.10).

Excellent reviews exist that describe all these technologies (Hübert et al., 2011). Catalytic combustion-based sensors are the most numerous because they are the least expensive and provide adequate service in many environments. There are two types: pellistor and thermoelectric. In a pellistor, the sensing signal is provided by the imbalance of a Wheatstone bridge, which includes a Pt or Pd catalyst bead. In a thermoelectric type sensor, the sensing signal arises from the Seebeck effect, which takes place when the temperature differential increases in conductor or semiconductor materials.

The catalytic combustion-based sensors are proven technology with good performance and excellent reliability. They have a few weaknesses: (1) they are not selective, as they may react with other combustible gases; (2) like all catalytic devices, they may become inactive because of exposure to poisons such as chlorinated and sulfur compounds; and (3) they require oxygen to operate. So, they should be used in locations where they can operate at their best.

10.4.2 Elimination of hydrogen

The undesired formation of hydrogen in various processes can be mitigated by the elimination of this hydrogen afterwards. Because hydrogen oxidation is the reaction most sensitive to the action of catalysts, especially precious metals, hydrogen can be removed selectively in the presence of other gases. Some caution has to be exercised concerning the heat release during oxidation. As a rule of thumb, the combustion of 1 vol.% hydrogen in a gas mixture raises the temperature by 80°C in an adiabatic enclosure. Usually for pressure drop issues and improved control of transport phenomena, gas treatment is performed with monolithic supports that may be ceramic or metallic. The choice of either one is be determined by the hydrogen concentration in the blend, with arguments similar to those used for car exhaust treatment. For

the removal of hydrogen traces in the oxygen stream of electrolyzers, platinum on ceramic monoliths are usually the preferred combination.

The most important commercial application of catalytic hydrogen oxidation is found in nuclear plants. In the case of a serious accident, hydrogen generated by the reaction of water with the fuel rods could be released into the reactor building. To curtail the risk of an explosion, recombiners are often installed. Recombiners are devices that are designed to be able to destroy the eventual incoming hydrogen by triggering its reaction with oxygen.

There are thermal recombiners that require electricity to operate and this has proved to be a poor solution as the power may be cut during an accident, such as the Fukushima Daiichi nuclear disaster (WNN, 2012). Passive versions based on hydrogen catalytic oxidation emerged in the 1990s and have now been installed in nuclear plants all over the world. They take advantage of the fact that on platinum catalysts, the oxidation takes place spontaneously at room temperature. The recombiner is described as passive because it is self-starting and self-feeding and requires no external energy. It starts to operate as soon as the hydrogen concentration begins to increase over 1–2 vol.%.

The treating capacity corresponds to the hydrogen flow that could be expected in the case of an accident. The largest size sold by AREVA (Figure 10.11) can treat up to 1500 Nm^3/h, which is the amount that would be required by a large-size hydrogen bus refueling station ($\sim$100 fuel cell buses/day).

The platinum catalyst is supported on stainless steel metallic plates located at the bottom of the unit. The 1500 Nm^3/h AREVA passive autocatalytic recombiner (PAR)

Figure 10.11 AREVA's high-capacity passive autocatalytic recombiner (PAR), with a gas treating capacity of up to 1500 Nm^3/h. Height is 1.4 m for the largest model (Areva, 2015).

contains 150 plates. Weight is 130 kg. Upon contact with the catalyst in the lower part of the unit, the oxidation takes place. The heat of reaction causes a reduction in gas density and induces convective flow currents, which contribute to the mixing of the gases in the containment for an optimum efficiency of the recombination.

Platinum is the catalyst of choice for PARs. However, platinum, which has been evaluated as being 400 times more efficient than palladium for that application, is more prone to iodine poisoning. Alloys permit the high platinum activity to be maintained and are less susceptible to poisoning (Morfin et al., 2004).

Recombiners are also used in large battery applications. The high cost of platinum is a barrier for the development of the market. The search for less expensive nonprecious metal catalysts continues, especially in the fuel cell area for vehicle and stationary/CHP applications. Promising results are regularly announced but they still have to reach the commercial stage (e.g., UNIST, 2013).

10.5   Sources of further information

National/government programs on hydrogen energy
    http://www.iphe.net/ Australia, Austria, Brazil, Canada, China, EC, Germany, France, Iceland, India, Italy, Japan, Republic of Korea, Norway, Russian Federation, Republic of South Africa, United Kingdom, United States
Hydrogen implementing agreement of the international energy agency
    http://ieahia.org/
International association for hydrogen energy
    http://www.iahe.org/
Companies involved in hydrogen catalytic combustion
    http://www.catator.se/
    http://www.precision-combustion.com/
Historical perspective
    Peter Hoffmann, 2012. Tomorrow's Energy, Revised and Expanded Edition. Hydrogen, Fuel Cells, and the Prospects for a Cleaner Planet. The MIT Press. ISBN: 9780262516952.

References

Altfeld, K., Pinchbeck, D., 2013. Admissible hydrogen concentrations in natural gas systems, gas for energy 03, ISSN 2192–158X DIV Deutscher Industrieverlag GmbH, www.gas-for-energy.com.

Anonymous, 2015. Hydrogen turbines, http://kraftwerkforschung.info/en/hydrogen-gas-turbines/.

Areva, 2015. http://us.areva.com/EN/home-1495/new-challenges-proven-solutions-mitigation-passive-autocatalytic-recombiner-par.html.

Baird, B., Etemad, S., Karim, H., Alavandi, S., Pfefferle, W.C., 2010. Gas turbine engine test of RCL catalytic pilot for ultra-low NOx applications. Catal. Today 155, 13–17.

Baukal Jr., C.E., 2001. The John Zink Combustion Handbook. CRC Press, Boca Raton.

Benjaminsson, G.J., Benjaminsson, J., Boogh Rudberg, R., 2013. Power to Gas—a technical review, SGC Rapport 2013:284, Svenskt Gastekniskt Center AB.

Booth, D., Pyle, W., 1993. Cookin' on hydrogen, Home Power, 33 February/March.

Burgess, R., Buttner, W., Post, M., 2009. DOE annual merit review hydrogen program & vehicle technologies hydrogen safety sensors, May 22, 2009 NREL project ID # SCS 02 burgess.

Carroni, R., 2009. Combustion chamber with burner and associated operating method, U.S. Patent 7,568,907.

COSPP, 2014. http://www.cospp.com/articles/2014/12/microturbine-market-boosted-by-chp-applications.html.

Cowan, E.J., 1986. Everything you wanted to know about hydrogen but were afraid to ask. In: ASGE-1 National Conference. 16/05/1986.

Dalla Betta, R.A., Schlatter, J.C., Nickolas, S.G., Cutrone, M.B., Beebe, K.W., Furuse, Y., Tsuchiya, T., 1997. Development of a catalytic combustor for a heavy-duty utility gas turbine. J. Eng. Gas Turbines Power 119 (4), 844–851. http://dx.doi.org/10.1115/1.2817063.

DeCorso, S., Mumford, S., Carrubba, R.V., Heck, R., 1977. Catalysts for gas turbine combustors—experimental test results. J. Eng. Gas Turbines Power 99 (2), 159–167.

Dennis, R., 2006. http://www.netl.doe.gov/research/coal/energy-systems/turbines/publications/handbook.

Deutschmann, O., Warnatz, J., 2002. Diagnostics for catalytic combustion. In: Kohse-Höinghaus, K., Jeffries, J.B. (Eds.), Applied Combustion Diagnostics. Taylor & Francis, New York.

Dzubiella, M., Eder, A., 1977. Le brûleur catalytique Matrix, GWA 713.

Element Energy, E4tech. and PURE Energy Centre, 2006. Novel hydrogen applications—review of status and prospects. Information Resource for Highlands & Islands Enterprise.

Etemad, S., Baird, B., Alavendi, S., 2011. Catalytic combustion for ultra-low NOx hydrogen turbines. Final report, Department of Energy, Contract # DE-FC26-05NT42647.

Gasperetti, G.S., Faleni, M., Benelli, G., Cimino, S., Russo, G., Stanzione, V., 2007. Development of catalytic elements for hydrogen fuelled gas turbine. In: Proceedings of the 3rd European combustion meeting ECM.

H2sense, 2014. http://www.h2sense.bam.de/en/data_sheet/index.htm, http://www.fch-ju.eu/prpage/presentations-0, 2014 Project Review days.

Hayes, R.E., Kolaczkowski, S.T., 1997. Introduction to Catalytic Combustion. Gordon and Breach Science Publishers, Amsterdam.

Hoffmann, P., 2012. Tomorrow's energy, hydrogen, fuel cells, and the prospects for a cleaner planet. The MIT Press, Cambridge, ISBN: 9780262516952.

Howell, J.R., Hall, M.J., Ellzey, J.L., 1996. Combustion of hydrocarbons within porous inert media. Prog. Energy Combust. Sci. 22, 121–145.

Hübert, T., Boon-Brett, L., Black, G., Banach, U., 2011. Hydrogen sensors—a review. Sens. Actuators B157, 329–352.

HYINDOOR, 2014. http://www.hyindoor.eu/.

Jannasch, A.K., 2010. Catalytic Burner for gas stove and cooking plate applications, http://www.catator.se/?p=524.

Johnson, T.A., Kanouff, M.P., 2012. Development of a hydrogen catalytic heater for heating metal hydride hydrogen storage systems. Int. J. Hydrogen Energ. 37 (3), 2304–2319.

Karim, H., Lyle, K., Etemad, S., Smith, L.L., Pfefferle, W.C., Dutta, P., Smith, K.O., 2003. Advanced catalytic pilot for low NOx industrial gas turbines. J. Eng. Gas Turbines Power 125, 879–884.

Ladaki, M., Houser, T., Roberts, R.W., 1965. The catalysed low-temperature hydrogen-oxygen reaction. J. Catal. 4, 239–247.

Lamb, A.B., Scallone, C.C., Edgar, G., 1922. The preferential catalytic combustion of carbon monoxide in hydrogen. J. Am. Chem. Soc. 44 (4), 738–757. http://dx.doi.org/10.1021/ja01425a007.

Laster, W.R., 2005. Development of a catalytic combustor for fuel flexible turbines. In: 23rd Annual International Pittsburgh Coal Conference.

Lee, S., Ahn, K.Y., Lee, Y.D., Han, J., Im, S., Yu, S., 2012. Flow uniformity of catalytic burner for off-gas combustion of molten carbonate fuel cell. J. Fuel Cell Sci. Technol. 9 (2). http://dx.doi.org/10.1115/1.400561, 021006-021006-6.

Logue, J.M., Klepeis, N.E., Lobscheid, A.B., Singer, B.C., 2014. Pollutant exposures from natural gas cooking burners: a simulation-based assessment for southern California. Environ. Health Perspect 122 (1), 43–50. http://dx.doi.org/10.1289/ehp.1306673.

Lyubovsky, M., Smith, L.L., Castaldi, M.J., Karim, H., Nentwick, B.F., Etemad, S., LaPierre, R.B., Pfefferle, W.C., 2003. Catalytic combustion over platinum group catalysts: fuel-lean versus fuel-rich operation. Catal. Today 83, 71–84.

Melaina, M.W., Antonia, O., Penev, M., 2013. Blending hydrogen into natural gas pipeline networks. A review of key issues. NREL technical report. NREL/TP-5600-51995.

Milani, A., Wünning, J.G., 2002. What is flameless combustion? IFRF online combustion handbook.

Moliere, M., 2004. Hydrogen-fuelled gas turbines: status and prospects. In: 2nd CAME-GT conference, Bled, Slovenia, April 29–30. http://www.modernpowersystems.com/features/featuredaesan-unit-burns-95-per-cent-hydrogen-fuel/.

Morfin, F., Sabroux, J.C., Renouprez, A., 2004. Catalytic combustion of hydrogen for mitigating hydrogen risk in case of a severe accident in a nuclear power plant: study of catalysts poisoning in a representative atmosphere. Appl. Catal. Environ. 47, 47–58.

Pfefferle, W.C., 1973. Catalytically-supported thermal combustion. US patent 3928961.

Pyle, W., Healy, J., Cortez, R., Booth, D., 1993. Heatin' with hydrogen. Home Power# 34, April–May.

Roesler, J., 2009. CATHY-IFP Brûleur radiant catalytique pour la combustion des mélanges gaz naturel hydrogène, Agence Nationale de la Recherche, ANR: PAN-H.

Shankleman, J., 2015. http://www.businessgreen.com/bg/news/2395931/eu-to-ban-gas-guzzling-ovens-and-hobs-from-tomorrow.

Sharer, J.C., Pangborn, J.B., 1975. Utilisation of hydrogen as an appliance fuel. In: Veziroglu, T.N. (Ed.), Hydrogen Energy. Plenum Press, New York, pp. 875–888, Pt. B.

Silversand, F., 2013. HeatCore—an ultra-compact and fuel flexible catalytic boiler concept, SGC [Svenskt Gastekniskt Center AB], Rapport, 255.

Smith, L.L., Karim, H., Etemad, S., Pfefferle, W.C., 2005. Catalytic combustion of gasified coal for low-emissions gas turbines. In: Proceedings of the 22nd Annual International Pittsburgh Coal Conference.

Smith, L.L., Karim, H., Castaldi, M.J., Etemad, S., Pfefferle, W.C., 2006a. Rich-catalytic lean-burn combustion for fuel-flexible operation with ultra low emissions. Catal. Today 117 (4), 438–446.

Smith, L.L., Etemad, S., Karim, H., Pfefferle, W.C., 2006a. Catalytic combustion, In: Dennis, R. (Eds.), Chapter 3.2.2. http://www.netl.doe.gov/research/coal/energy-systems/turbines/publications/handbook.

UNIST, 2013. Ulsan National Institute of Science and Technology, non-precious metal catalysts outperforming Pt-based one. ScienceDaily. 23 September 2013. www.sciencedaily.com/releases/2013/09/130923143630.htm.

Veziroglu, T.N., 1995. Twenty years of the hydrogen movement: 1974–1994. In: Yürüm, Y. (Ed.), Hydrogen Energy System. In: NATO ASI Series, Series E: Applied Sciences, vol. 295. Kluwer Academic Publishers, Dordrecht.

Veziroglu, T.N., Escher, W.J.D., 1979. Solar energy utilization in advanced residential and commercial applications through hydrogen energy. In: Sayigh, A.A.M. (Ed.), Solar Energy Application in Buildings. Academic Press, Inc., New York.

WNN, 2012. World Nuclear News (WNN), Hydrogen fix for Japanese reactors, October 19.

This page intentionally left blank

Electrochemical applications of metal hydrides

11

K. Young
BASF-Ovonic, Rochester Hills, MI, USA

Abbreviations

11.1   Introduction

Metal hydrides (MH) are, in general, products of chemical reaction between hydrogen and metals. While the nature, synthesis, characterization, properties, and applications of MH are available in a recent publication (Young, 2013), the electrochemical applications, especially in the nickel-metal hydride (Ni-MH) battery, will be discussed in detail in this chapter. Different from gaseous phase hydrogen storage where electrically neutral hydrogen atoms enter MH, the electrochemical reaction of MH usually requires supplying or removing of electrons through an external circuit accompanied with absorption or desorption of protons through the MH–electrolyte interface (Figure 11.1). Therefore, a good MH candidate for an electrochemical application has to be a good conductor for both protons and electrons. That leaves transition metal elements and their alloys (both solid solutions and intermetallic alloys) the major players in electrochemical applications, such as Ni-MH battery, MH-air battery,
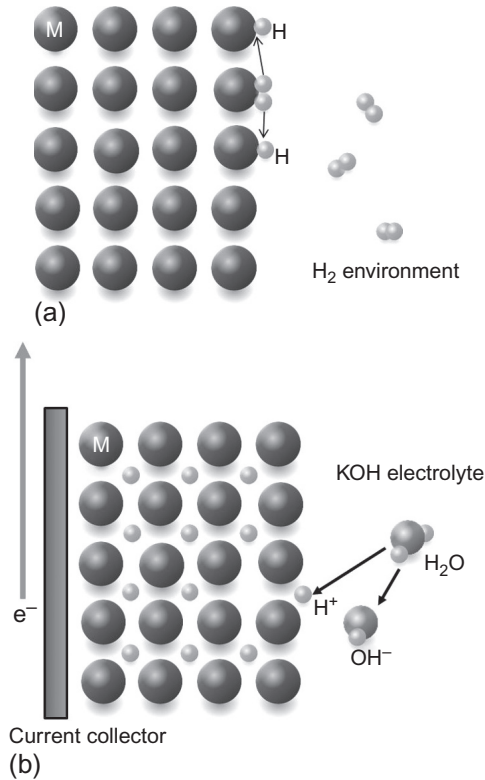
Figure 11.1 Comparison of hydrogen absorption through gaseous phase (a) and electrochemical reaction (b).

Ni-hydrogen battery, Li-ion battery, alkaline fuel cell, and water-decomposition cell (for a review, see Young and Nei, 2013). Among these applications, the Ni-MH battery, a US$4 billion (annual) business that powers billions of portable electronic devices and over 6 million hybrid electrical vehicles (HEV), is no doubt the largest application of MH. Therefore, the application of MH as active materials in negative electrode (anode) of the Ni-MH battery will be the main topic of this chapter.

The Ni-MH battery usually consists of a MH negative electrode, a transition metal hydroxide positive electrode, a grafted polyethylene (PE)/polypropylene (PP) separator, 30 wt.% KOH electrolyte, a Ni-plated (inside) stainless steel can, and a pressure release valve (except for a button cell or a coin cell). At the negative electrode, a microporous surface oxide layer is formed at the MH surface after a proper formation process is conducted, which allows the penetration of electrolyte into MH alloy. There are nanosized metallic (mainly Ni) clusters embedded in the surface oxide layer acting as catalyst for the electrochemical reactions. At the positive electrode, the active components are a highly disordered (both compositional and structural) hydroxide mixture of Ni, Co, and Zn. Ni is the main functional element in the battery reaction, which switches between +2 (discharge) and +3 (charge) oxidation states, while Co and

Zn are additives to raise the oxygen gas evolution potential and prevent swelling (generating gamma─NiOOH). To ensure a good conducting path between the active materials and the current collector, a conductive CoOOH network on the surface of the current collector was formed either by Co precoating before the positive electrode was loaded or by adding additives of CoO or Co metals to the positive electrode materials during the electrode formation process. As a general practice, a small amount of Y_2O_3 or Er_2O_3 is added in the positive electrode to retard the oxide formation on the negative electrode surface. Both the negative and positive electrodes can be made through dry compaction or wet pasting method into conducting substrates, such as Ni-plated stainless steel plate, Ni-foam, Ni-mesh, or expanded metal. In recent years, the sulfonated PE/PP separator has been used widely due to its capability of trapping nitrogen species during cycling to hinder self-charge issue. In the electrolyte, NaOH and LiOH additives are used to improve the high- and low-temperature performance, respectively.

11.2   Criteria of metals for Ni-MH battery applications

Many considerations need to be taken into account when it comes to choosing a proper metal for an alkaline Ni-MH battery. The first one is good electronic conductivity, which excludes those metals that form a covalent or ionic bond with hydrogen. This leaves only elemental metals and their alloys in the arena. The next concern is the compatibility of the element/alloy metal with KOH electrolyte. Heavy corrosion (formation of a soluble oxidation product—usually a complex ion) or passivation (formation of a thick and dense surface oxide layer) of the metals or metal alloys in an alkaline environment (pH value > 14) can cause a severe capacity degradation. It is one of the reasons why high percentages of Ni, which is inexpensive and robust in KOH, are used in all hydrogen storage alloys in Ni-MH batteries. In addition to resistance to corrosion and passivation, Ni-MH battery suitable metals or metal alloys must also carry good hydrogen storage capacity (>1.2 wt.%), fast bulk hydrogen diffusion ($D > 1 \times 10^{-10}$ cm s^{-2}), adequate metal–hydrogen bond strength (hydride formation heat between -25 and -45 kJ mol H$_2^{-1}$), acceptable cost, environmental safety, and electrochemically active surfaces after activation. Last but not least, the lattice expansion during hydrogenation should be within a reasonable range ($<15\%$) to prevent severe pulverization during hydriding/dehydrid cycling.

11.3   Classification of metals used in a Ni-MH battery

Conventional materials that are used as an active component in a Ni-MH battery negative electrode can be classified into two categories: element metals and metal alloys; both of which rely on the metallic nature of the interstitial hydrogen in the host metal lattices to store hydrogen. Recently, ionic compounds such as perovskite oxides and phosphates with hydrogen storage capability were also investigated as negative

electrode material for Ni-MH battery applications. In addition, metal borides and semiconductors, such as NiSe, can be used as negative electrodes in the Ni-MH battery as well.

11.3.1   Elemental metals

The investigation of hydrogen absorption in metals started from precious metals, such as Pt, Au, and Pd, about 100 years ago, which was followed by an interest in rare earth metals, and it finally found its way to transition metals. $PdH_{0.7}$ and VH_2 have been studied the most thoroughly due to their adequate hydride formation heat (ΔH_h, $-41\ kJ\ mol^{-1}\ H_2$ for $PdH_{0.7}$ and $-34\ kJ\ mol^{-1}\ H_2$ for VH_2), at room temperature for hydrogen storage. Other elemental metals with lower ΔH_h, such as MgH_2 ($-74\ kJ\ mol^{-1}\ H_2$), TiH_2 ($-124\ kJ\ mol^{-1}\ H_2$), ZrH_2 ($-163\ kJ\ mol^{-1}\ H_2$), and LaH_3 ($-208\ kJ\ mol^{-1}\ H_2$), are also being researched due to their relatively high hydrogen storage capacity. The elemental metals can be further classified by their crystal structures into body-centered-cubic (BCC), face-centered-cubic, and hexagonal-closest-pack types. The hydrogen occupation sites in these three structures are either surrounded by four (tetrahedral sites) or six host metals (octahedral sites). An example of a hexagonal-closest-pack $LaNi_5$ structure together with its possible hydrogen occupation sites is shown in Figure 11.2.

11.3.2   Intermetallic compound metals

Because the choices of elemental MH are very limited, the investigation of the room temperature MH extended to intermetallic compound (IMC) about 50 years ago. TiFe, Ti_2Ni, TiNi, MgNi, Mg_2Ni, and ZrV_2 binary alloys in this category were studied first. It was not until the hydrogen storage capability of rare earth-based AB_5 was accidently discovered in the Philips Research Laboratory that practical applications of MH alloys started to take place and became the main stream of research in the area of electrochemical application of MH. To adjust the metal–hydrogen bond strength and modify various gaseous phase or electrochemical hydrogen storage properties, substitutions in both A and B-sites of AB_x ($x = 0.33$, 0.5, 1, 2, 3, and 5) IMC were investigated to
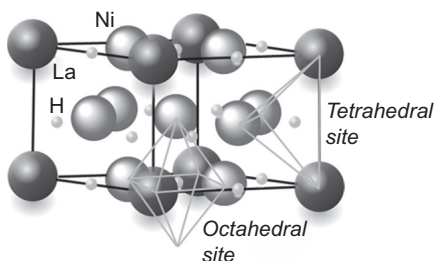
Figure 11.2 Tetrahedral and octahedral hydrogen occupation sides inside a $LaNi_5$ host metal crystal lattice (hexagonal-closest-pack).

Table 11.1 **Common pseudobinary alloy systems for hydrogen storage purposes**

Stoichiometry	Available crystal structural	A site element	B site element	Typical hydrogen storage (wt.%)
A_3B	FCC	Zr, Er	Fe, Rh, Al, Co	Up to 2.1
A_2B	Hexagonal	Mg	Ni, Cu	Up to 3.6
AB	B2	Ti	Cr, Fe, Ni, Mn, V	Up to 3.5
AB_2	C14, C15, C36	Ti, Zr, Hf	V, Cr, Mn, Fe, Co, Ni, Cu, Zn	Up to 3.0
AB_3	Hexagonal	Mg, Ca, Y, La, Ce, Pr, Nd, Sm	Ni, Co, Mn, Al, Fe, Cu	Up to 1.8
A_2B_7	Hexagonal	Mg, Ca, Y, La, Ce, Pr, Nd, Sm	Ni, Co, Mn, Al, Fe, Cu	Up to 1.6
AB_5	$CaCu_5$	Ca, Y, La, Ce, Pr, Nd, Sm	Ni, Co, Mn, Al, Fe, Cu	Up to 1.4

produce pseudobinary IMC. The widely used MH alloy in today's Ni-MH battery with a chemical composition of (La, Ce, Pr, Nd) (Ni, Co, Mn, Al)$_5$ is a good example of such a pseudobinary system. Other examples of AB_x systems can be found in Table 11.1. The stoichiometry of IMC always has a limited range of solubility due to the existence of defects such as vacancies and antisites. The off-stoichiometry in MH IMC may benefit gaseous phase and electrochemical hydrogen storage properties (Young, 2012).

11.3.3   Solid solution metals

When two or more metals with similar size and electronegativity melt together the solidified product is usually a solid solution with a wide composition range. This is different from the AB_x IMC where A and B atoms have quite different size and electronegativity (A atoms are larger with smaller electronegativity compared to B atoms). The search for a solid solution metal for hydrogen storage application started from two elements that are capable of storing hydrogen at room temperature, V and Pd. TiVCr-based body-centered-cubic MH is a classic example that has been widely studied due to its relatively high hydrogen storage capability at room temperature (3.6 wt.%). Another example of a solid solution metal for hydrogen storage is Rh-Ag alloy, which has a similar electronic structure to Pd, although neither Rh nor Ag can store hydrogen. The wide compositional range of this group of alloy allows for composition engineering fulfilling different applications.

11.3.4   Amorphous metals

Not only the crystalline metals can absorb hydrogen, so too can their amorphous siblings. Compared to their crystalline counterparts, the amorphous MH alloys usually have the following characteristics:

1. A higher hydrogen storage capacity.
2. A shorter plateau region and a steeper curve in the pressure-concentration isotherm.
3. Less lattice expansion resulting in less pulverization during hydriding/dehydriding cyclings.
4. More surface active sites available to facilitate chemical/electrochemical reactions.

For example, the amorphous Zr-based MH can absorb 1.8 times more hydrogen compared to the same material with a crystalline structure (Burlakova et al., 2011). Another example is the Mg-Ni MH system. Because neither of the only two possible IMCs in the Mg-Ni binary phase diagram ($MgNi_2$ and Mg_2Ni) has the adequate metal-to-hydrogen bond strength for a room temperature application, an amorphous alloy closed to MgNi composition is engineered to be used at room temperature (Young, 2012). Electrochemical discharge capacity of 720 mAh g^{-1} was reported on a MgNiCoMn-based amorphous thin film prepared by RF sputtering (Ovshinsky and Fetcenko, 1996). Later on, bulk production with similar composition and the same microstructure was achieved by combining melt-spin and mechanical alloying together. The best discharge capacity achieved was 791 mAh g^{-1} (Ovshinsky et al., 1997).

11.3.5   Perovskite oxides

In a generalized definition, conducting perovskite oxides (ABO_3) are considered as metals and can be used as negative electrode in a Ni-MH battery. They are conductive either due to the transition metal atoms with multivalence in the B-sites or based on distorted perovskite oxides (the high-temperature superconductor $YBa_2Cu_3O_{7\text{-}\delta}$, for example). Some of these conductive perovskite oxides show impressive hydrogen storage capabilities at near room temperature. For example, $LaFeO_3$ has a discharge capacity of 530.3 mAh g^{-1} measured at 333 K (Deng et al., 2010). With this promising result, intense research is expected to be focused on lowering the operating temperature while maintaining a reasonable amount of discharge capacity (Lim et al., 2013a).

11.3.6   Other oxides

In addition to the perovskite oxides mentioned in the last section, $FePO_4$ was also proposed as a low-cost hydrogen storage negative electrode for the Ni-MH battery (Lim et al., 2013b). The crystalline $FePO_4$ has a slightly larger discharge capacity (109 mAh g^{-1}) compared to that of its amorphous counterpart (81.4 mAh g^{-1}). While the surface exchange current density of $FePO_4$ is at the same level as MH alloys used in the Ni-MH battery, its bulk diffusion constant is at least five orders of magnitude lower. The lower power performance limits its applications to those occasions where slow-rate discharge (clock, for instance) is sufficient. Recently, we performed tests of

using the disordered hydroxide of transition metals with a high initial conductivity as new cathodes material and progress is encouraging.

11.3.7   Metal borohydrides

A few compounds made from metal and borohydride (BH_4) were found to be able to store a large amount of hydrogen reversibly to a certain degree. Examples are $LiBH_4$ (13.9 wt.%), $NaBH_4$ (7.9 wt.%), Be $(BH_4)_2$ (20.8 wt.%), $Mg(BH_4)_2$ (14.9 wt.%), and $Al(BH_4)_2$ (16.9 wt.%). However, the metal-to-hydrogen bonds in most of these compounds are too strong to be used as the Ni-MH battery anodes, which require a ΔH_h between -25 and -45 kJ mol^{-1}H$_2$ to be able to release the absorbed hydrogen. Fortunately, mixed metal borohydrides have demonstrated the properties to overcome this issue. A recent work by Wang et al. showed results of using low-cost $La_{15}Fe_{77}B_8$-type of boride as negative electrode in the Ni-MH battery, which achieves 310 mAh g^{-1} capacity with a retention of about 50–75% of the original capacity after 50 cycles (Wang et al., 2014). The capacity is maintained.

11.3.8   Semiconductor

Hollow semiconducting NiSe nanospheres were reportedly used as negative electrode for the Ni-MH battery (Shi et al., 2013) as well. Despite the acceptable discharge capacity of 340 mAh g^{-1}, it's the relatively low energy density due to the low discharge voltage (0.44 V) that limits the application of NiSe as electrode materials. Other semiconducting nanostructured compounds in this category, such as Bi_2S_3, $Cu(OH)_2$, CuO, Fe_3S_4, and MoS_2, were also investigated for hydrogen storage purposes.

11.4   Current status of MHs research for Ni-MH battery application

A review paper on MH research for the electrochemical application was published recently (Young and Nei, 2013). It covers the efforts to improve the MH alloy performance for all the MHs, such as rare earth-based AB_5, Laves-based AB_2, Ti-Ni-based, Mg-Ni-based, Laves-BCC, Zr-Ni-based and other alloy systems. The energy density, cycle life, and wider temperature range have been investigated in the Ni-MH battery anode as elaborated in the following sections.

11.4.1   Strategies to increase the energy density of the Ni-MH battery

The key issue of the Ni-MH battery for consumer and electrical vehicle applications is the energy density when compared to the Li-ion battery, especially the gravimetric energy density. While a 18,650 Li-ion battery using lithium-cobalt-oxide as cathodes can easily achieve 250 Wh kg^{-1}, the best high energy of a AA Ni-MH cell is only about

105 Wh kg^{-1}. Efforts have been made to improve the energy density of new materials for both anode and cathode, as well as electrolyte. In the positive electrode, multielectron transferring alpha-Ni(OH)$_2$ has been proposed for many years as a high-energy density substitute for positive electrode material, but there is still no commercial product. In the negative electrode, both AB$_2$ and A$_2$B$_7$ MH alloys with higher hydrogen storage capacities than the conventional AB$_5$ MH alloy were used in commercial products. However, it is tough for the Laves phase-related BCC MH alloys (Young et al., 2014a) to penetrate the market due to the high cost of one key element, vanadium, although they demonstrate high storage capacity (Figure 11.3). Inexpensive MgNi-type of AB alloys, on the other hand, suffer from capacity degradation due to oxidation from the KOH electrolyte (Figure 11.3), which makes it impossible for commercialization despite their very high initial capacities (>700 mAh g^{-1}). As to the electrolyte, less corrosive salts with lower conductivity are used to substitute a portion of the 30% KOH electrolyte in the commercial Ni-MH battery with a trade-off of power performance for applications where the high power is not an essential requirement. Moreover, proton-conducting ionic liquid or organic solvent-based electrolyte were investigated as well for possible use as electrolyte in the Ni-MH battery, to minimize corrosion so that cheap and high-energy MgNi-based AB type of MH alloys can be used.

11.4.2 Battery failure mechanism

Various Ni-MH battery failure modes reported in recent publications are summarized in Figure 11.4 (Kong et al., 2012; Zhou et al., 2013; Young et al., 2014b), together with suggested solutions. The main failure mode is the increase of the internal impedance
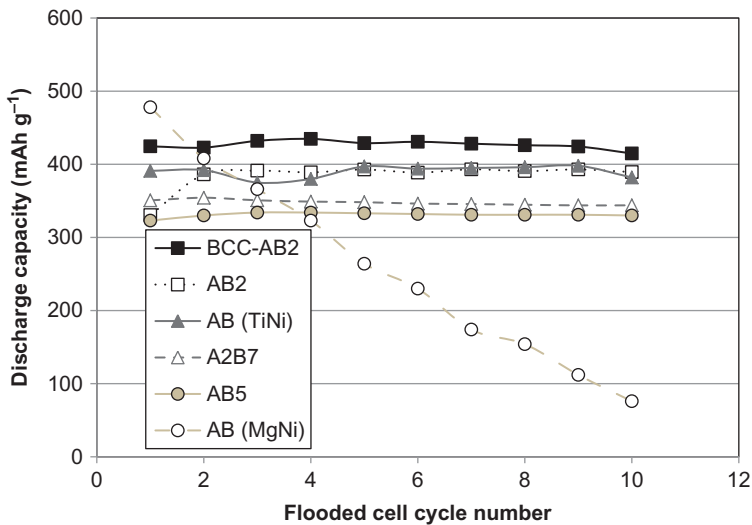
Figure 11.3 State-of-the-art discharge capacities measured with a current density of 10 mAh g^{-1} of MH alloys used as negative electrode in Ni-MH battery. BCC-AB2 is a Laves phase-related BCC alloy that has about 20% C14 and 80% BCC phases.
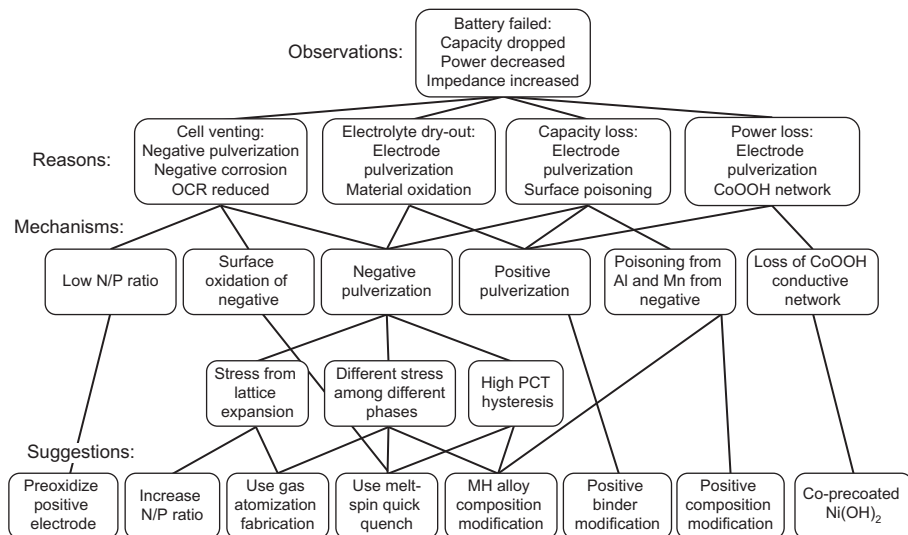
Figure 11.4 The schematic of the possible failure modes of Ni-MH battery and several suggested solutions. N/P ratio is the negative-to-positive capacity ratio and is typically between 1.2 (high energy type) and 2.0 (high power type). OCR and PCT stand for overcharge reservoir (Young et al., 2012) and pressure-concentration-temperature isotherm (Young et al., 2009).

due to the dry-out of the electrolyte during excessive oxidation and venting, which increases the charge voltage (refuse to be charged) and decreases the cell voltage (no output). Other failure modes include negative electrode pulverization, oxidation, passivation, leaching-out, microconducting network formation and separator collapse, CoOOH network breakdown, Al-contamination, formation of nonreversible gamma-NiOOH, and pulverization of the positive electrode and a very large surface area in both electrodes competing for the remaining electrolyte due to severe pulverization. A well-designed Ni-MH battery has to balance all the degradation mechanisms in the battery during cycling.

11.4.3 Strategies to increase the cycle life of a Ni-MH battery

Although Ni-MH battery applications in consumer products require less extended cycle life (typically 200–500 cycles is sufficient), some applications, such as in automotive propulsion and in the daily energy storage system of solar or wind farms, demand longer service life. In recent years, many efforts in different areas have been put together to fulfill market needs. For example, rare earth Mg-based A_2B_7 superlattice alloys without Mn and Co elements were designed to eliminate the poisoning to the positive electrode (Yasuoka et al., 2006); cocoated $Ni(OH)_2$ was developed to enhance the durability of the positive electrode during cycling; and additives in the negative electrode were developed to reduce the oxidation of the MH alloy (Tanaka et al., 2009). By improving further the abovementioned A_2B_7 superlattice
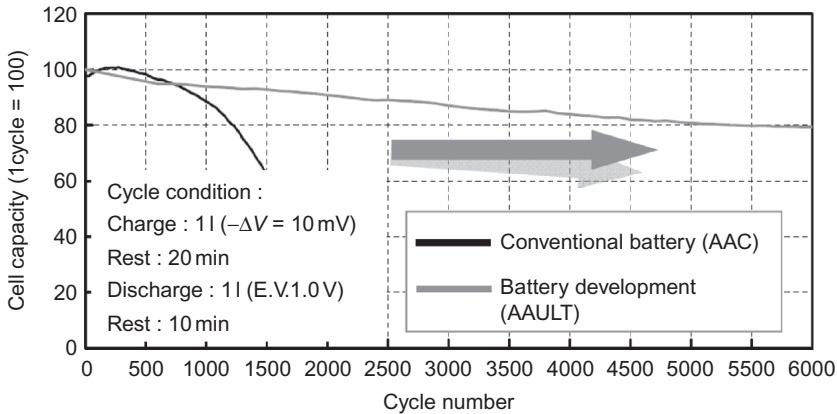
Figure 11.5 Improvement in the 1C/1C cycling performance combining improvements from both electrodes, separator, cell design, and electrolyte. Courtesy of FDK Corporation.

alloy and designing a high-durability cell in which the performance of the high-corrosion superlattice alloy is maximized, Fuji Denki Kagaku (FDK) Corporation was able to demonstrate a Ni-MH battery capable of 6000 cycles with 100% state-of-charge and 100% state-of-discharge (Figure 11.5). Two main directions for future MH alloy development are the elimination of both pulverization and oxidation. Engineering in both electrode material compositions and producing processes were found to be effective to serve these purposes in the past (Young et al., 2010, 2011).

11.4.4 Strategies to improve the low-temperature performance of the Ni-MH battery

One of the most promising opportunities for the Ni-MH battery in the consumer market is as a replacement for the environmentally hazardous Ni-Cd rechargeable battery. Compared to Ni-Cd, a Ni-MH battery has a higher energy density, similar power density, better cycle life and charge retention, but an inferior low-temperature performance. Their discharge chemical reactions are different:

$$MH + OH^- \rightarrow M + H_2O + e^- \, (in \, Ni - MH \, battery) \tag{11.1}$$

$$Cd + 2OH^- \rightarrow Cd(OH)_2 + 2e^- \, (in \, Ni - Cd \, battery) \tag{11.2}$$

The low end of the applicable temperature range of an alkaline battery (-30 to -40 °C) is close to the freezing temperature of the 30% KOH. The water generated from the discharge of a Ni-MH battery dilutes the KOH concentration locally and increases the chance of electrolyte freezing. Special engineering in the pore structure of the surface oxide is needed for even lower temperature applications. For example, by adding Cu to the AB$_5$ MH alloy, channel-type pores are created to better deliver the electrolyte to the electrode surface (Fetcenko et al., 2007). Adding elements, such as Si and Y, were

also found to be effective to enhance the low-temperature conductivity by either increasing the surface catalytic ability (Young et al., 2013a) or increasing the surface area (Young et al., 2013b).

11.4.5 Strategies to improve the high-temperature performance of the Ni-MH battery

There are two issues that need to be addressed during high-temperature operation of a Ni-MH battery. The first one is charge acceptance at elevated temperature and usually associated with decreasing oxygen evolution potential causing an insufficient charge, which requires remediation from a new positive electrode recipe (Fierro et al., 2006). Additives in the electrolyte, such as Na_2WO_4, also can be used to raise the oxygen evolution potential (Shangguan et al., 2013). The second issue is associated with the increased amount of oxidation in the MH alloy at higher temperature (Balogun et al., 2013; Khaldi et al., 2013; Yao et al., 2014; Karwowska et al., 2014). A related issue is the oxidation of the MH alloy by KOH electrolyte due to its strong oxidizability, especially at high temperature. The oxidation of MH alloy causes either corrosion to form soluble complex ions (in the case of AB_2, for example) or passivation to form thick surface oxides, which prevent further electrochemical reactions (in the case of AB_5, for example). For the MH alloy chosen as the negative electrode, the surface has to be kept "fresh" without sacrificing too much of the active material. For example, phases containing high percentages of Ni and Cr can be used to protect AB_2 MH alloy from heavily corroding at high temperature; oxides of other rare earth elements (Y_2O_3, Er_2O_3, or Yb_2O_3) were added to retard the formation of La_2O_3 on the AB_5 surface. The addition of a B2 secondary phase close to $AlMnNi_2$ with a higher solubility in KOH (Young et al., 2014c) may be beneficial to keep the surface active during the high-temperature storage.

11.4.6 Strategies to reduce the raw material cost of MH alloy used in the Ni-MH battery

To achieve a good balance between various electrochemical properties, a conventional AB_5 alloy usually contains about 11, 1, and 3 wt.% of expensive Co ($30 per kg), Pr ($132 per kg), and Nd ($66 per kg), respectively. The costs of these three elements share 25% of the overall cost. Therefore, in order to make the Ni-MH battery cost-effective versus its Li-ion rivals, two approaches were taken to reduce the raw material cost: elimination of Pr and Nd in the A-sites and reduction/elimination of Co in the B-sites. Both approaches sacrifice cycle life and a small amount of capacity (Moussa et al., 2013; Young et al., 2014c,d) to achieve a lower cost target. Replacement of Co with Fe and/or Cu decreases the c/a lattice ratio in the unit cell while increasing the pressure-concentration-temperature (PCT) hysteresis, which consequently increases the pulverization rate of MH alloy during cycling. Remedies such as Zr and Si additions and hyperstoichiometry (B/A > 5) were proposed to extend the cycle life of these Cu- or Fe-substituted AB_5 MH alloys (Young et al., 2014c).

11.5   Current market forces and future trends of the Ni-MH battery

There are currently three major markets for Ni-MH batteries: consumer electronics, HEV, and stationary energy storage units. Among these, the growth in HEV and stationary applications are very strong compared to the almost saturated consumer electronics market. The current market status and future trends for each application will be discussed in the following sections.

11.5.1   Consumer applications

The rechargeable Ni-MH battery was originally created to replace the toxic Ni-Cd battery. The first application of the Ni-MH battery was in portable electronic devices. Although Ni-MH and Li-ion were invented at about the same time, Ni-MH dominated portable consumer applications (cell phones, for example) due to it being free of safety concerns compared to the Li-ion battery in the earlier days before the safeguard separator was invented and used in the Li-ion battery. After the safety issues in the Li-ion battery were solved, it soon took over the market due to its higher energy density (240 in Li-ion vs. 100 Wh kg^{-1} in Ni-MH). The remaining consumer market for the Ni-MH battery includes retailers (mainly AAA and AA batteries), cordless phones, smart vacuum cleaners (e.g., iRobot), power tools, shavers, and toothbrushes. There are two main reasons the Ni-MH battery is still alive: voltage compatibility to dry cell (the primary nonrechargeable alkaline battery) and unbeaten safety, especially in high-power applications. The cost of the Ni-MH battery is close to that of the Li-ion battery with 10% variation in energy. The price fluctuation of the Ni-MH battery is mainly due to the price volatility and uncertainty of rare earth metals (the key components in the AB$_5$ MH alloys used in the negative electrode), which makes the battle against the Li-ion battery in the consumer market more difficult. Except for the 10% yearly increase in smart vacuum cleaner sales with a 14 million unit sales volume in 2013, there is no substantial growth for the Ni-MH battery in other consumer markets.

11.5.2   Automotive propulsion applications

The current battery market for HEV propulsion is dominated by the Ni-MH battery. More than 6 million HEV cars on the road today are powered by the Ni-MH battery due to its excellence in abuse tolerance, high charge and discharge rates, and freedom from the expensive battery management system and liquid-cooled thermal management system. Toyota is the leading car company in the HEV market using Ni-MH batteries made by its wholly owned subsidiary, Primearth EV Energy (PEVE, formerly, Panasonic EV Energy). The market share of HEV battery sales by Toyota was over US$2 billion in 2012 and increases at a yearly rate higher than 10%. The increase is expected to be even higher in the use of the Ni-MH battery for HEV applications especially when the joint venture between Toyota and Corun starts to manufacture Ni-MH batteries for HEV in China this year. In addition to HEV, the Ni-MH battery is also used in a 12 V energy

recovery system (10 D-cells) installed in Nissan and Mitsubishi's passenger vans. The application of the Ni-MH battery in a commercial battery-powered electrical vehicle (BEV) was first demonstrated in EV-1 made by General Motors with a drive range of 180 miles per charge in 1999. After that, the car companies switched their attention to the lighter Li-ion battery for BEV applications. However, Li-ion-powered BEV still has a long way to go in overcoming economic and engineering obstacles. Recently, BASF was granted with a US$4 million funding to develop a low-cost, long-range, and safe Ni-MH battery for BEV under an ARPA-E research contract. It is expected that a more practical Ni-MH battery with an extended driving range and a more affordable price can be developed for BEV applications by the end of 2016.

11.5.3 Stationary applications

The stationary battery market is a relatively new battery industry with many competing technologies, such as Li-ion, flow-battery, and molten-salt battery wrestling in this field. The Ni-MH battery with its long cycle and calendar life at a wide temperature range and superior abuse tolerance is the technology of choice. With a current cost of about $500/kWh, 20% of the stationary market can accept the Ni-MH battery but with heavy competition from the Li-ion battery. There are just a few categories for the stationary applications of energy storage: UPS (uninterrupted power supply), energy storage for alternative energy generation (solar and wind farms), and buffer between alternative energy and the electrical grid. The UPS can be further classified into device-oriented UPS: UPS for personal computers (0.5–1 kWh), UPS for household units (2–10 kWh), UPS for telecommunications (20–100 kWh), and UPS for buildings (1–10 MWh). Each application has its own special requirements. For example, in 2012 Telcordia published a list of generic requirements for Ni-MH battery systems for telecommunications applications (Telcordia, 2012). In this list, the requirement for a deep-discharge cycle life is not as stringent as other stationary applications, such as daily energy storage for a solar farm. So far, only FDK Corporation in Japan is mass-producing large quantities of Ni-MH cylindrical batteries for stationary application (24 kWh systems, for example), and Kawasaki Heavy Industries in Japan is producing a bipolar prismatic Ni-MH battery up to 205 (Takasaki et al., 2013) and 1500 Ah per cell (Nishimura et al., 2013). The entire stationary battery market is about 50 GW, into which the penetration of the Ni-MH battery heavily depends on the cost of the battery system.

11.6 Sources of further information

Reddy, T., Linden's Handbook of Batteries, fourth ed. McGraw-Hill Professional, NY, ISBN 007162421X.

Schlapbach, L., Hydrogen in Intermetallic Compounds I: Electronic, Thermodynamic, and Crystallographic Properties, Preparation. Springer-Verlag, Berlin, ISBN 3540183337.

Schlapbach, L., Hydrogen in Intermetallic Compounds II: Surface and Dynamic Properties, Applications. Springer-Verlag, Berlin, ISBN 3540546685.

Wipf, H., Hydrogen in Metals III. Springer-Verlag, Berlin, ISBN 354061639X.

References

Balogun, M., Wang, Z., Zhang, H., Yao, Q., Deng, J., Zhou, H., 2013. Effect of high and low temperature on the electrochemical performance of $LaNi_{4.4-x}Co_{0.3}Mn_{0.3}Al_x$ hydrogen storage alloys. J. Alloys Compd. 579, 438–443.

Burlakova, M.A., Baranov, V.G., Chernov, I.I., Kalin, B.A., Svetlov, A.V., 2011. Amorphous and crystalline alloys for reversible hydrogen storage. Inorg. Mater. Appl. Res. 2, 452–456.

Deng, G., Chen, Y., Tao, M., Wu, C., Shen, X., Yang, H., Liu, M., 2010. Electrochemical properties and hydrogen storage mechanism of perovskite-type oxide $LaFeO_3$ as a negative electrode for Ni-MH batteries. Electrochim. Acta 55, 1120–1124.

Fetcenko, M.A., Ovshinsky, S.R., Reichman, B., Young, K., Fierro, C., Koch, J., Zallen, A., Mays, W., Ouchi, T., 2007. Recent advanced in NiMH battery technology. J. Power Sources 165, 544–551.

Fierro, C., Zallen, A., Koch, J., Fetcenko, M.A., 2006. The influence of nickel-hydroxide composition and microstructure on the high-temperature performance of nickel metal hydride batteries. J. Electrochem. Soc. 153, A492–A496.

Karwowska, M., Jaron, T., Fijalkowski, K.J., Leszczynski, P.J., Rogulski, Z., Czerwinski, A., 2014. Influence of electrolyte composition and temperature on behavior of AB_5 hydrogen storage alloy used as negative electrode in Ni-MH batteries. J. Power Sources 263, 304–309.

Khaldi, C., Boussami, S., Tliha, M., Azizi, A., Fenineche, N., El-Kedim, O., Mathlouthi, H., 2013. The effect of the temperature on the electrochemical properties of the hydrogen storage alloy for nickel-metal hydride accumulators. J. Alloys Compd. 574, 59–66.

Kong, L., Chen, B., Young, K., Koch, J., Chan, A., Li, W., 2012. Effects of Al- and Mn-contents in the negative MH alloy on the self-discharge and long-term storage properties of Ni/MH battery. J. Power Sources 213, 128–139.

Lim, D., Im, H., Singh, B., Park, C., Song, S., 2013a. Electrochemical hydrogen charge and discharge properties of $La_{0.1}Sr_{0.9}Co_{1-y}Fe_yO_{3-\delta}$ (y = 0, 0.2, 1) electrodes in alkaline electrolyte solution. Electrochim. Acta 102, 393–399.

Lim, D., Singh, B., Kang, J., Kim, J., Song, S., 2013b. Study of electrochemical hydrogen charge/discharge properties of $FePO_4$ for application as negative electrodes in hydrogen batteries. Ceram. Int. 39, 6559–6568.

Moussa, M.B., Abdellaoui, M., Lamloumi, L., Percheron Guégan, A., 2013. Investigation on the structure, thermodynamic and electrochemical properties of the $MmNi_{3.55}Mn_{0.4}Al_{0.3}Fe_{0.75}$ compound used as negative electrode in Ni-MH batteries. J. Alloys Compd. 575, 414–418.

Nishimura, K., Takasaki, T., Sakai, T., 2013. Introduction of large-sized nickel-metal hydride battery GIGACELL for industrial applications. J. Alloys Compd. 580, S353–S358.

Ovshinsky, S., Fetcenko, M.A., 1996. Electrochemical hydrogen storage alloys and batteries fabricated from Mg containing base alloys, US Patent 5,506,069.

Ovshinsky, S., Fetcenko, M.A., Reichman, B., Young, K., Chao, B., Im, J., 1997. Electrochemical hydrogen storage alloys and batteries fabricated from Mg containing base alloys, US Patent 5,616,432.

Shangguan, E., Li, J., Chang, Z., Tang, H., Li, B., Yuan, X., Wang, H., 2013. Sodium tungstate as electrolyte additive to improve high-temperature performance of nickel-metal hydride batteries. Int. J. Hydrog. Energy 38, 5133–5138.

Shi, W., Zhang, X., Che, G., 2013. Hydrothermal synthesis and electrochemical hydrogen storage performance of porous hollow NiSe nanospheres. Int. J. Hydrog. Energy 39, 7037–7045.

Takasaki, T., Nishimura, K., Saito, M., Fukunaga, H., Iwaki, T., Sakai, T., 2013. Cobalt-free nickel-metal hydride battery for industrial applications. J. Alloys Compd. 580, S378–S381.

Tanaka, T., Magari, Y., Yasuoka, S., 2009. Negative electrode for alkaline storage battery and alkaline storage battery, US Patent Application 20090061317.

Telcordia, 2012. Generic requirements for Nickel metal hydride battery systems for telecommunications use. Available online at http://telecom-info.telcordia.com.

Wang, L., Yan, H., Xiong, W., Li, B., Li, J., Kong, F., 2014. The influence of boron content on the structural and electrochemical properties of the $La_{15}Fe_{77}B_8$-type hydrogen storage alloy. J. Power Sources 259, 213–218.

Yao, Q.R., Zhou, H.Y., Wang, Z.M., Pan, S.K., Rao, G.H., 2014. Electrochemical properties of the $LaNi_{4.5}Co_{0.25}Al_{0.25}$ hydrogen storage alloy in wide temperature range. J. Alloys Compd. 606, 81–85.

Yasuoka, S., Magari, Y., Murata, T., Tanaka, T., Ishida, J., Nakamura, H., Nohma, T., Kihara, M., Baba, Y., Teraoka, H., 2006. Development of high-capacity nickel-metal hydride batteries using superlattice hydrogen-absorbing alloys. J. Power Sources 156, 662–666.

Young, K., 2012. Stoichiometry in inter-metallic compounds for hydrogen storage applications. In: Innocenti, A., Kamarulzaman, N. (Eds.), Stoichiometry and Materials Science—When Numbers Matter. InTeck, Croatia. ISBN 978-953-51-0512-1.

Young, K., 2013. Metal hydrides. In: Reedijk, J. (Ed.), Elsevier Reference Module in Chemistry, Molecular Sciences and Chemical Engineering. Elsevier, Waltham, MA. http://dx.doi.org/10.1016/B978-0-12-409547-2.05894-7.

Young, K., Nei, J., 2013. The current status of hydrogen storage alloy development for electrochemical applications. Materials 6, 4574–4608.

Young, K., Ouchi, T., Fetcenko, M.A., 2009. Pressure-composition-temperature hysteresis in C14 Laves phase alloys: part 1. Simple ternary alloys. J. Alloys Compd. 480, 428–433.

Young, K., Koch, J., Banik, A., Fetcenko, M.A., 2010. Study of AB_2 alloy electrodes for Ni-MH battery prepared by centrifugal casting and gas atomization. J. Alloys Compd. 496, 669–677.

Young, K., Ouchi, T., Banik, A., Koch, J., Fetcenko, M.A., Bendersky, L.A., Wang, K., Vaudin, M., 2011. Gas atomization of Cu-modified AB_5 metal hydride alloys. J. Alloys Compd. 509, 4896–4904.

Young, K., Wu, A., Qiu, Z., Tan, J., Mays, W., 2012. Effects of H_2O_2 addition to the cell balance and self-discharge of Ni/MH batteries with AB_5 and A_2B_7 alloys. Int. J. Hydrog. Energy 37, 9882–9891.

Young, K., Ouchi, T., Huang, B., Reichman, B., Blankenship, R., 2013a. Improvement in −40°C electrochemical properties of AB_2 metal hydride alloy by silicon incorporation. J. Alloys Compd. 575, 65–72.

Young, K., Reichman, B., Fetcenko, M.A., 2013b. Electrochemical performance of AB_2 metal hydride alloys measured at −40°C. J. Alloys Compd. 580, S349–S352.

Young, K., Nei, J., Wong, D.F., Wang, L., 2014a. Structural, hydrogen storage, and electrochemical properties of Laves phase-related body-centered-cubic solid solution metal hydride alloys. Int. J. Hydrog. Energy 39, 21489–21499. http://dx.doi.org/10.1016/j.ijhydene.2014.01.134.

Young, K., Wong, D.F., Yasuoka, S., Ishida, J., Nei, J., Koch, J., 2014b. Different failure modes for V-containing and V-free AB_2 metal hydride alloys. J. Power Sources 251, 170–177.

Young, K., Chao, B., Huang, B., Nei, J., 2014c. Studies on the hydrogen storage characteristics of $La_{1-x}Ce_x(NiCoMnAlCuSiZr)_{5.7}$ with a B2 secondary phase. J. Alloys Compd. 585, 760–770.

Young, K., Chao, B., Huang, B., Nei, J., 2014d. Effects of Cu-substitution on $La_{0.62}Ce_{0.38}(Ni-CiMnAlSiZr)_{5.3}$ metal hydride alloy. J. Alloys Compd. 588, 235–241.

Zhou, X., Young, K., West, J., Regalado, J., Cherisol, K., 2013. Degradation mechanisms of high-energy bipolar nickel metal hydride battery with AB_5 and A_2B_7 alloys. J. Alloys Compd. 580, S373–S377.

Index

Note: Page numbers followed by *f* indicate figures and *t* indicate tables.

As part of a four volume series, *Compendium of Hydrogen Energy, Volume 3: Hydrogen Energy Conversion* focuses on the methods of converting hydrogen into useful energy. The other three volumes focus on hydrogen production and purification; hydrogen storage and transmission; and hydrogen use, safety, and economy, respectively. Many experts believe that, in time, the hydrogen economy will replace the fossil fuel economy as the primary source of energy. Once hydrogen has been produced and stored, it can then be converted via fuel cells or heat engines into useful energy. This volume highlights how different fuel cells, hydrogen-fuelled combustion engines, and turbines work.

The first part of the volume investigates various types of hydrogen fuel cells, including solid oxide, molten carbonate, and proton exchange membrane. The second part looks at hydrogen combustion energy and explores the use of metal hydrides in hydrogen energy conversion.

Compendium of Hydrogen Energy, Volume 3: Hydrogen Energy Conversion is a key reference text for R&D managers in the industry, who are interested in the development of hydrogen conversion technologies. The volume is also a valuable resource for academic researchers and postgraduate students working in the wider field of the hydrogen economy.

Professor Frano Barbir is Chair of Thermodynamics for the Faculty of electrical engineёring, mechanical engineering, and naval architecture at the University of Split, Croatia. Professor Angelo Basile is a senior researcher at the Institute of Membrane Technology (ITM) for the Italian National Research Council (CNR) in Italy. Dr T. Nejat Veziroglu is President of the International Association for Hydrogen Energy (IAHE) in the United States, and has been nominated for a Nobel Prize in Economics.